Hamburger Wasserbau-Schriften

Band 14

Herausgegeben von

Prof. Dr.-Ing. Erik Pasche†

Institute of River and Coastal Engineering, Hamburg University of Technology

2011

Abstract

Bank Erosion in Alluvial Rivers With Non-Cohesive Soil In Unsteady Flow

So far the theory of bank failure in non-cohesive soils is limited to the avalanche of loose, not compacted, fully saturated discrete grains, applicable mainly to gravel banks. However, the present field investigation indicated that undercutting of the riverbank, slip failure of the submerged zone of the bank, as well as cantilever failure of the overhang are the dominant processes in non-cohesive dense (sandy) soils under unsteady flow conditions. These processes have been modelled in the present work by an innovative method, which has been validated by field measurements. The results showed that the method enhanced the simulation accuracy up to six times in comparison to the earlier methods.

Böschungserosionsvorgänge im alluvialen Gewässer mit nicht kohäsiven Boden bei Instationären Strömungen

Bislang ist die Theorie der Böschungsbruchvorgänge für kohäsionslosen Boden auf ebenen Gleitfugen in einem rollenden, nicht verdichteten und voll gesättigten Boden mit diskreten Körnern begrenzt und damit vor allem für Kiesboden anwendbar. Die vorliegende Felduntersuchung hat aber gezeigt, dass Unterspülung und Gleitfugen unterhalb des Wasserspiegels sowie Abbruch der Überhänge die dominanten Prozesse im kohäsionslosen verdichteten (sandigen) Boden unter instationären Bedingungen sind. Diese Prozesse wurden in der vorliegenden Arbeit durch eine innovative Methode modelliert, die durch Feldmessungen validiert wurde. Die Ergebnisse zeigten, dass diese Methode die Genauigkeit der Simulation im Vergleich zu den bisherigen Methoden bis zu sechsmal verbessert.

Cover Design: Kerstin Schürmann, www.formlabor.de

Editorial office:Katrin Coelius

Print: Planet Study GmbH

ISBN 978-937693-14-9 1. Edition, Institut of River and Coastal Engineering, TUHH, Hamburg

ISSN 1612-8699

Vorwort

Liebe Leserin
Lieber Leser
der Wasserbau-Schrift 14,

Am 1. Dezember vor einem Jahr ist Professor Erik Pasche, der Leiter und Gründer des Instituts verstorben. Sein Wirken, seine Tatkraft und seine fachliche Kompetenz fehlen sehr. Sie sind aber auch Ansporn für die Mitarbeiter, die Arbeiten und Projekte mit Engagement und Tatkraft weiterzuführen.

Die in dieser Schrift 14 behandelte Thematik der Böschungserosion in alluvialen Gewässern in instationärer Strömung wurde von Professor Pasche angeregt und bis zur fachlichen Fertigstellung betreut.

Zur Einschätzung der Komplexität der Sedimentbewegung möge die folgende Anekdote einen Hinweis geben:
Als Albert Einstein erfuhr, dass sein Sohn Hans-Albert Einstein über die Sedimentbewegung forschen wollte, hat er ihm empfohlen sich lieber mit der Relativitätstheorie zu beschäftigen, da käme er eher zu Ergebnissen[1].

In der Tat ist alles, was mit Sedimentbewegung und gar Quantifizierung von Sedimentations- und Erosionsvorgängen zu tun hat, sehr komplex und es bedarf einiger Erfahrung, gründlicher Wertung und kritischer Prüfung um Vorgänge in der Natur charakteristisch wiederzugeben und zu modellieren.

Mit dem Thema

Bank Erosion in Alluvial Rivers With Non-Cohesive Soil In Unsteady Flow
Böschungserosion in alluvialen Gewässern mit nicht kohäsiven Böden bei instationären Strömungen

kommt noch eine erdstatische Komponente hinzu, sicherlich eine Erhöhung der Komplexität.

Bei Berechnungsansätzen ist grundsätzlich zu unterscheiden, ob das Material kohäsiv oder nicht kohäsiv ist. Für kohäsive Materialien wurden in den letzten 10 Jahren entscheidende Fortschritte erzielt.

Die nichtkohäsiven Materialien wurden lange Zeit als weniger problematisch angesehen und mit einfachsten Ansätzen behandelt. Die Anschauung zeigt aber, dass dies für die meisten Situationen in der Praxis nicht ausreicht. Der Boden ist zum einen verdichtet und „verklebt“ (cementation) und es tritt negativer Porendruck auf. Zum anderen liegt in der Natur an der Geländeoberfläche ein starker Einfluss durch pflanzliche Durchsetzung vor, der die

[1] Der Titel der Doktorarbeit von Hans Albert Einstein ist "Bed Load Transport as a Probability Problem"

Erosionsvorgänge und –formen signifikant verändert. Es entstehen komplexe Bruchflächen und -formen. Dies alles trifft auf ein sehr komplexes Strömungssystem, besonders in Flusskrümmungen.

An dieser Stelle setzt die Arbeit von Herrn Nasermoaddeli an. Aus der Anschauung der örtlichen Verhältnisse wurde sehr deutlich, dass die einfachen Ansätze in keiner Weise das tatsächliche Geschehen nachbilden können.

Auf der Grundlage von intensiven Messungen der Ufer- und Sohländerungen, der Bodenverhältnisse und der Strömungen in der Natur, und unter Heranziehung bekannter Gleichungen der Sedimentbewegung und der Strömungsmechanik, entwickelte er einen analytischen Ansatz der Ufererosionsvorgänge in instationären Strömungen als Grundlage für die numerische Modellierung. Eingangsparameter sind Sedimentgehalt, Strömungsgeschwindigkeit, Bodeneigenschaften, Böschungsneigung, Porendruck, Grundwasserstand, Verfestigung durch Wurzeln und Wasserstand im Gewässer.

Die Veränderungen werden in vier aufeinander aufbauenden numerischen Modellen berechnet.

Die Arbeit von Herrn Nasermoaddeli liefert eine hervorragende Lösung der Problematik der Ufererosionsvorgänge, deren Nutzung durch die Implementierung als weiteres numerisches Modell für das freie Programmsystem KALYPSO erleichtert wird.

Karl-Friedrich Daemrich

Kommissarischer Leiter des Instituts für Wasserbau

Bank Erosion in Alluvial Rivers With Non-Cohesive Soil in Unsteady Flow

Vom Promotionsausschuss der
Technischen Universität Hamburg-Harburg

zur Erlangung des akademischen Grades
Doktor Ingenieur

genehmigte Dissertation

von
Mohammad Hassan Nasermoaddeli

aus Shiraz

2011

1. Gutachter: Prof. Dr.-Ing. Jürgen Grabe
2. Gutachter: Prof. Ana Maria A.F. da Silva

Tag der mündlichen Prüfung: 11.11.2011

Acknowledgement

This dissertation would not have been possible without the support, guidance and encouragement of a few special people who contributed their valuable assistance in the preparation and completion of this work.

My first, and most earnest, acknowledgment must go to my adviser Prof. Erik Pasche† for his scientific contribution throughout the work. I wish to express my appreciation to all his contribution of time, ideas and funding to make my Ph.D. work productive and stimulating. Throughout my dissertation-writing period, he provided encouragement, sound advice, and lots of good ideas. Unfortunately, he could not accompany the final stage of reviewing my dissertation. I was inspired by his joy and enthusiasm for research, invincible spirit and his pioneer ideas. One simply could have not wished for a friendlier supervisor. I hope that the current dissertation is in his sense.

I owe my most sincere gratitude to Prof. Ana Maria A.F. da Silva for her scientific contribution and sound advices to improve my dissertation, and for encouraging me after the unexpected demise of Prof. Pasche. I warmly thank her for reviewing my dissertaion as the second examiner. I would like also to acknowledge her for providing me the opportunity to have a short scientific stay in her Hydraulic Laboratory in Queen's University, Kingston, Canada in 2008.

I would like to show my gratitude to Prof. Grabe, who made his support available for reviewing my dissertation as the first examiner after Prof. Pasche and for his valuable recommendations for improving the final dissertation.

My warm thanks are due to Prof. Schlüter as chair of my examination committee and additional reviewer of my dissertation.

I am heartily thankful to Dr.-Ing. Karl-Friedrich Daemrich, the provisional Head of the Institute of River and Coastal Engineering, for his valuable comments on editorial improvement of my dissertaion and providing me an open and friendly working atmosphere after Prof. Pasche.

I am indebted to many of my colleagues for supporting me during my Ph.D. work. I am grateful to Josef Hoika for novel designing and building the traverse system and other mechanical apparatuses, as well as assisting me during the measurements. My thanks go to Jens Winkelbauer who developed innovative techniques making discharge and bank failure monitoring possible. I would also like to warmly thank Katrin Coelius for assisting me in

bathymetry measurements and scanning the bank surface using laser scanner. I am grateful to Anneliese Fey for assisting me in keeping my computer running, when it did not want. At this point I would like to acknowledge other colleagues, whose fruitful discussions and brainstorming brought me of new ideas.

My warm thanks go to Prof. Giselher Gust for providing me the opportunity to apply microcosm instrument and Dr. Volker Müller, who made the measurement, analysis and post-processing of the results.

The German Federal Ministry of Education and Research (BMBF-IPSWaT) is highly acknowledged for awarding me a three-year doctoral scholarship under the grant number IPS05/6P2.

Finally, I am forever indebted to my wife, Sharareh, for her understanding, encouragement, companionship, endless patience and giving love during whole these years. She receives all my everlasting love for being everything that I am not. I owe my lovely thanks to my daughter, Nazanin, and my son Shayan, for the time I could not share with them during this research work.

Mohammad Hassan Nasermoaddeli
Hamburg 15.12.2011

Index

List of figures

List of tables

List of symbols

A	shear surface area [m^2]
A_b	unit volume of locally derived bank debris deposition at the bank-toe [m^3/m]
A_f	unit volume of bank failed material deposited in an upstream cross section [m^3/m]
$A_{T,\ failed}$	total failed area in conjugate domain [m^2]
a_n	n^{th} coefficient of a polynomial of order n [-]
A_r	area of shear surface occupied by the roots [m^2]
A_s	total unit volume of bank-derived sediment stored at the bank-toe [m^3/m]
a_x	average spacing between vegetation elements in x-directions [m]
a_y	average spacing between vegetation elements in y-directions [m]
C'	effective cohesion [Pa]
C'_i	effective cohesion of the i^{th} layer [Pa]
c	depth-averaged sediment concentration [kg/ m^3]
C_a	apparent cohesion [Pa]
c_b	non-equilibrium near-bed suspended sediment concentration [m^3/ m^3]
c_{b*}	equilibrium near-bed suspended sediment concentration [m^3/ m^3]
C_d	damping factor of sediment deposition [-]
C_e	damping factor of sediment entrainment (erosion) [-]
c_{eq}	equilibrium total sediment concentration or potential transport capacity [m^3/ m^3]
c_f	friction factor [-]
c_r	additional cohesion due to the root reinforcement [Pa]
C_s	empirical factor in Smagorinsky turbulent model [-]
c_s	total concentration of sediment in source term flow [m^3/ m^3]
c_{wr}	form drag factor of the vegetation elements [-]
D	deposition rate [m/s]
d	horizontal distance of a node to a reference point in conjugate domain [m]
d_{50}	median diameter of sediment particles size [m]
d_{90}	representative sediment diameter at 90% of cumulative distribution [m]

d_p	average diameter of the vegetation elements [-]
E	entrainment rate [m/s]
e^*	dimensionless diffusivity coefficient [-]
F	driving forces per unit width [N/m]
f	form drag coefficient [-]
f_m	minimum required measurement frequency
F_c	Coriolis force per unit volume [N/m^3]
F_r	resisting forces per unit width [N/m]
f(x)	polynomial function [-]
g	gravity acceleration [m^2/s]
g_j	mapping from FE-domain to the conjugate domain [-]
h	flow depth [m]
h_b	water depth at bank-toe [m]
H_p	total pressure head [m of water]
h_p	matric head [m of water]
I_e	energy gradient [-]
k	turbulent kinetic energy [m^2/s]
k_s	equivalent sand roughness [m]
k_y	hydraulic conductivity in horizontal (y) direction [m/day]
k_z	hydraulic conductivity in vertical (z) direction [m/day]
L	length of the failure plane [m]
l	Prandtl mixing length [m]
L_e	non-equilibrium adaptation length [m]
$L_{eff.}$	length of the shear plane passing through vegetation zone [m]
L_i	length of the failure plane within the i^{th} layer [m]
L_s	length of deposited bank material [m]
M(x)	cumulative distribution function of mass [-]
m	empirical parameter [-]
N	component of weight force per unit width normal to the bank surface [N/m]
n	empirical parameter [-]
N	sample size of data [-]
P	confining water pressure force in the river per unit width [N/m]
Q	boundary unit flux [m^2/ m day]
q	non-equilibrium bed load transport rate [m^3/ms]
q_{br}	frictional (fluvial) erosion rate [m^3/ms]
q_{eq}	equilibrium bed load transport rate [m^3/ms]
q_l	longitudinal total sediment transport rate [m^3/ms]
q_r	radial total sediment transport rate [m^3/ms]
q_s	source term discharge [m^3/m^2s]

q^s_x	suspended sediment transport rate in x-direction [m^3/ms]
q^s_y	suspended sediment transport rate in y-direction [m^3/ms]
q_x	specific volumetric bed load transport rate in x-direction [m^3/ms]
q_y	specific volumetric bed load transport rate in y-direction [m^3/ms]
q_x^T	total sediment transport rate in x-direction [m^3/ms]
q_y^T	total sediment transport rate in y-direction [m^3/ms]
R	hydraulic radius [m]
Re	Reynolds number [-]
S	matric suction force per unit width [N/m]
S_e	net deposition or erosion rate [m/s]
S_{bank}	rate of sediment inflow due to bank failure [m/s]
SF	safety factor in stability of riverbank [-]
S_i	fraction of the failed bank material assigned as source term to the Finite Element node i [kg/m^2s]
$S_{i,\ cantilever}$	failed mass rate received by the lower node due to the cantilever failure [kg/m^2s]
$S_{i,\ shear}$	failed mass rate received by the lower node due to the shallow shear failure [kg/m^2s]
$S_{i,\ tensile}$	failed mass rate received by the lower node due to the tensile failure [kg/m^2s]
S_r	soil shear strength [Pa]
T	total sampling time [s]
t	time [s]
T^+	dimensionless shear stress parameter [-]
T_B	mean bursting period [s]
t_c	adaptation timescale [s]
t_d	adaptation timescale for deposition [s]
t_e	adaptation timescale for entrainment [s]
T_r	tensile strength of vegetation roots [Pa]
U	hydrostatic pore water pressure force per unit width under the tension crack [KN/m]
U	depth-averaged horizontal (resultant) flow velocity [m/s]
u	depth-averaged flow velocity in x-direction [m/s]
$\tilde{u}$	instantaneous flow velocity in x-direction [m/s]
$\hat{u}$	deviation of the depth-averaged flow velocity from its vertical profile in x-direction [m/s]
$\overline{u}$	time-averaged flow velocity in x-direction [m/s]
u´	velocity fluctuation in x-direction [m/s]
u_*	shear (friction) velocity [m/s]
u_{*bed}	shear (friction) velocity at bed [m/s]
u_a	pore air pressure [Pa]

U_i	hydrostatic pressure on the failure surface per unit width [N/m]
u_i	flow velocity in *i*-direction [m/s]
u_j	flow velocity in *j*-direction [m/s]
U_{max}	maximum flow velocity [m/s]
u_s	velocity of source term in momentum equation in x-direction [m/s]
u_w	pore water pressure [Pa]
V	hydrostatic pore water pressure force per unit width in the tension crack [N/m]
v	depth-averaged flow velocity in y-direction [m/s]
$\tilde{v}$	instantaneous flow velocity in y-direction [m/s]
$\hat{v}$	deviations of the depth-averaged flow velocity from its vertical profile in y-direction [m/s]
$\overline{v}$	time-averaged flow velocity in y-direction [m/s]
v´	velocity fluctuation in y-direction [m/s]
v_s	velocity of source term in momentum equation in y-direction [m/s]
V(t)	instantaneous velocity magnitude [m/s]
V_x	measured velocity in x-direction [m/s]
V_y	measured velocity in y-direction [m/s]
V_x'	rotated measured velocity in x-direction [m/s]
V_y'	rotated measured velocity in y-direction [m/s]
W	weight of the (failing) soil block (layer) per unit width [N/m]
w	sediment fall velocity in still water [m/s]
$\tilde{w}$	instantaneous flow velocity in z-direction [m/s]
$\overline{w}$	time-averaged flow velocity in z-direction [m/s]
w´	velocity fluctuation in z-direction [m/s]
W_i	weight of the i^{th} layer of the soil block per unit width [N/m]
X	state variable vector [-]
x	Cartesian horizontal axe [m]
y	Cartesian horizontal axe [m]
z	Cartesian vertical axe [m]
z_0	bed elevation [m]
α	Parameter [-]
α_0	recovery coefficient in net sediment vertical flux [-]
α_{lat}	lateral bed slope [-]
β	slope of the bank surface [-]
Γ	mixing coefficient [m^2/s]
Γ_{disp}	longitudinal dispersion coefficient [m^2/s]
Γ_x	turbulent diffusion coefficient in x-direction [m^2/s]
Γ_y	turbulent diffusion coefficient in y-direction [m^2/s]
γ_w	unit weight of water [N/m^3]

Δ	geometrical length scale in Smagorinsky turbulent model [m]
Δ'	dune height [m]
Δd	horizontal length of the element in profile domain [m]
Δt	numerical time step [t]
ΔV_i	receiving failed volume corresponding to the node i at bank-toe [m^3]
δ	Kronecker delta [-]
δd	horizontal distance between two mutual ADCP bins
ε	empirical parameter [-]
κ	von Karman constant [-]
ϑ	soil water content [m^3/ m^3]
Θ	space comprising the nodes in conjugate domain[-]
θ	weighing parameter [-]
θ'	shear distortion from vertical [degree]
ϑ_r	residual soil-water content [m^3/ m^3]
ϑ_s	saturated soil-water content [m^3/ m^3]
θ_r	rotation angle [-]
Λ	space comprising the nodes of finite elements along the cross sectional profiles [-]
λ	soil porosity [-]
λ_d	Darcy-Weisbach friction factor due to dunes [-]
λ_f	Darcy-Weisbach friction factor [-]
λ_v	Darcy-Weisbach friction factor due to vegetation [-]
λ_T	total friction factor of Darcy-Weisbach [-]
ρ	fluid density [kg/m^3]
ρ_s	sediment density [kg/m^3]
σ	effective stress [Pa]
σ_t	Schmidt number [-]
τ_b	bed shear stress [Pa]
$\tau_{b,x}$	bed shear stress in x-direction [Pa]
$\tau_{b,y}$	bed shear stress in y-direction [Pa]
τ_{ij}	fluid shear stress tensor in jk-plane in j-direction [Pa]
τ_{xx}	depth-averaged fluid shear stress tensor in yz-plane in x-direction [Pa]
τ_{xy}	depth-averaged fluid shear stress tensor in yz-plane in y-direction [Pa]
τ_{yx}	depth-averaged fluid shear stress tensor in xz-plane in x-direction [Pa]
τ_{yy}	depth-averaged fluid shear stress tensor in xz-plane in y-direction [Pa]
τ_w	wind shear stress [Pa]
ν	kinematic viscosity [m^2/s]
ν_t	eddy viscosity [m^2/s]
Φ_i	linear approximation function of Finite Element node i [-]

φ	internal friction angle or angle of repose for loose granular particles [-]
ϕ^b	angle expressing the strength increase rate relating to the matric suction [-]
ϕ^c	critical angle of repose of dense sand, shortly “dense angle of repose” [-]
ϕ^u	critical angle of repose of unsaturated dense sand, shortly “unsaturated angle of repose” [-]
ψ	positive force produced by matric suction [KN/m]
ψ	positive pressure produced by matric suction [KN/m^2]
ψ'	slope of the deposited material [-]
Ω	space defining the river bathymetry [-]
ω	rate of bank retreat [m/s]
$\bar{\omega}$	Portion of failed material assigned as source term [-]

1 Introduction

1.1 Problem and challenges

Rivers and their margins have been the cradle of civilization since a few thousands years of known history such as Mesopotamia, the land between the Tigris and Euphrates rivers. Ancient people (for example China, Iran, Egypt, India) had learned to utilize the river water for agricultural and municipal purposes, for example, by building dams on the rivers such as Band-e-Bahman in Fars province, Iran about 1800 years ago (Javan, 1996). Such anthropogenic modifications of rivers have impacted the morphology of the rivers and consequently the aquatic and riverine life over many years.

Anthropogenic- and climate changes within catchments do have a strong impact on the flow regime of the rivers. They cause extreme events such as extreme floods as well as low flow situations to occur more often. Since the morphodynamics of rivers is directly linked to the flow regime, it can be expected that the hydrological changes will also have a strong impact on the river morphology and meander migration. Riverbank erosion associated with meander migration claims every year fertile agricultural lands in the margin of the rivers all around the world and contributes to the suspended sediment load (often contaminated with agricultural nutrients and pesticides) in the rivers. Land loss through bank erosion endangers floodplain dwellers, bridge crossings, bank protection works, buildings and other hydraulic constructions. Neglecting this process during flood events may result in underestimation in risk analysis of flooding areas. Flood prone areas are defined by the German Water Act (WHG) as the areas that may be inundated by a 100-year flood event, which is purely based on water elevation. While, the effect of lateral migration of the river channel due to the bank erosion during the flood events has not been considered in the mentioned definition.

Apart from the above-mentioned environmental impacts on river morphology, modern practices in river engineering call for deliberate morphological alteration (restoration) of rivers to their natural form and function, to promote the preservation and health of the related eco-system and utilize their natural flood retention capacity as a means to mitigate floods. The call for such practices is embedded in the EU Water Framework Directive addressing the

natural ecosystem functions of rivers and streams, and also under the EU Flood Directive, addressing flood management strategies.

Since natural streams tend to meander, stream re-naturalization often involves the return of a stream to either its natural or to an engineered meandering state. However, the process is not a simple one, as meandering streams are very dynamic entities, involving downstream migration and lateral expansion of meander bends. These processes occur simultaneously and are closely related to bed deformation, with the bed scouring in some places and material depositing at other places. Thus, returning a stream to a more natural state implies also the return to (natural) situations, characterized by substantial bed scour, downstream transport and deposition, as well as intense bank retreat accompanying the lateral and downstream migration of bends. This can endanger the structural integrity or functioning of existing major infrastructures, both in-stream and lying on the floodplain. Thus in a cultured landscape, re-naturalization needs to be carefully planned and carried out, so as to minimize its possible negative impacts.

In this context, it is essential to have reliable, physically-based numerical methods available for the prediction of medium and long-term river evolution, encompassing both the bed and bank evolution, and to be used in the planning and re-assessment processes. To meet this requirement, the physical processes involved in riverbank and bed evolution need to be well understood.

As Vanoni (1975) well pointed out, all boundaries of a river are free surfaces. Therefore, bed and bank evolutions are integrated processes in morphological changes in rivers. Mainly, interaction of these two processes along river bends results in meander migration. Neglecting the effect of bank retreat or advancement in morphological studies may result in great inaccuracy. When the bank slope looses its stability or is eroded by fluvial erosion, it retreats and the width of the river is increased. On the other hand, deposition of sediment in the form of berms at bank-toe makes the bank advance hence the width of river decreases.

Retreat of riverbank due to mass failure is often initiated by bank-toe erosion through the incision of bank-toe and increasing the height and angle of the riverbank (Fig. 1-1a). Furthermore, undercutting of the bank surface can result in failure of the bank to a certain height, allowing formation of overhang at top of the bank (Fig. 1-1b). The overhang may fail through the mechanism of cantilever failure.

a) b)

Figure 1-1 Steep bank profile due to bank erosion (a). Formation of overhang due to riverbank incision and continuous fluvial erosion of bank-toe (b)

Soil properties of the riverbank, such as cohesion, soil type (classification), homogeneity (homogeneous, composite and layered soil), porosity, moisture content and other physical and mechanical properties such as tension crack (Darby and Thorne, 1994,1997) play important roles in the stability of the riverbank. Physical and chemical properties of bank material are of great importance in the phenomena of freeze and heave, soil sapping and piping. Bank shape, angle and height are other significant parameters that influence the stability of riverbank (Thorne and Abt, 1993). The higher the bank height the less stable is the bank. Additionally, with the increase of bank slope the probability of bank failure increases. The vegetation roots may have stabilizing or de-stabilizing effect depending on the form and diameter of roots (Lawler et al., 1997b).

Recently, a significant contribution has been made to understanding and modelling of the process of riverbank erosion in cohesive soils in respect to the flow regime. In this regard, the analytical methods of slope stability have been modified and extended with special reference to riverbank stability problems in cohesive soils. The recent advancement in the field of bank erosion in cohesive soils can open new prospects in the study of riverbank erosion mechanisms and modelling in non-cohesive soils.

So far the mechanism of bank failure in non-cohesive (sandy) soils is limited to the avalanche of loose fully saturated discrete grains applicable mainly to gravel banks. But in sandy soils negative pore pressure as well as compaction of soil plays an important stabilizing role, allowing formation of steep bank slopes (Fig. 1-1a). This provides the possibility of formation of overhang in upper region of the bank following undercutting of the lower part (Fig. 1-1b). The mechanisms of undercutting and subsequent overhang failure (cantilever failure) in such soil types are even different from cohesive soils.

Another relevant process is the mechanism of distribution and transport of failed bank material. They may remain intact on the bed in the form of a block or dispersed due to the impact energy with bed and deposited there. The soil blocks are eroded mainly due to the form drag (Wood et al., 2001), while in the latter case it might be further eroded due to bed

shear stress and transported depending on local flow pattern. There is still little understanding on the mechanism of break down of the failed blocks, which depends on the physical-chemical properties of the intact blocks and underlying soil layer as well as flow regime.
In this context, it is essential to study these processes in dense non-cohesive soils systematically in more detail to enable developing analytical and mathematical models based on the physical processes.

1.2 Motivation and general objectives

The generally accepted framework to mathematical modelling of the natural evolution of the rivers consists of integrating a hydrodynamic model, a bed evolution model, and a bank evolution model. One of the most critical issues in this regard is proper modelling of the bank evolution based on well-understood physical processes and mechanisms involved. In the available riverbank erosion models for non-cohesive soils, the mechanism of bank failure is limited to the avalanche of loose granular materials, which occurs when the bank slope exceeds the angle of repose of the soils. The effect of other parameters such as compaction/ cementation, pore water pressure and vegetation is ignored in this approach.
In dense non-cohesive soils, other bank failure mechanisms such as undercutting and cantilever failure seem to prevail, which are the result of interaction of the above-mentioned parameters with bank erosion driving parameters. Riverbank erosion in such soils results in the formation of complex natural bank geometry, comprising cavity and overhang zones, which exhibits discontinuities in bank profile. The mentioned mechanisms and parameters have been yet ignored in non-cohesive bank evolution modelling.
It is an overall target of this research work to improve the understanding of riverbank retreat in dense non-cohesive soils in response to the dynamics of the flow regime (including flood frequency and duration) and to develop, on this basis, a theoretical method by which these processes can be modelled in a predictive way. The main focus will be on bank failure mechanisms due to undercutting and cantilever failure in homogeneous sandy soils. Nevertheless, continuous fluvial erosion along the wetted perimeter is addressed through studying bed shear stress distribution across a river bend especially near outer bank-toe. The present study is accomplished in a shallow meandering river (width to depth ratio greater than 10[1]) in which the effect of secondary currents on bank-toe erosion is assumed to be negligible.
A 2D formulation will form the theoretical basis for the mathematical model of the flow and sediment transport. A 3D formulation should give the best flow structure in meandering streams. However in practice, if the problem is deformation of bed and bank, which are long-term processes, affecting large spatial domains, then the utilization of a 3d model makes the calculation extremely computer intensive and very expensive.

[1] Channels with width to depth ratio greater than 5 (Chang, 1988,page 213) or 10 (Yalin,1992,page 2) can be considered wide and consequently shallow.

Dispersion terms in 2D depth–averaged momentum equations, emerging because of the depth-integration of advection terms in the three dimensional momentum equations, are assumed not to have significant impact on the bank retreat process in the shallow rivers under study.

The above-mentioned model is a contribution to improve the tools for assessment of flood risk and hazard as well as planning river rehabilitation and other river engineering practices.

To accomplish the above-mentioned objectives, the present research work has been founded on four equally important pillars: (1) Experimental Study, (2) Analysis and development of theory, (3) Numerical implementation, and (4) Validation.

As process understanding is crucial, but far from being complete, in pillar (1) an experimental study has been carried out in the field (and partly in the hydraulics laboratory of Queen's University, Kingston, Canada). This study has been contributed to extend the present state-of-the-art in knowledge on bank erosion and failure processes in non-cohesive soils. In pillar (2) a theoretical concept has been developed and by analysis of the experimental data new analytical methods have been derived and their empirical parameters determined. In pillar (3) the new analytical knowledge has been implemented into an existing mathematical model, namely the Open Source software product Kalypso (Lippert et al., 2009). In pillar (4) the model has been verified on the basis of experimental data resulting from the present field studies.

2 Problem analysis

2.1 Riverbank erosion process

Evolution of the riverbank in non-cohesive soils can be considered to involve three main processes, namely, bank-toe erosion, riverbank erosion as well as distribution of failed bank materials.

The first process is a consequence of fluvial erosion at the bank-toe. The second process, riverbank erosion, is well known to occur in form of continuous erosion as well as sudden bank failure (Thorne, 1982; Lawler et al., 1997a; ASCE Task Committee, 1998; etc.). Continuous erosion of the bank is due to the fluvial erosion (particle by particle) resulting from mass imbalance between bed load transport rate q_{sb} and suspended load transport rate q_{ss} at the bank-toe (basal zone) and bank surface (Fig. 2-1). Therefore, the process of fluvial erosion is closely connected to the sediment transport process as well as bed and bank shear stress distribution along the wetted perimeter. Bank retreat due to pure continuous erosion of the bank surface is negligible compared to the sudden bank failure in dense non-cohesive soils as well as cohesive soils. However, it is not negligible in loose non-cohesive (coarse grain) soils as shown by Millar and Quick (1993) as well as Kovacs and Parker (1994) among the others. In the third process, the failed bank materials are partly deposited at bank-toe and partly transported by the flow, depending on the flow field and local sediment transport capacity. A bank failure event supplying sediment to the basal zone tends to increase the bank stability (by decreasing bank slope) unless fluvial conditions result in generation of bed shear stress beyond the critical shear stress for removal of this material (Thorne, 1982).

2.1.1 Process of bank-toe erosion

The effect of bank-toe erosion in riverbank failure is well known (Thorne, 1982, Darby and Thorne, 1996,a, b; ASCE Task Committee, 1998; Simon et al.2000; Wood et al., 2001; Rinaldi, et al., 2004; etc.). Bank-toe (basal area) erosion is linked to the bank failure through the concept of basal endpoint control (Carson and Kirkby, 1972; Thorne, 1982; Thorne, 1991). According to this concept, bank-toe erosion occurs if the rate of removal of sediment

from bank-toe exceeds the rate of materials supplied from bank erosion process, sediment feeding from upstream as well as across the channel. In this case fluvial erosion of the basal area of the bank causes both the bank height and the slope of the bank to increase to the extent that eventually riverbank mass failure occurs (Fig. 2-1). Bank-toe aggradation and berm formation occurs when the sediment feeding to this zone exceeds the removal rate of the sediment at the bank-toe and it contributes to the stabilization of the riverbank (Thorne, 1982).

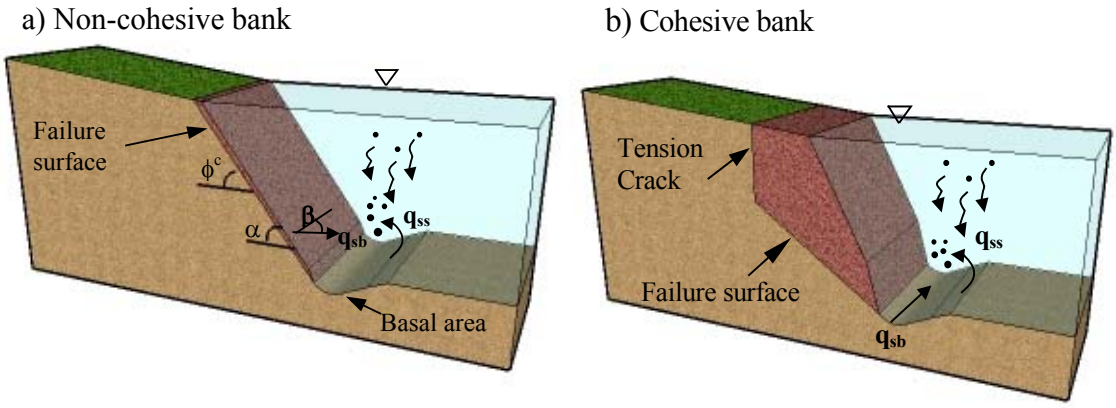

Figure 2-1 Continuous and abrupt bank retreat processes. The dark area on the bank surface depicts an avalanche (or shear shallow failure in (a) and a planar failure in (b)

Bank-toe erosion in non-cohesive soils begins by detachment and entrainment of individual particles, when fluid forces (lift and drag) exceed resisting forces (friction and inter-locking due to compaction). For calculating erosion of non-cohesive sediments, the fluid forces can be represented by boundary shear stress, because the latter scales on the same parameters of the flow intensity as do the lift and drag forces (Vanoni, 1975; Wieberg and Smith, 1987). However, bed level change due to bank-toe erosion is the result of sediment imbalance at the basal area and does not necessarily occur when the bed shear stress exceeds a critical shear stress for initiation of motion.

The imbalance in sediment transport along the basal area can be due to the non-uniformity of the channel geometry, curvature of the river or limited sediment supply to the river, for example, due to the dynamics of the flow regime. The shape of the channel geometry influences isovels, secondary flow and bed shear stress distribution across straight channels (Rhodes and Knight, 1994; Knight et al., 1994). In a river bend, the well-known secondary currents of Prandtl's first kind (Nezu and Nakagawa, 1993) generate circulation cells in the plane of cross section with outward flow near the free surface and inward near the bottom. They generate a net outward momentum transport thus increasing velocity and shear stress towards the outer bank (de Vriend, 1981; Johanneson and Parker, 1989). The maximum depth-averaged flow velocity occurs near the inner bank at the bend apex in a sine-generated rectangular channel with mild deflection angle (30°) (da Silva et al., 2006), while it occurs closest to the outer bank substantially downstream of the bend apex or even near cross over

section in a sine-generated trapezoidal channel with a large deflection angle (70°), (Wilke, 2008). Yalin (1992) states that in meanders with mild (small) deflection angles (smaller than 30°,da Silva et al., 2006), the maximum depth-averaged flow velocity is close to the inner bank around bend apex, while it is shifted towards the outer bank downstream of the apex in meanders with large deflection angles (Yalin, 1992). Kühner (2003) showed that the maximum bed shear stress occurs near the bend apex and slightly downstream of it in the first and second meander bend in a trapezoidal laboratory channel with deflection angle of 60°, for rigid as well as loose bed. In the first bend, the location of maximum bed erosion coincided with that of maximum bed shear stress, whereas in the second bend it deviated from maximum bed shear stress at the bend apex due to upstream propagation of the pool zone (talweg) formed downstream of the bend apex.

While the mentioned studies are limited to laboratory channels, field measurements in shallow rivers (such as the one under present study) are needed to investigate if secondary currents play a role in shifting the locations of maximum depth-averaged velocity and bed shear stress as well as the location of maximum bed erosion. Furthermore, the role of aggradation of bank-toe (berm formation) on bed evolution and flow re-distribution across the river sections is not clear, especially in shallow river bends and along outer bank. Measurements of the flow velocity and bathymetry along shallow river bends are required to understand this process and its role in respect to the dynamics of the flow regime.

Considering the dynamics of the flow regime, duration of exposure of bank surface to fluvial erosion is maximal at bank-toe, which implies that erosion at bank-toe is more than at the bank surface. During degradational phase of the channel[1], bank-toe erosion proceeds even during low water stage (Luppi, et al., 2009), and it is faster in non-cohesive soils than in cohesive soils. Since low and normal water stages have often a much longer duration than high flow events, the amount of bank-toe erosion might be comparable during these periods, especially in non-cohesive soils. Therefore, study of bank erosion by using a single discharge and water level (for example bank full discharge) is not sufficient, since ignoring low and normal flow stages in the study of bank erosion may lead to underestimation of the amount of bank erosion.

In the case of the presence of a berm, bank-toe erosion may proceed at berm-toe in place of bank-toe during low water stage in the river. This may cause later concentration of flow near bank-toe in high water stages (Luppi, et al., 2007), which have often shorter duration than low and normal water stages, but larger sediment transport capacity which increases the probability of the bank failure due to bank-toe erosion. Literature is particularly lacking on the berm evolution in respect to the dynamics of the flow, especially in river bends.

[1] Channel incision, or bed degradation due to erosion, occurs due to the deficit of sediment supply in respect to the sediment transport capacity of the channel.

2.1.2 Process of riverbank failure

Bank failure is a complex process depending on the geotechnical properties of bank material, stratigraphy and geometry of the bank (Thorne, 1991), as well as dynamics of the flow regime in the river and bank. Riverbanks may be broadly classified on the basis of material and stratigraphy as non-cohesive, cohesive and layered (Thorne et al., 1997). In riverbanks composed of non-cohesive soils, shear strength increases faster with depth than does shear stress, so that critical conditions are more likely to occur at shallow depths. In cohesive soils, shear stress increases more rapidly than shear strength with increasing depth so that critical surfaces tend to be located deep within the bank (Terzaghi and Peck, 1948).

In non-cohesive materials failure occurs by dislodgment and avalanche of individual particles or shear failure along shallow, planar or very slightly curved slip surfaces (Thorne, 1991; ASCE Task Committee, 1998) (Fig. 2-1a). In cohesive soils, deep-seated failure occurs along a rotational (circular) failure surfaces (Fig. 2-2a) in high, mildly sloped (less than 60°) stream banks, while planar failure (Fig. 2-2b) occurs often in steep banks, with the failed block sliding down into the channel (Thorne, 1982). During the process of temporal incision of channels, planar failures often occur earlier than rotational failures in the adjustment sequences when banks are lower (Simon, 1989) and it can occur along any critical failure surface irrespective of whether this plane passes through the bank-toe. This type of failure is a consequence of bank-toe erosion and generation of a near vertical tension crack (Lohnes and Handy, 1968; Thorne et al., 1981).

Cantilever failure (Fig. 2-2c) prevails on composite banks when erosion of the erodible underlying layer by flow generates undercutting to the extent that triggers this type of failure (Thorne and Lewin, 1979; Thorne and Tovey, 1981; Pizzuto, 1984). Three modes of cantilever failure, namely shear, beam and tensile failure have been addressed by Thorne and Tovey (1981). Shear and beam failures result in a similar vertical bank profile after failure (Fig. 2-3), due to existence of tension cracks in cohesive soils, which represents the weakest failure plane. On the other hand tensile failure yields a horizontal bank profile.

Beam failure occurs in cohesive soils in the form of rotation of the overhang block around its neural axis forward towards the river. This failure occurs along a vertical plane, where 90% of the failure surface over neutral axis is in tension and the rest in compression (Pizzuto, 1984). The neutral axis itself is neither in compression nor in tension. However, if the bank surface is vegetated such a failure is not expected, except when a tension crack already exists (Pizzuto, 1984).

Shear failure occurs when the block fails along a vertical plane without rotation, which is the most commonly observed type of cantilever failure (Thorne and Tovey, 1981). This happens when the weight of the block exceeds the shear strength along the failure plane. The failure may occur due to increase of block density because of saturation of the block due to rainfall or snow melting.

Tensile failure occurs if a weak plane exits along the horizontal plane in cohesive soils or due to saturation of the lower soil (Pizzuto, 1984). Riparian vegetation roots can increase the stability of the overhang and tensile failure can occur below vegetation roots, leaving root-

bounded overhangs, which fail subsequently by shear or beam failure (ASCE Task Committee, 1998). However, it is believed that vegetation roots can have positive and negative influence on stream bank stability (Endo and Tsuruta, 1969; Wu et al., 1979; Pizzuto, 1984; Thorne, 1990; Pollen, 2004; etc.).

Grasses and shrubs usually increase the stability by spreading tiny roots in the bank profile forming a reinforced soil like a natural geo-textile net (Waldorn, 1977). On the other hand, trees may reduce the bank stability by expanding their thick roots in the bank, dislodging and disintegrating the soil matrix, increasing infiltration into the soil profile and causing additional overburden on the soil due to their weight.

Pizzuto (1984) addressed the influence of the side grown roots on enhancement of tensile strength of the soil and its resistance against cantilever failure. Fibrous roots of vegetation in soil build a reinforced composite material, which increases the shear strength. Pollen (2004) found that the force required for pulling out the vegetation element is almost equal to their tension failure. Further information on the topic is given by Cancienne et al. (2008).

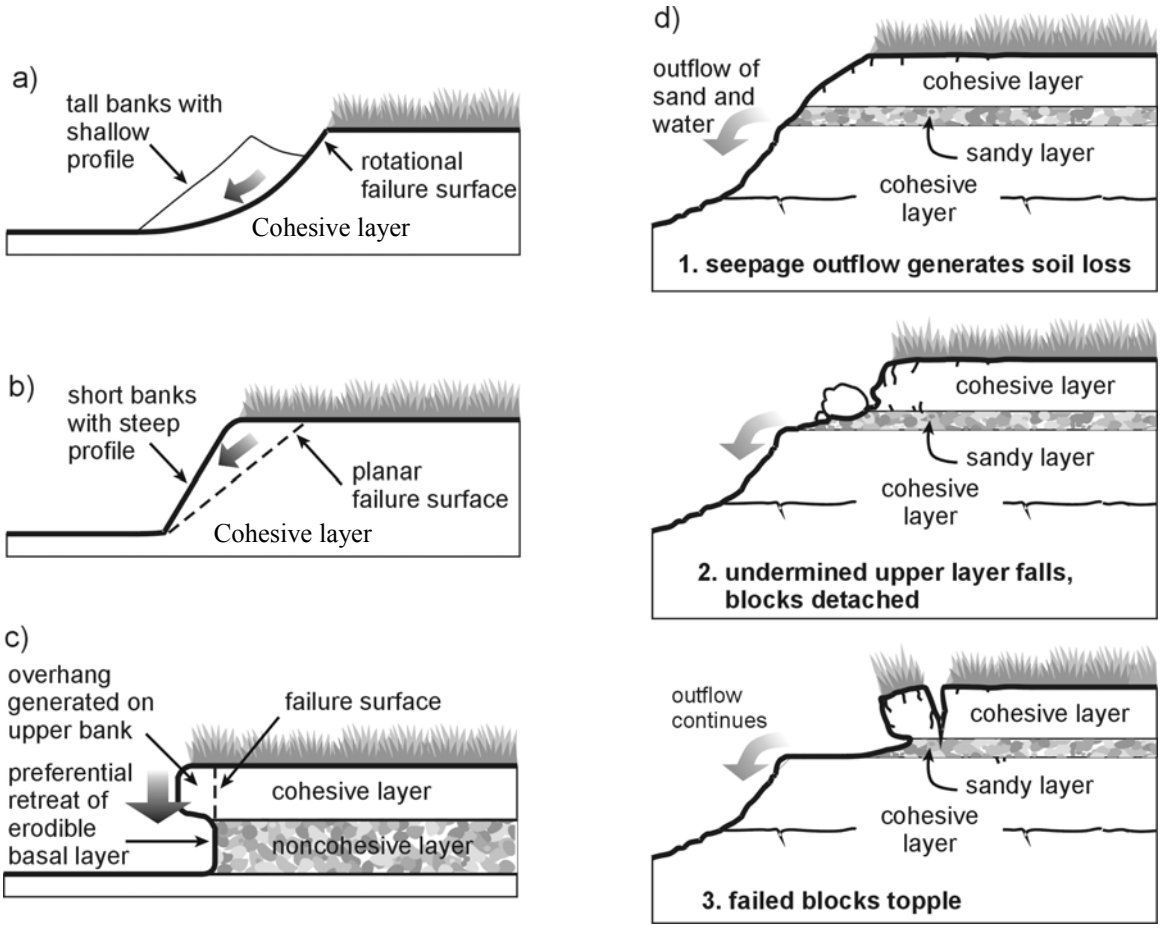

Figure 2-2 Different types of the riverbank failure in cohesive and composite soils (Thorne *et al., 19*81). A) rotational bank failure in tall banks. B) Planar failure in short steep banks. C) Cantilever failure in riverbanks with multilayer soil profile with underlying non-cohesive layer. D) Sapping failure process in riverbanks in multilayer soil profile with underlying non-cohesive layer.

As seen from Fig. (2-4), cantilever failure can also occur in dense non-cohesive soils covered with vegetation. Further research is needed to find out if cantilever failure mechanisms are identical to those in cohesive soils. Moreover, the parameters that affect the stability of the overhang needed to be studied systematically. Additionally, failure slopes can be different in these two soil types, since tension cracks are not normally present in non-cohesive soils.

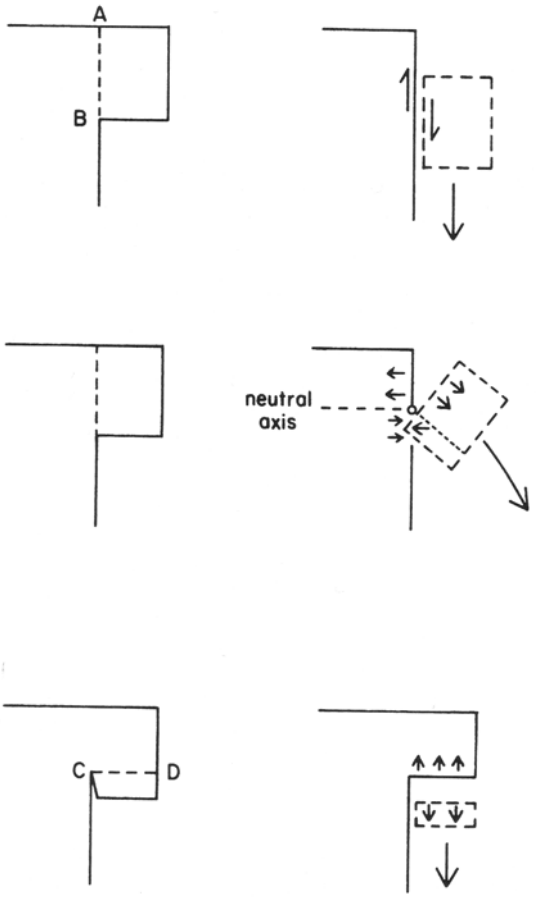

Figure 2-3 Schematic illustration of modes of cantilever failure (Thorne and Tovey, 1981). Top: shear failure; middle: beam failure and bottom: tensile failures

Figure 2-4 Cantilever failure of the overhang in dense non-cohesive soils in Hardebek-Brokenlander Au

There are other, so called, preparatory mechanisms or sub aerial processes such as wetting and drying of soil, freeze and thaw, which weaken the surface of the bank prior to the fluvial erosion (Wolman, 1959; Lawler et al., 1997b; Simon et al., 1999; Couper and Maddock, 2001, 2002), and play a secondary effect in bank erosion and over a longer period. Other types of bank failure, which are closely related to the dynamics of the flow regime, are illustrated later in the following.

Dynamics of the flow regime in the river, comprising water rise and drop during rising and falling limb of the hydrograph, respectively, as well as fluctuation of water table in the riverbank have a significant effect on the process of bank failure. The latter process is manifest in pore water pressure. Pore water pressure is defined as the pressure of water filling the voids in soil. The effect of pore water pressure on the mechanical properties of soil has been first presented by Terzaghi (1936). In fully saturated soils all soil pores are filled with water, and a part of stress is born by the water in soil body. Hence the effective stress is the difference between the total normal stress and pore water pressure.

In unsaturated soils, however, the voids (pores) are partly occupied by water and partly by air. Water adheres to the surface of soil particles leaving the rest of the voids occupied by the air. The pore water pressure is less than pore air pressure in unsaturated zone (due to the surface tension). Since the gauge air pressure is zero (in equilibrium with atmosphere), the pore water pressure above the water table is negative. The difference between air pressure and pore water pressure is called matric suction. Matric suction is a positive quantity. Measurement of matric suction can be made using tensiometer (Fredlund and Rahardjo, 1993). The presence of matric suction in unsaturated soils increases the shear strength of the materials which is often manifested in steeper bank slopes than those indicated by the angle of repose (Simon et al., 2000).

Low water stage

During this stage, erosion of bank surface is limited to the bank-toe (Fig. 2-5A). Duration of the low flow and subsequently bank-toe erosion can result in occurrence of bank failure in loose non-cohesive soils but it is not likely in cohesive soils as studied by Casagli et al. (1999), Rinaldi and Casagli (1999) and Simon et al. (2000). It is not clear if bank failure is likely to occur during low water stage in dense non-cohesive soils, but it can be expected that failure may not occur due to the existence of negative pore pressure in most part of the riverbank above the water stage.

Intermediate water stage

By rising water level in the river during intermediate flow stage, a larger portion of the riverbank is wetted and shear stress at bank-toe increases causing more bank-toe erosion (Fig. 2-5B). In loose non-cohesive soils, increase of bank-toe slope beyond the angle of repose, due to further bank-toe erosion, causes failure of the riverbank in form of dislodgment and avalanche of individual particles. Hasegawa (1981) and Nagata et al. (2000) suggested a failure slope equal to the angle of repose for submerged zone of the bank and a larger angle of failure for the dry region of the bank over water surface equal to the observed slope of the

natural riverbank. Based on this postulation, once failure occurs in the submerged zone, the upper part of the bank in the dry zone fails along this larger slope, which seems not to hold generally, as it is seen from Fig. (2-7). Referring to this figure, the lower part of the riverbank is steeper than the angle of repose and the upper part of the riverbank has remained stable after erosion of the lower part, causing generation of undercut and overhang zones in the riverbank composed of non-cohesive dense soils.

A) Low water stage

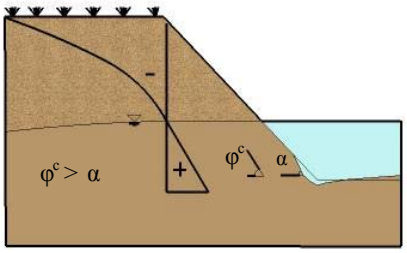

D)High water stage

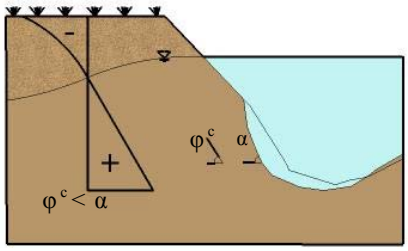

B) Rising water stage (normal flow)

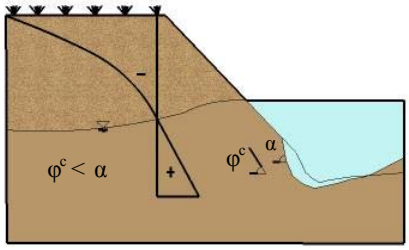

E) Undercutting due to shallow shear failure

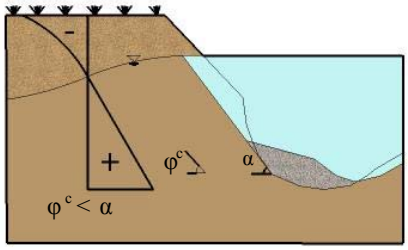

C) Shallow shear failure

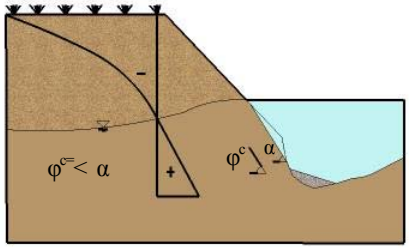

F) Cantilever failure showing possible failure planes

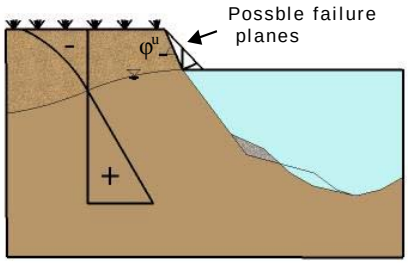

Figure 2-5 Postulated bank erosion process in dense non-cohesive soils in respect to dynamics of the flow regime. A) Bank-toe erosion in low water stage. B) Further development of bank-toe erosion in intermediate water stage. C) Shear slip failure and deposition at bank-toe in intermediate water stage. D) Continuation of bank-toe erosion in high water stage. E) Undercutting due to the shear failure and berm formation. F) Cantilever failure along possible failure planes. G) Sapping due to the sudden draw down of water stage.

G)Sapping

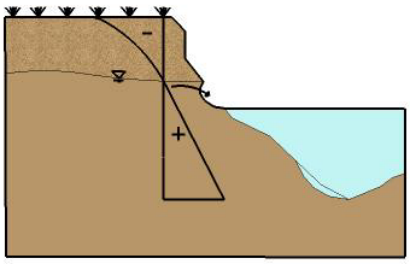

Figure 2-5 Continuation form previous page

The erosion in the submerged zone can be associated with the bank-toe erosion and subsequent shear failure due to the loss of matric suction (Fig. 2-5C). The existence of steep bank surface in Fig. (2-7) might be correlated to the effect of soil compaction and negative pore pressure. It is not clear if stability of the overhang is solely due to the vegetation roots or negative pore pressure above the water surface or even both, but it is expected that the overhang remains stable for a period of time.

Figure 2-6 Undercutting due to the slip failure in Hardebek-Brokenlander Au

In cohesive soils, the failure plane extends through tension crack to the top of the bank (Lohnes and Handy, 1968; Simon, 1989a; Thorne, 1990; Darby and Thorne, 1994, 1997), avoiding formation of an overhang. In intermediate water stage, a transition zone occurs in the riverbank, in which the pore water pressure changes from positive to negative pore water pressure above the water surface (unsaturated or vadoze zone). The negative pore water pressure above the water surface acts as an apparent cohesion and resists against failure, which increases the stability of the bank in cohesive soils (Casagli, et al., 1997, 1999; Curini, 1998; Simon et al., 2003, Rinaldi, et al., 2004). On the other hand, the positive pore pressure reduces the stability of the riverbank, by reducing the effective stress. In layered soils, erosion

of the submerged underlying weak layers results in formation of overhang at intermediate water stage (Fig. 2-2c).

It is essential to explore if the knowledge gained on the effect of pore water pressure on the stability of cohesive soils is directly transferable to dense non-cohesive soils or whether it acts differently in the stability of the latter soil type.

Figure 2-7 Formation of overhang due to undercutting in Hardebek-Brokenlander Au

High water stage (bank full)

During high water stage bank-toe erosion proceeds more intensively (Fig. 2-5D) resulting eventually in bank failure in non-cohesive soils as shown in Fig (2-8) and schematically in (Fig. 2-5E, F). In the case of cohesive soils, confining pressure of the water stage in the river increases the stability of the riverbank (Darby and Thorne, 1996b; Casagli, et al., 1999). However, prolonged wetting periods increase the probability of bank failure (Simon et al., 1999). Luppi et al. (2009) reported that the failure might occur during the flood peak or even shortly before that, due to the effect of bank-toe erosion in destabilizing the riverbank prior to the occurrence of peak flow. Therefore, the timing of bank failure, which depends on several parameters such as flow regime, soil types and bank stratigraphy, is still a subject of debate among researchers.

In case of submergence of the overhang in cohesive soils, loss of negative pore pressure and increase of bulk soil density may result in partial failure of the submerged part of the overhang in form of tensile failure along a horizontal plane (Pizzuto, 1984). There is particularly no similar investigation in dense non-cohesive soils. However, it can be expected that soil saturation occur faster in submerged zone and slightly above it due to capillary effect, so that tensile failure does not occur along a horizontal plane but a plane with negative slope.

Figure 2-8 Riverbank failure during high water stage in dense sandy soil (Hardebek-Brokenlander Au)

Draw down of water stage

During a rapid draw down stage in the channel following saturation of the bank during high water stage, a perched water table in the riverbank is developed above a water-restricting layer (Wilson et al., 1991; Jones, 1997) or between two layers with contrasting conductivities (Hagerty 1991). As perched water table rises above such less permeable layers, soil particles are entrained in seeping water out of the soil, when a critical hydraulic gradient is reached.

The process of erosion by seepage, termed seepage erosion or sapping (Ullrich et al., 1986; Hagerty, 1991), results in local failure of the bank (leaving cavities or undercutting zones) (Fig. 2-5G). Sapping has been especially observed in conductive soils such as loamy sand with underlying water restrictive layers, which has initiated cantilever failure preceded by undercutting due to sapping (Fox et al., 2007; Wilson et al., 2007 and Cancienne et al., 2008).

This has also been known as the most critical condition in the stability of the cohesive riverbanks (ASCE Task Committee, 1998; Casagli et al., 1997, 1999; Simon et al., 2000; Dapporto et al., 2003) due to the loss of matric suction in the riverbank and resisting forces of confining pressure in the river in cohesive soils.

It should be further studied if this process also occurs in single layer riverbanks especially consisting of sandy soils, due to, for example, hysteresis effect (Corey, 1986), and determine if it plays a similar role in bank failure mechanism in dense non-cohesive soils as in cohesive soils.

In fluctuating water stages due to frequent moderate peak river flow, alcove-type failure has been reported to occur in fine-grained banks (Dapporto et al., 2001,2003). This type of failure is characterised by sliding (failure) of a portion of bank material from the middle part of the bank, which leaves a characteristic alcove-shaped surface after failure. Bradford and Piest (1980) as well as Thorne et al. (1998) have referred to this type of failure as pop-out failure and have associated it to the saturation and strong seepage out of the bank surface. However, Dapporto et al. (2001) suggested that this type of failure can occur in sandy silt soils when the

soil is partly saturated without development of excess pore water pressure and strong seepage forces.

Such a type of failure preceded by undercutting and bank-toe erosion is shown in (Fig. 2-9). The combination of bank-toe erosion and alcove-type failure/ sapping in this figure has caused an unstable situation of the bank, so that with the next rise of water to intermediate stage, bank failure may occur. It seems that this type of failure does not play a primary role in bank failure, particularly when it is not combined with undercutting and bank-toe erosion. Dapporto et al. (2001) states that the initial geometry of the bank plays an important role in the occurrence of this type of failure. Further study is required to explore how often such type of failure occurs in the river under study and if it plays a significant role in bank failure process.

Figure 2-9 Alcove-type failure in Hardebek-Brokenlander Au

2.1.3 Process of distribution of failed bank materials

Failed bank material may be transported as wash load or suspended load, or it may deposit at the toe of the bank as intact blocks (Simon et al., 1991) as well as on the bank surface where the slope is mild (Fig. 2-10). The failed bank material can also be broken into several smaller pieces depending on the height of the bank (Thorne and Tovey, 1981). For example, in the case of non-cohesive soils, it may break into very small pieces, while blocks with grown vegetation remain longer together. Depending on the composition of the failed bank material and flow regime, the failed blocks may remain intact for a longer time at bank-toe or eroded away by flow.

In case of intact blocks at the bank-toe, Wood et al. (2001) showed that cohesion between the failed bank material at the bank-toe and substrates could provide an additional strength to resist direct fluvial entrainment, by studying this process in Goodwin Creek, Mississippi.

Therefore, it is not sufficient to estimate block entrainment in the basal area from block size or bed roughness alone, as in Shields type approach.
The failed bank material may improve the stability of the bank, by reducing bank height and slope. Additionally, in the case of berm formation the high flow velocity zone can be pushed away from the bank, protecting the bank from fluvial erosion. The process of distribution of bank material has not been well understood and requires more investigation.

Figure 2-10 Deposition of failed bank material at bank-toe (left) or bank surface (right) in Hardebek-Brokenlander Au

2.2 State-of-the art in the theory of the riverbank failure analysis

Bank failure occurs when the (moment of) driving forces (weight of the slipping block and positive pore water pressure) acting on the most critical slip surface exceeds the (moment of) resisting forces (Coulomb friction, apparent cohesion forces and hydrostatic confining pressure in the river) following an increase in bank height and slope due to bank-toe erosion (Osman and Thorne, 1988; Thorne and Darby, 1996b). Stability of the riverbank is commonly expressed in terms of a safety factor, which is defined as the ratio of resisting forces to the driving forces (Thorne, 1991, Millar and Quick, 1998; Darby and Thorne, 1996a,b; Casagli et al., 1999; Rinaldi and Casagli, 1999; Simon et al., 2000; etc.). Riverbank fails when the safety factor is less than 1, and is conditionally stable when it is between 1 and 1.3 (Simon et al., 1999).
In non-cohesive soils, the driving force in the shear failure of the riverbanks is the shear stress on the failure plane due to the component of the weight in down slope direction. The resisting forces include the shear strength of the potential failure plane due to the internal friction. Such types of failures can be analysed using Taylor's infinite slope approach (Terzaghi and Peck, 1948) as follows:

$$SF = \frac{F_r}{F} = \frac{W \cos\beta \tan\varphi}{W \sin\beta} = \frac{\tan\varphi}{\tan\beta} \qquad (2\text{-}1)$$

In the above equation, F_r (= N tan φ = W cos β tan φ) is the shear strength along failure slope, W is the dry or submerged weight of the slipping mass, β is slope of the bank and φ is internal friction angle (angle of repose). These forces are illustrated schematically for safety factor (SF) equal to 1 in Fig. (2-11).

In well-drained banks (loose coarse material), failure occurs when the bank slope exceeds the angle of repose. In poorly drained banks (non-cohesive materials) failure can occur because of the reduction of friction due to pore pressure (Thorne, 1991). In the case of saturated soils, it can be shown that the maximum stable bank slope in loose non-cohesive soils reduces to less than half of the angle of repose (Kolymbas, 1998).

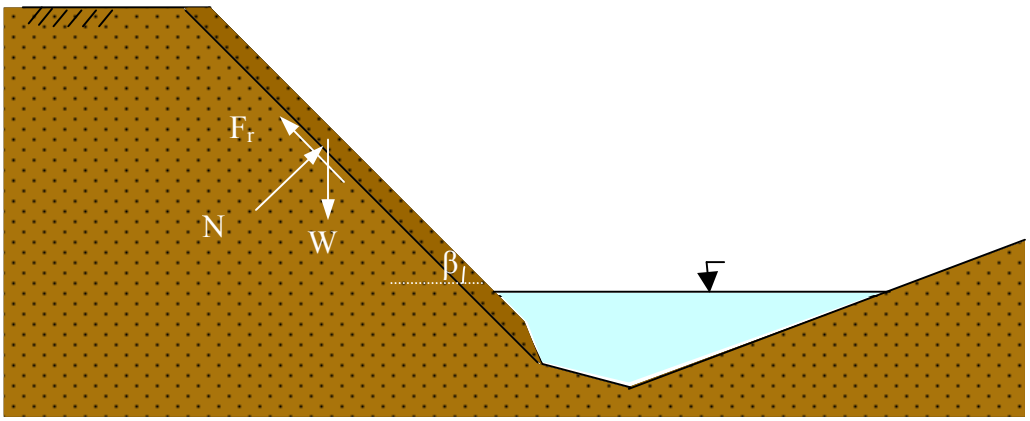

Figure 2-11 Shear failure of non-cohesive banks in critical condition (α = φ)

The above mentioned analysis has been unjustifiably and frequently applied to the failure analysis of the dense non-cohesive (for example sandy) riverbanks (Hasegawa, 1981; Nagata et al, 2000; Schmautz, 2003; Jang and Shimizu, 2005; Chen and Duan, 2006; etc.), while in reality this method is limited by the fact that most of the alluvial bank materials exhibit some cohesion due to silt and clay fractions, or apparent cohesion due to capillary suction in unsaturated zone, or the binding effect of vegetation roots and rhizomes (Thorne, 1991), or due to compaction and cementation. The presence of these factors can allow non-cohesive banks to stand at steep bank angles (Thorne et al., 1997). Millar and Quick (1993) proposed a raised angle of repose for gravels to account for the effect of compaction and cementation due to the finer particles as well as vegetation in increasing critical shear stress in computation of fluvial erosion process of the bank. They suggested estimating this angle based on the field measurements of the steepest stable bank angle. Further research is needed to investigate if the effect of compaction and cementation in shear failure analysis of non-cohesive soils can be explained by a raised angle of repose. Additionally, inclusion of the effect of negative pore pressure, hydrostatic confining pressure and vegetation in shear failure of such type of soil is almost completely missing in the literature.

In contrast to the case of non-cohesive soils, there are plenty of studies on the analysis of cohesive riverbank failure (planar and rotational types), even if these studies were often limited as the contribution of bank-toe erosion in triggering failure were neglected and a wedge shape failure geometry was only considered (Lohnes and Handy, 1968; Thorne et al., 1981; Spangler and Handy, 1982; Huang and Tsai 2000; Huang et al., 2002). Osman (1985), as well as Osman and Thorne (1988), presented stability analysis for planar and rotational failure by taking into account the effect of bank-toe erosion and considering a more realistic failure block geometry (composite slip surface). Pore water pressure and hydrostatic confining pressure were included in the analysis of bank stability first by Simon et al. (1991). Darby and Thorne (1996c) proposed an approach to consider the effect of the change in positive pore water pressure and hydrostatic confining pressure on the stability of the riverbank. Nevertheless, they assumed eleven predefined scenarios for pore water pressure state (assuming water table is parallel to the ground surface) in respect to the water stage in the river, ignoring the dynamic interaction between the two parameters.

Casagli, et al. (1997), Curini (1998), Simon and Curini (1998) made valuable contributions to understanding the effect of pore water pressure and matric suction (in vadoze zone) on the stability of the riverbank and outlined the need of special treatment to the riverbank stability analysis rather than conventional approaches like the ones in landslide problems.

Casagli et al. (1999) and Simon et al. (2000) included the effect of negative pore pressure in their stability analysis (considering positive pore pressure and hydrostatic confining pressure) but retaining the simple wedge-shape failure and ignored bank-toe erosion. Rinaldi and Casagli (1999) improved the mentioned approach by including the effect of dynamics of water stages in their stability analysis, keeping simplified bank geometry. They analysed stability of the riverbank in two conditions: 1) minor flow events, where the river stage does not reach the tension crack, and 2) major flow events, where the river stage exceeds the base of tension crack. They proposed the following formula for computation of safety factor for general case and analysed peak flow and draw down conditions as in Fig. (2-12)

$$SF = \frac{C'L + S\tan\phi^b + \left[W\cos\psi - U - V\sin\psi + P\cos(\beta - \psi)\right]\tan\phi}{W\sin\psi + V\cos\psi - P\sin(\beta - \psi)} \qquad (2\text{-}2)$$

where P is confining water pressure force in the river, U and V are pore pressure (uplift) forces under and in the tension crack on failure surface respectively, S is matric suction force, L is the length of the failure surface, and W is weight of the failed block. ϕ^b is the angle expressing the strength increase rate relating to the matric suction. This parameter varies for all soils, and for a given soil with moisture content (Fredlund and Rahardjo, 1993; Simon et al., 2000) within a normal range of 10-20° (Simon et al., 2000; Casagli et al., 1999). Data on this parameter are particularly lacking for alluvial materials. For this reason ϕ^b should be calculated by measurements using Tensiometer or similar devices. Other parameters are depicted in Fig. (2-12).

Although each of the already mentioned works has its own limitations, nevertheless compared to the analysis method of bank failure in non-cohesive soils, it is clear that a significant

advancement has been attained in the field of the analysis of failure in cohesive soils. It is to be explored which portion of the advancement gained in the failure analysis of cohesive riverbanks can be applied in the failure analysis of the dense non-cohesive soils.

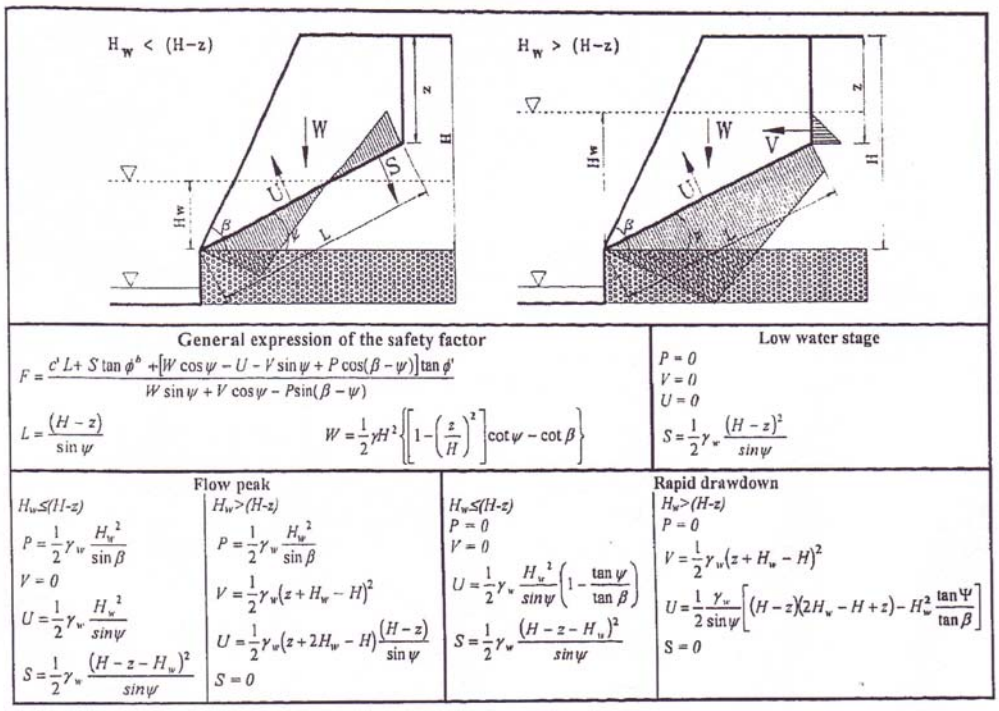

Figure 2-12 Planar failure analysis in cohesive soils (Rinaldi and Casagli, 1999)

Advancement in the field of the mechanical analysis of riverbank failure in layered soils are limited to a few works on planar failure (Simon et al., 2000; Langendoen and Simon, 2008b), sapping (for example Fox et al., 2007) and cantilever failure (Thorne and Tovey, 1981 and Pizzuto, 1984). The safety factor for the case of shear type of cantilever failure can be computed for layered soils as follows (Langendoen and Simon, 2008b):

$$SF = \frac{\sum_{i=1}^{I}\left(C'_i L_i - U_i \tan\phi_i^b\right)}{\sum_{i=1}^{I} W_i} \tag{2-3}$$

where C'_i = effective cohesion of i^{th} layer (kPa); L_i = length of the failure plane incorporated within the i^{th} layer (m); W_i = weight of the i^{th} layer (kN); U_i = the hydrostatic (positive or negative) pressure force on the failure surface (kN/m);

An equation similar to Eq. (2-3) can be derived for the analysis of tensile failure. For the analysis of beam failure, the reader is referred to Thorne and Tovey(1981). The current knowledge in mechanism of cantilever failure is limited. Available analysis methods are limited to idealized mechanisms, ignoring the effect of vegetation, negative pore pressure and

submergence of the overhang block. Analysis of cantilever failure in dense non-cohesive soils is virtually non-existent in the literature.

2.3 State of the art in modelling of bank erosion

2.3.1 Bed erosion

Bed evolution in non-cohesive soils is the result of imbalance in conservation of sediment in the water column. If the net flux of sediment through a control volume of water column (including bed load layer) undergoes a deficit with respect to the sediment transport capacity of the flow, then the bed compensates it through erosion, provided that there is no restriction in sediment availability. On the other hand, if this net flux of sediment undergoes a surplus then the additional sediment is deposited on bed. The mentioned process in the basal zone leads to the evolution of the river bank-toe.

Sediment in rivers is assumed to be transported virtually in two layers, namely bed load and suspended load layers. Hence modelling of bed evolution requires mathematical description of these two layers. Suspended load transport in rivers has been consistently modelled using the well-known advection-diffusion equation, sometimes called convection-diffusion equation (Gresho and Sani, 2000) or advection-dispersion equation. Bed load transport can be mathematically expressed using either equilibrium or non-equilibrium transport models, which will later be addressed briefly.

Bed evolution process in non-cohesive soils is usually modelled using the well-known sediment transport continuity equation, known also as Exner equation:

$$(1-\lambda)\frac{\partial z_0}{\partial t}+\frac{\partial q_x}{\partial x}+\frac{\partial q_y}{\partial y}+(D-E)=0 \tag{2-4}$$

Here λ is the porosity of bed material, t is time, z_0 is bed elevation with respect to an arbitrary reference datum, x and y are Cartesian longitudinal and lateral directions, q_x and q_y are the components of the specific (per unit width) volumetric bed-load rate in x and y, directions, and D-E is the volumetric flux of sediment exchange between the bed and water column, in which D stands for deposition rate and E for entrainment rate (e.g. van Rijn, 1993). In equilibrium transport models D is equal to E. Bank-toe aggradation due to deposition of the failed bank material is not included explicitly in the above equation. This subject will be discussed in detail later in Ch. 2.3.3.

What distinguishes the different approaches adopted by researchers in using Eq. (2-4) are the choice of application of equilibrium or non-equilibrium load, bed or total load formulation, one layer or multiplayer bed with sediment mixture, and evaluation of the source term.

Sediment continuity equation for total load can be expressed as follows (Wu et al., 2000):

$$(1-\lambda)\frac{\partial z_0}{\partial t}+\frac{\partial ch}{\partial t}+\frac{\partial q_x^T}{\partial x}+\frac{\partial q_y^T}{\partial y}=0 \tag{2-5}$$

In the above equation[1], h is the water depth, c is the depth-averaged concentration and the second term (storage term), accounts for temporal change of sediment concentration, which can be neglected in, steady state (van Rijn, 1987). q^T is the total sediment transport rate determined by summation of suspended load [2] and bed load. The non-equilibrium bed load transport rate (q) can be computed as follows (Wu et al., 2000):

$$\frac{1}{L_e}(q-q_{eq})+\frac{\partial q_x}{\partial x}+\frac{\partial q_y}{\partial y}+(D-E)=0 \tag{2-6}$$

In the above equation, q_{eq} is the equilibrium bed load transport rate, determined by any available empirical formula such as van Rijn (1984a), and L_e is the non-equilibrium adaptation length for bed load transport rate. This parameter is purely empirical and is often used as a calibration parameter.

Alternatively, bed level change in non-equilibrium transport models can be determined as follows under the assumption that suspended load is negligible (Phillips and Sutherland, 1989):

$$(1-\lambda)\frac{\partial z}{\partial t}=\frac{1}{L_e}(q-q_{eq}) \tag{2-7}$$

Observe that Eq. (2-6) can be obtained by substituting Eq. (2-7) in Eq. (2-4).

Although the non-equilibrium models seem to be more advanced than the equilibrium ones, there has been no systematic study to convincingly prove the superiority of the former method over the latter one, because of the uncertainty associated with both of them (Cao and Carling, 2002a).

It should be noted that in the above models, a single layer homogenous bed material has been assumed, while for bed materials with mixed grain sizes comprising sorting and armouring processes, modification to these equations are required (for example Gessler et al., 1999; Wang and Wu, 2004). This topic, however, is beyond the scope of the present work.

Success in application of the mentioned models in basal area is affected by near wall flow structure, lateral bed slope as well as secondary currents in the river bends. Several empirical formulas have been developed to consider the effect of transverse slope and secondary currents on bed load transport along the river bends (Engelund, 1974; Kikkawa, et al., 1976;

[1] It should be noted that in this equation, the source term (D-E) is cancelled out due to its inclusion in suspended as well as bed load layers with opposite signs.

[2] The suspended sediment load can be calculated in a two-dimensional depth-averaged model as follows: $q_x^s = u\partial hc/\partial x - \partial/\partial x(\Gamma_x h\partial c/\partial x)$, $q_y^s = v\partial hc/\partial y - \partial/\partial y(\Gamma_y h\partial c/\partial y)$.

Hasegawa, 1981; Ikeda, 1982; Struiksma, 1985; Bridge, 1992; etc.). However, formulas incorporating the effect of secondary currents are, with no exception, limited to the central region of the river and away from the sidewalls. This results in inaccurate computation of bed evolution near sidewalls. For example, in simulation of meander migration of a laboratory channel by Nagata et al. (2000), represented here as Fig. (2-13), bed degradation in the section downstream of the apex started and developed in the form of point bar along the inner bank, while in the experiment, it started and grew at the middle of the channel causing bank-toe erosion at outer bank and finally formation of berm there. This resulted in underestimation of the bank-toe erosion by their model, which implies that the applied method of Engelund (1974) and Hasegawa (1981), for considering the effect of secondary currents on bed load transport, overestimated the amount of transversal bed load transport in the bend, which resulted in underestimation of the amount of sediment transport along the outer bank-toe due to feeding from upstream. Similar problems can be observed in the result of simulation of bank-toe erosion along outer bank of the bends in several other works (for example, Amiri-Tokaldany, et al., 2007; Hafner, 2008; Jia et al., 2010). This problem has not been sufficiently solved and needs further study.

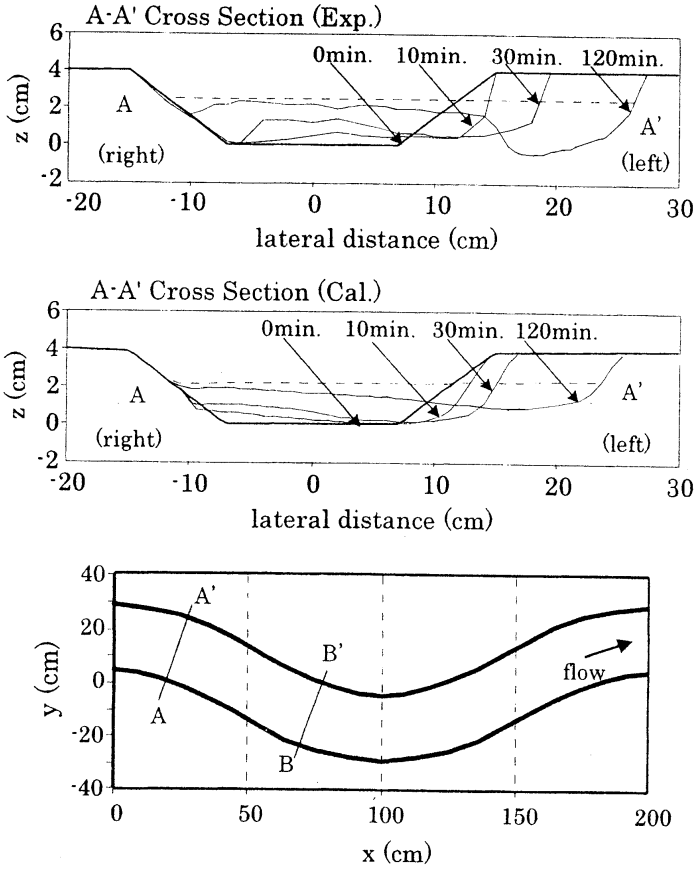

Figure 2-13 Temporal alteration of cross sectional profile (from Nagata et al.2000)

In determination of the source term in Eq. (2-4), it is a common practice to assume that the deposition rate (D) can be related to (hindered) fall velocity (w) near bed and near-bed suspended sediment concentration ($D = w.c_b$). Computation of entrainment rate (E) is still a debating issue among researchers (Sumer and Deigaard, 1981; Cheng, 1984; Rashidi, et al., 1990; Kaftori, et al., 1995; Cao, 1997,1999; Fu et al., 2005). This is due to the complexity of interaction of sediment dislodgement and turbulent structures (bursting) near bed and comparatively limited understanding of the physical processes occurring at the movable bed surface, particularly in natural rivers. Therefore, it is not surprising that in most of the current practical approaches, it is simply assumed that entrainment occurs at the same rate as it does under equilibrium condition (Chang, 1988; van Rijn, 1993; Wu et al., 2000; Duan and French, 2001; etc.).

$$D - E = \alpha_0 w(c_b - c_{b*}) \tag{2–8}$$

Here $\alpha_0 \leq 1$, is a recovery coefficient indicating that only a fraction of deficit of suspended sediment concentration with respect to the equilibrium concentration is compensated by means of bed evolution. There is little experience on the determination of the parameter α_0, which thus is often used as a calibrating factor. Equilibrium near-bed suspended sediment concentration (c_{b*}) can be computed with the aid of the equation proposed by van Rijn (1984). However, determination of c_b[1] requires knowledge on suspended sediment concentration profile very close to the bed, which is not resolved in either two-dimensional depth-averaged or three-dimensional approaches. Therefore, several assumptions and empirical relations are incorporated in the determination of near bed suspended sediment concentration, including a presumed vertical distribution of suspended sediment and velocity, vertical dispersion coefficient, near bed reference elevation, etc. (van Rijn, 1993; Gessler et al., 1999;Wu et al., 2000; Duan and French, 2001; Olsen, 2003). In this way the problem of determination of entrainment rate shifts to the problem of determination of near bed suspended sediment concentration. This issue is still a matter of debate among researchers and needs further studies, especially in the field.

2.3.2 Bank erosion

In the last two decades, modelling of the riverbank retreat has been a major interest among researchers. A variety of methods have been developed to describe and model channel geometry and morphological adjustments of the rivers.

Regime theory explains the equilibrium state of the river geometry, assuming constant discharge, which will not go under geometrical alteration any longer, in ideal case. A summary of different methods based on regime theory can be found in Yalin (1992). As mentioned by this author, seven parameters should be known beforehand in regime theories, which can present some difficulties in engineering practice. Extremal methods (among which, Chang 1980, White et al., 1982) rely on the hypothesis that the river tends to attain an

[1] For derivation of an empirical-analytical equation for c_b refer to Appendix A-1

equilibrium state through minimization of an energy related characteristic, for a given constant discharge (for example bank-full discharge). Since river channel formation is the result of constantly changing flow and sediment discharge with additional anthropogenic impacts, the mentioned methods cannot yield reliable results. Furthermore, bank failure mechanism had not been considered in the mentioned methods.

Millar and Quick (1993) developed an analytical model of bank erosion based on extremal hypothesis to determine the influence of the bank stability of gravel rivers on stable width and depth of alluvial gravel-bed rivers. They found that bank erosion has a great influence on equilibrium geometry of the rivers. In their method only fluvial bank erosion was considered and bank failure due to bank-toe erosion was neglected. They employed the method of Knight (1981) and Knight et al. (1984) to compute bed shear stress distribution along the wetted perimeter. The critical shear stress was then related to the angle of repose of the gravel using a simple relation. They suggested increasing the angle of repose in formulation of critical shear stress to compensate for the effects of compaction, vegetation as well as cementation by fine particles like silt and clay. They performed a sensitivity analysis on this parameter and showed that an increase of the angle of repose to a value of 74.1° yields good agreement with field measurement of the width of several gravel rivers with strong vegetation effect. It should be investigated if a similar approach is applicable in the analysis of shear failure in dense non-cohesive soils such as fine sand.

Duan et al. (2001) suggested a fluvial bank retreat model of non-cohesive soils using a two-dimensional hydrodynamic model, neglecting bank failure mechanism. The rate of bank retreat (ω) due to the fluvial erosion of bank surface was computed using mass balance within a prismatic control volume adjacent to the bank (with its edge at bank-toe) as follows:

$$\omega = -\frac{(\frac{\partial q_l}{\partial l}\frac{dr}{2} + q_r - q_{br})}{h_b} \tag{2-9}$$

Where ω is actual bank erosion rate, q_l and q_r are longitudinal and radial total sediment transport rates, respectively and q_{br} is frictional (fluvial) erosion rate. These authors attributed the rate of mass deficit over bank surface to the rate of bank retreat. However, this does not account for bank-toe erosion as well as the subsequent bank failure and assumes parallel bank retreat. Furthermore, validation of their model with the laboratory measurements of Nagata et al. (1997) in a sine-generated channel revealed that their model underpredicts bank erosion rate at the outer bank downstream of the apex where bank failure was supposed to have occurred.

Olsen (2003) developed a steady state three-dimensional fluvial model (with k-ε turbulent model) to simulate the self-forming process of meandering. He ignored the bank failure mechanism and only considered fluvial erosion process. Comparison of the simulation results with laboratory experiments of Zimpfer (1975) in a rectangular sand-bed channel showed only a qualitative agreement in reproduction of meander characteristics. This model underpredicted the meander wavelength, and downstream migration rate. This shows that improvement of computation of bed shear stress distribution as well as sediment transport

(using 3D approach) and consequently fluvial bank erosion is not sufficient in modelling of meander migration even in case of a constant flow discharge.

The above-mentioned authors did not provide a method to calculate bank failure due to bank-toe erosion. Pizzuto (1990) showed that inclusion of fluvial erosion without bank failure mechanism could not result in widening of the gravel-bed channels with mild lateral slope, since fluvial erosion near water surface is negligible. He developed a slumping model for simulation of straight gravel river widening, in which as the bank slope reaches beyond the angle of repose, the over-steepened area of the bank fails along an inclined line extended to the top of the bank with the slope of the angle of repose. The failed bank material is distributed at bank-toe forming a plane surface so that the eroded volume (A_e) is equal to the deposited volume (A_d) with the upper edge of the deposited material coinciding with the lower edge of the failure plane as shown in Fig. (2-14). A cross sectional analytical model was applied to compute bed shear stress distribution across the channel, given a bank-full discharge. This model provided close agreement with laboratory measurements of Ikeda (1981), however, was limited to a constant discharge, channels with lateral mild slope and a simple bed shear stress model.

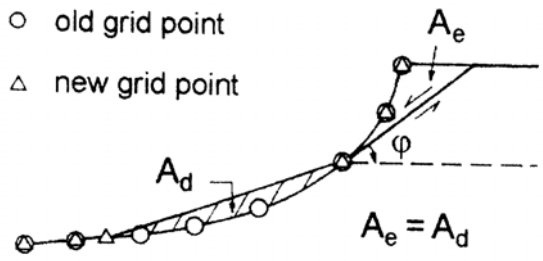

Figure 2-14 Numerical simulation of bank erosion in gravel soils (Pizzuto, 1990)

Li and Wang (1993) developed a three-dimensional unsteady fluvial model to simulate the river width adjustment in gravel rivers, neglecting suspended sediment transport. While their hydrodynamic model had a great advantage over that of Pizzuto, they applied a slumping bank failure model identical to the method of Pizzuto, with similar limitations. Comparison of their model results with the laboratory measurements of Ikeda (1981) showed over-prediction of the channel width.

Kovacs and Parker (1994) developed a vectorial bed load formula and integrated it with a two-dimensional sediment continuity equation (neglecting suspended sediment) for simulation of fluvial bed and bank erosion in straight gravel rivers. They simulated bank failure process by computing the time development of the front of erosion moving upward to the top of the bank once the erosion started at bank-toe, except when dynamic equilibrium is reached. While their method is more consistent with the physical process of bank failure mechanism in gravel soils; because of the assumption of constant discharge, their approach has limitations in application to natural rivers in which the discharge is hardly constant. Their

hydrodynamic model was a cross sectional flow model similar to that of Pizzuto. Their model too showed over-prediction of the channel width measured in laboratory by Ikeda (1981).

The differences among the three above-mentioned models in predicting the channel width of a laboratory test could be related to the different parameters (critical shear stress and angle of repose) they used in their simulations (ASCE Task Committee, 1998). However, for this reason, the accuracy of their models cannot be directly compared.

Nagata et al. (2000) developed a two dimensional numerical model in body-fitted coordinate system for simulation of bed and bank erosion in sandy bed rivers (ignoring suspended sediment transport). Bank failure and the effect of secondary currents on bed load transport were included in this model. The bank failure model was based on the model of Hasegawa (1981), which assumes that bank failure in non-cohesive soils occurs when the failing volume (A) is equal to the deposited volume (B) as is shown in Fig. (2-15). The slope of bank before and after failure (β_k) was assumed to be equal to the angle of repose. The bank retreat ΔB_c was defined so that A= B. After bank failure, the bank surface retreats parallel to the initial bank surface. The slope of the bank over water surface remains equal to the initial state, which could have been larger than the angle of repose due to the negative pore water pressure. The effect of negative pore pressure was not included quantitatively in this model; therefore no overhang was allowed to form. Furthermore, a physical basis is missing in their bank erosion model and the model is limited to constant discharge. For validation of the model, experimental results on mild sine-generated laboratory channels were used. Simulations were run for three different constant discharges with at least one non bank-full. The simulation of the temporal evolution of the bank retreat across a section downstream of the apex represented underprediction of the rate of the bank erosion in submerged as well as non-submerged zone in intermediate stages compared to the measured ones. This can be related to the shortcomings in computation of bank-toe erosion, as addressed in the previous chapter, application of a not physically based bank erosion model, and probably incorrect estimation of the angle of repose. As it is seen from Fig. (2-13), the slope of the eroded bank surface in laboratory experiment is much larger than that in the simulation.

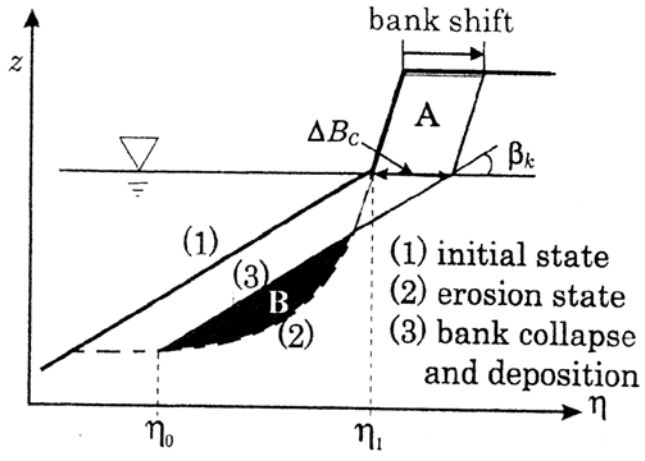

Figure 2-15 Non-cohesive bank erosion model (Nagata et al., 2000)

Schmautz (2003) developed a riverbank-widening model for non-cohesive riverbanks in straight channels assuming bank full discharge. In this model, if the bank slope reaches beyond the angle of repose due to fluvial erosion on an element, the upper node of the element is lowered, while the lower node is raised, so that the slope of the element is equal to the angle of repose, to preserve mass conservation, as is shown in Fig. (2-16). This is a simplification of the real process and it seems that the mentioned procedure requires iteration to attain a stable slope over all numerical elements on the bank. It is not clear if distribution of the failed bank material can be modelled properly by this method. Comparison of simulation results of bank width with the laboratory measurements in a straight channel showed a relative good agreement. However, this model underpredicted bank-toe erosion.

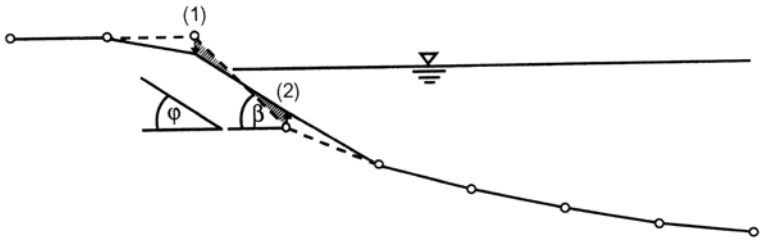

Figure 2-16 Non-cohesive bank erosion model (Schmautz, 20003)

Farshi and Minor (2004) developed a two-dimensional depth-averaged model to simulate bank erosion in non-cohesive soils on an unstructured triangular grid by introducing a new form of bed stress components in order to consider bed topography and some two dimensional effects of the flow. The hydrodynamic model used was too simplified neglecting eddy viscosity. A bank erosion model similar to that of Schmautz (2003) was implemented, but extended to unstructured triangular elements. In this model if the maximum slope of a computational triangular element exceeds the angle of repose, the element is rotated around a rotational axis so that the mentioned slope reduces to the angle of repose. The rotation axis is determined so that the eroded area of the element becomes equal to the aggregated area. This method requires iterations over all surrounding elements on the bank. The result of simulation of one test section of a laboratory test in a straight channel using this method showed underprediction of bank width in the dynamic stage of the bank evolution and good agreement with the final equilibrium stage of the channel width. This model is also limited to constant discharge.

Jang and Shimizu (2005) developed a two-dimensional fluvial model in body-fitted coordinate system to study the behaviour of the alternate bars in rivers with erodible banks. The bank failure model of Hasegawa (1981) was extended to include the effect of bank-toe erosion and the bank failure plane was computed as in Pizzuto (1990). Comparison to laboratory results under constant flow discharge showed a qualitative good agreement with bar formation and meandering due to alternate bars. However, a quantitative comparison of bank width simulation with measurements is missing in this work. Moreover, the bank failure model does not account for dynamics of the flow regime.

Hafner (2008) extended the applicability of the model of Schmautz (2003) to river bends by including the dispersion terms in the two-dimensional depth-averaged hydrodynamic model. However, other limitations of the bank erosion model of Schmautz (for example the condition of bank full discharge) remained unchanged. The result of Hafner's simulated and measured profiles at two cross sections, namely 40 and 90, of a meandering laboratory flume, nearly 50 numerical days after the beginning of the experiment, are shown in Fig. (2-17). It is observed from these figures that indeed the deviation between measured and computed cross sectional profiles is very large at these two sections in spite of inclusion of dispersion terms and secondary currents effect in bed load transport. This confirms the need of substantial improvement in modelling of secondary currents and their effect in bed load transport.

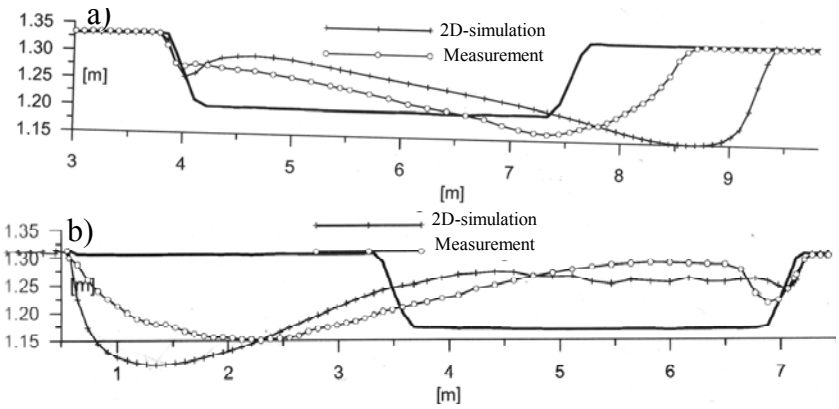

Figure 2-17 Simulation of bank erosion versus laboratory measurements, a) cross section 40, b) cross section 90 (from Hafner, 2008)

The above-mentioned models are all limited to a constant discharge and the effect of (positive/negative) pore water pressure, compaction as well as vegetation have not been considered directly in bank stability models. Additionally, they have been mainly tested using laboratory measurements. These limitations give rise to simplifications, which make these models not capable of reproducing the bank failure mechanisms (such as undercutting and cantilever failure) as well as discontinuities in bank profile geometries (comprising steep or negative bank slope) observed in the natural dense non-cohesive riverbanks (refer to Figs. 2-4 to 2-9).

Modelling of undercutting (due to fluvial erosion or seepage) as well as cantilever failure is limited to a few research works on multi-layer cohesive soils. Darby et al. (2007) modelled fluvial undercutting in cohesive layer of soil by an excess shear stress model. The applied shear stress was calculated by an empirical function relating the mean cross sectional shear stress to the distribution of shear stress along wetted perimeter in a straight rectangular channel. This approach is highly idealized for computation of shear stress distribution on the bank surface and the authors have achieved no validation of the model.

Dapporto et al. (2001) analysed bank failure process in respect to alcove-type failure, but did not verify their analysis with measurements. Langendoen and Simon (2008b) included modelling of cantilever failure in simulation of the bank erosion along a bend way in

Goodwin Creek in Mississippi over five years. Jia et al. (2010) incorporated undercutting and cantilever failure into a three-dimensional hydrodynamic model to simulate bank retreat along the outer bend in a reach of the Yangtze River in China. The results of the mentioned two works have been explained in Ch. 2.3.4. It remains open if the just existing models of undercutting and cantilever failure in cohesive soils are applicable to dense non-cohesive riverbanks along shallow river bends.

Modelling of pore pressure in riverbanks and advancements in understanding of the role of the negative pore pressure on the riverbank stability have emerged from and been restricted to the studies of bank erosion in cohesive soils (Casagli et al., 1999; Simon et al., 1999, 2003; Rinaldi and Casagli, 1999; Rinaldi et al., 2004; Dapporto et al., 2001, 2003; Darby et al., 2007; etc.). These works suggest that additional apparent cohesion due to the negative pore pressure needs to be accounted for in the analysis and modelling of riverbank stability, especially when the flow is below bank full stage in the river and a considerable portion of failure surface may pass through unsaturated soil.

Negative pore water pressure (matric suction) in the riverbank is not a static entity but fluctuates in response to the rainfall, soil temperature, variation of river stage, evapotranspiration, and variations of capillary fringe sustained by water table (Casagli, et al., 1999).

Rainfall and rise of water stage in the river as well as water table in the riverbank increase the water content of soil and consequently positive pore water pressure, resulting in a decrease of matric suction and loss of apparent cohesion in the riverbank. On the other hand, magnitude and duration of high soil temperature during hot seasons as well as evapotranspiration by vegetation cover on the riverbank increase the matric suction, especially in the upper soil layer, by loss of soil water content.

Therefore, dynamics of pore pressure in the riverbank can impact the stability of the riverbank. It is generally accepted that the dynamics of pore pressure can be modelled using equation of conservation of mass in unsaturated flow, known also as Richards equation (Eq. 2-10).

$$\frac{\partial \vartheta}{\partial t} = \frac{\partial}{\partial z}\left[k_z(\vartheta)\left(\frac{\partial H_p}{\partial z} \right) \right] + \frac{\partial}{\partial y}\left[k_y(\vartheta)\left(\frac{\partial H_p}{\partial y} \right) \right] + Q \tag{2-10}$$

Where ϑ is soil-water content, H_p is the total pressure head, k_z and k_y are hydraulic conductivity in z and y directions, respectively and Q is the boundary flux (rainfall / evaporation) . The total pressure head is the algebraic sum of elevation head (z) with matric head (h_p):

$$H_p = h_p + z \tag{2-11}$$

Matric head accounts for the effect of matric suction, which reads as follows:

$$h_p = -\frac{(u_a - u_w)}{\gamma_w} \tag{2-12}$$

Where γ_w is unit weight of water, which is also dependent on saturation degree. In case of saturated flow h_p in the above equation reduces to $h = u_w / \gamma$.

In particular, application of such seepage modelling to study the effect of pore water pressure distribution in the stability of the cohesive riverbanks were achieved by Dapporto et al. (2003); Rinaldi et al. (2004) and Darby et al. (2007).

In unsaturated flow, hydraulic conductivity is a function of the degree of saturation, (Corey, 1986), which, in turn, is a function of matric head. However, direct measurement of hydraulic conductivity and water content in unsaturated soils is very difficult. Therefore, empirical formulas are applied to compute these terms based on their saturated counterparts. A widely used approach to determine ϑ and k in unsaturated soils is that suggested by van Genuchten (1980), whose equations read as follows:

$$\vartheta = \vartheta_r + \frac{(\vartheta_s - \vartheta_r)}{\left[1 + \left(\varepsilon |h_p|\right)^n\right]^{1-\frac{1}{n}}} \tag{2-13}$$

k can be also expressed in terms of matric head as follows:

$$k(h_p) = k_s \cdot \frac{\left[1 - \left(\varepsilon |h_p|\right)^{n-1} \left(1 + \left(\varepsilon |h_p|\right)^n\right)^{-m}\right]^2}{\left[1 + \left(\varepsilon |h_p|\right)^n\right]^{m \cdot l_1}} \tag{2-14}$$

The empirical parameters ε, n, m, as well as residual and saturated soil-water content, ϑ_r and ϑ_s, respectively, are computed from soil-water retention curve, determined by field measurements; k_s is saturated hydraulic conductivity in the desired direction. l_1=0.5 has been widely used for all soil types.

This form of Eq. (2-10) is commonly referred to as mixed form, because h_p has been prescribed in relation to both k as well as ϑ; whereas its combination with Eqs. (2-13) and (2-14) yields a h_p-based formulation. Alternatively, k and h_p can be expressed in terms of ϑ so that Eqs. (2-10) is only a function of ϑ (called also ϑ-based). Application of k (h_p) typically exhibits hysteresis (Bastos de Vasconcellos and Amorim, 2001), while it is less pronounced by $k(\vartheta)$ (Nielsen et al., 1996). Nevertheless, the numerical formulation of mixed form has shown to be mass conservative (Raff and Ramirez, 2005) while the other mentioned forms suffer from large mass error (Celia et al., 1990). Simulated pore pressure in riverbank showed to be very sensitive to these parameterization functions (Rinaldi et al., 2004). To improve the accuracy of these parameterization relations in simulation of pore pressure distribution in riverbanks, Rinaldi et al. (2008) applied a ϑ-based formulation using in-situ field measurements combined with empirical formulae. It should be noted that field measurements

for determination of soil-water content can be subject to hysteresis, which adversely affects the measurement results.

Darby et al. (2007) analysed the effect of bank evolution on pore pressure distribution in a multi-layered cohesive riverbank along Sieve River in Italy by integrating seepage modelling, fluvial erosion and bank failure models (including cantilever failure). They applied a very simplified shear stress model, which governed fluvial erosion without utilizing a hydrodynamic model. Comparing different simulation scenarios with and without fluvial bank erosion and bank failure, they showed that pore water pressure field in near-stream region is modulated by bank deformation. They argued that exposure of interior region of the bank with higher matric suction due to bank erosion (undercutting and failure) causes a reduction of (positive) pore water pressure below what it would be without considering bank evolution. The deformation of the bank surface leads to alteration of hydraulic gradients driving infiltration to the bank. The simulation scenario including the effect of bank evolution showed that during draw down stage of the hydrograph, water table in the riverbank remains in equilibrium with water stage in the river at least in the vicinity of the bank surface. It is still not clear if these findings are general to cohesive soils or restricted to the hydrologic and sedimentary set up of the studied riverbank. Furthermore, their simulation results were not verified by measurements.

It is obvious that the reliability of pore pressure modelling depends largely on authentic determination of k and ϑ. This constitutes the greatest part of uncertainty in pore pressure modelling due to the difficulty in reliable determination of the embedded empirical parameters in their formulations. Additionally, application of seepage modeling requires a number of data and parameters, which are often not available. In such cases, simplified methods based on the (reasonable) hypothesis of pore pressure distribution in the riverbank can be desirable. Based on this requirement, Dapporto et al. (2001) assumed linear distribution of negative pore pressure similar to hydrostatic pressure distribution in the failure analysis of a riverbank in a small reach of Arno River in Italy and obtained similar results to riverbank failure analysis achieved by including complete seepage modelling in the same river reach.

It can be perceived that full dynamic simulation of pore water pressure can reveal detailed information of pore pressure distribution in the riverbank, given reliable required parameters, while simple assumptions on pore pressure distribution might be enough to evaluate pore pressure distribution along the failure plane. Furthermore, exact computation of pore pressure distribution might not be necessary in non-cohesive soils, since in such soils bank failure occurs in a shallow layer, so that the pore pressure might remain in equilibrium with water stage in the vicinity of the bank surface (Darby et al., 2007) due to the relative higher permeability of such soils compared to cohesive soils.

Rinaldi et al. (2008) further extended the approach of Darby et al. (2007) in computation of bed shear stress at bank-toe by integrating a two-dimensional depth-averaged version of hydrodynamic model of DELFT3D with the seepage, bank erosion and fluvial models. The coupled model was used to simulate erosion of a multi-layer cohesive bank along a 80m reach of a sharp river bend by means of considering a single representative outer bank profile. The

simulations were achieved for three flood events occurring during a two months period. In spite of the fact that the applied hydrodynamic model included an empirical approach to approximate the effect of the secondary currents in the main flow region, it had limitations in the near bank zone where bank-toe erosion was of concern. Furthermore, the model is limited to fixed bed, neglecting bed evolution along the river bend, which adversely affects shear stress distribution along the outer bank-toe. The simulation results of bank erosion after three flood events showed that bank-toe erosion in lower loose gravel layer has been largely overestimated by the model, yet good result of the bank retreat of the top bank could be attained, although the bank geometry (comprising middle packed gravel layer and upper cohesive layer) could not be reproduced well. Extension of the simulation period to four further flood events by Luppi et al. (2009) revealed that the model generally underpredicts the volume of mass failure. The origin of errors in the method remains open, though simplification in hydrodynamic model and consequently fluvial erosion of bank-toe, idealization of bank failure mechanisms and parameterization of the seepage model might have adversely affected the simulation results.

Quantification of the effect of vegetation roots in bank stability is difficult since, several vegetation parameters such as root intensity, dimensions and tensile strength have to be measured. The fibrous roots of vegetation are strong in tension increasing soil (shear) strength. The additional strength due to vegetation roots can be calculated using a fiber-break mode, force-equilibrium equation in the following form (Waldorn, 1977; Wu et al., 1979), which has been frequently applied in the literature (Simon and Collison, 2002; Pollen et al., 2004; Luppi, 2007; Cancienne et al., 2008, among the others).

$$c_r = T_r\left(\cos\theta'\tan\phi + \sin\theta'\right) \cong 1.2T_r\left(\frac{A_r}{A}\right) \tag{2-15}$$

In the above equation c_r is the shear strength (cohesion) due to the roots, T_r is the tensile strength of roots (KPa), A_r/A is the root-area-ratio or the fraction of soil cross sectional area occupied by the roots, θ' is the shear distortion from vertical (in degree) and ϕ is the friction angle of the soil. Pollen and Simon (2005) demonstrated that the above equation may overestimate root reinforcement by 50% due to the fact that the roots in soil-root matrix have different shear strength and break progressively and proposed another method called fiber-bundel approach. Apart from uncertainties associated with determination of parameters θ', T_r and A_r in the above equation, it is not clear if the method applies similarly to non-cohesive soils, which requires further measurements.

2.3.3 Distribution of failed bank material

It is difficult to derive a physically based relation for distribution of failed bank material (deposition and subsequent erosion and transport) but generally there are three possible ways for failed bank materials to be transferred to the stream. These are wash load, bed material and bed load (Simon et al., 1991). Wash load is transported by flow as suspension, bed material is a direct deposition at the bed and bed load is transport of failed material over and

in contact with the bed surface. Nevertheless, for simplification reasons, authors have often assumed that the entire failed bank material deposits at the bank-toe with the angle of repose in accordance to a slump model (Pizzuto, 1984; Nagata, et al., 2000; Jang and Shimizu, 2006; etc.), which seems to be more appropriate for coarse none-cohesive materials (Darby et al., 2002).

Amiri-Tokaldany et al. (2007) developed a method for computation of bank-toe evolution in steep riverbanks due to the failed bank material by portioning failed bank material to wash load and bed material. The latter portion was assumed to deposit at the bank-toe with the angle of repose. The horizontal and vertical length scale of deposited bank material (Fig. 2-18) are calculated as follows in their work:

$$L_s = \frac{h_1 \cos\alpha_0}{\sin(\alpha_0 + \psi')} \tag{2-16}$$

$$h_1 = \sqrt{\frac{2A_s}{1/\tan(\alpha_0 + \psi') + \tan\psi'}} \tag{2-17}$$

Here, L_s is the length of deposited bank material; ψ' is the slope of the deposited material equal to the angle of repose; α_0 is the lateral bed slope angle, h_1 is the depth of the slump along the line normal to the surface of deposit and A_s is the total unit volume of bank-derived sediment stored at the bank-toe, which is equal to ($A_b + A_f$). A_b is the unit volume of locally derived bank debris deposition at the bank-toe (excluding wash load) and A_f is the unit volume of failed material originally deposited in an upstream cross section by bank failure, but which has been subsequently mobilized and re-deposited locally. The latter parameter should be calculated using sediment transport laws (see Amiri-Tokaldany et al., 2007 for details). As the comparison of their simulation with field measurement results show, bank failure as well as bank-toe erosion have been largely overestimated so that validation of their model of distribution of failed bank material has not been possible. The reasons that the model fails to simulate correctly the distribution of failed bank material remains open. Nevertheless, it can be recognized that the above mentioned method is based on the assumption of non-cohesive deposited failed material, while the angle of repose of deposited failed bank material had been used as a calibrating parameter in case of the cohesive material in the studied case.

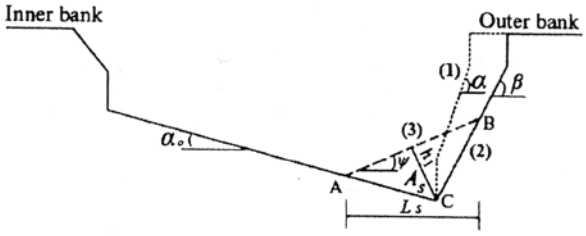

Figure 2-18 Schematic illustration of distribution of failed bank material (Amiri-Tokaldany et al., 2007)

Darby et al. (2002) suggested that the distribution mechanism of failed bank material is controlled by the particle size distribution. They assumed that the fraction of failed bank materials finer than 0.062 mm is transported as wash load and the larger fraction of the materials still smaller than 10 mm is transported as bed load material. The coarse fraction material (>10 mm) was assumed to be transferred instantaneously to the bank-toe, similar to the slump deposition model of Pizuuto (1990) and Nagata et al. (2000). In contrast to the mentioned slump methods, in which distribution at bank-toe is based on the angle of repose, they assumed that the failed bank material is distributed within one bank height from the unstable bank, by adjusting the inclination of the surface of the deposition to maintain mass conservation. The portion transported as bed material is summed with the eroded bank-toe material due to basal erosion and assigned as source term to the sediment continuity equation. They assumed that this portion of failed material is distributed over the computational cells of the bank-toe region across the channel section within a bank height distance from the bank. A linear decreasing distribution function towards the channel centre was applied. The result of validation of this model will be presented later in Ch. 2.3.4. Mosselman (1992) applied a delta Dirac function as distribution function for cohesive failed material and assumed that the failed material is distributed evenly across the section.

Notwithstanding the fact that the method proposed by Darby et al. (2002) seems to be more comprehensive than other common approaches, it can be recognized that the postulation of controlling distribution mode by size fraction is a simplification of real processes, in which flow transport capacity controls the mode of transport. Furthermore, the failed bank materials are not completely disintegrated into smallest components but may remain as blocks at bank-toe, reducing the portions contributed to the suspended and bed loads. The removal of such fail blocks cannot be computed using Shields type approaches due to their apparent cohesion with underlying layer in case of cohesive soils. Wood et al. (2001) proposed an empirical relation to account for additional apparent cohesion between failed blocks and underlying bed, which was added to the critical shear stress. In their proposed method this apparent cohesion was measured directly in the field, which makes the practical application of this method limited.

The mechanism of erosion and transport of intact blocks becomes even more complicated by the presence of vegetation cover and roots within the blocks. Therefore, current approaches to model this process are far from reality and requires further research.

2.3.4 Temporal and spatial scales of morphodynamic models

Most of the existing morphodynamic bank erosion models for non-cohesive soils have been assessed using a few different laboratory experiments with different set-ups and constant discharge, mainly bankfull stage (e.g. Pizzuto, 1990; Kovacks and Parker, 1994; Nagata et al., 2000; Duan and French, 2001; Schmautz, 2003; Jan and Shimizu, 2005; Hafner, 2008, among the others). While constant discharge is rare in natural rivers, the magnitude, duration and frequency of the flow events have a crucial implication in morphological evolution. As Wolman and Millar (1960) states, low-magnitude, relatively high-frequency flow events are

more important than rare floods events in terms of their cumulative sediment transport in sandy-bed rivers. Hence, authenticity of the mentioned models should be examined using field data within appropriate timescales (short to medium timescales[1]).

There are few event-based assessments of morphodynamic bank erosion models using field data in cohesive and multi-layer soils (Darby, et al., 2007; Amiri-Tokaldany et al., 2007; Rinaldi, et al., 2008; Luppi et al., 2009). In these studies a few flood events with duration of a few days but with multiple flood peaks have been separately simulated. Therefore, the contribution of low as well as minor flow episodes between simulated flood events had not been considered in the context of bank-toe erosion and dynamics of pore pressure in these works. Additionally, the mentioned simulations have been achieved for a single, representative bank profile within a short river reach.

Morphodynamic bank erosion modelling has not been conducted over longer temporal and larger spatial scales, with a very few exceptions (Darby et al., 1996, 2002; Langendoen and Simon, 2008; Jia et al., 2010) restricted to cohesive or multilayer soils.

Darby et al. (1996) developed a quasi two-dimensional quasi-steady model that took into account bank erosion as well as failure mechanism (planar and curved). They included suspended load and bed load, but neglected the effect of pore water pressure on the stability of the riverbank and the model was applicable only to straight channels. This model was applied for simulation of bank erosion over 24 years along 13.5 Km reach of a tributary to the Mississippi river. The result of river widening could be only qualitatively reproduced.

Darby et al. (2002) integrated a two-dimensional depth-averaged hydrodynamic model with bed and bank evolution models (including a special method for distribution of failed bank material, explained already above) to simulate bank erosion process over approximately six years along 800 m meandering reach of Goodwin Creek river in Mississippi. The model could reproduce the locations and patterns of bank migrations correctly, however, the magnitude of bank retreat were extremely underestimated. They have related this to the simplifications in hydrodynamic and sediment transport model and systematic underprediction of their bank evolution model.

Langendoen et al. (2008a,b) developed a one-dimensional fluvial model coupled with bank erosion model, which accounted for planar and cantilever failure in multi-layer soils. The effects of confining water stage, positive as well as negative pore water pressure was included in this model. The latter two parameters were assumed to have linear distribution in contrast to the full seepage modelling in Dapporto et al. (2001) and Simon et al. (2003). The model was applied to simulate bank erosion along a bend way in Goodwin Creek in Mississippi over five years. The simulation results showed a relatively acceptable reproduction of the channel geometry across six selected sections. However, the model predicted generally steeper bank

[1] Lawler (1993) suggested that short timescale in the study of bank erosion spans between a few months to a few years, whereas it spans between 10 to 30 years in medium (intermediate) timescale. Short timescales have been often applied to define causes, processes and mechanisms of bank failure, while medium timescale are more appropriate for establishing bank retreat (migration) rate (Thorne et al., 1997).

profile than the measured ones. They attributed the poor results to the large underestimation of tension cracks in the riverbank.

Recently, Jia, et al. (2010) developed a model of bank erosion for a composite two-layer riverbank by coupling a three dimensional hydrodynamic model with a three-dimensional bank erosion model. Cantilever (beam) failure for the upper cohesive soil and parallel bank retreat (with critical bank slope equal to the angle of repose) for the lower gravel layer have been accounted for in the bank erosion model. Erosion of underlying loose layer resulted in undercutting of the upper cohesive layer, yielding overhang formation and eventually cantilever failure in this model. It is not clear if the submergence of the overhang has been considered in the flow simulation and bank failure model. The model has been applied to simulate bank erosion over a two-year period along 15 km reach of a meander bend in China. The comparison of their simulation results with field measurements revealed that the model has only reproduced main channel migration and bank retreat qualitatively. The mentioned deviations have been attributed to the neglecting other factors affecting bank erosion processes such as vegetation and sediment supply from upstream. These might be also related to the simplification of the modelling of bank erosion process in underlying non-cohesive soil in respect to the effect of compaction and dynamics of the flow regime.

It can be inferred from the mentioned works, there is an absolute absence of published works on modelling of bank erosion in “dense” non-cohesive soils in natural rivers considering dynamics of the flow over short to medium timescales.

2.4 Open questions and refined objectives of this work

The challenges in the field of the study of riverbank erosion in dense non-cohesive soils can be divided into three groups, namely process understanding, theory and modelling. Basically, the effect of the dynamics of the flow regime in short and medium timescales establishes one of the most challenging issues in all three mentioned disciplines.

Under the process understanding, further research is required on the following issues:

- Bed evolution process along river bends and its interaction with bank erosion in the context of a changing flow regime,
- Bank failure processes (including shallow shear failure, cantilever failure and sapping), their interactions and importance in respect to the dynamics of hydrological parameters such as water stage in the river and ground water table of the bank zone
- Deposition and distribution of failed bank material at bank-toe and along river bends considering flow regime, sediment composition and vegetation

In the theory of bank failure mechanics of dense non-cohesive soils proper answers should be proposed for the following questions:

- How can the effects of compaction, vegetation and negative pore pressure be included in the analysis of bank failure?
- Are the existing analytical approaches (including those for cohesive soils) sufficient to analyse shallow shear failure, cantilever failure as well as sapping and determine the most critical failure plane in complex natural bank geometries?

Modelling bank erosion encounters the main following challenges:

- Proper modelling of outer bank-toe erosion along river bends including the effect of secondary currents on flow and sediment transport near side walls,
- Simulation of undercutting, cantilever failure and discontinuities in bank profile as well as their advancements in respect to the dynamics of the flow regime,
- Development of simple approaches to simulate dynamics of pore pressure to approximate full seepage modelling,
- Modelling of deposition and distribution of failed bank materials along river bends
- Short to medium timescale simulation of bank erosion process

Not all of the mentioned issues could be addressed in this work. The main objective of the present work is to improve the understanding of the main physical processes in evolution of dense non-cohesive banks along river bends, their interactions as well as their mathematical modelling.

In this context, bank failure process along outer bank of a shallow river bend will be studied with respect to the dynamics of the flow regime. Bed evolution along the river bend and its interaction with bank failure will be investigated. Deposition of failed bank material at bank-toe and its effect on bed evolution and flow field alteration will be addressed. To meet these goals a comprehensive field measurement methodology using state-of-the-art technology in flow field, bathymetry and three-dimensional bank surface measurements will be introduced.

Based on the gained knowledge in the measurement phase, mathematical approaches will be developed to enable computation of riverbank erosion due to the undercutting and cantilever failure, including the effect of compaction, water pore pressure and vegetation. In this regard a special method should be developed to account for discontinuities in the riverbank and kinematics of the development and advancement of such discontinuities in respect to the dynamics of the flow regime. It is assumed that sapping failure has a secondary role in bank retreat and will not be considered here, which should be validated by measurements. The distribution of failed bank material is assumed to be representable by a probability mass distribution function.

It is assumed that the current two-dimensional depth-averaged mathematical approaches for simulation of flow and sediment transport are sufficient to describe the flow field and bed evolution along a shallow meandering river. An attempt will be made to introduce a simple approach for modelling of negative pore pressure in the vicinity of bank surface. Clearly, such

an approach cannot account for complex interaction of hydrological parameters, like rainfall and evaporation, with pore water pressure.

The above mentioned morphodynamic model will be applied to simulate bank retreat of a shallow meandering river over a short timescale including complete cycles of low to high flow regimes.

3 Theoretical basis

Morphological processes are directly linked to the flow regime in the river. Tractive force of the flow (bed shear force) is the driving force for sediment transport and bed evolution. Transport of sediment causes erosion in some places of the river and deposition in other places, which can initiate bank-toe erosion and consequently bank failure as discussed in Ch. 2.1. Bank retreat causes lateral migration of river channel and river bends. This migration accompanied by bed evolution dictates a new pattern of flow field, building up a closed chain of interactive processes. The dynamics of the flow regime has a significant impact on these processes.

The mathematical concept in the present work consists of four theoretical components, namely, fluid flow, sediment transport, bed evolution and bank evolution. A two-dimensional depth-averaged approach forms the basis of the first three components and the latter component is based on a 2 ½ dimensional approach. The underlying theory of each component is discussed in the following chapters.

3.1 Mathematical description of flow

As the aim of the current work is the study of morphological evolution in unsteady flow, the full time-dependent hydrodynamic equations are required. The 2D depth-averaged Navier-Stokes Equations, also called shallow water equations (SWE) are derived by integrating the 3D incompressible Reynolds Averaged Navier-Stokes Equations (RANS) over the flow depth. The derivation is based on two assumptions:

- The pressure distribution is hydrostatic (no vertical acceleration)
- The vertical momentum exchange is negligible and vertical velocity component w is very small compared with horizontal velocity components (u and v).

Based on the above assumptions the non-conservative form of 2D depth-averaged SWE for unsteady flows reads as follows (for the detailed derivation of the equations, the reader is referred to Kuipers and Vreugdenhil, 1973):

$$\frac{\partial h}{\partial t}+h(\frac{\partial u}{\partial x}+\frac{\partial v}{\partial y})+u\frac{\partial h}{\partial x}+v\frac{\partial h}{\partial y}=q_s \tag{3-1}$$

$$h\frac{\partial u}{\partial t}+hu\frac{\partial u}{\partial x}+hv\frac{\partial u}{\partial y}=-gh\frac{\partial}{\partial x}(z_0+h)+\frac{1}{\rho}\frac{\partial(h\tau_{xx})}{\partial x}+\frac{1}{\rho}\frac{\partial(h\tau_{xy})}{\partial y}+\frac{\tau_{w,x}-\tau_{b,x}}{\rho}$$
$$+\underbrace{h\frac{F_{c,x}}{\rho}}_{\text{Coriolis force}}-\underbrace{u_s q_s}_{\text{source term}}\underbrace{-\frac{1}{\rho}\frac{\partial}{\partial x}\int_{z_0}^{z_0+h}\rho\hat{u}\hat{u}dz-\frac{1}{\rho}\frac{\partial}{\partial y}\int_{z_0}^{z_0+h}\rho\hat{u}\hat{v}dz}_{\text{Dispersion terms}} \tag{3-2}$$

$$h\frac{\partial v}{\partial t}+hu\frac{\partial v}{\partial x}+hv\frac{\partial v}{\partial y}=-gh\frac{\partial}{\partial y}(z_0+h)+\frac{1}{\rho}\frac{\partial(h\tau_{xy})}{\partial x}+\frac{1}{\rho}\frac{\partial(h\tau_{yy})}{\partial y}+\frac{\tau_{w,y}-\tau_{b,y}}{\rho}$$
$$+\underbrace{h\frac{F_{c,y}}{\rho}}_{\text{Coriolis force}}-\underbrace{v_s q_s}_{\text{source term}}\underbrace{-\frac{1}{\rho}\frac{\partial}{\partial x}\int_{z_0}^{z_0+h}\rho\hat{u}\hat{v}dz-\frac{1}{\rho}\frac{\partial}{\partial y}\int_{z_0}^{z_0+h}\rho\hat{v}\hat{v}dz}_{\text{Dispersion terms}} \tag{3-3}$$

Eq. (3-1) is the 2D depth–averaged continuity equation and Eqs. (3-2) and (3-3) are 2D depth-averaged momentum equations in x and y directions, respectively. Note that in the above equations velocities in x and y directions (u and v, respectively) and Reynolds shear stresses (τ) are depth-averaged values. τ_w and τ_b are wind and bed shear stresses, respectively; $\hat{u}$ and $\hat{v}$ (as functions of z, vertical direction) are the deviations of the depth averaged flow velocities from their vertical profile in x and y directions, respectively. Moreover, q_s is the source term, u_s and v_s are the velocities of the source term in x and y directions, respectively, h is the flow depth and z_0 is the bed elevation; F_c is the Coriolis force of unit volume; g is the gravity acceleration and ρ is the density of fluid. Wind shear stress as well as Corilios force is assumed to have negligible effect on the flow, since they are generally significant in large water bodies. Dispersion terms in the above equation will not be considered in the current work. They are responsible for reproduction of a well-known feature of meandering flows, namely the shift of maximum flow velocity towards the outer bank due to secondary currents. The difficulty in the evaluation of the dispersion terms rests on the fact that this requires knowledge of vertical distribution of flow velocity in longitudinal and lateral directions. As these are not known unless the flow is fully resolved, one has no alternative but to assume some vertical distribution for these quantities. Usually it is assumed that vertical distribution of longitudinal velocity follows the logarithmic law. This assumption seems to be generally regarded as acceptable, even if not exactly valid in the neighbourhood of the banks. However, the same cannot be said with regard to the assumptions made for the vertical distribution of lateral (radial) velocity. This distribution is invariably assumed to be that of the purely circulatory flow of the type occurring in a “fully developed circular flow”. Strictly speaking, this flow can only occur in an infinite circular channel (spiral channel), or in the central region of a circular channel having a finite length (Yalin, 1992).

Most rivers do have a large aspect ratio. For these channels, this assumption leads not only to an unrealistic large shifting of the maximum depth-averaged velocity towards the outer bank

but also adversely affects the bed load transport direction in the river bends, resulting in over estimation of bed erosion at the bank-toe (see Hafner, 2008).

ATV-DVWK (2003), Lippert (2005) and Hafner (2008) showed that for rivers with mild to moderate river bend curvature, the effect of secondary currents on transversal distribution of depth-averaged velocity distribution can be modelled using approaches such as Lien et al.(1999), but they do not impact so much the overall result. In Fig. (3-1) the negligible effect of inclusion of dispersion term on computation of depth-averaged velocity can be observed across a bend section of Isar river, in the south of Germany, with a width to depth ratio of about 21.

Thus without better understanding of secondary currents in shallow meandering rivers, it is sufficient to include the secondary currents effect (dispersion effect) through a Boussinesq type approach (refer to Eq. 3–4).

To solve Eq. (3-1) to (3-3), a turbulence closure model is required to model Reynolds shear stresses, which is presented in more detail in the following.

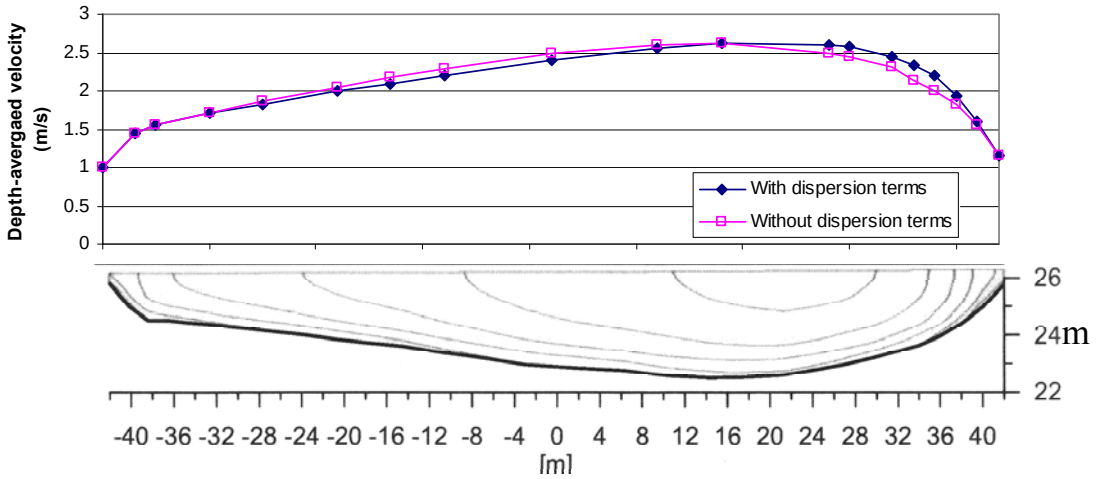

Figure 3-1 Effect of inclusion of dispersion term on velocity distribution across a meander of the river Isar (after Hafner, 2008)

3.1.1 Turbulence

Turbulence in open-channels comprises a wide range of temporal and spatial scales. Resolving all turbulent scales is only possible by directly solving the exact time-dependent Navier-Stokes equation (DNS). This is computationally too intensive and expensive even for supercomputers and is interesting only for pure basic research in turbulence. Using large eddy-simulation (LES) method, the large-scale turbulent motion is resolved by a given numerical grid, while finer-scale turbulent motions are approximated using a sub-grid scale model. These types of calculation should be three dimensional (Nezu and Nakagawa, 1993), and hence they require also a large computational effort. Fortunately, most of the hydraulic engineering applications do not require such details of turbulence. That is the reason why the application of RANS equations with relative low numerical effort is so common in hydraulic

engineering science. In this method, the generated turbulent shear stress terms, due to the time averaging, present the correlations between turbulent velocity fluctuations (momentum exchange). Because of the appearance of these terms, which adds to the number of unknowns of the governing equations, a turbulence model should be introduced to close RANS equations. Most of the turbulence models applied to open channel flows are based on the eddy-viscosity concept of Boussinesq (1877). This concept suggests that turbulent shear stresses arising from the cross correlation of fluctuating velocities are proportional to the mean velocity gradients with a proportionality factor named eddy viscosity (ν_t), in analogy to viscous stress in laminar flow. Applying eddy-viscosity concept, the shear stresses are described as follows (in tensor notation):

$$\frac{\tau_{ij}}{\rho} = -\overline{u_i' u_j'} = \nu_t \left(\frac{\partial u_i}{\partial x_j} + \frac{\partial u_j}{\partial x_i} \right) - \frac{2}{3} k \delta_{ij} \tag{3–4}$$

where δ is Kronecker delta, and k is turbulent kinetic energy, which is defined as follows:

$$k = \frac{1}{2} \left(\overline{u'^2} + \overline{v'^2} + \overline{w'^2} \right) \tag{3–5}$$

The eddy viscosity is not a fluid property, unlike the molecular viscosity. Its value differs from point to point depending on turbulence structure (Launder and Spalding, 1972). At this stage, a turbulence model is required to represent eddy-viscosity in relation to the mean velocity. There are several simple to complicated turbulence models including zero equation models, one equation models, two equation models, Reynolds-stress-equation models and algebraic stress models. Almost all of the mentioned turbulent models include empirical parameters, which have been determined mostly in laboratory and there is a range of choice for them in literature. Hence, the suggested values for these empirical parameters should be applied in field applications with care. The value of these empirical parameters should be verified by field measurements, which will be discussed in Ch. 7.1.

In several publications (among which Pasche, 1984; Schmautz and Aufleger, 2001; Malcherek 2002; Lippert, 2005; Pasche et al., 2006) it could be shown that the zero equation models can quantify the turbulent shear stresses in natural rivers sufficiently, with the advantage of a low computational effort. These approaches comprise empirical parameters, for which a range of values is suggested in the literature. Depending on flow conditions, these methods and their parameters are required to be validated using field measurements (refer to Ch. 7). To choose the most appropriate zero-equation turbulent model for the present application, the following four turbulent models have been examined. Independently of the assumptions of flow and the available data on local velocities, following approaches provide sufficient theoretical basis for accounting the turbulence in the two-dimensional SWE.

3.1.1.1 Constant eddy viscosity

This simple approach can be applied if measurements of velocity distribution are available. It is assumed that the eddy viscosity is constant over depth and is not a function of the flow field (velocity or water depth). This method can be useful for those engineering applications in wide rivers, in which the water level computation is mainly in question. In this regard, Lippert (2005) and Plöger (2007) showed that good results could be obtained in calculation of the water depth. Even in this case, it might yield poor results in the case of unsteady flow (Pasche et al., 2006). In the case of compound channels with relatively small width to depth ratio, the velocity distribution across rivers may not be computed properly using this method due to the impact of sidewalls on turbulence in the main channel. The disadvantage of this model is that the eddy viscosity should be determined experimentally.

3.1.1.2 Bottom generated turbulence

This turbulence approach is suitable for flow situations in which the turbulent boundary layer is dominant and turbulence is generated mainly through the riverbed (very wide channels, for example). In a wide channel with uniform flow, under the assumption of logarithmic velocity law and linear distribution of shear stress, the theoretical distribution of eddy-viscosity ($\nu_t(z)$) can be shown to be of parabolic form (Nezu and Nakagawa, 1993) as follows:

$$\upsilon_t(z) = \kappa u_* z\left(1-\frac{z}{h}\right) \tag{3–6}$$

where κ is von Kármán constant , h is the flow depth and u_* is the shear (friction) velocity which is a measure of the intensity of turbulent eddies and momentum transfer due to eddies ($u_* = \sqrt{|\tau|/\rho} = \sqrt{\left|\overline{u'v'}\right|}$). The depth-averaged form of Eq. (3–6) reads as follows:

$$\upsilon_t = \frac{1}{6}\kappa h u_* = 0.07 h u_* \tag{3–7}$$

The proportionality factor (0.07) is only valid for bed-induced turbulence and too small for compound channels with significant horizontal momentum exchange.
The ASCE Task Committee on turbulence models in hydraulic computations (1988) suggested that the proportionality factor should be computed as the production of Schmidt number (σ_t) and a dimensionless diffusivity coefficient e^*as follows.

$$\upsilon_t = e^* \sigma_t h u_* \tag{3–8}$$

Applying the Darcy-Weisbach friction law for the determination of friction velocity in Eq. (3–8) yields:

$$\upsilon_t = e^* \sigma_t \sqrt{\frac{\lambda_f}{8}} h U \tag{3–9}$$

For Schmidt number a range of 0.5 to 1.0 has been suggested by Rouvé and Schröder (1994). Webel (1982) suggested an average value of 0.15 for dimensionless diffusivity coefficient (e^*) in rectangular laboratory channels. In natural channels, dispersion due to the gradient of flow velocity in lateral and vertical direction is larger than the pure turbulence diffusion, which should be accounted for in e^*. Furthermore, other factors such as secondary currents in natural meandering rivers, variation of bed roughness, irregularity of the riverbed and banks, width to depth ratio as well as geometry of the channel impact the value of this parameter. To account for the effect of the secondary currents in depth-averaged hydrodynamic models, Pavlovic (1981) suggested a value of $e^* = 0.6$. Pasche (1984) showed that this parameter is not constant across compound channels and suggested a range of 0.5 to 0.7 for laboratory compound channels. Fischer et al (1979) suggested a value of 0.6 based on field experiments on diffusion of dye in natural rivers. A range of 0.075 to 0.9 has been suggested by Rouvé and Schröder (1994). Schmautz (2003) used a value of 0.6 for straight trapezoidal channels and 0.9 for naturally formed compact channels. Lippert (2005) used a value of 0.25 for the product of both parameters ($e^*.\sigma_t$) to simulate flow in river Lippe. Hafner (2008) reported that an increased value of e^* may give rise to overestimation of flow velocity near bank zone, especially in the inner bank zone. Therefore, this parameter should not be considered constant across the channel as suggested by, for example, Pasche (1984), and need to be estimated or determined by measurements. The above-mentioned effects have been further discussed in Ch. 3.2.2.

3.1.1.3 Prandtl Mixing length model

Estimation of the parameter e^* is avoided by the method of Prandtl (1925) who proposed a hypothesis, known as mixing length theory, which states that the eddy viscosity is proportional to the mean velocity gradient, the proportionality factor being the square of a characteristic length scale of turbulent motion, called mixing length, i.e.:

$$\upsilon_t(z) = l^2 \frac{\partial U}{\partial z} \tag{3–10}$$

This model is restricted to vertically two-dimensional boundary layer flows, ignoring the horizontal turbulent momentum exchange. The generalized Prandtl mixing length model for three-dimensional flows considering vertical and horizontal turbulent momentum exchange can be written in tensor form as follows (see Rodi, 1978 and Spannring, 1999, among others):

$$\upsilon_t(z) = l^2 \left[\left(\frac{\partial u_i}{\partial x_j} + \frac{\partial u_j}{\partial x_i} \right) \frac{\partial u_i}{\partial x_j} \right]^{\frac{1}{2}} \tag{3–11}$$

Several empirical formulae for l can be found in literature. For example, in the case of free shear layers, Rodi (1993) assumed that l is constant across the layer and proportional to δ (local layer width). The proportionality factor ranges from 0.07 to 0.16 depending on the type

of free shear layer (Rodi, 1993). However, estimation of the Prandtl's mixing length for more complex flows is not simple.

Smagorinsky (1963) suggested a method for the computation of l for the case of finer turbulent motions in sub-grid scale model in LES:

$$\upsilon_t(z) = (C_s\Delta)^2 \left[\left(\frac{\partial u_i}{\partial x_j} + \frac{\partial u_j}{\partial x_i} \right) \frac{\partial u_i}{\partial x_j} \right]^{\frac{1}{2}} \tag{3–12}$$

Here $l = C_s \Delta$, where C_s is an empirical factor between 0.065 to 0.23 (Forkel, 1995), and Δ is the third root of the element volume (in three-dimensions) or square root of the element area (in two-dimensions). Therefore, the empirical factor in Smagorinsky model is dependent on element geometry. The influence of element geometry on computation of flow velocity and water depth should be further studied and will be referred to in Ch. 7.1. In the case of large discretization grids, this model has the advantage to Prandtl's mixing method that it compensates the numerical diffusion error (Pasche et al., 2006).

To model only horizontal turbulent momentum exchange in depth-averaged models, Eq. (3–12) is occasionally reduced in two-dimensional form by neglecting vertical velocity as well as the velocity gradients in vertical direction and substituting the horizontal velocities by their depth-averaged counterparts (Eq. 3–13).

$$\upsilon_t(z) = l^2 \left[2\left(\frac{\partial u}{\partial x} \right)^2 + 2\left(\frac{\partial v}{\partial y} \right)^2 + \left(\frac{\partial u}{\partial y} + \frac{\partial v}{\partial x} \right)^2 \right]^{\frac{1}{2}} \tag{3–13}$$

Lippert (2005) obtained relative good results in the simulation of the flow in the rivers Rhine and Lippe using this method. But this author could show that the model underestimates the eddy viscosity in the main channel, as here botttom-generated turbulence is dominant.

3.1.1.4 Combined bottom-generated and horizontal turbulence model

To account for the effect of vertical as well as horizontal momentum exchange in turbulent eddy viscosity Eq. (3–11) can be integrated over water depth to present a two-dimensional depth-averaged model of eddy viscosity. Such approaches are accompanied by further assumptions and often introduce new unknown parameters (refer to Appendix C). Pasche et al. (2005) proposed a linear superposition of Eq. (3–13) with Eq. (3–9) as follows:

$$\upsilon_t = e^* \sigma_t \sqrt{\frac{\lambda_f}{8}} hU + l^2 \left[2\left(\frac{\partial u}{\partial x} \right)^2 + 2\left(\frac{\partial v}{\partial y} \right)^2 + \left(\frac{\partial u}{\partial y} + \frac{\partial v}{\partial x} \right)^2 \right]^{\frac{1}{2}} \tag{3–14}$$

Pasche et al. (2006) applied this approach in simulation of several flow events in different small to large rivers in Germany. They concluded that the model overestimates water depth in

compact small channels, but very good results are accomplished for flow depth as well as flow velocity in rivers with large aspect ratios (width to depth ratio greater than 20) such as the river Lippe.

3.1.2 Bed shear stresses

Bed shear stress is the key parameter connecting flow and bed processes. It transfers the impact of the flow field on the bed deformation through bed load transport, playing an important role in evolution of the riverbed. If the bed shear stress does not exceed the critical value, no bed load transport takes place. In the case of assuming equilibrium sediment transport, this means that no bed evolution occurs. The bed shear stress is affected by bed geometry, roughness, water depth and velocity. The exact computation of bed shear stress is only possible through direct measurement or direct numerical simulation of the flow field from water surface down to the bed surface. Direct bed shear stress measurement is only feasible in laboratory, while direct numerical simulation is not practical in river engineering practices due to the enormous computational demand. In practice, instead of resolving the velocity field close to the bed by many numerical grids, the bed shear stress is approximated by an empirical formula, such as the logarithmic law of the wall.

Analytical methods for computation of bed shear stress are more accurate than simplified methods, but they are complicated and often applicable only to straight channels. Such methods are especially attractive in combination of detailed flow velocity measurements to investigate bed shear distribution across a stream section (such an analytical approach applicable in river bends has been developed in the present work, the derivation being presented in Appendix A). On the other hand, simple methods of determination of bed shear stress, such as von Kármán, have been successfully tested for general applications in hydrodynamic and even morphodynamic modelling (Schmautz, 2003; Hafner, 2008), however, they are limited in complicated flow fields. As the main focus of this research is not improvement of bed erosion modelling, the common method of the quadratic stress (resistance) law of von Kármán is adapted in this work for modelling bed shear stress.

3.1.2.1 Quadratic stress law

Assuming uniform parallel flow, the bed shear stress can be computed on the basis of the empirical method of quadratic stress (resistance) law by von Kármán as follows:

$$\tau = \rho u_*^2 = c_f \rho U^2 \tag{3-15}$$

In which U is the resultant velocity ($U = \sqrt{u^2 + v^2}$), u_* is the friction velocity and c_f is the friction factor.

Under the assumption that the bed shear stress follows the same path as the depth-averaged velocity direction, the bed shear stress can be divided into two components in x and y directions as follows:

$$\tau_b = \begin{pmatrix} \tau_{b,x} \\ \tau_{b,y} \end{pmatrix} = \begin{pmatrix} c_f \rho\, u\sqrt{u^2+v^2} \\ c_f \rho\, v\sqrt{u^2+v^2} \end{pmatrix} \tag{3–16}$$

For determination of the friction factor in this equation, the method of Darcy-Weisbach is generally preferred to the other two methods (Manning-Strikler and Chézy formula), because the other two methods are purely empirical in contrast to the selected method (DVWk, 1989; BWK, 1999; Pasche et al., 2006). Based on the method of Darcy-Weisbach, friction factor in quadratic stress law can be defined as follows.

$$c_f = \frac{\lambda_f}{8} \tag{3–17}$$

For determination of Darcy-Weisbach's friction factor (λ_f) in the above equation for rough open channels, Schröder (1965) suggested the following equation on the basis of Colebrook-White formula.

$$\frac{1}{\lambda_f} = -2.03\log\left(\frac{2.51}{f\cdot \mathrm{Re}\sqrt{\lambda_f}} + \frac{k_s}{14.84 f\cdot R}\right) \tag{3–18}$$

In the above equation k_s is the equivalent sand roughness; R is hydraulic radius; $Re=uR/v$ is Reynolds number and f is the form drag coefficient, which depends on the channel geometries deviating from circular channels for which this factor is equal to unity. Several empirical formulae exist for determination of f for different geometry of cross sections in the literature (for example, BWK, 1999/1).

In addition to the bed friction, form friction (drag) due to vegetation elements in the flow should be considered in natural rivers. This has been accounted for using the method of Pasche (1984), in which the effect of vegetation elements on flow friction can be determined as follows:

$$\lambda_v = \frac{4\cdot h\cdot d_p}{a_x \cdot a_y}\cdot c_{wr}\cdot \cos\alpha_{lat} \tag{3–19}$$

In the above equation c_{wr} is the form drag factor, which depends on the ratio of approach velocity to the disturbed velocity in vegetation zone and should be calculated using an iterative approach (Pasche, 1984); α_{lat} is the lateral bed slope; d_p is the average diameter of the vegetation elements, and a_x as well as a_y are average spacing between vegetation elements in x and y directions.

Applying the principle of linear superposition, the friction factor of bed (λ), the additional friction factor due to vegetation elements (λ_v) as well as that due to the dunes (λ_d) can be added to form the overall bed friction factor ($\lambda_T = \lambda_f + \lambda_d + \lambda_v$), in case no significant variation of roughness structure across the river section exists (for more information on the topic, the

reader is referred to BWK, 1999/1). λ_d can be computed using the method of Yalin (1992) or van Rijn (1993).

3.2 Sediment transport

Depending on the particle size, density, shape and flow condition, sediment is transported by water in three forms, namely, bed load, suspended load and wash load. Wash load consists of a portion of fine sediment, which is washed away easily in suspension by the flow. Therefore, it can be included in suspended load. Wash load is originated from run-off erosion (land surface erosion) and consists of clay and silt particles. Einstein (1950) suggested that the largest sediment diameter of the wash load can be arbitrarily defined as d_{10} (10% of sediment is finer than this diameter).

Depending on bed shear stress and particle size, the sediment can move by rolling and sliding, in saltation and in suspension. Given a specific particle size and density, as the bed shear stress just exceeds the threshold of initiation of motion, the sediment particles begin to move in contact with the bed in the form of rolling and sliding. With increasing shear stress, the particles move along the bed in the form of more or less regular jumps (saltation). When the magnitude of the shear stress exceeds the fall velocity of particles, they are entrained into suspension (van Rijn, 1993).

Bed load is usually considered to comprise a portion of sediment transported in the vicinity of the bed, while suspended load is considered to be the sediment over this layer. This distinction is made for simplicity of mathematical formulation, otherwise, there is physically no distinct boundary between bed load and suspended load.

The present conceptual model is based on total sediment transport, in which the bed load and suspended load layers are taken together as one layer (well applicable to 2D depth-averaged and one dimensional models). The advantage of this method is that there is no need to include sediment flux exchange between the two mentioned layers in the equations explicitly. The main disadvantage of this method is that the effect of bank and bed slope as well as secondary currents cannot be included properly in the equilibrium total sediment transport as long as suspended sediment and bed load are computed together.

3.2.1 Total sediment transport

The conceptual model of sediment transport is illustrated schematically in Fig. (3-2). It is assumed that the flow is in (potential) transport capacity, which is equal to the equilibrium total load transport. Potential transport capacity is the maximum amount of sediment that the flow can transport without net deposition or erosion (Fig. 3-2-a), assuming sediment availability. In this case, net erosion or deposition is zero (either erosion and deposition rate are equal, D=E, or they are zero, D=E=0). If the total sediment concentration is less than the transport capacity, net erosion occurs (Fig. 3-2-b) by entraining bed material. On the other

hand, if the total sediment concentration is greater than the equilibrium total sediment transport capacity, net deposition occurs (Fig. 3-2-c).

There are different methods available to compute equilibrium total load transport. Among these, the methods of van Rijn (1993), Ackers-White (1973) and Brownlie (1981) have been tested in this work, since they are appropriate for transport of sand (for the corresponding formula refer to Appendix B). In the first method, bed load and suspended load are calculated separately and summed up to form the total load. In the other two methods, the total load transport is computed directly.

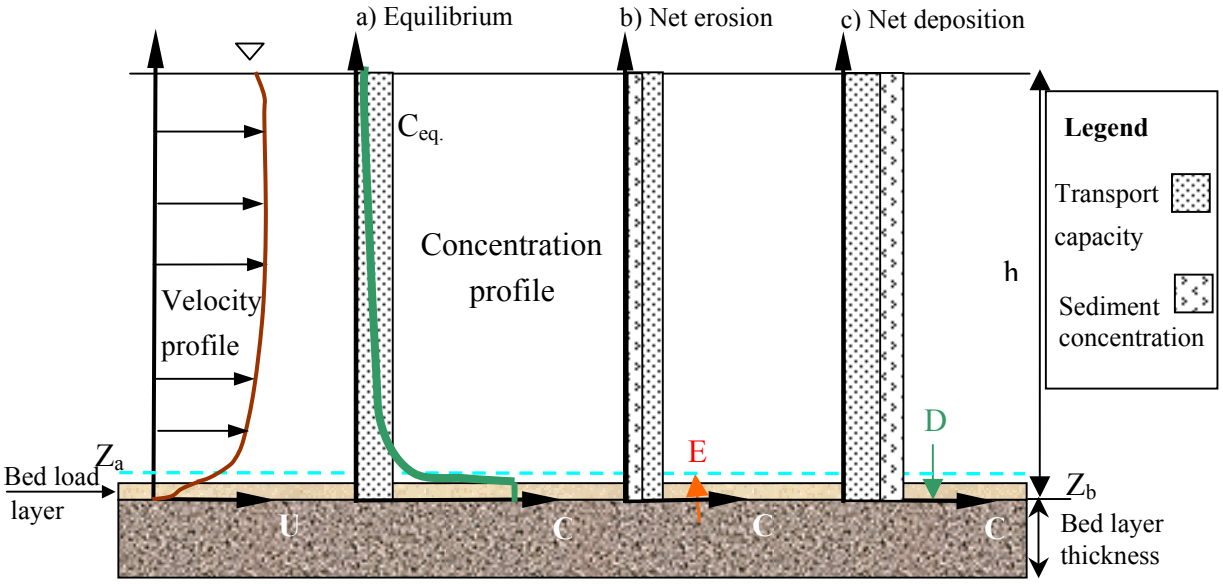

Figure 3-2 Conceptual model of total sediment transport in equilibrium. a) a typical vertical distribution of concentration in equilibrium capacity and its depth averaged magnitude ($C_{eq.}$). b) Deficit of sediment concentration and net erosion. c) Excess sediment concentration and net deposition.

The instantaneous total sediment concentration in the water column (including bed load layer) can be computed by the 2-dimensional depth-averaged advection-diffusion equation as follows:

$$h\frac{\partial c}{\partial t}+uh\frac{\partial c}{\partial x}+vh\frac{\partial c}{\partial y}-\frac{\partial}{\partial x}(\Gamma_x h\frac{\partial c}{\partial x})-\frac{\partial}{\partial y}(\Gamma_y h\frac{\partial c}{\partial y})-S_e-S_{bank}-q_s(c_s-c)=0 \qquad (3\text{–}20)$$

In which c is the depth-averaged sediment concentration, q_s and c_s are discharge and concentration of a source flow, respectively; S_{bank} is the rate of sediment inflow due to bank failure, h is the local water depth, S_e is the net deposition or erosion rates, and Γ is the horizontal mixing coefficient. When the later term includes turbulent diffusion as well as dispersion, the above equation is sometimes named advection-dispersion equation. The turbulent diffusion is in analogy to molecular diffusion. Inclusion of dispersion in the mixing coefficient is due to unresolved three-dimensional features in a two-dimensional approach

such as the effect of secondary currents in lateral mixing. Additionally, the effect of transversal distribution of longitudinal velocity on longitudinal mixing is accounted for by longitudinal dispersion. Effect of dispersion due to secondary currents can be alternatively included separately in the above equation in a similar way as dispersion terms in momentum equation. It has been shown that such an approach may improve the estimation of lateral depth-averaged suspended sediment distribution in a river bend, however not near riverbanks (for example Fang et al., 2005). However, the major focus of the current work is on bank failure mechanisms, and especially the fluvial processes near bank-toe, which cannot be improved by the mentioned approach. Furthermore, inclusion of dispersion terms due to depth averaging inherits the same problems as those in momentum equation and requires further research.

The net deposition or erosion rate (S_e) can be computed based on the potential transport capacity concept by the following equation.

$$S_e = \frac{h}{t_c}(c_{eq} - c) \tag{3–21}$$

In the above equation S_e is negative for deposition and positive for erosion; t_c is the adaptation timescale, which is determined in case of deposition ($c_{eq.} < c$) using Eq. (3–22) and for erosion ($c_{eq.} > c$) using Eq. (3–23), given by McAnally (1989).

$$t_c = t_d = \text{ Larger of } \begin{cases} C_d \dfrac{h}{w} \\ \Delta t \end{cases} \tag{3–22}$$

$$t_c = t_e = \text{ Larger of } \begin{cases} C_e \dfrac{h}{U} \\ \Delta t \end{cases} \tag{3–23}$$

where Δt is the numerical time step, and C_d is a damping factor, reflecting the effect of flow velocity in damping sediment deposition compared with still water; and C_e is the damping factor of re-entrainment which compensates for the application of resultant depth-averaged velocity (U) instead of near-bed velocity in Eq. (3–23). In the case that the computed adaptation timescale is smaller than Δt, the latter value is applied. This implies that the adaptation timescale should be resolvable by the designated time step. In other words, the adaptation timescale should be larger than the numerical time step.

In the above equation w is the sediment fall velocity and for a range of sediment diameter 100-1000 μm, it can be determined by Zanke (1977):

$$w = \frac{10\nu}{0.8 d_{50}} \cdot \sqrt{\left(1 + \frac{0.01 g (\rho_s/\rho - 1)(0.8 d_{50})^3}{\nu^2}\right)} - 1 \qquad (3\text{–}24)$$

In the above equation ρ_s is the grain density, d_{50} is a mean grain diameter (50% of grains are smaller than this diameter) and ν is kinematic viscosity of fluid. Eqs. (3–21) to (3–23) are equivalent to Eq. (2–8) and the above-mentioned damping factors are equivalent to $1/\alpha_0$ in the latter equation.

3.2.2 Mixing coefficient

Mixing in shallow meandering rivers is due to turbulent diffusion and dispersion. Turbulent diffusion coefficient is the proportionality factor relating flux to concentration gradient in turbulent flows in analogy with molecular diffusion. This analogy was derived first by Taylor (1921) for a stationary homogenous turbulent flow, such as a flow in an infinitively long straight uniform channel with constant depth and great width. In Taylor analysis, the time of presence of particles in flow was larger than the Lagrangian timescale[1] ($t > T_L$). In this case the diffusion coefficient can be assumed to be constant (in time). In reality, turbulence is often not homogenous as was originally assumed by Taylor. The theory of spatially varying diffusion coefficient was first introduced by Kolmogorov (1931, 1933). Eq. (3–20) is a simplified 2-dimensional depth-averaged version of Kolmogrov equation (in the latter, the diffusion coefficient are not scalar but tensor). In summary, the turbulent diffusion coefficient in Eq. (3–20) is applicable to situations in which particles are longer in the flow than Lagrangian timescale and have spread over a distance larger than Lagrangian length scale of turbulent motion (for example several water depth in a uniform straight channel).

Spreading in flow direction is primarily due to the velocity gradient in cross section in rivers and estuaries (Fischer et al., 1979). This lateral gradient of velocity increases the spreading speed of the particles in such shear flows. The time and length scales of spreading are much different from those of molecular diffusion, therefore different values of diffusion coefficient are expected, which is named dispersion coefficient (since it results from shear flow dispersion). While turbulent diffusion coefficient represents the point diffusion, dispersion coefficient is actually a bulk (for example cross sectional average) transport coefficient expressing the diffusive property of the velocity distribution, by assuming balance between the lateral diffusive transport and longitudinal advective transport (Taylor's assumption, 1953). This assumption is only attained, when after a long time the lateral diffusive transport has evened out the lateral distribution of concentration and the particles have been spread over a long distance in longitudinal direction. Under this circumstance, the longitudinal shear flow dispersion tends to retain a relatively constant concentration along the channel and concentration gradient in longitudinal direction remains constant.

In meandering rivers the dispersion effect has to be included in the mixing coefficient. The lateral and vertical mixing coefficient for mass are considered to be equal to their counterpart-

[1] It is "a measure of how long the particles take to lose memory of its initial velocity" (Fisher et al., 1975)

mixing coefficient of turbulence. They are proportional to friction velocity and flow depth as follows:

$$\Gamma = e^{*} u_{*} h \tag{3–25}$$

In the above equation "Reynolds analogy" has been applied and e* is dimensionless diffusivity coefficient, which is about 0.067 for vertical turbulent mixing and 0.1-0.2 for lateral turbulent mixing (Fischer et al., 1979). In natural streams, bends and irregularity of the side walls (such as existence of groin field) as well as flow depth have thought to have negligible effect on the vertical turbulent mixing, since the scale of vertical motion is limited by the local water depth. Hence the above equation with the mentioned proportionality factor has been customarily applied for vertical mixing. However, the mentioned factors can largely impact transverse mixing, as already discussed, so that the proportionality factor ranges from 0.3 to 0.8 with an average of 0.6 (Fischer et al., 1979; Pavlovic, 1981; Pasche, 1984). Therefore lateral mixing (assuming e* =0.6) is almost 10 times larger than vertical mixing (e* =0.067). As a result vertical mixing can be regarded as instantaneous compared to transverse mixing leading to the assumption that the effluent is uniformly distributed in vertical direction in practical problems (Fischer et al., 1979).

It is difficult to separate the effect of dispersion from turbulent diffusion in longitudinal direction, but it is presumed that longitudinal turbulent mixing is of the same rate as lateral mixing (Fischer et al., 1979). According to Elder (1959), the longitudinal dispersion coefficient can be determined as follows:

$$\Gamma_{Disp} = 5.93 u_{*} h \tag{3-26}$$

The proportionality factor is about 40 times the expected magnitude of the turbulent mixing coefficient. Since these two terms are additive, the turbulent diffusion coefficient can be ignored. However, experiments in natural streams have shown that the proportionality factor ranges from 140 to 500 and even 7500 in Missouri River (see in Fischer et al., 1979). Therefore, Elder's result does not apply to natural streams as explained by Fischer. In the mentioned results either dye or radioactive materials have been invariably applied. Whereas the properties of sediment, such as settling velocity and diameter, can affect the value of dispersion coefficient. This can be recognized in simulation of sediment transport in rivers for example by Xu (1998), in which a dispersion coefficient of 0.8 (in Eq. 3-26) for longitudinal as well as transverse mixing has been used. Diffusion/dispersion coefficient for sediment transport has been frequently computed using the following equation (for example, Celik and Rodi, 1988; Wu et al., 2000; Olsen, 2003; Duan and Nanda, 2006 and etc.):

$$\Gamma = \frac{\upsilon_t}{\sigma_c} \tag{3-27}$$

In the above equation σ_c is turbulent Schmidt number and υ_t is eddy viscosity. This equation can be obtained by substituting e* from Eq. (3–8) in Eq. (3–25).

The Schmidt number reflects the ratio between fluid diffusivity and sediment particle diffusivity. This parameter has been used as calibration parameter to include the effect of sidewall and bed irregularities as well as secondary currents, which cannot be resolved by Eq. (3–20). For two-dimensional depth-averaged models, Ye and McCorquodale (1997) suggested that the Schmidt number should be significantly reduced to account for increased mass diffusivity in river bends and recommended a value of 0.15, while Duan and Nanda (2006) used a value of 0.02 in the calibration of a two-dimensional depth-averaged advection-diffusion model for pollutant transport in a channel bend. Wu et al (2000) adopted a value of σ_c =1 in modelling of flow and sediment transport in a 180° trapezoidal channel bend, in which sediment has been mainly transport by bed load.

Depending on the ratio of particle size to turbulence length scale as well as particle Stokes number, turbulence can be attenuated or enhanced by suspended particles (refer to Cao and Carling, 2002b). In the current work, Eq. (3-27) will be applied with the restriction that suspended sediment has no effect on modulating horizontal turbulence. In case low concentration of suspended sediment or fine particle size, this restriction should be justifiable (Muste and Patel, 1997). This implies that the diffusion coefficient (Γ) in Eq. (3–20) is practically equal to the turbulent eddy viscosity in Eq. (3-27), implying Schmidt number equal to one (Wu et al., 2000; Olsen, 2003). Since, the sediment is transported mainly as bed load in the current study case, this value of Schmidt number seems to be reasonable (Wu et al., 2000). It should be noted that the above-mentioned discussion applies to suspended sediment transport, while in the current application a mixture of bed- and suspended load, total sediment transport, is being considered in Eq. (3–20).

3.3 Bed evolution

Bed erosion along the wetted perimeter of the river occurs through an imbalanced exchange of sediment particles between bed and water column in non-cohesive soils. This imbalance is the result of deficit or excess in the sediment concentration in the water column with respect to the sediment transport capacity of the local flow. To be more specific, it can be assumed that the sediment exchange occurs between a transient layer over rigid bed and the water column (including bed load layer), namely active bed layer. This layer constitutes a mixing zone in which sediment of different sizes may be eroded and deposited frequently forming an unconsolidated layer, whereas the rigid bed layer is a relatively more consolidated layer. To model this process mathematically, several methods have been developed including single grain size models assuming no active layer to more complex models considering graded size sediment with sediment sorting and active multi-bed layer models (Borah et al., 1982; Spasojevic and Holly, 1994; Gessler, et al., 1999, Wright and Parker, 2005, etc.)

In the present work, alluvial river with uniform sandy bed has been considered relaxing the requirement of considering armouring and grain sorting. This assumption will be later justified by measurement of sediment properties (refer to Ch. 6.1). A Lagrangian method has been applied, in which bed evolution occurs through exchange of (single-sized) sediment in

water column (including bed load layer) with a single active bed layer, utilizing the concept of potential transport capacity (schematically shown in Fig. 3-3). In this context, bed load layer plays the role of a transient layer for vertical exchange between underlying active bed layer and overlaying suspended load layer by assuming that the local bed load layer remains always at its potential transport capacity (C_{b*}), which depends on the local flow and sediment properties. This permits application of total sediment transport method, by considering bed and suspended load as one layer regardless of the details of interaction between these two layers.

The top of active bed layer has been considered as the actual bed level. When total sediment transport is equal to potential transport capacity (net deposition or erosion is zero), no bed level change takes place (Fig. 3-3a). In case, suspended sediment concentration in water column is less than potential transport capacity (Fig. 3-3b), the deficit is compensated by removing sediment from underlying layer (bed load layer). However, since bed load layer remains in potential transport capacity, this removal of sediment is balanced by removing sediment from the underlying active bed layer, which results in degradation of bed surface.

On the other hand, if suspended sediment concentration in water column is greater than the potential transport capacity (Fig. 3-3c), the excess sediment is deposited into the bed load layer. This increases the concentration of the bed load layer beyond its potential transport capacity, which causes deposition on underlying active bed layer and aggradation of the river bed.

Accordingly, sediment flux just above bed load layer does not influence change of bed load layer thickness, but active bed level. This allows considering bed load layer together with suspended load layer as one layer with an average potential transport capacity, above which bed aggradation and below which bed erosion occurs.

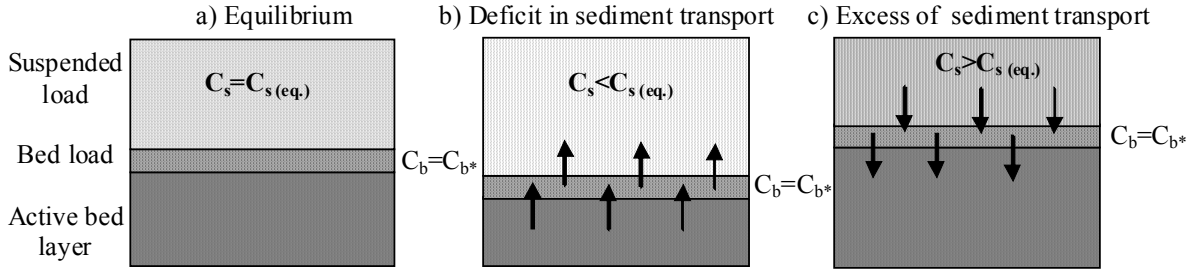

Figure 3-3 Conceptual model of bed erosion and deposition in case of potential transport capacity

In other words, local bed erosion or deposition rate is proportional to the difference between total sediment transport capacity and total sediment transport rate (King, 1993):

$$\rho_s(1-\lambda)\frac{\partial z_0}{\partial t} = \frac{h}{t_c}(c - c_{eq}) \tag{3–28}$$

In the above equation λ is the porosity of bed material, z_0 is bed elevation with respect to a datum, h is water depth, ρ_s is the sediment density, t is time and t_c is the adaptation timescale

(already introduced). c and c_s are total sediment concentration and potential transport capacity (equilibrium total sediment concentration) in [kg/m^2/m of depth], respectively. The latter is computed by any of the total sediment transport capacity formulation addressed in Ch. 3.2.1.

3.4 Bank evolution

In the present mathematical approach, bank failure mechanisms including undercutting (due to fluvial erosion on bank surface and bank-toe as well as because of shear failure along a shallow slip surface) together with cantilever failure (shear and tensile failure types) have been considered. It should be noted that bank retreat due to the fluvial erosion of the bank surface in dense non-cohesive (sandy) soils is negligible compared to the sudden failure due to the shear failure. Sapping has been regarded here as a minor process in bank retreat, since it mainly occurs above a water-restricting layer or between layers with contrasting conductivities (Wilson et al., 1991; Hagerty, 1991; Jones, 1997). Therefore, it will not be considered here because of treating single layer riverbank with homogenous sandy soil.

3.4.1 Undercutting

The process of undercutting in the submerged zone is the result of the sequence of bank-toe erosion and shear failure along a shallow slip failure surface (Fig. 3-4A). Bank-toe erosion is determined using the same equation as for bed evolution (Eq. 3–28). Shear failure occurs due to the imbalance between resisting and driving forces. The imbalance is caused because of the loss of support at the basal zone and matric suction in the submerged zone. In this zone, it is assumed that the water table in the riverbank is in equilibrium with the water stage in the river at least in the proximity of the bank surface and along the failure plane. This implies that in the submerged zone, matric suction is diminished along the shallow failure plane. Hence, modelling of pore water pressure can be avoided in this region in contrast to the cohesive soils in which the deep-seated failure plane may pass through regions with negative pore pressure due to the sharp gradient of the phreatic line near bank surface. In unsteady flow, the water table changes in response to alteration of water stage in the river. Therefore, the theoretical approach presented in the following is restricted to the situations in which the rate of the water stage alteration in the river is slow or rapid draw down occurs seldom so that equilibrium state between water table and water stage in the river can be assumed to hold.

Based on the above-mentioned hypothesis, the remaining resisting forces in submerged zone are friction force and apparent cohesion due to compaction. The former is correlated to the friction factor of the sand (a physical property depending on the type of the soil) and specific weight of the sand. The latter is a function of soil property, soil moisture and compaction energy. It is assumed that the stabilizing effect of compaction (and cementation) in the submerged zone can be represented through a raised angle of repose, designated here as "critical dense angle of repose (φ^c)". It is further presumed that failure occurs along a critical surface, which has a slope equal to φ^c. The riverbank slope remains stable as long as the

resisting forces (F_r) along the mentioned surface can compensate the driving forces (F) (Eq. 3-29).

$$F_r - F \geq W \tan\varphi^c \cos\beta - W \sin\beta \geq 0 \tag{3-29}$$

Here, the parameters have been already defined in Fig. (2-11). Simplification of the above equation yields:

$$\cos\beta(\tan\varphi^c - \tan\beta) \geq 0 \tag{3-30}$$

Since cos β is a positive entity for submerged natural slopes, the bank remains stable as long as $\varphi^c \geq \beta$. This relation is often presented in form of a safety factor as follows:

$$SF = \frac{\varphi^c}{\beta} \geq 1 \tag{3-31}$$

Thus as soon as the slope of (a part of) the riverbank in the submerged zone reaches beyond its crtical dense angle of repose, the bank material of the over-steepened area (up to the water surface) slides in a planar shallow layer into the scoured bank-toe leaving a hanging zone in bank profile over water surface and an undercutting zone beneath it (Fig. 3-4B). The failure surface may be parallel to the initial bank surface but it is not necessarily so. The failed bank material is deposited at the bank-toe with a maximum slope of angle of repose for loose materials (φ).

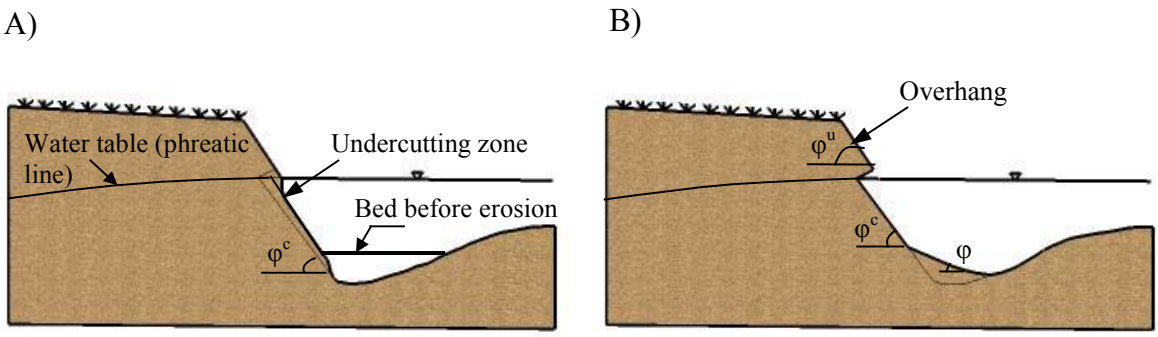

Figure 3-4 Schematic demonstration of undercutting process in non-cohesive banks according to the measurements. A) Continuous erosion of bank (-toe) before undercutting takes place. B) Undercutting, formation of the overhang and deposition on the bank-toe.

3.4.2 Cantilever failure

In contrast to the failure in submerged zone, failure plane can assume a steep (up to 90°) to reverse slopes (larger than 90°) in cantilever failure of dense non-cohesive soils. This can be contributed to the effect of negative pore water pressure and vegetation roots. In the overhang

zone, pore water pressure passes through a transient zone from positive to negative values above water table (Fig. 3-5). Therefore, pore pressure is no more in equilibrium with water stage in the river and it should be considered in stability analysis of the overhang. This is particularly notable when dealing with dynamics of the flow regime. The methods of computation of negative pore pressure distribution above the water table as well as additional cohesion due to the vegetation root have been presented in Ch. 3.4.4 and 3.4.5.

Two types of cantilever failure have been considered in the present work, namely, shear and tensile failure (Fig. 3-5). The overhang failure along steep (positive) slopes is a shear failure type while along reverse (negative) slope is a tensile failure type. However, failure plane in tensile failure has been here assumed to be parallel to the water surface or slightly upward (Fig. 3-5). This is consistent with the hypothesis of equilibrium state between water table and water stage. This type of failure occurs due to the loss of matric suction when the lower part of the overhang becomes saturated because of the submergence during rise of water stage.

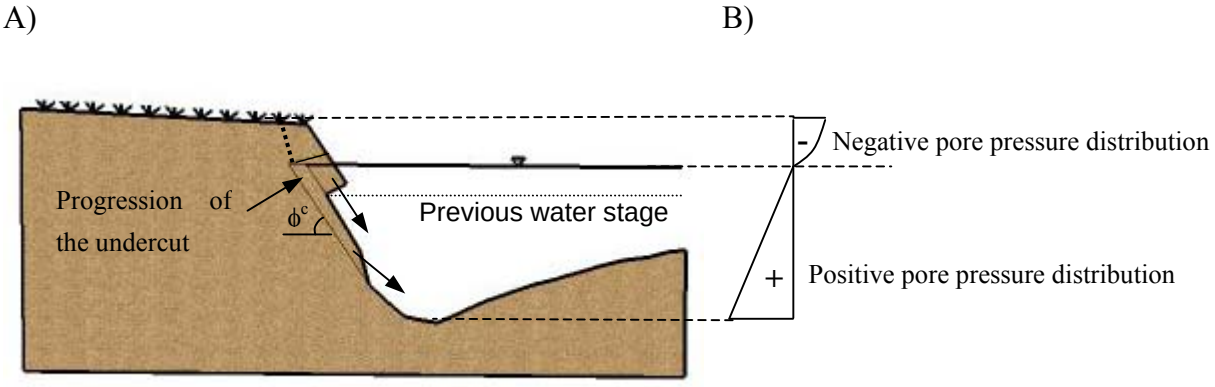

Figure 3-5 Progression of undercutting and cantilever failure in unsteady flow. A) Slip and tensile failure of the submerged bank and overhang. B) Pore water pressure distribution in the riverbank.

Shear failure

Shear failure is triggered when undercutting front has advanced enough to destabilize the overhang, given a flow regime. The balance between resisting and driving forces determines the stability condition. It is assumed that shear failure occurs along a failure plane with a slope equal to a raised angle of repose, which accounts for the effect of compaction (and cementation) as well as negative pore pressure, named here as " unsaturated dense angle of repose (φ^u)". The resisting force (F_r) along the failure plane comprises apparent cohesion force due to the matric suction ($\psi \tan\phi^b$), internal friction force ($N \tan\phi = W \cos\varphi^u \tan\phi$) and additional cohesion force due to the vegetation roots ($c_r L_{eff.}$). The driving force is the weight component of the failing block along failure surface. The balance of the mentioned forces can be shown as follows:

$$F_r = \left(c_r L_{eff.} + \psi \tan\phi^b + W \tan\phi \cos\varphi^u \right) \geq W \sin\varphi^u \qquad (3\text{-}32)$$

In the form of a safety factor this equation can be expressed as follows:

$$SF = \frac{\left(c_r L_{eff.} + \psi \tan\phi^b + W \tan\phi \cos\varphi^u\right)}{\left(W \sin\varphi^u\right)} \tag{3–33}$$

Here c_r is additional cohesion due to the root reinforcement, which will be illustrated in more details in Ch. 3.4.5; $L_{eff.}$ is the effective length (area per width) of root zone; ψ is positive force produced by matric suction on the unsaturated part of the failure surface (kN/m). Determination of this parameter has been described in Ch. 3.4.4; and W is weight of the soil block (kN). The term ϕ^b should be determined by in situ measurement as referred to in Ch. 3.4.4 or should be determined as a calibration parameter.

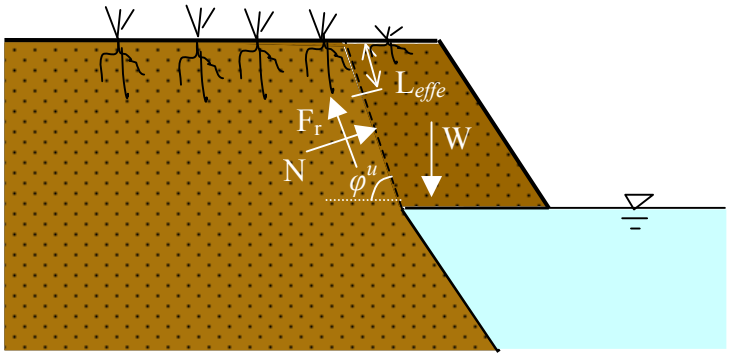

Figure 3-6 Schematic illustration of shear type cantilever failure

Tensile failure

Tensile failure occurs when the soil matrix is in tension. The failure occurs along a failure plain, which may assume a horizontal or an oblique surface (reverse or negative slope) in non-cohesive dense soils, as shown in Fig. (3-7). The most critical failure plane is however an unknown parameter. For simplicity, it is assumed here that this failure plan is horizontal. Nevertheless, the associated inaccuracy needs to be investigated in validation of the model. Under the mentioned assumption, the weight of the block is normal to the failure plane (Fig. 3-7) and the resisting forces (also normal to the failure plane) are those due to the vegetation and matric suction. Hence, the balance of forces yields:

$$F_r = \left(c_r L_{eff.} + \psi \tan\phi^b\right) \geq W \tag{3-34}$$

The above equation can be written in the form of a safety factor as follows:

$$SF = \frac{c_r L_{eff.} + \psi \tan\phi^b}{W} \tag{3–35}$$

It can be seen from the above equation, if matric suction (ψ) reduces to zero the second term in numerator diminishes. Therefore, it can be assumed that as soon as a part of the overhang is submerged, it gets fully saturated (assuming equilibrium condition), which leads to the loss of matric suction. Tensile failure then occurs if the failure plane does not pass through the vegetation root zone or the cohesion force due to vegetation is less than the weight of the soil block.

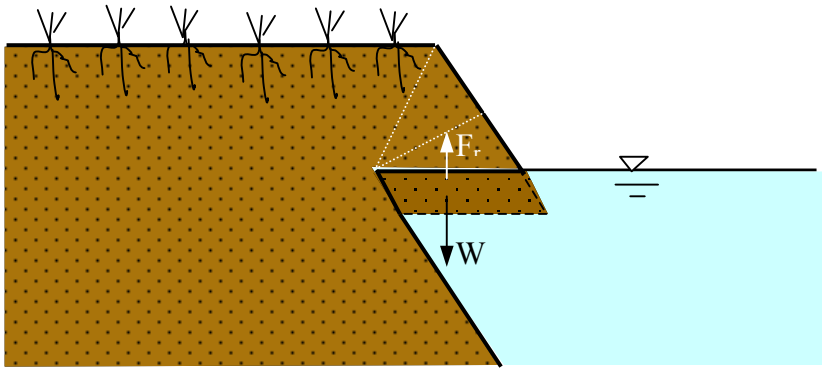

Figure 3-7 Schematic illustration of tensile failure showing the alternative possible failure planes

3.4.3 Distribution of failed bank materials

Failed bank materials slip to the talweg or deposits as a block at bank-toe (for example in the case of cantilever failure). The bank-toe geometry and slope influence the location of deposition of the failed bank material. In the case of steep slope of bank-toe, the particles and blocks may roll down the slope and deposit at the bank-toe, while in the case of mild bank-toe slopes it may remain intact in the beginning or middle part of the bank slope.

Distribution of the failed bank material is additionally dependent on flow situation at the time of failure. In case that the failure occurs during high water stage, most of the failed bank material may be removed, when the water stage remains high for a longer period. While in low water stage, if cantilever failure occurs the failed blocks may remain intact at bank-toe or middle of the bank and be further stabilized by growth of vegetation. Such types of sudden addition of bank material to bank-toe may not alter the overall geometry of the bank-toe region, but the transport of upstream failed bank material as well as near bank sediment transport capacity determine the final geometry of bank-toe, which may give rise to berm formation or bank- or berm-toe erosion.

Along the river bend, erosion of failed bank material is more pronounced at the apex or downstream of it due to the helical flow structure in river bend even in moderate water stage (as long as depth to width ratio is large enough to allow formation of secondary currents). Therefore it is difficult to derive a precise relation to describe this process. Two approaches have been developed to model the distribution of failed bank material, which are explained in the following.

Physically based method

In this method, it is assumed that the failed mass contributes directly or partly to the total sediment transport. In the former case the total failed bank material is assigned as a source term in sediment transport equation (S_{bank} in Eq. 3–20) and the sediment transport model takes care of how to transport the failed mass across and along the river. For the case of shallow slip failure in the submerged zone, it can be presumed as re-suspension of the whole failed material into to the water column as source term and further transport or deposition determined by sediment transport equation.

In the latter case, the rest of the failed material is assumed to deposit directly at bank-toe as bed material causing increase of the local bed elevation. Determination of these two portions is not trivial, as already explained in Ch. 2.3.3, therefore for simplicity reasons, the upper 10% portion of the cumulative grain size distribution has been assumed to deposit directly as bed material in the latter approach.

A problem of such an approach is numerical implementation of source term in transport equation, which may cause numerical instability due to the addition of a large amount of failed mass in a limited zone of the flow field at once.

Slump method

Alternatively, the whole failed mass can be summed to a lumped mass and assumed to deposit at bank-toe zone using a distribution function. This seems to be justifiable for non-cohesive soils such as sand particles with relative large settling velocity, which can be assumed that they are not commonly transported for a long period as suspended load in the water, but deposited immediately at bed. It is obvious that this is a simplification of the physical process. To model this process mathematically, the failed mass resulting from all failure modes (shallow slip failure, tensile and shear failure) are summed (lumped) and distributed over bank-toe by the following set of equations:

$$M(x_i) = \int_{x_0}^{x_i} m\, f(\xi) d\xi \tag{3–36}$$

$$m = \int_{x_0}^{x_i = x_L} M(x) f(x) dx \tag{3–37}$$

$$\int_{x_0}^{x_L} f(x) dx = 1 \tag{3–38}$$

$$f(x) = \frac{n}{(x_L - x_0)^n} x^{n-1} \tag{3–39}$$

In these equations M(x) is the cumulative distribution function of mass (probability mass function) and m is the total failed mass; f is a polynomial function featuring a unit area over the range $<x_0,x_L>$ (starting and ending point of distribution, respectively) which has a similar feature like the delta Dirac function but in a bounded domain. (n-1) is the order of the polynomial function. With the set of above equations mass can be distributed over bank-toe smoothly. It should be noted here that as the order of polynomial increases, a larger portion of the failed mass is concentrated towards the end-point of the bank-toe (Fig. 3-8). While with this method numerical stability may be improved, it is noted that this is not a physically based approach.

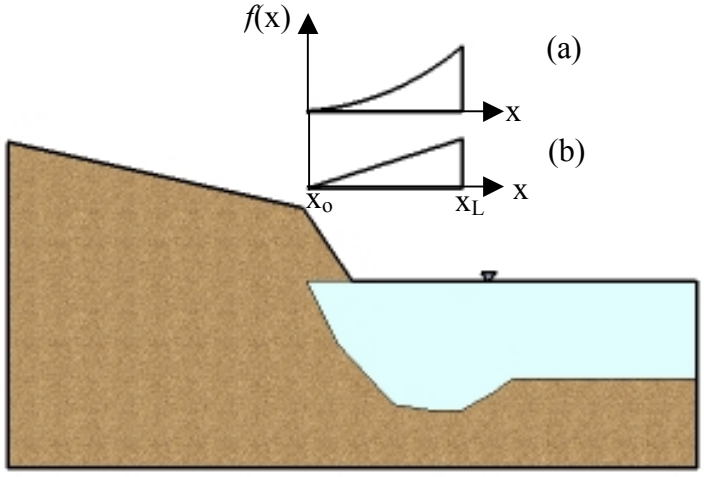

Figure 3-8 Schematic presentation of mass distribution function over the bank-toe. The distribution starts from the water edge on the bank and ends at the deepest point at the bank-toe. (a) polynomial mass distribution diagram (b) linear mass distribution diagram

3.4.4 The effect of pore water pressure

The presence of negative pore water pressure in unsaturated soils increases the shear strength of material which is often manifested in steeper bank slopes than those indicated by friction angle, φ (Simon et al., *20*00). The increase in shear strength due to an increase in matric suction is described by the angle ϕ^b. Fredlund et al., (1978), incorporated this effect into standard Mohr- Coulomb equation as follows:

$$S_r = C' + (\sigma - u_a)\tan(\varphi) + (u_a - u_w)\tan(\phi^b) \tag{3-40}$$

where S_r is shear strength, C' effective cohesion that can be assumed zero in non-cohesive soils, σ is total stress, u_a is pore air pressure, u_w is pore water pressure and φ friction angle in terms of effective stress. The value of ϕ^b is always less than φ ranging between 7° and 26° and increases with degree of saturation (Fredlund and Rahardjo, 1993). In fully saturated soil ($u_a = u_w$), the suction component in Eq. (3-40) disappears and the equation reduces to the standard Mohr- Coulomb equation. The extended form of Mohr-Coulomb failure envelope for an

unsaturated soil can be plotted in a three dimensional diagram with shear strength, and two stress state variables, namely (σ- u_a) and (u_a – u_w), as three axes (Fig. 3-9).

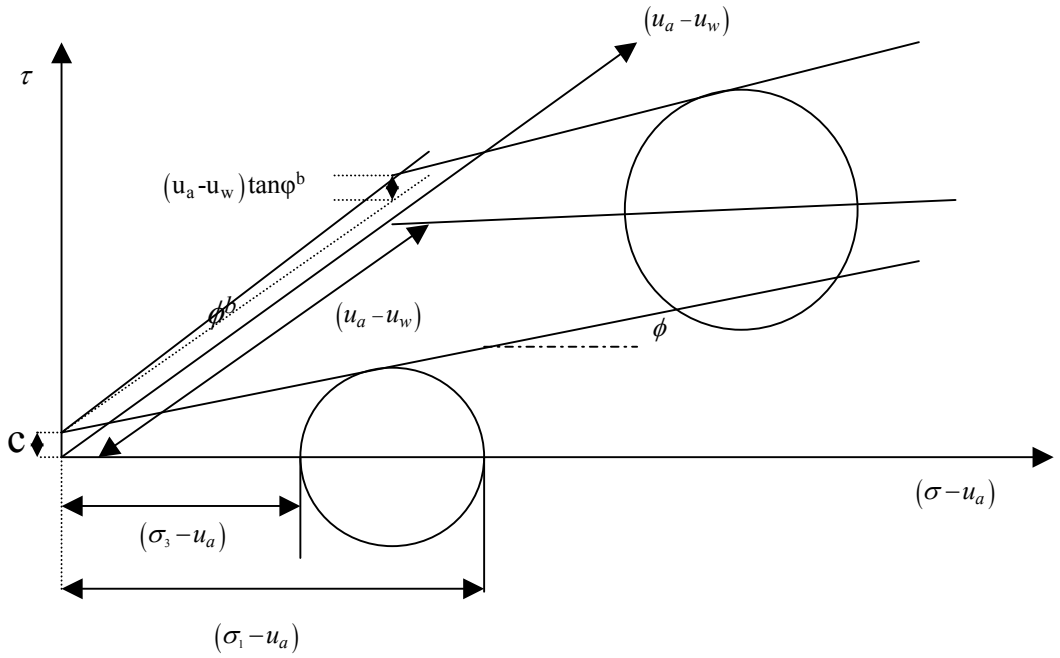

Figure 3-9 Mohr-Coulomb circles for unsaturated soils in three dimensions (Fredlund and Rahardjo, 1993)

The extended failure envelope can be presented as a projection onto the shear stress versus σ-u_a plane (Fig. 3-9). For a given matric suction, the projection is presented as a line with the following equation:

$$S_r = C_a + (\sigma - u_a)\tan(\varphi) \tag{3-41}$$

where C_a is total or apparent cohesion given by:

$$C_a = C' + (u_a - u_w)\tan(\phi^b) = C' + \psi\tan(\phi^b) \tag{3-42}$$

The above equation includes the effect of matric suction (ψ) as well as effective cohesion (C′), although it does not signify that the matric suction is a form of cohesion (Fredlund and Rahardjo, 1993). Using the above equation, the parameter ϕ^b can be calculated if the results of in situ shear strength tests and pore pressure measurements (for example by means of tensiometer) are available (Rinaldi and Casagli, 1999).

As already mentioned, matric suction is a dynamic entity. The effect of a few environmental and hydrological parameters on distribution of matric suction above water table in the soil layer has been schematically illustrated in Fig. (3-10-a to d). As it is seen from these figures matric suction increases rapidly near ground surface, much faster than the equivalent rate of increase of hydrostatic pressure distribution. Furthermore, the distribution of matric suction

depends on several parameters such as seasonal fluctuation of water table, surface cover, evaoptranspiration, rainfall and etc. Therefore, it is required that the pore water pressure and its dynamics be considered in the stability analysis of the riverbank, and in the present case overhang failure.

Modelling of dynamics of the pore pressure distribution and seepage in the soil layer can be achieved by solving the two-dimensional unsaturated flow conservation equation, called Richard's equation (Eq. 2-10). This can be avoided by assuming that the water stage in the river is in equilibrium with the water table in the riverbank in the vicinity of the bank surface. A simple polynomial function (Eq. 3–43) has been introduced to consider the effect of the vertical distribution of negative pore pressure in the unsaturated zone of the riverbank. Hydrostatic pressure distribution has been assumed in saturated zone.

As it is inferred from the graphs in Fig. (3-10), the major part of them can be approximated by a polynomial function, although it may not be generally true. This has brought the idea to use such functions to approximate the vertical distribution of matric head over water table in the absence of dynamic simulation of pore pressure distribution, which can be generally represented as following:

$$h_p = \frac{\psi}{\gamma_w} = \sum_{n=1}^{i} a_n h^n \qquad (3\text{–}43)$$

here ψ is matric suction in [Pa] and h_p is matric head in [m], h is elevation over water table (which is assumed to be in equilibrium with water stage in the river) and a_n is the n^{th} coefficient of the polynomial function of order n. The coefficients and order of the polynomial function should be determined as calibration parameters. Such polynomial functions of second and third order are depicted in Fig. (3-11) together with hydrostatic distribution (n=1). The computed matric suction profiles in this figure seem to be comparable with those in Fig. (3-10-a). However, matric suction distribution may not be well reproduced by such functions near the ground surface for some cases including vertical infiltration of rainfall.

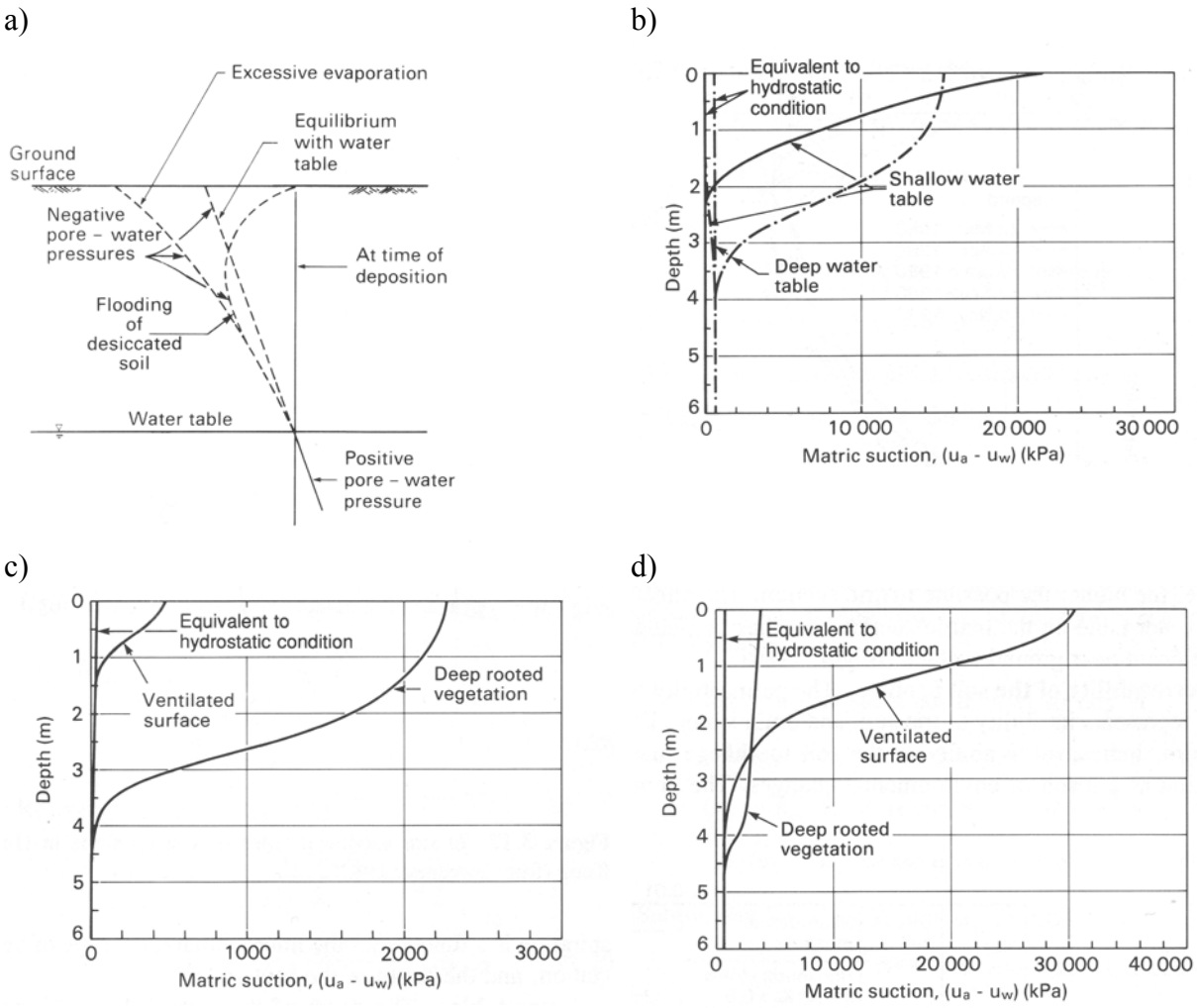

Figure 3-10 Typical distribution of pore pressure and the effect of environmental parameters on its distribution (Fredlund and Rahardjo , 1993). (a) Typical pore pressure distribution. (b) Typical suction profile due to seasonal fluctuations of water table. (c) Drying influence on shallow water table. (d) Drying influence on deep water table

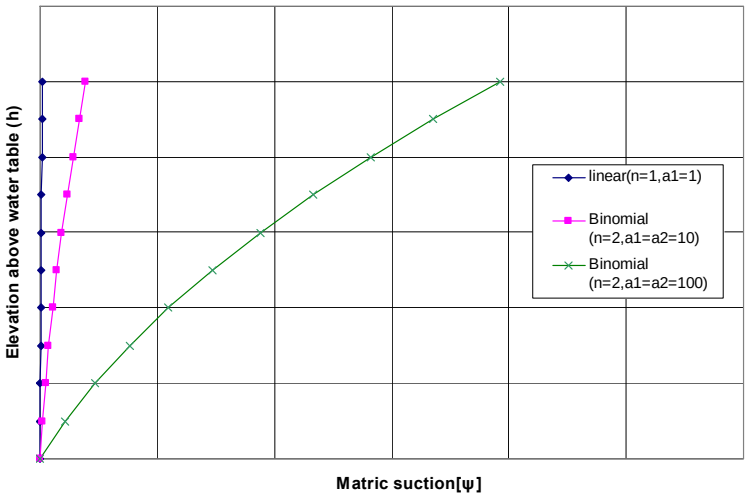

Figure 3-11 Matric suction distribution over water table using polynomial approximation functions for order of n=1 (equivalent to hydrostatic distribution) and n=2 (Binomial).

3.4.5 Vegetation effect on bank stability

Vegetation covering top of the bank impacts the stability of the riverbank. In case of grasses and shrubs the root fibers increase the stability of the riverbank through additional tensile strength created by building a reinforced soil-matrix. However, this increase of stability is limited to the root zone and does not impact the overall stability of the riverbank. Nevertheless, in the overhang zone it may play a significant stabilizing role against cantilever failure, which necessitates inclusion of this factor in stability analysis of the overhang.

The tensile strength due to root reinforcement is considered as additional shear strength or cohesion in the soil. To include this effect, Eq. (2-15) presented in Cancienne et al. (2008) has been used to account for the local stabilizing effect of root zone along the critical failure plane as follows:

$$c_r \cong 1.2T_r\left(\frac{A_r}{A}\right) \tag{3–44}$$

T_r (the tensile strength of roots in KPa) needs to be determined by field measurements. For different types of vegetations a range of c_r values has been provided in Cancienne et al., (2008). Impact of overburden of vegetation mass on bank stability is not needed to be considered here (due to small vegetation).

3.5 Closure

The process of undercutting and cantilever failure in non-cohesive soils under the influence of dynamics of the flow regime needs to be experimentally investigated to prove the developed theory in the present work. The proposed mathematical approach includes assumptions and hypothesis that should be proved by measurement and verified by numerical simulations. The velocity distribution across the river bend should be measured to prove if secondary currents are negligible in the present shallow meanders. Turbulent models and their parameters need to be determined by measurement and verified by simulation. Diffusion/ dispersion parameter in sediment transport model is required to be determined by measurement and verified by simulation.

In the bank evolution model the hypothesis of equilibrium state between water stage in the river and water table needs to be proved. Furthermore, the following parameters should be determined by experiments and/or validation of the model: dense angle of repose, unsaturated dense angle of repose, additional cohesion due to vegetation roots as well as parameters and order of pore pressure distribution function.

4 Numerical approach

4.1 General concept

The numerical approach in the present work for morphodynamic simulation is based on the decoupled[1] solution of four mathematical models, namely, a hydrodynamic model, a sediment transport model, a bed evolution model and a bank failure model, as shown schematically in Fig. (4-1).

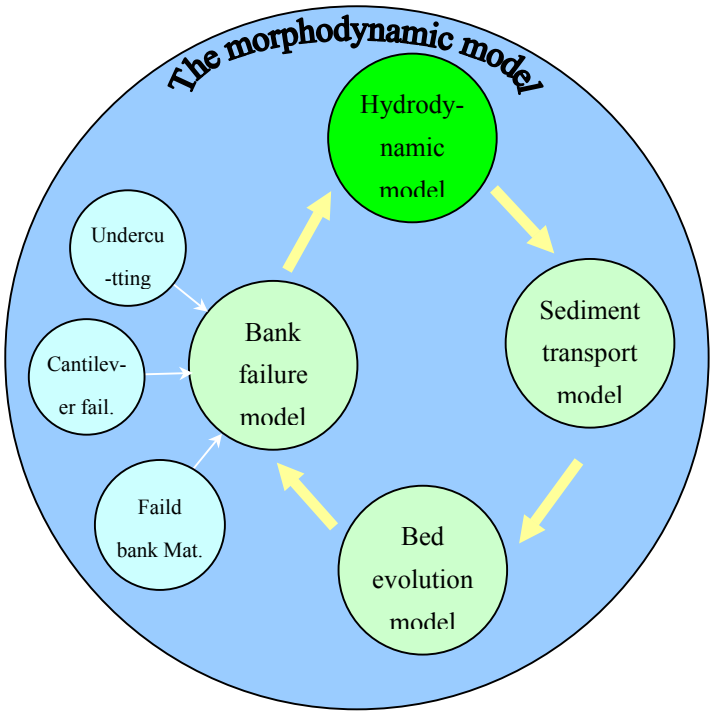

Figure 4-1 Conceptual process of morphodynamic simulation of the riverbank erosion

[1] Decoupled solution means the governing equations of mathematical models are solved sequentially and not at the same time.

A novel numerical model for simulation of bank evolution (undercutting and cantilever failure) has been developed based on the theory presented in Ch. 3. This new model has been implemented in the fully unsteady 2D depth-averaged morphodynamic model of RMA-Kalypso. This is based on the well-known model RMA-10 developed by King (1993), which has been further refined and modified by Lippert (2005), Nasermoaddeli and Pasche (2006), Plöger (2007), Schrage and Pasche (2009). The hydrodynamic model, sediment transport and bed evolution equations used in this model have already been presented in Chs. 3.1, 3.2, and 3.3, respectively. These equations are discretized using Finite Element Method (FEM). It is not intended here to present the discretization of the hydrodynamic and sediment transport equations (for details, the reader is referred to King, 1993), but rather to demonstrate mainly the developed bank evolution model. Therefore, only key issues regarding the discretization and solution method in RMA-Kalypso are presented in the following.

The numerical domain can be composed of triangular as well as rectangular finite elements with corner and mid-side nodes. Velocity terms and concentration are approximated using quadratic approximation functions, while the pressure term (water depth), the bed elevation and the source term in sediment transport are approximated using linear approximation functions.

The hydrodynamic and sediment transport equations are solved decoupled using the iterative method of Newton-Raphson. A semi-implicit finite different scheme is applied for the numerical solution of time derivatives of state variables:

$$\left(\frac{\partial \mathrm{X}}{\partial t}\right)_{t+\Delta t} = \frac{\theta}{\Delta t}\left(\mathrm{X}^{t+\Delta t} - \mathrm{X}^{t}\right) - \left(\theta - 1\right)\left(\frac{\partial \mathrm{X}}{\partial t}\right)_{t} \tag{4–1}$$

here, X is the state variable vector and the superscript denotes the time step; θ is a weighting parameter. Setting θ =0 converts Eq. (4–1) to a fully explicit scheme, while with θ =1 it is changed to a fully implicit scheme, and with θ = ½ it is identical to Crank-Nicolson scheme. As $\theta \rightarrow 2$, the numerical stability decreases, and with θ =2 a time centred semi-implicit scheme is obtained. Explicit methods are numerically unstable for Courant-Friedrichs-Lewy (CFL) greater than 1, while implicit methods are unconditionally stable. A value of θ =1.8 was adopted in this work, without experiencing numerical instability.

For calculation of net deposition or erosion rate, Eq. (3–21) is applied. Updating of bed elevation due to the net deposition/entrainment is achieved using Eq. (3–28), which is computed numerically on each corner node (Fig. 4-2) by means of the following equation, while the mid-side nodes are linearly interpolated.

$$\Delta z = \frac{h \cdot \Delta t}{\left(1-\lambda\right)\rho_s}\left\{\left(\frac{1}{\theta}\right) S_e^{\,t+\Delta t} + \left(\frac{\theta - 1}{\theta}\right) S_e^{\,t}\right\} \tag{4–2}$$

The source term (S_e) in this equation is computed using Eq. (3–21).

The new bank erosion model comprises three main sub-models: undercutting, bank failure (tensile and shear failure) and distribution of failed bank materials (refer to Ch. 3.4). The effect of negative pore pressure (Eq. 3–43), vegetation (Eq. 3–44), and cementation (by means of increased saturated angle of repose) are considered in the stability analysis of the riverbank (Eqs. 3-31, 3–33, 3–35). Distribution of the failed bank material can be computed using any of the methods presented in Ch. 3.4.3.

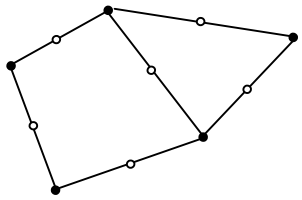

Figure 4-2 Depiction of corner nodes (solid black circles) and mid-side nodes (hollow circles)

In the decoupled method, after each converged hydrodynamic time step, the suspended sediment transport and bed evolution models are run sequentially to compute new bed elevation in the river. Having updated the riverbed topography, it is investigated if the riverbank is stable by the methods described in Ch. 3.4. Provided that no riverbank erosion and failure occurs, the model computes the next time step in an unsteady simulation, otherwise the bank and bed profile are updated after distributing the failed bank material. The mentioned computation procedure is depicted in the flow chart diagram in Fig. (4-3).

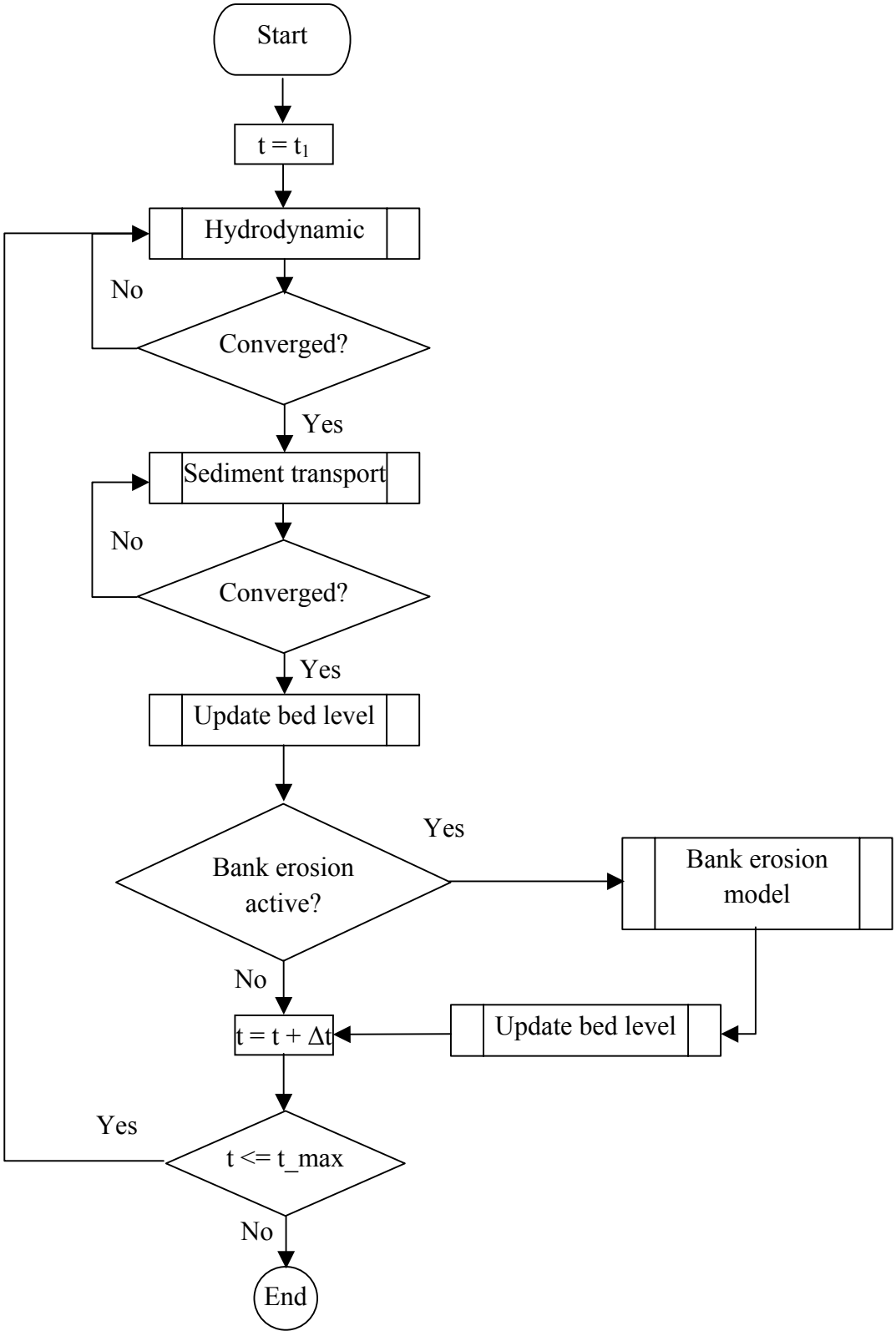

Figure 4-3 Flow chart diagram of the morphodynamic model.

4.2 Bank evolution model

4.2.1 Concept of conjugate domain (2 ½ dimensional model)

Since undercutting creates vertical and negative slope in the riverbank, it is not possible to model it directly using common methods of generation of 2D numerical mesh or even 3D-layered numerical mesh. To remove this limitation, an innovative conjugate domain concept was developed, which is described in the following.

In a semi-structured finite element domain, comprising rectangular as well as triangular elements (see Fig. 4-4a), cross sectional profiles that join the sides of the rows of finite elements (the dark green thick lines in the mentioned figure) can be used to establish a domain, which is here called "conjugate domain" or equivalently "profile domain". It is common to study temporal evolution of the riverbank by means of such typical cross sections across the river reach under study in a domain comprising vertical and lateral dimensions (z and d in Fig. 4-4b). This transfers two-dimensional elements in FE-domain into one-dimensional elements (sides of 2D elements) in profile domain.

a)

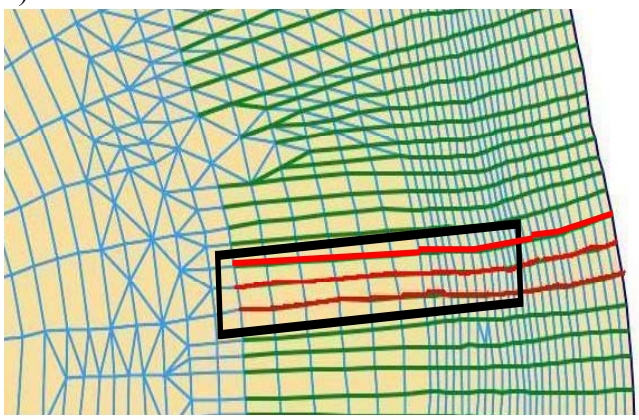

b)

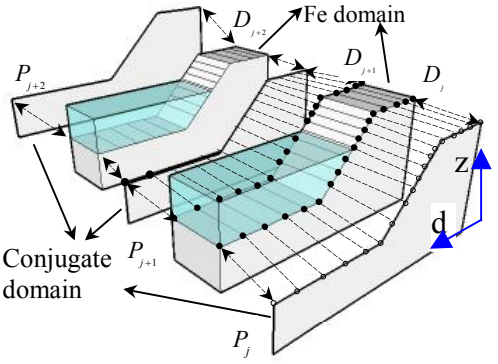

Figure 4-4 Illustration of (half) cross sectional profiles (green lines) across an eroding river bend reach joining sides of FEs (a) and a schematic initial bank profile prior to erosion in FE- and conjugate domains corresponding to the red marked elements (b)

Although, it is not necessary to establish profiles from both sides of a row of elements, as shown in the just mentioned figure, this is, however, recommended especially for long-term simulations. Since in such cases a substantial amount of morphological evolution might be expected, which would be included only along one side of the elements, if both sides of the elements were not included in conjugate domain. This can result in undesired distortion of finite elements.

The more straight the line the mentioned element sides build, the less error is associated with the transformation to the profile domain. The cross sectional profiles do not need to span the whole cross section, although generally it may span from one flood plain to the other. However, it should be extended enough towards the main channel to enable considering the

effect of fluvial bank-toe erosion in bank evolution in conjugate domain. It is recommended to apply triangular element in the long-term morphological simulations, since the nodal displacement in triangular elements is not likely to result in distortion of the element, while in rectangular elements relative displacement of the nodes may result in bending of the element and generation of folded surfaces as shown in Fig. (4-5).

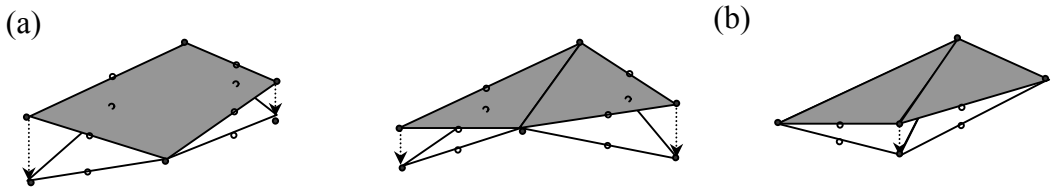

Figure 4-5 Illustration of deformation of elements due to nodal displacement (solid circles are corner nodes and hallow circles are mid side nodes). a) A quadratic element, b) triangular elements. Dark areas show the element surface before deformation. Arrows show the displacement of corner nodes. The mid side nodes are linearly interpolated

Flow field, sediment transport and bed evolution are computed in FE-domain comprising an idealized bank profile, excluding probable vertical faces or reverse bank slopes (for example overhang zone). The complex riverbank geometry is discretized on conjugate domain, in which morphological evolution of the riverbank is computed based on stability analysis. The initial geometry of the profiles in conjugate domain can be either identical to FE domain (Fig. 4-4b) or in a complex natural form, determined by field measurements, including discontinuities (Fig. 4-6).

Mathematically, Ω is defined here to be the space comprising the river bathymetry, Λ the space including the nodes of finite elements along the cross sectional profiles (FE-domain), and Θ the space comprising the nodes in conjugate domain. Thus the mapping (g_j) from FE-domain to the conjugate domain can be defined as follows:

$$\Lambda \subset \Omega \subset \mathbb{R}^3$$
$$\#\{\Lambda\} < \infty$$
$$\#\{\Lambda\} = n \in \mathbb{N}$$
$$\Theta \subset \mathbb{R}^2$$
$$\#\{\Theta\} < \infty$$
$$\#\{\Theta\} = k \in \mathbb{N}$$
$$\Lambda = \bigcup_{j=1}^{m} \Lambda_j \ , \ \Lambda_j \cap \Lambda_i = \varnothing \quad i \neq j,\ i, j = 1,...m \in \mathbb{N} \tag{4–3}$$
$$\Theta = \bigcup_{j=1}^{m} \Theta_j \ , \ \Theta_j \cap \Theta_i = \varnothing \quad i \neq j,\ i, j = 1,...m \in \mathbb{N}$$
$$g_j : \begin{cases} \Lambda_j \to \Theta_j \\ \begin{pmatrix} x \\ y \\ z \end{pmatrix} \mapsto \begin{pmatrix} \left\| \begin{pmatrix} x \\ y \end{pmatrix} - \begin{pmatrix} x_{1_j} \\ y_{1_j} \end{pmatrix} \right\| \\ z \end{pmatrix} \end{cases}$$

The data set (x_{1j} y_{1j}) in this equation shows the FE- coordinates of the first node in the cross sectional profile j as shown in Fig. (4-6). As it is noted from this definition, the number of nodes in conjugate domain may not be equal to those in the FE-domain. This can already be seen in Fig. (4-6). The reverse mapping $\mathcal{F}$: $\Theta_j \to \Lambda_j$ includes only updating the z coordinate in FE-domain based on those in conjugate domain.

The two mentioned domains are linked together by means of mutual nodal assignment. This has been achieved by linking Finite Element nodes along desired cross sections to the profile nodes in conjugate domain and vice versa (Fig. 4-4b). However, the profile nodes of conjugate domain in overhang zone (nodes between the front of undercutting to the upper edge of the overhang shown in Fig. (4-6), are not directly linked to those in FE domain.

The details of connectivity of nodes between these two domains, mesh adaptation during bank evolution as well as data model created to accomplish this task are demonstrated in the following.

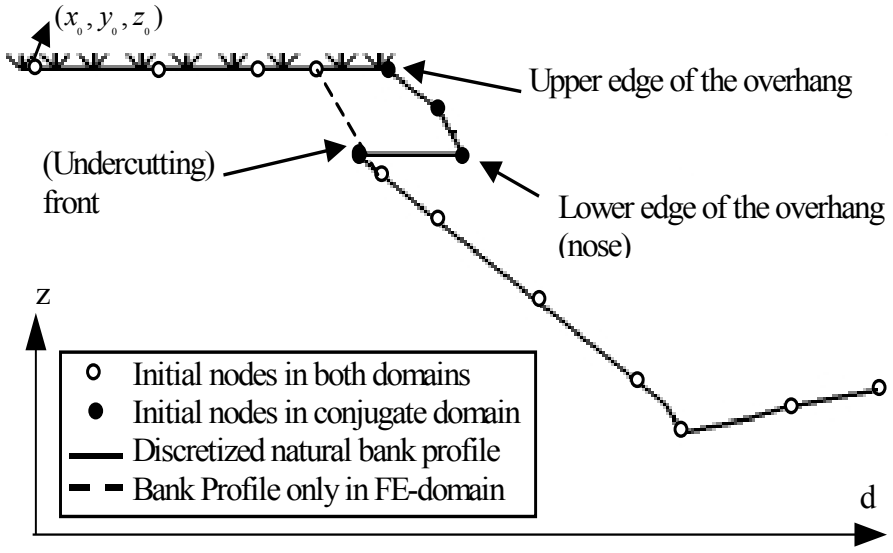

Figure 4-6 Schematic presentation of modelling eroded bank profile in FE- and conjugate domains comprising discontinuity

4.2.2 Implementation

The bank evolution model was implemented in modular form (using FORTRAN programming language) so that each bank erosion process is encapsulated in a module and all modules together form the bank erosion model (BKEM). Before representing the algorithm of the BKEM, it is required to demonstrate the developed data model, which has efficiently enabled modelling of bank erosion using a special adaptive mesh algorithm as well as its linkage with FE domain.

4.2.3 Data model

To represent the conjugate domain and model bank erosion process, a data model using derived data types has been developed consisting of nodes and profiles and their connection to FE-domain (Fig. 4-7, for more details see Appendix D). Connectivity between FE domain and its conjugate (morphological) domain has been established as shown in Fig. (4-7). As explained in the next section, it is not required that all of the profile nodes be linked to the FE-nodes and vice versa. In the array of profile nodes, the attribute of the nodes of each profile describes the function of the node in the profile (for example “Nose” means the edge of the overhang and “Front” implies the front of advancement of undercutting as shown in Fig. 4-6; the remaining attributes will be explained later).

In the case of formation of overhang on both sides of the riverbank, the profile node number corresponding to the control nodes of the overhang geometry (nose and front) are saved in for the left and right banks in Lnose, Lfront, Rnose and Rfront, respectively. If no overhang is formed in either side of the riverbank, these variables are set to zero. Assignment of the

attributes to the nodes is achieved automatically during the simulation of the evolution of bank profile. Currently only one pair of front and nose is allowed for each side of the bank.

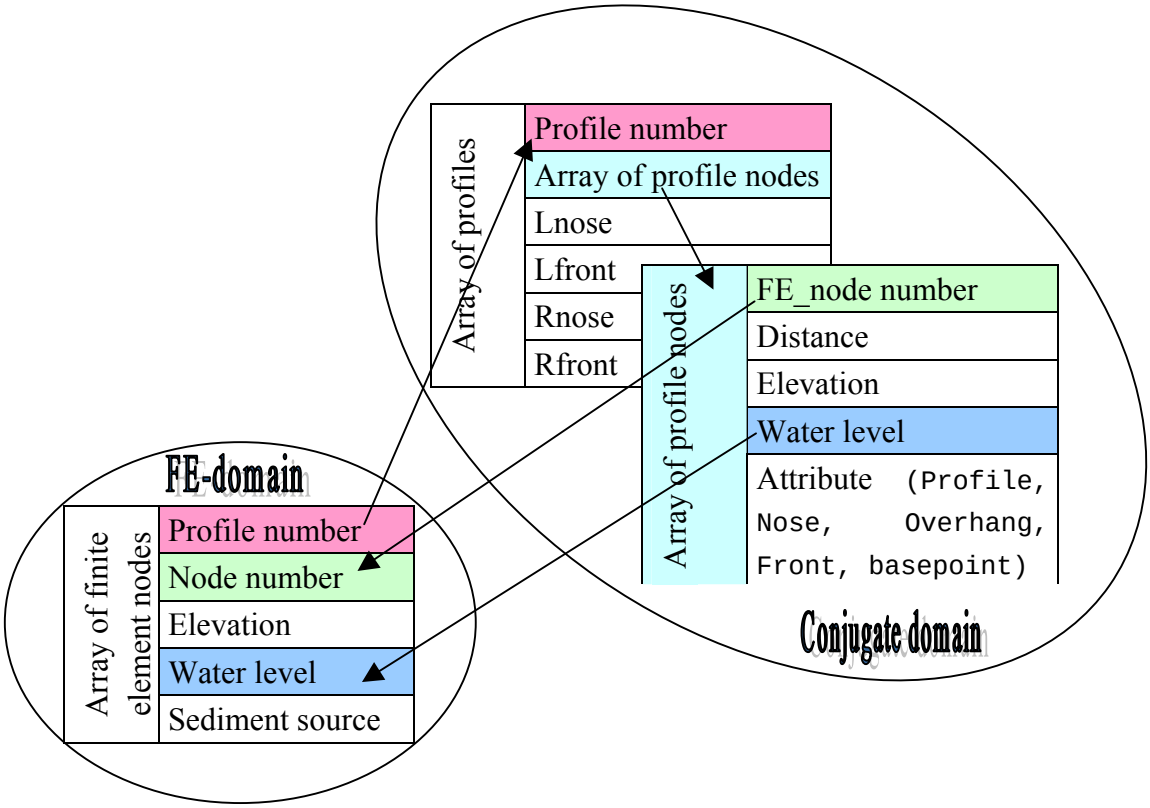

Figure 4-7 Linking nodes between FE- and conjugate domains

4.2.4 Algorithm of bank erosion and mesh adaptation

Bank erosion analysis is conducted in conjugate domain and the profiles in this domain are adapted to the new geometry after bank evolution. The elevation of Finite Element nodes are then updated according to the new status of bank profiles, before beginning a new hydrodynamic time step. This gives rise to alteration of those Finite Element nodes, which are linked with profile nodes by means of data structure, as explained in the previous sub-chapter. Before starting computation of bank erosion, first the finite element nodes (FE array of data type: finite_element_node, see Appendix D) and then the profile nodes of all profiles (PR array of data type: Profile, see Appendix D) are updated to the new bed (nodal) elevations resulting from erosion/deposition calculated in the sediment transport model. Then three failure modes are sequentially examined for each activated profile in the following order: tensile failure, undercutting and shear failure. In case either of these failure types takes place, the failed mass is distributed over bank-toe as explained in Ch. 3.4.3. Then the bank profile and elevation of the FE nodes are updated, and the next time step starts with hydrodynamic simulation using the new bed and bank elevation data. The above-mentioned procedure is illustrated in Fig. (4-8).

To allow for continuous evolution of the riverbank, an adaptive mesh algorithm was developed to represent the conjugate domain. The profile nodes are added, deleted and displaced to adjust to the new geometry of the riverbank after erosion. The mesh adaptation algorithm will be first explained for the simple case of steady flow, followed by the algorithm for unsteady flow.

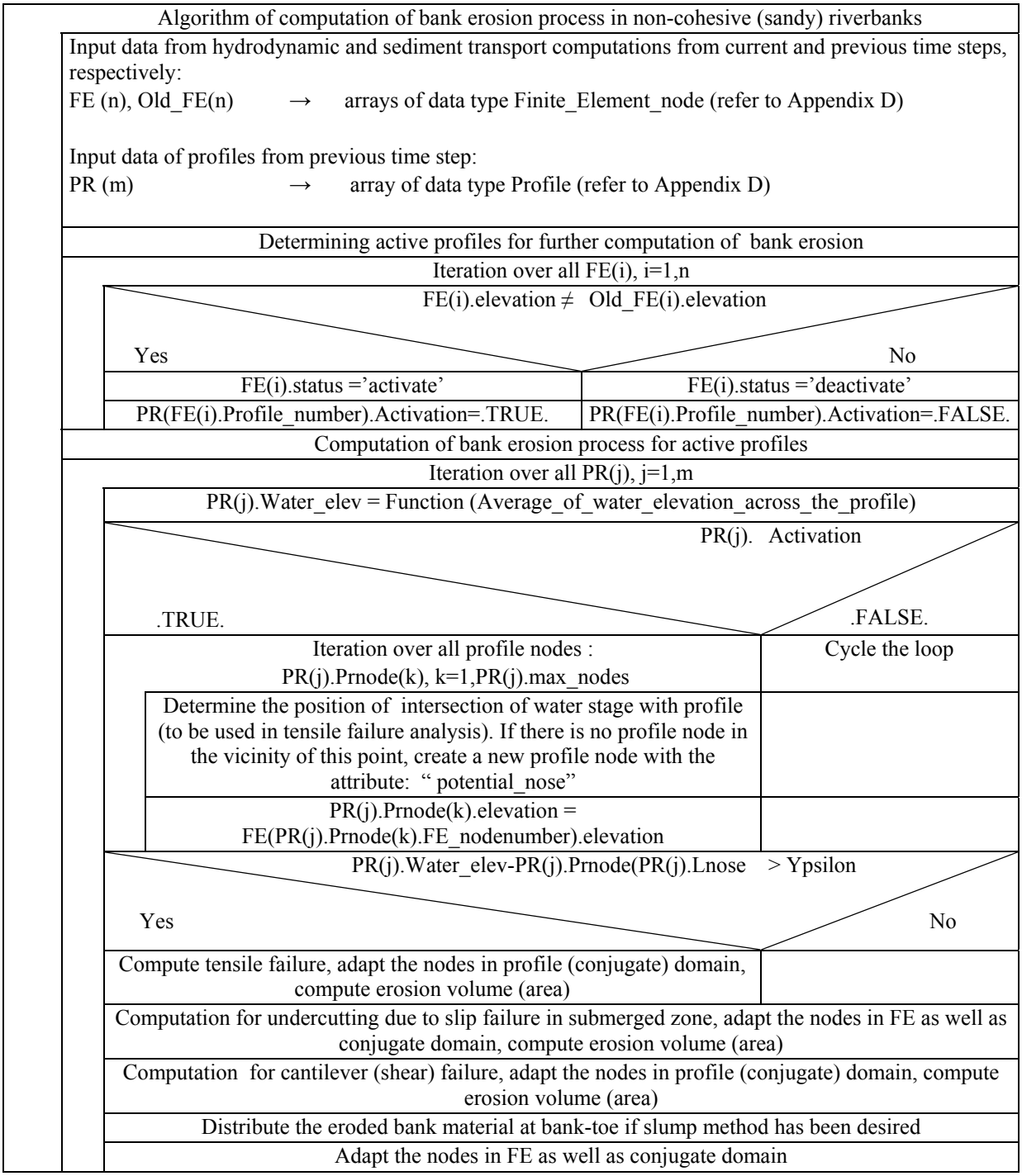

Figure 4-8 Structural diagram (Nassi-Schneidermann diagram) describing bank erosion algorithm

4.2.4.1 Mesh adaptation for steady flow

Here steady flow refers to a situation in which alteration of water elevation over a few numerical time steps is negligible with respect to a desired accuracy. This reduces unnecessary mesh adaptation when alteration of water elevation is negligible. In steady case, no tensile failure of the overhang is expected, however, the process of fluvial bank and bank-toe erosion as well as undercutting in submerged zone can proceed and result in cantilever (shear) failure of the overhang.

Bed and bank level alteration due to fluvial processes (erosion and deposition) are simulated in FE domain by vertical nodal displacement. This has been shown schematically in Fig. (4-9 A), in which corner nodes ABCD are displaced vertically to A´B´C´D´ as a result of erosion in FE-domain.

The same procedure is followed for submerged nodes in conjugate domain (Fig. 4-9 a). In case, the slope of a submerged element in profile domain exceeds the critical dense angle of repose due to the fluvial erosion, the upper node of the element (B in Fig. 4-9 b and 4-10) is lowered vertically (to the point B´ in these figures) so that the slope of the element reduces to the critical dense angle of repose (Fig. 4-9b). This procedure simulates the shallow slip failure of the bank in submerged zone. The equation of such a vertical projection shown in Fig. (4-9b) is as follows:

$$\left(\frac{z_B - z_A}{\Delta d}\right) > \tan(\varphi^c) \Rightarrow z_{B'} = z_A + (-1)^j \tan(\varphi^c)\ (\Delta d) \qquad (4\text{–}4)$$

where j=1 for the left bank and 2 for the right bank (refer to Fig. 4-10); Δd is the horizontal length of the element in profile domain (between the two nodes of the over steepened element); and z is elevation of the nodes of the over-steepened element. Subscript lower and upper stand for lower and upper node of an element. The superscript new stands for the new elevation of the node after projection.

The above-mentioned procedure is applied at all elements of each profile in conjugate domain, starting from deepest node of the bank profile (talweg) up to the last submerged node (Fig. 4-9a to c and in Fig. 4-10 the displaced nodes in submerged zone shown using solid red arrows). The elevation of FE-nodes linked to the mentioned profile nodes in conjugate domain are updated accordingly to the new elevation. Up to this stage, which simulates the process of slip failure, the elevation of nodes in FE- and conjugate domains are identical (Fig. 4-9A to C). However, the creation of undercutting front as well as overhang occur only in conjugate domain (Fig. 4-9d-e), while the vertical node displacement is continued up to the top of the bank in FE-domain, as if the bank failure plane would have been extended to the top of the bank (Fig. 4-9D-E). However, the slope of this virtual failure in FE-domain is equal to the unsaturated angle of repose. The whole mentioned process is repeated for the other bank side (left or right), if it is present.

The key issue in the algorithm of undercutting is the formation of undercut front and simulation of its advancement, which represents the discontinuity in the profile in conjugate domain. Prior to determination of the position of the undercutting front it is required to

compute the position of the lower edge of the overhang (named "Nose", refer to Fig. 4-9c), which is going to be formed following undercutting. In case that water level coincides with a node, this node is considered as "Nose" and a duplicate of this node is projected vertically on the bank surface in submerged zone using Eq. (4–4). These nodes have been shown schematically in (Fig. 4-9d) as N and M, respectively. The node "N" looses its link to the corresponding FE-node (N in Fig. 4-9D) and the node "M" becomes conjugate to the projected node of N in FE-domain, which is the node N´ in (Fig. 4-9D). Hence, the node "M" does not have any counter part in FE-domain anymore. This linkage (node association) procedure is achieved using setting the variable "Fe_nodenumer" (refer to Appendix D) equal to the node number of the FE-node (Fig. 4-10). In case of non-coincidence of water level with a node, a new node with attribute "Nose" is added to the profile in conjugate domain, and the mentioned variable is set to zero (Fig. 4-10).

The position of the undercutting front is determined by extrapolating a line from point M (in Fig. 4-9d)[1] to the water surface with the slope equal to the dense angle of repose using Eq. (4–5) and a node with attribute "Front" is created at this position (F in Fig. 4-9d).

$$\begin{aligned} d_F &= d_M + (-1)^j \tan^{-1}(\varphi^c)\ (z_{water} - z_M) \\ z_F &= z_{water} \end{aligned} \qquad (4–5)$$

If the node F is directly below another node in the overhang (node L in Fig. 4-9d), then the same linkage procedure is achieved as already explained above for the case of coincidence of "Nose" with a node.

The lateral advancement of undercutting front is simulated by lateral displacement of F, by repetition of the above procedure. The mentioned two nodes ("Front" and "Nose") form the horizontal lower edge of the overhang along water stage in the river (average of the variable water_level in data type finite_element_node).

Having generated the lower edge of the overhang, the profile nodes in overhang spanning between the nodes with attribute "Nose" and top of the bank above the undercutting front (the zone shown with a green double headed arrow in Fig. 4-10) are projected on the submerged zone of the profile. These nodes retain their original position in overhang in conjugate domain therefore adding additional nodes between the last submerged node and the node with attribute "Front" in submerged zone (the displaced nodes in Fig. 4-10 shown with dashed red arrows). These additional nodes represent the new position of the FE-nodes, which were formerly positioned in the above-mentioned zone of the overhang. As illustrated in Fig. (4-10), the sign of the inked FE-nodenumber of these profile nodes in overhang zone in conjugate domain are turned to negative, signalising that duplicate of these profile nodes have been projected on the submerged zone of the profile. Additionally, the profile nodes with negative FE-nodenumber are no longer directly linked to the FE-nodes implying that changing of the FE- nodes' elevation does not directly affect these nodes. Depending on the arrangements of profile- and FE nodes above and between the last submerged node and front

[1] Alternatively from the virtual projection of the Nose node in case of the mentioned non-coincidence.

node, more complicated situations may occur for adaptation of the profile's mesh and undercut front. These have been schematically demonstrated in Appendix E.

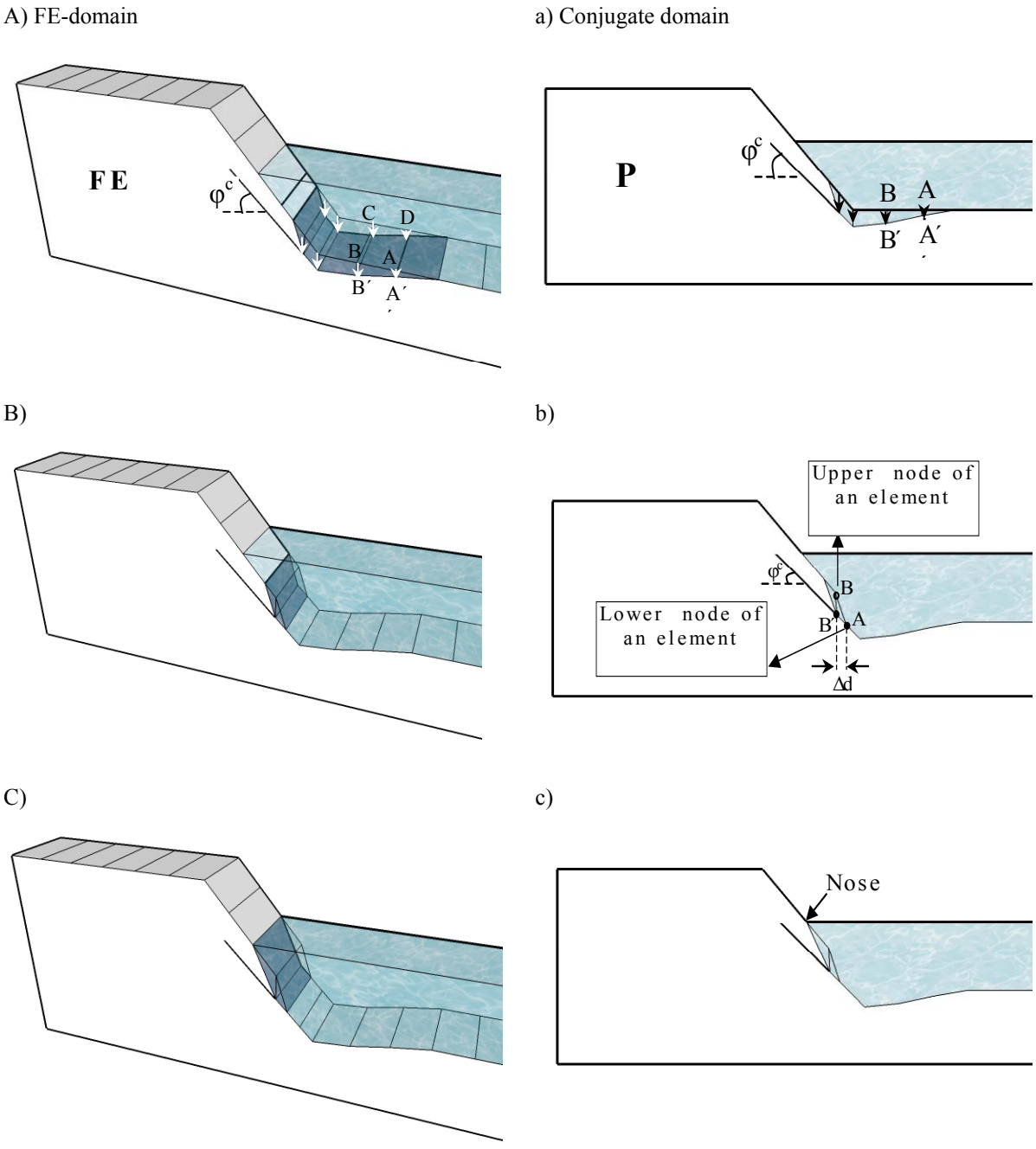

Figure 4-9 Schematic illustration of mesh adaptation following undercutting and cantilever failure in FE- (left) and conjugate domain (right)

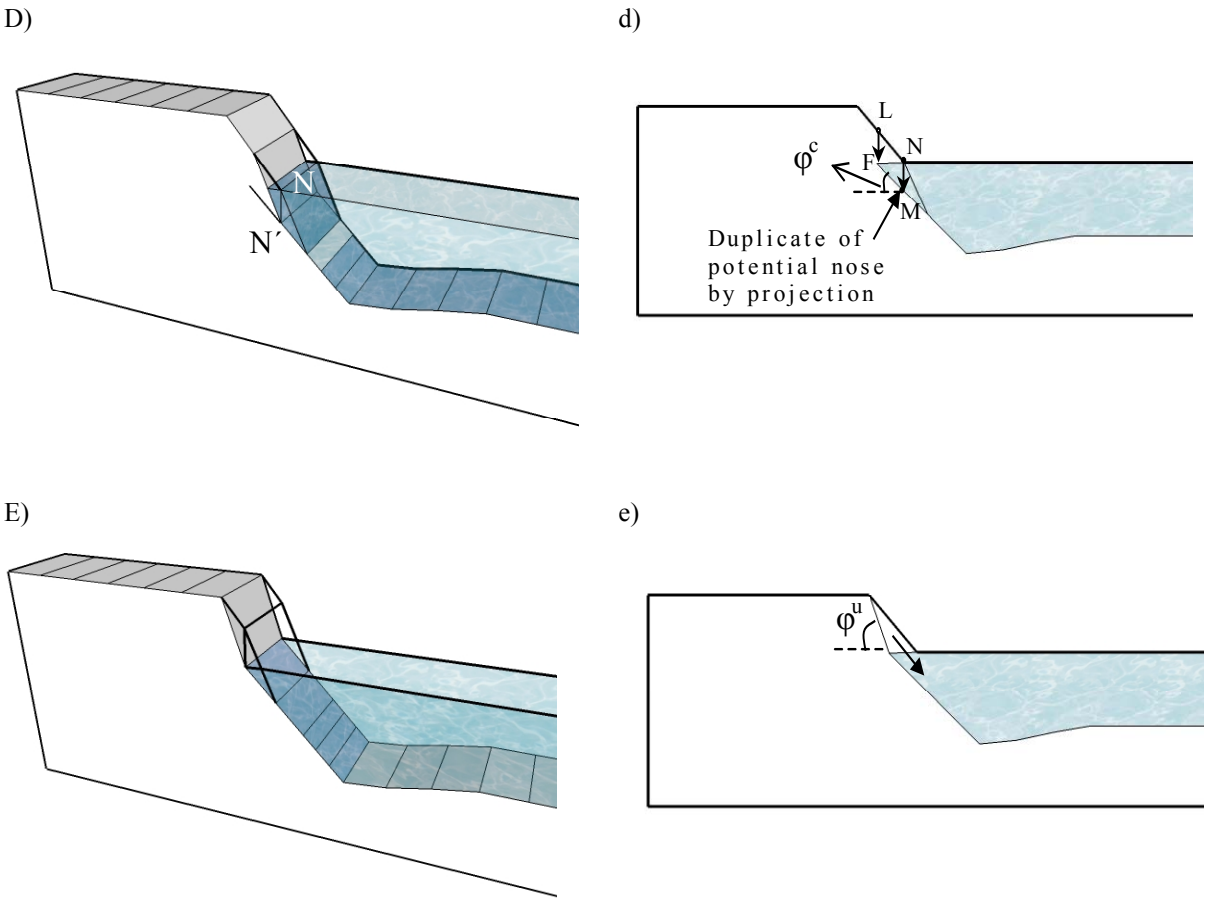

Figure 4-9 Continuation from previous page

To this stage, the mesh adaptation in submerged zone as well as formation and kinetic of undercutting front have been illustrated (see Appendix I for the structural diagram of the algorithm). The rest of the FE-nodes in overhang spanning between the zone starting above the "Front" and the first node of the overhang (the zone left to the dotted red line in Fig. 4-10) are projected on the most critical failure surface (unsaturated angle of repose), as shown with dashed red line in Fig. (4-10). This results in omission of the overhang in the FE-domain. In the mentioned zone, the profile nodes maintain their position and the positive sign of "Fe_nodenumer", retaining the overhang in conjugate domain. In case of cantilever (shear) failure, the profile nodes in this zone are vertically projected on their linked FE-nodes on the mentioned failure slope and the rest of the profile nodes in overhang with attribute "overhang" as well as "Nose" are omitted from the profile. This results in identical bank geometry in both domains. As it is seen from Fig. (4-10), the exclusion of the overhang in FE-domain implies no error in hydrodynamic calculations, since the overhang includes exclusively the dry nodes.

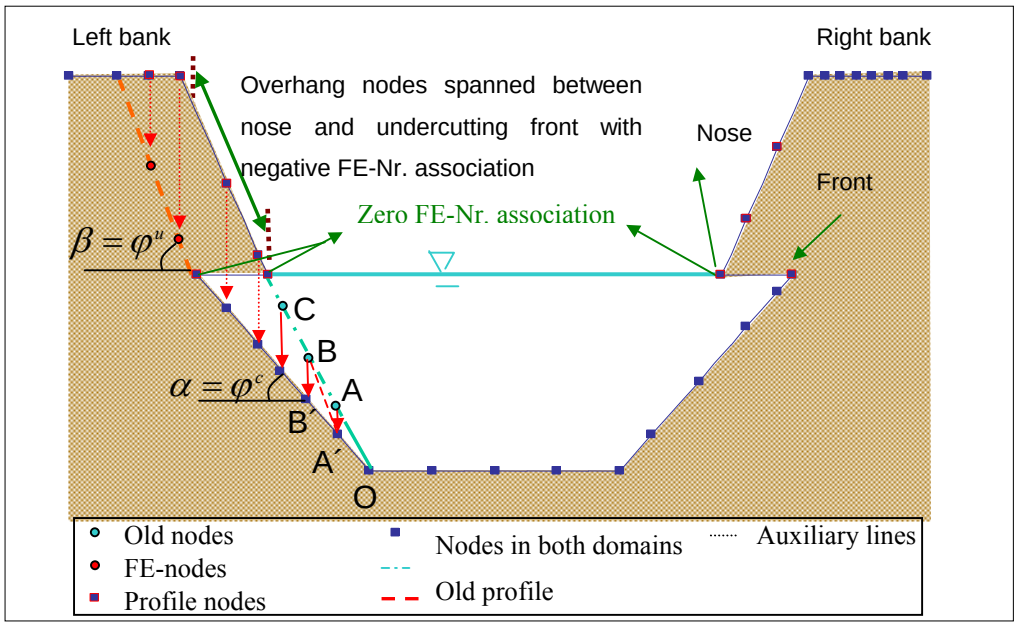

Figure 4-10 Schematic explanation of mesh adaptation in FE- and conjugate domains as well as FE-node linkage in conjugate domain following undercutting

4.2.4.2 Mesh adaptation for unsteady flow

Due to the alteration of water level in unsteady flow the undercutting front may change its position not only laterally but also vertically. Two situations can occur in unsteady flow, a rise or a drop of water level.

In the first situation, when water rises over the elevation of the overhang nose, the submerged zone of the overhang is assumed to immediately fail due to the tensile failure (see Ch. 3.4.2). This is achieved by omitting submerged nodes from overhang profile and the new "Front" and "Nose" are added to the profile as illustrated in (stage 1 in Fig. 4-11). The intersection of water level with overhang profile in conjugate domain marks the position of the nose. The coordinate of this point is calculated similar to Eq. (4–5), but with the slope of element in place of φ^c and coordinate of the old "Nose" in place of those of "M", in this equation. The coordinate of the new "Front" is computed also using Eq. (4–5), by substituting the coordinates of old "Front" in place of the coordinate of the point "M" in this equation.

As a result, the lower edge of the overhang shifts upward parallel to the old one (stage 2 in Fig. 4-11) and undercutting fronts advances. Mesh adaptation through undercutting and shear failure are similar to those of the steady case and are referred to as stages 1 and 3 in Fig. (4-11), respectively.

If there are FE- or profile nodes available in the overhang spanning between old "Front" and the new one, they are projected on the profile line connecting these two mentioned points,

provided that the FE-nodenumber of profile nodes be not equal to zero. In case the old "Front" has not been associated (linked) with a FE-node, it is removed from the profile in conjugate domain.

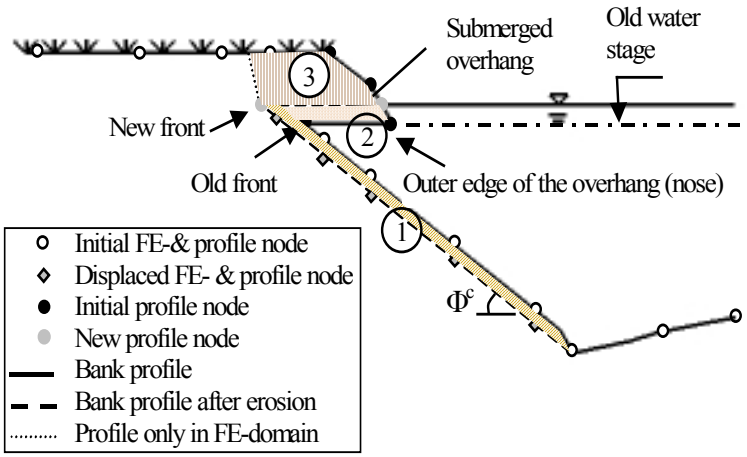

Figure 4-11 Illustration of mesh adaptation for undercutting (stage 1) and tensile failure (stage 2) during rise of water stage in unsteady flow. The failure area of each failure stage is shaded differently

In the case of water level drop, the process may become even more complex, if the water stage remains relatively constant for a longer period so that undercutting is developed below an already existing undercutting zone. This introduces additional "Nose" and "Front" in the profile, which makes the adaptation of the mesh and implementation of the stability analysis of the overhang more complicated. This process has been simplified. As soon as below the lower edge of an existing overhang is eroded due to the undercutting process in a water stage draw down phase, it is assumed that the new generated overhang below the old one fails immediately in form of shear failure along a shear plane starting from the new undercutting front (additional front in Fig. 4-12) with a slope equal to the unsaturated angle of repose, as illustrated in this figure. At the intersection of the shear plane with the existing bank profile, a new profile node is added with the attribute "Basepoint". Depending on the arrangement of the original (actual) Front node and "Basepoint", several situations may be expected for adaptation of the profile's mesh (refer to Appendix D).

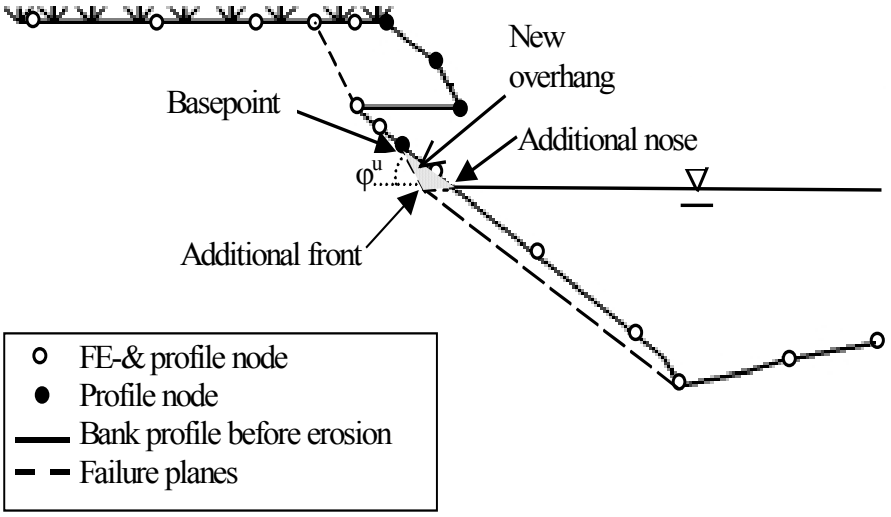

Figure 4-12 Mesh adaptation in case of undercutting in water stage draw-down phase

4.2.5 Mass distribution over bank-toe

Two methods for distribution of failed mass were developed here, namely, physically-based (using Eq. 3–20) and slump method (Eqs. 3–36 to 3–39). As a portion of the collapsed bank material usually deposits immediately at the bank-toe and the rest is transported by flow, a mixture of the two mentioned methods was additionally examined. These methods are described in the following.

4.2.5.1 Slump method

In this method, it is assumed that the failed mass resulting from all types of considered failure mechanisms (slip, shear and tensile failures) are principally rolled down the bank slope and deposited entirely over the bank-toe (the zone between talweg and the last submerged node). Therefore, they are added directly to the riverbed as bed material assuming no re-suspension. This method is a simplification of the real processes, which may deviate largely from the mentioned assumptions depending on material composition, bank geometry and near bank flow field. The advantage of this method is the simplicity and the possibility to choose an appropriate mass distribution function for the problem under study. In this method, the failed mass is computed in terms of the volume per unit length, which is actually the area in the profile plane.

In shallow slip failure of the riverbank, the over-steepened zone of the bank slides down towards the bank-toe along the most critical failure plane. This is modelled in conjugate domain by means of a cascade of vertical nodal displacement of over-steepened elements (projection of the upper node on the plane having the slope of critical dense angle of repose) starting from the deepest node in the profile up to the last submerged node (refer to the Figs.

4-9 b-d and 4-10). To compute the volume (per unit length) of failure, the failed area due to the vertical displacement of two sequential nodes (for example, the area OABA´ in Fig. 4-10) is computed as partial failed area and the procedure is repeated over all adjacent submerged nodes from talweg to the last submerged node (for example the area A´BCB´ in Fig. 4-10 and so on). Finally, all of the partial failed areas are added together to result in lump eroded area (volume per unit length) due to the undercutting (slip failure).

For tensile failure, the total area of submerged overhang (area of stage 2 in Fig. 4-11) is computed and summed up with the already computed lump area of the failed mass due to the slip failure (area of stage 1 in Fig. 4-11). For shear (cantilever) failure the area of the overhang (area of stage 3 in Fig. 4-11) is computed in the same way and summed up with the already calculated failed areas. This total failed area is distributed over the bank-toe zone using Eq. (3–36) to (3–39). The area is converted to the nodal displacement using the following equation:

$$\Delta z_i = \frac{A_{T,failed}}{\left(d_i - d_{i-1}\right)} \cdot \int_{d_{i-1}}^{d_i} f(\xi) d\xi \qquad (4\text{–}6)$$

where Δz_i is the bed displacement at node i due to the distribution of total failed area ($A_{T,\,failed}$) between node i-1 and i (given, i=1 as the first profile node starting from top of the bank). The integrand is the probability mass function, described in Ch. 3.4.3.

Since the total area of the failed zone is distributed directly over the bank profile, the mass is conserved to area at each profile in conjugate domain. In FE-domain, the vertical nodal displacements due to this kind of mass deposition are linearly interpolated for mid-side nodes (refer to Fig. 4-5).

4.2.5.2 Physically-based method

It is here assumed that the failed mass is primarily added into the water column as source term in the sediment transport equation and this equation determines where and when they will deposit.

The mass of failed material in shallow slip failure is computed in FE-domain in contrast to the previous method. However, the amount of nodal displacement of over-steepened elements is computed in conjugate domain as explained in the previous method. The displacement of linked nodes in FE-domain gives rise to the loss of volume (mass) between the previous and new stage of the elements (Fig. 4-13). The lost mass due to the vertical displacement of the upper node (node A in Fig. 4-13) is redistributed on the lower node (node B in Fig. 4-13) as nodal source term (variable sed_source in data type finite_element_node, see Appendix D) in sediment transport equation. This simulates the process of mass slide from upper part of the over-steepened element to its lower part. To accomplish this task, it is considered (King, 1993) that to each finite element node an effective area can be assigned (hatched area in Fig. 4-14). The summation of the effective areas of all surrounding elements connected to a node establishes the contributory area (blue area in Fig. 4-13 and 4-14). On this basis, redistribution

of the lost mass from upper node to the lower node can be made proportional to their contributory areas.

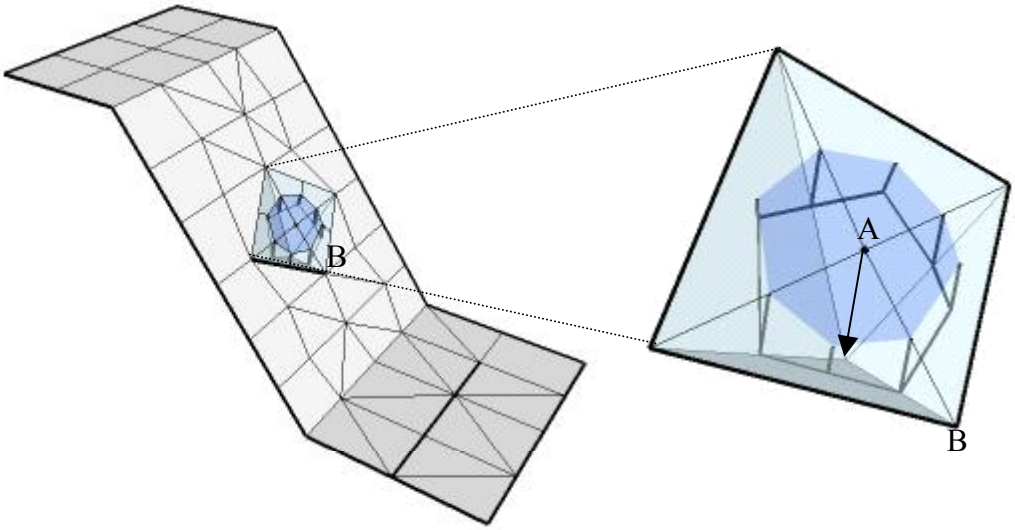

Figure 4-13 Schematic description of volume loss due to nodal displacement in FE-domain. The blue coloured area demonstrates the contributory area of the node A and the corresponding volumetric share of this node

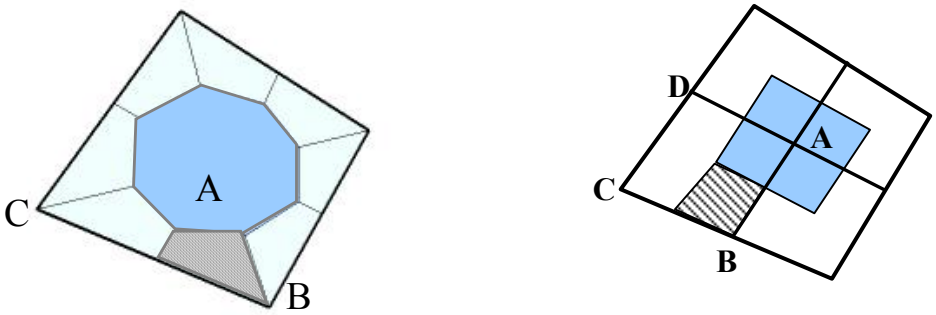

Figure 4-14 Schematic representation of the effective area of an element for each of its nodes (i.e. hatched area in triangular element ABC or rectangular element ABCD for node B). The blue area around point A is the contributory area of the surrounding element

Accordingly, the nodal source term is computed as follows:

$$S_{i,\,shear} = (1-\lambda)\,\rho_s \cdot \Delta z_{i-1} \cdot \frac{A_{i-1}}{A_i \cdot \Delta t} \qquad [Kg/m^2 s] \qquad (4\text{–}7)$$

here $S_{i,shear}$ is the failed mass rate received by the lower node due to the vertical displacement of the upper node, i-1, (in order to reduce the element slope to the stable slope); ρ_s is the sediment density, Δz_{i-1} is the displacement of the upper node; Δt is the computational time step. A_{i-1} and A_i are the contributory areas of the upper and lower nodes, respectively. The above equation states that the failed mass of the contributory area of the upper element is

removed and re-distributed over the contributory area of the lower node with a ratio of their contributory areas.

In the case of tensile failure, the mass rate of failed material is calculated in conjugate domain, since the overhang does not exist in FE-domain. It is assumed that each overhang's node has a virtual submerged node on the lower edge of the overhang (the solid grey circles in Fig. 4-15) as well as along the shear plane in the submerged zone of the overhang (the dotted line in Fig. 4-15). The submergence depth of each virtual node is converted to mass rate per area and assigned as mass source term to the FE-nodes directly below it using Eq. (4–8). Provided that the nodes directly below the overhang nodes have no conjugate FE-node, the failed mass rate is assigned to the next lower FE-node.

$$S_{i,\,tensile} = (1-\lambda)\,\rho_s \cdot \frac{\Delta z_{i,overhang}}{\Delta t} \tag{4–8}$$

Where $\Delta z_{overhang}$ is the depth of submergence for each virtual submerged node.

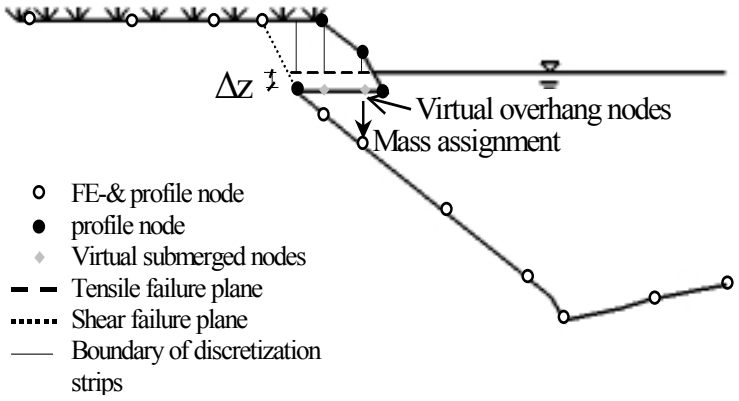

Figure 4-15 Distribution of failed mass in tensile failure using virtual overhang submerged nodes

In the case of cantilever shear failure, the affected area of the overhang is discretized to vertical strips in conjugate domain. The volume of the mentioned strips is computed by multiplying the height of the strips at each node by the contributory area of their conjugate FE-nodes. The total volume of the overhang is then the summation of the volumes of these vertical strips, which is later distributed over the near bank zone using the distribution function already explained above. The so calculated volumetric nodal failed mass is divided then by the contributory area of each receiving node at the bank-toe zone to calculate the rate of failed mass as follows:

$$S_{i,\,Cantilever} = (1-\lambda)\,\rho_s \cdot \frac{\Delta V_i}{A_{i,tributary}\,\Delta t} \tag{4–9}$$

here ΔV_i is the receiving failed volume corresponding to the node i at bank-toe, and $A_{i,contributory}$ is the contributory area of receiving node.

Having computed the "rate" of failed mass [g/(m^{2}s)] for each node using Eqs. (4–7 to 4–9) the total rate of failed mass received as source term by a finite element is computed using Eq. (4–10). This element source term is assigned as bank source term to the discretized form of the sediment transport equation (Eq. 3–20).

$$S^n_{bank} = \sum_{i=1}^{k} \sum_{j=1}^{3} \Phi_i \cdot S^n_{i,j} \tag{4–10}$$

Where, S^n_{bank} is the sediment source term assigned to the element number n; Φ_i is the linear approximation function; k is the number of corner nodes of the element n; and j is the type of failure (shear, tensile and cantilever shear failure for j=1,2 and 3, respectively).

4.2.5.3 Mixed method

This approach is a mixture of the two already mentioned method of mass distribution. It is based on the fact that not all of the failed sediments from bank failure may deposit at the bank-toe as bed material, but a portion of these may be transported by the flow. To model this process, the rate of mass failure is computed in the same way as in the " physically-based method". However only a portion of this rate is assigned as source term to the FE-nodes in advection-diffusion equation. The rest is converted to the bed elevation change as in the "Lump method" (Eq. 4–11). The ratio divided between lumped and physically based methods needs to be quantified by experiments.

$$\begin{aligned} S_i &= \bar{\omega} \cdot \sum_{j=1}^{3} S_{i,j} \\ \Delta z_i &= \left(1 - \bar{\omega}\right) \cdot \frac{\Delta t}{\rho_s} \cdot \sum_{j=1}^{3} S_{i,j} \end{aligned} \tag{4–11}$$

Here $\bar{\omega}$ is the portion of failed material assigned as source term and j=1 to 3 implies the three already-mentioned failure processes.

5 Measurement methodology

In the theoretical section several questions have been raised to the physical processes and a couple of parameters have been introduced, which need quantification. Therefore, an extensive experimental field study has been carried out in the present work.

One of the main advantages of field measurements is experimenting in real world with all its complexity. On the other hand, in such a complex environment, the experiments are not repeatable and controllable, which increases the risk of missing some information and data.

A complementary laboratory experiment in the hydraulic laboratory of Queen's University was achieved to explain the interaction of bed and bank processes.

The result of the above-mentioned field measurement program and a part of the laboratory experiments is presented in Ch. 6 and in this chapter following issues will be presented:

- Field measurement programs and their scopes
- Instrumentation applied and their specifications
- Principles of operation of the instruments
- Accuracy of the measurements
- Installation of the instrument and specification of the installation sites
- Deployment of the instruments
- Pre-processing of data

5.1 Field measurement program

The study was carried out in the river Hardebek-Brokenlander Au, which discharges to the upper reach of the river Stoer near Neumuenster in North of Germany (Fig. 5-1). This river was selected, since it is a shallow, sandy-bed meandering river with dense non-cohesive banks. In 2002, a 350 m reach of the river was restored to a natural meandering river in place of the former straight canalised river reach. Neither bed nor bank has been stabilized so that a natural self-forming meandering river could develop. A complete meander wavelength, including two bends at the beginning of this new river reach formed the basis for the monitoring program. The length of the study reach has been about 100 m including the

straight reach upstream of the selected meander. The second bend, which has been the most active meander (in sense of morphological evolution) in the river, formed the main focusing reach of morphological study of the riverbed and bank. As shown in Fig. (5-1), three representative sections (entrance to the bend, bend apex, and a section in between) were chosen for further analysis. The average bank full width of the river was approximately 7 m with average flow depth of 0.28 to 1.0 m, depending on the time of the year. The bank has been covered with grass and the soil profile consisted of a fine sandy layer (d50 =0.22 mm) with an overlaying homos layer of 25 to 40 cm thickness. Hydrological and morphological data of the river are summarized in Table (5-1).

An innovative monitoring program was developed and carried out using state-of-the-art measurement techniques. In the first phase of the measurements, from January to April 30, 2007, flow discharge and water level were monitored using an innovative institute-modified mini ADCP[1] and differential pressure sensors, respectively. Additionally, the outer bank surface of the river bend has been scanned intermittently using a high-resolution 3D terrestrial laser scanner (Leica Cyrax HDS2500) from December 2006 to April 2007. A wireless remote camera recorded the moment of bank failure during this period.

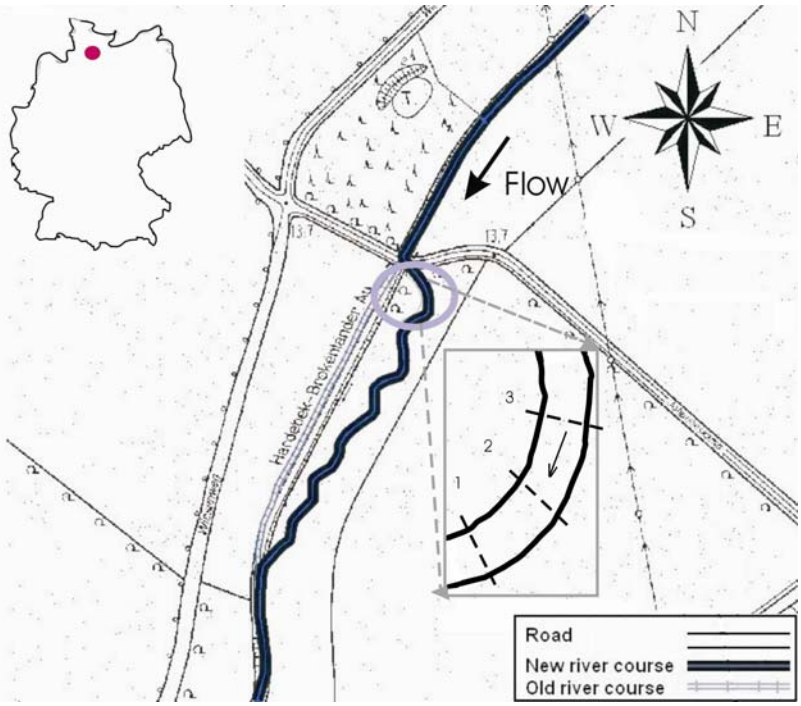

Figure 5-1 The geographical location of the study site

During the second phase of the measurements (July 2007 to March 2008), laser scanning of the outer riverbank was accompanied by bathymetry measurement of the river bend using a shallow water echo-sounder (Fahrentholz BBES 700 kHz) integrated with a RTK-DGPS[2] system (Leica 500-SR350). Vertical distribution of the mean and turbulent flow velocity

[1] StreamPro® ADCP (Acoustic Doppler Current Profiler) a product of RDI.

[2] RTK-DGPS (Real Time Kinematic-Differential Global Positioning System)

across the river bend along two sections were measured on April 2008, using ADV[1] (SonTek, Hydra®) and the mini ADCP mounted on a rigid traverse system. Water level upstream and downstream of the meander bend under study was monitored continuously from January to April 2008 in the second measurement phase.

Table 5-1 Hydraulic and morphological characteristics of the study reach of the river

Flow Parameters	Measured in 2007
Discharge (m^3/s)	0.31-1.36
Mean velocity (m/s)	0.21-0.45
Bank full width (m)	5.3-9.0
Average water depth range (m)	0.28-1.0
Mean bed slope(%)	0.12
Meander Properties	
Radius of curvature (m)	16.40
Meander length (m)	50.44
Sinuosity	1.25

5.2 Sediment properties

Physical properties

Five distorted soil samples from the riverbank and bed were collected for determination of the nominal diameter of the riverbed and bank material by the standard sieve analysis method.

By means of two undistorted soil specimens, soil density (ρ_s), soil dry density (ρ_d), porosity (the ratio of the volume of voids to the total volume) and degree of saturation were determined based on DIN standard (18 125-LA, 1997).

To determine the properties of the suspended sediment, a sample of water and suspended sediment was taken from the river. Due to the very small amount of suspended sediment in the river and thereby in the probe, it was not possible to determine sediment size distribution using Hydrometer analysis. Therefore, the average of particles diameter was determined using electron microscope. To prepare the probe, a small amount of the water sediment mixture was given on a small plate coated with a thin layer of gold, as a medium with very good electric conductivity. Then using electron microscope, the diameter of several particles was measured directly and the mean diameter of suspended sediment was determined.

Geotechnical properties

Geotechnical properties of the soil were determined from a direct shear test (DIN 18 137-DSR) at three undisturbed samples from the riverbank. It should be noted that the test gives the effective shear strength, only when the specimen is saturated. Therefore, in the current

[1] ADV (Acoustic Doppler Velocimeter)

tests, in which the natural in situ saturation of the specimen was preserved, the measurements included also apparent shear strength.

5.3 Critical shear stress

This parameter can be calculated using Shields diagram, given the mean diameter and density of the particles. Taking d_{50} as mean diameter, the critical shear stress was calculated as 0.12 Pa using Shields diagram.

Furthermore, the shear stress was measured using microcosm instrument (Gust, 1990). The instrument was originally developed to determine the critical shear stress in benthic sediments. This instrument consists of a Plexiglas cylinder (30 x 35 cm, diameter x height) in which a sediment sample is placed at its bottom, and then filled with water (undisturbed sample of the bed material from outer bank-toe was used). A radial flow is generated in the cylinder by means of a rotating stirrer attached to a hollow shaft mounted over the top end of the cylinder. At the same time water is pumped out of the hollow shaft into a re-circulating system generating suction at the middle of cylinder. By means of the adjustable rotation speed of stirrer, different shear stress magnitude could be generated at the bottom over the sediment sample. The revolution speed of the propeller had been already calibrated for computation of bed shear stress (friction velocity) using the 3D hydrodynamic model of COMET. Mean error of the resulting bed shear stress at any point and any time on the surface of the substrate in the instrument is less than 10% (Gust, 1990).

A high speed high resolution CCD camera directed at Plexiglas cylinder recorded the sediment movement through a Plexiglas window attached to the cylinder, which was filled with water to compensate the light refraction. Two lamps light up the cylinder for better observation and higher colour contrast. Using a software, the turbidity of water (in terms of colour codes) in four horizontal planes (virtual windows) with different elevations from the bed is analysed. These colour codes are representative for the concentration of sediment suspension. The higher the colour code the higher is sediment concentration.

By plotting turbidity versus bed shear stress (friction velocity) for each virtual window a series of curves are generated, from which the initiation of sediment motion at the bed and into suspension can be determined.

5.4 Water level

The water level (stage) has been measured downstream of the study reach (river bend) from January 5, 2007 till April 10, 2007 during the first monitoring phase. This was achieved by installing a differential pressure sensor (P-LOG520 from Driesen+Kern) within a perforated stainless steel pipe in the middle of the river above bed surface and another in the river margin to measure the air pressure. The latter was necessary because the applied sensors measured

the absolute pressure requiring independent air pressure measurement to calculate water gauge pressure.

The resolution of the instrument was 6 Pa (0.6 mm of water) with the accuracy of 0.05% of measurement range. The instruments were set to record pressure in 10 minutes intervals. The effect of temperature on pressure was internally corrected using an internal thermometer.

An additional differential pressure sensor was installed upstream of the bridge, which recorded data from January 30, 2007 till April 10, 2007, after which the instrument went missing. The instrument was to serve as a water stage gauge station for later generation of discharge-stage relation.

The cross sectional profile of the river at the installation location of upstream pressure sensor was surveyed using tachymeter to enable water level-flow area calculation. A FORTRAN program was written to compute flow area based on the water stage and cross sectional profile of the upstream gauging station. It was used to generate discharge time series using Eq. (6–2) as described in Ch. 6.3.

Almost every two to three weeks the pressure sensors were read by transferring recorded data on computer. The last recorded data from upstream pressure sensor dated back to March 20, 2007. Each time before and after reading the pressure sensors, their elevation was read by tachymeter to correct the water level elevation in case of minimal displacement.

During the second phase of monitoring from January 23, 2008 to April 10, 2008 the above-mentioned water level measurement system was installed again, however this time accompanied with an online flood warning system. The flood warning system consisted of three water level gauges in a perforated PVC pipe attached to the bridge side at three threshold levels. It was designed so that three levels of a flood wave could be signalled by SMS over GMS networks. If the water level in the river rises beyond the bank-toe, middle of the bank and below the root zone, three SMS are sent to inform the about the flood situation. This was achieved for facilitating proper time of high flow discharge and sediment measurement. The same sets of SMS are sent in reverse order in flood recession period, after which it is the most proper time for scanning of the bank surface and bed.

Post processing

The water pressure recorded by the sensors was subtracted from air pressure recorded by the air pressure sensor. The so-computed pressure difference (in mBar) was converted to cm of water by dividing the pressure by specific weight of the water. To include the effect of temperature on water density (ignoring the effect of salinity, measured 0.2 ppm), the following equation was used (McCutcheon et al., 1993):

$$\rho(\mathrm{T}) = 1000\left(1 - \frac{(\mathrm{T}+288.9414)}{(508929.2\times(\mathrm{T}+68.12963)}\right)\cdot(\mathrm{T}-3.9863)^2 \qquad (5–1)$$

here T is temperature in Celsius and ρ(water density) in kg/m^3. The time series of water level has been presented in Ch. 6.3 together with discharge time series

5.5 Flow discharge

In the past, discharge measurement in the rivers was based on several point measurements of the flow velocity over water depth and across the river by means of, for example, a propeller flow meter, a magnetic flow meter or an acoustic Doppler velocity meters. Apart from their application problems, such as those originated from their intrusive nature, one of the main drawbacks of these methods are the relative large measurement time (depending on the river width and depth) and time consuming post processing of the collected data. Non-intrusive distributed discharge measurement methods have replaced the point based measurement methods with advancement of radar and acoustic Doppler technology. These instruments enable velocity measurement of a portion of flow at once. The large data produced by these methods are analysed directly by software during measurements or later by post processing, which is much faster than point based measurements.

The acoustic Doppler current profilers (ADCP) are more practical than those based on radar technology for small to medium rivers. They are either mounted on a small boat or a catamaran for measurements in small rivers or mounted on the side or front of a boat for larger rivers. However, for very large rivers it takes a relatively long time to measure discharge, using ADCP. This limits the application of ADCP especially in large tidal rivers, in which the water level and discharge may change much faster than the measurement duration using ADCP. In the mentioned situations radar technology is applied in two variants, land-mounted system (terrestrial), remote sensing using helicopter (Melcher et al., 2002) or satellite (Bjerklie et al., 2002). These methods are used for discharge measurement as well as discharge monitoring.

In the small river under study, the application of ADCP is best suited. However, the very shallow water in Hardebek-brokenlander Au made the application of ADCPs developed mainly for deep water impossible. Therefore, a new mini ADCP (StreamPro ADCP from firm RDI®) was used for discharge measurement as well as discharge monitoring. Since this instrument is not originally designed for monitoring applications, a novel innovative technique was developed to meet this challenge.

5.5.1 Principle of velocity measurement using ADCP

Velocity measurement in ADCP is based on the principle of *Doppler shift*. The ADCP transmits acoustic signals in water and receives the echo reflected back from floating particles. By measuring the change of frequency of the reflected signal, the velocity of the floating particle is measured. The broadband ADCPs of RD Instrument measure time dilation using phase measurement[1]. Each generated acoustic signal is called a ping. The instrument generates pings with a high rate and then averages over several pings to compute the time-averaged velocity at a specified frequency.

[1] For further information the reader is referred to "Acoustic Doppler current Profiler: Principles of Operation, a Practical Primer, 1999, RD Instrument"

Depending on the number of velocity components measured by ADCPs, they possess up to three transducers for current measurement in three dimensions (for some models, for example those from RDI, a fourth transducer is installed for error measurement to evaluate the quality). Each pair of beams (in four beam models) computes a horizontal and a vertical component of the velocity. Therefore, the instrument measures two horizontal components and two estimates of vertical component, from which one is used for error estimation. The most important feature of ADCP is its ability to measure velocity over a profiling range at once. This is achieved by dividing echo signals internally into different cell depths (bins) with equal heights, depending on their time of return. Echo from far ranges take longer to be received by the instrument than those close to it. The internal processing of these echoes separately enables computation of velocity in three dimensions over the water depth at once.

Usually a distance in front of the instrument, called blanking distance, cannot be measured due to the ringing effect. This is related to the fact that the transducers vibration should first rest before receiving the echoes. Therefore, the echoes reflected from very close distance to the instrument can not be measured properly. A blanking distance also exits near to the bed (down-looking installation) or near the water surface (up-looking installation). This is due to the fact that the energy of the reflected echo from such surfaces is much higher than that from floating particles, which makes the instrument unable to detect the actual echoes. Therefore, ADCP cannot measure water velocity in such blanking zones, reducing the measurable depth. However, in these regions the velocities are internally approximated in the instrument's processor using theoretical velocity distribution profile, for example logarithmic or power law.

5.5.2 Discharge measurement using moving StreamPro®

StreamPro®, a 2 MHz mini ADCP with 1 Hz sampling rate (Fig. 5-3), was used for intermittent discharge measurements. The transducer head with a 13.5 cm height and 3.89 cm diameter was the smallest of its type at the time of application making the instrument unique for shallow water applications (see Appendix F for specifications of the instrument). To maintain this small size, the transducer unit is separated from the electronic unit by a standard 1m cable. However, for the present application a 10 m cable configuration was used. Furthermore, deployment of the unit, storing the data as well as online data processing are achieved on a portable pocket computer using StreamPro software. The on-line data transfer between electronic unit and pocket computer is accomplished over a wireless Bluetooth® communication. Therefore, standard StreamPro® cannot be applied for standalone applications such as long term stationary measurements (monitoring) without special modifications.

Before starting the discharge measurement, a trail measurement needs to be conducted to reassure that the bed is not moving (high rate of bed load transport is not present). In such cases the measurement is erroneous, since the boat velocity is computed internally by assuming that the bed is fixed. In such cases a bias is introduced to the velocity calculations. Additionally, the near bank zone, where no velocity measurement is possible due to the very

shallow depth, needs to be marked in this stage. This is achieved by moving the ADCP as closely as possible to each bank, so that a minimum of two reliable measurement cells is available. These two positions are marked so that each transacts starts and ends exactly at these positions, while being held as still as possible to collect a user-defined number of velocity ensembles. Moving of ADCP at these two positions is a source of error in discharge calculation. The collected velocity data at these two locations are used to estimate the discharge in the unmeasured zones close to the bank using linear interpolation. Depending on the geometry of the bank, rectangular or triangular profile can be selected in StreamPro program for unmeasured zones.

By pulling the ADCP over water surface from one riverbank to the other (mounted on a boat or catamaran), vertical velocity profile data are collected across the river. During a discharge transact across the river, the velocity magnitude of each measured bin (cell) is observed in the form of a colourful cell as in Fig. (5-2). The discharge in the measured zone is calculated internally or in post processing by means of multiplication of each velocity magnitude cell by the cell area. The corresponding ship track is presented in Fig. (5-2). The velocity vectors (blue lines in this figure) should be as uniformly spaced as possible and normal to the ship track, to provide good measurement results. This can be attained by uniformly and slowly pulling the catamaran over water.

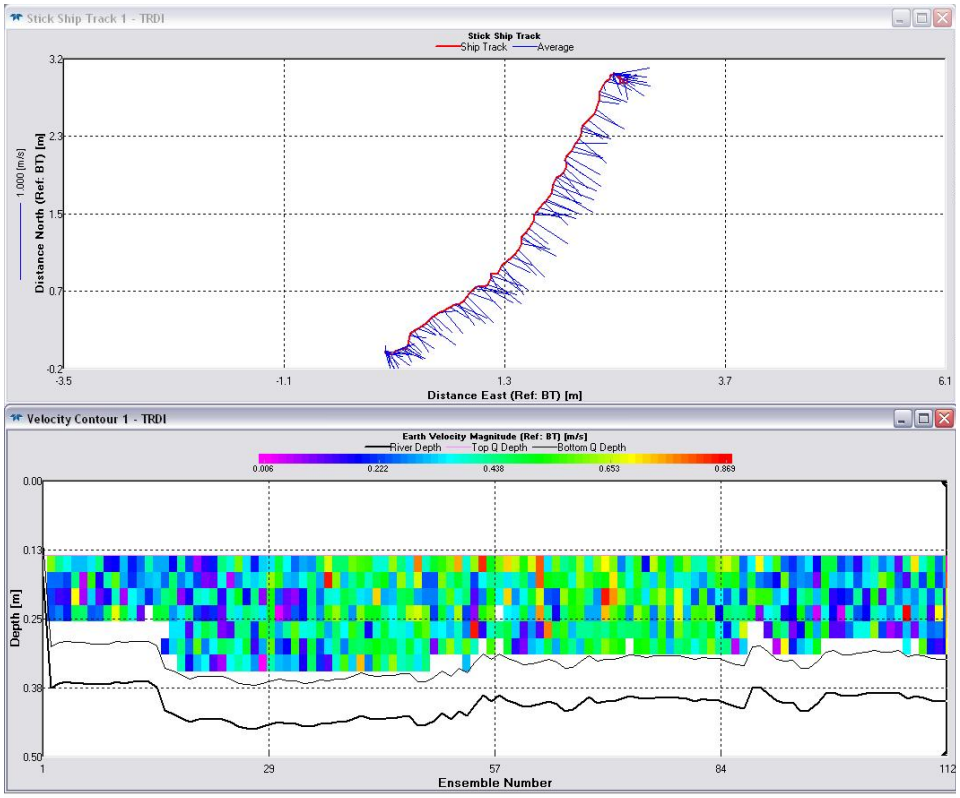

Figure 5-2 Velocity magnitude (below) and ship track (above) measured by moving ADCP

The measurements were achieved by pulling the mini ADCP over water using a pulley system installed on both sides of the river just upstream of the bridge. The catamaran was attached to

the pulley system via a rope (Fig. 5-3). Each transact was repeated a few times (usually 3 to 4 times) to reach to a discharge deviation of less than 5% among all of transacts. The unmeasured zones, which were estimated as explained earlier, comprised between 38 to 64 percent of the area in the accomplished measurements from January 2007 till April 2008 (please refer to the Table 6-4for an example of measured zones). This constitutes the largest part of uncertainty in the discharge measurements.

Another important issue that impacts measurement quality is the uniformity and the speed of pulling the boat over water. The pulling speed should be lower than the mean velocity of the river and it should be done as uniformly as possible. Furthermore, the instrument should approach slowly the banks. However, during the transact the path of the boat does not need to be completely straight (Fig. 5-3)

Each discharge measurement consisted of a few transacts across the river taking a total amount of 10 to 20 minutes, depending on how well discharge had been estimated in each transact. The discharge measurement was terminated when at least four transacts with less than 5% deviations from the mean discharge had been attained.

Discharge measurements were carried out nine times between 13 December 2006 and 2 April 2007, from which five were considered for later analysis (refer to Ch. 6.3). These discharge measurements were used later to generate a continuous discharge time series by the method explained in Ch. 6.3.

Figure 5-3 Moving boat application of StreamPro by de-montaging the electronic unit and keeping it in a water proof housing for subsequent continuous monitoring application.

5.5.3 Discharge monitoring using Stationary StreamPro®

For morphological studies of the river, continuous record of discharge and water level is required to enable establishing a correlation between flow regime and morphological evolution. Therefore, it is necessary to install in the river a stationary ADCP, instead of moving ADCP. Generally there are two installation possibilities of ADCP, namely horizontally (side looking) and vertically (upward-looking). By horizontal installation, the ADCP is installed horizontally at one side of the river in a position in which it remains submerged during the measurement period. If the instrument is installed close to the bed the acoustic beams may eventually hit the bed close to the instrument, introducing error in the measurements. This reduces the measurable flow area, which leads to less accuracy and reliability of the measurements. These limitations have forced the industry to manufacture horizontal or H-ADCP type, which minimizes these effects. This type of instrument is especially recommended for application in wide rivers, which enables more flow area to be measured. Nevertheless its application in shallow water is still limited due to the mentioned factors.

The upward-looking installation on the river bed, on the other hand, has the advantage that it remains always submerged, making it best suited for shallow waters, since the conical from of acoustic beams do not meet the bed surface (Fig. 5-4). However, the transmitters should be installed above the mean riverbed, to eliminate the risk of being covered by bed load transport.

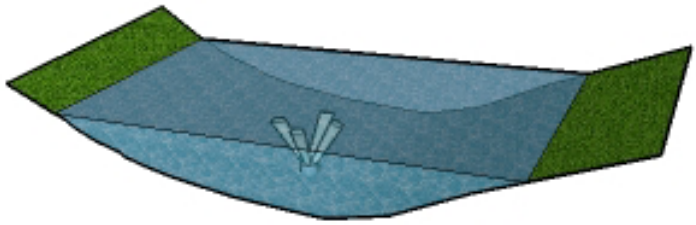

Figure 5-4 Upward looking ADCP for monitoring purposes, depicting conical acoustic beams

Due to the aforementioned reasons, an upward-looking installation of StreamPro® in the river bed upstream of the bridge was used. The detachable transducer unit was installed as explained below in the river bed and the electronic unit was demounted from catamaran and secured in a water proof metal box at the side of the bridge (Figs. 5-3 and 5-6a). The electricity was supplied by means of a 12V car battery kept in the same metal box.

Installation of the transducer at the riverbed required protection measures for the transducer head as well as the connected cable. For this sake, two stainless steel cylinders were constructed to accommodate the mini-ADCP in the riverbed. One cylinder was fixed in the river bed by a large (0.5 m) metal nail so that the upper edge of the cylinder was located about 10 cm above mean bed level to avoid probable covering of the transducer head by bed load. The second cylinder, made in form of two centric cylinders, was fitted inside the fixed one (Fig. 5-5a) so that the second cylinder could be pulled out (Fig. 5-5a) from the fixed cylinder

for subsequent moving ADCP application. This simple mechanism permitted a flexible deployment of the mini-ADCP in stationary as well as moving configurations and as a stable robust installation against washing out by bed erosion.

a) b)

Figure 5-5 (a) Fixed cylinder depicting the portable cylinder inside it. (b) Removing portable cylinder from riverbed for moving ADCP application

The portable cylinder (Fig. 5-6b) was constructed so that the transducer could be fixed via special PVC fitting in the middle centric cylinder. This special construction of the portable cylinder prevented cable-transducer joint from rapture by accommodating a portion of the cable inside the larger cylinder. The rest of 10m cable was protected within a detachable corrugated PVC pipe (Fig. 5-6b).

The most challenging problem faced by the stationary application of StreamPro® was the absence of an internal control unit like other ordinary ADCPs to configure the instrument and setting up the measurements. Therefore, it was decided to leave the pocket computer (the deploy unit) after measurement initiation in a waterproof housing box (Fig. 5-6a). However, the crystal display of the pocket computer (iPAQ) could get damaged in cold temperature and the temperature of iPAQ should be kept always above zero centigrade (minimum operating temperature). Hence, the pocket computer was laid on a heating system (connected to a processor and a temperature sensor, to avoid overheating the instrument) both embedded in a Styrofoam box for isolation of temperature. The excess electrical voltage of car battery, not used by the pocket computer and electronic unit, was applied to this aluminium plate to heat it.

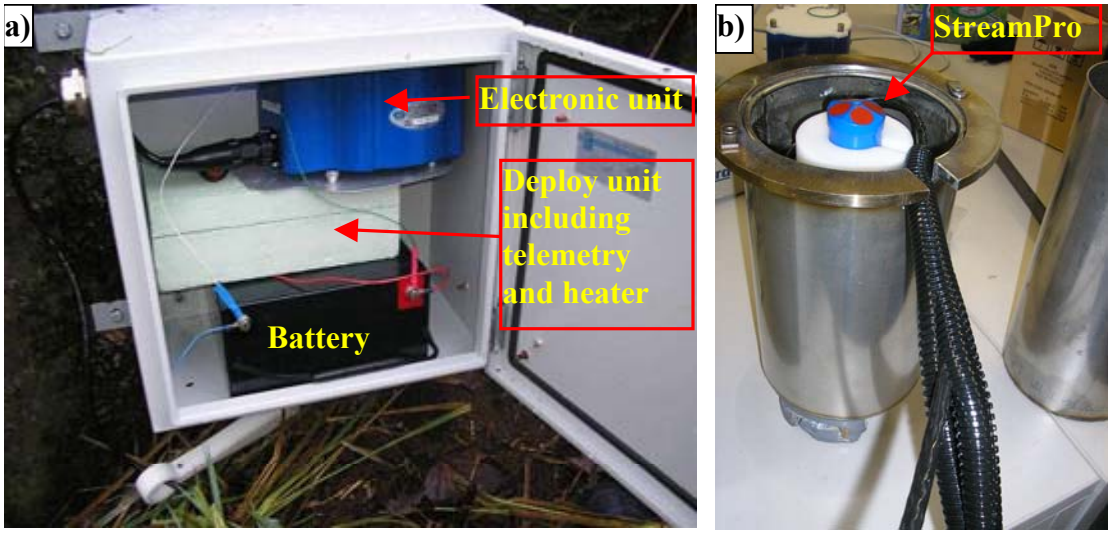

Figure 5-6 Stationary installation of StreamPro ADCP in Brokenlander-Au river. (a) water proof housing accommodating: electronic unit (above), deploy unit together with telemetry and heating unit in Styrofoam (middle) and the battery (below). (b) StreamPro transducer head in the portable stainless steel cylinder, depicting the protecting corrugated pipe of cable

Furthermore, the system was then equipped with a telemetry system over GSM to inform its probable shut down due to, for example, loss of electricity or any other reasons. In such cases, it would send a SMS message to a mobile phone, informing the shut down of the instrument. This innovative system set up a reliable and robust system of monitoring.

Using the above mentioned novel measurement approach, the StreamPro® was made for the first time applicable for long-term discharge monitoring, even beyond the capabilities of standard stationary ADCPs.

The method of analysis of data and correlation of vertical velocity profile collected by stationary StreamPro with actual discharge measurement using moving StreamPro is presented in Ch. 6.3.

5.5.4 Monitoring program

By applying the above-mentioned instrumentation, discharge was monitored from 12 December 2006 till 10 April 2007. However, the monitoring was interrupted at the beginning due to the electricity failure after 9 days of operation. It took 15 days to improve the system for a longer operation time. Later on 5 January 2007 the system failed due to the damage of the iPAQ. It took more than a month to develop a reliable system and the measurement started again on 14 February 2007 with the new system. The whole monitoring system was stopped due to corruption of a part of monitoring system by vandalism.

During the operation time, before exchanging the battery with a fully charged one (almost every two weeks), the measurement was stopped and the recorded data of continuous velocity profile measurement (near 0.7 GB data) was transferred from iPAQ flash card to a laptop for

post processing. Then the mini-ADCP was pulled out of the fixed cylinder (Fig. 5-5b) and it was assembled again on the catamaran (Fig. 5-3) for discharge measurement. Having finished the discharge measurement as explained in Ch. 5.5.2, the transducer was replaced in the cylinder in the riverbed and another cycle of continuous velocity profile measurement was started after installation of the recharged battery. By this method, the stationary velocity profile measurements could be correlated with direct discharge measurement; from which a time series of discharge could be obtained.

5.6 Flow velocity

5.6.1 Mean flow velocity measurement

For the purpose of validation of the hydrodynamic model, flow velocities at few locations along the river were measured using StreamPro ADCP on August 14, 2007 in low flow (Q=0.464 m^3/s) and on December 6, 2007 during high flow (Q=1.06 m^3/s) conditions. Avoiding swinging of the ADCP's catamaran on the water surface was impossible leading to changing position during velocity recording (Fig. 5-7). Therefore, the velocity data collected in this way introduced an error due to spatial averaging of velocity bins. This swinging of catamaran was more pronounced on the latter date due to the higher flow velocity. In the river bend, it was even not possible to measure with ADCP due to the large drifting and swinging of the catamaran. Therefore, the flow velocities were measured at the same locations across the river bend using Acoustic Doppler Velocimeter (ADV) from SonTek Company, mounted on a rigid traverse system. Measurement using ADV has the advantage of precise point measurement, while it takes more operation time.

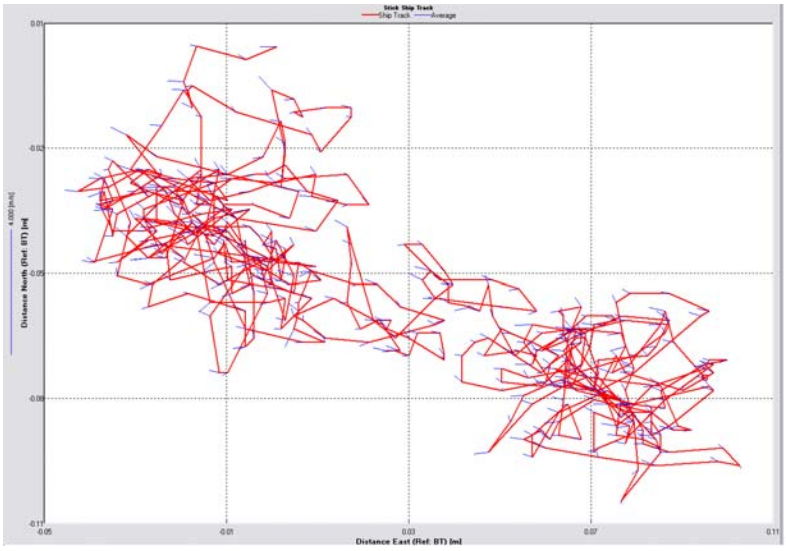

Figure 5-7 Ship track of StreamPro during vertical velocity profiling at section V-2-1 with almost 15 cm drift to the East and 11 cm to the North. Blue lines are velocity magnitude vectors

The elevation of the sampling volume over the bottom of the riverbed was recorded by ADCP and ADV. The horizontal coordinates of the measurement location were additionally surveyed using a tachymeter with high accuracy (1 mm). The elevation data measured by tachymeter was used for correction of the measured depth of sampling volume using ADCP and ADV. This was done, because the maximum accuracy of ADCP sampling position was about 0.5 cm (for a sampling bin of 1 cm height). Even the high accuracy of 1 mm for measuring the position of sampling volume and bed location by ADV is biased with acoustic noise, apart from the fact that the ADV instruments from SonTek had often problem for detecting the location of the boundary. The measurement locations are shown in Fig. (5-8).

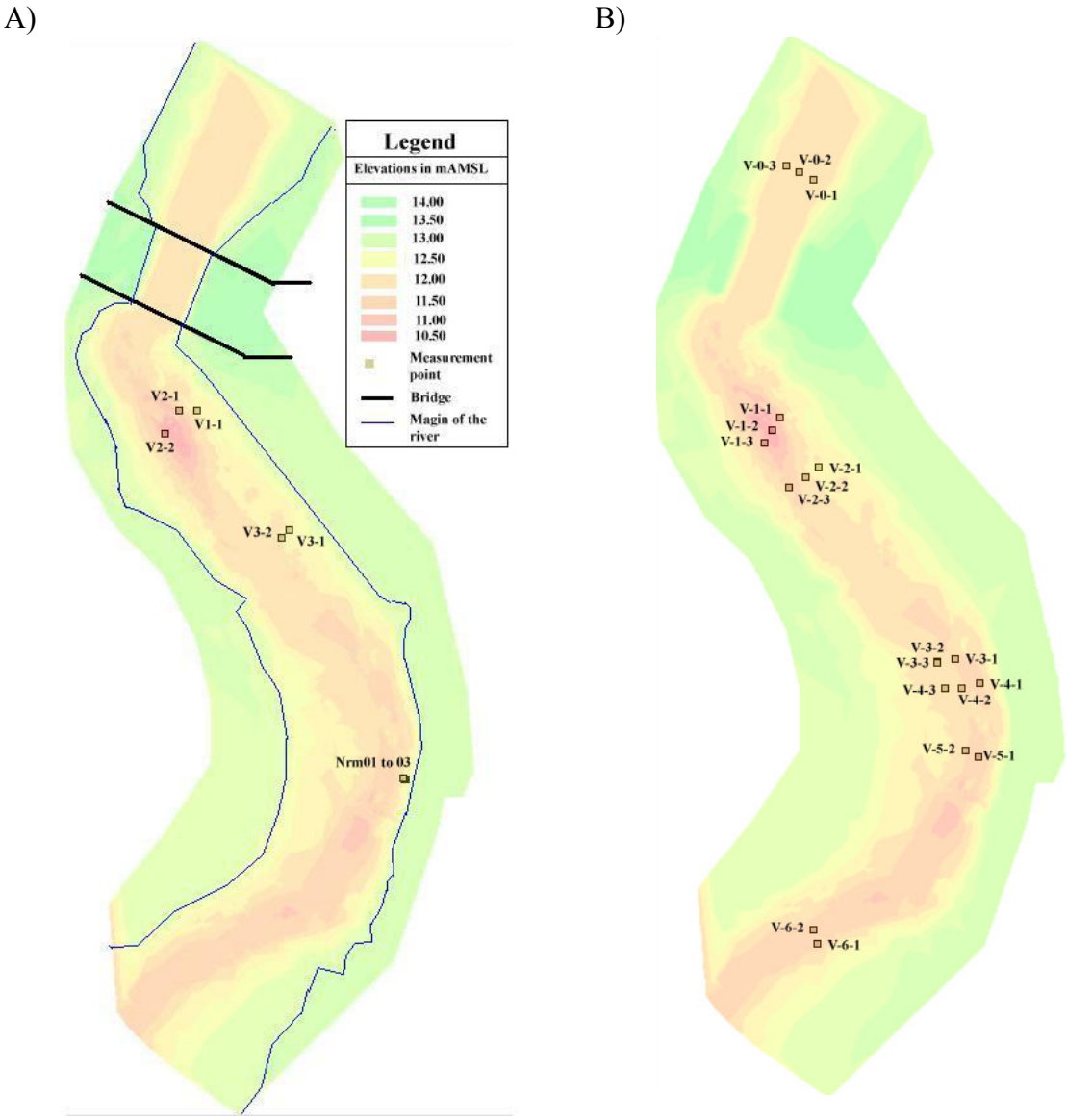

Figure 5-8 Velocity measurement locations in the river for validation purpose. A) December 6, 2007, B) August 14, 2007

5.6.2 Vertical profile of velocity across the river bend

One of the objectives of the current work was to investigate bed shear stress distribution across the river bend. To meet this goal, precise measurement of the vertical profile of the flow velocity in turbulent boundary layer was required. As already mentioned above, fixing the position of a catamaran or boat in its position on the stream was not generally possible. However, a precise measurement of flow velocity requires a very still platform. To meet this ambitious requirement, an innovative portable aluminium traverse system was constructed to span the 10-meter width of the river at the river bend. The measurement instruments (ADV or ADCP) were mounted on this traverse system as explained below.

Portable traverse system

The traverse system was made of a 12m long aluminium truss with rectangular cross section (0.40 x 0.42m, W x H) (refer to Fig. F-1 in Appendix F-7) and a remotely adjustable carrying wagon (Fig. F-2 in Appendix F-7). The wagon consisted of a rolling platform (Figs F-4 and F-5 in Appendix F-7) on which a vertically adjustable shaft (Fig. F-6 in Appendix F-7) was mounted. The measurement instrument has been mounted on this shaft and the whole system could be rolled along the traverse system over six bearings (two in lower edge and four under the upper edge) manoeuvred by means of a pulley system. The wagon as well as the shaft was remotely adjusted from the riverbank using two separate pulley systems and two sets of special ropes (Fig. F-3 in Appendix F-7). This unique system enabled manoeuvre of the traverse system in two axes (horizontal and vertical) with a step less adjustable mechanism. Furthermore, the structure was designed and constructed in a way that it could be easily transported and fixed on precisely (using tachymeter) levelled pedestals installed at both sides of the riverbank across three sections (Fig. F-3 in Appendix F-7).

Acoustic Doppler Velocimeter(ADV)

The principle of operation of ADV is somewhat different from that of ADCP, even though both systems rely on Doppler shift effect. The former instrument comprises one transmitter in the middle and three receivers (depending on the number of velocity component being measured) surrounding it (some models have four receivers such as Vectrino® from NorTek). Both transmitter and receiver generate narrow acoustic signals, which meet each other at a distance from the transducer called sampling distance. The volume of water in which these beams meet forms the sampling volume. As a pulse (generated by the transmitter) travels through water, a portion of its energy is reflected in all directions. However, the receiver is sensitive only to the acoustic waves reflecting from a very narrow angular range. As the pulse approaches the sampling volume, the signal strength detected by the receiver increases. The ADV does the measurement when the received signal has reached its maximum strength at the centre of the sampling volume.

To carry out precise three-dimensional velocity measurements in turbulent boundary layer close to the river bank, a 10MHz Acoustic Doppler Velocimeter (ADV), Hydra® from SonTek, with maximum 25Hz sampling rate was used. For the rest of the cross section,

StreamPro ADCP was used to measure mean flow velocity distribution across the river bend, since it would have required too much time to measure all of vertical velocity profiles solely by ADV.

Hydra® ADV has a standard sampling volume (in the form of a cylinder) with 6mm diameter and 7.2 mm height (0.25^{cc}) which is located 10 cm away from the transmitter. The vertical edges of sampling volume is defined within ±0.5 mm accuracy and could be configured so that a minimum sampling height of 1.2 mm could be reached. It should be noted that such a small sampling size is subjected to signal strength as well as spatial averaging. This ADV can typically detect boundary condition within 25 cm away from its transmitter with an accuracy about 1 mm (for detailed specification of the instrument, see Appendix F). This excellent feature was utilized to carry out measurements in the boundary layer.

Measurement program

A preliminary three-dimensional velocity profile measurement, using both ADV and ADCP was achieved on September 21, 2007 to determine bed shear stress and Reynolds shear stress distribution in the bank-toe region. The second velocity measurement close to the outer bank in the river bend was carried out by means of solely ADV on December 6, 2007 to determine mean depth-averaged velocity as validation data for the hydrodynamic model (see Sec.5.6.1). Two other measurement campaigns were achieved using both ADV and ADCP to study secondary currents and bed shear stress distribution in detail across two sections (Figs. 5-9 to 5-11), namely, at the bend apex and upstream of it on 10 and 22 April 2008, respectively.

Each measurement program started by positioning and fixing the traverse system across the considering cross section on designated pedestal on both sides of the river. The first three vertical profiles close to the riverbank were measured using ADV and the rest of the other vertical profiles by means of ADCP (Fig. 5-9). This was due to the fact that measurements using ADV would take so long (2-4 hours for three vertical profiles, depending on the number of measurement points) that it would not be possible to measure enough points across the entire river using exclusively ADV in one day. Furthermore, the most interesting measurement area was the bank zone, at which the velocity was measured solely using ADV. After mounting the instrument on the vertical shaft and fixing it in the desired elevation, the orientation of the probe was aligned manually along the main flow direction and measured using a compass. A laser distometer, with better than 1mm precision, was installed on the upper side of the traverse system to measure the distance of the shaft to the reference point on the outer bank. Additionally, the position of the shaft and consequently each single sampling volume as well as bed elevation were measured by means of a tachymeter. The water level was measured by a piezometer about 2m downstream of the traverse system. This unique high precision field measurement technique enabled a very accurate robust system of measurement in the turbulent boundary layer.

The number of measurement points in each velocity profiling was dependent on the water depth (Figs. 5-10 and 5-11). Application of ADV made it possible to conduct measurements very close to the bed (0.6 cm) and adopt a flexible spacing of measurement points. On the other hand, velocity measurements using ADCP comprised blanking zone near the bed and a

uniform spacing of the measurement points. Blanking distance of 11 cm under water surface using both instruments was inevitable. To compare the accuracy of ADCP versus ADV, velocity profile measurements using both instruments at the same profile (third profile) was achieved on April 22, 2008 as it is observed from measurement points in Fig. (5-10). In the following, the deployment set up of the ADV is demonstrated.

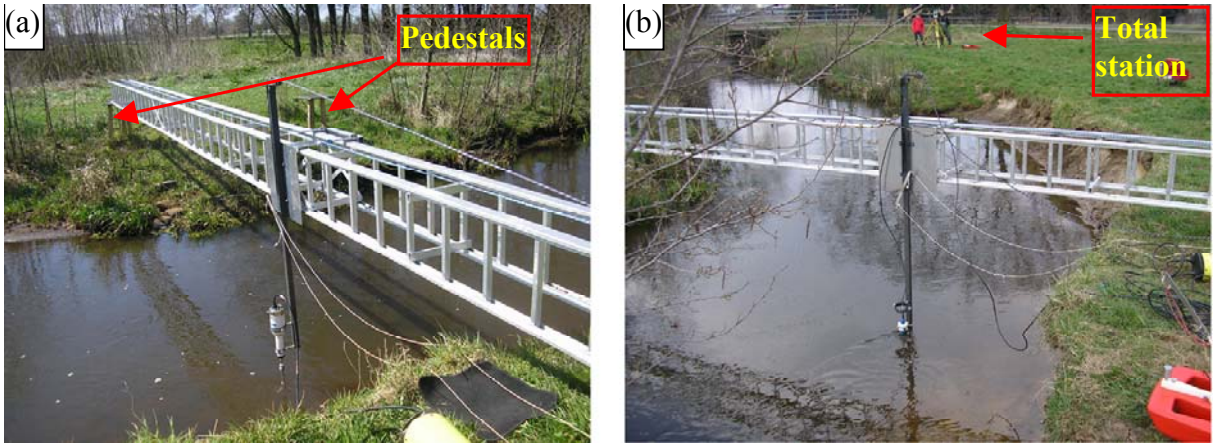

Figure 5-9 Precise velocity measurement using an innovative traverse system by means of (a) ADV; (b) mini ADCP

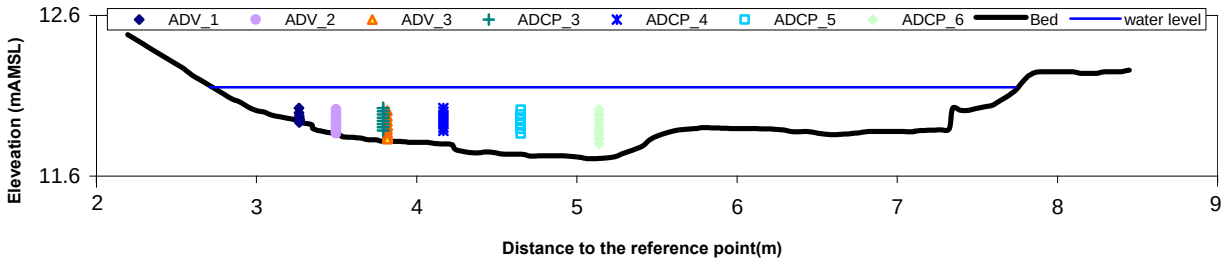

Figure 5-10 Velocity measurement points across the river upstream of the bend apex (section –2)

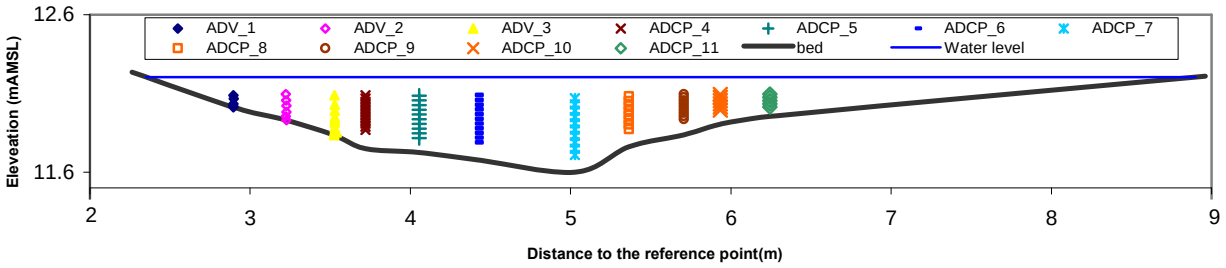

Figure 5-11 Velocity measurement points across the river bend apex (section-1)

Measurement frequency

Between 5000 to 6000 data samples with 20Hz frequency (250-300 seconds) were collected using ADV for each measurement to produce sufficient samples for computation of mean velocity in Dec. 2007. While in the last three set of measurements in April 2008 the sampling rate of ADV was set to 25Hz collecting between 5000 to 15000 samples (200 to 600 seconds) for turbulent velocity analysis. According to Nezu and Nakagawa (1993) a minimum of 5000 samples should be available to examine turbulent structures for which the minimum required measurement frequency (f_m) can be estimated by the following equation:

$$f_m > 2 f_{\max}$$
$$f_{\max} \approx \left(\frac{50}{\pi}\right)\left(\frac{u}{h}\right) \tag{5–2}$$

here u is the depth average velocity and h is the local water depth. The minimum required measurement frequency was calculated to be between 10 to 26 Hz using Eq. (5–2) and measured flow velocities (tables 6-6 and 6-7), which justifies the selected measurement frequency. To estimate the appropriate total sampling time (T), Nezu and Nakagawa (1993) suggested the following formula:

$$\left(\frac{T}{T_B}\right) \approx \left(\frac{N}{50}\right)$$
$$\frac{T_B U_{\max}}{h} = 1.5 - 3 \tag{5–3}$$

where T_B is the mean bursting period and N denotes the sample size of data. Assuming the minimum sample size of 5000, a total measurement period of 214 to 500 seconds is computed using Eqs. (5–2) and (5–3). The above-mentioned calculations justify the time and sample size adopted in this work for the study of turbulent structure.

Pre-processing

The velocity data measured by ADV was analysed by WinADV software. As can be inferred from Fig. (5-12), the correlation coefficient was high enough (>70%) to indicate a reliable low noise velocity measurement. This reflects the high quality of the measurements.

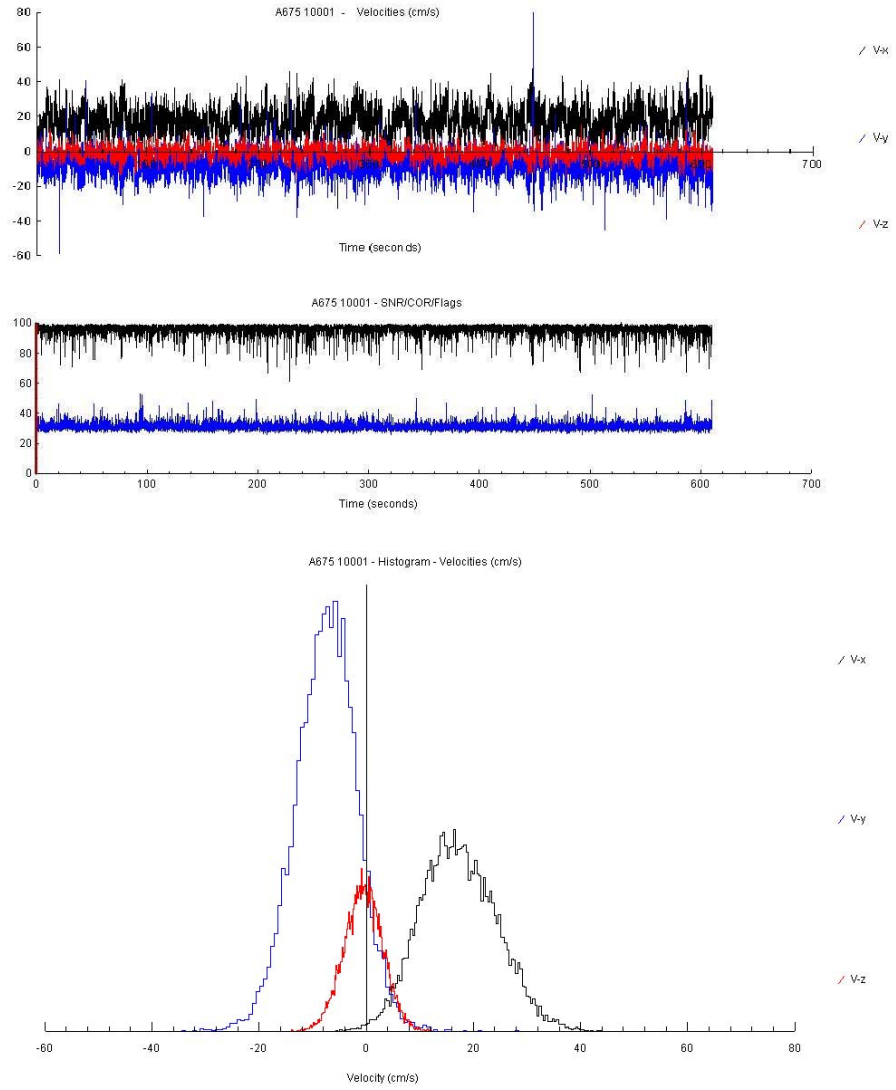

Figure 5-12 A typical instantaneous velocity measurement using ADV on April 10, 2008 analyzed by WinADV software.(a) Velocity Time series (b) Correlation and Signal to Noise Ratio (SNR). (c) Histogram

Furthermore, in this figure a good SNR (Signal-Noise-Ratio) value greater than 15% indicates that enough particles were present in the sampling volume to produce a reliable measurement. All of the achieved measurements possessed almost the same measurement quality as just explained.

In spite of the high quality of the measurements, existence of noise in data is inevitable. Such noises as it is observed in form of spikes in Fig. (5-12), must be filtered out before processing the data. This was achieved using WinADV software by despiking method of Phase-Space Threshold (Goring and Nikora, 2002) and filtering out data with correlation less than 70%. Afterwards time-averaged values of flow velocity components, velocity magnitude and Reynolds shear stresses have been computed using the mentioned software. Time-averaged velocity magnitude may be computed in two ways in the software, either as the resultant of the time-averaged velocity components or time-averaged of time series of velocity magnitudes. In the former case, the velocity components in x, y and z directions are first

separately averaged over time from which the velocity magnitude is computed (Eq. 5–4). In the latter case, first the resultant velocity (velocity magnitude) is computed and then the developed time series is averaged over time (Eq. 5–5).

$$\bar{V} = \sqrt{\bar{u}^2 + \bar{v}^2 + \bar{w}^2} \tag{5–4}$$

$$V(t) = \sqrt{\tilde{u}^2 + \tilde{v}^2 + \tilde{w}^2}$$
$$\bar{V} = \frac{1}{t}\int_t V(t)dt \tag{5–5}$$

Where $V(t)$ is the instantaneous velocity magnitude; $\tilde{u}$, $\tilde{v}$ and $\tilde{w}$ instantaneous velocity components in x, y and z directions, respectively; the bar over the variables indicating their time-averaged values. The calculated time-averaged velocity magnitude profile using these equations for one profile measured on April 10, 2008 is shown in Fig. (5-13). As can be observed from this figure, the calculated velocities using Eq. (5–5) are generally greater than those computed using Eq. (5–4) from 6 to 12% in this case. The question is now, which one of these approaches is correct.

To answer this question, it is important to notice that velocity is a vector quantity and turbulent velocity may change not only its magnitude but also its direction in every instance. Therefore, the direct addition of the magnitude of velocity vectors of each ensemble seems not to be correct for the computation of time-averaged resultant velocity. Furthermore, in deriving the time-averaged mathematical equations of flow motion (Reynolds Averaged Navier-Stokes equations), each velocity component is separately averaged over time. Hence, Eq. (5–4) was preferred to Eq. (5–5) for computation of time-averaged velocity magnitude in the rest of the analysis, including depth-averaged velocity.

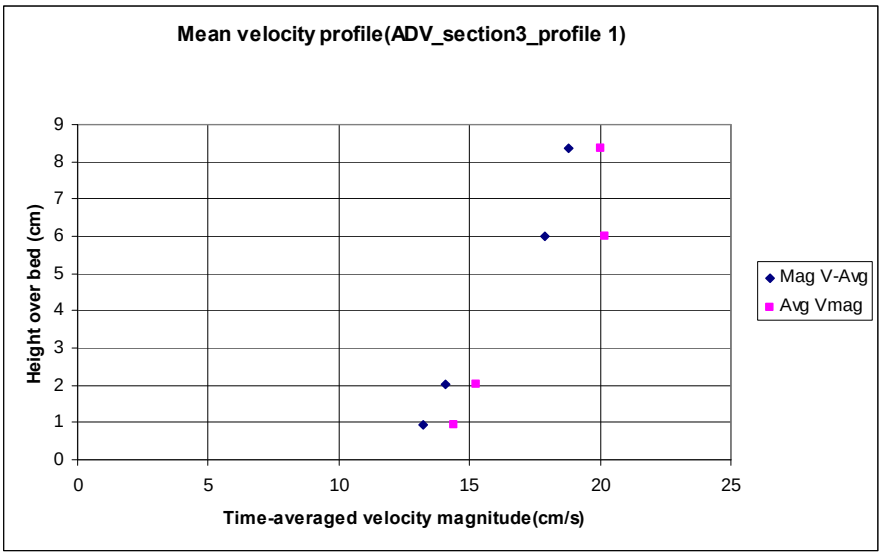

Figure 5-13 Time-averaged velocity profile: Mag V-Avg (Eq. 5–4) and Avg Vmag (Eq. 5–5)

The measurement sensors were aligned so that V_x of the ADV probe had been in the main flow direction while V_y of ADCP against the main flow direction (Fig. 5-14). Therefore, to convert the latter velocity component in the correct main flow direction, V_y of ADCP has been multiplied by cos (180). For investigation of secondary currents it is important to have the lateral velocity in radial direction of the river bend curvature. To determine this lateral direction precisely, the curvature of the river bend was approximated by a circle with a radius of curvature of 21.855 m (as shown in Fig. 5-15).

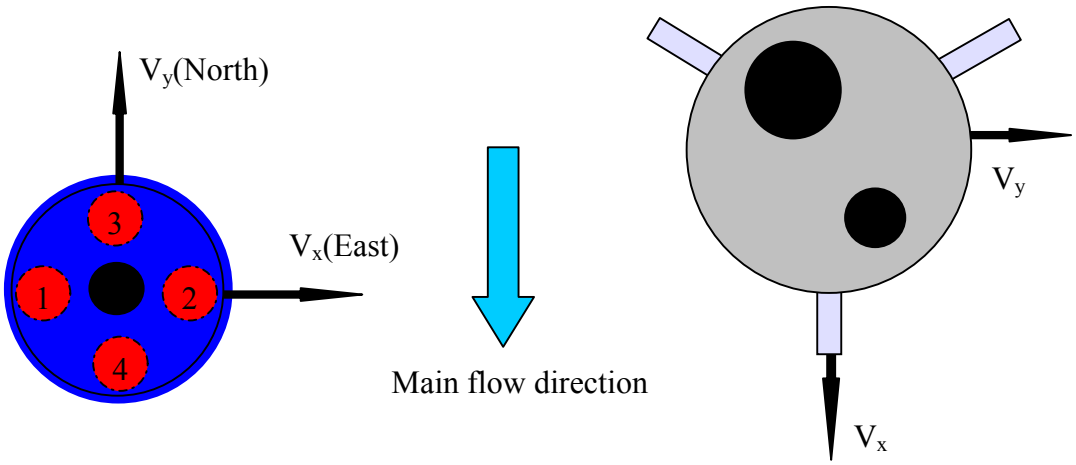

Figure 5-14 Orientation of ADV and ADCP during measurement mounted on traverse (viewing from tail to tip). The dimensions are not scaled

As can be observed from this figure, due to irregularity around the apex of the river bend, a second circle with radius of curvature of 9.191 m was fitted to the river bend around the apex to get a more precise radial direction for section (1).

Furthermore, it was required to compensate the misalignment of the traverse system and consequently the sensors at each measurement point with respect to the radial direction (Fig. 5-15). To meet this requirement, the rotation angle (θ_r) of the coordinate system of the probes at each measurement point had to be determined. Assuming that the streamlines in the river bend follow the curvature of the mentioned approximated circles at each measurement point, a radial ray starting from the centre of the circle (for section (1) the smaller circle was used) extending through the considered measurement point were drawn on the map (as an example the black radial ray through measurement point in Fig. 5-15).

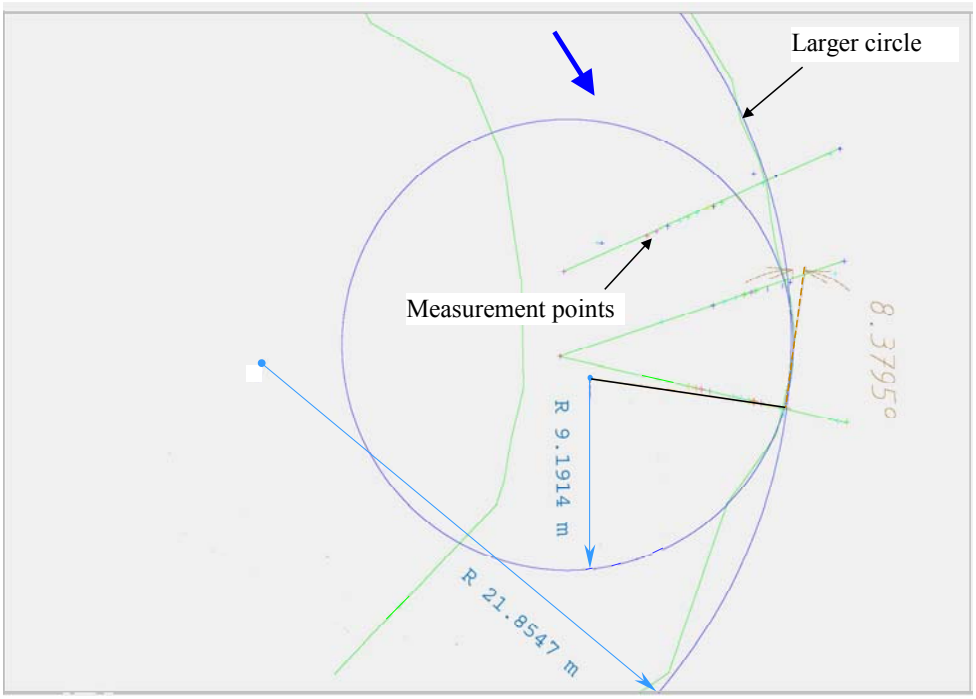

Figure 5-15 The river bend under study depicting the measurement points (+) and sections thin lines as well as the radial ray passing through the first measurement point of the most downstream section

A tangential line was drawn to the intersection point of this line and the circle (the brown tangential line to the circle in Fig. 5-15) to compute the tangential angle (here 8.38° azimuth, the clockwise angle made to the North), which represents the theoretical longitudinal direction of the flow at that measurement point.

To compute the lateral flow component along the drawn ray at each point, the measurement axis was rotated (in this example clockwise 11.38°) so that the longitudinal axis of the probe became parallel to the tangential line (see Fig. 5-16 for clarification of the calculation procedure). The so-calculated rotation angle for each measurement point and azimuth angle of tangential lines are given in Table (5-2) as θ_r and α_t, respectively.

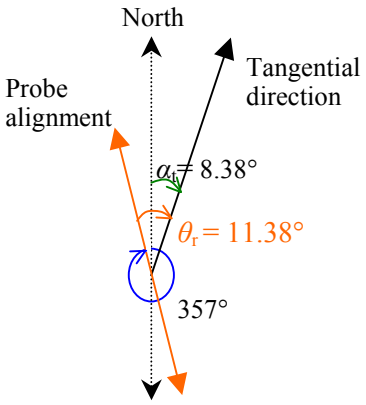

Figure 5-16 A typical computation of the rotation angle of the measurement probe at a measurement point

The velocity components in the new coordinate were computed using rotation matrix (Eq. 5–6),

$$\begin{bmatrix} V_x' \\ V_y' \end{bmatrix} = \begin{bmatrix} \cos\theta_r & -\sin\theta_r \\ \sin\theta_r & \cos\theta_r \end{bmatrix} \begin{bmatrix} V_x \\ V_y \end{bmatrix} \tag{5–6}$$

where the velocities with prime denote the rotated velocity. The rotation angle (θ_r) accounts for the misalignment of the instrument as well as traverse system, which was not exactly perpendicular to the river bend curvature. The computations were achieved using WinADV and WinRiverII software for ADV and ADCP data, respectively. In WinADV the rotation angle is positive in the counter clockwise direction, while it is positive in clockwise direction in WinRiverII, if the option "magnetic variation" is used or positive in counter clockwise direction when option "Beam 3 misalignment" is used for correction. The latter method was used here for ADCP data. The rotation angles of each measurement point are given in Table (5-2).

Table 5-2 Rotation angle of each measurement point due to the misalignment.

Measurement section	Vertical Profile number	Probe alignment angle (Azimuth)	α_t	θ_r
3	ADV_sec1-1	357	8.38	-11.38
3	ADV_sec1-2	357	8.15	-11.15
3	ADV_sec1-3	357	7.87	-10.87
3	ADCP_sec1-0	15	7.99	7.01
3	ADCP_sec1-1	15	7.99	7.01
3	ADCP_sec1-2	15	7.48	7.52
3	ADCP_sec1-3	15	7.2	7.8
3	ADCP_sec1-4	15	6.11	8.89
3	ADCP_sec1-5	15	5.94	9.06
3	ADCP_sec1-6	15	5.44	9.56
3	ADCP_sec1-7	15	4.47	10.53
2	ADV_sec2-1	330	-8.61	-21.39
2	ADV_sec2-2	330	-8.67	-21.33
2	ADV_sec2-3	330	-8.31	-21.69
2	ADCP_sec2-1	335	-8.31	-16.69
2	ADCP_sec2-2	335	-8.4	-16.6
2	ADCP_sec2-3	335	-7.97	-17.03
2	ADCP_sec2-4	335	-7.77	-17.23

The misalignment of the traverse system introduced a longitudinal displacement error of the measurement location with respect to the radial direction of the river bend curvature as given in Table (5-3).

Table 5-3 Range of longitudinal displacement error due to the misalignment of the traverse system

Measurement sections	Min. displacement (m)	Max. displacement (m)
1	0.010	0.260
2	0.210	0.853
3	0.365	0.74

As can be inferred from the procedure of rotation of the measurement axes, there is a source of error in estimation of the river bend curvature, computation of the tangent to the curvature and measurement of the orientation using compass. Therefore, a sensitivity analysis was carried out on the rotation angle to investigate the effect of this parameter on horizontal velocity components. The results of this analysis are presented in Fig. (5-17) and (5-18) corresponding to the ADV measurements on April 22, 2008 over the third vertical profile.

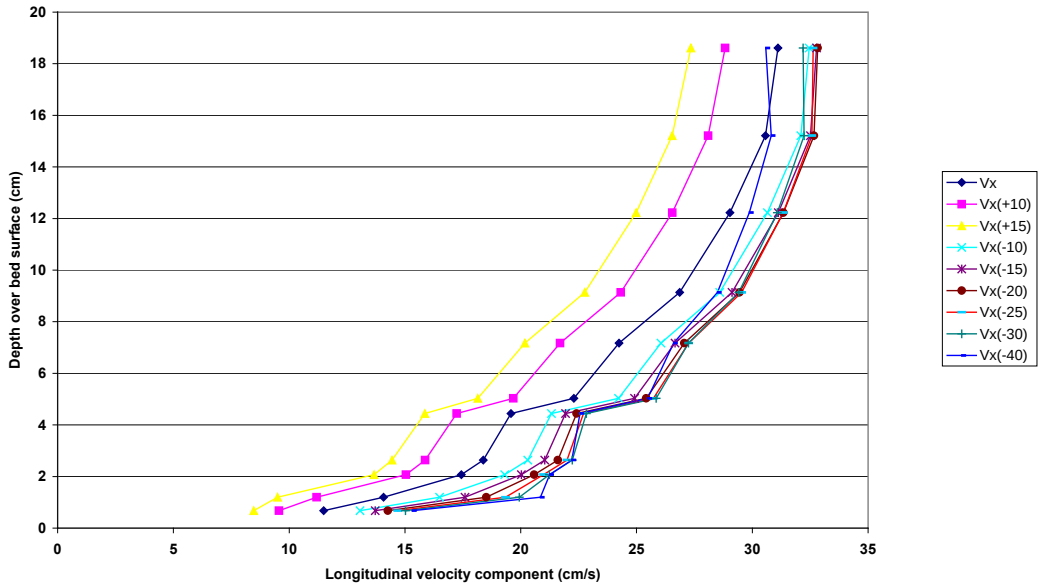

Figure 5-17 Effect of rotation angle (–25° to +10°) on longitudinal velocity profile, section (2) profile (3)

As can be inferred from these two figures, the lateral velocity profile is much more sensitive to the rotation angle than the longitudinal velocity profile. This shows how important is the correct orientation of the probes for the study of secondary currents, which may introduce more than 100% error in the measurement of lateral velocity.

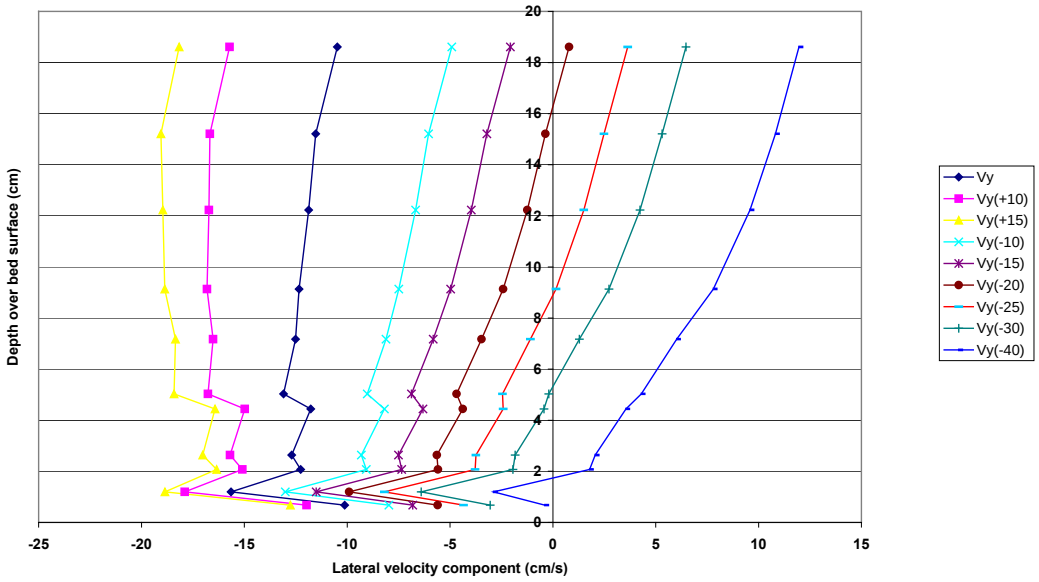

Figure 5-18 Effect of rotation angle (from –25° to +10°) on lateral velocity profile, section (2) profile (3)

5.7 Sediment transport

As is well known, bed evolution is the result of sediment imbalance. Therefore, data on sediment concentration can provide validation data for sediment transport model, which impacts bed evolution simulation results. Several techniques have been used to measure suspended sediment concentration in field, for example, bottle sampling, pump sampling, focused beam reflectance, laser diffraction, nuclear method, optical backscatter and acoustic methods. The advantages and disadvantages of these and other techniques can be found in Wren et al. (2000). In the current work, a sophisticated laser sensor (850 nm) turbidity profiler (ASM-IV®, ARGUS) was used to measure sediment concentration at the upstream section where discharge was measured. This instrument works with the principle of common optical backscatter sensors with the advantage of providing sediment concentration profile over the whole water depth down to the bed profile.

The gathered data was aimed to provide the required boundary condition for solution of the sediment transport equation (Eq. 3–20). Three measurement campaigns were conducted on February 22, 2007; March 9 and 20, 2007. On the latter date, it was tried meanwhile to establish correlation between ADCP acoustic backscatter intensity and sediment concentration. Due to the very low measured values of suspended sediment concentration (an average of less than 100 mg/l), further measurements of suspended sediment concentration were avoided. The results of the above-mentioned measurements and their analysis are presented in Ch. 5.7. In the following, the principle of operation of ASM-IV and its calibration are presented.

5.7.1 The principle of operation of turbidity profiler

The turbidity profiler, ASM-IV, comprises an array of optical backscatter sensors (OBS), embedded with a vertical spacing of 10 mm, in a stainless steel rod (Fig. 5-19). The length of the sensor section of the instrument was 80 cm (an array of 80 OBS sensors). Each sensor consists of an infrared laser (850 nm) transmitter and a photo sensor as receiver. The transmitter emits laser light into the sampling volume of 10 cc in a range of 10 cm in front of the sensor. A portion of emitted light is reflected from, for example, suspended material. The photo sensor beside each transmitter detects the backscatter signal. The strength of the backscatter signal is used as a measure of sediment concentration. Therefore, site-specific calibration of the instrument is required since the reflected optical signal depends on the sediment concentration as well as particle characteristics, such as size and shape. For example, only a small portion of clay in suspension avoids registration of coarser sediment (Kondolf and Piegay, 2003), while light scattering from clay particles (4μ) with platy shape is 20 times more effective than that mass concentration of coarse silt (Foster et al., 1992). To a lesser extent the optical signal is sensitive to the particle composition (organic or mineral for example) and colour. Therefore the time of the year in which samples are taken for calibration can be important. For example in flood events in winter, where less green cover is expected, more clay particles may be transported in the river than normal flow. Such a situation in rivers with mainly sandy sediment may result in large error in measurement of sediment concentration. Therefore, the largest uncertainty and error in measurement can be related to the calibration.

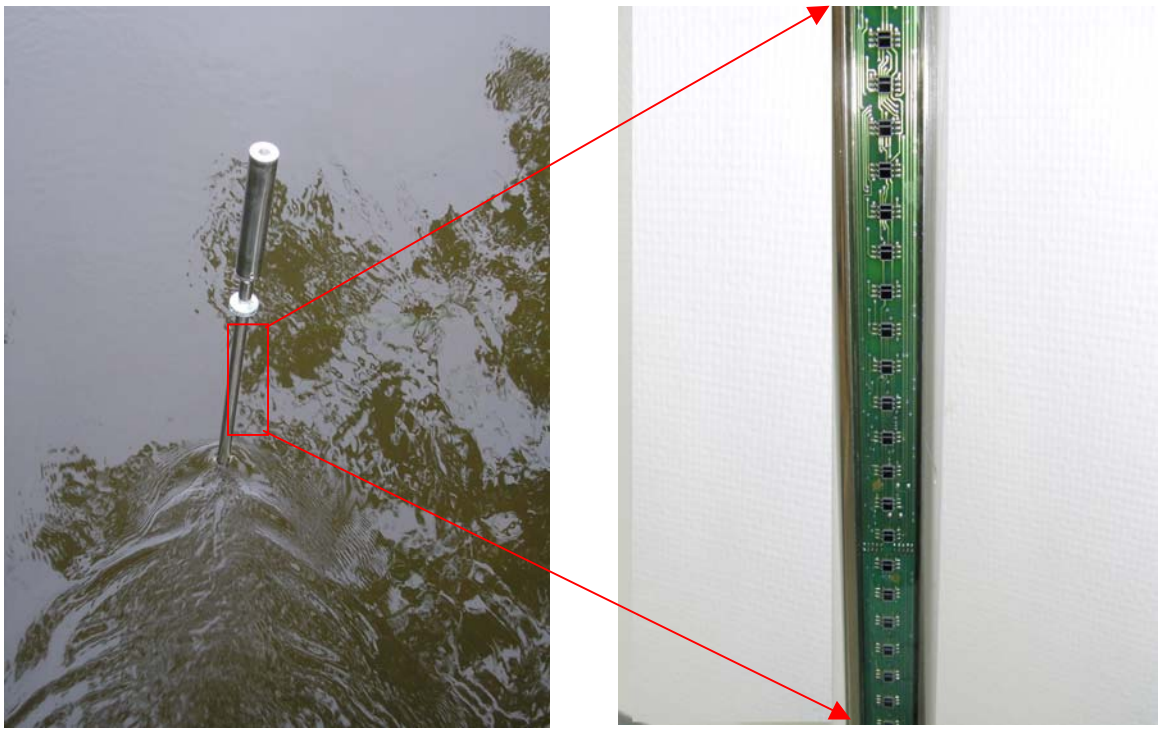

Figure 5-19 Muti-optical backscatter sensor (ASM-IV) during deployment (left) and the close-up view of OBS array

5.7.2 Calibration of the backscatter sensor

As discussed earlier, the calibration of backscatter probes is site specific. Therefore, at first a sample of suspended sediment was sent to the firm ARGUS for calibration of the ASM-IV probe. However due to the very low suspended sediment concentration and consequently reduction of reliability of calibration, it was decided to use another sample for calibration, which included not only suspended sediment but also the bed material of a thin upper layer. Using such a sample calibration was achieved for a range up to 1000 mg/l. For the details of calibration procedure, the reader is referred to ASM-IV manuals.

5.8 Bed evolution

The sandy bed of alluvial rivers may undergo large fluvial evolution during short and even very short timescale (during one flood event). Since the evolution of the riverbank, especially along the river bend, is closely connected to the bed evolution at the bank-toe, periodical bathymetry measurement is important, at least, in the context of morphological studies. Such a bathymetry measurement, especially in small spatial scale such as the case in the current study, requires higher resolution than common survey with tachymeter or GPS. In this regard, application of multi-beam echo sounders has become very common in marine applications, where enough water depth is available. However, such instruments can not be applied in shallow waters like Hardebeck-Brokenlander Au. Even common commercial single-beam echo sounders were not applicable due to the very shallow water depth in this river until a special shallow water single-beam echo sounder (Fahrentholz BBES 700 kHz) was acquired in Mai 2007. Therefore, no reliable bathymetry data could be acquired prior to this date. The echo-sounder was integrated with the rover antenna of the RTK-DGPS system (Leica System 500-SR350) and mounted on a floating round Styrofoam to form the bathymetry measurement system (Fig. 5-20). The whole system was then towed across and along the stream with much closer cruising paths (higher spatial resolution) in the river bend than elsewhere. Nevertheless, the measurement resolution is much less than multi-beam echo sounder. On the other hand, the spatial measurement resolution is much higher than tachymeter and GPS, with two further advantages. First, the accuracy of the measurement is higher due to the fact that, the levelling staff (or reflector pole) penetrates into the bed, especially in sandy soils, and introduces errors and uncertainty in measurements. Second, protrusion of levelling staff in water together with the feet of surveyor disturb largely the bed profile, especially in rivers with sandy beds, while the applied method is a non-intrusive one.

The mentioned echo-sounder transmits a 700 KHz sound wave and measures the time of returned echo from the bed surface to the transducer in order to measure the depth and records them in 10 Hz with an accuracy of 1 cm. A maximum of 2 cm horizontal accuracy by RTK-DGPS system could be reached during the measurements.

Figure 5-20 illustration of application of integrated RTK-GPS with single-beam echo-sounder installed within a float

In the second phase of the measurements, bathymetry measurement were conducted on 20 July, 24 Oct., 10 Dec. 2007, Feb. 5 and March 7, 2008 to explore the interaction between bed and bank evolution process, especially in near outer bank-toe along the river bend.

The main difficulties during both measurement phases were first loosing the connection between GPS and satellites or reduction of number of visible satellites, which resulted in impairing the accuracy of horizontal positioning; and second, the growth of algae and other vegetations at the river bed, which introduced error in measurement of bed surfaces, especially on Oct. 24, 2007.

A FORTRAN program was developed to filter out the contaminated data such as those due to low accuracy (<4cm in position) of GPS data as well as noise caused by floating objects and bed vegetation. The deleted points were then interpolated by triangulation method, achieved in Fledermaus software with a maximum resolution of 5 cm. This procedure led to omission of a large amount of data near the outer bank-toe on Oct. 24, 2007, which resulted in reducing the accuracy and spatial resolution of the generated digital elevation model (DEM). The result of bathymetry measurements and their analysis are presented in Ch. 6.6.

5.9 Bank evolution

The focus of the present work is the study of riverbank erosion mechanisms. Different methods are used for monitoring and measurement of bank erosion depending on spatial and temporal scale of study. Lawer (1993) made a comprehensive review and discussion on the measurement techniques for the study of bank erosion and divided them into seven categories depending on the temporal and spatial scale of the study, among which, erosion pins, PEEP (Photo Electric Erosion Pins) and terrestrial photogrammetry are applied to short timescale.

The mentioned methods suffer from either or both spatial and temporal resolution (Lawer et al., 1993) and are labour-intensive in pre- and post processing phases.

Most of the above-mentioned measurement techniques were unable to quantify small-scale changes in the riverbank, which trigger large-scale morphological changes. However, technical advances in hardware used for surveying and software for post-processing of large amount of data, paved the way for acquiring more accurate data with higher resolution. High precision tachymeter surveying (Fuller et al., 2003), Real-Time Kinematics Global Positioning System (RTK-GPS) (Brasington et al., 2000; Mitasova et al., 2002) and airborne LiDAR (Light Detection and Ranging) techniques (Thoma et al., 2001, 2005) have been applied in the study of river and coastal morphology.

Tachymeter offers a very high accuracy but relatively low spatial resolution. In the case of very steep or vertical riverbanks, it is also not appropriate. The same limitations hold for GPS in addition to its lower accuracy. Airborne LiDAR systems provide relatively high accuracy and high spatial resolution. However, it is feasible for the study of large areas with limited temporal resolution. Application limitations of the mentioned methods are discussed in Heritage and Hetherington (2007) and Milan et al. (2007).

With recent developments in LiDAR technology, very high spatial resolution and accuracy is attainable by terrestrial laser scanning, with much higher temporal resolution than its airborne version and lower costs on small- and moderate-size reaches. This technique has been often applied in industry, piping, architecture, as well as archaeology and has found its way into geology and landslide studies (Bitelli et al., 2004), in-stream habitat quantification (Large and Heritage, 2007), study of gravel-bed forms (Entwistle et al., 2007) and assessment of erosion and deposition in proglacial rivers (Milan et al., 2007).

Detailed study of erosion and deposition processes of the natural riverbanks with complex surface requires a very high spatial resolution to reduce the possibility of un-scanned areas due to the shadowing effect of roughness elements and overhanging zones.

A high-resolution terrestrial 3D laser scanner was used in the current work to study the morphological changes of the steep riverbank along the river bend. The probability of unscanned zones due to shadowing effect of roughness elements and overhanging zones in this method is also minimized due to proximity to the target and the possibility of scanning from different angles and overlapping the scanning results.

In the following, application of the aforementioned technique to investigate the riverbank erosion and deposition mechanism is illustrated. This technique has been combined with RTK-GPS integrated with a shallow-water single-beam echo sounder for the measurement of the bed surface under water surface (bathymetry), where laser scanner is not applicable.

The length of the study reach was over 13 m of the outer bank of the river bend with 0.80 to 1.3 m bank height (Fig. 5-21). Scanning was achieved intermittently in two phases over flooding periods of October 2006 to April 2007 and October 2007 to March 2008 using Leica Cyrax HDS2500 3D laser scanner. Additional riverbed bathymetry was achieved in the second phase, using the method addressed in the previous subchapter, which enabled investigation of interaction of bed and bank processes.

Figure 5-21 The outer riverbank of the meander under study

5.9.1 Laser scanner Leica Cyrax HDS2500

The instrument measures the distance based on the principle of "time of flight". A pulsed green visible (VIS) laser source (wave length of 532 nm, safety class II) is emitted to the target and the time of receiving the reflected wave is measured and converted to distance, knowing the light velocity. The emission of the laser source is controlled by a servo motor-driven spinning plane mirror.

The single point accuracy of the instrument in the range between 1.5 and 50 m is 6 mm (position), 4mm (distance) and 0.003° (angle); and the accuracy of the modelled surface is 2 mm. The highest scan resolution is 0.25 mm point-to-point spacing (vertical and horizontal) in 50 m range. The vertical and horizontal measurement spacing can be defined independently. The instrument field of view is 40° x 40° (horizontal x vertical). The maximum application range of the instrument is 100 m.

The study area was scanned in two overlapping regions due to the instrument's small field of view. Six targets were placed in each region and scanned with extra dense resolution for later registration of two overlapping scans and merging in Cyclone® 4.0 (the post-processing object oriented software of the laser scanner). Each merged point cloud was geo-referenced in the mentioned software using surveyed coordinates of the targets by the tachymeter Leica TCR705.

Surveying using laser scanner was achieved on Oct. 25 and Dec. 12, 2006; Jan. 5 and 30, 2007; Feb. 14 and April 16, 2007, designated as first phase. On the second phase, scanning of bank surface was accomplished on Oct.24, 2007, Jan. 23, 2008; Feb. 5, 2008 and March 7,

2008. The second measurement phase was accompanied by bathymetry measurement using the already mentioned method. The aim of the latter measurement phase was integration of the high-resolution laser scanning data with low-resolution echo sounder data for the study of interaction of bank and bank-toe processes.

5.9.2 Pre-processing

All of the point clouds were cut first by a defined three-dimensional polygon as a bounding region, common to all scans by means of a FORTRAN program. The bounding limit was dictated by different water stages at the time of scanning and the elevation of vegetated layer over the top of the bank.

A Fortran program was developed to filter the over-hanging grasses from the point clouds. In fact, hanging grasses were closer to the measurement origin than actual bank surface. This was used to generate an algorithm for filtering these data. The filter program algorithm creates a vertical grid over the bank surface and transforms the coordinates to a local cylindrical coordinate system with laser scanner as its origin. Then, it computes the average and standard deviation of radial distance of the points to the origin within each grid cell. The points within each grid cell with a standard deviation larger than a user specified threshold are deleted.

Having bounded and filtered the point clouds, surface models (TIN and DEM, depending on the software applied) were created from point clouds for the computation of erosion and deposition surfaces with different softwares. However, the generated surface models in commonly available softwares, such as FlederMaus®, Surfer®, ArcView® and Sycode TerrainCad plug-in for AutoCad®, were erroneous in the zones with vertical and negative slopes as shown as an example in Fig. (5-22). The reason is the vertical to negative slope of the bank, which does not present an unfolded surface, so that more than one elevation can be attributed to a single point in a horizontal plane. Therefore, a DEM model can not be correctly created for such surfaces.

Although the Cyclone® 4.0 software could generate a complex 3D folded fine mesh, it could neither achieve surface difference computations between two meshes in the software nor export the mesh to be analysed in another software. Even if it would be the case, it would not be possible to create a difference surface with traditional methods (vertical subtraction of two elevation models), due to the local folded zones in the mesh surface. A simple novel coordinate translation and rotation was achieved, as explained in the following, to remedy the mentioned problems.

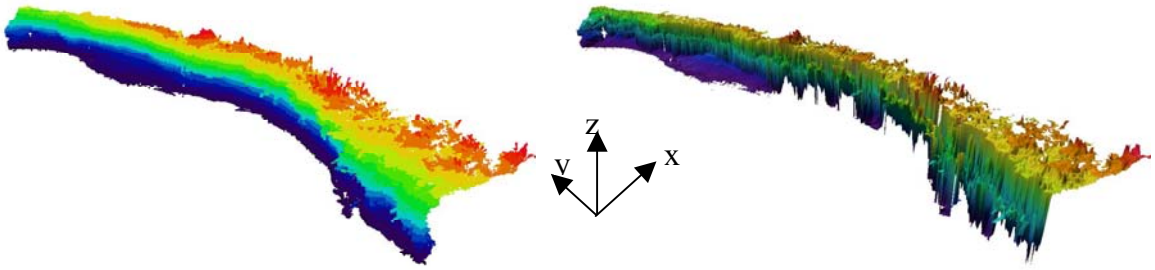

Figure 5-22 Error in generation of DEM of the riverbank in the vertical- and negative-slope regions of the riverbank. Left: original point cloud in Cyclone software. Right: generated digital elevation model in FlederMaus software

The Gauss-Krueger coordinate system were translated to a local coordinate (with a scaling factor for horizontal plane) and rotated about y axis 90° counter-clockwise, so that the bank surface lay on the horizontal plane (y-z plane) with x axis directing down in negative direction of the former z axis (Fig. 5-23). Therefore, in the analysis of the riverbank, later presented in Ch. 6, the horizontal local coordinate is negative. The DEM model was created in the new mentioned transformed coordinate system in FlederMaus® (Fig. 5-23a). The coordinates were then rotated back for visualization purposes in graphical environment of the software (Fig. 5-23b).

In the case of the data of 24 Oct.2007, the original laser scanner data of bank-toe were integrated to the echo-sounder data and a DEM model was generated for investigating bed and bank-toe processes. The so-generated 3D digital elevation models (DEM) of the scanned bank surfaces were subtracted sequentially to produce erosion/deposition surfaces and their distribution along the river bend.

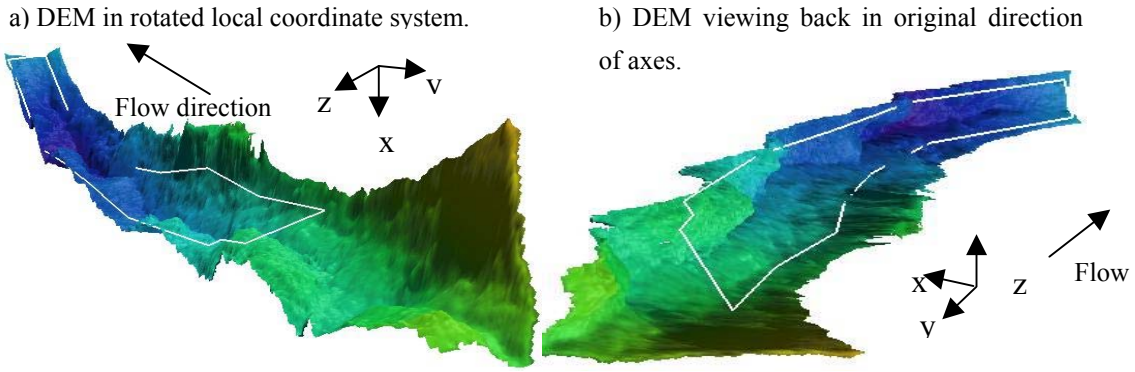

Figure 5-23 Generated DEM model of outer riverbank. The white polygon is the bounding limit.

5.10 Moment of bank failure

Registering the time of failure is an important issue for the investigation of the effect of flood frequency and duration on different types of undercutting and cantilever failure. Furthermore, time of bank failure is of interest not only for validation of bank stability model, but also for its influence on deposition and redistribution of failed bank material at the bank-toe. In the case of cantilever failure occurring during high water stage, it is expected that a larger portion of the failed material be transported by flow, depending on the sediment transport capacity of flow. At low flow stages, if cantilever or sapping failure occurs, it is expected that most of the failed bank material deposits at the bank-toe, depending on the bed slope at the bank-toe.

To the knowledge of the author, the only available technique for recording the timing of bank erosion is the Photo-Electric Erosion Pins (PEEP) developed by Lawler. The advantage of the instrument is simultaneous recording of the amount as well as time of punctual erosion or deposition. However, it has several disadvantages such as pin movement, intrusion into water and impacting local flow, influence on erosion and high price for a network of such pins. Furthermore, application of such pins is more appropriate for fluvial erosion than bank failure, since it may reinforce the soil in overhang zone or conversely deteriorate soil structure and soil stability. For further information on advantages and disadvantages of erosion pins, the reader is referred, for example, to Couper and Maddock (2002) as well as Lawler (1993).

A novel technique was developed to record semi-automatically the time of bank failure. A remote GSM/GRPS-camera from Nokia (PT-6) was installed in a special weatherproof box and mounted on a 4 m timber mast located on the inner bank (Fig. 5-24). Power was supplied to the system by a pack of rechargeable batteries, which was recharged automatically by means of a solar panel. The camera was able to send (stream or still) images of the outer bank over GSM/GPRS network to mobile phone or email. The images could be captured on request (by sending SMS to the camera), at set times or automatically by detection of motion (for example failure of bank). Since no sudden change of water level was expected in this river (for example no tidal effect), the mode of “capture on request” was chosen. This had the advantage to adjust the number of captured images depending on flow situation.

In contrast to PEEP this system is non-intrusive and applicable to bank failure monitoring. Furthermore, it captures a larger area of the bank at once (view angle 55°). On the other hand, it is not able to measure the amount of erosion neither under nor over water surface. However, the bank surface change (erosion/deposition) has been measured here separately using laser scanner.

Figure 5-24 Remote camera system with solar panel mounted on a timber mast.

6 Measurement analysis and results

Understanding the bank erosion process is one of the main objectives of the present work. This can only be attained by a comprehensive measurement and monitoring program. The analysis of the measurement results constitutes a deep insight into factors governing the process as well as their interactions in bank erosion process. Furthermore, the data obtained by means of measurements will be applied to verify the new developed morphodynamic model of bank erosion.

6.1 Sediment properties

6.1.1 Physical properties

Physical properties of the riverbed and bank are the primary parameters needed for the analysis of sediment transport, bed level change and bank erosion and failure. They were determined using the methods described in Ch. 5.2. A typical result of sediment sieve analysis is shown in Table (6-1) and Fig. (6-1). For a complete result of sieve analysis, the reader is referred to Appendix G.

Table 6-1 Physical properties of the riverbed and bank material excluding the homos layer of the bank

Sediment properties (bed)	
D_{10} (mm)	0.11
D_{30} (mm)	0.17
D_{50} (mm)	0.22
D_{60} (mm)	0.25
$C_c=D_{30}^2/(D_{60}xD_{10})$	1.1
$C_u=D_{60}/D_{10}$	2.2
Sediment properties (bank)	
D_{10} (mm)	0.12
D_{30} (mm)	0.17
D_{50} (mm)	0.22
D_{60} (mm)	0.23
$C_c=D_{30}^2/(D_{60}xD_{10})$	1.1
$C_u=D_{60}/D_{10}$	1.94

According to the Unified Soil Classification System (USCS), the bed and bank materials are in SP category (poorly graded sand), which means sand with uniform particle size distribution. This confirms that the sediment mixing and armouring effect are not required to be taken into account in bed evolution modelling. In well-graded sediments, larger grain sizes cover the finer grains so that an armouring layer is established on the bed surface, resisting erosion. Furthermore, the riverbank can be considered to consist of a single layer of soil (neglecting the agricultural homos layer covering the bank top, 20-30 cm thick). This confirms the assumptions made in the development of theory (Ch. 2.4) regarding single-layered soil and uniform sediment.

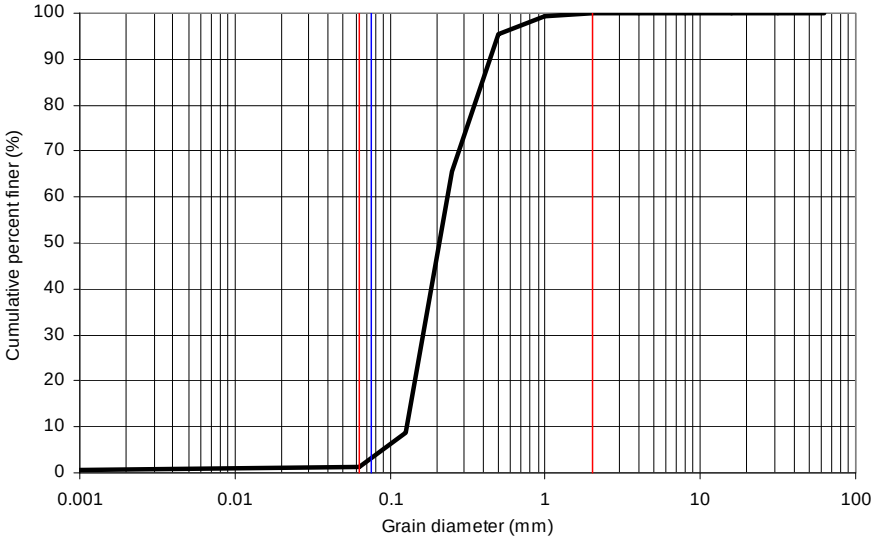

Figure 6-1 A sample grain size distribution of the riverbank material

The average of main physical properties of the sediment is given in Table (6-2). The specific gravity of the sediment can be taken to be 2.65 with adequate reliability, since over 90% of the sampled materials are composed of quartz with the mentioned specific gravity.

As already mentioned in Ch. 5.2, using electron microscope, the diameter of several suspended sediment particles was measured directly with the average of 77.6 μm nominal diameter. A typical measurement is shown in Fig. (6-2). The vertical and horizontal white lines in this figure show how the nominal diameter of the particle was determined. Further analysis of the sample by the method of Spectromatography revealed the constituent of the suspended sediment with Au, Ca, Cl, Si and Fe as major components. Moreover, the practical salinity of the water was measured 0.2 ppt, which is almost zero.

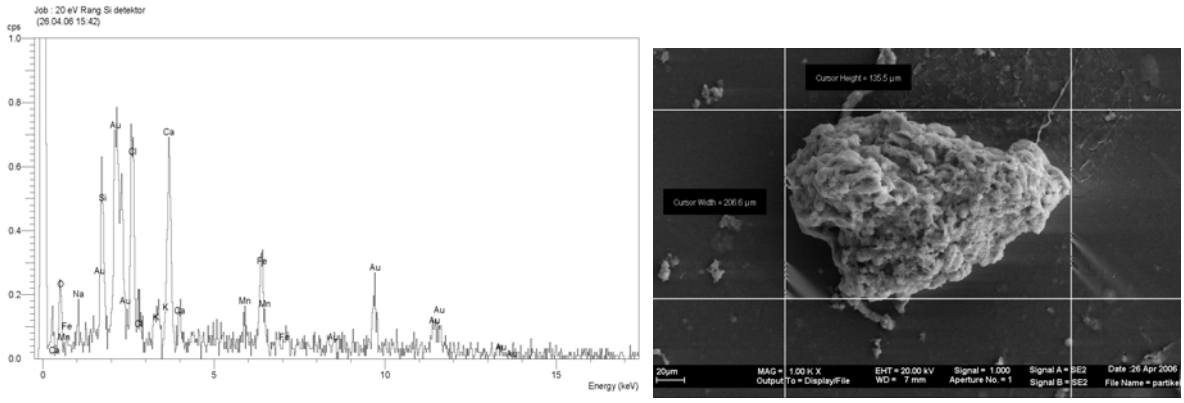

Figure 6-2 Result of Spectromatography of suspended sediment (left) and a sample particle measurement using electron microscope (right)

6.1.2 Geotechnical properties

Geotechnical properties of soil are the required parameter in the analysis of the riverbank stability. The results of direct shear test (DIN 18 137-DSR) to determine geotechnical properties of soil are given in Table (6-2)[1]. The high value of soil cohesion (14.6 kN/m^2) is not ordinary for sand material and is comparable with clay soil. The average value of cohesion of fine sand is 5 to 8 kN/m^2 according to DIN 1055-2. However, it should be noted that the applied test gives the effective shear strength, only when the specimen is saturated. The averaged measured degree of saturation of the samples was 55%, which means that the samples were in unsaturated condition. This implies that the measured cohesion should have been mainly due to the apparent cohesion and not effective cohesion. As already explained in Ch. 3.4.4, apparent cohesion is the summation of effective cohesion and cohesion due to the matric suction (Eq. 3-42). The measured physical properties of the sand probes (with clay and silt fraction of less than 1.4%) indicate that the measured soil cohesion can be mainly due to the matric suction and shows what a high cohesion can be developed in soil matrix of fine sandy soils due to the matric suction. The measured angle of repose (42.3°) is also much

[1] For the laboratory report of direct shear test refer to Appendix G-1.

higher than the average value given for normal sand (35°-37.5°). Angle of repose as high as 46.5° has been also determined in direct shear test by Schmautz (2003). Furtheremore, it should be noted that the range of normal stresses applied in the laboratory test (50 to 100 kN/m^2, Appendix G-1) have been much larger than those in natural situation.[1] Therefroe, an insitu test might have yielded other results.

Table 6-2 Physical and geotechnical properties of the river material (bed and bank), excluding the homos layer of bank

Phase properties	
Soil density: ρ_s(g/cm^3)	2.65
Dry density: ρ_d (g/cm^3)	1.678
Porosity (%):	36.7
Void ratio:	0.58
Degree of saturation	0.55
Geotechnical properties	
Friction angle φ	42.3°
Cohesion c (kN/m^2)	14.6

6.2 Critical shear stress

Critical shear stress is required for determination of equilibrium bed load transport. Using Shields diagram, the critical shear stress was calculated as 0.12 Pa, taking d_{50} =0.22 mm as mean diameter of sediment. As already explained in Ch. 5.2, the shear stress was measured additionally using Microcosm instrument. The plots of measured turbidity versus bed shear stress (friction velocity) for all four measurement-windows of this instrument are shown in Fig. (6-3).

In the following the result of measurements using this graph accompanied by visual observations recorded by a video camera are discussed. While visual observation depends on the investigator's definition of how much movement constitutes initial motion (Neill and Yalin, 1969; Wilcock 1988), the combination of this graph with visual observation improves the certainty of computations.

As can be observed from this figure, in the range of friction velocity less than 0.82 cm/s no change of turbidity is observed in the diagram. Only the fuzz over the bed was re-suspended initially into the water column. The alteration in turbidity of the first plane, which represents bed layer, occurs at a friction velocity of 0.922 cm/s (τ = 0.085 Pa). By observing the film captured during the experiment, initiation of motion of sediment in the form of rolling started at this stage.

[1] The specimens were obtained from bank surface in a depth of approximately half of a meter.

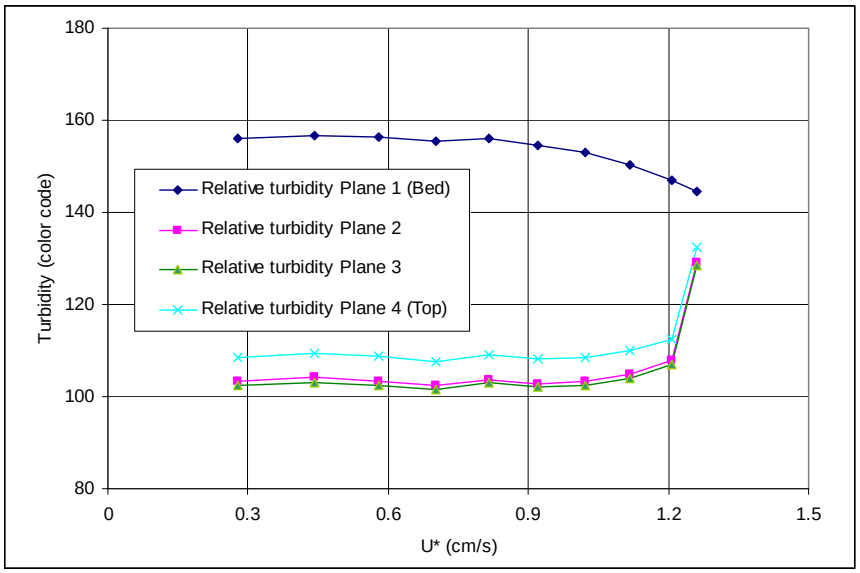

Figure 6-3 Plot of turbidity in Benthic Simulator versus friction velocity to determine critical shear stress

At a shear velocity of 1.021 cm/s (τ = 0.104 Pa) this curve deflects further downwards. By observing the aforementioned recorded film, initiation of saltation took place at this stage. By further increase of bed shear stress to τ = 0.125 Pa, almost most of the bed sediment were in movement in the form of rolling as well as saltation and bed forms started to form. This stage can be observed in Fig. (6-3) at u_*= 1.12 cm/s. As can be inferred from this figure, at this stage all of the four curves show a change in the value of turbidity, meaning that the smaller sediment sizes have been brought to suspension. At a τ = 0.146 Pa, the bed material went into suspension near bed and bed forms were clearly developed. This situation is associated with u_*= 1.2 cm/s in Fig. (6-3). As can be observed from this figure, the last measured point depicts a sudden change of gradient in three curves (planes 2-4), reflecting sudden change of sediment concentration in the water column. At this stage sediment was injected into the water column over the formed dunes like a jet, creating a very turbid water column. The detail of the experiment has been summarized in Table (6-3).

Table 6-3 Calculation of shear stress using Benthic

Revolution speed [1/min]	u_* [cm/s]	Relative turbidity (Plane1)	Relative turbidity (plane2)	Relative turbidity Plane(3)	Relative turbidity Plane(4)	Bed shear stress (kPa)
5	0.279	156	103	103	108	0.008
10	0.443	157	104	103	109	0.020
15	0.580	156	103	103	109	0.034
20	0.703	155	102	102	108	0.049
25	0.816	156	104	103	109	0.067
30	0.922	154	103	102	108	0.085
35	1.021	153	103	103	109	0.104
40	1.117	150	105	104	110	0.125
45	1.208	147	108	107	112	0.146
48	1.261	145	129	129	133	0.159

From the above mentioned measurement and observation, a shear stress of τ_c = 0.125 Pa was determined as initiation of bed load transport (critical shear stress), which is close to its theoretical value using Shields diagram (0.12 Pa).

6.3 Discharge monitoring

As already mentioned in Ch. 5.5.2, five direct discharge measurements (Table 6-4) were selected for the generation of discharge time series using the method explained in the following. To correlate the continuous velocity profile measurements to the direct measured discharges, the method of index-velocity was used. Based on this method, the mean velocity, calculated by dividing the direct measured discharge by the flow area, is correlated to the index-velocity. The latter is the local depth-averaged velocity computed based on vertical profile of the velocity magnitude measured by an instrument such as a stationary ADCP. To obtain a good correlation, the closest velocity ensembles of stationary ADCP to the time of direct discharge measurement were selected. The measured vertical profile of velocity was first averaged over the selected ensemble time interval using Eq. (5–4) and then the so-calculated velocity profile was integrated over the effective depth (the actual measured zone) to yield the index-velocity. By repetition of this process for each period of direct discharge measurement, a time series of mean velocity versus index-velocity was generated. Using regression analysis between these two sets of data, an equation was obtained for calculating mean velocity, given index-velocity. Then the so-calculated mean velocity was multiplied by the flow area to obtain discharge time series. This process for generating discharge time series is explained in the following.

Table 6-4 Flow measurements by moving mini ADCP calculated by StreamPro software

Row	Date	discharge (m^3/s)	area(m^2)	Mean velocity (m/s)	Measured area (%)
1	13.12.2006 12:18	0.751	2.0	0.38	49.80
2	20.12.2006 13:03	0.619	2.1	0.292	49.50
3	05.01.2007 12:45	1.052	2.4	0.437	54.24
4	14.02.2007 15:19	0.878	2.3	0.391	52.67
5	20.03.2007 15:19	1.310	2.9	0.451	61.91

Time-averaging

First of all a sensitivity analysis was achieved to explore the effect of averaging time (30 sec., 1, 2, 3, 4,5 and 10 min.) on vertical profile of velocity as well as index velocity. It was concluded that the magnitude of time averaging impacts the shape of the vertical velocity profile but not the depth-averaged value (index-velocity). A comparison of seven stationary measurements revealed that the smoothest vertical velocity profiles were obtained by 5 to 10 minutes time-averaging interval (see Appendix G). However, as can be observed from Fig. (6-4) the index-velocity was not sensitive to the time averaging, having a variance of 2.26×10^{-6} to 1.44×10^{-4} m/s depending on the mean velocity magnitude. This implies that any of the mentioned time averaging interval could be applied. However, to smooth out the effect of this selection, an average of all seven time averaging variants was used to calculate the index-velocity.

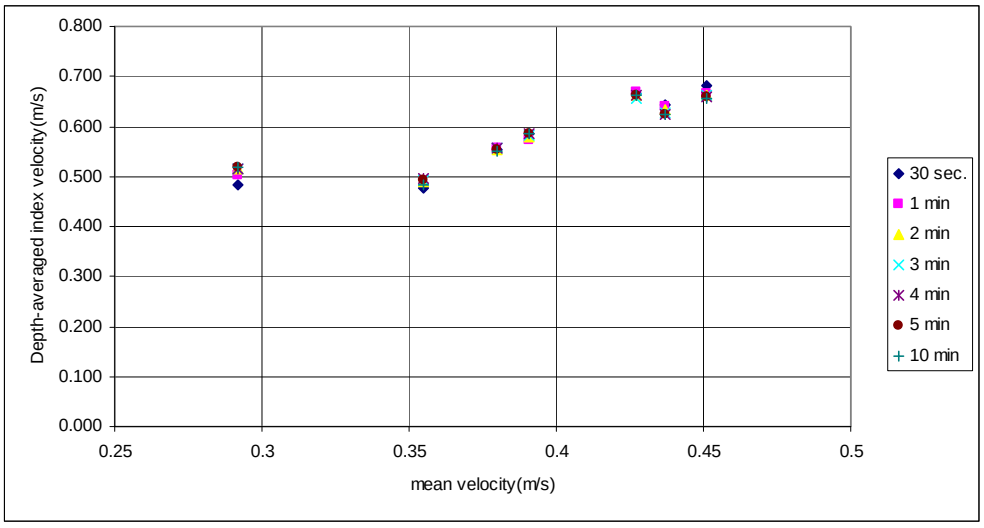

Figure 6-4 Comparison of the effect of time averaging on computation of index-velocity

Regression

The so-calculated index-velocity versus mean velocity is plotted in Fig. (6-5). By inclusion of the zero point in both time series, the following regression equation was obtained.

$$V_{mean} = 0.5153 U_{index}^2 + 0.3587 U_{index} - 0.0005 \qquad (6\text{–}1)$$

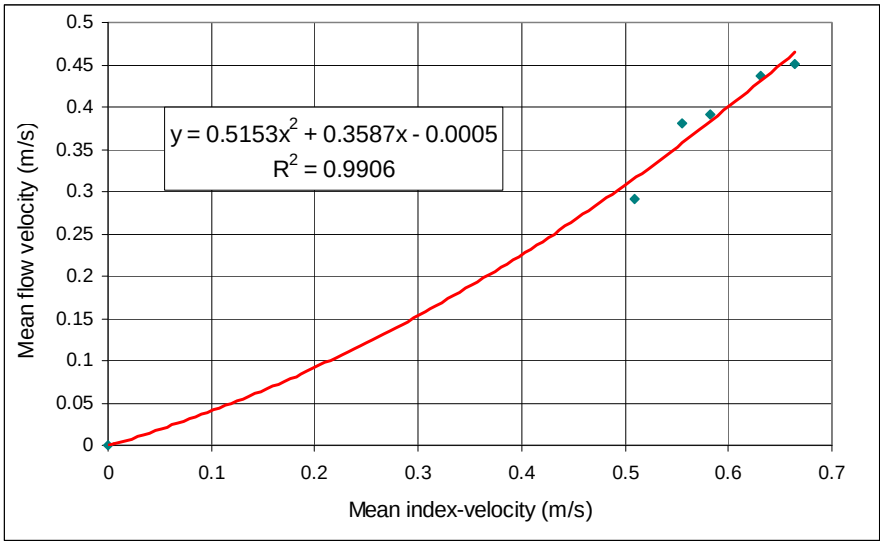

Figure 6-5 Mean velocity versus index-velocity and their functional relation using regression

Discharge time series

To generate the time series of discharge based on the long-term measurements of vertical profile of velocity, a FORTRAN program was written to calculate the time series of index-velocities from discharge measurement time series. The program reads the ASCII output data file generated by WinADCP program and filters out the missing and blank cells. In the next step, for each cell (bin) a time-averaged velocity magnitude (resultant of the three velocity components calculated by StreamPro) is computed and then the index-velocity is computed by depth-averaging the time-averaged velocity magnitude. Finally, using Eq. (6–1) and water level- flow area relation (refer to Sec. 5.4) discharge is computed as follows:

$$Q = V_{mean} \cdot A \tag{6–2}$$

The above-mentioned process was achieved for the whole time series of measured vertical profile of velocity and generated discharge time series for the measurement periods. To close the gap of unmeasured periods, due to the instrument failure as already explained in Ch. 5.5.3, the calculated discharge time series using Eq. (6–2) was correlated to the measured water level time series at upstream and downstream using regression analysis, to generate a Q-H relation. For the period of upstream water level missing data, downstream water level was applied for the mentioned regression analysis and for the rest upstream water level data was utilized as explained below.

The discharge calculated using Eq. (6–2) for the period of 27 February till 4 March 2007 was correlated once to the upstream water stage and the other time to the downstream water stage at the same period. This period was chosen because it comprised a full flood hydrograph (rising and recession period) comparable with the lost data and enabled the detection of a probable hysteresis effect in water stage discharge relation. As can be observed from Fig.

(6-6), no hysteresis effect was observed and a good correlation could be obtained for both cases.

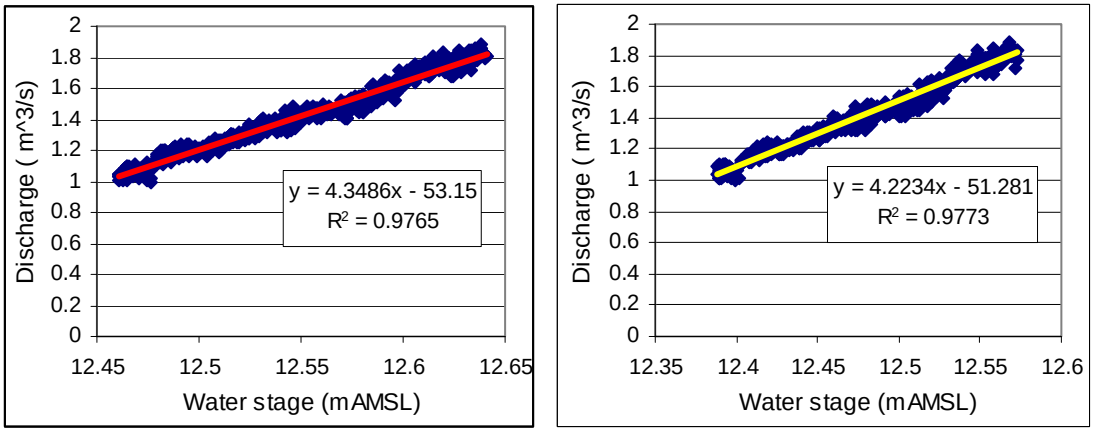

Figure 6-6 Discharge-stage (Q-H) relation based on the measurements of 27.02 to 4.03.2007. Left: Q-H relation based on upstream water stage. Right: Q-H relation based on downstream water stage

The regression equations shown in Fig. (6-6) were used to generate discharge time series for the whole period of available water stage data in 2007. The so-calculated discharges together with upstream and downstream water stages are depicted in Fig. (6-7). As it is observed from this figure, in two periods the discharge calculated using upstream water stage is higher than those calculated based on downstream water stage. As only the downstream water stage was available for the whole mentioned period, the discharge time series based on the downstream water stage was chosen. It should be noted that the correlation coefficient of the regression was even higher for the calculations based on the downstream water stage than that of the upstream water stage (Fig. 6-6).

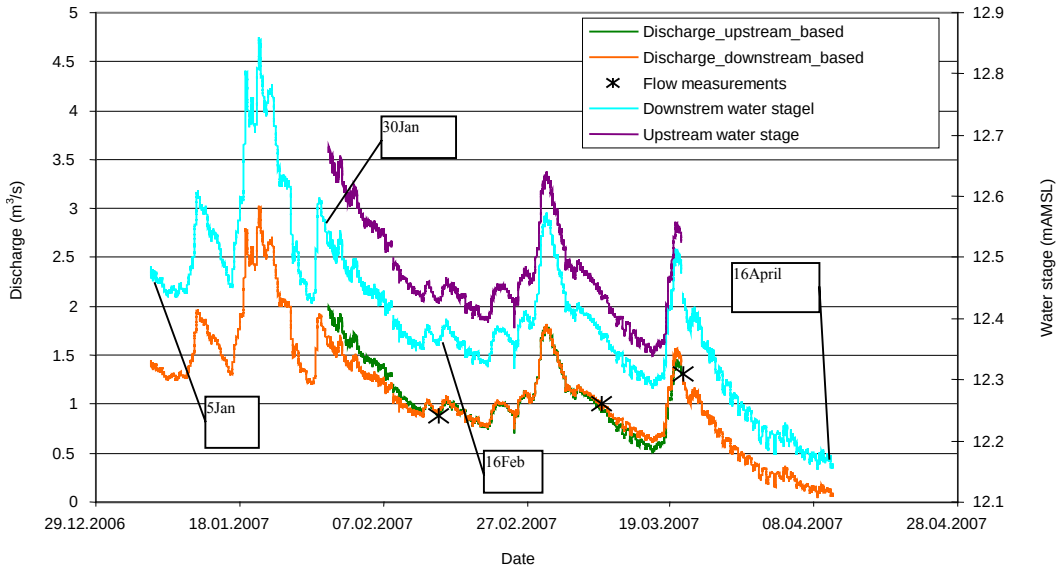

Figure 6-7 Discharge time series based on upstream and downstream water stages (2007)

As shown in Fig. (6-7), the computed discharges agree very well with the three direct measured flow discharges, depicted by stars in this figure. The computational error compared with these measurements is additionally presented in Table (6-5).

As shown in Fig. (6-7), the characteristics of high flow events are different. The first flood event comprises a multi-peak hydrograph and a trailing flood event with a very long recession period and a rapid rising period. The next two flood events, especially the last one, include only one main discharge peak. The different shape of flood hydrographs can impact the morphological evolution of the river differently, as is presented and discussed in Chs. 6.6, 6.7 and 8. In the rising limb of the first hydrograph the discharge has increased from less than 1.5 to about 3 m^3/s (the discharge level of the first peak among multi-peaks) in less than two days (17 to 18th January). The recession period, in contrast, has taken more than 5 days (22 to 27th January) to reach the previous discharge of less than 1.5 m^3/s. The last flood event exhibits also a similar trend with a relatively slow draw-down phase similar to that of the trailing peak of the first flood event.

Table 6-5 Computational error of discharge calculation method based on downstream water level

Datum	Measured discharge (m^3/s)	Computed discharge (m^3/s)	Error (%)
14.02.2007 15:19:29	0.878	0.89265129	1.669
09.03.2007 12:11:29	0.997	0.962934554	-3.417
20.03.2007 15:19:29	1.310	1.313945779	0.301

Based on the above-mentioned analysis the water level stage and associated discharge was calculated for the second period of monitoring as depicted in Fig. (6-8). As seem in this figure, the discharge hydrograph calculated using downstream water level deviates substantially from that of upstream in March. By comparing the flow events during this period with the similar period in 2007, can be observed that the cycle of flooding events seems to be the same. A flow peak has occurred around 7th February and another at the beginning of March in both years. However, the high flow event in March 2008 is lower in magnitude, but higher in peak frequency and longer in peak duration compared to the same period in the previous year (the former peak period is from 29th Feb. to 7th March 2008, while the latter peak period spans from 28th Feb. to 2th March 2007). Generally the flow discharge was lower in 2008 than 2007.

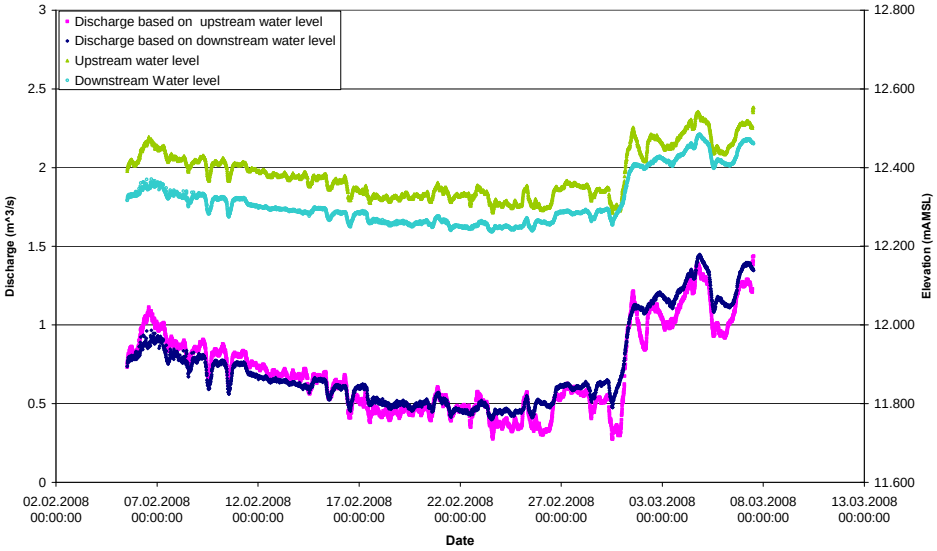

Figure 6-8 Discharge time series based on upstream and downstream water stages

6.4 Flow velocity

6.4.1 Mean flow velocity

For the validation of the hydrodynamic model, mean flow velocity was measured along the river using StreamPro ADCP, as explained in Ch. 5.6.1. The measurement duration was 5 minutes at each measurement point. The time-averaged horizontal velocity components were used to calculate the resultant velocity magnitude at each sampling volume. As already explained in Ch. 6.3, the depth-averaged velocity was not sensitive to the time averaging period. The velocity magnitude at the lower unmeasured zone close to the bed was approximated by means of linear extrapolation. Furthermore, it was assumed that the upper unmeasured zone is outside the turbulent boundary layer, above which flow velocity may be extrapolated as a constant value. This was justified by comparing the change of velocity magnitude among the first three measurement bins below the water surface, where for all measurements this change was between 0.2 to 4 percent. Failing to approximate the velocity in the unmeasured zones can result in large deviation from actual depth-averaged velocity in shallow waters, since a large portion of water depth may be located in the unmeasured zone. Finally, the so-generated vertical velocity profile was averaged over the whole water depth to compute approximated depth-averaged velocity. The latter has been compared with the depth-averaged velocities computed by ignoring the unmeasured zone in tables (6-6) and (6-7). The computed depth-averaged velocity by approximating the unmeasured zone has been later applied for validation of the hydrodynamic model. The location of the measurement points

listed in the just mentioned tables can be observed in Fig. (5-8), where these measurement points are ordered from up to down and right to left.

Table 6-6 Depth-averaged velocity on August 14, 2007

Vertical profiles	Depth-averaged velocity [m/s]		Difference between the two depth-averaging velocities [%]
	Including unmeasured zone	Only measured zone	
v-0-1	0.334	0.368	10.08
v-0-2	0.470	0.535	13.86
v-0-3	0.374	0.427	14.15
v-1-1	0.199	0.252	26.16
v-1-2	0.211	0.252	19.52
v-1-3	0.410	0.415	1.24
v-2-1	0.330	0.398	20.79
v-2-2	0.367	0.450	22.54
v-2-3	0.396	0.465	17.30
v-3-1	0.280	0.334	19.32
v-3-2	0.408	0.469	14.81
v-3-3	0.413	0.486	17.63
v-4-1	0.280	0.334	19.32
v-4-2	0.400	0.478	19.44
v-4-3	0.383	0.462	20.62
v-5-1	0.381	0.451	18.44
v-5-2	0.397	0.469	17.90
v-6-1	0.472	0.543	15.18
v-6-2	0.416	0.452	8.72
Average			16.69

Table 6-7 Computed depth-averaged velocity measured on December 06, 2007

Vertical profiles	Depth-averaged velocity [m/s]		Difference between the two depth-averaging velocities [%]	Measurement instrument
	By approximation	Pure measurement		
V1-1	0.453	0.483	6.65	ADCP
V2-1	0.216	0.238	10.52	ADCP
V2-2	0.490	0.554	13.07	ADCP
V3-1	0.418	0.450	7.48	ADCP
V3-2	0.408	0.471	15.34	ADCP
Nrm-01	0.137	0.137	0.03	ADV
Nrm-02	0.158	0.159	0.67	ADV
Nrm-03	0.194	0.199	2.36	ADV
	Average		7.01	

6.4.2 Velocity distribution in river bend

Secondary currents across river bends cause the maximum depth-averaged flow velocity to shift across river bend, and consequently impact on the distribution of bed shear stress. Therefore, investigation of the three-dimensional pattern of flow across natural river bends brings insight into the process of development and decay of secondary currents along the river bend, compared to the theoretical fully developed pure circular flow. Furthermore, investigation of bed shear stress distribution across river bend lightens the bed erosion pattern along the river bend and its effect on bank-toe erosion.

Flow velocity along the river bend was measured across two sections using ADV and ADCP mounted on a traverse system, as described in Ch. 5.6.2. The first section refers here to the section at the bend apex, where most bank and bank-toe erosion were measured. The second section refers to the one between bend apex and bend entrance with moderate bank erosion rate.

Computation of depth-averaged velocity magnitude in a river bend is not trivial. Due to the existence of secondary currents in river bends, the depth-averaged longitudinal flow velocity and depth-averaged lateral flow velocity should be computed separately from which the depth-averaged velocity magnitude can be computed. For computation of longitudinal flow velocity in unmeasured zones, a law of the wall, such as wake log-law, might be applied to allow for integration of the whole velocity profile over the entire depth. However, such a generally acceptable reliable mathematical method does not exist yet for describing the theoretical vertical distribution of lateral velocity for the whole cross section of the river bends. Therefore, the following approach was adopted.

The velocity magnitude was computed for each sampling volume of ADCP and ADV measurements by the time averaging method already described in Ch. 5.6.2. The so-calculated velocity profile was linearly extrapolated to the bed, in case of measurements using ADV, since measurements very close to the bed could be achieved. For the case of the ADCP, the measured velocity magnitude in this zone was extrapolated using log-law (except the last 1-2 cm near bed which was linearly extrapolated). The upper unmeasured zones for both instruments were approximated using log-law, except in the case where the unmeasured zone was located outside the turbulent layer. In the latter case, a linear extrapolation was used. The velocity magnitude (resultant velocity) was used to compute bed shear stress vector across the river bend based on the log-law.

In the following, the results and analysis of flow velocity distribution across the mentioned two sections are presented separately. Furthermore, distribution of depth-averaged flow velocity, lateral and vertical velocities, Reynolds shear stresses, and finally bed shear stress across sections (1) and (2) are presented.

6.4.2.1 Section (1)

The velocity measurements at this section were accomplished on April 10, 2008 and took about 4.5 hours (excluding 1 hour of set up of instruments and traverse system). The duration

of each measurement point was about 5-6 min. The discharge of 0.619 m^3/s was measured using mini ADCP before starting the velocity measurements. The vertical distributions of the measured flow velocity magnitude together with the approximations in unmeasured zones are presented for each measured velocity profile in Fig. (6-9) (ADV1 to 3 in these figures refer to the first three profiles from outer bank followed by ADCP profiles whose locations have been already presented in Fig. 5-11).

ADV-measurements were carried out over 4 to 5 minutes in continuous mode of ADV with a sampling rate of 25Hz at each measurement point. The same time interval was applied for mini-ADCP measurements at each profile, however with 1 Hz sampling frequency. Due to the low frequency of the ADCP, the turbulence structure could not be resolved[1].

As can be observed from these figures, the measured velocity magnitude follows relatively well the logarithmic profile in the turbulent boundary layer except that of ADV-2 and ADV-3. In profile ADV-2, apart from one outlier data point in a distance of 10 cm from the bed, the rest of data shows a good agreement with logarithmic profile. The closest velocity point to the bed (0.66 cm away from bed, y/h = 0.025) depicts a sudden brake in velocity magnitude profile, which may imply its location in the viscous sublayer.

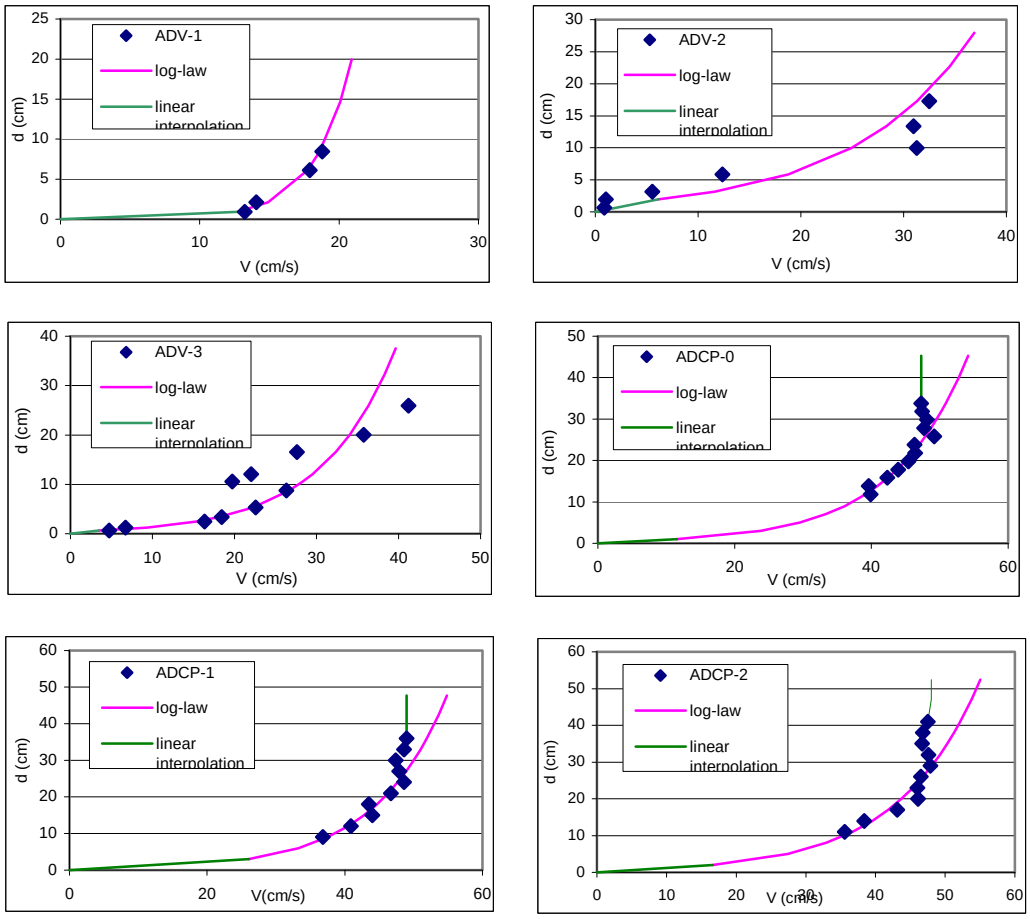

Figure 6-9 Extrapolation of velocity magnitude profile using linear approximation and log-law

[1] For computation of the minimum required frequency to study turbulent structure refer to Ch.5.6.2.

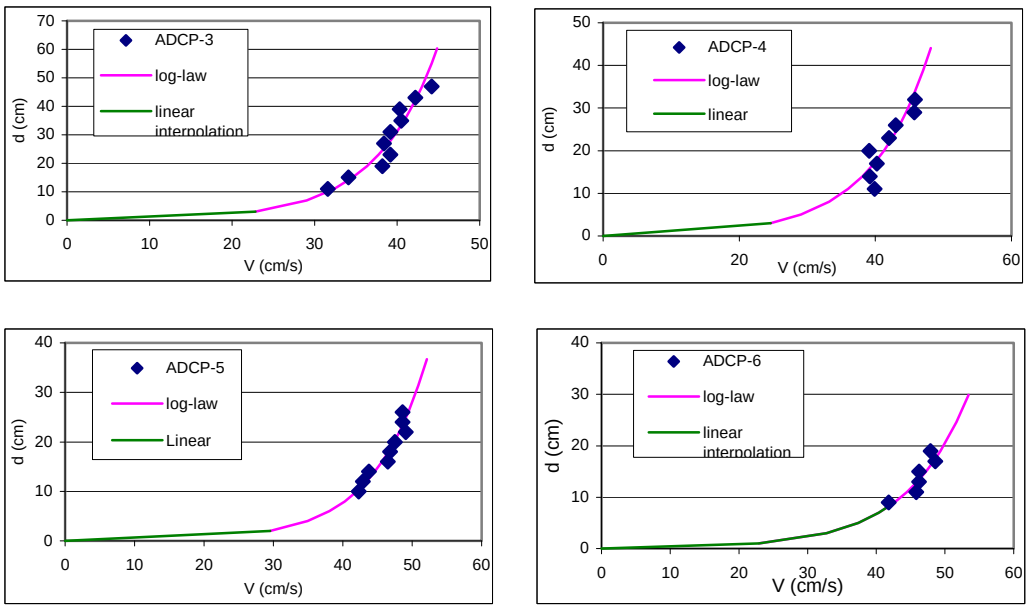

Figure 6-9 Continuation form previous page

In profile ADV-3, the trend of the velocity profile seems to be interrupted and shifted to the left over 10.548 cm of depth. Since the velocity measurement was achieved from water level down to the bed surface, taking almost 55 minutes, it seems that as the measurement started below this elevation, the bed had been eroded, for example by displacement of a stone over which the velocity profile was being measured. This claim can be supported by the boundary distance measurement of ADV, in which the above-mentioned elevation was primarily measured 1.532 cm and the measured boundary distance of the next sampling volume increased unexpectedly to 8.694 cm. This sudden increase of boundary distance can be only associated to a sudden deepening of the bed. However, the elevation of the sampling points presented in Fig. (6-9) has been corrected by recorded elevations surveyed by means of total station. Therefore, the velocity profile of ADV-3 is not reliable.

It can be concluded that even in the river bend the vertical profile of flow velocity magnitude follows a logarithmic profile[1] in the turbulent boundary layer. However, outside this layer within free shear outer layer (the upper 35% depth of the measured velocity magnitudes of profiles ADCP-1 to ADCP-3) the velocity magnitude remained almost constant (within almost 1% deviation from their mean), implying that the measurement points in this zone had been outside the turbulent boundary layer. Therefore, the velocity magnitude in the upper unmeasured zone of these profiles can be assumed to be constant.

The distribution of depth-averaged flow velocity together with the contour plot of velocity magnitude across section-1 is presented in Fig. (6-10). For a portion of the inner bank (right in the figure) no velocity measurement could be conducted using mini ADCP due to the very shallow water depth (less than 20 cm). Therefore, no depth-averaged velocity was computed for this zone. However, the computation of velocity contours in this region has been achieved

[1] This does not imply that the velocity profile follows the *universal* log-law, as it will be shown in Ch. 6.4.3.

by linear interpolation, assuming zero velocity at the river bed surface. The rest of unmeasured zone was computed as already explained above.

As can be observed from Fig. (6-10), a local maximum depth-averaged velocity magnitude occurs near the outer bank (left of this figure), while its absolute maximum is shifted towards the inner bank. The latter is due to the fact that shifting of the maximum depth-averaged velocity in river bends depends on the curvature of the river and lateral bed slope. In the current measurement, the local maximum velocity magnitude near the outer bank can be associated with the larger lateral bed slope in this region as it will be presented in the following (remembering that velocity magnitude is the resultant of lateral and longitudinal velocity components). It can be observed from Fig. (6-10), that the talweg does not form where the highest (depth-averaged) velocity magnitude occurs. Furthermore, it is shown that the location of maximum velocity magnitude coincides with maximum depth-averaged flow velocity.

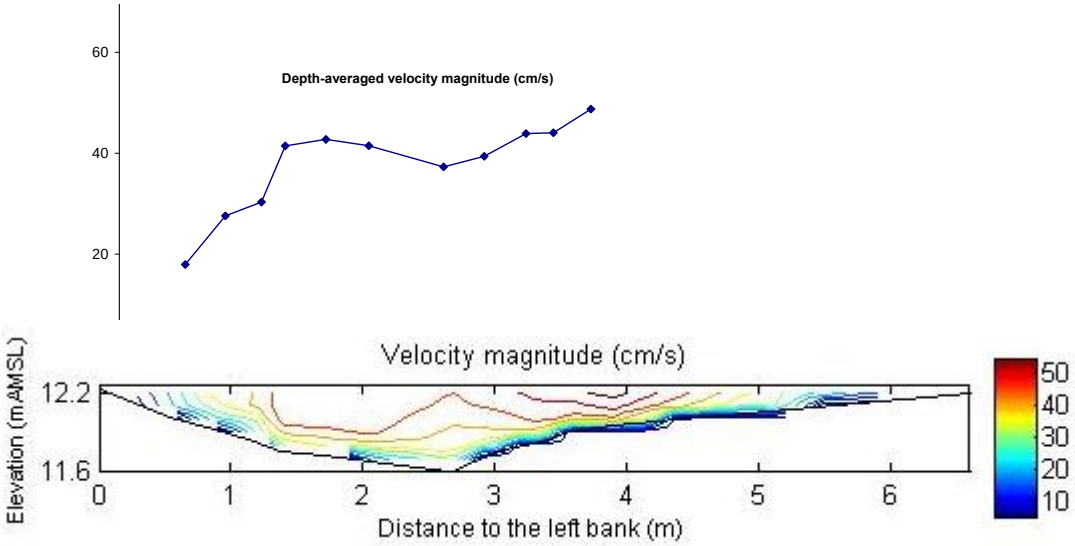

Figure 6-10 Distribution of velocity magnitude and depth-averaged velocity across the bend apex

The lateral and vertical velocity distributions across the river bend are presented in Fig. (6-11) and (6-12). As can be observed in these figures, in the first 11 cm under water, no measurement could be achieved due to the instrument limitations (Ch. 5.6.1). In Fig. (6-11), the lateral velocity closest to the bed at the first profile (from left) seems to be higher than that of the next two profiles, while bed shear stress is not higher (Ch. 6.4.3) as will be shown later. There is an uncertainty in the measurement results of lateral velocity of the third profile, as already described above. Therefore, the relatively large negative velocity zone (defining positive lateral velocity towards the outer bank) seems not to be reliable.

Considering the negligible vertical velocity of the first three profiles (from left) in Fig. (6-12) and assuming that its trend does not change towards the water surface in unmeasured zone, it can be concluded that the flow in this region (outer bank) is of pure lateral flow (refer to Fig. J-1-c in Appendix J). This can be clearly observed in Fig. (6-13), where the lateral velocity vector at these three sections is parallel to the local bed surface, implying the effect of bed

topography in the deformation of lateral velocity profile. This effect of bed topography has been also addressed by Bridge (1977) and Jackson (1976). As can be observed from this figure, this zone of pure lateral velocity acts as a suppressing zone, which pushes the central secondary current cell away from the bank-toe. This is in agreement with the conclusions derived from laboratory measurements achieved by Blanckaert and Graf (1999). This type of flow is not a cross circulatory flow for which the existing experimental secondary current distribution formulae have been developed. That can explain the reason of overestimation of the shifting of the maximum depth-averaged flow velocity towards the outer bank by such formula, as well as the fact that they are applicable only to a portion of central flow region as can be observed from Fig. (6-11). In this figure, only the 4^{th} and 5^{th} profiles seem to have equal portion of positive and negative areas of lateral velocity, where the currently available secondary current distribution formulae are applicable. This justifies exclusion of the inefficient available dispersion models from hydrodynamic model in the current work. Since the near bed lateral velocity for the rest of vertical profiles lay in the unmeasured zone of ADCP the effect of lateral bed slope on secondary current in this portion of inner bank cannot be explained.

As can be observed in Fig. (6-12), vertical velocity on the left bank is very small and downward (in the figure towards left). This implies that in the outer bank the main velocity component is the lateral velocity in this plane. At the third vertical profile in this figure, the maximum downward velocity (3.39 cm/s) occurs near the bed (3.16 cm above the bed), implying the potential of deposition of suspended sediment at this level (the settlement velocity was computed to be 1.35 cm/s). Furthermore, it is observed that the vertical velocity increases generally as the water depth increases at the outer bank. As seen from the velocity vector field in the central and inner regions (upslope of talweg), the lateral velocity near the bed is clearly towards the inner bank, which implies the radial direction of transport of sediment towards the inner bank in the river bend.

The vertical velocities measured by ADCP seem to be much higher than those by ADV, irrespective of their position. This can also be observed in Fig. (6-13), where the vertical components of the velocity vector measured by means of ADCP show an exaggerated downward flow. This matter has been investigated in the next measurement on April 22, 2008 and is presented in Ch. 6.4.2.2. Apart from the aforementioned issue, the downward flow is partly due to the local lateral bed slope, which causes the deflection of the flow downwards in the upper layer, while the lateral flow near the bed travels upslope towards the inner bank. This cross circulation process is outlined by red arrows in Fig. (6-13).

By analyses of the ADV data, it was found that the ratio of measured lateral velocity to longitudinal velocity increased from 8% to more than 77 % towards the bed surface, indicating the increasing role of lateral velocity near the bed at the outer bank, which has an implication for the main direction of bed load transport towards the inner bank at the bend apex. An order of magnitude analysis of the same data set showed that the ratio of the measured vertical velocity to lateral velocity was from 13% to 60 %. Increasing trend of this ratio towards the bed surface was computed for the first two vertical profiles, in contrast to the

third vertical profile (Fig. 6-14). Furthermore, this ratio was damped closer to the outer riverbank, probably due to the shallower water depth.

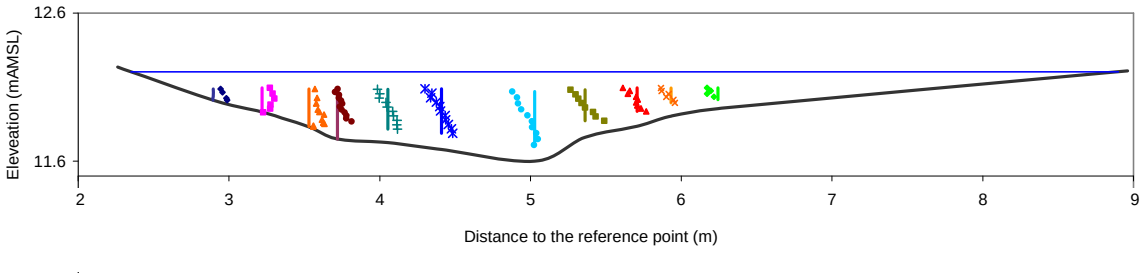

Figure 6-11 Lateral velocity distribution across section (1). Left side corresponds to the outer bank.

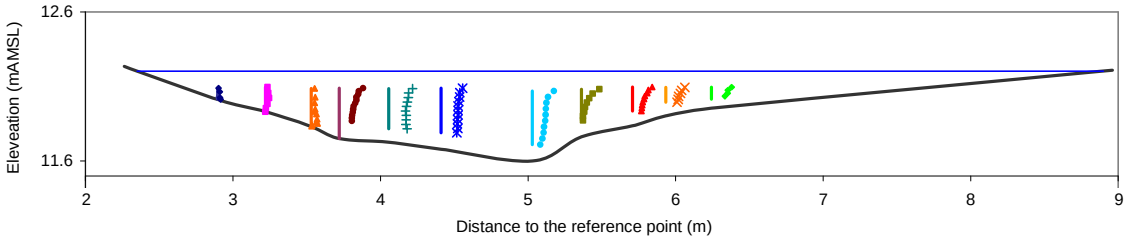

Figure 6-12 Vertical velocity distribution across section (1).

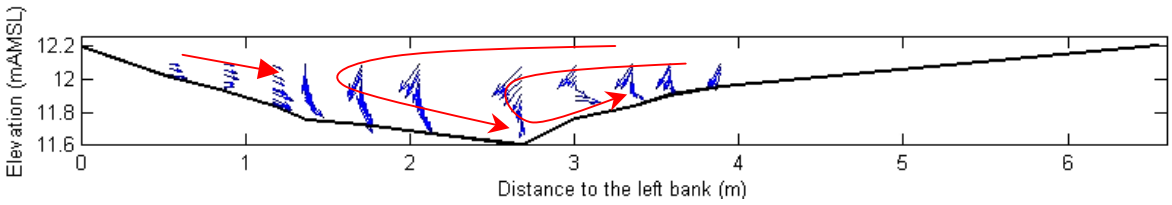

Figure 6-13 Velocity vector filed across section (1)

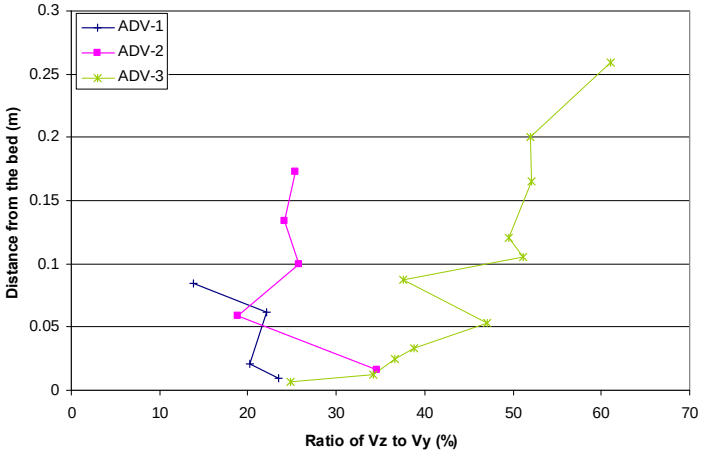

Figure 6-14 The change of ratio of V_z to V_y in respect to the depth

6.4.2.2 Section (2)

Velocity profile measurements were carried out on April 22, 2008 at this section and took more than 5 hours (excluding 1 hour of set up of instruments and traverse system). The discharge was measured to be 0.435 m^3/s using mini ADCP before starting velocity profile measurements. This value of discharge was lower than that in the first measurements on April 10, 2008. Due to the very shallow water depth at the inner bank, no reasonable measurements could be achieved in this zone, resulting in only six velocity profile measurements across the river bend. Apart from these six profiles, as already mentioned in Ch. 5.6.2, an additional velocity profile measurement using ADCP was achieved over the third profile of this section to compare its accuracy with that of ADV measurements at the same profile. The result of this comparison is presented in Fig. (6-15).

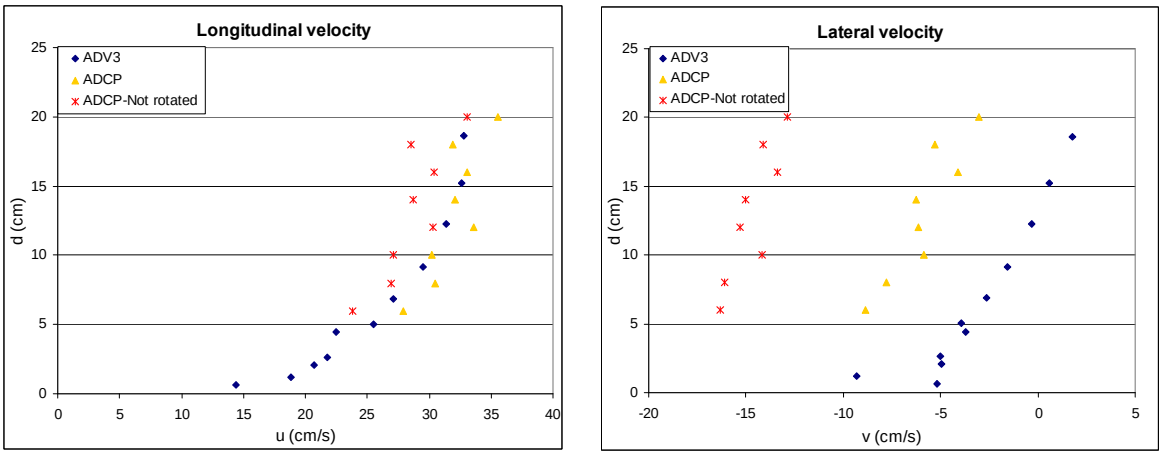

Figure 6-15 Comparison of velocity measurement using ADV and ADCP at third profile from left bank

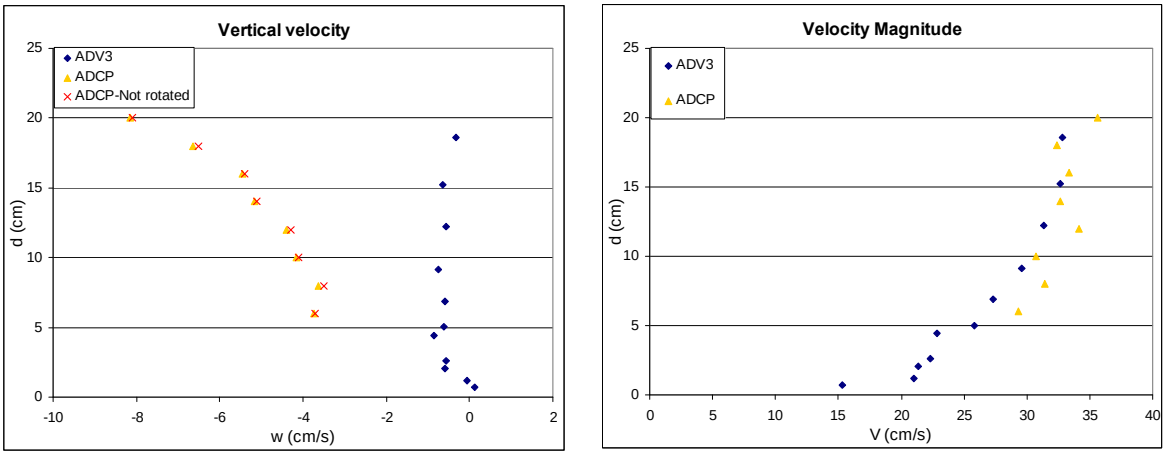

Figure 6-15 Continuation form previous page

In this figure, the longitudinal velocity profile measured by means of mini ADCP seems to have a relatively good agreement (maximum of 7% deviation) with that of the ADV measurement. Almost the same condition prevails for the case of velocity magnitude. However, the mini ADCP overestimated the lateral velocity (up to 20%), although the trend of lateral velocity measured using mini ADCP seems to be identical with that of ADV measurement. The larger deviation in lateral velocity computation in river bend is associated, in fact, to the principle of operation of the ADCP. The four beams of the instrument sample the velocity in four bins spreading away with an angle of 20°. The horizontal distance between two mutual bins in a vertical distance of Δz under the probe head can be easily evaluated as follows:

$$\delta d = 2 \cdot Sec(20) \cdot \Delta z = 2.128\,\Delta z \qquad (6\text{–}3)$$

For example, in a depth of 10 cm under the mini ADCP head the horizontal distance between two mutual sampling bins is more than 21 cm. The longitudinal velocity of the flow in such a relatively small distance might not change significantly in a river bend. However, across the river bend this distance might not be negligible.

The worst accuracy of mini ADCP is by the vertical velocity measurement with a maximum of 30% deviation from that of ADV. Furthermore, even the trend of the vertical velocity profile does not agree with that of ADV. It can be observed in Fig. (6-15) that the closer is the sampling bin to the mini ADCP head, the larger is the overestimation of the vertical velocity.

These large inaccuracies in lateral and vertical velocity measurements by mini-ADCP can be additionally attributed to the timescale of the eddies in lateral and vertical directions in the river bend, which could be much smaller than the sampling frequency of the mini-ADCP (1 Hz). This comparison suggests that the application of mini-ADCP should be limited to discharge measurement and mainly to longitudinal or resultant velocity measurement in river bends and it is not recommended for turbulent flow measurements.

Furthermore, the effect of coordinate rotation (Ch. 5.6.2) on the velocity profile is shown in these figures. As observed, lateral velocity is much more sensible to rotation than longitudinal velocity, as was also the case for ADV measurements (Fig. 5-17 and 5-18). As observed in Fig. (6-15), the lateral velocity deviation measured by mini ADCP would have been much larger without coordinate rotation.

To compute the depth-averaged flow velocity, the same method explained in Ch. 6.4.2.1 was used here. The comparison of the velocity magnitude profiles with logarithmic distribution is presented in Fig. (6-16). As can be observed in this figure, the velocity profiles measured by means of ADV agree well with logarithmic distribution. Moreover, those measured by mini-ADCP agree even better than those of section (1). This implies that in the course of development of secondary currents along the river bend, more deviation of longitudinal velocity profile from logarithmic distribution is expected. The outlier values closest to the bed in the case of ADCP measurement are not included in the computation of logarithmic profile, since these data might have been contaminated with acoustic echo reflected from the bed.

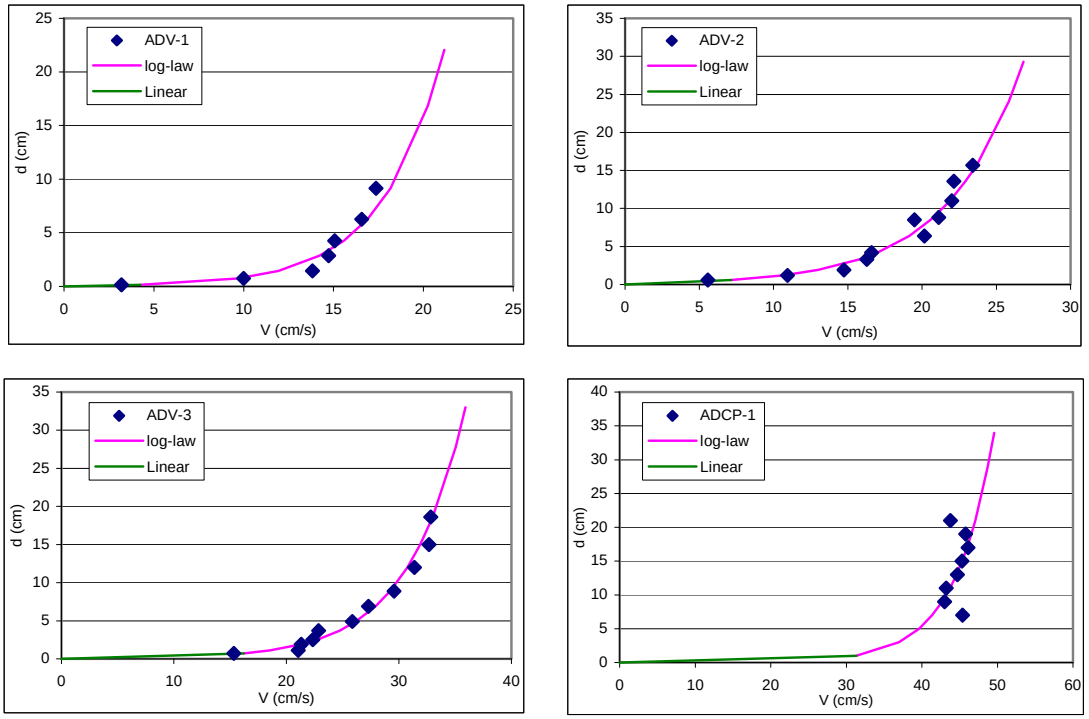

Figure 6-16 Vertical distribution of velocity magnitude across river bend versus logarithmic function

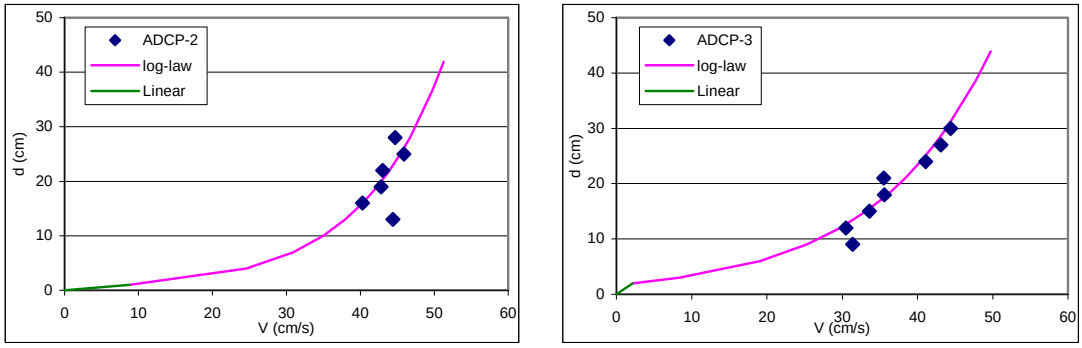

Figure 6-16 Continuation form previous page

The depth-averaged velocity distribution across section (2), computed from the velocity profiles already depicted in Fig. (6-16), is shown in Fig. (6-17), together with contours of velocity magnitude across this section. The contours beyond measured profiles (from local distance of 2.7m to the right bank in this figure) are the result of interpolation in the unmeasured zones. As shown in this figure, the maximum depth-averaged flow velocity shifts towards the outer bank. The same can be observed from the contour of maximum velocity, although it does not coincide exactly with the location of maximum depth-averaged velocity, unlike in section (1). Assuming that the change of flow discharge between two measurement dates at section (1) and (2) has not influenced the pattern of flow across and along the mentioned two sections, it seems that the zone of maximum flow velocity at section (2) has been redistributed in downstream across section (1) (see Fig. 6-10). This has resulted in widening of the maximum flow velocity zone at the latter section and the shifting of maximum depth-averaged velocity magnitude towards the inner bank. This process of shifting maximum depth-averaged velocity along a channel bend is in accordance with previous studies (for example Kühner, 2003; da Silva et al., 2006; Wilke, 2008).

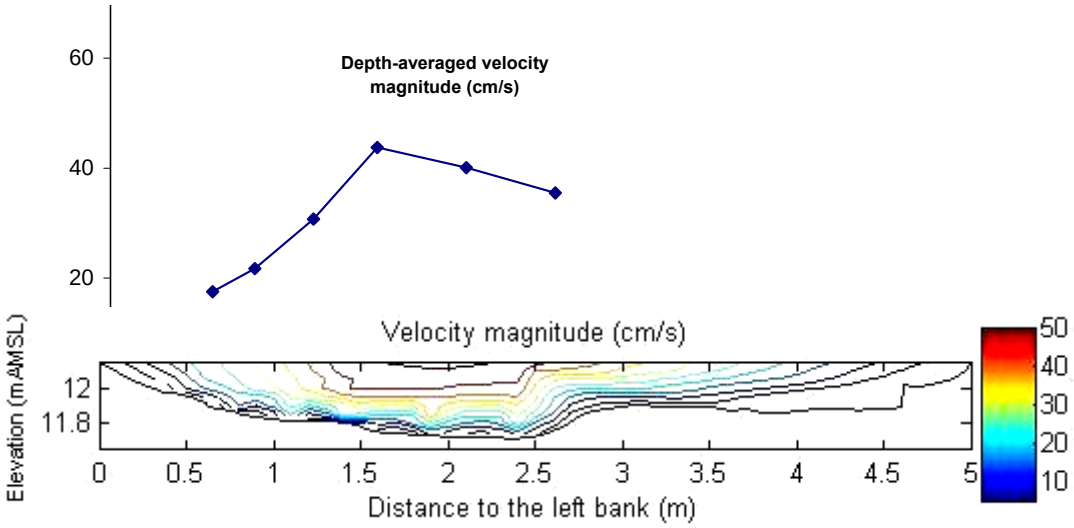

Figure 6-17 Distribution of velocity magnitude and depth-averaged velocity across the river bend section 2

The distribution of lateral flow velocity has been presented in Fig. (6-18). On the third profile (from left), the measured velocity profile using ADCP has been shown using dark yellow marks. The pattern of velocity profiles in this figure shows the existence of superposition of a pure laterally oscillating flow (refer to Fig. J-1c in Appendix J) with circulatory flow (refer to Fig. J-1b in Appendix), since the area of negative velocity[1] seems not to be equal to the positive zone. The same pattern of lateral velocity profile as that of section (1) can be observed on the first profile, with relatively high velocity close to the bed. This pattern of high gradient of lateral velocity is observed even on the third profile.

As observed from the velocity vector field in Fig. (6-20), the lateral flow towards the inner bank is parallel to the bed at the outer bank (first three profiles from left) and diminishes towards the water surface, implying the existence of secondary flow at this zone in contrast to the pure lateral flow in cross section (1). The lateral velocity close to the bed is accelerated towards the third profile, showing the effect of local bed slope on the lateral velocity field. Effect of bed topography on near bed flow might be different from that in the upper layer, as can be observed from the last measured profile. The large lateral slope of the bed at this profile has caused the lateral outwards flow to deflect towards the bed, while the near bed flow is upslope towards the inner bank (the dashed arrow). The flow velocity field across the cross section can explain the sediment transport direction across the river bend.

An order of magnitude analysis of ADV data showed that the ratio of lateral velocity to longitudinal velocity ranges from 3 % to 60%, increasing towards the bed (although very close to the bed this ratio decreases substantially). The ratio of vertical velocity to lateral velocity in the first two vertical profiles reached to 300% near bed surface. An increasing trend of this ratio towards the riverbed was computed for these two profiles and a decreasing trend for the third vertical profile as in section (1). In the latter profile this ratio reached near 200% in the upper measured zone. Comparing this analysis with the same one achieved for section (1), it follows that the ratio of vertical velocity to the lateral velocity decays towards the bend apex near the outer bend, while the ratio of lateral velocity to the longitudinal velocity grows towards the bend apex. This is an implication of the main direction of sediment transport along the outer bend upstream of the bend apex, which changes towards the inner bank at the bend apex.

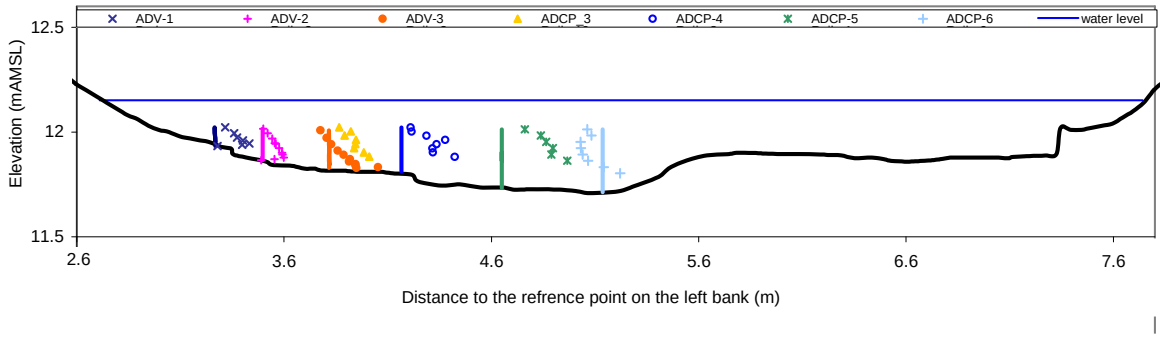

Figure 6-18 Lateral velocity distribution across section (1). Left side corresponds to the outer bank

[1] The zone of lateral velocity profile skewed towards the inner bank (right) is conventionally negative.

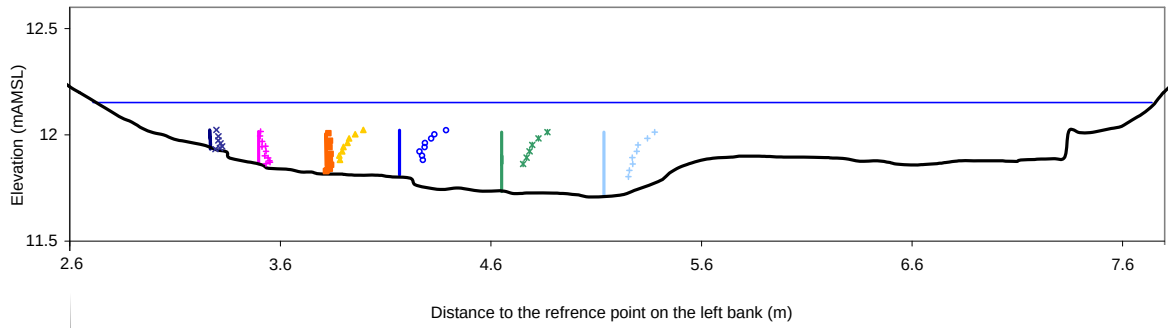

Figure 6-19 Vertical velocity distribution across section (2).

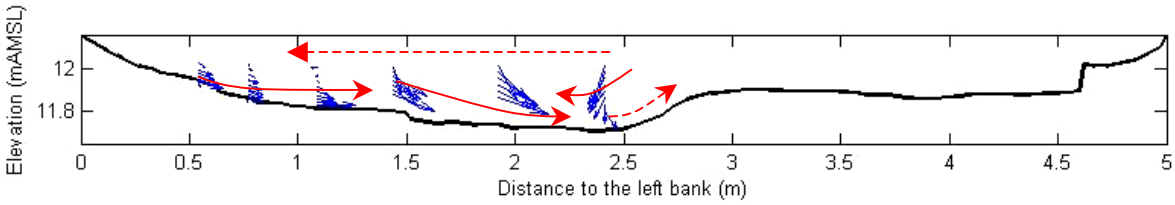

Figure 6-20 Velocity vector field across section (2). The dashed arrows represent the probable flow direction in unmeasured zones.

6.4.3 Bed shear stress across the river bend

The distribution of bed shear stress across the river bend and its shifting pattern along the river bend can help to understand the bed evolution process along the river bend. There are mainly seven methods to determine bed shear stress or equivalently bed friction velocity based on the measurements (Nezu and Nakagawa, 1993, Biron et al., 2004) as follows (other less common methods can be found, for example, in Stapleton and Huntley, 1995; Wolf, 1999)

1. Assuming steady uniform flow, the average friction velocity across a channel section can be computed using energy slope (I_e) and hydraulic radius (R) as follows:

$$u_* = \sqrt{g.R.I_e} \tag{6–4}$$

This method is not appropriate for computation of local shear stress or direct shear stress distribution across channels.

2. Using log-law (Eq. 6-5) in conjunction with measured flow velocity profile. There is a great uncertainty in computation of the reference height (z_0) in this method.

$$\frac{u(z)}{u_*} = \frac{1}{\kappa}\ln\left(\frac{z}{z_0}\right) \tag{6-5}$$

In this equation, z_0 is a characteristic roughness length (at which u = 0), which is of the order of magnitude of the thickness of viscous sublayer in hydraulically smooth flow. This is assumed to be proportional to the equivalent sand roughness height, k_s, (Schlichting, 2006). Setting z_0 proportional to k_s in the above equation yields the following equation for rough beds.

$$\frac{u(z)}{u_*} = \frac{1}{\kappa}\ln\left(\frac{z}{k_s}\right) + A_r$$
$$A_r = \frac{1}{\kappa}\ln\left(k_s^+\right) + A \qquad (6\text{-}6)$$

Here $k_s^+ = u_* k_s/\upsilon$ is the dimensionless equivalent sand roughness. The proportionality factor is about 1/30. For completely rough bed regime A_r=8.5 (Nezu and Nakagawa,1993) or A_r =8.0 (Schlichting, 2006).

3. Using measured Reynolds stress very close to the bed and the following equation:

$$u_*^2 = -\overline{u'w'}\Big|_{at\,bed} \qquad (6\text{–}7)$$

This method is relatively sensitive to any deviation from uniform two-dimensional flow (Nezu and Nakagawa, 1993) and to sensor misalignment with local streamlines (Stapleton and Huntley, 1995; Wolf, 1999; Kim et al., 2000). A height of 0.1 water depth from bed has been suggested for the position of the measurement point (Biron, et al., 2004). However, further investigation is required to verify this position over different bed roughness and geometries. This method was found to be appropriate for smooth boundary layers (Biron, et al., 2004).

4. Using extrapolation of theoretical Reynolds stress profile to the bed by fitting measured data to the following equation (Nikora and Goring, 2000; Song and Chiew, 2001;):

$$\frac{-\overline{u'w'}}{u_*^2} = \left(1 - z/h\right) \qquad (6\text{–}8)$$

The normalized Reynolds stress profile may deviate substantially from linear distribution in a non-uniform flow (Yang and Lee, 2007) and flows with secondary currents (Nezu and Nkagawa, 1993; Papanicolaou and Elhakim, 2007). This method is especially appropriate for smooth boundaries (Biron et al., 2004) and is preferred to the third method, when vertical Reynolds stress profile is available.

5. Using measured total kinetic energy (TKE) near the bed, where the turbulent energy production is assumed to be equal to the turbulent energy dissipation, following equation for computation of bed shear stress holds:

$$\tau = c_l \rho\left[0.5\left(\overline{u'^2} + \overline{v'^2} + \overline{w'^2}\right)\right] \qquad (6\text{–}9)$$

The term in bracket is TKE and the value of c_l is commonly assumed to be constant (Soulsby, 1983). However, Wolf (1999) computed a value between 0.17 to 0.27 for c_l in tidal flow. This method is widely applied in oceanography. Biron et al.,(2004) found that this method yields the best results in the computation of bed shear stress in flow around deflectors. However, the value of c_l should be further investigated in case of natural rivers. The appropriate measurement point is the same as in method (3).

6. Using measurements in viscous-sublayer, if this exists.
7. Direct shear stress measurement using for example hot film or Preston tube.

Generally, those methods, which incorporate profile of velocity or Reynolds shears stress, are more reliable than single point measurements due to the uncertainty in the correct position of measurement point in respect to the bed surface and sensibility to sensor misalignment with local streamlines.

The above methods are not generally appropriate for complex flows in natural rivers such as flow in river bends. With the advancement in measurement techniques in the last decade, it is now possible to measure three dimensional flow velocity profile, allowing for more accurate bed shear stress computation. Therefore, a general method is suggested here (for detailed derivation refer to the Appendix A):

$$u_{*bed}^2 = gz(\sin\theta - \frac{\partial h}{\partial x}\cos\theta) - \left(\int_{z_0}^{z} \frac{\partial}{\partial x}(u^2 + \overline{u'^2})dz\right) - \left(\int_{z_0}^{z} \frac{\partial}{\partial y}(u.v + \overline{u'v'})dz\right) - u\cdot w\Big|_z - \overline{u'w'}\Big|_z \qquad (6\text{–}10)$$

The first term in the parenthesis is the energy gradient (I_e). For z=h the last two terms on the right are zero (at water surface) and by substituting the continuity equation in the second term in the integral the following equation is obtained:

$$u_{*bed}^2 = gzI_e + \int_{z_0}^{h}\left(2u(\frac{\partial v}{\partial y} + \frac{\partial w}{\partial z}) - \frac{\partial \overline{u'^2}}{\partial x}\right)dz - \left(\int_{z_0}^{h} \frac{\partial}{\partial y}(u.v + \overline{u'v'})dz\right) \qquad (6\text{–}11)$$

Assuming that the normal Reynolds stress is negligible with respect to the lateral one in a river bend, the above equation is simplified to the following equation:

$$u_{*bed}^2 = ghI_e + 2\int_{z_0}^{h} u(\frac{\partial v}{\partial y} + \frac{\partial w}{\partial z})dz - \left(\int_{z_0}^{h} \frac{\partial}{\partial y}(u.v + \overline{u'v'})dz\right) \qquad (6\text{–}12)$$

In case measurements are available for the three-dimensional flow field over the flow depth, bed shear stress can be computed almost accurately by means of Eq. (6–12). However, in the current measurement, due to the already mentioned limitations in measurement technique with respect to the very shallow depth, measurements are available only for a portion of the velocity profile. Therefore, only Eq. (6–10) can be applied to compute bed shear stress. This

method, however, requires intensive pre-processing of data, therefore, it will be not applied in the current analysis.

In the following, to compare the performance of the above-mentioned methods, bed shear stress computation using methods 2 to 5 are presented. As can be observed from the vector fields in Figs. (6-13) and (6-20), the velocity vectors are parallel to the bed close to it. Therefore, as is also well known (for example, Pavlovic, 1981; Yang et. al., 2004; Khodashenas and Paquier, 1999) the velocity profile normal to the inclined bed should be used for computation of bed shear stress. However, at first, it is assumed that the lateral and longitudinal bed slope is small and negligible, allowing the direct application of measured velocity profiles in the calculation of the bed shear stress. Later, the contours of velocity magnitude are used to compute bed shear stress based on the normal distance to the bed.

6.4.3.1 Bed shear stress distribution computed using Log-law

The measured velocity magnitude was first plotted versus the distance of measurement point to the bed (z). Those data of each profile were selected for the analysis, which resulted in the highest correlation coefficient of the logarithmic regression (Eq. 6–13)

$$u = a \cdot \ln(z) + b \tag{6–13}$$

This equation is equivalent to the log-law (Eq. 6-5), for which $a = u_* / \kappa$ (the slope of the regression line) and $b = -u_* / \kappa \cdot \ln(z_0)$. Once u_* is determined from 'a', z_0 can be determined from 'b'. A value of $\kappa = 0.41$ was used throughout the analysis (Nezu and Nakagawa, 1993).

Section (1)

The result of this analysis for section (1) is presented in Fig. (6-21).

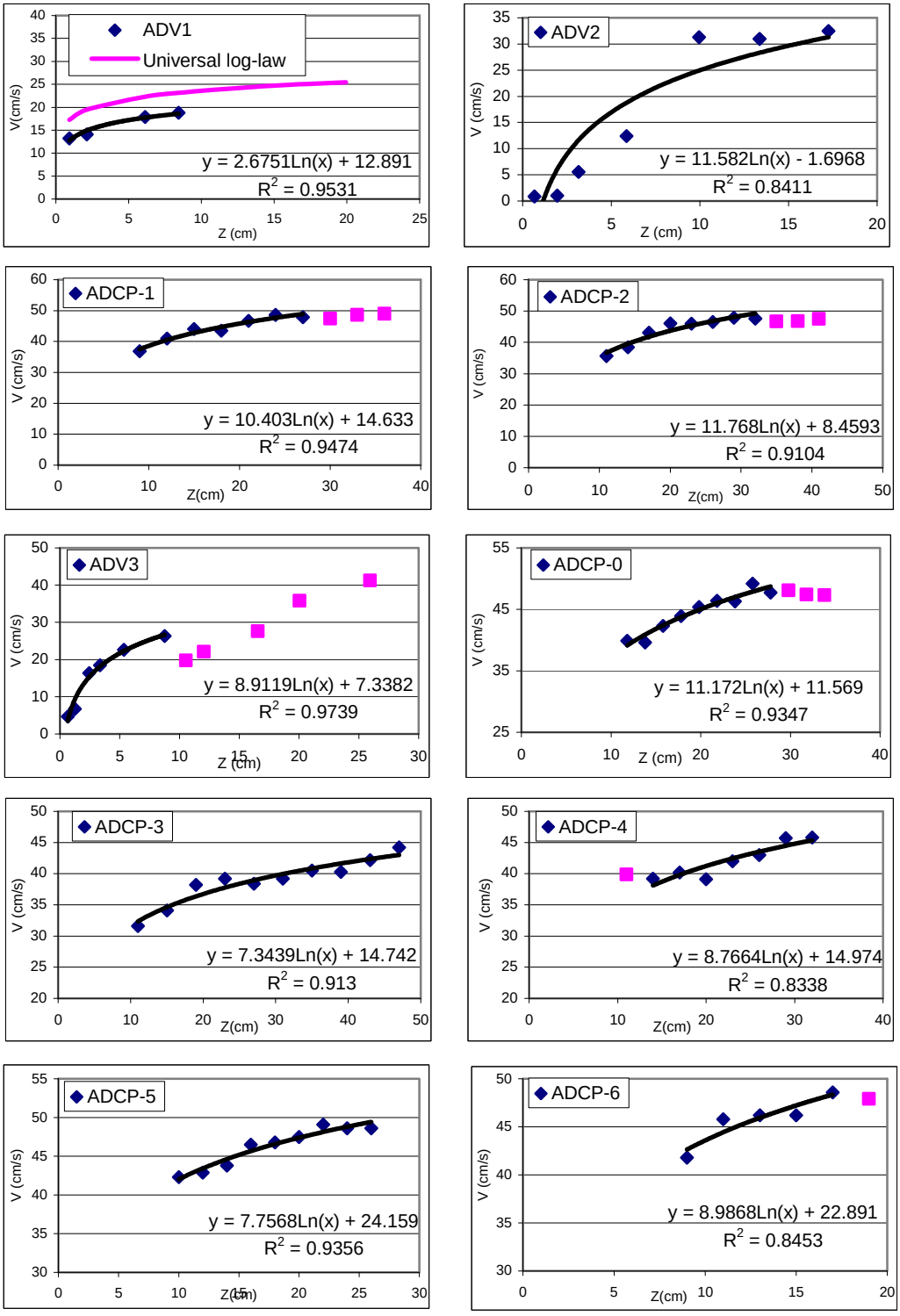

Figure 6-21 Analysis of velocity profile of section (1) using Log-law. The purple points are data, which have been not used in regression. In regression equation y and x are V and Z, respectively

As can be inferred from Fig. (6-21), the selected velocity data agree well with logarithmic profile. The value of the computed shears stress and z_0 are given in Table (6-8).

Table 6-8 Parameters of log-law computed for section (1) (with d_{90}=0.045 cm)

Profile	U_*(cm/s)	$_{z0}$(cm)	k_s (cm)	k_s / d_{90}	$k_s^+ = u_* k_s / \upsilon$	A_r
1	1.096791	0.00807578	0.00269193	0.066467361	11.7953306	6.869279938
2	4.6328	1.15777863	0.38592621	9.529042218	49.8229905	-5.372459238
3	3.653879	0.43892976	0.14630992	3.612590605	39.2952812	-2.875767362
4	4.58052	0.35503629	0.11834543	2.92210939	49.2607504	-2.358403009
5	4.26523	0.24497148	0.08165716	2.016226186	45.8699952	-1.453334204
6	4.82488	0.48731759	0.1624392	4.010844394	51.8886959	-3.130832379
7	3.010999	0.13434015	0.04478005	1.105680233	32.3814917	0.011950669
8	3.594224	0.18120745	0.06040248	1.491419307	38.6537274	-0.717970015
9	3.180288	0.04439815	0.01479938	0.365416846	34.2020935	2.712383046
10	3.684588	0.07830214	0.02610071	0.644462081	39.6255381	1.328536118
11	3.645761	0.0393511	0.01311703	0.323877391	39.207977	3.0067092

As shown in this table, the value of bed friction velocity is above its measured threshold value (1.12 cm/s), except on the first profile indicating that bed forms should have been formed. This has been also observed by in situ observation. The large value of friction velocity in the second to fifth profiles indicate the potential area of bank- and berm-toe erosion due to high bed shear stress. However, it does not necessarily imply that bed erosion should occur in these zones, because according to Eq. (2-4), bed erosion is the result of local mass imbalance.

As shown in this table, the value of z_0 is not constant as in the universal log-law for which $z_0=k_s/30$. The high value of z_0 is due to bed forms (dunes) developed because of the prevailing high bed shear stress. Such bed forms have been also observed in the river bend. The value of k_s in Table (6-8) was computed assuming the just mentioned relation with z_0. A unique relation between k_s and the characteristic diameter of the sediment does not exist in the literature. For a stationary flat bed with uniform sediment, Nikuradse suggests k_s = D (sand diameter). However, in non-uniform sediment, it can be taken as equal to d_{50} (Wu et al., 2000; Song and Graf, 1994) or a factor of it. A number of relations have been used in literature, a few of which are listed in Table (6-9).

Table 6-9 A few suggested values of K_s in the literature

Yalin and da Silva (2001)	$k_s = 2d_{50}$
Mahmood (1971)	$k_s = 5.1d_{84}$
Ackers & White (1973)	$_{ks} = 1.25d_{35}$
Charlton et al (1978)	$k_s = 3d_{84}$
Hey (1979)	$k_s = 3.5d_{84}$
Einstein & Barbarossa (1952)	$k_s = d_{65}$
Engelund & Hansen (Kuelegan Eqn.)	$k_s = 2d_{65}$
Van Rijn (1984)	$k_s = 3d_{90}$

The proportionality factor with respect to d_{90} for the current measurements, listed in the fifth column of Table (6-8), ranges from 0.07 to 9.53. This large range shows that the effect of other parameters such as bed forms is included in this proportionality factor (Gonzalez et

al.,1996). The larger values of k_s are related to the larger bed roughness, for example due to the bed forms.

The universal value of A_r in Eq. (6-6) is 8.5, assuming $\kappa = 0.40$ or 8.30, for $\kappa = 0.41$.In the last column of Table (6-8), the constant of universal log-law was derived for each profile based on the assumption of $k_s = 3d_{90}$. As is shown in this table, the value of A_r is not constant, which might be due to the state of transient rough bed ($5 < k_s^+ < 70$). However, the reported range of A_r (Schlichting, 2006, pp.528) varies between 8 and 9.5. Nevertheless, it is here between -3.13 and 6.87. To the extent of knowledge of the author, negative values of A_r have not yet been reported in the literature. This suggests that more study is required on the value of A_r in the transient rough bed in natural rivers with uneven bed (bed forms). The lower values of A_r indicate the increase of bed friction and downward shifting of velocity profile (Papanicolaou et al., 2007). This has been shown also in Fig. (6-21) by comparing the velocity profile of ADV-1 with that of universal log-law. It should be noted that uncertainty in the parameter A_r does not influence the calculated friction velocity.

The computed friction velocity, as explained above, is plotted together with the lateral distribution of depth-averaged velocity in Fig. (6-22) for section (1). As shown in this figure, the friction velocity is minimum near outer bank and increases suddenly to a maximum at the bank-toe. The trend of bed shear stress distribution matches that of the depth-averaged velocity magnitude only across half of the river channel at the bend apex. However, the location of maximum bed friction velocity does not coincide with the maximum depth-averaged velocity, but with the local maxima of depth-averaged velocity magnitude. As the bed friction was computed using the velocity magnitude profile, the effect of lateral velocity is already included in friction velocity, which might be here referred to friction velocity magnitude.

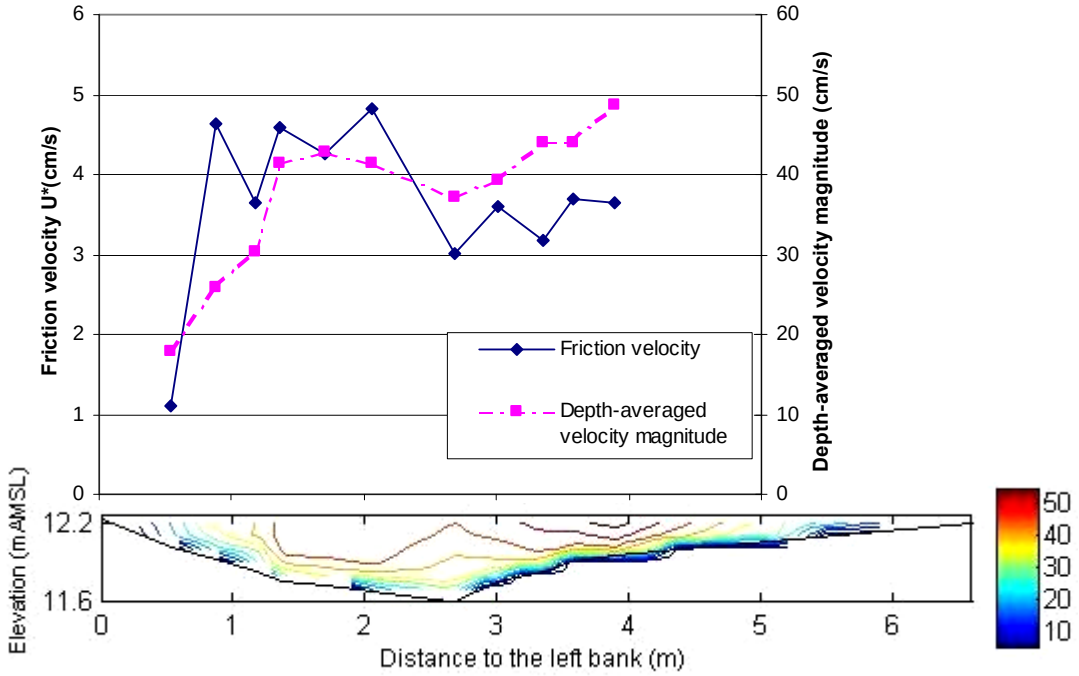

Figure 6-22 Bed shear stress and velocity magnitude distribution across section (1)

The maximum friction velocity is close to the outer bank (bank-toe), which can describe why more bank-toe and berm-toe erosion occurred in this section (as explained in Ch. 6.7).
Similar patterns of maximum depth-averaged velocity and bed shear stress at bend apex have been reported by Kühner (2003) in the first bend of a fixed-bank, mobile bed circular meandering laboratory channel with an opening angle of 60° (figure 66 in his work). However, at the bend apex of the second bend of this laboratory channel, the location of the maxima of both parameters coincided close to the inner bank.

Section (2)

The same analysis of bed shear stress has been achieved for section (2), as presented in Fig. (6-23). As observed from this figure, the selected data fit the log-law even better than those of section (1). This can be because the secondary currents are not as developed as at the bend apex and at this section vertical flow velocity is much less than those at section (1) (compare velocity vectors in Figs. 6-13 and 6-20). Therefore, it can be concluded that as long as the vertical flow acceleration (vertical velocity component) is not significant and the assumption of hydrostatic pressure distribution is less violated (which is one of the main assumptions for derivation of log-law), the vertical profile of velocity magnitude follows well a logarithmic profile in the river bends. However, as shown in Table (6-10), the constant of the logarithmic equation deviates substantially from the constant of the universal log-law. Although this deviation can be mainly correlated to the lateral bed slope and bed forms, nevertheless, the

absence of a generally applicable method to compute z_0 makes the present logarithmic function not applicable in numerical modelling of shear stress across river bends.

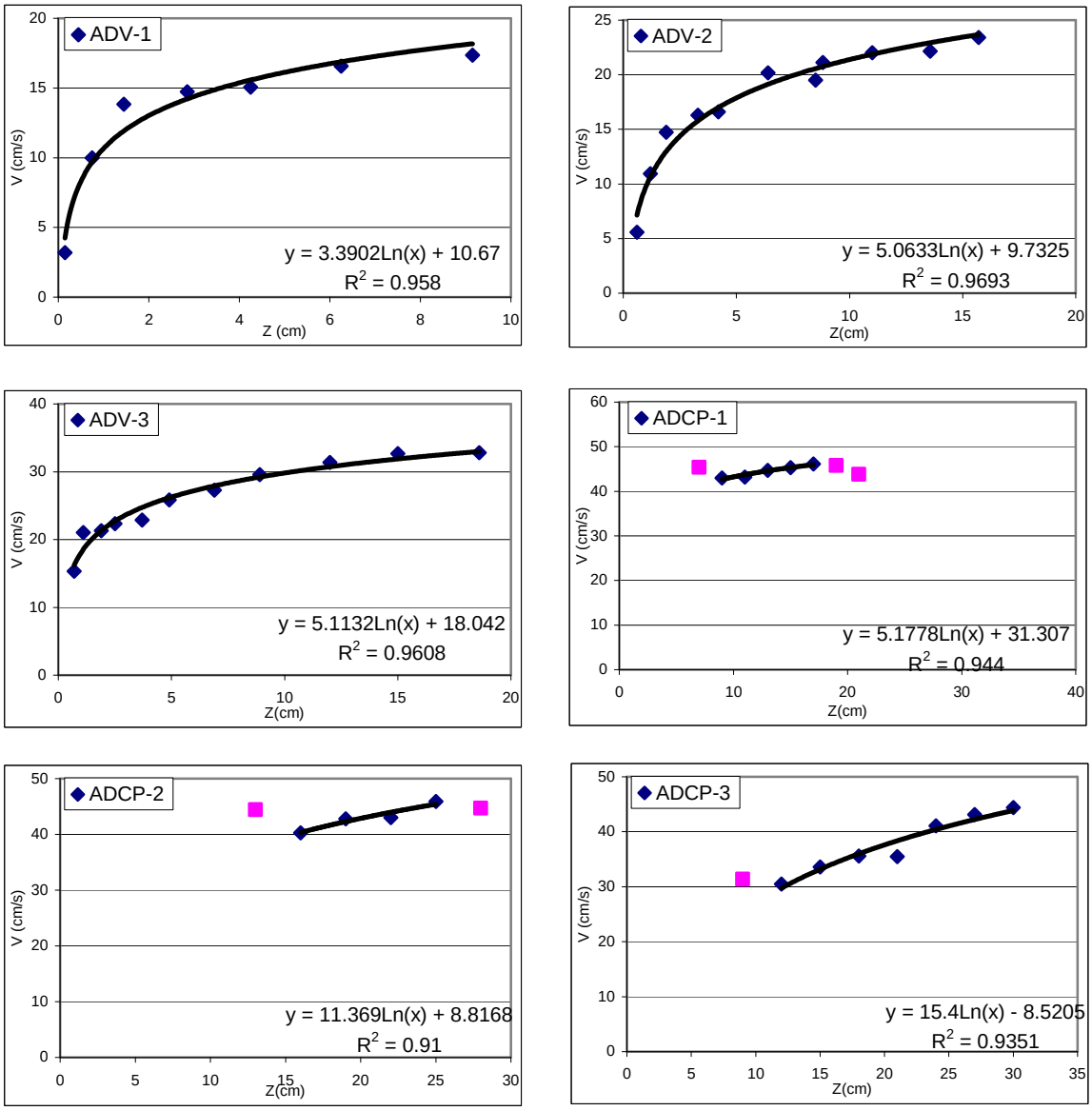

Figure 6-23 Analysis of velocity profile of section (2) using Log-law. The purple points are data, which have been not used in regression. In regression equation y and x are V and Z, respectively

Over section (2), the friction velocity is generally higher than the critical value of 1.12 cm/s, indicating that the bed is active across this section. The larger magnitude of maximum z_0 than in section (1) suggests that the bed forms might have been larger at this section or their arrangement have impacted more the velocity profile (for example profile 5).

The computed proportionality factor between k_s and d_{90} in Table (6-10) is not constant and ranges from 0.019 to 14.31. Although the lateral bed slope is milder here than in section (1), the range of this parameter is larger, suggesting that only the effect of bed forms has

influenced the k_s value. The same trend of A_r as in section (1) is observed also here. The value of computed A_r =9.86 in the case of profile (4) is even larger than the standard value of 8.30. Similar value of A_r ($4.2<A_r<10.64$) has been reported also by Song and Gra (1996) for unsteady flow in laboratory channel. In the case of availability of measurements of bed form characteristics, the following equation proposed by van Rijn (1984) can be used to take the effect of bed forms on k_s into account.

$$k_s = 3d_{90} + 1.1\Delta'\left(1 - e^{-25\Psi}\right)$$
$$\Psi = \frac{\Delta'}{\lambda} = 0.015\left(\frac{d_{50}}{h}\right)^{0.3}\left(1 - e^{-0.5T^*}\right)\left(25 - T^*\right) \qquad (6\text{–}14)$$

Table 6-10 Parameters of log-law computed for section (2) (with d_{90}=0.045 cm)

Profile	U∗(cm/s)	Z_0(cm)	k_s (cm)	k_s / d_{90}	$k_s^+ = u_* k_s / \upsilon$	A_r
1	1.389982	0.04296769	0.01432256	0.3536435	15.1377517	2.79225962
2	2.075953	0.14628984	0.04876328	1.20403165	22.6083942	-0.19589052
3	2.096412	0.02934848	0.00978283	0.2415513	22.8312052	3.72203398
4	2.122898	0.00236639	0.0007888	0.01947645	23.1196539	9.86319478
5	4.66129	0.4604678	0.15348927	3.7898584	50.7642909	-2.99260523
6	6.314	1.73894607	0.57964869	14.3123133	68.7633107	-6.2335603

The computed friction velocity across the section was added to Fig. (6-17) and re-plotted here (as solid line) in Fig. (6-24). Bed shear stress (equivalently friction velocity) increases towards the middle of the channel, in this figure, and reaches its maximum (to the measured extent) at the talweg, while the maximum velocity magnitude is shifted towards the outer bank and does not coincide with the location of maximum bed shear stress. Relatively similar pattern of shifting and adjustment lag of maximum depth-averaged velocity and shear stress across bend section has been reported by Kühner (2003), however, at the beginning of the first circular bend and not just upstream of the apex. In his experiment the maximum bed shear stress is close to the inner bank at this section and not at the center of the channel. These differences indicate the influence of curvature of the river in the process of shifting maximum depth-averaged flow velocity and bed shear stress.

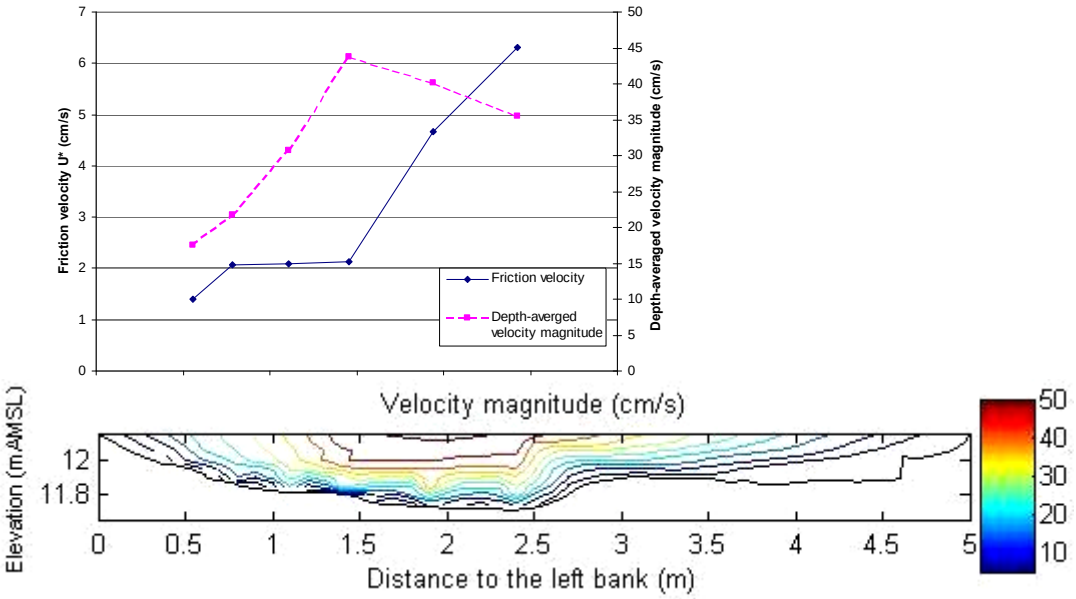

Figure 6-24 Bed shear stress distribution across section (2)

6.4.3.2 Comparison of different methods of computation of bed shear stress

To examine the reliability of the computed bed shear stresses, bed shear stress was computed using three further methods. It was first investigated if the method of Reynolds stress profile (Eq. 6–8) is applicable here. For this purpose, the time-averaged Reynolds stress (-u´w´) was computed for a 5 min period for each measurement point, primarily for the third profile (ADV-3) of section (1). The so-created vertical profile of Reynolds stress for this section is plotted in Fig. (6-25) and compared with Eq. (6–8). As follows from this figure, the Reynolds stress increases from bed to a maximum at a distance over the bed and then reduces monotonically towards the water surface. A similar profile has been measured by Song and Graf (1994) and Afzalimhr et al. (2007) in decelerating flows and Fedele and Garcia (2001) over dunes. The latter authors have referred to the elevation for maximum Reynolds stress as equilibrium or reference layer and postulated that the maximum Reynolds stress corresponds to the form drag, while extrapolation of Reynolds profile in the lower portion of the graph to the bed is an estimate of grain stress.

The most conspicuous pattern seen in this figure, is the reduction of Reynolds shear stress towards zero near bed, which is in contrast to the result of Song and Graf (1996) for unsteady flow as well as Song and Graf (1994) and Afzalimhr et al. (2007). This discrepancy can be related to the different bed material used in the above-mentioned literatures (gravel) and the current work. The smoothness of sand bed causes a reduction in turbulent production ($G = -\overline{u'w'}\,\partial u/\partial z$) close to the bed, thereby reducing Reynolds shear stress $-\overline{u'w'}$ close to zero (0.17 u_*) at near bed.

Velocity and Reynolds stress profiles have been experimentally shown to be different over dunes than in plane bed (Bennet and Best, 1995; Nezu and Nakagawa, 1993). However, as it

was shown here, the velocity profiles followed a logarithmic profile, which is similar to the result of velocity profile measurement on dunes by Holmes and Garcia (2002).

The upper half of the data applied for regression has been marked with green triangles in Fig. (6-25). As shown in this figure, the relation between dimensionless Reynolds stress and dimensionless depth remains linear in this zone. However, this relation does not agree with Eq. (6–8), plotted also in this figure. Furthermore, according to Yang and Lee (2007), in gradually varied flow the sum of the Reynolds shear stress and momentum flux in longitudinal direction remains linear and should follow the line plotted with label "Eq. 6-6" in Fig. (6-25). Such a relation has been plotted with blue circles in this figure. Although this relation remains linear in the upper portion of data, it still deviates substantially from the line "Eq. 6-6". This deviation indicates that neither Eq. (6–8) nor the method of Yang and Lee (2007) are applicable to describe the Reynolds stress profile in situations with secondary currents or pure lateral flow. This shows the importance of application of more comprehensive equations such as Eq. (6–12) to compute bed shear stress. Therefore, this method was not used for the analysis of the rest of data.

To investigate the effect of sensor misalignment in this method, the data corresponding to non-rotated horizontal velocity components are plotted in this figure. As it is shown, even 22.3° rotation angle does not induce pronounced influence on the Reynolds stress profile, which shows that this method is not sensitive to the misalignment of sensors.

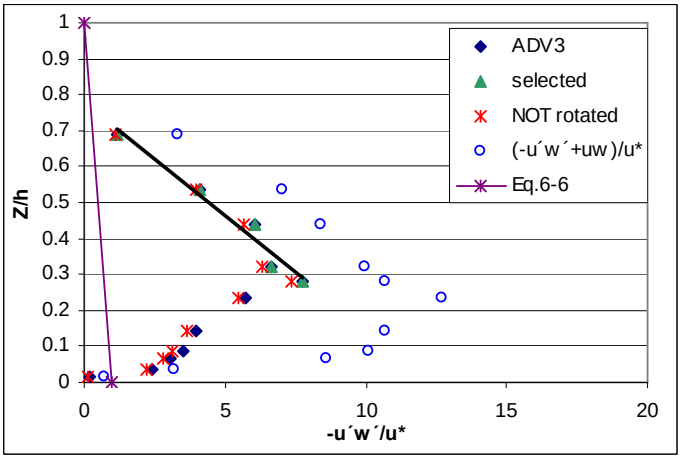

Figure 6-25 Vertical distribution of Reynolds stress for the third profile (ADV3) at section (1)

In the rest, only the result of three methods are compared, namely, log-law, Reynolds stress at one point and TKE. Since the velocity close to the bed could be measured only using ADV, the result of bed shear stress computation on the first three profiles of the first section have been compared in the following.

As shown in Fig. (6-26), representing the comparison of these methods for section (1), the result of the three methods are close only at the third profile. Otherwise, no specific trend is observed, which indicates the great uncertainty inherited in the mentioned methods of bed shear stress computation in complex flows, such as those along a river bend. This issue is

significant in morphodynamic modelling, in which the accuracy of computation of morphological evolution depends partly on the correct estimation of bed shear stress.

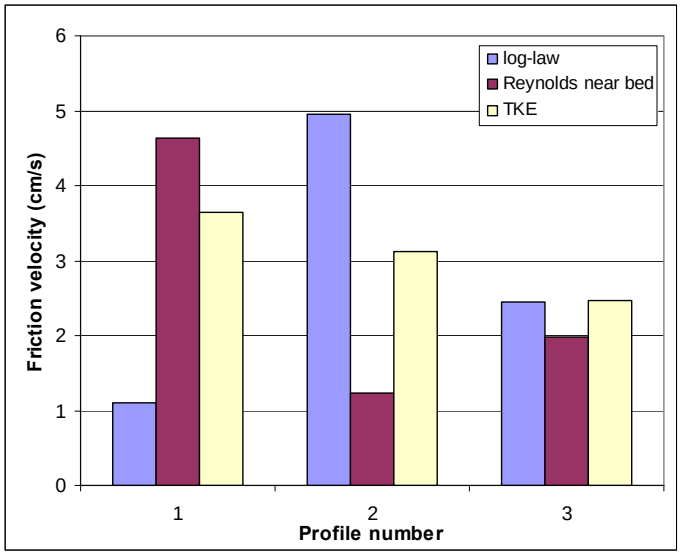

Figure 6-26 Comparison of three methods to compute bed shear stress on the first three profiles at section 1

The same comparative analysis has been carried out for section (2) and the result is presented in Fig. (6-27). In contrast to the case of section (1), in this figure a trend can be observed among these methods. TKE yields in all profiles the highest value of friction velocity, followed by Reynolds stress method. The lowest friction velocity was computed using log-law. This is in sharp contrast to the laboratory results of Biron et al. (2004), in which log-law yielded in all their test cases the largest value of bed shear stress.

The values of computed bed shear stress using these three methods are closer together in section (2) than in section (1). This implies that none of these three methods is reliable when the flow deviates substantially from a hydrostatic pressure distribution (negligible vertical velocity acceleration), as is the case at bend apex. This issue should be further investigated in different flow situations and width-depth ratios.

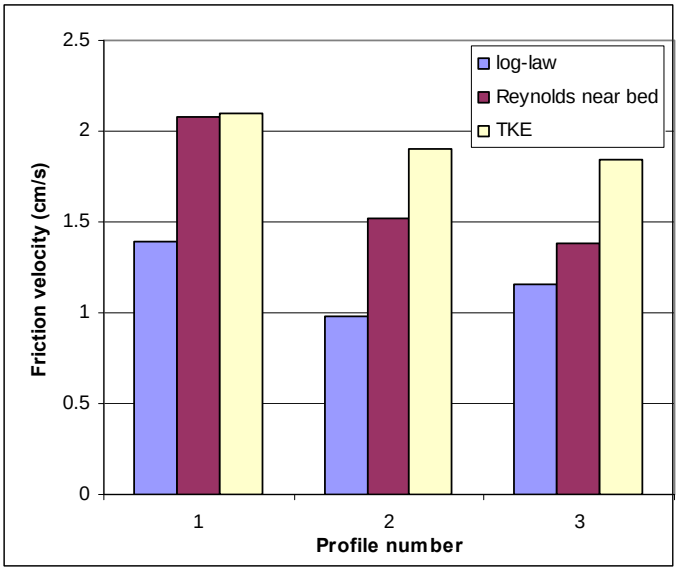

Figure 6-27 Comparison of three methods to compute bed shear stress on the first three profiles at section 2

6.4.3.3 Log-law normal to the bed

The bed shear stress distribution was already determined for both cross sections assuming that the lateral bed slope is negligible. In the following, it is assumed that the bed slope is not negligible and the velocity profile should be analyzed normal to the inclined bed to compute bed shear stress (Pavlovic, 1981; Khodashenas and Paquier, 1999; Yang et. al., 2004).

The resultant velocity distribution over the bank surface across section (2) was analyzed once along the normal vector to the bank and next along a special curvilinear coordinate system composed of isovel curves and their normals. The latter coordinate system is similar to that used by Chiu and Lin (1983) to divide the flow field across the channel for computation of shear stress. The two mentioned coordinate systems along with isovel curves (resulting from velocity measurements) are shown in Fig. (6-28). For the result of application of the latter coordinate system, see Nasermoaddeli and Pasche (2008b).

The normal axis to the bed surface was extended up to the isovel curves with maximum resultant velocity magnitude as an effective length scale for defining the limiting extent of the influence of the core flow on the shear stress of the bank. A similar method has been used to define the influencing area by Papanicolaou and Elhakim (2007). A review of methods of dividing flow area for computation of shear stress across a channel section is given in Yang et al. (2004).

Due to the blanking distance of ADCP and the sampling distance of ADV, the first 13 cm depth under water surface could not be measured by the instruments. In this region the velocity profiles were extrapolated from the data by a power function. Therefore, for the sake of accuracy, it was decided to limit the current normal profiles to an elevation below the unmeasured zone (the dark thick line in Fig. 6-28). Using the isovel curves, the velocity profiles were plotted for three normal profiles (Fig. 6-28).

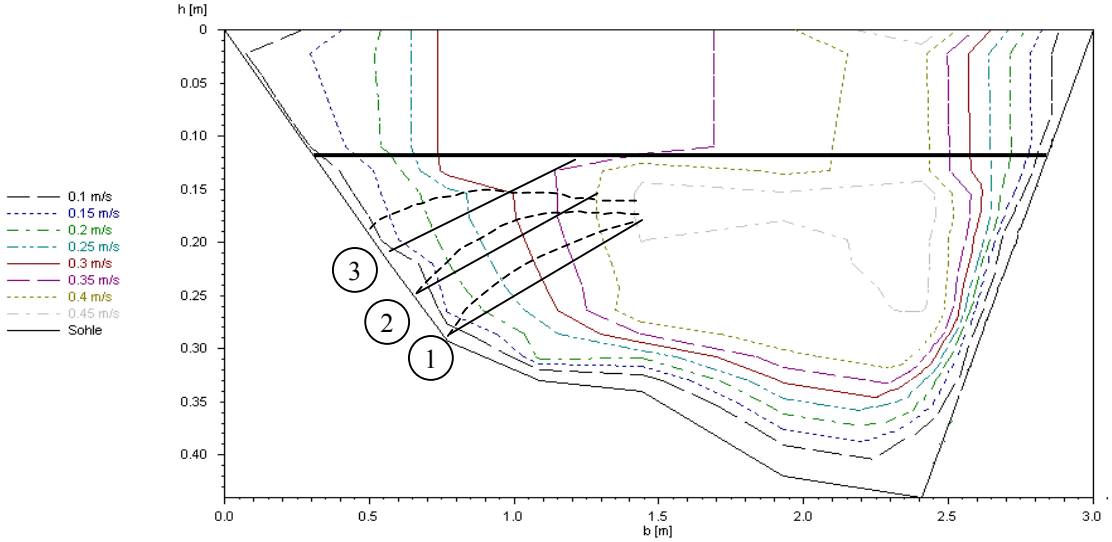

Figure 6-28 Isolvels plotted using Q-software at section (2). Dashed lines are curvilinear orthogonal lines to isovels. The vertical axe is distorted for better visualization.

By fitting a logarithmic function to the thus plotted data, u_* (bank friction velocity) and the constant A_r of the log-law was determined by rewriting the log-law as follows:

$$u = \underbrace{\frac{u_*}{\kappa}}_{m} \ln(y) + \underbrace{u_* \left(-\frac{1}{\kappa}\ln k_s + A_r\right)}_{A} \qquad (6\text{–}15)$$

where k_s is the equivalent sand roughness ($k_s = d_{50} = 0.22$ mm) and κ is von Kármán constant (equal to 0.41), y is the vertical distance to the bed and u_* is the shear velocity.

However, since the data are analysed in the normal direction to the bank, y was substituted for y′(normal distance to the bank) and k_s was first substituted for its projected value on the normal vector of the bank, $k_s \cos(\theta)$, where θ is the bank slope (equal to nearly 20.5°). It was found that the differences in computed A_r were between 1% and 3%. Therefore, k_s was not altered in Eq. (6–15) throughout the analysis.

By setting the slope of the fitted curve to m and the intercept to A in the above equation, u_* and the constant A_r of the log-law formula were determined. To determine the range of applicability of the log-law, the data limited to the inner region ($y'/h < 0.2$, where h is the effective distance) were examined first, since log-law is applicable normally in this region for a rough bed. As observed from Fig. (6-29), the velocity profiles follow a logarithmic profile very well ($R^2 > 0.99$) in this region. Then the same procedure was repeated by extending the applied range of data beyond the inner region to $y'/h < 0.4$ and it still showed a very good agreement with log-law ($R^2 > 0.98$).

In spite of extending the range of included data to $y'/h < 0.70$, a good agreement with log-law ($R^2 > 0.98$) was obtained. Finally, all of the data were used for the computation of the logarithmic profile and still a good agreement with log-law ($R^2 > 0.98$) was attained.

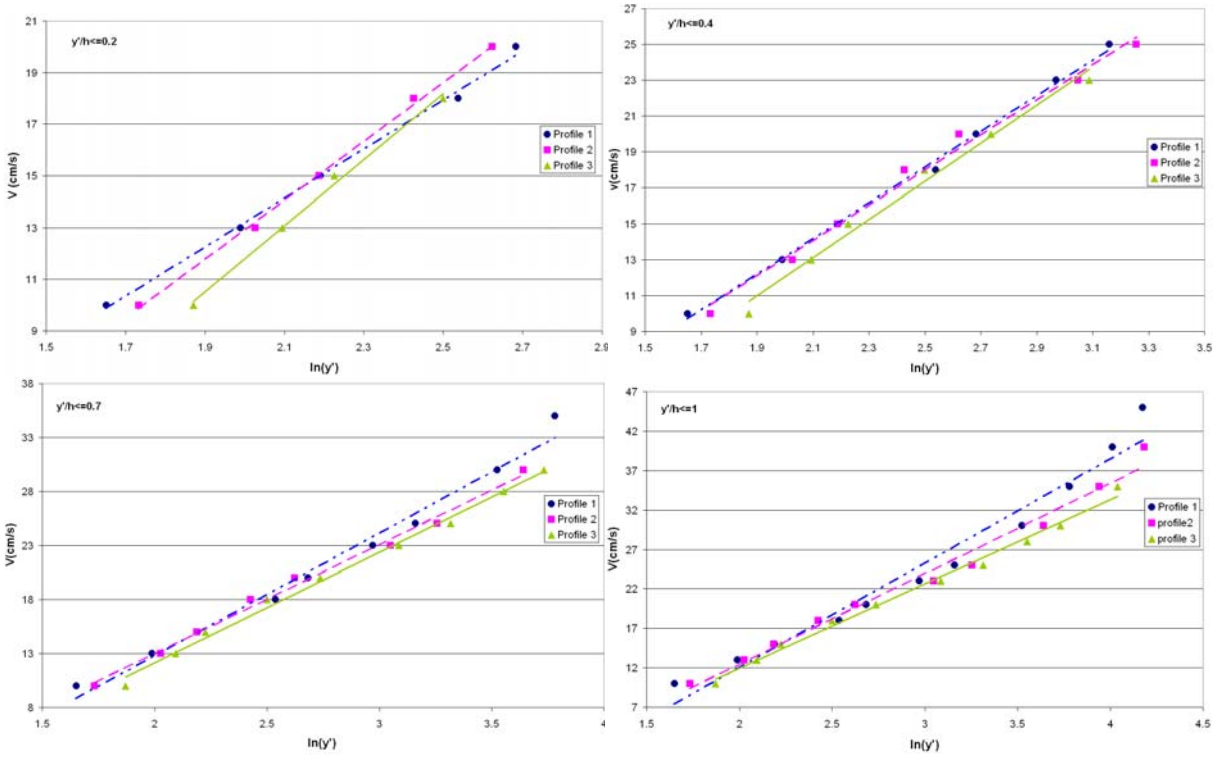

Figure 6-29 Velocity distribution v.s. logarithm of normal distance to the bank and the corresponding fitted lines for profile 1 to 3.

According to the correlation coefficients, it seems that log-law can describe well the velocity distribution normal to the bank even for the whole effective length scale. Nevertheless, a more detailed investigation of the differences between the thus calculated shear velocity among these regions revealed large differences.

The computed bed friction velocities, the intercept of log-law (A_r), correlation coefficient of the fitted curves together with the percent of differences in calculated values of the shear velocity in the above mentioned regions and that of the inner region are given in table (6-11). As shown in this table, with the expansion of data set to an extent of y´/h< 0.4, the computed shear stress by log-law shows a small difference (<6%) with that of the inner region for the first profile. However, this difference increases by including the whole data set for the first profile, while it decreases from 14% to 0.3% for the second profile. It can be inferred that a typical boundary layer exits in the inner region normal to the outer bank-toe surface of the river bend under study and the flow velocity profile follows a logarithmic distribution.

With no exception among the three profiles, negative values were obtained for A_r in all cases, these values remaining nearly constant ($A_r \approx -11.5$). As seen from Eq. (6–15), the constant of log-law has no influence on the value of shear velocity.

Based on the calculated u* shown in table (6-11), the value of k_s^+ was calculated in the range of $6.13 < k_s^+ < 8$ for the three normal profiles. This shows that the flow over the outer river

bank-toe is in transitionally rough region. Moreover, since $y^+ = yu_*/\upsilon$>1600, the data in the inner region are in overlapping region of the boundary layer, where the log-law is applicable.

The above analysis proved that the uncommon range of values of A_r obtained in the first analysis, in which the vertical velocity profiles instead of normal velocity profiles were applied, are not due to the coordinate of velocity profile chosen, but mainly due to the bed forms and k_s^+ value (transient rough region).

Tracy and Lester (1961) suggested that in a smooth rectangular channel, the shear velocity at the centre of the channel can be presented by a log-law with two different shear velocities on both sides of the equation. Yang et al. (2005) showed that if u/u_{*0}[1] is plotted against $u_{*w}z/\upsilon$ [2], the near wall velocity profile can be expressed well with logarithmic function along the bed and bank in a smooth rectangular channel. Furthermore, Yang et al. (2004) proposed the following form of the log-law for the velocity distribution in an open channel with complex geometry (Eq. 6–16).

$$\frac{u(y',z')}{u_{*0}} = 2.5 \quad \ln(f_1 \frac{y'}{y_0}) \tag{6–16}$$

Where z′ is the coordinate along the bank surface, u(y′,z′) is the velocity normal to the bank, y_0 is a reference height equal to the roughness height divided by 30; $f_1 = u_{*w}/u_{*2d}$, in which u_{*2d} is the shear velocity at the channel centre= $(gHS)^{0.5}$, H is the water depth at centre. In the following, the validation of Eq. (6–16) in the natural river under study is examined.

Table 6-11 Computed velocity distribution parameters normal to the bank according to the log-law.

	u_* (cm/s)	B	R^2	y′/h<	Percent difference in u_*	α factor in Eq. (6–17)
Profile 1	3.898	-11.03	0.9966	0.22	-	0.01
	4.096	-11.20	0.9973	0.36	5.05	0.01
	4.662	-11.67	0.9847	0.68	19.56	0.008
	5.441	-12.21	0.9824	1.00	39.58	0.007
Profile 2	4.692	-11.67	0.9982	0.21	-	0.008
	4.0295	-11.17	0.9896	0.4	-14.12	0.01
	4.141	-11.28	0.9930	0.58	-11.74	0.01
	4.706	-11.76	0.9818	1.00	0.30	0.008
Profile 3	5.247	-12.17	0.9953	0.20	-	0.008
	4.344	-11.64	0.9861	0.39	-17.20	0.009
	4.194	-11.53	0.9943	0.70	-20.07	0.008
	4.379	-11.70	0.9918	1.00	-16.54	0.007

For Eq. (6–16) to hold, then the slope of the curves fitted to the velocity measurements should be constant and equal to 2.5. To examine this hypothesis, the velocity in the inner region was

[1] $u_{*0}=(gRS)^{0.5}$ is the overall mean shear velocity, in which R is hydraulic radius and S is energy slope.

[2] u_{*w} is local wall shear velocity determined from the local boundary shear stress.

re-plotted as depicted in Fig. (6-30). The overall mean shear velocity was computed to be 7.75 cm/s, which seems to be very high. As observed from this figure, the slope of the fitted lines are not constant, but the correlation coefficient is high (R^2>0.99). Therefore, the denominator of the left hand side of Eq. (6–16) can not be constant, which indicates that no universal log-law constant is attainable. It implies that the two different shear velocity log-law model proposed by Yang et al (2004) may not be applicable here.

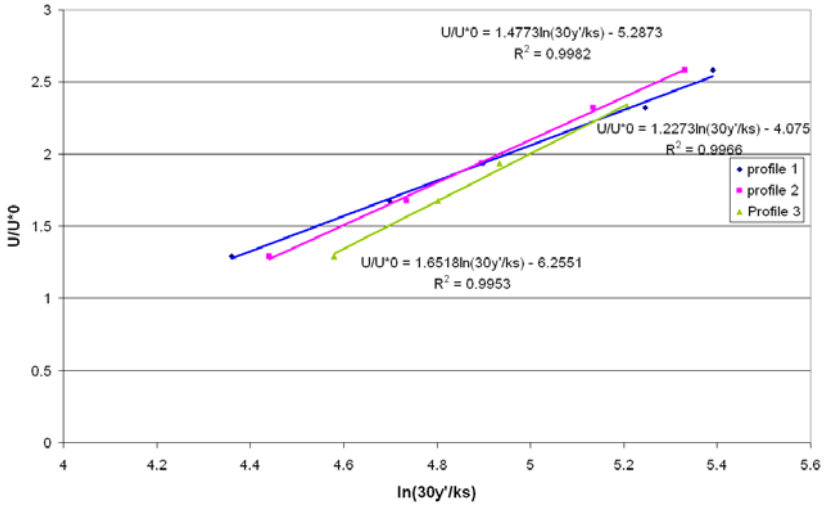

Figure 6-30 Re-plotting velocity data in a form compatible with Yang(2004) formula

Aforementioned analysis showed that the velocity distribution could be well represented by a log-law in the inner region with a single shear velocity parameter. It was then tried to explore if a universal constant of log-law can be obtained for such a logarithmic profile. For this purpose Eq. (6–15), was reformulated in the following form to investigate if a constant value of parameter α can be determined so that all three-velocity profiles collapse on one.

$$\frac{u}{u_*}=\frac{1}{\kappa}\ \ln(\frac{y'}{y_0})$$
$$y_0=\frac{k_s}{\alpha} \qquad (6–17)$$

Using the same regression method presented in Fig. (6-29) for the inner region and k_s =0.022 cm, α was determined 0.01, 0.008 and 0.007 for the profiles 1 to 3, respectively. It seems that α decreases with a decrease in water depth near the riverbank. An average value of 0.0085 was considered for this parameter according to table (6-11). Assuming this value for α, the data were re-plotted in Fig. (6-31).

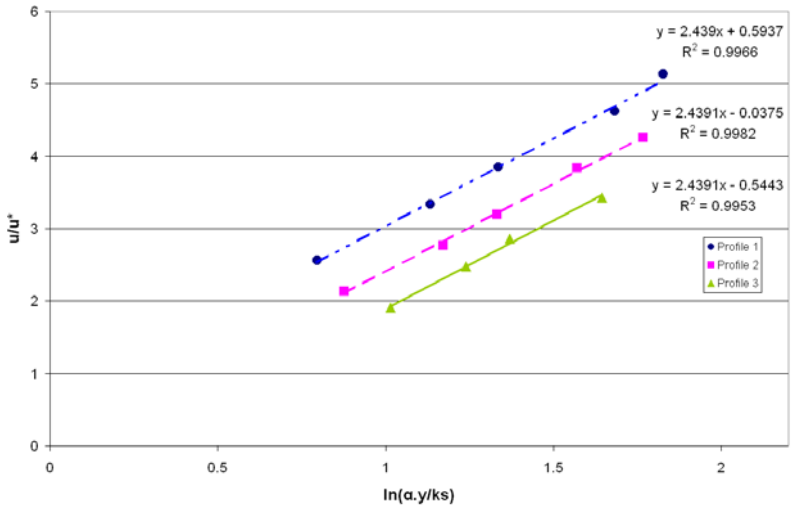

Figure 6-31 Re-plotting the measured velocity profile in inner region with α=0.0085

As seen from Fig. (6-31), the fitted lines are all parallel and the slope of the lines is equal. However, the intercepts are different and the data do not collapse on one line. This means that a universal constant could not be attained, i.e., the universal log-law does not hold, although bed friction velocity could be determined.

6.5 Sediment transport

The aim of the present study is not the study of sediment transport process along the river bend, but bank failure mechanisms. Therefore, it was decided not to conduct measurement of sediment transport along and across the river bend. Furthermore, the small amount of measured suspended sediment in the river justified this decision.

Monitoring of sediment discharge in the river is required as upstream boundary condition for simulation of the sediment transport. Since a depth-averaged model is used here, the temporal variation of depth-averaged concentration of total sediment (bed and suspended load) is required. This can be achieved in three main ways. The best method is the direct long-term monitoring of sediment transport using ASM optical backscatter array. The second method is correlation of backscatter intensity of ADCP with measured sediment concentration after calibration of these two parameters, in which case the process of calibration is complicated and is not always successful. The third method, the simplest and less accurate one, is correlation of flow discharge with sediment concentration using rating curve based on the measurements.

Due to some security limitations, it was not desired to leave the instrument without attendance at the measurement site. Therefore, the first method was not applied here. The second method was examined on March 20, 2007 by simultaneous measurement of discharge using stationary mini-ADCP (StreamPro) and sediment concentration profile at the same position using ASM. However due to the poor correlation between sediment concentration and backscatter

intensity, as will be presented in the following, finally the third method was used to compute the sediment transport rating curve.

Sediment concentration in the water column (down to the bed surface) at the inflow section to the river, where the discharge measurement was carried out, has been measured using optical back scatter profiler (ASM) in the river mainly three times on February 22, 2007; March 9 and 20, 2007. The sampling rate was 1Hz with 2 samples per burst cycle, which means every two samples averaged as an ensemble.

6.5.1 Measurement on February 22, 2007

The temporal variation of sediment concentration in the water column measured on February 22, 2007 from 10:30 to 11:45 is shown in Fig. (6-32). The flow discharge was computed based on the downstream water level measurement using the method explained in Ch. 6.3. The discharge variation was negligible (between 0.973 to 0.991 m^3/s) during this period.

The red zone at the bottom of Fig. (6-32) represents the variation of local bed in front of the array of optical sensors. The timescale of bed evolution represents the existence of an active bed with a bed change of about –3 (erosion) to +4 cm (deposition) in 1:15 hours. The sediment entrainment at the bed surface is shown by orange to blue colours. As can be observed in this figure, the sediment concentration in the water column is generally low (less than 150 mg/l). The colourful strips seen in horizontal direction at the elevation of about 12 and 17 cm show attachment of algae to the instrument forming an obstacle on the sensors. The same is true for the case of oblique colour stripes, which indicate slipping down or up of an obstacle along the array of the sensors over time. The corresponding measured data were filtered out manually before analysis of sediment concentration.

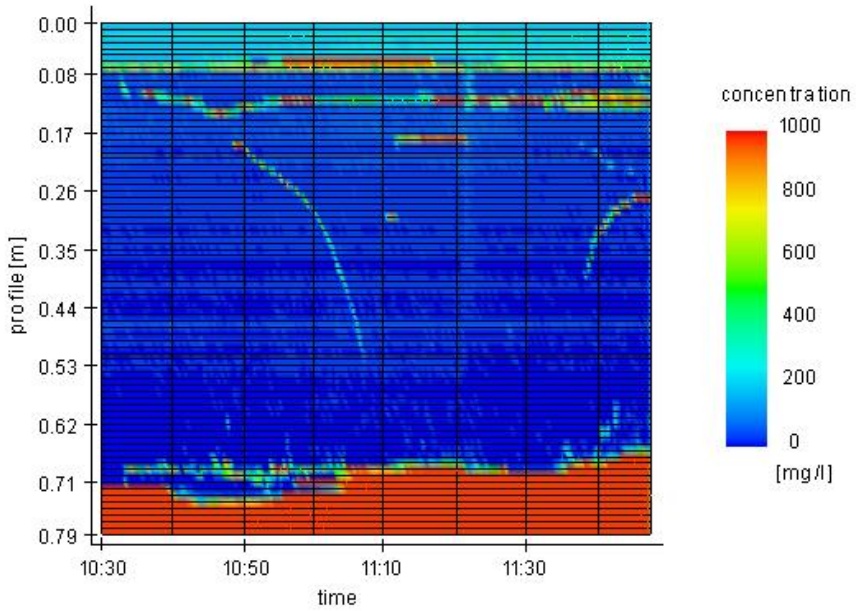

Figure 6-32 Temporal variation of sediment concentration profile from bed to the water (0.08 cm under reference) measured on 2007.02.22

The sediment concentration was first averaged over depth and then over 1 minute interval to examine the relation between sediment concentration and flow discharge. After excluding the range of contaminated data with obstacles, the extent of sensors used for averaging of concentration was from sensor 16 (nearly 8 cm under water surface) to the bed. At this level the concentration was measured a maximum of 1000 mg/l (red colour in Fig. 6-32). The layer close to the bed was considered to account for bed load transport (saltating sediment layer) to keep consistency with the conceptual model of total sediment transport.

As evidenced by Fig. (6-33), no clear trend between depth-averaged sediment concentration and discharge could be observed. Due to the small variation of discharge, no reliable rating curve could be obtained solely from this set of measurement.

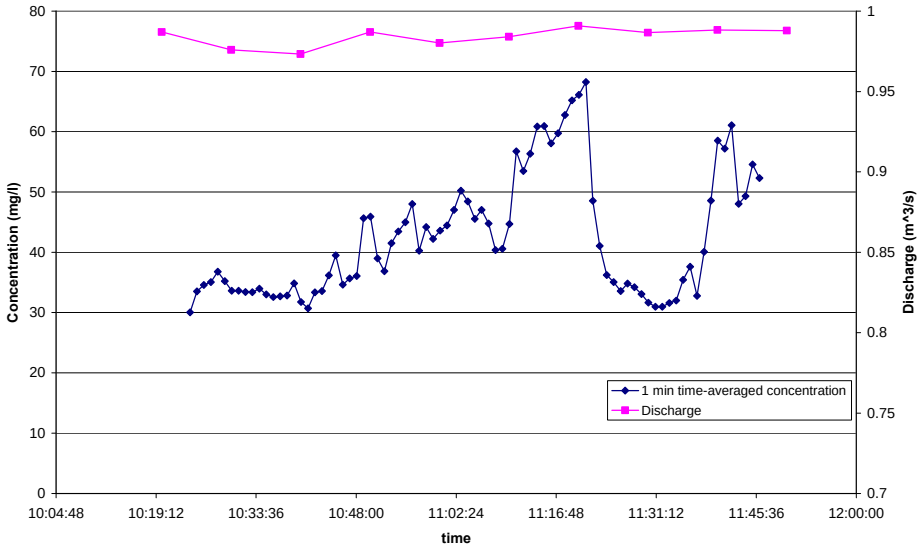

Figure 6-33 Temporal variation of depth-averaged sediment concentration with respect to discharge

6.5.2 Measurement on March 09, 2007

The longest sediment concentration measurement (about 3 hours) was conducted in this measurement campaign (Fig 6-34), where the discharge was computed with the same method as in the previous measurement. The discharge variation was larger than in the previous measurement (between 0.946 to 0.981 m^3/s), however still not significant. The border of light blue color with dark blue in the upper part of this figure (near elevation 0.18 m) represents the interface of air with water. The sediment concentration in the water column seems to be even smaller than that of the previous measurement (most of the water column possesses a dark blue colour, meaning concentration less than 50 mg/l). In contrast to the previous measurement, the bed level changes slightly (about maximum of 2 cm) during the measurement period. Around 10:30 more suspended sediment in the water column is visible for a period of half an hour. The range of 7 cm below water surface was excluded from depth

averaging due to contamination of data by sticking of algae to ASM (the light blue strip in the figure).

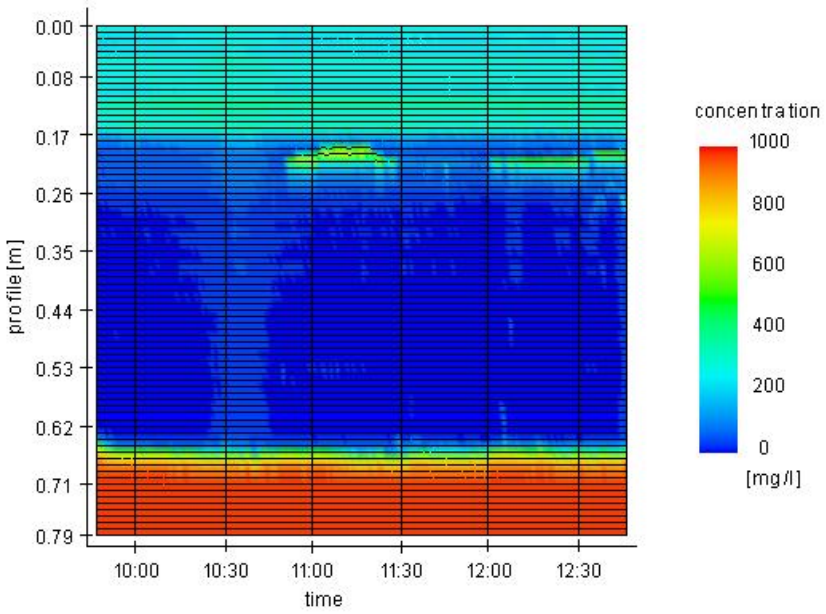

Figure 6-34 Temporal variation of sediment concentration profile from bed to the water surface measured on 2007.03.09

The depth-averaged sediment concentration for 1-minute time averaging is plotted against discharge variation in Fig. (6-35). In the first half of the hydrograph, a trend between sediment concentration and flow discharge is observed. The sediment concentration increases in the rising limb of the flow hydrograph (accelerating flow), with a delay in peak of flow discharge with respect to the peak of the sediment concentration. This is due to the lag of maximum flow discharge with respect to the maximum bed shear stress in accelerating flow (Song and Graf, 1996), which results in re-suspension of more sediment into the water column in the rising limb of the hydrograph. According to these authors, Reynolds shear stress on the rising limb is generally larger that on the falling limb in open channel flows. However, Gordon (1975), in his experiment on tidal flows, suggested that due to the effect of hysteresis in Reynolds stress, the Reynolds Shear stress could be higher in the falling limb (decelerating flow) than in the rising limb, which increases the sediment concentration. Similar trend of sediment concentration with respect to the flow discharge as those in Fig. (6-35) has been also reported in Chanson et al (2007) for tidal flow in estuary.

Since the water level was measured in 10 minutes interval, the depth-averaged sediment concentration was also computed for 10 minutes intervals. This shows a better correlation to discharge than 1-minute interval in this figure.

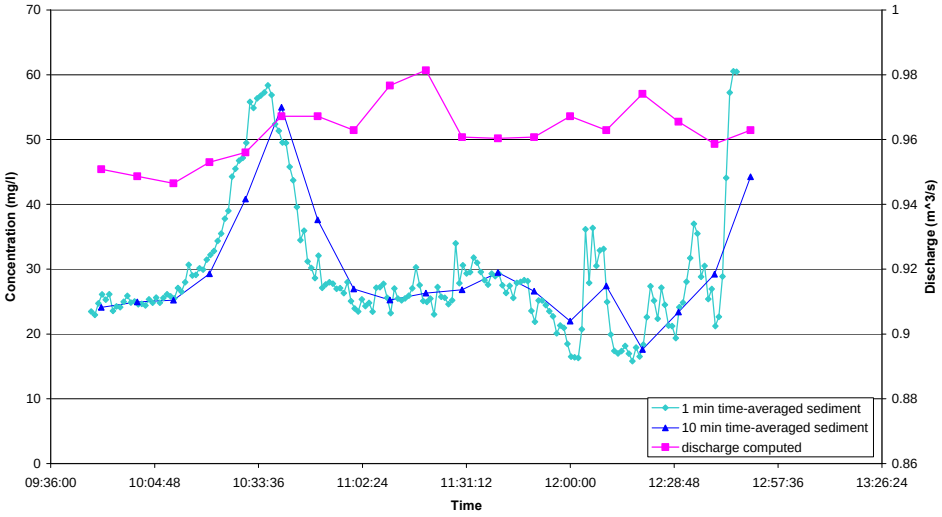

Figure 6-35 Temporal variation of depth-averaged sediment concentration with respect to discharge

6.5.3 Sediment rating

There are two main methods to establish sediment rating (Kondolf and Piegay, 2003). The first method consists of collecting concurrent measurements of sediment concentration and flow discharge and plotting concentration versus flow discharge (C-Q relation). A linear or logarithmic regression may explain the collected data. In this method it is important to have data on high flow range (Miller, 1951). The second method involves explicit estimation of sediment concentration with an empirically derived multivariate relation, relating it to other processes or controls such as sediment supply, season and long-time trend, hysteresis, etc. (Kondolf and Piegay, 2003).

The first of these two methods was used in the present work for the sake of simplicity. The above-mentioned measurements were used to establish the sediment concentration rating curve, assuming that the vertical profiles measured are representative of sediment concentration across the channel. As the measurement location was in a straight reach of the channel with small width (almost 3 m), large lateral variation of sediment transport may not be expected, except near the banks. Therefore, the mentioned assumption seems to be justified.

The two mentioned measurements together with that on March 20, 2007 (used mainly for correlation of backscatter intensity of ADCP with sediment concentration) were used as "index" samples to generate the sediment-discharge rating curve. Further measurements of index samples were not carried out due to the very low measured (suspended) sediment concentration in the river. Because most of the measured sediment concentrations have been almost lower than the minimum measurable range of the instrument (50 mg/l), which is associated with large uncertainty. Therefore, the uncertainty in computed sediment discharges using the already mentioned index samples might be comparable with those in measurement

of sediment concentration. Sediment rating assessed yield may show an error as large as a factor of 10 (Walling and Webb, 1988), which is mainly due to the absence of high discharge data values in regression (Kondolf and Piegay, 2003).

The result of such a C-Q relation using the above-mentioned collected data is presented in Fig. (6-36). As shown in this figure, a high sediment concentration measurement corresponding to the high flow discharge of March 20, 2007 is included in the regression. However, more data on higher concentrations would increase the reliability of the regression equation.

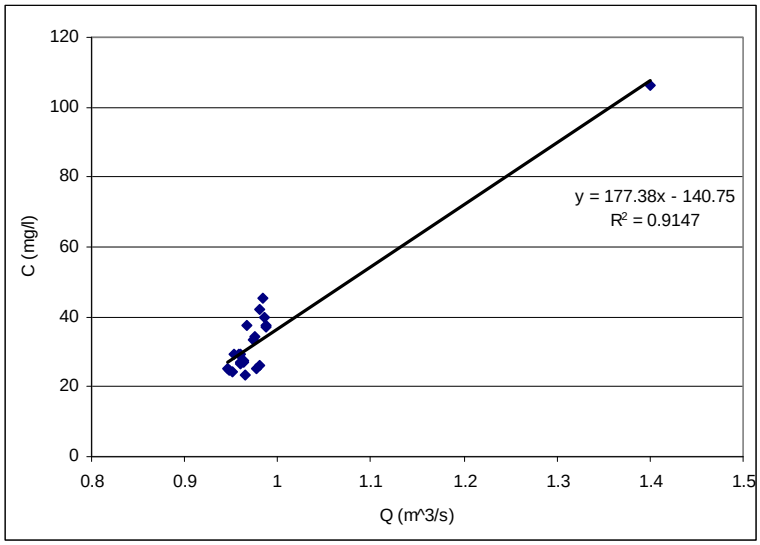

Figure 6-36 Sediment rating curve based on 10-min averaged sediment concentration

6.5.4 Suspended sediment measurement using ADCP

Backscatter intensity of acoustic signals can be used to estimate sediment concentration, which depends on sediment concentration, particle shape and size as well as density (Creed et al., 2001). A change in size distribution is interpreted as a change in concentration (Gartner, 2002). Furthermore, based on the scattering theory of Rayleigh (long wave length), acoustic analysis is restricted to the particles whose ratio of circumference to wave length is less than unity. This restricts the maximum particle size for which an acoustic instrument with a fixed single frequency (like ADCP or ADV) can appropriately measure the sediment concentration. In addition, the wave attenuation falls off significantly when the ratio of circumference of particle to the wave length of acoustic source is near 0.01 to 0.1, which sets a lower limit to the single frequency acoustic method (Gartner, 2002). Therefore, in the case of StreamPro ADCP with 2000 kHz acoustic source and assuming sound velocity in water to be 1500m/s, the most appropriate range of particles is those with diameter of 0.025 to 0.25 mm. This corresponds to a circumference/wave length ratio of approx. 0.1 and 1, respectively. This range covers a part of the lower range of sediment material over the bed ($d_3<d<d_{60}$), as well as the suspension sample in the present experiment. However, it should be noticed that the mean

particle diameter measured for suspended sediment (Ch. 6.1.1) was limited to only one probe, which may inherit large uncertainty in particle diameter of suspended sediment in different flow regimes, such as flood events.

To calibrate the acoustic backscatter intensity (ABI) of the ADCP with sediment concentration (SC), a concurrent measurement was achieved over 20 minutes on March 20, 2007 upstream of the bridge site. The measured discharge was 1.31 m^3/s and the water depth was 1.05 m. The ADCP was mounted in stationary position and the ASM was installed beside it. A range of ASM sensor was selected for the analysis, which corresponded to the ADCP bins. Having converted the backscatter intensity of the mini ADCP from count to (dB) (using the factor of 0.41(dB/count), given by the factory) the sediment concentration as well as backscatter intensity was averaged over depth and a time series of data with 2-second interval was generated.

According to Thevenot et al (1992) and Gartner (2002), in most simplest way, logarithm of SC time series can be linearly correlated to the concurrent measured relative ABI (more sophisticated methods such as Deines, 1999 have not been followed here). Such a diagram is shown in Fig. (6-37). Note that the vertical axis in this figure is in logarithmic scale. As can be seen in this figure, ABI remains almost constant (between 62 to 65 dB), for a range of 25 to 325 mg/l. of SC, indicating no correlation between these two parameters.

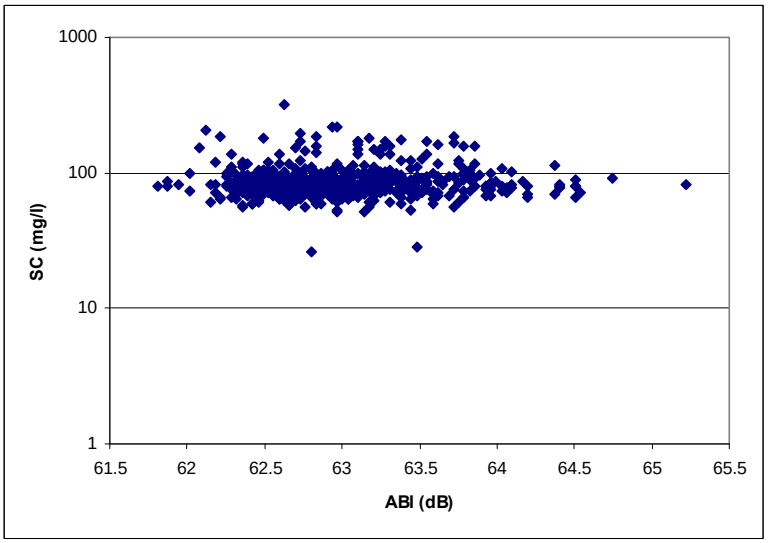

Figure 6-37 Measured sediment concentration in water column versus acoustic backscatter intensity of ADCP

There could be two reasons for this result. First, the optical signals are more sensitive to small particles (proportional to the cross sectional area), while acoustic signals are more sensitive to large particle sizes (Gartner, 2002). As already described above, the measured suspended sediment could have been so small that it would be out of the effective measurement range of ADCP (less than 0.025 mm of diameter), while the optical sensor could still register them. Second, due to the relative low sediment concentration, no significant variation in ABI can be expected. That is the reason why ABI shows almost no sensitivity to different low

concentrations. Therefore, it was decided to use the sediment concentration rating curve for further application in the simulation of sediment transport.

6.6 Bed evolution

Different bed processes have been found out along and across the river bend by means of bathymetry measurements. In this chapter these processes are presented and analysed for each campaign of bathymetry measurement. These processes include:

- Bi-directional pool development
- Berm formation
- Bank-toe erosion
- Inner bend aggradation, degradation
- Mechanism of distribution of failed bank material across the river bend
- Quantification of scouring and deposition

For the purpose of the investigation of the bed and bank-toe evolution along the river bend, bathymetry measurement with special focus on the river bend was carried out using single-beam echo sounder integrated with a RTK-DGPS system on July 20, 2007, Oct. 24, 2007, Dec. 10, 2007, Feb. 5, 2008 and March 7, 2008. The average and absolute accuracy of GPS and echo-sounder for these measurements was about 0.02 m and 1 mm, respectively. Digital elevation models (DEM) of these measurements were generated from filtered bathymetry data in form of raster data with 5 to 10 cm resolution as shown in Fig. (6-39). The DEMs, presented here cover the region between entrance and apex of the bend. Due to the very shallow water depth, the toe of the bank could not be measured using echo sounder on July 20, 2007 and Oct. 24, 2007. Three cross sections are indicated on the first three DEMs with orange lines in this figure. These typical cross sections will be later used to discuss the evolution of the talweg along the river bend presented in Ch. 8. The DEMs have been utilized to quantify the distribution of erosion and deposition along the river bend and explore the bed evolution process along the river.

Bed forms can be observed on the inner bed of the river bend in Fig. (6-39a). However, no specific regular bed form type (dune for example) can be recognized, due to the low resolution of single beam echo sounder compared to multi-beam echo sounders. Indeed bed forms (ripples) were observed by visual inspection. (Fig. 6-38).

Figure 6-38 Bed forms along outer bank-toe

As evidenced by the DEM of July 20, 2007, the pool width and depth increase toward the bend apex. The inner bank comprises a very mild lateral slope while that of outer bank increases towards the outer bank, where it becomes relatively steep. The higher slope of the bank-toe around the bend apex is an evidence that justifies the argument presented in Ch. 6.4.3 regarding the process of shifting maximum bed shear stress from central region upstream of the apex towards the outer bank at the bend apex and its effect on bed erosion (Fig. 6-22 and 6-24).

The generated DEM of Oct. 24, 2007 suffers from contamination of bathymetry data with large growth of vegetation at riverbed, especially along the pool, which had to be filtered out. Therefore, the relatively flat shape of pool in Fig. (6-39b) is the result of filtering out the data in this region and linear interpolation by triangulation. In this measurement, a zone of bank-toe over water surface, which has been isolated from the rest of the scanned bank by means of laser scanner, was integrated with bathymetry data to yield a seamless DEM of the river bend including bank-toe. In the mentioned figure, the formation of berm at the bank-toe can be clearly recognized. The berm width reduces from the entrance of the bend towards the bend apex due to the berm-toe erosion. Furthermore, the development of berm at the bend entrance caused concentration of flow in the central part, thereby deepening the pool.

a) July 20, 2007(with indication of section 3).

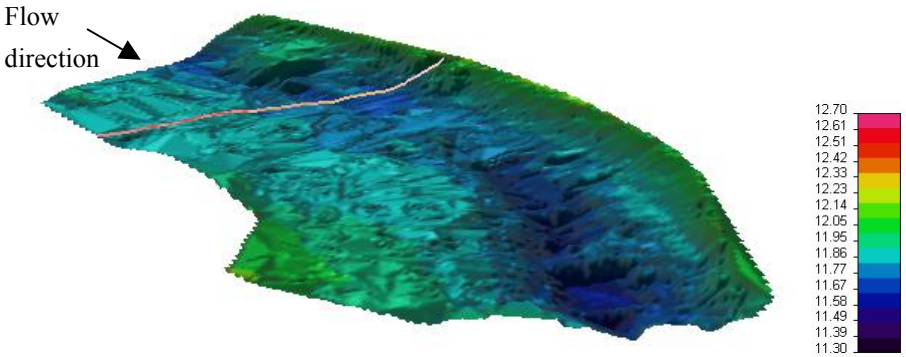

b) Oct. 24, 2007(with indication of section 2).

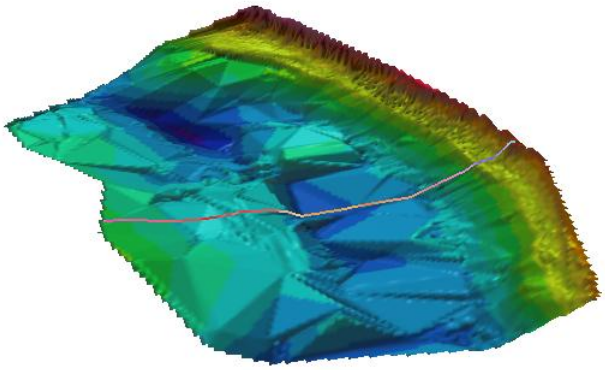

c) Dec. 10, 2007 (with indication of section (1)

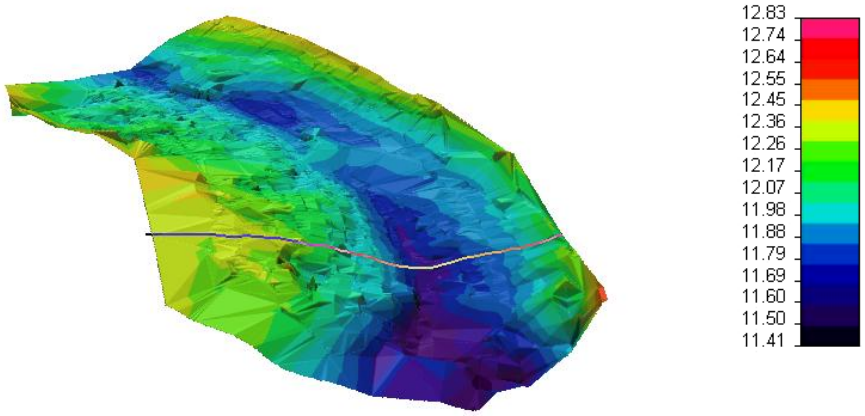

Figure 6-39. DEM models of the river bend using echo-sounder data, with vertical scale of two

d) Feb. 5, 2008

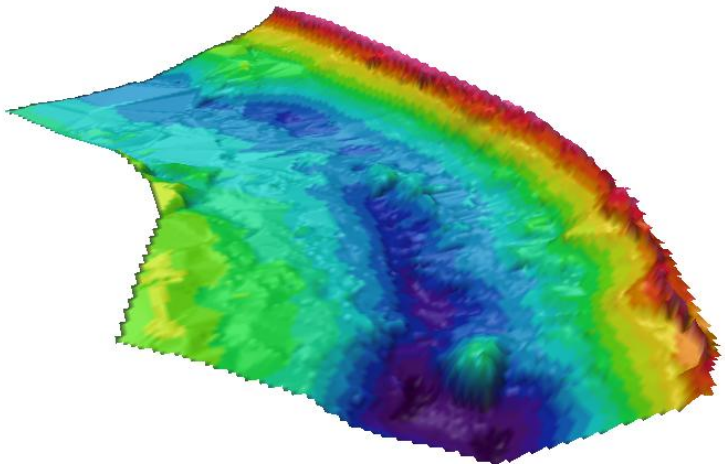

e) March. 7, 2008

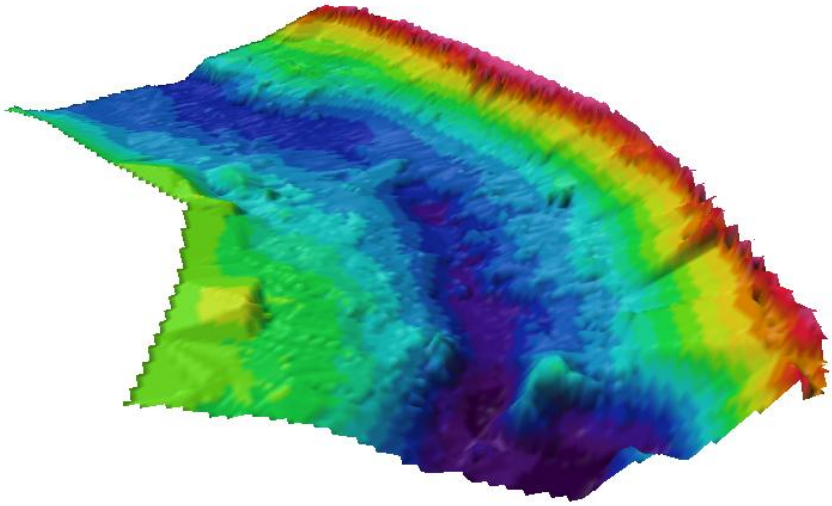

Figure 6-39 Continuation form previous page

During the high water stage on 10 Dec. 2007, flow in the river channel was close to the bank full stage. Hence laser scanner was not applicable. Nevertheless, most of the bank-toe area could be measured by echo sounder. Due to the low spatial resolution of echo sounder in comparison with laser scanner, the development and evolution of berm can not be recognized well in Fig. (6-39c). Further development of the pool and its deepening can be clearly observed in this figure, especially at the entrance section. The pool at the bend apex has been further scoured, destabilizing the riverbank near this zone. This can be a result of helical flow motion and secondary currents. This fact describes the reason of increasing trend of bank failure towards the bend apex.

The developed technique of integrating laser scanner data of the outer bank-toe and bathymetry data was used in the 2008 measurement, to study the processes of bank-toe and berm evolution. Development of berm formation can be observed along the outer bank in yellow to red colours in Fig. (6-39d). Further deepening and widening of pool towards the

inner bank can be observed, especially at the entrance and apex on Feb. 5, 2008. This is probably due to the flow concentration at the centre of the section because of berm formation. Deposition of failed bank material in the form of a bar can be observed near the outer bank at the bend apex and upstream of it. This can describe the mechanism of deposition of failed bank material, in which a part of failed bank material remains intact at the bed and forms a bar, along which further bed erosion may occur.

The pool and bank-toe of the outer bank seem to be the most dynamic zones of the river bend. Berm-toe erosion and deepening as well as widening of the pool proceeds on the measurement of March 7, 2008 (Fig. 6-39d). Indeed, in this period the pool has generally shifted closer to the outer bank, especially at the entrance and upstream of the apex. Bar formation near the bend apex has been expanded due to further bank erosion and consequently deposition of failed bank material in this zone, as will be shown in the next chapter.

The most important issues which can be observed from sequences of bathymetry measurements in (Fig. 6-39) is, first, the widening process of the pool, especially at the bend apex, and second, its upstream propagation. As it is seen from (Fig. 6-39a), two distinct pools can be observed at the bend entrance and apex. In (Fig. 6-39b to d) they are extended in upstream as well as downstream directions, so that they have become closer together. In Fig. (6-39e), the upstream propagation of the pool at the bend apex and downstream propagation of that at the bend entrance met each other at the middle of the bend, forming an almost continuous pool throughout the river bend. Finally, the larger deepening and widening of the pool staring near the bend apex in the mentioned figure suggests the existence of a still more intensive bi-directional development of pool downstream of the bend apex, which has reached the bend apex.

To determine the quantity as well as distribution of erosion and deposition zones (bed evolution) in four subsequent periods, the common area of each DEM surface (Fig. 6-39) were subtracted from that of the previous one sequentially. In this way, DEMs of the difference surfaces have been generated as shown in Fig. (6-40).

In the differential surface shown in Fig. (6-40a), a strip of bar formation associated with pool along the outer bank can be recognized. This relatively large bar formation could be mainly biased due to the data contamination by filtering vegetation elevation in DEM, as already explained. However, to a lesser extent, it can be due to the settlement of fine particles in low water stage due to the flow retardation created by growth of vegetation in this zone, as was observed during in situ inspections. The scour zones along the berm become larger and deeper with the size of the berm. The larger deposition zone at the bend apex, probably due to deposition of failed bank material, is accompanied by deepest erosion depth at this section, which justifies the already mentioned process of pool deepening due to the flow concentration.

In the next period (Fig. 6-40b), the outer bank underwent slight erosion along the bank-toe. However, a large zone of deposition formed on the inner bank. This forced the talweg to shift towards the outer bank. The dark blue zone along the centre of the river illustrates this. However, the magnitude of erosion is biased due to the reason just mentioned above.

a) Difference surface of Oct. 24and July 20, 2007

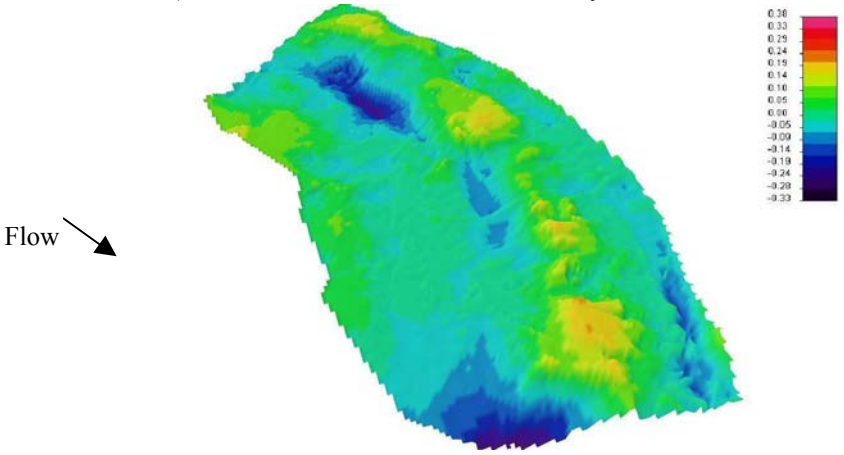

b) Difference surface of Dec. 10 and Oct. 24, 2007

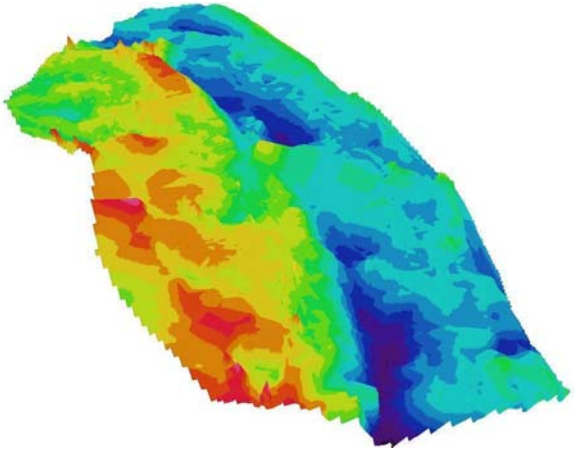

c) Difference surface of Feb.5, 2008 and Dec.10, 2007

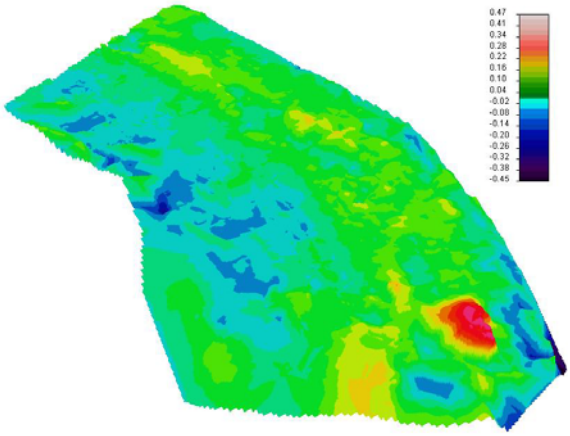

Figure 6-40 Bed erosion and deposition along the river bend in meter.

d) Difference surface of March 7 and Feb.5, 2008

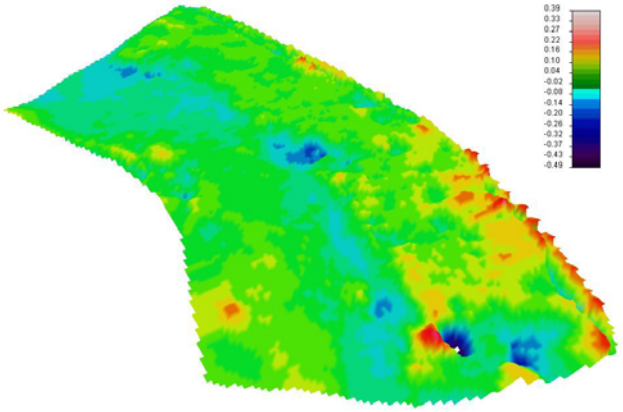

Figure 6-40 Continuation form previous page

Further deepening of the pool near the bend apex and its trend of upstream propagation can be inferred from (Fig. 6-40c) by observing the erosion zone along the river centreline. At the outer bank, deposition is generally observed in this period, while erosion has occurred along the inner bank. This confirms the process of inner bend degradation by means of two interconnected processes. Deposition at the outer bank causes a shift and concentrates the flow at the river centre, thereby shifting the pool towards the inner bank in the form of widening accompanied by deepening. The latter causes more flow discharge over the inner bank, which results in inner bend degradation. Furthermore, formation of bar due the deposition of bank material can be observed along the outer bank in this figure.

In the last period, large scour holes can be observed around the bars, formed due to deposition of collapsed bank material at the outer bank-toe. Additionally, berm formation in the form of distributed deposition zones along the outer bank can be recognized in Fig. (Fig. 6-40d), especially near the bend apex. Furthermore, bi-directional development of pool can be clearly observed along the eroded centreline of the riverbed. At the central region of the river bend, erosion can be considered related to the deposition at the inner as well as the outer bank and concentration of flow in this region.

The computed mean erosion and deposition depth and net volume of erosion or deposition has been quantified and summarized in table (6-12). As shown in this table, in three of the four mentioned periods, a net deposition has occurred, indicating that a surplus in sediment balance existed due to upstream feeding of bed sediment and deposition resulting from bank erosion. The negative net volume in the last period can be attributed to the local scouring around formed bars and bi-directional pool development at the channel centreline. In a few cases, failure of the vegetated overhang and sliding to the bank-toe has caused retardation of flow velocity and deposition of suspended sediment over the failed block (Fig. 6-41). This has consequently contributed to the bar formation.

Table 6-12. Mean erosion (-) and deposition (+) depth (volume /surface) and net volume change along the river bend.

Row	Reference surface	Overlaying layer	Erosion depth(m)	deposition depth (m)	Net volume change(m^3)
1	2007.07.20	2007.10.24	-0.047	0.051	0.167
2	2007.10.24	2007.12.10	-0.081	0.129	1.266
3	2007.12.10	2008.02.05	-0.056	0.064	0.585
4	2008.02.05	2008.03.07	-0.061	0.051	-0.774

Figure 6-41 Collapse of vegetated overhang at bank-toe and growth of vegetation at river bed

6.7 Bank evolution

Bank erosion often occurs along outer bank of the river bends (Pizzuto, 1984; Nasermoaddeli and Pasche, 2008a). Therefore, the core of this investigation has been monitoring and analysing the bank surface evolution along the outer bank using high resolution terrestrial laser scanning technique. Since the riverbank downstream of the bend apex was stabilized by woody trees and no bank retreat was observed there, the investigation reach was limited between the bend entrance and the bend apex. The following issues that were studied are presented in this chapter.

- Undercutting process
- Cantilever failure
- Complex bank geometry after undercutting and cantilever failure
- Non-uniform rate of bank retreat along the river bend

- Bank evolution in respect to the dynamics of the flow regime
- Moment of bank failure
- Spatial distribution and quantification of bank erosion along the river bend
- Effect of vegetation on bank erosion process
- Distribution of failed bank material

In two monitoring phases, namely from Oct. 25, 2006 to April 16, 2007 and from Oct. 24, 2007 to March 7, 2008,respectively, ten measurement campaigns were conducted. In the first phase, the scanning of bank surface was accompanied by flow measurement to study the dynamics of bank evolution with respect to the flow regime. In the second phase, however, the main focus was the interaction between bed and bank erosion to explore the mechanism of fluvial evolution (bank-toe erosion and distribution of failed bank material at the bank-toe in the form of berm) and its effect on bank erosion. Hence in the second phase, the measurement campaigns were mostly accompanied by bathymetry measurement and only those conducted in 2008 were accompanied by flow measurements. The vertical and horizontal resolution of the bank surface scanning was between 2 mm to 1 cm grids.

After pre-processing of the data and rotation of coordinates as described in Ch. 5.9.2, the DEMs of the scanned riverbank were generated, for example, as shown in Fig. (6-42). This figure shows an oblique view of the outer bank. The outer bank of the river bend starts from the left side of the figure and ends in the apex at the right side. The larger amount of bank retreat upstream of the apex (shown in dark blue) as well as undercutting in form of large cavities with steep to negative slopes and formation of overhang at the bend apex are illustrated in this figure. It should be noted that the scale in radial direction (from the point of location of the laser scanner to the bank surface) is 10 times exaggerated to better show the structures of the bank surface. The three representative cross sections, already analysed in the previous chapter are indicted in this figure with white lines. Later in the following, the temporal evolution of bank surface will be investigated in more detail using these three sections. Furthermore, the spatial distribution of erosion and deposition zones along the outer bank was analysed by sequential subtraction of their elevation models similar to those conducted in previous chapter.

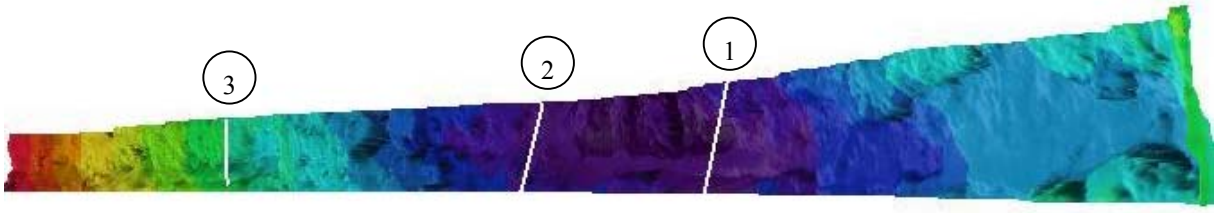

Figure 6-42 The DEM of the outer riverbank surface (March 7, 2008) with an oblique view from inner bank

6.7.1 First measurement phase

The lateral bend migration during this period is shown in Fig. (6-43) by means of plotting the plane view of the longitudinal profile of the upper part of the outer river bank. The largest amount of bank retreat is observed around section (2), shortly upstream of the bend apex, while negligible bank retreat occurred at the bend entrance (section 3). This is in agreement with field observations of Pizzuto (1984) in sandy rivers, in which hundreds of bank failures were reported in river bends, while only a few in straight reaches. The observed location of maximum bank retreat is in contrast with the laboratory results of Wilke (2008), in which bank erosion started shortly downstream of the bend apex and reached its maximum at the outer bank around the crossover to the next meander. As already explained in Ch. 6.4 the location of maximum bed shear stress and depth-averaged velocity is a function of bend curvature, therefore, it can be concluded that the location of maximum bank erosion, which is also a function of bank-toe erosion, is also dependent on the river bend curvature.

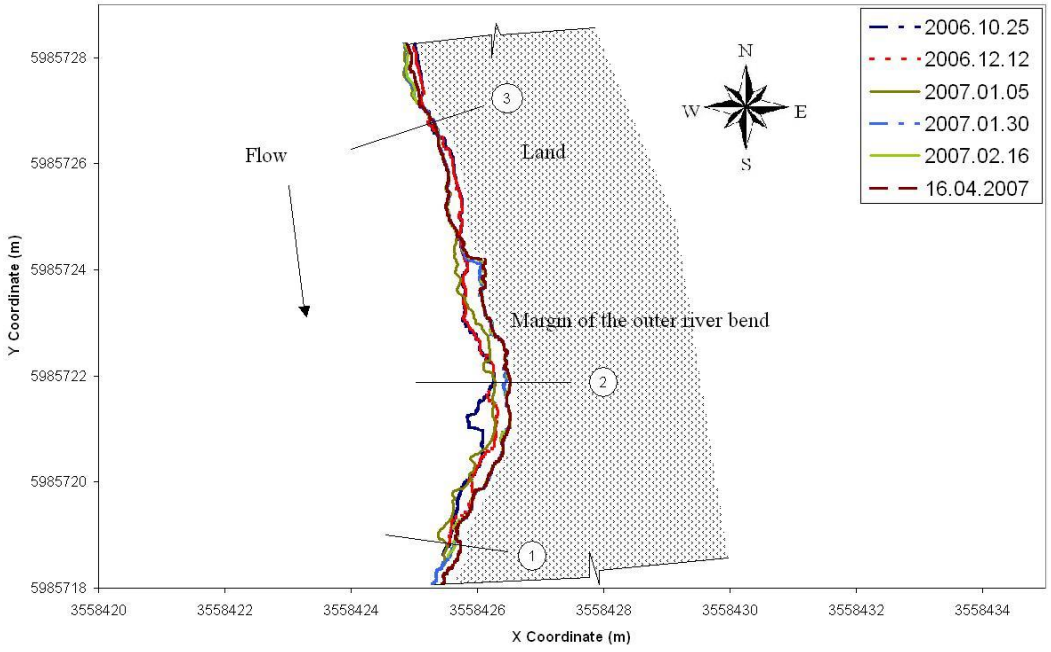

Figure 6-43 Outer bank retreat along the river bend during the first measurement period

As seen from Fig. (6-43), the riverbank retreat has been primarily restricted to a small reach downstream of section (2) from Oct. 25 to Dec. 12, 2006. However, it has been extended laterally as well as longitudinally in upstream and downstream directions between Jan 5 and jan.30, 2007, when the highest flow event occurred (refer to Fig. 6-7). As can be inferred from Fig. (6-43), no such a large bank retreat occurred in the rest of this study period, although two other flood events occurred between Feb. 16 and April 16, 2007. This indicates that the major bank retreat occurred during the flood event with higher discharge and multi-peak hydrograph. However, it should be noted that this trend of bank margin shows the longitudinal bank profile along the top of the bank. Later in the following the bank surface

will be studied in more detail to explore the bank retreat not only at the top of the bank but also over the whole bank surface. The total amount of bank retreat of the upper edge is given in table (6-13) for sections (1) to (3) in Fig. (6-43) during the first year and once for the whole measurement period. Although the major amount of bank retreat at section (1) (27 cm) occurred between April and December 2007, it is seen from this table that most of the bank retreat at this section, in fact, occurred in the first year, while in the second year, the bank retreat was negligible. At the two other sections, the amount of bank retreat is almost half of that for the first section in the first year and almost equal to that of section (1) for the whole period. The trend of the bank retreat along the river bend, presented in table (6-13), suggests the increase of bank retreat towards the bend apex and perhaps over a longer period.

Table 6-13 Amount of riverbank retreat (cm) at upper edge for the three representative sections

Measurement periods	Section (1)	Section (2)	Section (3)
First year (Dec. 2006-2007)	52	26	25
Dec.2006-March 2008	55	54	53

The result of scanned surfaces in the first measurement period is presented in Fig. (6-44). The images are sorted by ascending date. Furthermore, since the extent of scanned surfaces along the river bank was not the same at each measurement campaign, they are sorted horizontally so that the horizontal location of a specific point among the images remains fixed through all images. The stepping shape of the top of the bank at the left is purely due to the bounding of images in pre-processing phase. The difference in the height of images is due to the stage of water level that has dictated a lower limit of the image, below which the laser scanner technique was not applicable. The locations of the three mentioned sections are indicated using white lines on the first image from top. The dark blue colour in these images indicates the location of largest bank retreat measured in radial direction with respect to the location of the laser scanner on the inner bank, while light colours such as yellow imply a closer distance (in radial direction) of the surface to the reference point on the inner bank.

A horizontal narrow deep cutting strip along the bank surface can be recognized in all of these images in Fig. (6-44). This is an imprint of the highest water level on the bank surface, which has fluctuated over a longer period around the same elevation.

As observed in this figure, the bank retreat started upstream of the bend apex (section 2) and expanded in both downstream as well as upstream directions. Comparison of the bi-directional development of bank erosion with that of the talweg (pool) propagation shows the effect of the mentioned bed evolution on bank erosion along the river bend discussed in the previous chapter. This agrees with earlier research on the role of bank-toe erosion on bank failure (Carson and Kirkby, 1972; Thorne, 1982; Simon et al., 2000).

The large cavity, comprising steep as well as negative slope, observed on the right side of the image pertaining to 16th April, seems to be the result of superposition of sapping failure with a preceding fluvial undercutting or rather shallow slip failure. Referring to the flow hydrograph in this period (Fig. 6-7), it can be seen that two high flow events occurred between Feb. 16 and April 16, 2007. The water stage difference between flow peak and lowest water stage was

28 cm for the first event and 35 cm for the second event. The mentioned drop of water stage in the river together with high gradient of the falling limb of the hydrograph of the second flood event can be seen as evidence of the occurrence of seepage out of the bank surface and consequently probable sapping failure during this period.

The deepest zone normal to the retreated bank surface in all images can be recognized to be the upper part, which implies the occurrence of cantilever failure of the overhang. Overhang formation can be observed over most of the bank surface in these images.

It can be further recognized that in a few of these images (for example, Oct. 25 and Dec. 12, 2006), the bank surface suddenly changes its slope from almost vertical (or negative due to the overhangs) to a mild bank-toe slope. This is mainly due to deposition of failed bank material at the bank-toe. The deposition of failed bank material directly at the bank-toe can be clearly observed on the right side of the image of Jan 5, 2007. A pile of failed bank material at the bank-toe around section (3) on Oct. 25, 2006 is not visible in the next measurement on Dec. 12, 2006. This indicates that in less than a month the failed bank material was washed away by fluvial erosion at the bank-toe.

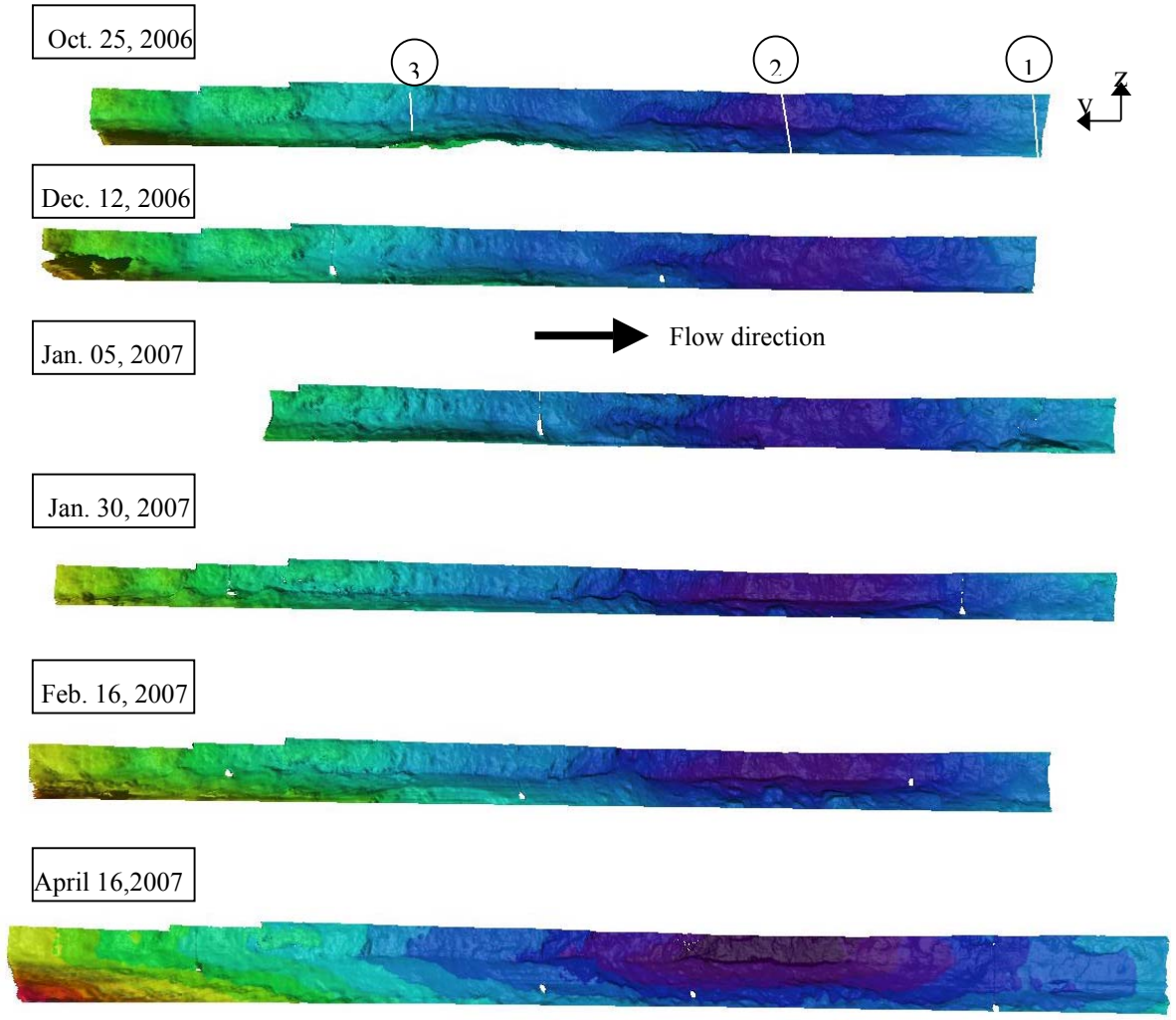

Figure 6-44 The DEMs of outer bank surface of the river bend measured using laser scanner

To quantify bank erosion and determine the spatial distribution of deposition and erosion along the outer river bend, difference surfaces were calculated as in the previous chapter. The results are presented in Fig. (6-45). For analysis purposes, the bank surface was divided in three vertical slices (I, II, III, meaning: downstream, middle and upstream reach of the river bend) and in three layers (Top, Middle, Bottom). For example, (IIB) means the zone locating in the middle slice and bottom layer and (III) means the whole third slice. Moreover, for each zone a representative cross section was introduced to explain the riverbank retreat process better. This will later be used for the analysis of bank erosion process at each mentioned zone. The positions of these cross sections have already been shown in Fig. (6-44).

As can be inferred from Fig. (6-45), during the first period (Oct. 25 to Dec. 12, 2006) , the middle layer(M) of the bank, especially in zones (I) and (II), was severely eroded by undercutting creating overhanging (positive depths in the legend) as well as bank failure (negative depths in legend) in layer (T). Moreover, the changes in the riverbank surface in zone (III) are small, whereas riverbank and bank-toe erosion are moderate in zone (II) and intensive in zone (I) due to the proximity of maximum bed shear stress to the outer bank (Fig. 6-22) and consequently more bank-toe erosion at the bend apex. The erosion and deposition volumes within this period were –0.299 m^3 and 0.026 m^3, respectively, which reflects the net erosion values in table (6-14). The rest of the eroded material should have been transported and deposited at the bank-toe, below water level, where the application of laser scanner has been limited.

In the second period (Dec. 12, 2006 to Jan. 5, 2007), bank-toe erosion combined with undercutting played the role of triggering cantilever bank failure through increasing bank height and slope (often negative slope). The collapsed bank material was mostly deposited on layers (B) and (M). Vegetation roots in the top layer allowed formation of the soil overhanging in a portion of the zone (IIIT). The erosion and deposition volumes of -0.088 m^3 and 0.442 m^3 were computed for this period, respectively. Other computed parameters are given in table (6-14). The deposition volume is larger than the erosion volume due to two reasons. First, the earth mass hanged from the top of the river and supported by vegetation roots (seen in zone IT and IIT) induced a positive volume bias. Second, this positive net deposition can be attributed, to a lower extent, to the transport of sediment from upstream.

The highest flood event with multiple peaks occurred (Fig. 6-7) in the third period (5 to 30 Jan. 2007). The four high peaks with water level ranging from 12.70 m and 12.86 m occurred in a relatively short duration (2007.01.18,17:23 and 2007.01.22, 23:53), leaving a cutting zone at the same elevation interval at layer (M) all along the river bend. It can be concluded that the frequency and duration of flood peaks can play a role in the erosion process of sandy banks.

Lane et al. (1994) and Lindsay and Ashmore (2002) addressed the issue of survey frequency and its effect on underestimation of erosion volume due to unaccounted erosion and deposition, which may occur within a single or multiple flood events. However, bank surveying was not feasible during high flow events to investigate the mentioned process in detail.

Undercutting (in zone M) induced almost no change in zone (IIIT), while it triggered intensive bank failure in zones (IT) and (IIT) in the form of cantilever failure. Collapsed bank materials were deposited on zone (IIB), while in zone (IB) they were eroded. This process is the result of intensification of helical flow motion towards the bend apex, which induces intensive bank-toe erosion and transportation of eroded materials downstream and towards the inner bank. The most severe erosion volume of –0.564 m^3 occurred during this period, with just a little amount of deposition (0.074m^3), indicating that most of the eroded material was deposited at the bank-toe under water surface or transported away.

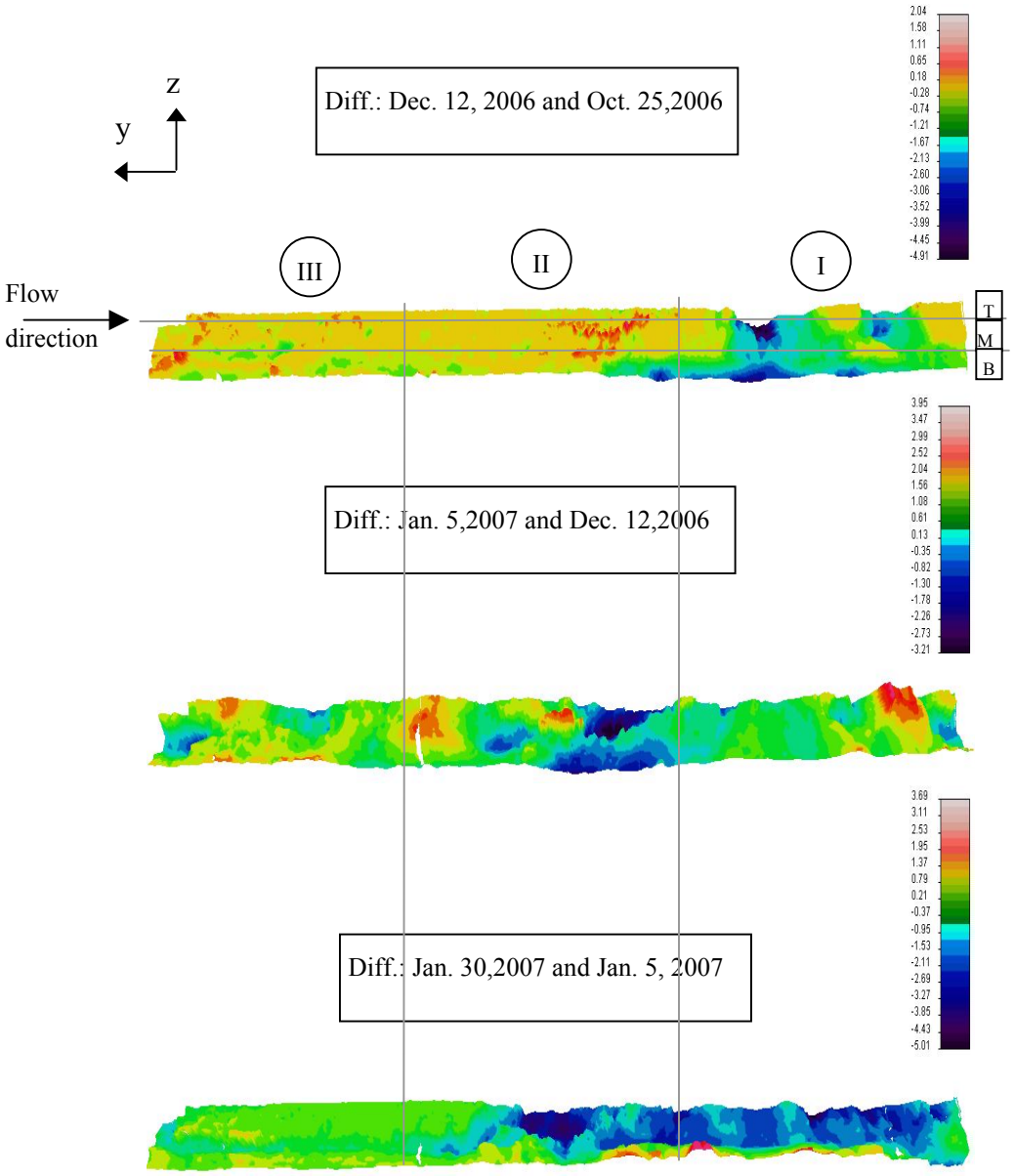

Figure 6-45 Spatial distribution of erosion and deposition along the riverbank in the rotated coordinate system within the bounded area. The erosion (-) and deposition (+) depths are in dm in x-direction (normal to the paper).

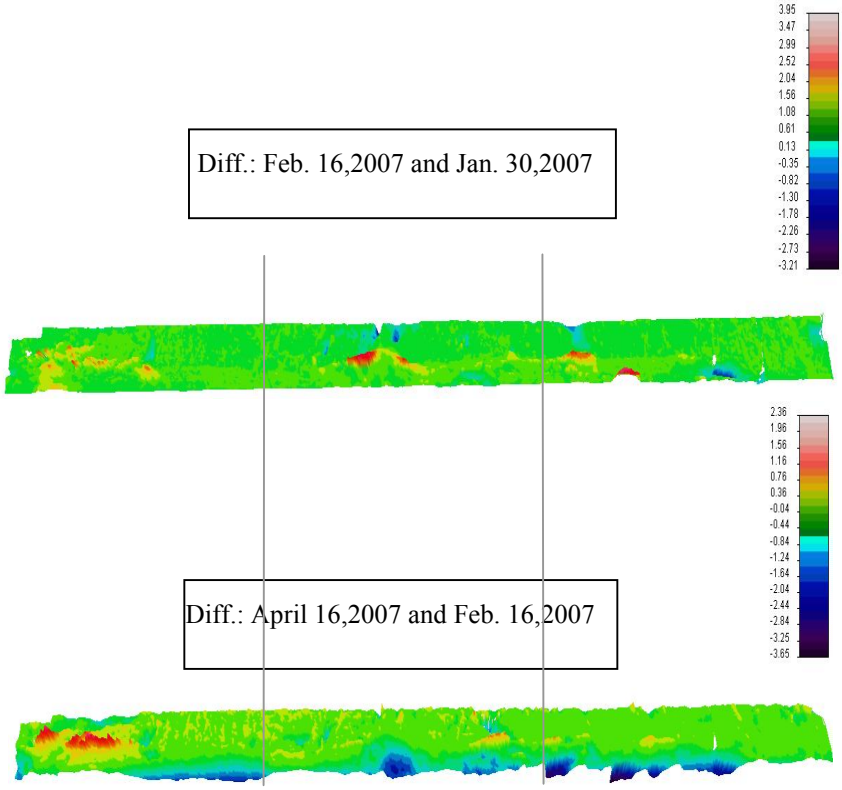

Figure (6-45) Continuation form previous page

During the phase of decreasing flow, between Jan. 30 and Feb. 16, 2007 (fourth period) no significant bank surface changes occurred, since the water level was under the bank-toe elevation. Nevertheless, low water level still plays a role on bed erosion close to the bank, as already addressed in the previous chapter. The computed net deposition of 0.014 m^3 confirms the negligible change in bank surface.

Table 6-14 Mean erosion (-) and deposition (+) depth (volume /surface) along the outer riverbank

row	Reference surface	Overlaying layer	Erosion depth(m)	deposition depth (m)	Net volume change(m^3)
1	2006.10.25	2006.12.12	-0.090	0.014	-0.274
2	2006.12.12	2007.01.05	-0.079	0.109	0.354
3	2007.01.05	2007.01.30	-0.153	0.049	-0.490
4	2007.01.30	2007.02.16	-0.016	0.014	0.014
5	2007.02.16	2007.04.16	-0.047	0.017	-0.107

Two flood events with relatively long duration occurred between Feb. 16 and April 16, 2007 (fifth period). This caused severe bank-toe erosion all along zone (B) on the fluctuating area of water level, through which the bank height and bank-toe slope have increased. An erosion volume of –0.143 m^3 was computed for this period, which shows less than one fourth of the erosion volume in the third study period. This indicates the importance of peak flow magnitude and frequency on bank erosion as well as bank retreat in sandy soils. Furthermore,

it shows the importance of non bank-full stage events in bank-toe erosion, which later triggers bank erosion (undercutting in non-cohesive soils). Therefore, consideration of intermediate stages of flow and morphological evolution is necessary for computation of bank erosion at least in short timescale.

The moment of cantilever failure was recorded by the remote camera described in Ch. 5.10. In contrast to previous studies (Casagli et al., 1999; Simon et al., 2003; Dapporto et al., 2001, 2003; Rinaldi et al., 2004), the bank failure occurred during the high flow regime as shown in Fig. (6-46). The reason is that, first, in the mentioned literature, only planar or circular failures were considered and not cantilever failure, which was the case here. Second, bank-toe is eroded more intensely in non-cohesive alluvial rivers than cohesive ones given a flood event, which results in faster fluvial erosion and consequent undercutting.

Figure 6-46 The moment of cantilever failure of outer bank, recorded at 9:28 on Jan. 20, 2007

The already mentioned morphological processes involved in the erosion of sandy riverbanks along the river bend can be categorized in four main processes, namely, bank-toe erosion, undercutting, cantilever failure and distribution of failed bank material. These are investigated in more detail in the following by means of the already defined representative bank profiles (sections in Fig. 6-43) presented here in cross sectional view in Fig. (6-47). As can be seen from this figure, all three bank profiles comprise vertical as well as negative slopes throughout almost the whole measurement period. This verifies a part of the theory presented in Ch. 3.4, regarding the mechanism of bank failure and considered geometry of the bank profile.

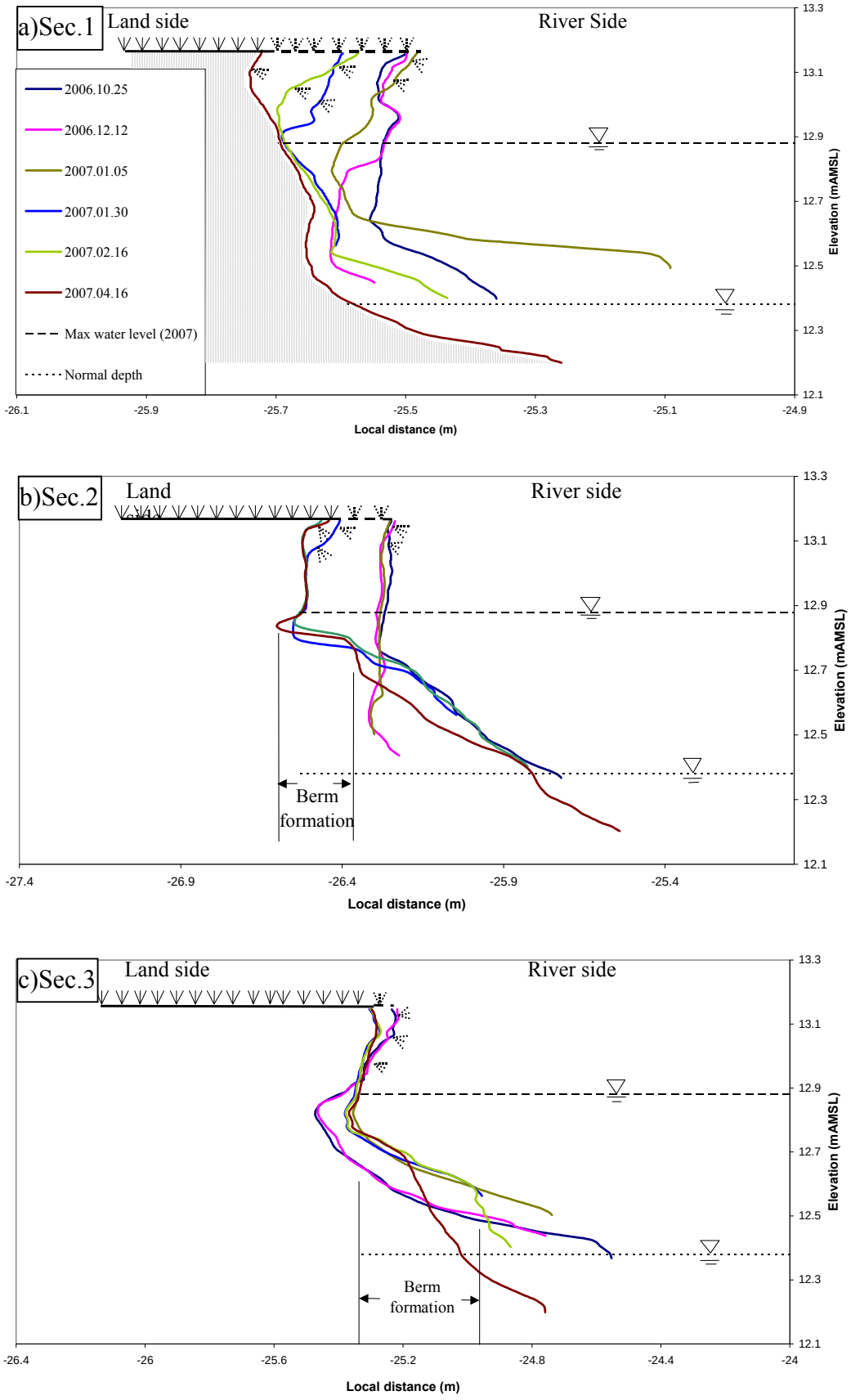

Figure 6-47 Outer bank evolution process along the river bend across three representative cross sections

Bank-toe erosion

As can be seen from Fig. (6-47), during the first period (Oct. and Dec. 2006), the bank-toe was largely eroded at section (1) and (2). This resulted in large and moderate amount of bank failure at section (1) and (2), respectively. Almost no bank-toe erosion and failure was measured at section (3) during this period. The same processes were repeated in the measurements carried out in January, February and April 2007, as shown in this figure. The pattern of bank-toe erosion along the outer riverbank at these sections explains two important mechanisms. First, it shows indirectly the effect of flow curvature in the intensification of bank-toe erosion towards the bend apex. Second, the increasing amount of bank-toe erosion along the river bend has resulted in increase of bank failure towards the bend apex. This confirms the role of bank-toe erosion in triggering bank failure through increasing bank height and bank-toe slope as recognized by earlier researchers (for example Carson and Kirkby, 1972;Thorne, 1982). This process of increasing bank height and bank-toe slope can be best observed at section (1) in the period between February and April 2007.

Fluvial bank-to erosion at section (1) during the third and fifth periods triggered shallow slip failure. In the case of formation of a berm at the bank-toe, as is the case in section (2) and (3), fluvial erosion is mainly limited to the berm-toe. This type of berm-toe erosion can be well recognized in the period between February and April 2007 by sharp slopes of berm in section (2) and parallel retreat of berm-toe at section (3).

Undercutting process

Undercutting can be observed among the three sections during the measurement period. This is manifested by steep to negative (reverse) bank slope, which has induced overhang at the upper portion of the bank. Steep bank slopes after failure suggest occurrence of slip failure, while negative bank slopes in the form of relatively small cavities imply occurrence of a sapping failure.

At section (1) (Fig. 6-47), it seems that bank-toe erosion primarily increased the bank height, bringing the stability of bank near critical, and then sapping failure induced the undercutting in the form of a cavity in the lower part of the bank profile, followed by a slip failure resulting in expansion of the cavity. This cavity induced formation of the overhang at this section, which has failed later in the next period.

Undercutting process occurred in the form of shallow slip failure at section (1), which can be observed as sequential parallel displacement of the bank surface in the lower part of the bank in undercutting zone in January, February and April 2007. The failure surface was extended up to the highest water stage on the third period (between Jan.5 and 30, 2007), above which the bank slope became reverse (negative) and leading to formation of overhang above the highest water stage. This form of undercutting suggests that the shallow slip failure plane is limited to the submerged zone of the bank. Note that the different bank slope resulted after shallow slip failure and sapping failure during the rest of the measurement period at this section.

The mentioned parallel bank surface displacement due to slip failure in submerged zone resembles those in loose non-cohesive (gravel) slopes due to the avalanche failure.

Nevertheless in avalanche failure, particles slip in the form of individual grains over a much milder slope, while in the mentioned slip failure it fails along a steep failure slope as a sudden continuous mass failure or at least as sequential progressive small slip failures starting from the bank-toe and propagating upwards towards water surface along the slip surface (the latter process was used in the numerical algorithm to simulate undercutting as already presented schematically in Fig. 4-9).

On the other hand, the steep failure surface (73° to 76°) observed at section (1) suggests a mechanism similar to planar failure in cohesive soils. However, there are two main differences between these two mechanisms. First, in sandy soils there is no cohesion, which causes the soil particles to stick together, especially in the saturated zone, apart from those due to compaction. Nevertheless, positive pore pressure in the submerged zone reduces the stabilizing effect of compaction. Second, the failure surface is not deep-seated as in cohesive soils.

Utilizing the above-mentioned analogy to avalanche failure and the mentioned similarity with planar bank failure, the shallow slip failure mechanism can be approximated by following hypothesis. When the bank-toe is eroded and its slope exceeds a critical value, the overlying soil slides in a shallow layer parallel to a steep failure surface due to loss of its basal support. The apparent cohesion in sandy soils almost diminishes due to the loss of matric suction in the submerged zone and due to the reduction of the effect of soil compaction because of establishing positive pore pressure in soil matrix. Loss of resistance forces from one side and increase of driving forces from the other side (due to soil saturation and loss of basal support) result in a slip failure of the river bank in a shallow layer confined to the submerged (saturated) zone. Such a failure occurs along a steep failure plain in the submerged zone. Nevertheless, in the unsaturated portion of the soil, riverbank failure may not occur due to the large apparent cohesion because of matric suction, as long as driving forces (moments) not exceeding the resistance forces (apparent cohesion and frictional resistance). The mentioned features of pore pressure limit the extent of shallow slip failure surface to the fully saturated portion of the river bank (under water stage) and allow formation of the overhang in unsaturated zone (above water stage) mainly due to the matric suction. The sequential occurrence of such shallow slip failures results in parallel bank surface retreat in submerged zone, since the most critical failure slope seems to remain almost constant (according to measurements, for example at section 1).

According to the above-mentioned argument, it can be further postulated that the thickness of failed layer in shallow slip failure process should be a function of pore pressure distribution inside the riverbank along the failure surface. In the case of long-lasting high water stage in the river, seepage into the riverbank saturates a deeper zone beneath the bank surface. Hence the failure surface can comprise a thicker layer than in case of sudden flash flood. Therefore, larger bank retreat can be expected in the case of occurrence of slip failure in long lasting flood events in sandy riverbanks.

The above-mentioned process of undercutting in non-cohesive soil justifies the developed theory in Ch. 3.4 regarding the type of failure which causes undercutting and the corresponding high slope of the shear failure plane, manifested there through dense angle of

repose (φ^c). The results of these measurements and developed theory explain why the current common practices of bank erosion modelling fail to model this process properly. These reasons are, first, unreasonable generalization of bank failure theory of loose particle soils (for example gravel) to non-cohesive compacted soils (sand) and second, application of the same failure plane for saturated and unsaturated zone of the soil, by neglecting the effect of (negative) pore pressure.

The undercutting process in section (2) resulted in different bank profile due to large amount of deposition of failed bank material at the bank and reducing bank height. This explains that in very shallow bank profiles undercutting may occur in the form of a sharp lateral cut of a stripe, which undercuts the bank in a narrow height and results in larger bank failure than in those banks with moderate height. This might be due to the different geometry of lower edge of the overhang in these two sections. At section (1), the lower edge of the overhang has a moderate to high negative slope, which supports the overhang just like a bracket support. However at section (2), the lower edge of the undercut is relatively horizontal, which introduces little support to the overhang. Generally, more frequent bank profile measurements is required during high flow events (for example by side-looking sonar systems) to explore more precisely the processes that occurred at section (2), which was not possible most of the time due to inherited limitations in measurement during high flow events.

Furthermore, to clarify the process of undercutting in respect to flow regime, the highest and normal water stages (refer to Fig. 6-7) are depicted in Fig. (6-47). The front of undercutting in all sections is located almost at the level of the maximum water stage. This justifies the theory and numerical approach developed in this work to simulate the dynamics of front of undercutting process and the fact that the shallow failure surface ends at the water level.

Cantilever failure

Cantilever failure was observed in the form of tensile and shear failures. The former was found to be in the form of failure of the lower edge of the overhang along a mild inclined (negative) failure slope, while the latter occurred in form of the failure of the overhang along a large positive or negative (reverse) slope. The cantilever failure is evident from the formation of overhangs and their subsequent failure. Nevertheless, the mechanism of cantilever failure seems to be different from that in cohesive soils, the latter resulting in vertical bank profiles. As can be observed from Fig. (6-47), the bank profile after failure generally has a negative slope except at section (2), which is vertical. The reason of this difference is primarily due to the physical properties of non-cohesive sandy sediment, for which effective cohesion is almost zero. The excess apparent cohesion, which caused the formation of such overhangs, is negative pore pressure, as already discussed in previous chapters. Hence the mechanism of cantilever failure in non-cohesive soils is in strong connection with dynamics of pore pressure in the riverbank. Vegetation roots can further improve overhang stability in non-cohesive soils.

The slope of cantilever failure surface at section (1) is almost constant and equal to about -69° to -76°, except that of Feb. 16, 2007, which has a slope of 52°. Surprisingly, the absolute slope of the lower part of the bank after shallow slip failure is almost equal to the absolute

value of upper bank slope after cantilever failure at this section. The slope of cantilever failure surface for section (3) is equal to -68° to -75°, which is almost in the same range as section (1). However the slope of cantilever failure surface at section (2) is almost 90°. This difference of failure slope might be due to the smaller bank height at section (2), nevertheless making it difficult to derive a simple rule for the computation of failure surface of cantilever failure. This indicates that more research is required to understand this process in non-cohesive sandy soils. Therefore, for simplicity, in the present developed theory this angle was assumed a large positive angle.

The lower edge of the overhang has a slope of –30 to –40 at section (1), while it is equal to -22° at section (2). This slope is most probably the result of tensile failure of the bottom of the overhang, while in the literature, this slope is assumed to be horizontal (Thorne and Tovey, 1981). Since the lower edge of the overhang is closest to the undercutting front, where it is in contact with water level, it can be concluded that the lower part of the overhang gets saturated thereby loosing its apparent cohesion (matric suction) as well as increasing the specific weight and consequently resulting in tensile failure of the lower part along the mentioned failure surface. Nevertheless, it is not simple to explain the reason of double fold range of this slope (-22° to -40°). Therefore, more research is required to explore the mechanism of tensile failure with respect to pore pressure and water stage in the river. However, for simplicity, in the presently developed theory, a horizontal failure surface was assumed for tensile failure due to submergence of the overhang.

Deposition of failed bank material

The failed bank material is deposited mainly on the bank-toe forming a berm at the beginning and middle part of the bend (cross sections 3 and 2, respectively), which decreases bank height and stabilizes the riverbank. Failed bank materials were mainly washed away at the bend apex (cross section 1), which caused increase of bank height and slope and destabilisation of the riverbank. The formation of a very mild bank-toe at this section (compared with already-described berm-toe slope during berm-toe erosion) can be correlated to the sediment supply from upstream, mainly originated from failed bank material at upstream. This is discussed in more details in Ch. 8.

The development of berm along the outer bank-toe has been already shown in Fig. (6-39b). In the second period, large amount of aggradation at bank-toe has occurred at section (1) and 3 as already quantified in table (6-14). Unfortunately, no hydrological data are available for this period to explore the reason of this large amount of aggradation. However, it is evident that the amount of bed aggradation is much higher than that of cantilever bank failure, confirming the process of upstream excess sediment supply, in similarity to the laboratory experiment of Wilke (2008).

It is shown in Fig. (6-47) that the bank-toe deposition and erosion is almost periodic. Bank-toe erosion generally occurred in the first, third and fifth periods, while in the second and fourth periods, bank-toe deposition took place. For the period of measured hydrological data (Jan. 5, to April 16, 2007) this process could be correlated to the flow regime. For example the second period (deposition) was followed by a large bank-toe erosion period due to the

high flow event of the third period. This is especially seen at sections 1 and 3. During the fourth period, flow drop stage, no significant bank evolution was observed, while in the fifth period, in which two successive high flow events occurred, large bank-toe erosion was observed.

It is also worthwhile to note that the berm-toe retreats in time due to berm-toe erosion, especially seen at section (3), and the slope of the berm (bank-toe) in erosion cycle is generally larger than in deposition cycles. Using this feature of deposition, which is correlated to the upstream excess sediment supply and bed load transport, it is possible to determine if the current bank-toe geometry is the result of erosion or deposition, when the frequency of surveying is high enough.

6.7.2 Second measurement phase

One of the major aims of this measurement phase was the integration of bed with bank processes to study the whole morphological process (bank-toe erosion, undercutting and cantilever failure) along the river outer bend. In the following, the bank evolution process during the second phase is presented first. The interaction of bed and bank processes will be presented in Ch. 6.7.2.2.

6.7.2.1 Bank evolution process

The structures of bank surface were similar to those in the first phase (see Appendix G). In the following, the result of difference surfaces, generated as in the first phase, are presented. Between Oct.24, 2007 and Jan. 23, 2008 (first period), bank erosion can be observed in most part of the bank along the river outer bend (Fig. 6-48). This is in the form of undercutting at the bend entrance (left in this figure), cantilever failure in the middle reach, and a combination of both around the bend apex. As can be seen from this figure, in the middle reach, where cantilever failure prevails, large amount of deposition occurred at the bank-toe. It can be concluded that primarily bank-toe erosion and consequent undercutting prevailed in this reach, as is the case in the apex reach. However, cantilever failure and associated deposition at bank-toe resulted in piling up at the bank-toe. Due to the pattern of bed shear stress in the middle reach (Fig. 6-24), in which maximum bed shear stress is near the centre of channel with low shear stress at the outer bank, the deposited materials remained intact at the bank-toe. At the bend apex, the eroded bank material was transported away from the bank-toe due to the proximity of maximum bed shear stress to the outer bank-toe (Fig. 6-22),

The magnitude of mean erosion and deposition depth, together with net volume change are presented in table (6-15). The large net erosion volume of -0.846m^3 should not be compared with data in table (6-14), since this large net volume change corresponds to three months.

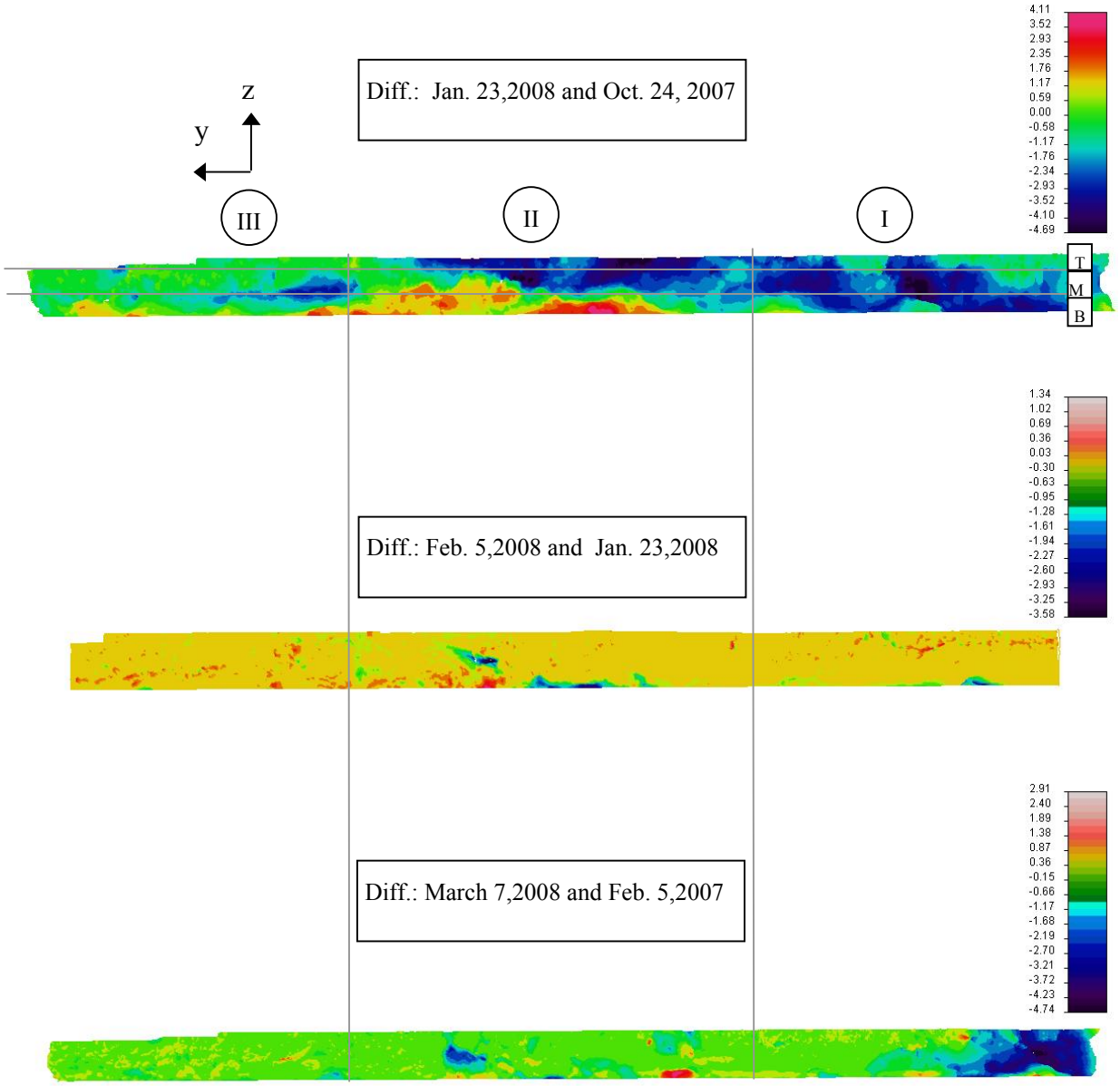

Figure 6-48 Spatial distribution of erosion and deposition along the riverbank. The erosion (-) and deposition (+) depths are in dm in x-direction (normal to the paper).

In the next period (Jan.23 to Feb.5, 2008), no significant erosion is observed, except slight bank-toe erosion in the middle reach. The same holds for the last period, except at the bend apex, in which undercutting and bank failure occurred. This negligible morphological evolution during the mentioned two periods is quantified in table (6-15). Whereas the net volume change in the last period is three times larger than the previous period. As observed from Fig. (6-8), a flood event occurred in March, 2008 to which the bank erosion at the apex in the last period can be correlated. By comparing the hydrograph of March 2007 with that of 2008 (Fig. 6-7), it can be concluded that although the duration of flood peak in the latter period has been longer than that of the former period, due to the lower water stage in the latter

period, less bank-toe erosion occurred in this period. This suggests that the elevation of water stage during a flood event plays a more important role in bank-toe erosion than the longer duration of flood event with a lower water stage. It should be recalled that bed erosion is a consequence of sediment transport imbalance. Therefore, existence of high bed shear stress alone over longer period does not necessarily result in bed erosion as long as the same amount of eroded material is supplied from upstream (equilibrium sediment transport). Furthermore, it is the imbalance of sediment transport due to non-uniformity of flow and along the river bend, which resulted in more bank-toe erosion near the bend apex.

Table 6-15 Mean erosion (-) and deposition (+) depth (volume /surface) along the outer riverbank

row	Reference surface	Overlaying layer	Erosion depth(m)	deposition depth (m)	Net volume change(m^3)
1	2007.10.24	2008.01.23	-0.16750777	0.10022315	-0.84627
2	2008.01.23	2008.02.05	-0.01588344	0.00575898	-0.038931
3	2008.02.05	2008.03.07	-0.02740706	0.01146551	-0.099169

For further investigation of bank processes in the second measurement phase, the same three reference sections as in the first measurement phase were used. They were integrated here with bank-to profile data extracted from the DTM model of the bed as depicted in Fig. (6-49). It can be observed from this figure that at section (1) between the last measurement campaign of the first phase (April 2007) and the first measurement campaign of the second phase (Oct. 2007), a large amount of bank retreat occurred, as addressed in Ch. 6.7.1. This erosion was accompanied by bank-toe erosion. However, due to the large temporal span between these two measurement campaigns, bank-toe aggradation due to deposition of mass failure and subsequent bank-toe erosion may have occurred in between, without being recorded. The general slope of the bank was steep in this period but not negative as in the first measurement phase.

Between Oct. 2007 and Jan. 2008 a relative large amount of bank erosion occurred, causing the initially positive bank slope to change to negative, while between Jan. and Feb. 2008 no changes in the upper bank profile was observed. Nevertheless, bank-toe erosion, which has resulted in undercutting at the lower portion of the bank profile can be clearly observed during the latter period. The so-generated overhang with negative surface slope failed through cantilever failure mechanism during the next period (Feb. 5, to March 7, 2008) leaving a still steeper (negative) bank surface slope after failure and deposited basically at the bank-toe. However, no further bank retreat of the upper edge of the bank was measured after Dec. 2007. Such a mentioned (cantilever) failure should have been the result of further bank-toe erosion and undercutting during this period. To prove this claim, it is enough to investigate flow stage during this period. As seen from the flow hydrograph (Fig. 6-8), water stage at the downstream section, being only a few meters away from this profile, did not exceed 12.55 (mAMSL). Such a water stage could submerge only a part of the undercutting zone (approximately up to the point of intersection of the lower bank profiles in the last two measurement campaigns) and mainly may have caused the loss of matric suction and probably

tensile failure only around a small portion of the lower edge of the overhang due to the capillary effect. From the mentioned discussion, sapping failure could not be the reason of bank failure. Such a complex mechanism of cantilever failure along a negative slope suggests the requirement for more systematic research on the mechanism and analysis of this type of failure, especially in non-cohesive (sandy) soils.

The general trend of bank-toe degradation at section (1) in this measurement phase ended by deposition of failed bank material and excess sediment transport over the bank-toe from upstream during the last period. The latter process can be justified by the deficit of the volume of eroded bank compared with the volume of bank-toe aggradation at this section as shown in (Fig. 6-49).

In contrast to section (1), no bank retreat occurred at section (2) during the first period (April to Oct. 2007) of the second measurement phase. However, large amount of berm-toe erosion resulted in diminishing of the berm as well as bank-toe erosion and subsequently advancement of undercutting front. Probably the advancement of the undercutting front caused tensile failure in the form of erosion of the lower edge of the overhang at this section.

On the other hand, relatively large amount of bank retreat was measured during the second measurement period (Oct. 2007 to Jan. 2008). It can be observed that during this period bank-toe erosion has proceeded, which resulted in advancement of undercutting and eventually cantilever failure of the overhang. Due to the relatively steep slope of the bank-toe, it can be expected that the failed bank materials have rolled down over the bank-toe and deposited further below the depicted region of bank-toe in this figure.

In the rest of the measurement period, little bank erosion and retreat has occurred at this section. In contrast to section (1), bank slope has remained almost vertical during the whole second phase of the measurement.

The largest bank retreat at section (3) occurred during the first measurement period, as seen in Fig. (6-49). At this section, berm was completely eroded during this period and the bank height increased through bank-toe erosion, as was the case at section (2). In spite of (relatively) large bank height and slope as well as incised bank-toe, the bank profile still remained stable at the end of the first period. In fact, at section (1) the bank slope and height are even larger than at this section in Feb. 2008 and remained still stable. Although no bank retreat was measured during the second period (Oct. 2007 to Jan. 2008), a large amount of bank erosion occurred causing the steep (near vertical) bank slope to turn negative through undercutting and cantilever failure. This negative bank slope remained for the rest of the measurement periods. It is noticeable that the zone of negative bank slope is in the upper part of the channel much farther above the largest recorded water sage (12.55 mAMSL) during the last period. This implies that undercutting could have not been the process causing the negative steep bank surface seen in Fig. (6-49) at section (3), but cantilever failure. In the rest of the measurement period, the bank profile at section (3) did not evolve further apart from a small cantilever failure of the lower edge of the overhang in the last period.

The slope of the outer bank-toe is almost identical across all sections and is equal to about 20° during outer bank-toe erosion cycles, while in deposition cycles this slope is milder. Finally, it

can be observed how the deepening process of talweg changed to widening process in this period.

Due to the relatively low frequency of scanning of bank surface, the process of parallel retreat of bank surface due to the undercutting failure could not be observed during the second measurement phase unlike the first measurement phase. Indeed, the scope of this measurement phase has been rather investigation of the interaction between bed and bank processes than the mechanism of bank erosion, although cantilever failure could be observed well during this phase. In the following, the interaction between bed and bank process is investigated.

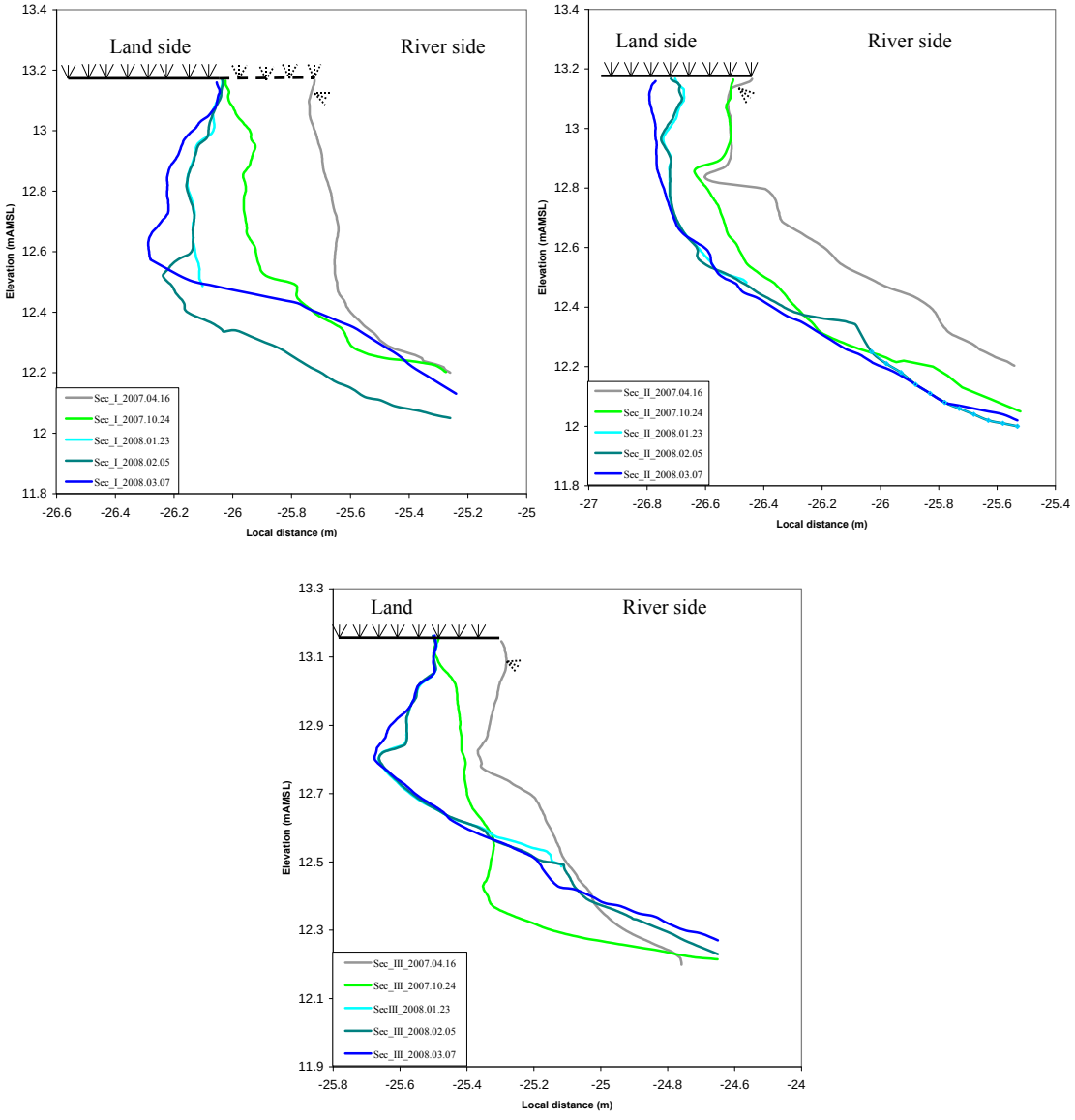

Figure 6-49 Evolution of the bank profiles in the second measurement phase integrated with bank-toe profile

6.7.2.2 Interaction of bed and bank evolution processes

The last two measurement campaigns in 2008 as well as that on Oct. 24, 2007 were accompanied by bathymetry measurement to enable coupling of bed with bank processes. The three already mentioned reference cross sections were used to analyse the integrated bed and bank profile. The result of such integration is shown in Fig. (6-50). As seen from this figure, river bank retreat between Oct. 24, 2007 and Feb. 5, 2008 is associated with bank-toe erosion and undercutting at section (1) (bend apex). Furthermore, the volume of eroded bank material was not deposited at the bank-toe, or if so, it was completely eroded and transported mainly downstream due to high bed shear stress (refer to Fig. 6-22) and partly toward the inner bank by secondary currents (refer to Fig. 6-13) at the time of measurement. This proves the hypothesis of excess upstream sediment supply to the outer bank-toe along the river bend. Note that aggradation of the inner bank is associated with increase of the lateral bed slope.

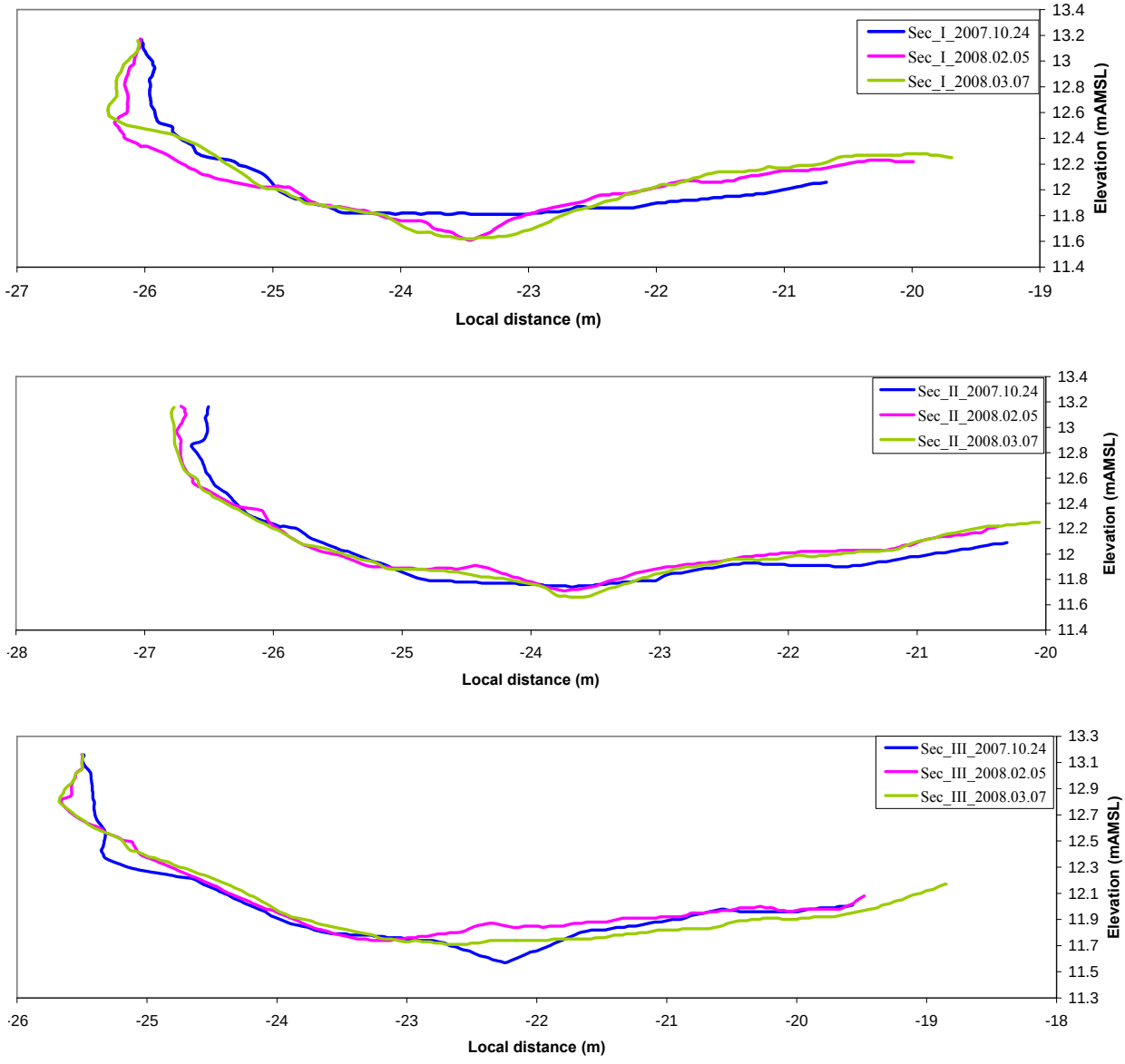

Figure 6-50 Morphological evolution across the channel section including river bank

On the other hand, deposition on the outer bank-toe at this section on March 7, 2008 contributed to widening of the talweg. It can be clearly observed that this deposition is to a lesser extent due to direct deposition of failed bank material and more due to imbalance of sediment over the outer bank-toe. Furthermore, negligible amount of deposition can be observed over the inner bank at of bend apex section in the last period. Considering the flow hydrograph (Fig. 6-8), the flood event that occurred during this period has reached to a water stage of less than 12.50. This elevation corresponds to the location of the bank, where the undercutting front is observed. Therefore, it can be recognized that the water depth over the bank-toe was very shallow, providing the required condition for deposition of suspended sediment at outer bank-toe. Furthermore, concentration of flow at the centre of the channel due to the position of talweg caused widening of the talweg.

At section (2) the same processes as mentioned above are observed in the first period, however with less intensity of outer bank and bank-toe erosion as well as talweg deepening in the first period. The eroded bank material seems to have slipped towards the bank-toe and deposited there. This deposition together with aggradation at the inner bed seems to have caused deepening of the talweg, by directing the flow to this zone. Similar to section (1), aggradation of the inner bank resulted in increase of lateral bed slope of the inner bank at this section. In the next period, the talweg was shifted slightly to the outer bank.

At section (3), the eroded bank material seems to have deposited directly at the bank-toe (berm), smoothly increasing the bed elevation and bank-toe slope. The talweg vanished by deposition and no deposition occurred on the inner bank-toe during the first period. During the second period, erosion over the inner bank occurred while no evolution at the outer bend and bank was observed.

7 Validation

The numerical solution of the governing equations of flow and sediment transport (Eq. 3-1 to 3-3 and 3–20) can be accomplished either in coupled or decoupled form. In the former method, all of the four mentioned equations are solved simultaneously, requiring several number of iterations, particularly when bed evolution is active, since alteration in flow field may give rise to change of bed elevation, which impacts the flow field in a self-repeating cycle. Therefore, a decoupled modelling approach is used here. This approach is especially time saving due to inclusion of bed and bank evolution. Moreover, due to the relatively large temporal scale of bed changes in comparison to flow field alteration, it can be reasonably assumed that the bed level does not alter within each time step appreciably, allowing decoupling sediment transport and bed evolution equations from hydrodynamic equation (provided that the time steps are not large and appreciable bed evolution is not involved). Furthermore, it is assumed that sediment density is low so that it does not impact the flow field (and water density). In decoupled method, after convergence of the solution of hydrodynamic equation, the sediment transport equation is solved. After this, the bed evolution and bank evolution equation are solved sequentially.

At the beginning, the hydrodynamic model was verified using the flow and water stage data of four flow events in 2007, after which the sediment transport model and bed load transport formula were qualitatively investigated for one high flow event. A quantitative validation of the sediment transport model was not possible due to the lack of measurement of sediment concentration along the river because of the reasons mentioned in Ch. 5.7. Furthermore, bed evolution model could not be verified quantitatively, since no reliable bathymetry measurement was possible during the applied validation period due to the reasons already explained in Ch. 5.8. Finally, the complete morphodynamic model, including bank erosion model, was verified for the high flow event of January 2007. The data of the second measurement phase in 2008 were not used, since no appreciable bank erosion was measured in this period (February to March, 2008).

7.1 Hydrodynamic model

It is often sufficient to verify a hydrodynamic model based on the measured water stages at gauging stations in simple engineering applications. However, in complicated problems such as modelling of flow in groin fields or problems concerning sediment transport, flow velocity distribution across and along the study reach should be verified based on the velocity measurements.

Three flow events were used to verify the hydrodynamic model of RMA-Kalypso including one low flow (August 14, 2007) and two high flow events (Feb. 27 and Dec.6, 2007). Two sets of flow velocity data corresponding to a high flow and a low flow event were collected for validation, as will be shown later in Ch. 7.1.4).

7.1.1 Elevation model

Among parameters influencing the result of flow simulation, perhaps bed elevation data play the most important role. To obtain elevation data of the river a few surveys were conducted using total station in 2007 and five surveys using echo-sounder after July 20, 2007. Since high resolution data of the bed and bank geometry along the river bend were required, the bathymetry data of Dec.10, 2007 were integrated with bank data of Jan. 5, 2007 (obtained by laser scanner) to generate the base elevation model for target simulation period of flood event of January 2007. The rest of the bed profile, which was not measured using echo-sounder, as well as bank geometry of the rest of the river were completed using survey data of Dec. 10, 2007 and Jan. 10, 2008 using total station.

Such an integration of elevation models spanning less than one year was inevitable due to the lack of detailed bathymetry data of the river bend during the target period of Jan. 2007. This can produce uncertainty in the validation of the bed evolution model along the river as well as validation of velocity field. Nevertheless, such a practice is common in engineering projects, in which a few different flood events spanning several years are simulated using a data elevation model, sometimes belonging to a completely different period. The above-mentioned elevation data were applied to generate the TIN (Triangulated Irregular Network) model already presented in Fig. (5-8).

7.1.2 Bed roughness

The next important parameter in hydrodynamic modelling is the bed roughness. The roughness of bed surface or vegetation influences the flow in form of bed shear stress as is shown in Eq. (3–19). The parameter required for Colebrook-White equation (Eq. 3–18) is the equivalent sand roughness (k_s). This parameter can be either estimated using flow measurement (for example Lippert, 2005) or adopted from tables such as those presented in BWK (1999/1). The latter method was used here to define the k_s parameter as well as vegetation parameters required in Eq. (3–19). These parameters are given in table (7-1) after

some modifications during the calibration of the model. The parameters in the two last columns have already been defined in Eq. (3–19). The spatial distribution of roughness zones given in this Table is presented in Fig. (7-1).

Table 7-1 Roughness parameter of model domain

Roughness class	Definition	k_s (m)	$a_x=a_y$ (m)	d_p (m)
1	Sand/gravel	4E-3	----	----
2	Fine sand	1.5E-4	----	----
3	Sand	4.0E-4	----	----
5	Concrete (bridge)	3.5E-3	----	----
6	Grass	0.2	----	----
7	Trees	0.5	5	0.2
9	Floodplain with vegetation	0.35	5	0.2
13	Rock embankment	0.15	----	----

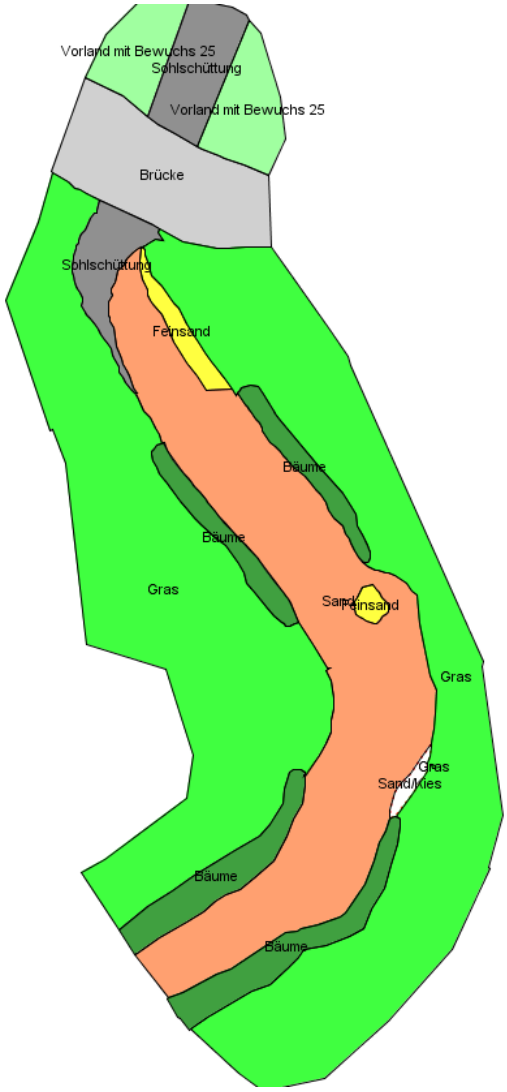

Figure 7-1 Spatial distribution of roughness zone given in Table (7-1)

7.1.3 The finite element grid

On the basis of bed roughness zones and special characteristics of elevation model (break lines, steep slopes, etc.) a non-structured finite element grid was generated with a total number of 3818 elements and 10735 nodes along the70 m reach of the river (Fig. 7-2). It was tried to keep the quadratic and triangular elements semi-structured along the river bend under study and aligned so that each radial row of elements having their upstream and downstream sides lined up. This was done to enable definition of profile domain as described in Ch. 4.

To improve the spatial resolution of discretization along the outer bank, elements as small as 0.11 x 0.30 m were generated in this region. In the rest of the domain, elements as large as (maximum) 0.6 x 2.3 m were used. The discharge was defined as upper boundary condition and water stage as downstream boundary condition.

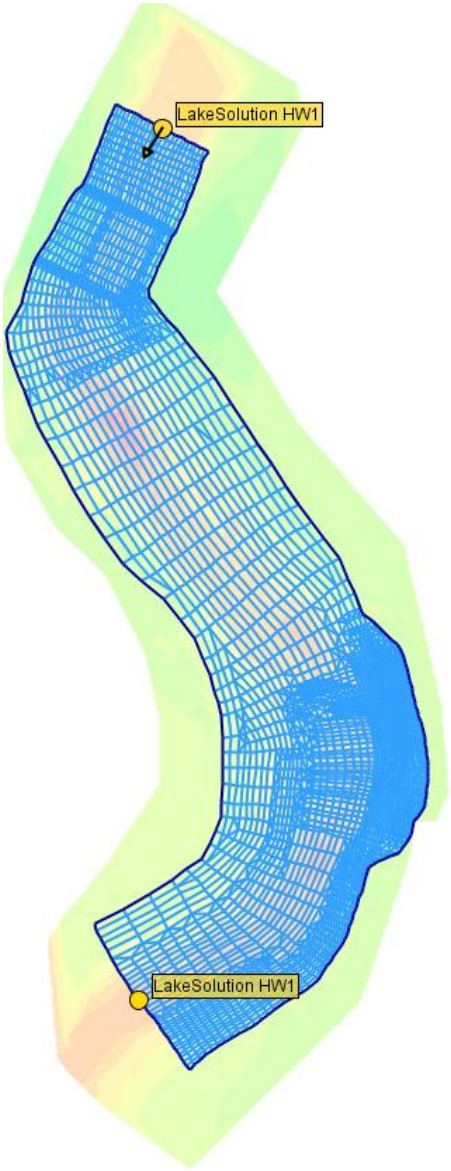

Figure 7-2 Finite element grid generated along the river reach under study (superimposed over TIN model)

7.1.4 Flow events

After calibration of the roughness parameters based on the flow measurement on Feb. 14, 2007 with a moderate discharge of Q=0.878 m^3/s, the validation of the hydrodynamic model was achieved on the basis of three further flow measurements. The mentioned flow events are summarized in Table (7-2). During the validation process, the proper turbulence model and corresponding parameters were determined.

Table 7-2 Flow events applied for calibration and validation of hydrodynamic model

Datum	Discharge (m^3/s)	Downstream water stage (mAMSL)	Upstream water stage (mAMSL)	purpose	Abbreviation used in RMA-Kalypso
2007.02.14	0.878	12.356	12.423	Calibration	Nw
2007.03.20	1.310	12.48	12.53	Validation	Hw1
2007.08.14	0.464	12.27	12.32	Validation	Nnw1
2007.12.06	1.057	12.39	12.46	Validation	Hw2

Three turbulence models were selected for validation, namely, Smagorinsky, Prandtl and combined form of Smagorinsky and bed induced turbulence model. The constant eddy viscosity model as well as combined bottom generated with Prandtl mixing length was ruled out during the calibration phase due to their poor results.

Constant eddy viscosity turbulence model produced the most unsatisfactory result of velocity distribution across the channel among others in the calibration phase. Only first at a value of ν_t =0.1 m^2/s the parabolic transverse distribution of flow velocity could be partly produced (Fig. 7-3), otherwise the velocity were computed uniform across the channel (in Lippert, 2005 a ν_t =0.15 m^2/s was applied for simulation of flow in Lippe). A high eddy viscosity resembles a high viscous flow, which results in a uniform flow velocity distribution. On the other hand, very low eddy viscosity results in overestimation of maximum velocity at the channel centre (Lippert, 2005). The constant eddy viscosity model can not properly reproduce the transverse velocity profiles of narrow channels due to the influence of the riverbanks. Therefore, it is not surprising that this method was used successfully in water level computation of wide rivers (for example Lippert, 2005; Plöger, 2007).

Bottom-generated turbulence model with a coefficient of e^* . σ_t =0.135 and 1.35 were examined in the calibration phase (Lippert, 2005 applied a value of e^* . σ_t =0.25). It was found that 10-fold range of the parameter had no appreciable influence on computed upstream water stage. Simulation results using this model showed the highest overestimation of upstream water level in the current application. That can be attributed to the dominating role of horizontal turbulence in narrow channels (width to depth ratio ≈ 11), especially when the bed roughness is not in hydraulically rough zone. As discussed in Ch. 6.4.3, the hydraulic regime of the flow was in transient rough region, which verifies this postulation. Such a performance of this model in narrow channel could be expected due to the principal assumption imbedded in this turbulence model, namely, wide channels.

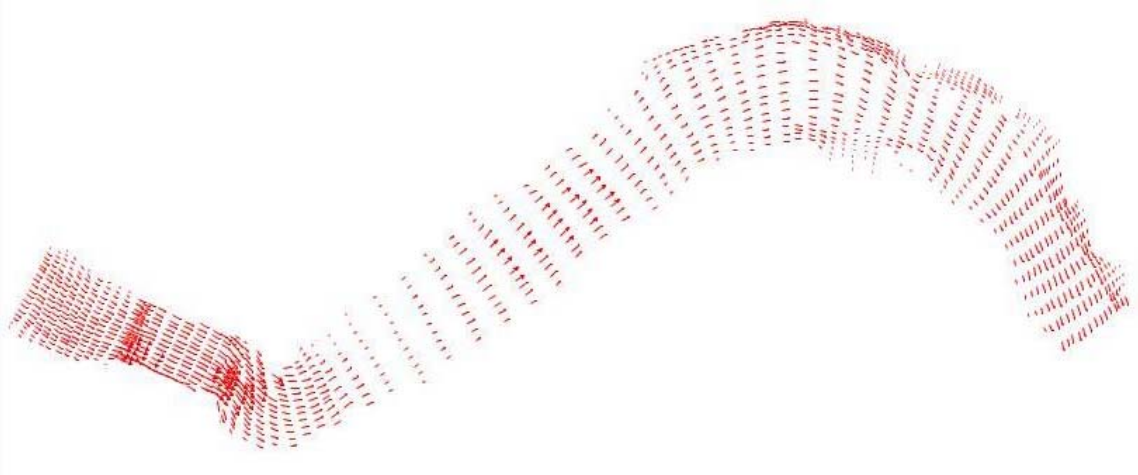

Figure 7-3 Velocity vector along the river reach computed using constant eddy viscosity model for Nnw1 (with $\nu_t = 0.1\ m^2/s$)

During the calibration phase, the shear layer thickness (l) in Prandtl method and c_s factor in Smagorinsky model were determined as 0.2 m and 0.2, respectively. Mason and Callen (1986) suggested the same value for the latter parameter, while Smagorinsky used a value of 0.197. The proportionality factor of 0.09 was used in Prandtl model as suggested by Lippert (2005). Only the Smagorinsky method was tested for the low flow event (Nnw1) in validation phase. Generally high flow events were of interest here due to the later validation of morphological model for a high flow event. The result of simulation of the three mentioned events using the selected turbulence models are summarized in Table (7-3). As seen in this table, the Prandtl method has largely overestimated the upstream water level although it was already calibrated for a moderated flow. Such a problem in simulation of high flow events using already calibrated simple turbulent models have been addressed by Pasche et al.(2006). The next worst result has been obtained by a combination of Smagorinsky model and bottom-generated turbulence model. This confirms Pasche et al. (2005 and 2006) who have shown that this model overestimates flow depth in compact channels. As already discussed above, the bottom generated turbulence model is suitable for wide channels and overestimates the water elevation in narrow channels. As seen from this table, with increase of the flow discharge (Hw1) the computational error of water depth increases. The best result of water level computation was obtained by Smagorinsky model, as seen in Table (7-3). For further investigation, the computed velocity vector by this model was compared with that of the Prandtl model. The pattern of the velocity vectors in the swirling zones (dead zones) was well reproduced qualitatively only with the Smagorinsky model as shown in Fig. (7-4). Such a swirling pattern was observed in the field investigations.

Table 7-3 upstream water level elevation simulated in validation phase for three flow events

Events	Turbulence models			Measured Upstream water stage (mAMSL)
	Smagorinsky	Smagorinsky + bottom generated turbulence	Prandtl	
Nnw1	12.314	-----	-----	12.32
Hw1	12.534	12.57	12.81	12.53
Hw2	12.450	12.48	12.72	12.46

As seen from this figure, the swirling zone occurs on the inner bank of the first bend beside the pool shown in yellow to red colours (just downstream of the bridge, not identified in this figure). Further investigation of the velocity vectors at the outer bank of the second bend (the reach under study), where very small elements were used, revealed no clear dependency of velocity magnitude with element size, as it is commonly believed in the case of Smagorinsky turbulence model.

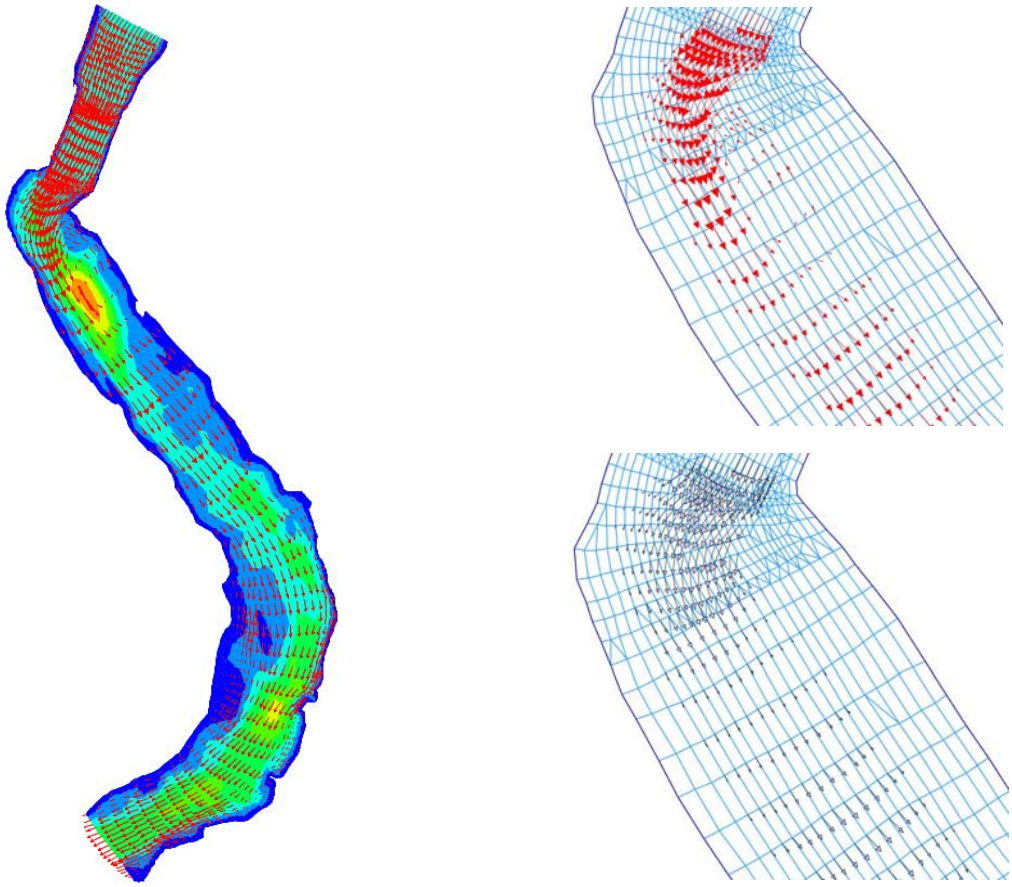

Figure 7-4 Results of computation of event HW1. Left: flow velocity distribution computed using Smagorinsky superimposed over water depth isosurface Right: Reproduction of swirling zone by Smagorinsky(above) and failing to reproduce it by Prandtl (below) turbulence models

The accuracy of the computed velocity by Smagorinsky model was investigated by comparing with the measured depth-averaged velocities already presented in tables (6-6) and (6-7). The

result of this comparison is shown in tables (7-4) and (7-5). It can be generally observed that this turbulence model underestimated the flow velocity about –25% in average. Close to the outer bank in the river bend (measurement points Nrm_01 to 3 in Table 7-5), the underestimation reached more than 100%. However, the simulated velocities near the outer bank of the river is not very reliable due to the uncertainty related to the DTM model near the bank-toe zone, as mentioned in Ch. 7.1.1. The general discrepancy between simulated and measured depth-averaged velocities can be partly associated to the just mentioned deficiency in generated bathymetry. Therefore, the Smagorinsky turbulence model was used for hydrodynamic modelling required for later morphological simulation.

Table 7-4 Measured versus computed depth-averaged velocity using Smagorinsky model (Nnw1)

Vertical profiles	Depth-averaged velocity [m/s]		Error [%]
	Measured	Simulated	
v-0-1	0.334	0.312	-6.66
v-0-2	0.470	0.337	-28.23
v-0-3	0.374	0.311	-16.87
v-1-1	0.199	0.12	-39.81
v-1-2	0.211	0.15	-28.91
v-1-3	0.410	0.16	-61.00
v-2-1	0.330	0.29	-12.06
v-2-2	0.367	0.31	-15.56
v-2-3	0.396	0.28	-29.36
v-3-1	0.280	0.26	-7.05
v-3-2	0.408	0.26	-36.34
v-3-3	0.413	0.26	-37.07
v-4-1	0.280	0.22	-21.35
v-4-2	0.400	0.293	-26.73
v-4-3	0.383	0.26	-32.16
v-5-1	0.381	0.25	-34.38
v-5-2	0.397	0.27	-32.06
v-6-1	0.472	0.282	-40.24
v-6-2	0.416	0.27	-35.02
Average			-28.47

Table 7-5 - Measured versus computed depth-averaged velocity using Smagorinsky model (Hw2)

Vertical profiles	Depth-averaged velocity [m/s]		Error [%]
	Measured	Simulated	
V1-1	0.453	0.29	-35.98
V2-1	0.216	0.15	-30.42
V2-2	0.490	0.53	8.12
V3-1	0.418	0.29	-30.66
V3-2	0.408	0.43	5.34
Nrm-01	0.137	0.09	-34.21
Nrm-02	0.158	0.13	-17.56
Nrm-03	0.194	0.39	101.00
	Average		23.18*

* Absolute averaged error ignoring the last data

7.2 Sediment transport model

The sediment transport model was not verified separately; because the measured sediment concentration in the river was close to the minimum measurable range of the ASM instrument (refer to the Appendix F-4). This impacts adversely the reliability of the measured data so that availability of such data would have been not so helpful and suitable for validation purposes.

Nevertheless, the simulation result of sediment transport in the river bend was qualitatively analysed compared to the field observations and a sensitivity analysis on the parameters involved in the sediment transport equation was carried out to help understand their effect in the present sediment transport model. The parameters investigated in sensitivity analysis included, boundary conditions, choice of equilibrium sediment transport formula and diffusion coefficient. The deposition as well as erosion damping coefficient were analysed later in the simulation of bank erosion and distribution of failed bank material.

7.2.1 Boundary conditions

The aim of this analysis was to examine the sediment transport process along the river bend with different constant sediment concentration as Dirichlet boundary conditions. Negative value of upstream concentration was used as downstream boundary condition, implying physically net zero sediment flux in the river reach. The erosion and deposition damping coefficients were initially set as high as 500 to avoid high rate of deposition, which could result in stability problem due to probable negative sediment concentration. The sediment transport formula of Ackers and White (1973) was used for this stage. Boundary conditions of 25,100,200 and 1000 mg/l were used with different initial conditions (10, 25, 120 mg/l) to investigate the downstream and lateral transport of sediment. These tests were achieved for event Hw1 with Smagorinsky turbulent model. The diffusion coefficients in x and y directions were equal to the eddy viscosity computed by the Smagorinsky method. A typical result of

such a simulation is shown in Fig. (7-5) for constant concentration of 200mg/l as upstream boundary condition. As seen in this figure, total sediment concentration is maximum along the outer bank of the first meander and inner bank of the second one. This qualitatively agrees with the inner bend aggradation observed in the bathymetry measurements of the second bend as will be discussed in Chs. 8.2 and 8.3, as well as with the observation of transport of bed material from upstream outer bank to the downstream inner bank of the next meander bend in experimental investigation at the hydraulic laboratory of Queen's University (refer to Ch. 6.4.3.1). Due to the simulation of total sediment transport, it was not possible to distinguish between processes causing transport of bed load along the inner river bend (bed shear stress) with those causing transport of suspended sediment transport along the outer bend (depth-averaged velocity). However, bed load transport could be considered as the main transport process due to the low measured suspended sediment. Simulation with other mentioned concentrations showed also the same trend of sediment transport along the river bend.

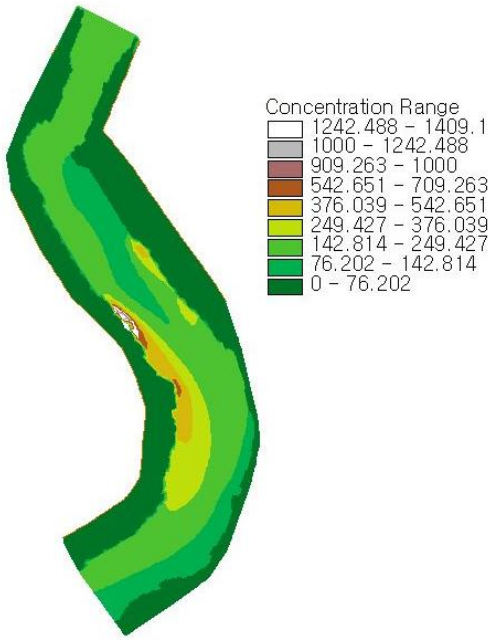

Figure 7-5 Total concentration (mg/l) distribution along the river by constant discharge of 200 mg/l to the river after half an hour with initial concentration of 120 mg/l using Ackers-White formula, for event Hw2,damping coefficient of 500

7.2.2 Choice of sediment transport formula

By the choice of sediment transport model, a comparison between van Rijn, Ackers-White as well as Brownlie methods was achieved with 200 and 1000 mg/l concentration boundary condition. The first two methods showed the same trend of sediment transport along the first and second bend as already explained above, while with the third method, the sediment was transported mainly along the outer bend (refer to Appendix H-1). Quantitatively, the first two methods computed the same order of sediment concentration and even lateral and longitudinal

distribution at the first bend, however the sediment concentration on the second bend, especially at the inner bend, calculated by van Rijn method was generally between 3 to 10 times larger than that computed by Ackers-White. By comparing a few methods of sediment transport over 266 data sets of rivers in USA, van Rijn (1993) concluded that arriving at accuracy better than 200% error in total load computation is almost impossible. However, here, due to the lack of measurements during the periods of events, it is difficult to judge the performance of each method. Due to the wide application of van Rijn method and its better performance compared with Ackers and White method (van Rijn, 1993), the method of van Rijn was used for the rest of the simulation. The method of Brownlie was not used, since total sediment transport could not be reproduced qualitatively as it has been observed in the field.

7.3 Morphodynamic model

After validation of the hydrodynamic model using three events, the present novel morphodynamic model was verified by simulation of the outer bank evolution in Hardebek-Brokenlander Au during the flood event of January 2007. The flow data presented in Ch. 6.3 for the period between Jan. 5 and 30, 2007, the elevation model illustrated in Ch. 7.1.1 and the measured bank profile for this period presented in Ch. 6.7 were used as validation data. At the beginning 34 profiles across the river bend were considered for reassuring the performance of the developed morphodynamic algorithm, after which only three profiles, already presented in Ch. 6.7, were considered for the rest of the simulation to reduce the amount of data produced and analysed. The initial state of these three profiles is depicted in Fig. (7-6) by plotting the measured profiles on Jan. 05, 2007 with the corresponding discretized profile in FE- and conjugate (profile) domain. It should be noted that no accurate bed profile measurements were available for these profiles; hence they are not shown in this figure. This is a source of uncertainty in the validation of the bed evolution model at all three mentioned sections, especially at the middle section (Fig. 7-6B).

As seen from this figure, the FE-nodes do not necessarily coincide with profile nodes especially in overhang zone and even in sharp slope of the bank surface. It should be noted that in Fig. (7-6A), the slope of the overhang's face at the bend apex could not be precisely discretized in the profile domain due to its negative slope. As already mentioned, currently only positive bank slopes can be simulated by the new developed numerical model. However, the rest of the profile especially the bank-toe was discretized precisely with small elements to improve the accuracy.

The same discretization problem of overhang as the above-mentioned section holds for the section upstream of the apex (middle section) as shown in Fig. (7-6B). However, in the latter case, this problem comprises also the top edge of the overhang, so that the profile node building the top edge of the overhang is 5 cm away from the actual one. This will be later indicted in analyses of simulation results. The sharp, almost vertical, face of the bank under the overhang could not be accurately discretized in Fe-domain due to limitation of FE-elements, however it has been precisely discretized in profile domain. Bar formation can be

recognized in the middle of this figure. This can be an indication of flow concentration near the bank-toe in low flow situation, which results in bank-toe erosion in these situations (Luppi et al., 2009). The bend entrance section could be well discretized in profile domain (Fig. 7-6C). It should be noted that farther from the bank-toe, the rest of the sections, which could not be measured by laser scanner, have been extracted from TIN model.

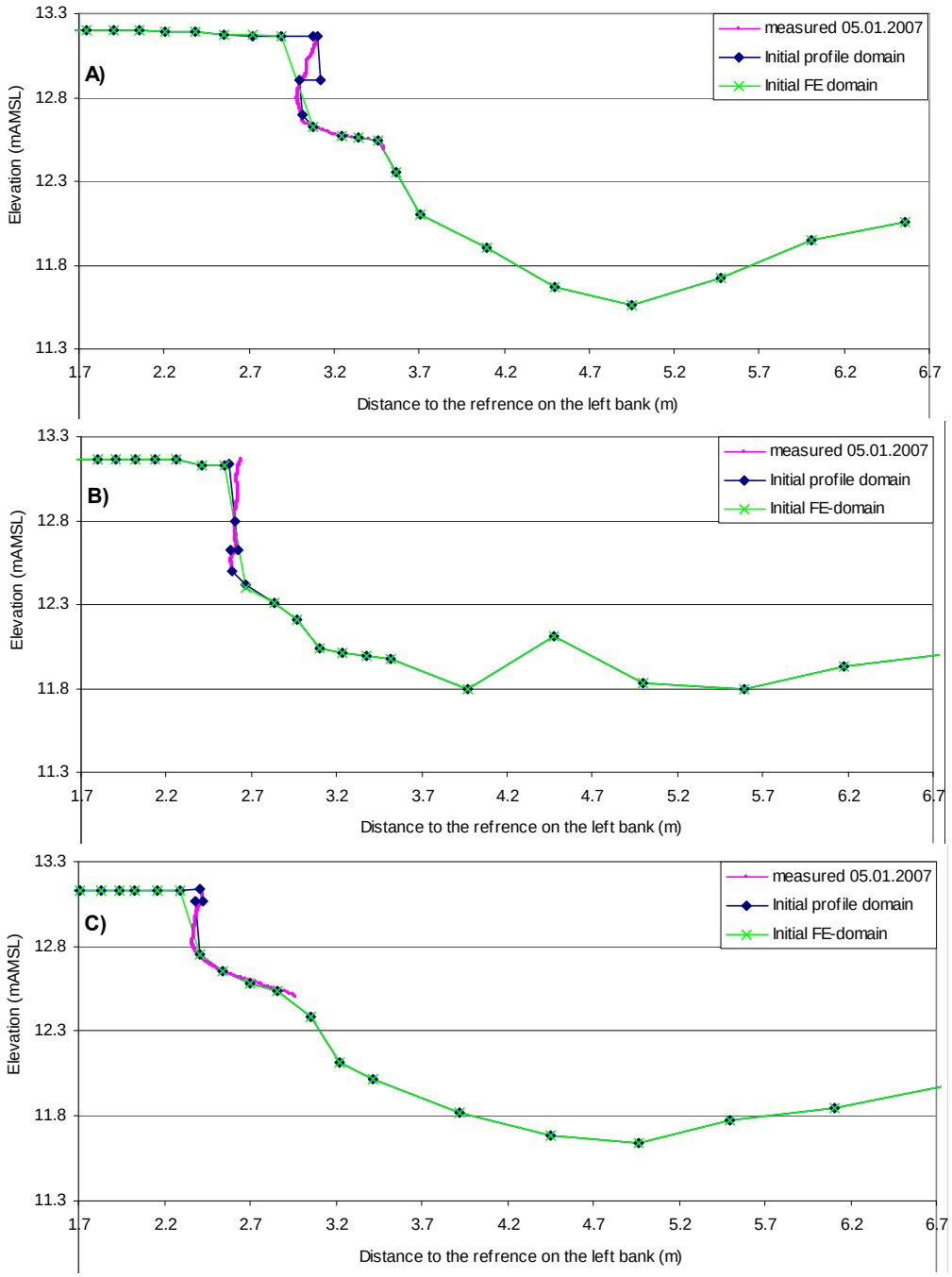

Figure 7-6 Initial condition of three selected profiles. A) Bend apex; B) upstream of the apex (middle); C) Bend entrance

In this phase of validation, five main parameters, which influence bank erosion process, had to be determined as follows:

- Critical dense angle of repose (φ^c)
- Unsaturated (dense) angle of repose (φ^u)
- Matric angle (φ^b)
- Order and coefficients of the polynomial of pore pressure distribution function
- Damping factor of erosion and deposition

Further parameters such as the order of distribution function of failed bank material and associated method of distribution as well as additional cohesion due to the vegetation roots had to also be determined. The measured angle of repose (refer to Ch. 6.1.2) was used as friction angle φ, for example, in Eq. (3–33). Slip failure was considered to be the major form of undercutting process. Deep-seated failures are rare in non-cohesive soils, since shear strength increases usually more quickly than shear stress with depth in such soils (Lawler et al., 1997). Two types of undercutting were studied. At the primary phase of validation, φ was assumed to be the most critical failure angle in saturated zone in analogy to the common practice in the analysis of bank failure in (granular) non-cohesive soils. The failure was however assumed to occur when the bank-toe slope exceeded beyond φ^c, to account for excess stability due to compaction and cementation. To simulate the case of shallow slip failure, φ^c was then assumed to be the most critical failure slope, beyond which failure of submerged bank occurs. Critical shear stress for threshold of sediment movement had been already determined as explained in Ch. 6.2.

The length of each numerical time step should be limited so that the assumption imbedded in decoupled approach of solving governing equation is not violated. As can be seen from Eq. (4–2) the bed change increases linearly with the length of time step. Therefore, according to Schmautz (2003), the time step should be determined in a way that the maximum change of bed elevation in each element does not exceed 5% of the corresponding water depth. On the other hand, in case of movable bank, erosion of the riverbank or increase of water stage results in activating new elements in solution matrix, as already explained in Ch. 4.2.4. This leads to unevenness in bank margin, which cause a change in the direction of the local velocity vector as well as local flow acceleration along bank margin. Such a local numerical acceleration due to mesh adaptation, results in raise of local bed shear stress (Schmautz, 2003). Therefore, in the current application, the variation of water stage has been considered as the limiting factor, which controls the length of morphological time step in bank erosion simulation.

The 25 days of simulation period of January 2007 were discretized into 195 time steps with variable temporal resolution from 6 minutes to 19 hours, depending on water stage. Short time steps were used during rapidly varying flow and large time steps when the flow level remained almost constant. The length of each time step was determined based on the water elevation change, so that at each time step water level had changed more than 1 cm but less than 2 cm with respect to the previous time step. Rinaldi et al. (2008) have also used similar

varying time steps (0.25 to 50 hours) for simulation of bank erosion in natural rivers. More than 51 simulation runs were conducted, on the high performance parallel computer cluster of Hamburg University of Technology to determine the above-mentioned parameters for best results. The result of validation processes is summarized in the following. It should be noted that the simulation result of the last time step forms the basis of comparison with the measurement result of March 30, 2007 during validation phase. At the first stage the method of distribution of failed bank material was investigated to ensure the stability of the sediment transport model, before starting to verify the bank erosion model. Next, the cantilever failure model was verified by adjusting the parameters related to pore pressure and cantilever failure. The damping factor of erosion/deposition was then examined to study their influence on bank-toe erosion, which can affect the undercutting process. Up to this stage the first type of undercutting with $\varphi^c = 60$ and $\varphi = 42.3$ was used. Then, undercutting parameters were adjusted to get the best result of bank profile in submerged zone including the second type of undercutting. Finally, effect of root reinforcement was included in simulations.

7.3.1 Distribution of failed bank material

The two already mentioned methods of distribution of failed bank material were examined. At first the physically based method (refer to Ch. 4.2.5.2) was examined. It was found that this introduced a numerical stability problem. It was then tried to apply the mixed method (see Ch. 4.2.5.3) to improve the stability. However, even with the assignment of 10% of failed bank material as source term to the sediment transport equation, numerical instability could not be removed. Therefore, the lump method was used in all simulations.

7.3.2 Order of pore pressure polynomial

As already explained the (negative) pore water pressure distribution plays an important role in stability and timing of cantilever failure. To estimate the distribution of negative pore pressure, a polynomial function was defined (Eq. 3–43), for which its order (n) and coefficients (a_n) were determined so that the time of bank failures match those captured by remote camera (see Ch. 6.7). The correct simulation of the time of failure is closely related to the resulting shape of overhang and corresponding volume of failure. For example, early failures allow formation of only a small overhang, which results in a small amount of failed volume.

In order to determine the order and coefficients of the mentioned polynomial function, a sensitivity analysis was performed while keeping other parameters constant. At the beginning, the first type of bank failure mechanism in submerged zone was considered with $\varphi^c = 60°$. The unsaturated angle of repose was assumed to be 78° and φ^b=16°. The effective cohesion as well as cohesion due to vegetation root were set to zero. The deposition and erosion damping coefficient were set primarily to 500.

The sensitivity analysis began first by considering a binomial function with zero constant ($a_0 = 0$) and its coefficients were kept equal ($a_2 = a_1$). Unsteady simulations were run for the

whole simulation period while varying these coefficients from 1 to 10. It was found that the best agreement between measurements and the simulated bank profiles at the end of the simulation was obtained with a coefficient of $a_2 = a_1 = 4$ for almost all three test profiles. A coefficient of 10 produced as satisfactory results as that of coefficients equal to 4, for section (3), while the worst result was for section (1), where no cantilever failure was computed during the simulation. This suggested that probably a unique solution may not exists for coefficients of binomial. Therefore, two cases of $a_2 = 4$ and $a_2 = 10$ were chosen for the rest of the analysis.

Six further simulations were run for $a_1 = 2$ to 6, while keeping $a_2 = 10$. It was found that $a_1 =$ 10, 6 and 5 produced the same and best result of bank profile for section (2) among the rest of coefficient values, while the worst result was obtained with $a_1 = 2$. The lower values of a_1 generally resulted in more bank retreat than the measured ones through cantilever failure of the overhang. However, for section (1), it was vice versa, so that with $a_1 = 2$ and 3 similar best results were obtained, while similar worst results were obtained by $a_1 = 4$, 5 and 6. Simulation of cantilever failure of section (3) was generally not sensitive to pore pressure parameter, confirming the fact that no cantilever failure had occurred at this section.

The same above-mentioned process was repeated with $a_2 = 4$, by varying a_1 from 4 to 7. The best result could be obtained by a value of $a_1 = 6$ for section (2) and 3, while a value of $a_1 = 4$ showed the best result for section (1). The result of this analysis is depicted in Fig. (7-7) and compared with that of $a_1 = 2$ and $a_2 = 10$. As seen from this figure, for section (1) the result of simulation of bank profile using the set of $(a_2, a_1) = (4,4)$ is completely identical with that of $(a_2, a_1) = (10, 2)$. This proves the supposition that there can be no unique combination of these two parameters for the best solution. Furthermore, it can be observed that with $(a_2, a_1) = (4,6)$ the simulation of bank profile at section (2) has been significantly improved, while the difference of the examined range of a_1 parameter is not very significant in the case of section (1).

Additionally, it was found that the number of occurrence of shear cantilever failure decreased with increasing value of the mentioned coefficient so that with $(a_2, a_1) = (1,1)$ a total number of 56 cantilever failures over the three mentioned sections was recorded during the simulation phase, the number of failures sharply reduced to 8 for $(a_2, a_1) = (1.5,1.5)$. The number of cantilever failures reduced further to 1 for $(a_2, a_1)=(10,10)$, in which cantilever failure was computed only once for section (2). For the case of $(a_2, a_1) = (4,4)$, one cantilever failure was computed for section (3), which should have not been the case according to the measurement. This was another reason for ruling out this combination. The number of simulated cantilever failure for the case of $(a_2, a_1) = (4,6)$ was two times at time step 81 and 83 for section (2) and (1) respectively. These time steps correspond to 18:23 and 19:53 on 18th January with downstream water level of 12.741 m and 12.777 m, respectively, which occurred in the rising limb of the recorded flood event. According to the photos recorded by the remote camera, at least one cantilever failure had occurred between 12:44 on 18th January and 9:15 on 19th January. However, the next recorded cantilever failure, which occurred between 15:46 on 19th January, and 9:28 on 20th January could not be simulated with the mentioned parameter combination. The mentioned times correspond to the numerical time steps 70 to 92 and 94 to

106. Although with (a_2, a_1)=(3.57,3.57) five simulated cantilever failures occurred, three of which in the just-mentioned later period (each profile one failure), nevertheless the amount of computed bank retreat showed one of the largest errors with respect to the measurements.

A separate series of computations was achieved, assuming a third order polynomial function. In this case the negative pore pressure increases over water table faster than binomial equation with equal polynomial factors. Two combination of polynomial factors were tested, namely, $a_3 = a_2 = a_1 = 4$ and $a_3 = a_2 = 4$ and $a_1 = 6$. The simulations introduced no improvement at the bend entrance and apex sections and worse results in the middle section. Therefore, continuation of further analysis of these parameters for n = 3 was avoided.

According to the above mentioned sensitivity analysis, a binomial function with (a_2, a_1) = (4,6) was selected for the sensitivity analysis of the rest of the parameters. Furthermore, it was concluded that the profile shape was generally less sensitive to the parameter a_1 than to a_2.

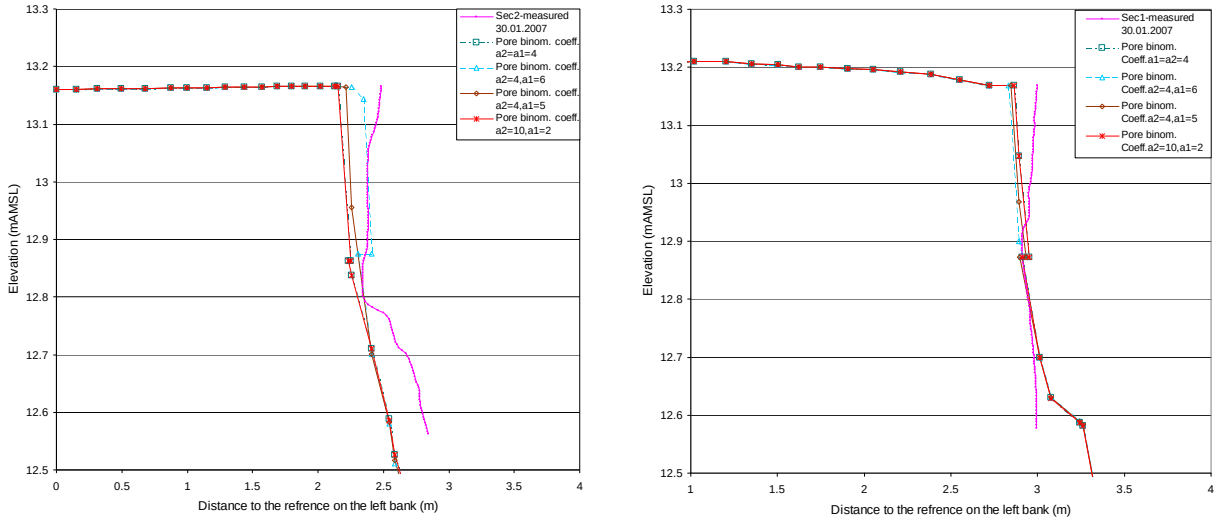

Figure 7-7 Effect of binomial coefficients of negative pore pressure on simulation of cantilever failure

7.3.3 Matric angle

Increase of matric angle enhances the apparent cohesion and stability of the bank. To investigate its effect in the rate of bank retreat, the matric angle values of 16°, 18° and 20° were examined preliminarily, which is in the normal range reported by previous authors.

The simulation result of bank profiles was identical for values of 16°, 18° and 20° for bend apex profile (section (1)) and for values of 18° and 20° for the middle profile (Fig. 7-8). On the latter profile, the simulation with larger matric angles, resulted in larger bank retreat than with $\varphi^b = 16°$. This is because of the timing of bank failure. The cantilever failure in the middle profile occurred at time step 81 (Jan. 18 at 18:23) for $\varphi^b = 16°$ and at time step 82 (Jan. 18 at 19:03) in the case of $\varphi^b = 18°$ and 20°. At time step 81, the overhang was not as large as at time step 82 (due to the advancement of undercutting in the latter case). Therefore, the failure of the larger overhang at time step 82 resulted in larger bank retreat. It can be

concluded that, it is not trivial to judge the effect of matric angle on bank retreat rate based only on Eq. (3–33).

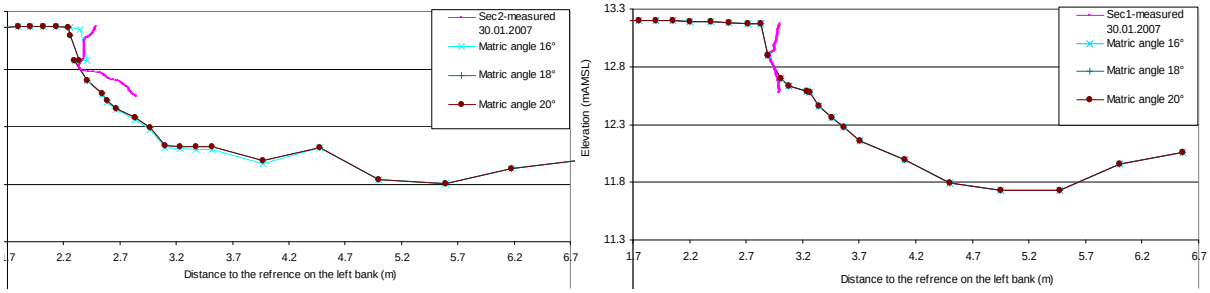

Figure 7-8 Effect of matric angle on simulation result of cantilever failure

7.3.4 Unsaturated angle of repose

No analytical method exists to determine the slope of the most critical failure plane in cantilever shear failure (unsaturated angle of repose). According to the current measurements this angle varies from a positive angle of 52° to 90° (relatively wide interval) and a negative angle of –68° to –78° (relatively narrow interval). This indicates a complex interaction between negative pore pressure, soil property and vegetation on cantilever failure in non-cohesive soils, which has made the analytical determination of most critical shear plane difficult. As already mentioned, only positive failure angles can be simulated with the currently developed method. This angle was increased from primary 78° to 83°-85°. As seen from Fig. (7-9) the increase of this angle does not necessarily result in formation of larger overhangs (for example at section 2). This parameter affects mainly the position of upper and lower edges (nose attribute in data model) of the overhang as can be observed from this figure. The best result was obtained by an unsaturated angle of repose of 85° (followed by 84°) for the bend apex profile (section 1). For the other two profiles the best results were obtained with $\varphi^u = 84°$. Therefore, this value was selected for the unsaturated angle of repose for the rest of the analysis.

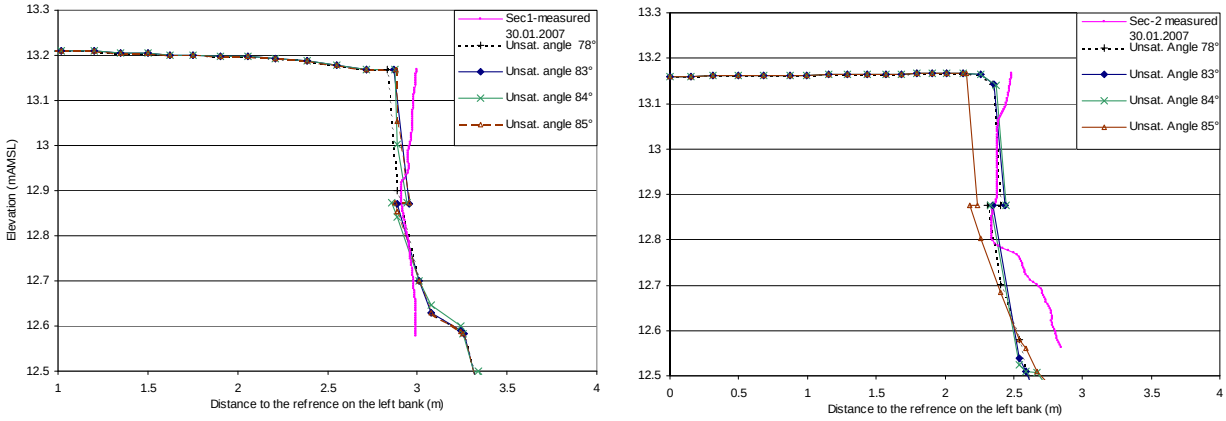

Figure 7-9 Effect of unsaturated angle of repose on simulation of cantilever failure and shape of the overhang

7.3.5 Damping factor of deposition and erosion rates

As can be seen from Eqs. (3–22 and 3–23), if the damping coefficients C_d and C_e are greater than one, the erosion and deposition timescale increase, which results in slowing the mentioned processes. This yields a reduction of net bed sediment flux (Eq. 3–21) and bed change (Eq. 3–28). In other words, as already mentioned, these two parameters are equal to $1/\alpha_0$ in Eq. (2–8). Therefore increase of damping factors is equivalent to reduction of α_0, which indicates that the deficit of total sediment concentration with respect to total equilibrium concentration is compensated only partly by bed evolution.

All of the already mentioned simulations were achieved with a high damping coefficient ($C_d = C_e = 500$), to ensure a stable simulation and because mainly the cantilever failure model was to be verified. This means only 0.2 % of the already defined deficit in sediment concentration is compensated by bed evolution.

To investigate the influence of these factors on bank-toe elevation, the damping factor was reduced to 80, 50, 40 and 30. Further decrease of this factor below 10 resulted in instability in sediment transport simulation. The unsaturated angle of repose was kept at 84° except the reference computation with damping factor of 500, which had $\varphi^c = 85°$. The result of this simulation is presented in Fig. (7-10).

As seen from this figure, reduction of these factors increases degradation at the bank-toe in form of berm formation with a maximum at the bend entrance profile and minimum at apex profile. This is in agreement with bed bathymetry measurements in which the berm width reduced towards the bend apex. It also conforms to the pattern of flow velocity along the outer riverbank, in which flow velocity accelerates towards the bend apex, therefore less sedimentation is expected at the apex than at the bend entrance section. Validation of these parameters was not possible due to the inevitable use of bathymetry data of Dec.10, 2007 for the elevation model of numerical simulations in January 2007 (see Ch. 7.1.1).

Bank-toe erosion was generally underestimated at the bend apex, as observed in Fig. (7-10a), and overestimated in the middle profile just upstream of the apex. A good estimation of bank-toe geometry and elevation was obtained at the bend entrance profile (section 3) by a damping

factor of 500. This indicates the effect of river bend on sediment transport, which could not be properly simulated in this work with the adopted total sediment transport model and distribution model of failed bank material. It should be noted that the results could also be mainly affected by improper bathymetry data.

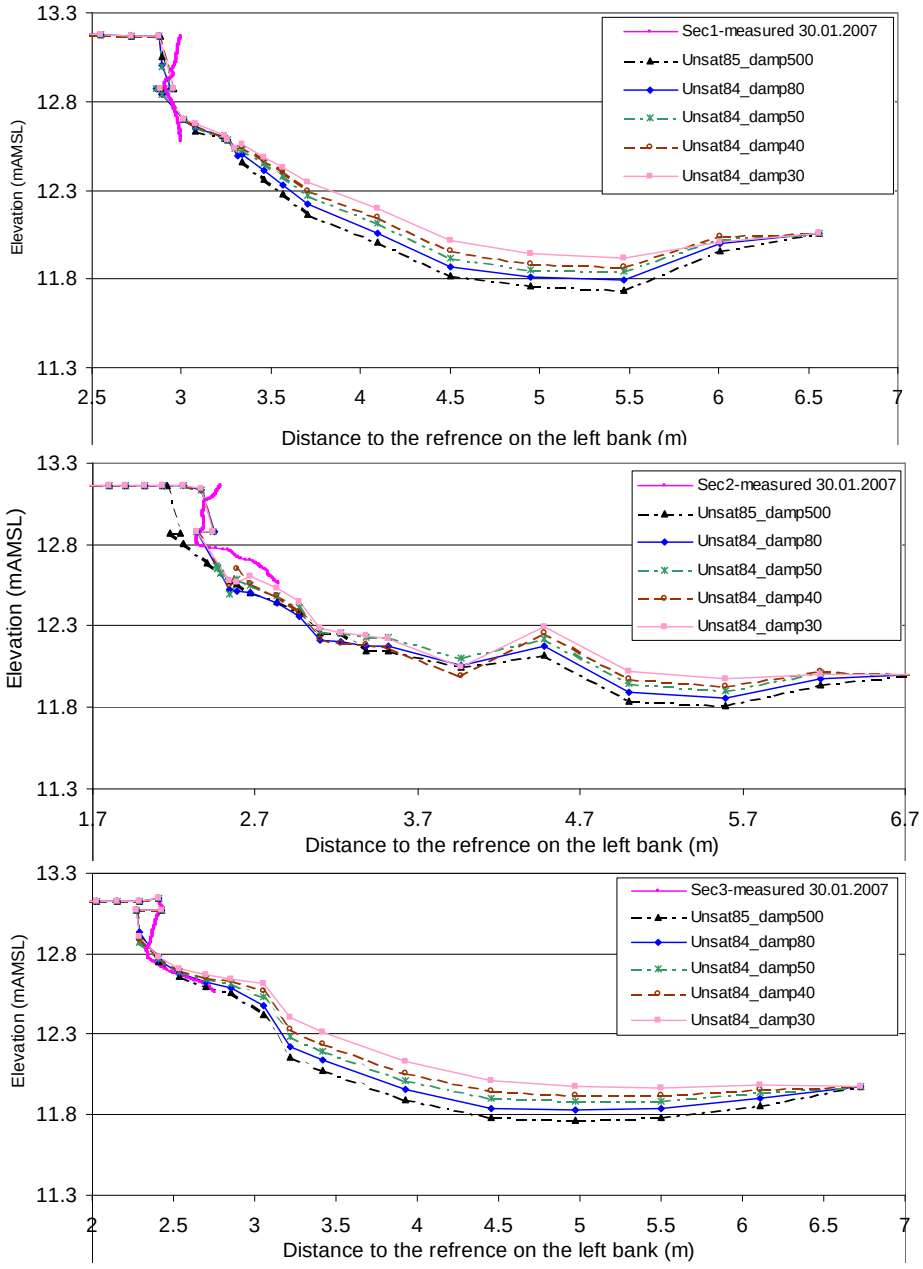

Figure 7-10 Effect of damping factor of deposition/erosion on simulation results of bank-toe evolution. The profiles from up to down are bend apex, middle and bend entrance profiles, respectively

7.3.6 Saturated dense angle of repose

This parameter is the most important one in the simulation of undercutting extent, which influences the position of undercutting advancement (front attribute in data model). The position of front directly affects the stability of overhang and its time of failure. Two further simulations using the second undercutting type with saturated dense angle of repose equal to $\varphi^c = 60°$ and 75° were achieved, assuming occurrence of shallow slip failure in which the failure plane is parallel to the bank surface in saturated zone ($\varphi^c = \varphi$). The damping factors of erosion and deposition were set to 50 for both simulations. Although the best result of the upper bank edge of the bend apex profile (with 8 and 5 cm error, respectively) could be obtained with these two values among all 51 simulation runs, the largest amount of underestimation of front advancement (6 and 7 cm) among all of the runs were obtained by $\varphi^c = 75°$. The front was correctly computed with $\varphi^c = 60°$ at this profile.

For the upstream profile of the bend apex, however, $\varphi^c = 60°$ yielded the best result among all simulation runs, not only in the undercutting zone but also in overhang zone. Here too, the front position was correctly calculated. However, its improvement over $\varphi = 42.3°$ was not significant (2.3 cm closer to the measurement at the upper edge of the overhang). With $\varphi^c = 75°$, the method largely overestimates the overhang size and underestimates undercutting extent. For the entrance profile to the bend, this value has substantially enhanced the simulation. Since no cantilever failure was either measured or simulated for this profile, undercutting plays an important role in bank evolution at this section. As seen from Fig. (7-11), the bank profile has a negative (adverse) slope from the bank-toe to top of the bank. Geometrical modelling of such a profile is beyond the capabilities of the current numerical model. It is, therefore, not surprising that by increasing φ^c, better results could be obtained, however not as satisfactory as in other profiles.

It can be concluded that shallow slip failure with the angle of $\varphi^c = 60°$ has best simulated the bank profiles generally and it supports the idea that the failure mechanism in the submerged zone has been mainly shallow slip failure although sapping failure could also have contributed to bank erosion in the middle section. Furthermore, it shows that an increased angle of repose can account for compaction and cementation effect in submerged zone.

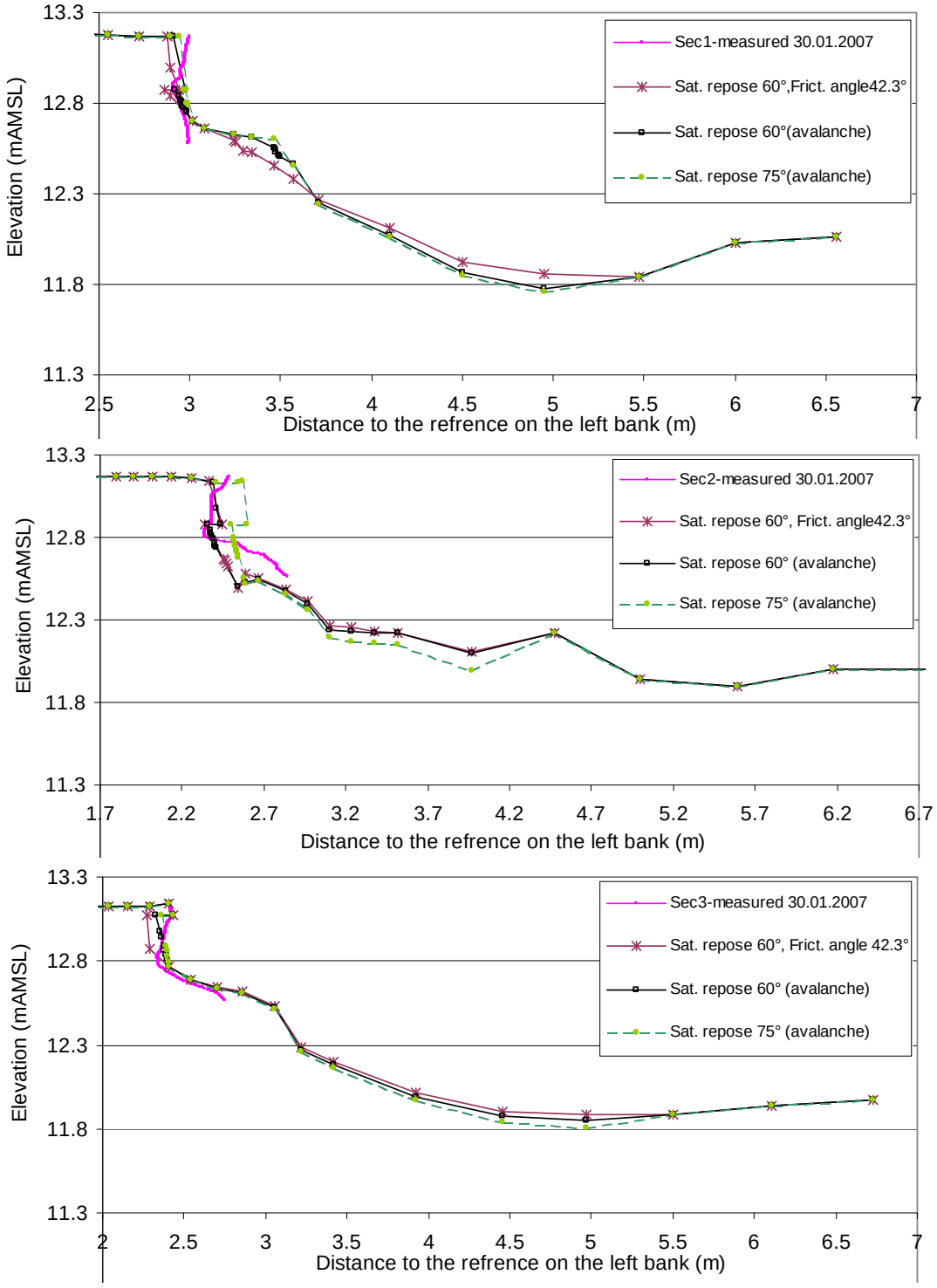

Figure 7-11 Comparison of measurements on Jan. 30, 2007 with simulation results using two methods of undercutting (deep seated and shallow slip failure φ^c =60° and 75°) with following parameters: φ^u = 84°, c_d=c_e= 50 and negative pore function coefficients (a_1, a_2)=(4,6).

7.3.7 Fine-tuning of matric angle

Based on the above-mentioned analysis, the best combination of calibrating parameters for simulation of bank erosion process for the flood event of January 2007 in Hardebek-Brokenlander Au has been determined as follows:

a) Saturated angle of repose for shallow slip failure in submerged zone $\varphi^c = 60°$.
b) Unsaturated angle of repose of shear type cantilever failure $\varphi^u = 84°$.
c) Matric angle $\varphi^b = 16°$.
d) Negative pore pressure binomial function in form of $f(\xi) = 4\,\xi^2 + 6\,\xi$, in which ξ is the elevation over water level and f is the corresponding matric head.
e) Damping factor of deposition and erosion could not be determined due to the uncertainty of bathymetry measurements. However, a value of $C_d = C_e = 50$ seemed to be closer to the applied range of α_0 in literature (0.1 to 1), therefore this value was also preferred here.

Among the above-mentioned parameters, matric angle is the only one, which allows further fine-tuning. As mentioned in Ch. 3.4.2, the minimum value of matric angle reported in literature is 10°. Applying the minimum value of matric angle in a new simulation run enhanced not only the simulated bank profiles but also the timing of the cantilever failure. As can be observed from Fig. (7-12) the simulated location of upper edge of the bank at section (1) has been significantly improved (4 cm reduction of absolute error) with $\varphi^b = 10$. At section (2) the simulated position of the upper bank edge (1 cm increase of absolute error) has not been improved. However, the geometry of bank face has been significantly improved in at the cost of increasing the deviation between simulated and measured lower cavity at the bank-toe. This parameter had no influence on section (3), since no cantilever failure was calculated for this section. Two further simulations with matric angle 13° and 15° were carried out. These showed to be identical and did not result in improvement of the simulation results, as can be inferred from Fig. (7-12).

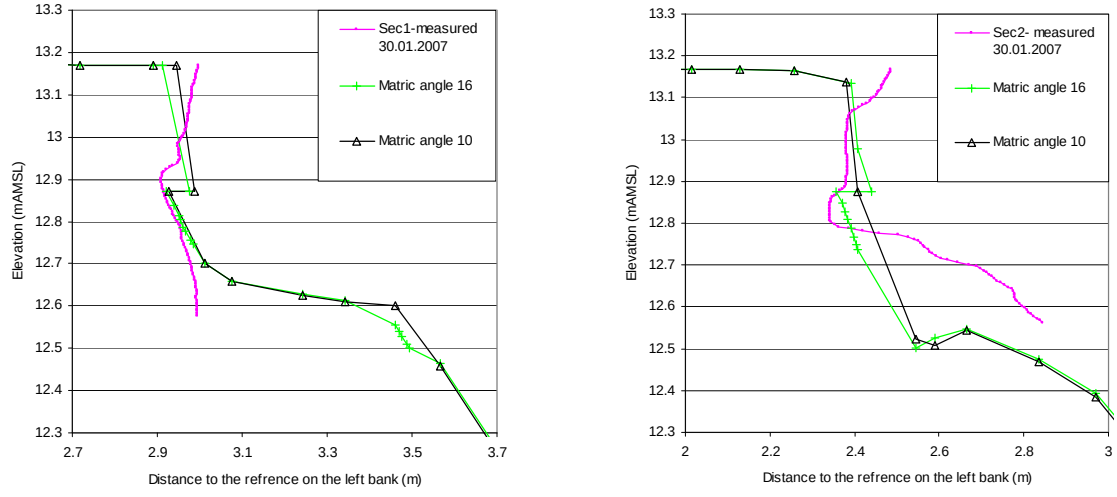

Figure 7-12 Application of refinement of matric angle in enhancement of simulation results

The timing of cantilever failure has also been significantly improved with $\varphi^b = 10°$. Two occurrences of cantilever failure were computed for section (2) at time steps 75 and 114 (16:33, 18.01.2007 and 19:13, 20.01.2007, respectively) and one for section (1) at time step 81 (18:23, 18.01.2007). As mentioned in Ch. 7.3.2, the combination of $\varphi^b = 16°$ and other above-mentioned parameters did not result in correct timing of camera-recorded cantilever failure events between 19 and 20 Jan. 2007. However, with this refinement of matric angle parameter, the new developed mathematical bank erosion model could simulate almost the correct timing of cantilever failure events. This implies that the proposed simplified pore pressure function could substitute the complicated and computer intensive seepage modelling of negative pore pressure with sufficient accuracy in the current case.

7.3.8 Cohesion due to vegetation roots

A sensitivity analysis was carried out to investigate the effect of cohesion of vegetation roots on the simulation of bank erosion. For this purpose, the root tensile strength (T_r) was varied from 0.5 to 10 kPa. This range corresponds to an additional cohesion (c_r) due to vegetation root from 0.4 to 6 kPa, assuming a root depth (L_r) of 0.1 to 0.2 m for the slip length (L) of 0.2 to 0.3 m. The latter two parameters were kept constant for each examined root tensile strength as shown in Table (7-6). This range of T_r covers the expected c_r for grass according to Cancienne et al. (2008).

Appling the best combination of parameters determined in Ch. 7.3.7, it was found that the simulation results using T_r = 4 to 10 kPa yielded no cantilever failure in profile sections 1 to 3. Reducing this parameter to 0.5 kPa, resulted in even larger bank erosion than in the case where root cohesion effect was disregarded. Generally, the result of bank erosion simulation was deteriorated by addition of the cohesion due to the roots (T_r = 0.5 to 10 kPa). Although in the case of the bank profile at section 2, the overhang nose and front were calculated precisely with respect to the measurements for T_r = 2.5 kPa, however the bank retreat of the top edge of the overhang has been over-predicted (Fig. 7-13 and Table 7-7).

At the next stage the effect of root cohesion was investigated assuming a hydrostatic distribution of negative pore pressure ((a_2, a_1)=(0,1)). Using this assumption, bank erosion simulations were run for a range of T_r = 1 to 10 kPa. No bank erosion was computed with T_r = 5 and 10 kPa, while for the case of T_r = 1 kPa, excessive bank erosion was computed for profile 1 and no bank erosion for profile 3. The best estimation of the location of top edge of the riverbank at profile 2 could be obtained for T_r = 2.5 kPa. However the profile of the overhang surface (nose) has not been correctly simulated (Fig. 7-13).

It can be seen from Table (7-7) that the deviation of the simulation results with the case of excluding the vegetation effect explicitly is generally very low. However, the closest result to this case could be obtained by T_r = 2.2 kPa with (a_2, a_1) = (0,1) for negative pore pressure. The timing of the simulated overhang failure with the mentioned parameters was also acceptable.

Table 7-6 Range of vegetation parameters for sensitivity analysis

				Additional cohesion (c_r) due to vegetation					
				Slip length (cm)					
T_r (kPa)	Root length (cm)			20			30		
10	10	---	---	6	---	---	4	---	---
5	20	10	---	6	3	---	4	2	
2.5	---	20	10	---	3	1.5	---	2	1
4	10	---	---	2.4	---	---	1.6	---	---
2	20	10	---	2.4	1.2	---	1.6	0.8	---
1	---	20	10	---	1.2	0.6	---	0.8	0.4
0.5	---	---	20	---	---	0.6	---	---	0.4

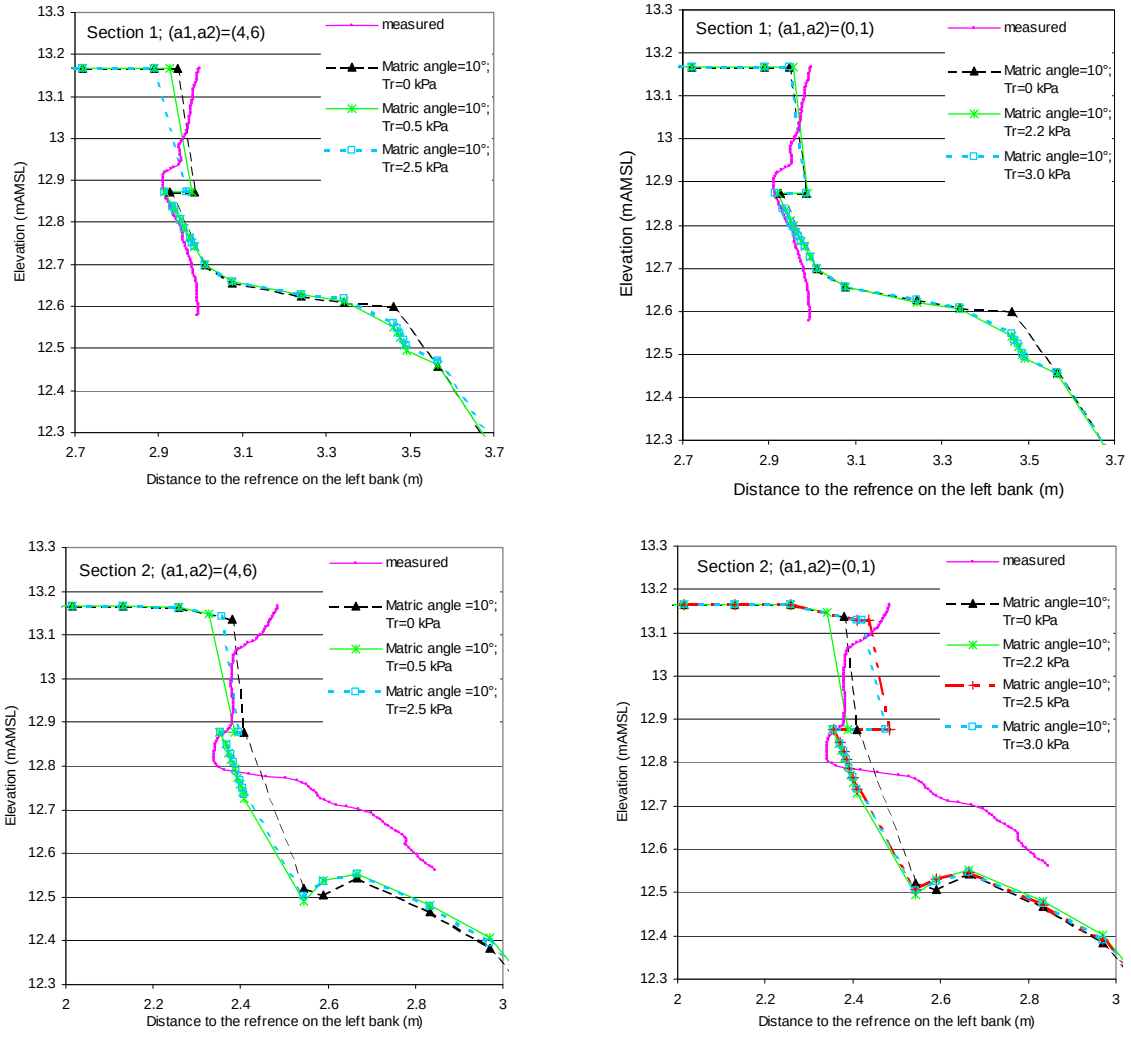

Figure 7-13 Simulated bank profiles after including the effect of root cohesion

Table 7-7 Simulation results of cantilever failure including the effect of cohesion due to the vegetation roots

Pore pressure parameter (a1,a2)	T_r (kPa)	Section	Overhang		Nose		Front		Time step of cantilever failure
			Horizontal position (m)	Deviation to the case without vegetation effect (%)	Horizontal position (m)	Deviation to the case without vegetation effect (%)	Horizontal position (m)	Deviation to the case without vegetation effect (%)	
M*	M*	P1	2.9926	1.57	2.9472	-1.34	2.9097	-0.60	70 to 106
		P2	2.3821	0.04	2.3414	0.00	2.3404	0.00	
		P3	2.4100	0.00	2.4300	-0.04	-----	-----	
(4,6)	0.5	P1	2.9276	-0.63	2.9802	-0.23	2.9145	-0.44	74
		P2	2.3284	-2.21	2.3863	1.92	2.3518	0.49	82, 112
		P3	2.4100	0.00	2.4300	-0.04	2.3260	-0.05	-----
	1	P1	2.9276	-0.63	2.9802	-0.23	2.9196	-0.27	83
		P2	2.4084	1.15	2.4672	5.37	2.3566	0.69	76
		P3	2.4100	0.00	2.4300	-0.04	2.3260	-0.05	-----
	2.5	P1	2.8905	-1.89	2.9665	-0.69	2.9146	-0.44	112
		P2	2.3574	-1.00	2.3950	2.29	2.3555	0.65	84
		P3	2.4100	0.00	2.4300	-0.04	2.3260	-0.05	-----
(0,1)	1	P1	2.8905	-1.89	2.9500	-1.24	2.9145	-0.44	1, 110
		P2	2.3426	-1.62	2.3932	2.21	2.3649	1.05	31,75,82,112
		P3	2.3426	-0.28	2.3882	-1.76	2.3512	1.03	84
	2	P1	2.9556	0.32	2.9905	0.11	2.9196	-0.27	1
		P2	2.3537	-1.15	2.3933	2.22	2.3537	0.57	67, 84
		P3	2.3195	-0.38	2.3818	-2.02	2.3432	0.69	113
	2.2	P1	2.9556	0.32	2.9905	0.11	2.9196	-0.27	34
		P2	2.3410	-1.68	2.3898	2.07	2.3518	0.49	70, 110
		P3	2.4100	0.00	2.4300	-0.04	2.3260	-0.05	-----
	2.5	P1	2.9556	0.32	2.9905	0.11	2.9196	-0.27	77
		P2	2.4353	2.28	2.4824	6.02	2.3573	0.72	72
		P3	2.4100	0.00	2.4300	-0.04	2.3260	-0.05	-----
	3	P1	2.9459	-0.01	2.9870	0.00	2.9145	-0.44	79
		P2	2.4208	1.67	2.4742	5.67	2.3569	0.71	74
		P3	2.4100	0.00	2.4300	-0.04	2.3260		-----

* M represents the result of direct measurements of bank profile with respect to the reference point on the left riverbank

7.3.9 Numerical process of bank evolution

The theory and measurement results regarding the three main bank evolution processes under study have been already presented in previous chapters. It is intended here to show the evolution processes numerically by means of a typical simulation result at section (2) (Fig. 7-14). As shown in this figure, tensile failure due to the rise of water level has caused the lower edge of the overhang profile to rise at time step 79 (17:53, 18.01.2007). It should be noted that water stage in the river is equal to the lower edge of the overhang in this figure.

Tensile failure results in advancement of the undercut front, which eventually leads to cantilever failure at this time step. Further shallow slip- and tensile failure process during the high flow stage of the simulation period resulted in the cantilever failure shown for time step 140. This time step corresponds to 01:30, 23.01.2007 just after the passage of the multi-peak flood event in the recession limb of the flow hydrograph (Fig. 6-7). By comparing this stage of bank profile with time step 195 (30.01.2007), no further bank evolution has been simulated for the rest of the recession period. However, aggradation has been computed during this flood recession period (between these two time steps), which seems to be realistic.

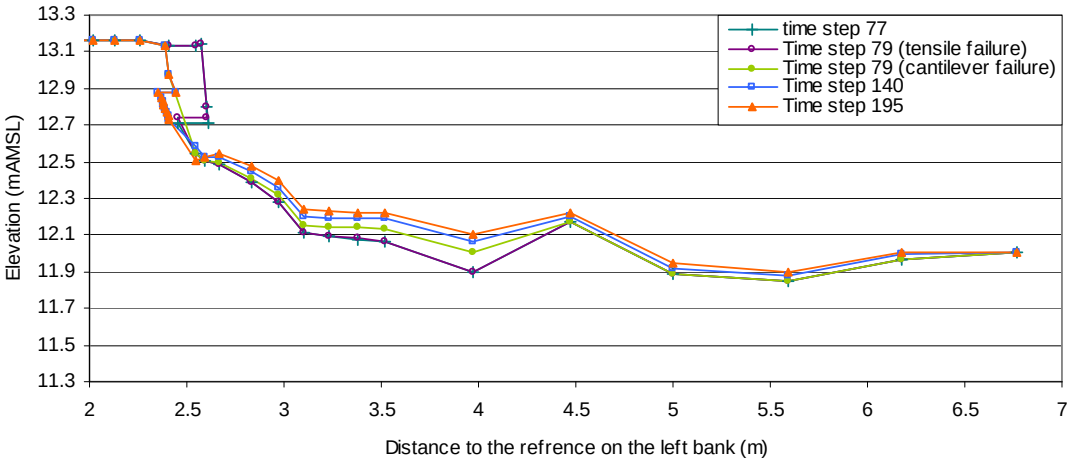

Figure 7-14 Presentation of numerical bank erosion processes at section (2)

8 Discussion

It is intended here to discuss the fluvial processes along and across river bend that cause bank erosion. This will be illuminated in the following by interpreting the interconnection between bed evolution and flow velocity (and bed shear stress) distribution across the river bend with respect to the dynamics of flow regime. Furthermore, the interaction of bed and bank evolution as well as the mechanism of bank evolution in non-cohesive (sandy) soils will be discussed with reference to the dynamics of flow regime. Finally, the results of the numerical simulations are discussed. It should be noted that the conclusions derived here regarding processes along the river bend are limited between the bend entrance and apex, since no measurements were carried out downstream of the bend apex in the river due to stabilization of riverbank by vegetation.

8.1 Velocity and bed shear stress distribution

The velocity contours at the two cross sections at the bend apex and upstream of it (Fig. 6-10 and 6-17) show that the velocity has one maximum zone at the latter section, while two maxima (a local and an absolute) in the former section. The latter situation has caused a more uniform depth-averaged velocity distribution across the bend apex than upstream of it showing a process of lateral dispersion of maximum velocity along the river bend.

In the river bend under study the maximum depth-averaged flow velocity magnitude shifts from the outer bank downstream of the bend entrance towards the inner bank at the bend apex (Fig. 6-17 and 6-10). Nevertheless, the depth-averaged velocity magnitude at the outer bank-toe at the bend apex is not much less than the maximum value. This shifting of the position of maximum depth-averaged velocity magnitude is mainly due to the change of pattern of transversal velocity along the river bend. In downstream development of secondary currents, a large secondary current cell (Fig. 6-20), which comprised most of the channel cross section downstream of the bend entrance, has been pushed away from the outer bank and towards the channel centre by pure lateral flow at outer bank at the bend apex (Fig. 6-13). It is mainly this pure lateral velocity, which pushes the flow and consequently the depth-averaged velocity magnitude towards the inner bank at the bend apex. Disregarding this phenomena can be sought as one of the major reasons that the application of the theory of fully developed

circulatory flow in determination of dispersion terms in momentum equations results in unrealistic shifting of maximum depth-averaged velocity towards the outer bank.

On the other hand, the maximum bed shear stress has shifted from the inner bank, downstream of the bend entrance, towards the outer bank at the bend apex (Fig. 6-24 and 6-22), neglecting that at the time of measurements on section (2), the flow discharge was lower than that of the measurement date of section (1). Similar shifting pattern of maximum bed shear stress (friction velocity) along a meandering flume has been also reported by Kühne (2003). The bed shears stress is more uniformly distributed across bend apex, with a wider large bed shear stress zone, than bend entrance.

By examining different flow discharges, Kühne (2003) concluded that discharge has almost no effect on the shifting pattern of maximum bed shear stress, given a trapezoidal cross section. However, in rivers with fine sandy banks, the slope of the bank can attain vertical and even negative slopes as already shown in Ch. 6.7, bringing the cross section of the river in high water stage closer to a rectangular geometry, even if for a short time before failure of the submerged steep bank. As is well known, the shear stress distribution across a trapezoidal channel is different from that in a rectangular channel. In the latter case, the bed shear stress near the bank is high, while in the former case that is low due to the small water depth and velocity over the sidewall.

8.2 Sediment transport across the river bend

The direction and magnitude of vertical velocity, especially near the bed, can be used to interpret potential re-entrainment and /or deposition of suspended sediment across the river channel. Referring to the order of magnitude analysis on lateral and vertical velocity profiles achieved in Ch. 6.4.2, it can be concluded that at the upstream of bend apex (and probably also at bend entrance) the larger relative downward vertical velocity (comparing to the apex), especially near the bed, suppresses re-suspension and accelerates deposition of suspended material at these two sections (ignoring re-suspension due to the bursting phenomena). This contributes to more berm formation at the bend entrance than at the bend apex (refer for example to Fig. 6-39b). Additionally, as it will be discussed in the following chapter, the pattern of bed shear stress along the river bend is another reason of decrease of berm width along the river bend.

It is well known that secondary currents have the potential to transport sediment from the outer bank to the inner bank across a river bend resulting in point bar formation on the inner bank. Depending on the type of cross circulation profile (refer to Fig. J-1), in streams with small width to depth ratio, the pure lateral velocity at outer bank-toe is responsible for transporting sediment mainly on the same eroded bank side, while circulatory flows across the river bend cause to transport the eroded material on the eroded side, at most, comparable to the amount transported across the channel (Yalin, 1992,p.192). The transport of eroded bank material along the outer bank-toe by means of pure lateral flow (Fig. 6-11) contributes to berm formation on this side of the river bank like that observed in the present field

measurements (refer to Ch. 6.7) as well as laboratory measurements (Fig. 8-4). From velocity vector field in Fig. (6-13), it can be concluded that in bank-toe region, where the velocity vector is parallel to the bed, no re-suspension of eroded sediment should be expected, apart from those induced by bursting phenomena, since the vertical velocity component is downward and negligible. This implies that the eroded outer bank material deposits at the bank-toe and remains primarily intact at the bank-toe if the bed shear stress does not exceed the threshold of motion.

The secondary currents (vectors) in the central region of the bend apex (Fig. 6-13) contribute to erosion of berm-toe and transport the eroded material towards the inner bank, resulting in aggradation of inner bank, which has been observed in the current achieved bathymetry measurements (Fig. 8-3). The direction of velocity vectors near bed upslope the talweg towards the inner bank (Fig. 6-13 and 6-20) indicates the direction of radial transport of sediment towards the inner bank.

Furthermore, the relative large velocity magnitude at the inner bank (Fig. 6-10) and low lateral velocity in this region (Fig. 6-11) implies that the transported sediment to the inner bank is further transported mainly downstream by longitudinal flow component on this side of the river. On the other hand, the local maximum depth-averaged flow velocity near the talweg at the apex (Fig. 6-10) is responsible for downstream transport of a portion of eroded bank material, which has been already discussed in Ch. 6.6. Similar processes have shown to hold for the section upstream of the apex as described in Ch. 6.4.2. Relative large longitudinal velocity in the bank-toe zone in both sections implies that a larger portion of the eroded and transported bank material are transported downstream along the bank-toe (as also conceptualised in Amiri-Tokaldany et al., 2007) since the lateral velocity is smaller than longitudinal velocity and a part of the rest is transported towards the inner bank. This longitudinal transport of sediment along the outer bank-toe cause downstream berm propagation along the outer bank and describe the concept of excess sediment feeding from upstream.

The above-mentioned discussion supports the concept of berm formation due to sedimentation of eroded bank material at bank-toe and mechanism of lateral transport of eroded bank material. In summary, in the process of downstream development of the secondary currents along the bend (due to bend geometry, lateral bed slope as well as pure lateral flow at outer bank) talweg becomes deeper and more sediment is transported towards the inner bank at the bend apex than upstream of it. The more intensive inner bank aggradation at this section contributes to more concentration of flow towards the outer bank, which results in more bank-toe erosion at the outer bank.

8.3 Sediment transport along the river bend

Along the shifting path of depth-averaged velocity magnitude from the outer to the inner bank along the river bend, the sediment transport capacity is also maximum, thereby, showing the main direction of suspended sediment transport along the river bend towards the bend apex.

On the other hand, the shifting pattern of maximum bed shear stress from the inner bank to the outer bank along the river bend represents the main bed load transport direction along the river bend. Furthermore, in the case of non-erodible banks, this process of shifting of the bed shear stress results in imbalance of bed load transport capacity in longitudinal direction as well as in lateral direction, which leads to the bed erosion along this path through increase of absolute magnitude of sediment transport gradient (note the role of gradient terms in Eq. 2-4). Therefore, the deepest erosion or pool should occur, where this gradient reaches its maximum (Yalin, 1992,p.200), which should coincide with the mentioned shifting path. Such a *longitudinal* "convective" behavior of flow and thus sediment transport has been already known to be the reason of bed deformation along wide meandering streams (da Silva et. al, 2006 and other references in this paper). However, in narrow meandering rivers, such as the one here, lateral "convective" behavior of flow plays an important role in increase of bed erosion and lateral sediment transport, as discussed above. The above-mentioned process justifies the occurrence of measured more bank and bank-toe (also berm-toe) erosion on section (1) than section (2) (Chs. 6.6 and 6.7).

In case of erodible banks, due to the large sediment supply from bank erosion in natural rivers, degradation at the bank-toe in the form of berm occurs as a consequence of sediment imbalance near the outer bank-toe. Nevertheless, the mentioned shifting process of maximum bed shear stress still causes the berm-toe to erode, resulting in decrease of berm width in downstream direction along the river bend as observed in Fig. (6-39b). This shifting of bed shear stress and consequent outer bank-toe erosion results in more bank retreat near the bend apex as shown in Fig. (6-43).

The position of maximum bed shear stress coincides with the talweg (pool) at the section upstream of the bend apex (Fig. 6-24), as was also mentioned by Yalin (1992), but not at the bend apex (Fig. 6-22). Similar findings have been also reported in fixed bank mobile bed experiment by Kühne (2003), for example in his figures (49) and (67). The reason of the mentioned non-coincidence at bend apex will be illustrated in Ch. 8.4.

Generally, it can be concluded that the path of maximum depth-averaged velocity defines the main path of suspended sediment transport and not necessarily bed erosion, especially at the bend apex. Therefore, the proximity of maximum depth-averaged velocity near the riverbank does not imply the maximum bank-toe erosion (refer to Fig. 6-10 and 6-17). On the other hand, the path of maximum bed shear stress represents the path of talweg (pool) upstream and downstream of the apex but not at bend apex in river bends with mild deflection angles such as in the present studied meander.

8.4 Bed evolution

In the following, the morphological bed evolution of the river bend in connection to the flow field is demonstrated based on the measurements presented in Ch. 6.6. One of the interesting features presented in this chapter was bi-directional development of pool along the river bend. Furthermore, as it has been pointed out above, the maximum bed shear stress does not

coincide with pool location at bend apex. The connection between these two mentioned issues is demonstrated first in the following. Finally, the dynamics of bed evolution across the river bend in respect to the flow regime is discussed.

The location of convectively accelerated and decelerated flow zones in meandering channels with corresponding increasing and decreasing sediment transport capacity, respectively, coincide with the erosion and deposition zones according to Eq. (2-4), assuming no suspended sediment (da Silva et al., 2006). Therefore, pool (talweg across a section) should form where the gradient of sediment transport (∇q) is maximum. In a sine-generated meandering channel with large deflection angle (70° in the mentioned laboratory test) this occurs downstream of the bend apex at outer bank, while in meanders with small deflection angles this should occur at the inner bank upstream of the apex (Yalin, 1992). The increase of local lateral bed slope due to the pool formation intensifies the local downward acceleration of flow similar to those generated across section (1) and (2) (Figs. 6-13 and 6-20), which results in deepening of talweg further.

8.4.1 Bed evolution along the river bend

In a uniform one-dimensional flow, the average bed shear stress increases linearly with hydraulic radius, given a constant energy slope. Therefore, it is expected that maximum bed shear stress occurs at the talweg (deepest water depth). However, as it has been mentioned above, the maximum bed friction velocity does not coincide with the location of talweg at the bend apex. This is due to the process of upstream propagation of the pool formed primarily downstream of the bend apex, where maximum bed shear stress coincides with the location of talweg (Kühne, 2003). Such a process has been also observed by the author in the laboratory experiment on bank erosion by Wilke (2008) in a sine-generated meandering rectangular channel at the hydraulics laboratory of Queen's University, for which the author had the opportunity to participate during his short scientific stay in March 2008. A similar process of upstream propagation of bed perturbation (for example, scour hole as a result of mining activities) in the river has been also reported by Martin-Vide and Ferrer-Boix (2005). The reason of such an upstream propagation of pool has been however not specified in the above-mentioned works.

In the above-mentioned laboratory channel, at the primary stage of erosion, the scouring pool started to form downstream of the apex (downstream of section 8_1 in Fig. 8-1) and extended gradually in downstream as well as upstream direction beyond the bend apex. The upstream propagation of the scoured pool was associated with lateral widening of the talweg. These observations suggest the existence of such process of upstream propagation of pool towards the bend apex mentioned in Ch. 6.6. The mechanism of upstream propagation of scouring pool can be explained as follows.

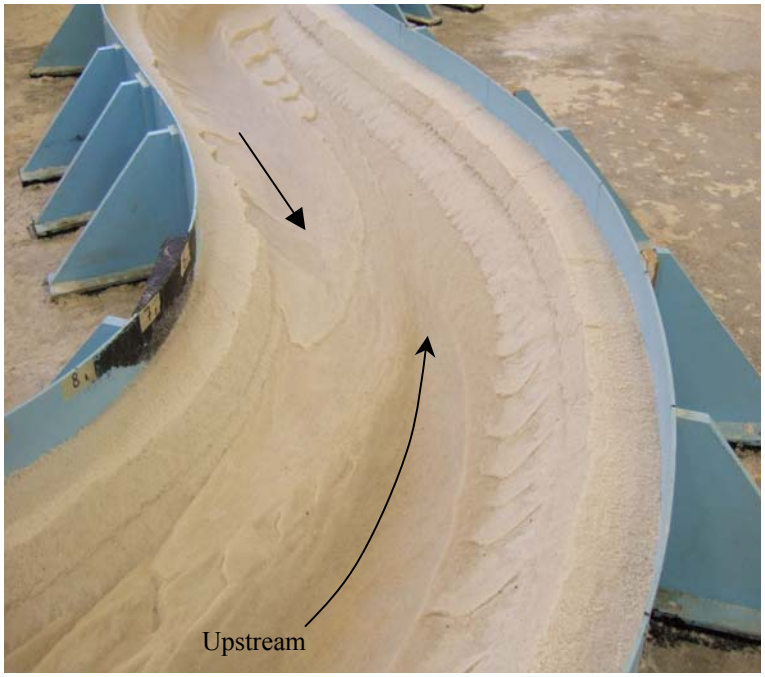

Figure 8-1 Upstream propagation of the pool in the sine-generated channel at Queen's University

Formation of the pool induces a perturbation in the riverbed, which propagates primarily downstream and with lower speed upstream. The downstream propagation is accelerated by intensification of cross circulation. Passage of the longitudinal flow over the upstream edge of the pool, which forms a step-like channel bed, results in flow separation in longitudinal direction (it is well-known that flow over a step results in flow separation depending on the step height and length; see e.g. Schlichting, 2006, Ch. 14.4). This kind of flow separation yields in formation of vertical eddies and reverse flow that transport sediments upstream of the pool thereby eroding the upstream face of the pool and elongating it in upstream direction (towards section 6_1 in Fig. 8-1). The mentioned mechanism of upslope-sediment transport is similar to that in scour hole upstream of a bridge pier, although with different origins but similar functionality, which cause upstream propagation of scour hole (Nasermoaddeli, 1999). Furthermore, the concentration of flow in the pool region causes the bed shear stress to increase, which results in further erosion of the pool due to sediment imbalance in this region. The local acceleration of flow by entrance to the pool is thought to be another reason for erosion of the chute-like pool entrance, which in turn results in upstream propagation and concave profile. A similar large scale process of concave profile of the rivers in longitudinal direction has been studied for example by Wright and Parker (2005).

In case of erodible banks, a large amount of eroded bank material from upstream bend is transported along the inner bank of the next meander bend (Fig. 8-2). This reduces the effective width of the channel section gradually towards the bend apex, which results in more concentration of the flow and cross circulation towards the centre and outer bank of the channel, contributing to the upstream advancement of pool. Additionally, it is well known that

cross circulation is mainly effective in point bar formation (for references see Yalin, 1992, p.199), which in turn reduces the effective channel width in a sense of self intensifying process. The propagation of the pool proceeds upstream (comprising bend apex) until a mild slope is reached at the upstream entrance to the pool so that no flow separation and reverse flow occurs (Schlichting, 2006, Ch. 14.4) and the longitudinal flow acceleration is not strong enough to cause erosion. Since the location of maximum bed shear stress is mainly a function of curvature, therefore, it does not coincide with the location of pool at bend apex due to the above-mentioned processes, which contribute to upstream propagation of the pool.

In contrast to the bend apex, the location of talweg in the process of its downstream propagation, coincides with the location of maximum depth-averaged velocity (also shown in Wilke, 2008 and Kühner, 2003) and maximum bed shear stress (Kühner, 2003) downstream of the bend apex. Similar process may have taken place to generate the talweg in Fig. (6-22). Therefore, it is not surprising that the maximum bed shear stress does not coincide with the location of talweg at the river apex, although this should be the case downstream as well as upstream of the bend apex.

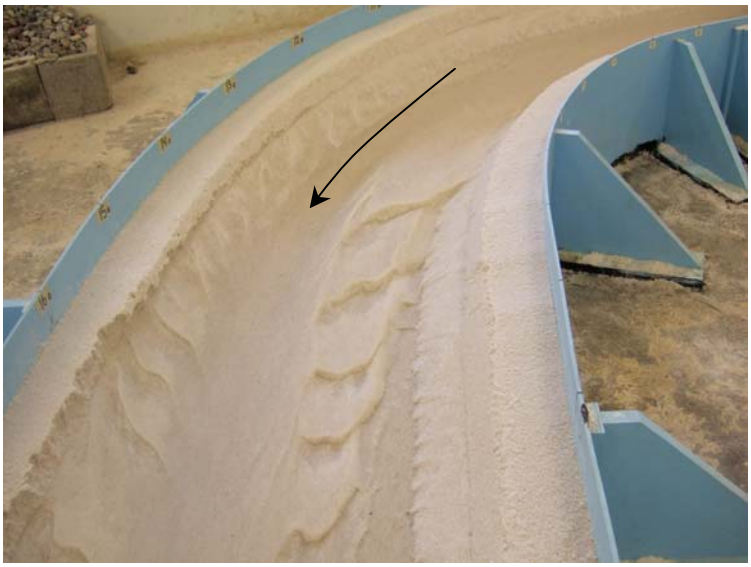

Figure 8-2 Effect of berm formation on upstream propagation of pool

8.4.2 Bed evolution across the river bend

For better investigation of the dynamics of bed evolution across the river, three typical cross sections have been selected from DEM of bathymetry (Fig. 6-39a to c), as depicted in Fig. (8-3). Due to the uncertainties regarding bathymetry measurements on Oct 24, 2007, as already illustrated in Ch. 6.6, this measurement was excluded from the current discussion.

During the first period, between July 20 and Dec. 10, 2007, the outer bank-toe has generally undergone erosion, which has resulted in deposition on the inner bank of all sections Fig. (8-3). The latter is partly due to the lateral transport of the eroded outer bank-toe material to

the inner bank by secondary currents, and partly due to excess sediment supply from upstream along the inner bank as discussed already above and in Ch. 8.3. The aggradation of the inner bank, in turn, contributes to deepening as well as pushing the talweg towards the centre of the channel as well as the outer bank. This results in more bed erosion near the outer bank-toe (or berm-toe) in a self-intensifying sense, especially at the apex.

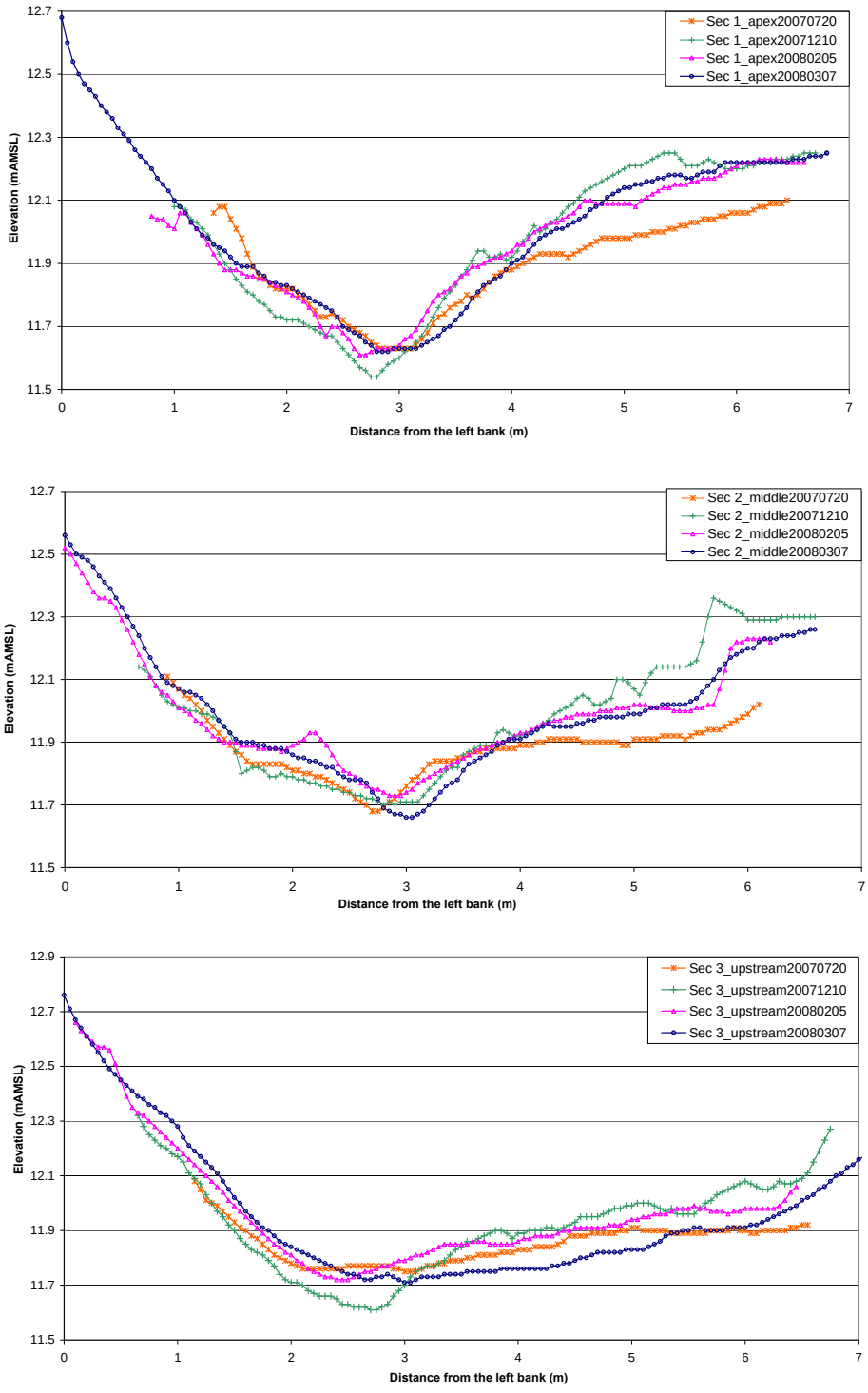

Figure 8-3 Shifting and widening of talweg. The vertical scale has been exaggerated for better observation

Differential bank surface scanning was not performed during the mentioned period, except once on Oct. 24, 2007. Therefore, it cannot be determined if the above-mentioned bank-toe erosion caused bank failure during this period.

Similar shifting of talweg due to excess sediment feeding from upstream along the inner bend has also been reported in the laboratory experiment of Wilke (2008). Assuming that the results of Wilke can be extended to the natural river here, it can be seen, for instance, from his figure B-16, reproduced here as Fig. (8-4), that the volume of deposited material at the inner bank is larger than the eroded volume at the outer bank-toe. Therefore, it can be concluded that the deposited material at this section of the inner bank is largely due to the transport of eroded outer bank material from upstream bend along the same bank side, as also illustrated by Yalin (1992,p.192). This process leads subsequently to shifting the talweg towards the outer bank.

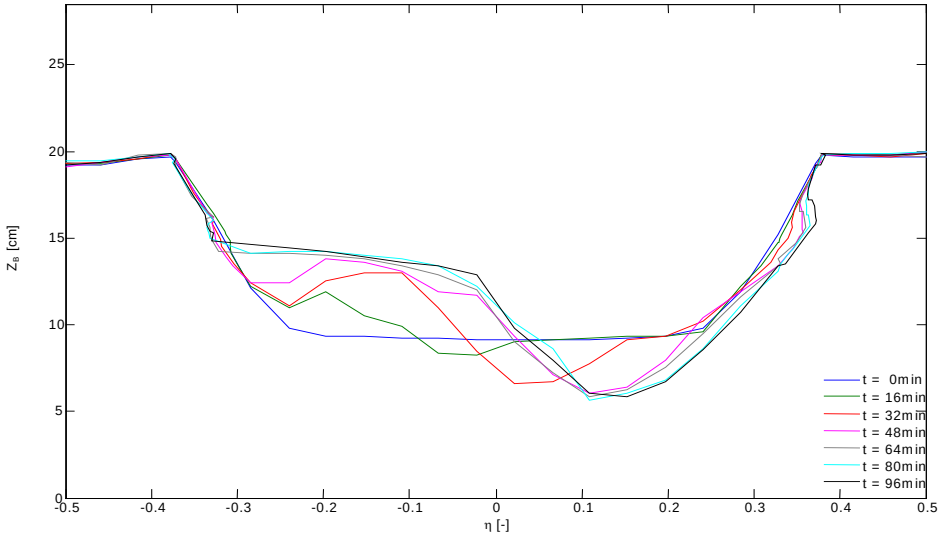

Figure 8-4 Section upstream of bend apex (7_2) in Wilke (2008). Positive value of η indicates outer bend

To examine this hypothesis for natural rivers, the net amount of sediment deposition /erosion across each section was computed for each period and summarized in Table (8-1). As seen from this table during the first period a large amount of net deposition across the river bend sections has been computed (at the bend apex, the deposition volume is more than three times the erosion volume). This shows a surplus of deposition across each section originating from upstream, considering the fact that deposition on the inner bank can be due to transversal and/or longitudinal sediment transport, assuming negligible deposition of suspended sediment due to the illustrated high flow velocity in this zone and measured low sediment concentration. The increasing amount of deposition towards the bend apex shows also accumulation of deposition volume towards apex, providing evidence for this hypothesis. The maximum and minimum erosion occurred at the bend apex and section (2), respectively.

Table 8-1 Net erosion (-) /deposition (+) per unit length across the three selected sections of the river bend

Period	Section	Deposition volume (m^3/m)	Erosion volume (m^3/m)	Net volume change (m^3/m)
1	1	0.45325	-0.1595	0.29375
	2	0.44375	-0.07	0.37375
	3	0.30325	-0.1445	0.15857
2	1	0.11125	-0.1320	-0.02075
	2	0.1375	-0.22025	-0.08275
	3	0.227	-0.117	0.11
3	1	0.118	-0.11375	0.00425
	2	0.08625	-0.12325	-0.037
	3	0.08625	-0.3295	-0.24325

In contrast to the previous period, outer bank-toe deposition associated with inner bank erosion was observed at all three sections along the bend in the second period (between Dec 10, 2007 and Feb 5, 2008). The deposition at the outer bank-toe reduced from bend entrance towards the bend apex, while erosion of inner bank is maximum at section (2) and minimum at the bend entrance. This pattern correlates well with the maximum bed shear stress path concept explained in Ch. 8.3, in which this path changes from inner bank at section (2) to the outer bank at section (1), bend apex. Therefore, more erosion has been measured at the inner bank at section (2) than at section (1). This shear stress pattern resulted in net deposition at the bend apex and net erosion at the two other sections as seen from Table (8-1). The deposition at the outer bank-toe should have been due only to bank failure during this period. However, no concurrent measurements of bank profile were carried out for this period to prove this claim.

But as observed from Fig. (6-49), between Oct. 24, 2007 and Jan. 23, 2008 (a time span within the above desired period) large bank retreat occurred along the outer bank, while between Jan. 23 and Feb. 5, 2008 no changes in bank profiles were observed. It is still unclear if the mentioned bank erosion took place exclusively between Oct. 24, 2007 and Dec 10, 2007 or includes the period till Jan. 23, 2008. To answer this question, it can be referred to the same period in the previous year. By comparing bank retreat process between Dec.12, 2006 and Jan. 30, 2007 (Fig. 6-47) with that between Oct. 24, 2007 and Jan. 23, 2008 (Fig. 6-49), it can be concluded that at least a part of bank retreat could have taken place between Dec 10, 2007 and Jan. 23, 2008, which has resulted in outer bank-toe deposition (Fig. 8-3). Nevertheless, deposition of fine material on the mild slope of the outer bank-toe during low flow regime could have additionally contributed to the outer bank deposition. The decreasing trend of bank-toe deposition volume towards the bend apex (Table 8-1), in spite of the almost increasing trend of bank retreat (Fig. 6-49), can be associated to the increase of bed shear stress near the bank-toe towards the bend apex, as explained above and in Ch. 8.3, which has removed more deposited material at the bend apex than at other sections.

The deposition at the outer bank-toe caused the flow to shift towards the inner bank by narrowing the talweg as well as aggradation of it. This resulted in more erosion on the inner

bank during the second period. Finally, it can be observed how the deepening process of the talweg has changed to widening process in this period.
In the third period, aggradation of the bank-toe proceeded and resulted in the talweg shifting towards the inner bank as well as deepening of the talweg. This process resulted in further erosion at the inner bank. As seen in Table (8-1), the net volume change across section (1) and (2) is close to zero, while at section (3), bend entrance, net erosion has occurred. According to Fig. (6-50), slight deposition at the bank-toe of section (2) and (3) is not due to deposition of failed bank material but rather to deposition of suspended sediment in the falling water stage during February 2008, as seen from the flow hydrograph in Fig. (6-8). This claim can be supported by the fact that the only significant bank failure occurred during this period at section (1), and most probably due to high flow event in March 2008 (Fig. 6-8). As observed from Fig. (6-50), the eroded bank material has not influenced the whole bed profile, but only the bank-toe. This suggests a limited effective width for deposition of failed bank material across the river channel. Additionally, it is clear from this figure that the aggradation volume at the bank-toe is larger than the erosion volume. By referring to Fig. (6-48) it is observed that bank erosion has occurred around bend apex. In Fig. (6-49), only a section of it has been presented, therefore, this imbalance of bank-toe deposition can be associated to downstream transport of failed bank material from adjacent failed bank material as well as bed load.

8.5 Interaction of Bed and bank processes

From the above-mentioned discussion, the interaction of bed and bank evolution process across the river bend can be summarized as follows in respect to the dynamics of the flow regime.
As shown schematically in Fig. (8-5), during high water stage, a relatively large amount of sediment is transported along the inner bend resulting in aggradation of the inner bank, which causes to shift talweg towards the outer bank (Fig. 8-5B) as measured during the first period mentioned above. This shifting of talweg towards the outer bank causes the flow to concentrate more in the talweg zone (pool) increasing the local bed shear stresses, which results in more bank-toe erosion. The steep outer bank profile in high water stage contributes to the rise of local bed shear stress near the bank-toe as well as development of secondary currents resulting in more bank-toe erosion and fluvial bank erosion. This leads to the increase of bank height and bank-toe slope beyond a critical value, which eventually triggers shallow slip failure along a steep failure surface, which may meet the bank profile under water stage (depending on the bank slope before failure) or extended as high as the water stage in the river.(Fig. 8-5B). In the latter case, an overhang is formed above the water surface, as shown in Fig. (8-5B). In both cases, an undercutting zone, comprising large positive slope (for example 76°) is created on the riverbank face in the submerged zone. Transport of eroded material by secondary currents to the inner bank, especially around the bend apex, contributes to the inner bend aggradation which results in more concentration of flow near the outer bank

and impacts the fluvial erosion and undercutting in a self-intensifying sense until eventually cantilever failure of the overhang occurs (Fig. 8-5C).

By deposition of failed bank material at the outer bank-toe and berm formation, the talweg is again shifted towards the inner bank (Fig. 8-5D), causing shifting of flow towards the inner bank. This results in inner bend degradation, as in second period mentioned above. The width of the berm crests reduces towards the bend apex due to the increase of intensity of the helical flow near the outer bank-toe and channel centre, as a consequence of formation of pure lateral flow.

It should be noted that the location of deposition of failed bank material depends not only on the slope of the bank-toe and bed near the bank-toe before the moment of failure but also on the type of failure and flow field. In the presence of berm with wide crest, the failure of the bank in the form of slump or undercutting results in aggradation of berm and does not primarily contribute to the bed evolution (section 3 in Fig. 6-50). In the case of relatively steep bank-toe, the failed bank material slips towards the talweg and deposits primarily there, forming a mild bank-toe slope. Generally, deposited failed bank material at the bank-toe as well as formed berm act as bank buttressing, which improves river bank stability. For more accurate analysis of near bank and bank-toe processes in submerged zones, a side-looking sonar system is required, since the applied RTK-GPS system could not measure at least a distance of 30 cm from side bank.

During low water stage, flow velocity and bed shear stresses are low over the mild slope of the outer bank-toe, especially upstream of the bend apex, resulting in deposition of sediment over outer bank-toe. This process is intensified during the summer by the growth of vegetation on the river bed, which causes more sediment deposition on the mentioned region. This type of deposition over or near the outer bank-toe results in the shifting of the talweg towards the inner bank and eventually inner bend degradation as observed in the above-mentioned last period. However, if the low flow event lasts for a longer period and is not followed by a high flow event (in contrast to the last period mentioned above) then bed erosion near outer bank-toe proceeds (Fig. 8-5E) and causes the shifting of the talweg towards the outer bank (Fig. 8-5F and G). Therefore, the dynamics of flow regime plays an important role in the morphological evolution.

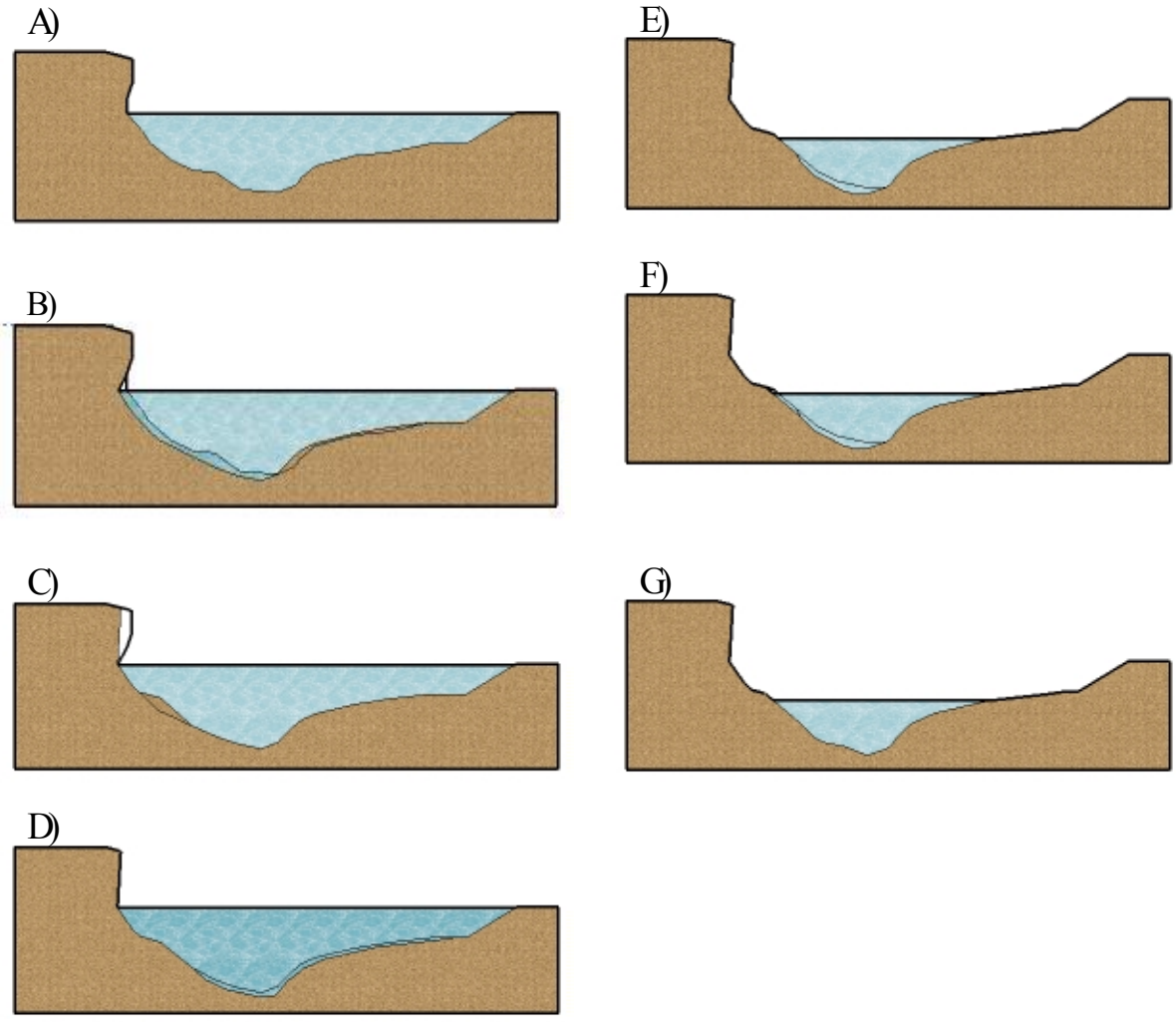

Figure 8-5 Illustration of interaction of bed and bank evolution in respect to the flow regime. A) Starting situation B) Bank-toe erosion and shallow shear failure in high water stage, causing undercutting. C) Cantilever failure and deposition of failed bank material forming berm. D) Pool (talweg) and inner bed erosion due to berm formation. E) Concentration of the flow near outer bank in low water stage and berm-toe erosion. F) Shear slip failure of berm-toe resulting in berm retreat G) Deposition of failed berm material at talweg. By rise of water stage the process starts from A again.

The bank evolution process gets even more complex during transient flow stages. In the rising flow regime, if the overhang submerges, tensile failure occurs due to the loss of matric suction in the submerged overhang zone and partly above it due to the capillary effect.

On the other hand, during flash drawdown period (flood recession) when water stage in the river drops fast compared to the water table in the river, the hydraulic head difference between perched water table and water stage in the river induces seepage flow from riverbank into the river. This process leads to the sapping failure leaving cavities in the bank surface.

Therefore, the shape of the flow hydrograph and frequency of peak flows play an important role in riverbank and bank-toe erosion. Flood frequency and duration are other significant factors in the intensity of bank erosion and the moment of the bank failure. The analysis of

laser scanning measurements revealed a considerable amount of bank erosion (15 cm^3/cm^2) in the bank-full flood event of 18 to 22 January 2007. This resulted from multiple flow peaks causing bank surface rewetting. On the other hand, during the two small flood events of 1 and 20 March 2007, each with a single peak, a relatively small amount of bank erosion (5 cm^3/cm^2) was measured (Nasermoaddeli and Pasche, 2008a).

8.6 Simulation of bank evolution

By means of the sensitivity analysis carried out in Ch. 7.3, the best combination of the parameters influencing intermediate morphological evolution were determined. Due to the lack of reliable bathymetry data of the riverbed for the period of simulation, the simulated profile of bed bathymetry was not used as a basis for assessment of the simulation runs and it will not be discussed here. Hence, bank profile especially the overhang shape formed the basis of judgment for determination of best value of parameters. Nevertheless, it can be observed from simulation results that bank-toe profile and its accurate simulation impact the undercutting process and its advancement. This suggests a need for better understanding of flow and sediment transport near bank-toe as well as distribution of failed bank material in this zone and across the river bend.

The performance of three of best simulation runs with coefficients of (a_2, a_1) = (4,6) for negative pore pressure binomial function are summarized in Table (8-2). For the assessment of the simulation runs the local distance of the upper edge and front of the overhang to the reference point on the left bank were used.

It is common in simulation of bank erosion to assess the accuracy of a numerical model according to the computed top edge of the bank. On this basis, the best simulation result was obtained in run number 45 with matric angle of 10° for all three profiles (Table 8-2), noting that the simulation results presented in this table show an excellent agreement with measurements (error is less than 4%) in all three runs. The result of this simulation runs and measured bank profiles at section (1) and (2) are depicted in Fig. (8-6) with respect to the initial measured bank profile as well as initial discretized mesh in conjugate domain. Neglecting the accuracy of simulation of bank-toe profile, due to the reason mentioned above, the face of the bank profile and most of the bank surface at section (2) was simulated very well in run 45. However, the small undercutting zone could not be reproduced in this run for this section. This can be related to effect of sapping, which was not considered in the present work. At section (1), overhang as well as bank profile could be simulated very well in run 45. This good result in spite of relatively large amount of bank retreat at this section, suggests that the current developed model should be capable of simulating bank erosion in longer periods with reasonable accuracy, although it should be still verified for other rivers with similar bank properties.

Table 8-2 Accuracy of bank erosion simulation

Section	Run	φ^u	φ^c	φ^b	Top edge (m)			Front(m)			Nose(m)		
					Simul.[a]	Meas.[b]	Error[c]	Simul.	Meas.	Error	Simul.	Meas	Error
1	30	85	60*	16	2.8805	2.9926	3.75	2.8779	2.9097	1.09	2.9523	2.9472	-0.17
	44	84	60	16	2.9116	2.9926	2.71	2.9197	2.9097	-0.34	2.9743	2.9472	-0.92
	45	84	60	10	2.9463	2.9926	1.55	2.9274	2.9097	-0.61	2.9871	2.9472	-1.35
2	30	85	60*	16	2.3643	2.3821†	0.75	2.3375	2.3404	0.12	2.4415	2.3414	-4.28
	44	84	60	16	2.3919	2.3821†	-0.41	2.3564	2.3404	-0.68	2.44	2.3414	-4.21
	45	84	60	10	2.3811	2.3821†	0.04	----- ‡	2.3404		----- ‡	2.3414	
3	30	85	60*	16	2.4101	2.4101	0.00	2.2762	2.4018	5.23	2.4310	2.4310	0.00
	44	84	60	16	2. 4101	2. 4101	0.00	2.3260	2.4018	3.16	2.4310	2.4310	0.00
	45	84	60	10	2. 4101	2. 4101	0.00	2.3272	2.4018	3.11	2.4310	2.4310	0.00

a Simulated distance in meter to the reference point on the left bank

b Measured distance in meter to the reference point on the left bank

c Error in percent calculated as (Measured - Simulated) / Measured × 100

* The (slip) shear failure type with most critical failure slope of 42.3° and largest allowable bank slope of 60°

† Ignoring the extra projection of the hanging soil block by vegetation roots on bank top with a distance equal to 2.4740 m

‡ No overhang has been predicted (a cantilever failure of overhang has been predicted)

The location of simulated "front" is one of the important indexes, as it shows how well undercutting advancement has been simulated. Based on this criterion the best simulation result was obtained in run 44, while in run 45, no overhang was predicted for section (2). River bank top at section (3) has been simulated precisely in all above-mentioned three runs, however relatively large error was associated with front calculation. This implies that undercutting has been overestimated at this profile. This might have been due to the inaccurate initial bed profile, which influences bank-toe slope and undercutting, respectively.

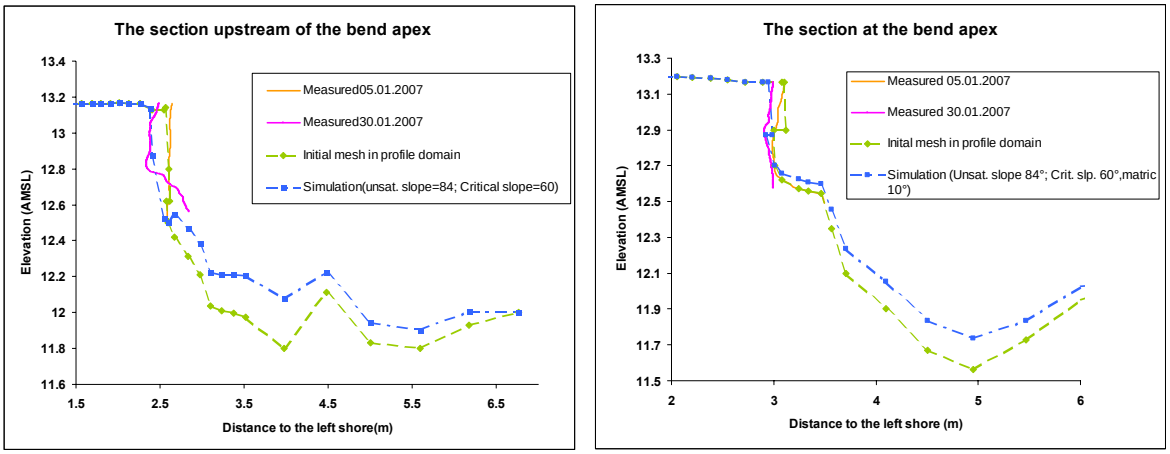

Figure 8-6 The simulated bank retreat versus the measured one for section (1)(right) and section (2) (left)

It is not expected here for the nose location to be computed precisely due to the limitation of positive unsaturated dense angle of repose imposed in the numerical model as well as the assumption of horizontal tensile failure plane (note the initial position of nose in conjugate domain compared with measured one for the section of bend apex in Fig. 8-6). Therefore, this

parameter has not been used here for assessment of accuracy. However, it is listed in Table (8-2) to show the associated error due to the mentioned limitation in the current model.

Appreciable improvement or deterioration in simulations was not attained by explicit inclusion of the vegetation effect. This can be related to two major reasons. First, there is great uncertainty associated with the applied equation, which accounts for cohesion due to the vegetation root (Eq. 3–44), as demonstrated by Pollen and Simon (2005). Second, the complex interaction of different parameters in bank erosion process in unsteady flow makes the effect of root reinforcement non-linear in respect to the time of the failure. Furthermore, the additional cohesion due to the vegetation roots is a function of the length of slip failure. The latter parameter is affected by the water stage and geometry of the bank, which in turn is controlled by undercutting process that depends on the water stage, flow regime, river bend curvature and the position of the profile under study along the bend way.

The simulation results suggest that the effect of cohesion due to the vegetation root on the stability of the overhang can be approximately included implicitly in the parameters of the pore pressure function. The approximately identical bank profiles at section (1) and (2) with and without inclusion of vegetation effect (Fig. 7-13) provides support for this hypothesis in simulations with the assumption of hydrostatic distribution of negative pore water pressure in the riverbank particularly at section (1).

To show the superiority of the present proposed method over the currently practiced methods, the result of run 45 has been compared in Fig. (8-7) with simulation runs assuming one critical slope for the whole bank profile (similar to the method of Hafner, 2008) and two different critical slopes for submerged and dry zone of bank without inclusion of pore pressure effect (similar to the method of Nagata et al., 2000). In the former case, the angle of failure surface was set to the critical angle of repose, which is commonly assumed to be equal to the friction angle (42.3°) and in the latter case, additionally, the stable bank angle in dry zone over water table has been set to 84°, as in run 45.

As seen from these figures, a large improvement has been obtained by application of the new proposed method. The associated error of computation of top edge of the bank using the mentioned methods is summarized in Table (8-3). In this table the amount of measured bank retreat of the upper bank edge has been compared with the amount of bank retreat in numerical domain (Fig. 8-6) during the simulation period. Since the simulated bank retreat for section (3) was equal to zero and equal to measurement, it is not presented in this table.

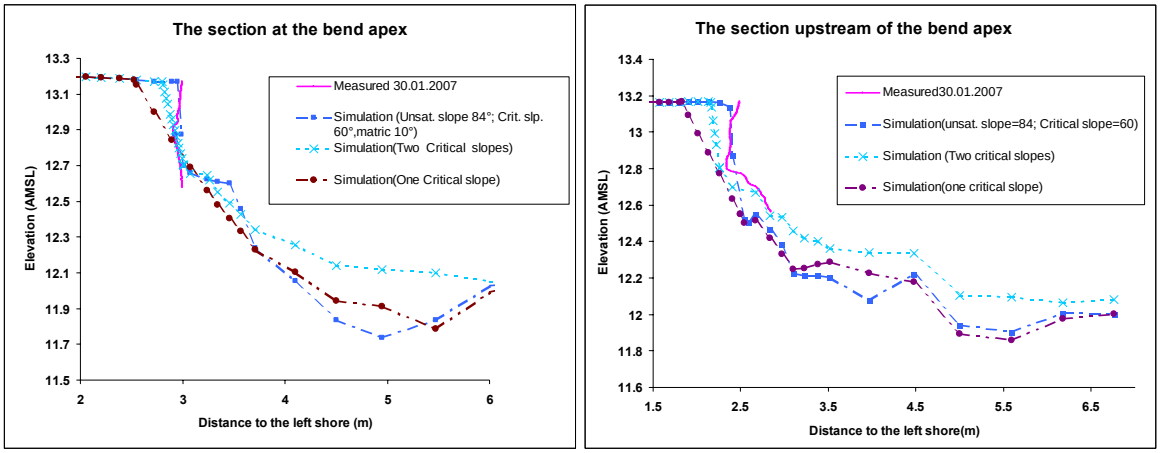

Figure 8-7 Comparison of the accuracy of the bank erosion simulation using the new proposed model and common methods

As seen from this table, the bank retreat has been overestimated 4.6 cm and 3.3 cm using the current proposed method for section (1) and 2, respectively. While the overestimation of bank retreat with common mention methods are from 19 cm to more than 58 cm. Although the present proposed method has not precisely computed the bank retreat, but it has largely improved the accuracy compared to the currently available methods. More investigation is required in different rivers to verify this new method. It should be noted that application of seepage modelling might enhance the simulation results with the price of more computational effort. However, the most important aspect in improvement of accuracy of bank erosion predication lies in more detailed investigation of overhang failure mechanism in non-cohesive soils, pore pressure distribution as well as bed evolution near outer bank.

Table 8-3 Bank retreat of the upper edge of the bank (measurement versus computation) during simulation phase

Section number	Measured bank retreat (m)	Proposed model		Double critical slopes		Single critical slope	
		Computed	Error*(%)	Computed	Error(%)	Computed	Error(%)
1	0.1137	0.1597	40.45	0.3075	170.44	0.5838	413.45
2	0.1559	0.1889	21.16	0.4151	166.26	0.7444	377.48
3	0.0000	0.0000	0.00	0.2525	------	0.2070	------

* Absolute over-estimation error of bank retreat (computed– measured) / measured × 100

9 Conclusions and suggestions for future research

9.1 Conclusions

Restoration of the rivers to their natural meandering form as well as environmental impacts of lateral migration of rivers on infrastructures and dwellers on margins of the rivers especially under climate change and anthropogenic effects, calls for a systematic improvement in understanding of the riverbank migration process. The complex processes of morphological evolution of the riverbed and -bank particularly along meanders have made the research on bank erosion processes challenging. The commonly available methods for the analysis of non-cohesive riverbank erosion are not sufficient to analyse and model the naturally dense non-cohesive (sandy) riverbank evolution processes in short to medium timescales. Since these methods have been originally developed for loose non-cohesive grains (such as gravel) and are either limited to bank erosion in bank full stage (for example, Pizzuto, 1990; Mosselman, 1992; Duan et al., 2001; Olsen, 2003; Schmautz, 2003; Hafner, 2008) or simplified methods of intermediate bank erosion ignoring overhang formation and cantilever failure (for example, Nagata et al., 2000). During intermediate flow stages (not bank full stage), bank erosion does proceed and causes retreat of non-cohesive riverbank mainly through a chain of bank-toe erosion, undercutting and cantilever failure processes. Ignoring such processes in the simulation of riverbank erosion results in overestimation of bank retreat.

The present work is a contribution to gain knowledge on riverbank erosion process including undercutting and cantilever failure in dense non-cohesive (sandy) soils. Application of the state-of-the-art techniques of measurement enabled acquiring novel knowledge on morphological processes of bed and bank evolution in a shallow non-cohesive alluvial river in the North of Germany. The difficulty in the analysis of digital elevation model of the complex three-dimensional riverbank surface was overcome by introducing a simple coordinate transformation. Based on the analysis of outer riverbank surface along the river bend, measured by laser scanner, and measurement of hydraulic parameters, it was found that undercutting due to the slip failure as well as cantilever failure were the major bank failure mechanisms in non-cohesive (sandy) soils. However, the measurement method could not provide either evidence of the occurrence or importance of sapping in the study site.

Furthermore, it was found that bank failure process in the submerged zone is mainly controlled by bank-toe processes and cantilever failure by undercutting process in non-cohesive (sandy) riverbanks. In this regard, the dynamics of flow regime (especially magnitude, frequency and duration of peak flow) is a key factor controlling bank erosion through affecting pore pressure, bed as well as bank-toe evolution.

The study of bank-toe process as an integrated part of the morphological evolution process across the whole river bend showed that it is controlled by a number of processes including flow and bed shear stress distribution as well as sediment transport across and along the river bends especially in compact channels such as the one in the study case. Therefore, it seems that considering the flow field and sediment transport only near the riverbank in modelling bank erosion process is not sufficient.

Quantifying the evolution of integrated bed and bank profiles revealed that the failed bank materials are mainly deposited at the bank-toe in form of berm and bar, protecting the riverbank from further erosion, especially at the bend entrance. However, around the bend apex, where maximum bed shear stress across the section is closer to the outer bank, berm-toe erosion causes the berm width to reduce, resulting in more bank erosion in this zone.

A mathematical method has been developed based on the gained knowledge to enable morphodynamic simulation of the riverbank retreat due to undercutting and cantilever failure in a predictive way. This was accomplished by developing a numerical $2^1/_2$ dimensional morphodynamic model with an innovative domain decomposition method, which enabled simulation of complex formation of riverbank. The complexity of the bank surface has been limited to the high positive slopes in submerged and overhang zones while allowing discontinuity of bank profile due to formation of the overhang.

A single-layered riverbank has been considered in the present work. The effect of compaction, negative pore water pressure as well as vegetation has been simplified in the mathematical model. Sapping failure due to the seepage from riverbank has not been considered. In the hydrodynamic model, dispersion terms were not included. The diffusion coefficient in the sediment transport model (ADV-DIFF equation) has been assumed to be equal to the eddy viscosity. Uniform sediment (poorly graded sediment) has been considered for the bed and bank material (based on the field measurements), which excludes armouring and grain size sorting effect.

The validation of the model proved that the current proposed approach is capable of simulating well the undercutting due to slip failure and cantilever failure process in unsteady flow. Furthermore, the good agreement of simulation results with measurement implies that the two mentioned mechanisms have been the prevailing bank erosion processes in the simulation period. Limitation of most critical shear failure slope of the overhang to positive values in the present simulation of cantilever failure resulted in deviation of overhang surface from the measured profiles.

The simulation results suggest that the effect of compaction of non-cohesive (sandy) soils in riverbank failure analysis can be considered by means of an increased angle of repose. Additionally, the timing of cantilever failure could be simulated reasonably well in spite of application of a simple binomial function for the computation of negative pore water pressure. Timing of the bank failure is an important index for validation of bank erosion models in unsteady flow condition. The results suggest that in the case of shallow slip failure, it is

reasonable to apply a simplified approach to model pore pressure dynamics in the riverbank. Neglecting the approximated negative pore pressure has proved to prevent formation of overhang (immediate failure of overhang as soon as it is formed) during the simulation period. Nevertheless, determination of the order and coefficients of the polynomial is not trivial and should be determined by trial and error.

Furthermore, the effect of additional cohesion due to small vegetation roots in the overhang could be implicitly considered in the parameters of the suggested function of negative pore water pressure. However, it should be noted that the complex interaction of these two parameters was found to be not linear with respect to the dynamics of the flow.

Although application of the lump method of distribution of failed bank material could solve the problem of numerical instability, the method is not physically based. Furthermore, it was not possible to assess the performance of this method, due to insufficient bathymetry measurement in the simulation phase.

Finally, the suggested mathematical approach should be further tested in natural streams over larger time scales.

The above-mentioned modelling system is a contribution to provide the engineers a better understanding of river migration and morphodynamic changes in natural rivers thereby supporting them in their task to restore good ecological conditions and natural retention to mitigate floods as requested by the EU Water Framework Directive and EU Flood Directive. Furthermore, it shall support the insurance companies with a more reliable tool for prediction of bank erosion-related risk assessment of infrastructures and dwellers along the margins of the rivers.

9.2 Suggestions for future works

9.2.1 Measurement techniques

The frequency of bathymetry and bank surface measurements plays an important role in quantification of (event oriented) morphological processes. It is suggested that such measurements be achieved before, during and after flood events as well as during the low flow events (at least once a month) to quantify the role of dynamics of flow regime on bed and bank morphological evolution more precisely and reliably. Online gauging stations together with weather forecast data can help deciding the right time of measurement, if the weather condition makes the measurement feasible during flood events.

Application of side looking sonar instrument is suggested for reliable investigation of bank-toe processes, especially the mechanism of distribution of failed bank material and its consequent evolution in high flow events.

For the investigation of mechanism and the effect of pore pressure distribution on different types of undercutting as well as cantilever failure, registering the time of failure is an important issue. As already mentioned the current measurement methods suffer either from low temporal or spatial resolution. Therefore, it is suggested to remove the limitation of PEEP method (light dependent), by applying a grid of tilting switch sensors arranged in series in

form of a shaft installed into the riverbank surface, so that the time of individual detachment of each of these sensors is recorded in a data-logger as the time of failure. In this way the failure moments occurring at night as well as the amount of erosion can be recorded.

It is recommended to install mini-tensiometers in the overhang zone of the bank to improve the understanding of the mechanism of tensile and shear cantilever failure in relation to the pore pressure dynamics in the sandy riverbanks.

9.2.2 Pre- and post processing

As already mentioned, due to the lack of proper tool for the generation and analysis of complex 3D pattern (including negative slopes) of bank surfaces, a special local coordinate transformation was applied. However, this led to some limitations in integration of bed bathymetry surfaces with bank surfaces for the purpose of analysis of interaction of bed and bank evolution in three dimensions. Therefore, there is a need for development of such tools to keep up with new technologies in the study of bank erosion, such as terrestrial laser scanning.

9.2.3 Theory

As shown in previous chapters, the distribution of bed shear stress across and along the river bend plays an important role in bank-toe and consequently bank erosion. Hence precise computation of bed shear stress in unsteady flow plays a key role in correct computation of the rate of bank retreat. The commonly available bed shear stress formulations, even those developed for unsteady or non-uniform flow, are not applicable in river bends, at least near the outer bank-toe. Therefore, it is suggested that the proposed general equations of bed and bank shear stress (refer to Appendix A-2) are examined, using detailed measurement of 3D velocity profile, to study the distribution of bed shear stress across river bends. Furthermore, it is suggested that the mentioned equations are implemented in numerical models for the computation of bed shear stress in sediment transport and bed evolution models.

It is required that in addition to the field measurements, controlled laboratory measurements be accomplished to investigate the mechanism of seepage failure as well as develop an analytical method for determination of failure surface in respect to the bank geometry, pore pressure distribution in the river bank, water stage in the river and soil properties. The same deficiency also holds for cantilever failure mechanism of non-cohesive riverbank, which should be investigated in the controlled laboratory experiments, in addition to field measurements

Furthermore, the pattern of riverbank failure is extremely irregular in longitudinal direction, which necessitates application of three-dimensional bank stability analysis in a deterministic way. Such methods have already been developed for slope stability of soils, which should be extended to riverbank failure analysis. Additionally, application of more sophisticated methods of stability analysis such as those based on numerical solution of the governing equations of the soil stress and deformation (using finite element method or smoothed particle hydrodynamics method) should be promising in the analysis of riverbank stability in saturated /unsaturated zones.

The mechanism of deposition and distribution of failed riverbank material has been less studied. Due to its significant effect on basal processes, this issue requires a special attention and much further laboratory and field investigation.

The process of bed load transport along a river bend has been invariably studied in the case of an ideal (infinite circular channel) bend, which can be at most applied to the centreline of a natural channel. There is an urgent need to investigate the bed load transport process along the outer bank-toe as well as inner bend in respect to the flow curvature and types of circulatory flow.

9.2.4 Numerical method

The current proposed discretization method and innovative data model showed a promising method for simulation of complex natural riverbank geometry. However, it is sill not capable to model negative bank slopes that might be generated due to seepage failure as well as cantilever failure. Therefore, it is recommended that the current method be improved to remove the mentioned limitations.

It is suggested to improve the numerical stability of discretized suspended sediment transport equation by further investigation of discretization of the source term due to eroded bank material. It is more realistic and physically based to allow flow field and sediment property to determine what percentage of which sediment size class is transported and where the rest is deposited.

References

[1] Ackers, P. & White, W.R., 1973. Sediment transport new approach and analysis. *J. Hyd. Div., ASCE*, 99, 2041-2060.

[2] Afzalimhr, H., Dey, S. & Rasoulianfar, P., 2007. Influence of decelerating flow on incipient motion of a gravel-bed stream. *Sadhana*, 32(5), 545-559.

[3] Amiri-Tokaldany, E., Darby, S. & Tosswell, P., 2007. Coupling bank stability and bed deformation models to predict equilibrium bed topography in river bends. *J. Hydr. Engrg*., *ASCE ,* 133(10),1167-1170.

[4] ASCE Task Committee on Hydraulics, Bank Mechanics, and Modelling of River Width Adjustment, 1998a. River width adjustment, I: Processes and mechanisms. *J. Hydr. Engrg*., *ASCE ,*124(9),881-902.

[5] ASCE Task Committee, 1998b. River width adjustment. II Modelling. *J. Hydr. Engrg*., *ASCE ,* 124(9), 903-917.

[6] ASCE Task Committee on Turbulence Models in Hydraulics Computations, 1988a. Turbulence Modelling of surface water flow and transport. Part I. *J. Hydr. Engrg*., *ASCE ,*114(9),970-991

[7] ASCE Task Committee on Turbulence Models in Hydraulics Computations, 1988b. Turbulence Modelling of surface water flow and transport. Part II. *J. Hydr. Engrg*., *ASCE ,*114(9), 992-1013

[8] ATV_DVWK, 2003. *Feststofftransportmodelle für Fließgewässer.* Arbeitsbericht WW-2.4.

[9] Bastos de Vasconcellos, C.A. & Amorim, J.C.C., 2001. Numerical simulation of unsaturated flow in porous media using a mass-conservative model. In: *Proceedings of 16th Brazilian Congress of Mechanical Engineering*. November ?, Uberlândia, Brasil.

[10] Bennett, S.J. & Best, J.L., 1995. Mean flow and turbulence structure over fixed, two-dimensional dunes: implications for sediment transport and bedform stability. *Sedimentology*, 42, 491-513

[11] Biron, P.M., Robson, C., Lapointe, M.F.& Gaskin, S.J., 2004. Comparing different methods of bed shear stress estimates in simple and complex flow fields. *Earth Surf. Process. Landforms,* 29, 1403–1415.

[12] Bitelli, G., Dubbini, M. & Zanutta, A., 2004. Terrestrial laser scanning and digital photogrammetry techniques to monitor landslide bodies, In *10thISPRS*

Congress, Istanbul, Tukey.

[13] Bjerklie, D.M., Dingman, S.L., Vorosmarty, C.J., Bolster, C.H. & Congalton, R.G., 2002. Evaluating the potential for measuring river discharge from space, *Journal of Hydrology*, 278 (1-4), 17-38.

[14] Blanckaert, K. &Graf, W.H., 1999. Outer-bank cell of secondary circulation and boundary shear stresses in open-channel bends. In proceedings of: *IAHR Symposium on River, Costal and Estuarine Morphodynamics*, Spt. 6-10, Genova, Italy.

[15] Borah, D.K., Alonso, C.V. & Prasad, S.N., 1982. Routing graded sediments in streams: formulations. *J. Hydr. Div. ASCE,* 108, No. HY12.

[16] Boussinesq, J., 1877. Théorie de l' écoulement tourbillant. *Mem. Pre. Par. Div. Sav.* 23. Paris

[17] Bradford, J.M. & Piest, R.F., 1980. Erosional development of valley-bottom gullies in the upper mid western united states. In: Coates, DR., Vitek, JD: (Eds.) *Thresholds in geomorphology*. George, Allen and Unwin Publishers, London. 75-101.

[18] Brasington, J., Rumsby, B.T. & McVey, R.A., 2000. Monitoring and Modelling Morphological change in Braided Gravel-Bed River Using High-resolution GPS-based Survey. *Earth Surface Processes and Land Forms*, 25, 973-990

[19] Bridge, J. S., 1977. Flow, bed topography, grain size, and sedimentary structure in open channel bends: a three dimensional model. *Earth Surf. Process. Landforms*, 2,401-416.

[20] Bridge, J. S., 1992. A revised model for water flow, sediment transport, bed topography and grain size sorting in natural river bends. *Water Resources Research,* 28(4), 993-1013.

[21] Brownlie, W.R., 1981.*Compilation of alluvial channel data; laboratory and field*, Report KH-R-438, W.M. Keck Lab. of Hydraulics and Water Resources, California Institute of Technology, Pasadena, California.

[22] BWK, 1999. *Hydraulische Berechnung von naturnahen Fließgewässern*, Merkblatt 1/1999

[23] Cancienne, R.M., Fox, G.A. & Simon, A., 2008. Influence of seepage undercutting on the stability of root-reinforced streambanks. *Earth Surf. Process. Landforms* 33, 1769–1786.

[24] Cao, Z., 1997. Turbulent bursting-based sediment entrainment function. *J. Hydr. Engrg., ASCE,* 123(3),233-236.

[25] Cao, Z., 1999. Equilibrium near-bed concentration of suspended sediment. *J. Hydr. Engrg., ASCE,* 125(12),1270-1278.

[26] Cao, Z. & Carling, P.A., 2002a. Mathematical modelling of alluvial rivers: reality and Myth, Part 1: General review. *Water and Maritime Engineering,* 154(3), 207-219.

[27] Cao, Z. & Carling, P.A., 2002b. Mathematical modelling of alluvial rivers: reality and Myth, Part 2: Special issues. *Water and Maritime Engineering,* 154(4), 297-307.

[28] Carson, M.A. & Kirkby, M.J., 1972. *Hillslope form and process.* University press, Cambridge.

[29] Casagli, N., Curini, A., Cargini, A., Rinaldi, M. & Simon, A., 1997. Effects of pore water pressure on the stability of steam banks: preliminary results from the Sieve river, Italy. In: Wang, S.S.Y., Langendoen,E,J., Shields,F.D.Jr. (Eds.), *Proceedings of the Conference on Management of Landscapes Distributed by Channel Incision*. 19-23 May, Oxford Campus, The University of Mississippi, 243-248.

[30] Casagli, N., Rinaldi, M., Cargini, A. & Curini, A., 1999. Pore water pressure and stream bank stability: results from a monitoring site on the sieve river, Italy. *Earth Surf. Process. Landforms*, John Wiley and Sons, 24, 1095-114.

[31] Celia, M.A., Bouloutas, E.T & Zarba, R.L., 1990. A general mass-conservative numerical solution for the unsaturated flow equation. *Water Resources Research*. 26(7), 1483-1496.

[32] Celik, I. & Rodi, W., 1998. Modelling suspended sediment-transport in nonequilibrium situations. *J. Hydr. Engrg., ASCE,* 114(10), 1157-1191.

[33] Chang, H.H., 1980. Geometry of gravel streams. *J. Hydr. Engrg., ASCE,* 106(9),1443-1456.

[34] Chang, H.H., 1988. *Fluvial processes in river engineering*. John Wiley & Sons, New York, NY, pp.420.

[35] Chanson, H., Takeuchi, M.& Trevethan, M., 2007. High-frequency suspended sediment flux measurements in a small estuary. In *Proceedings of* 6th *International Conference on Multiphase Flow, ICMF 2007*, 9 – 13 July, Leipzig, Germany.

[36] Chen, D. & Duan, J.G., 2006. Modelling width adjustment in meandering channels. *Journal of Hydrology* 321,59-76.

[37] Cheng, K.J., 1984. Bottom-boundary condition for Non-equilibrium transport of sediment. *J. Geophysical Research*, 89(c5),8209-8214.

[38] Chiu,C.L. & Lin, G.F., 1983. Computation of 3D flow and shear in open channels, *J. Hydr. Div., ASCE,* 109, 1424-1440.

[39] Corey, A.T., 1986. *Mechanics of immiscible fluids in porous media.* Water Resources Publications.

[40] Couper, P.R. & Maddock, I.P., 2001. Subaerial river bank erosion processes and their interaction with other bank erosion mechanisms on the river Arrow, Warwichshire, UK. *Earth Surf. Process. Landforms*, John Wiley and Sons, 26(6), 631-646.

[41] Couper, P.R. & Maddock, I.P., 2002. Insights into river bank erosion processes derived from analysis of negative erosion-pin recordings: Observations from three recent UK studies. *Earth Surf. Process. Landforms*, John Wiley and Sons, 27(1), 59-79.

[42] Creed,E.L., Pence,A.M. & Rankin,K.L., 2001.Inter-Comparison of Turbidity and Sediment Concentration Measurements from an ADP, an OBS-3, and a LISST. In: *Proceedings of OCEANS 2001 MTS/IEEE Conference*, Honolulu,

HI., 3, 1750-1754.

[43] Curini, A., 1998. *Analisi dei processi di sponda nei corsi d'acqua, Universita degli Studi di Firenze, Dipartimento di Scienze della Terra*, 147, unpublished thesis.

[44] da Silva, A.M.F., El-Tahawy, T., Tape, W.D., 2006.Variation of flow pattern with sinuosity in sine-generated meandering streams. *J. Hydr. Engrg., ASCE*, 132(10), 1003-1014.

[45] Dapporto, S., Rinaldi, M. & Casagli, N., 2001. Failure mechanisms and pore water pressure conditions: Analysis of a riverbank along the Arno river (Central Italy). *Engineering Geology*, Elsevier. 61, 221-242.

[46] Dapporto, S., Rinaldi, M., Casagli, N. & Vannocci, P., 2003. Mechanics of riverbank failure along the Arno river, Cental Italy. *Earth Surf. Process. Landforms*, John Wiley and Sons, 28(12), 1303-1323.

[47] Darby, S.E. & Thorne, C.R., 1994. Prediction of tension crack location and riverbank erosion hazards along destabilized channels. *Earth Surf. Process. Landforms*, John Wiley and Sons, 19, 233-245.

[48] Darby, S.E. & Thorne, C.R., 1996a. Stability analysis for steep, eroding, cohesive riverbanks. *J. Hydr. Engrg., ASCE,* 122(8), 443- 454.

[49] Darby, S.E. & Thorne, C.R., 1996b. Numerical simulation of widening and bed deformation of straight sand-bed rivers. I: model development. *J. Hydr. Engrg., ASC,*. 122(4),184-193.

[50] Darby, S.E. & Thorne, C.R., 1996c. Development and testing of riverbank-stability analysis. *J. Hydr. Engrg., ASCE,*122(8), 443-454.

[51] Darby, S.E. & Thorne, C.R., Simon, A.,1996. Numerical simulation of widening and bed deformation of straight sand-bed rivers. II: model evaluation. *J. Hydr. Engrg., ASCE,* 122(4),194-202.

[52] Darby, S.E. & Thorne, C.R., 1997. Discussion of "Development and testing of riverbank-stability analysis*". J. Hydr. Engrg., ASCE,*123(11), 1052-1053.

[53] Darby,S.E., Alabyan, A.M.& Van de Wiel, M.J., 2002. Numerical simulation of bank erosion and channel migration in meandering rivers. *Water Resources Research*, 38(9), 1163, 2, 1-21.

[54] Darby,S.E., Rinaldi,M. & Dapporto, S., 2007. Coupled simulations of fluvial erosion and mass wasting for cohesive river banks. *J. Geophysical Res*. 12 (F03022), 1-15.

[55] de Vriend, H.J., 1981. *Steady flow in shallow channel bends*. Report No. 81-3, lab. Fl. Mech. Dept. Civ. Eng. Delft Univ. Techn.

[56] Deines, K.L., 1999. Backscatter Estimation Using Broadband Acoustic Doppler Current Profilers. In: Anderson et al., (Eds.), *Proceedings of the IEEE 6th Working Conference on Current Measurement Technology*, pages 249-253.

[57] Duan, J.G. & French, R., 2001. Simulation of meandering channel migration processes with an enhanced two-dimensional numerical model. *In: World Water and Environmental Resources Congress, Bridging the gap: meeting the world's water challenges*. Orlando, Fla.

[58] Duan, J.G., Wang, S.S.Y. & Jia, Y., 2001. The application of enhanced CCHE2D model to study alluvial channel migration processes. J. Hydr. Res. 39(5), 1-12.

[59] Duan, J.G. & Nanda, S.K., 2006. Two-dimensional depth-averaged model simulation of suspended sediment concentration distribution in a groyne field. *Journal of Hydrology*, 327, 426-437.

[60] DVWK, 1989. *Hydraulische Berechnung naturnaher Fließgewässer*, Merkblatt Heft 220, Paul Parey Verlag, Bonn

[61] Einstein, H.A., 1950. *The bed load function for sediment transportation in open channels*. Technical Bulletin 1026, U.S. department of Agriculture, Soil Conservation Service, Washington, D.C.

[62] Einstein, H.A. & Barbarossa, N., 1952. River channel roughness. Transaction of the ASCE, 117 (2528).

[63] Elder, J.W., 1959. The dispersion of marked fluid in turbulent shear flow. *J. Fluid Mech*. 5, 544-560.

[64] Endo T & Tsuruta, T., 1969. *On the effect of tree roots upon the shearing strength of soil*. Annual Report of the Hokkaido Branch, Forest Place Experimental Station, Sapporo, Japan, 167–183.

[65] Engelund, F., 1974. Flow and bed topography in channel bends. *J. Hdyr. Div. ASCE,* 100 (HY11), 1631-1648.

[66] Engelund, F. & Hansen, E., 1967. *A monograph in sediment transport in alluvial streams*. Tekniks Forlag, Copenhagen, Denmark.

[67] Entwistle, N.S., Heritage, G.L., Johnson , K. & Hetherington, D., 2007. Repeat Terrestrial Laser Scanner Survey of Pebble Cluster Creation and Formation in response to flow change. *Annual Conference, Remote Sensing and Photogrammetry Society*, Newcastle, Upon Tyre.

[68] Fang, C., Mao, J. & Lu, W.2005. 2D depth-averaged sediment transport model taken into account of bend flows. In *US-China Workshop on Advanced Computational Modelling in Hydroscience & Engineering,* September 19-21, Oxford, Mississippi, USA.

[69] Farshi, D. & Minor, H.E., 2004. Two dimensional fluvial channel model with bank erosion on triangular grid. In: Greco,M., Carravetta,A., Della Morte,R. (Eds), *Proceeding of the 2nd International Conference on Fluvial Hydraulics, River flow 2004*. 23-25 June, Napoli, Italy, Routledge, USA, 999-1003.

[70] Fedele, J.J. & Garcia, M.H., 2001. Alluvial roughness in streams with dunes: a boundary-layer approach. In: Seminara, G. and Blondeaux, P., (Eds.), *River, Coastal and Estuarine Morphodynamics*, Springer, Berlin, 37-60

[71] Fischer, H.B., John List, E., Koh, R.C.Y., Imberger, J. & Brooks, N.H., 1979. *Mixing in inland and coastal waters*. Academic Press. Pp.483.

[72] Forkel, C., 1995. *Die Grobstruktursimulation turbulente Strömungs- und Stoffausbereitungsprozesse in Komplexen Geometrien*. Bericht Nr. 24, Institut für Wasserbau und Wasserwirtschaft RWTH Aachen, Aachen.

[73] Foster, I.D.L., Millington, R. & Grew, R.G., 1992. The impact of particle size

controls on stream turbidity measurement; some implications for suspended sediment yield estimation. In: Bogen, J., Waling, DE., Day, TJ., (Eds.), *Erosion and Sediment Transport Monitoring Programmes in River Basins*, *Proceedings of the Oslo. Symposium,* 24-28 August .Oslo, Norway, IAHS Publ. No. 210, 51-62

[74] Fox, G.A., Wilson, G.V., Simon, A., Langendoen E.J., Akay, O. & Fuchs, J.W., 2007. Measuring streambank erosion due to ground water seepage: correlation to bank pore water pressure, precipitation and stream stage. *Earth Surf. Process. Landforms*, 32, 1558–1573.

[75] Fredlund, D.G., Morgenstern, N.R. & Widger, R.A., 1978. The shear strength of unsaturated soil. *Canadian Geotechnical J.*, 15(3), 312-321.

[76] Fredlund, D.G. & Rahardjo, H., 1993. *Soil mechanics for unsaturated soils.* John Wiley and Sons. 1993. Pp.517.

[77] Fu, X., Wang, G. & Shao, X., 2005. Vertical dispersion of fine and coarse sediment in turbulent open-channel flows. *J. Hydr. Engrg., ASCE,* 131(10),877-888.

[78] Fuller, I.C., Large, A.R.G., & Milan, D.J., 2003. Quantifying development and sediment transfer following chute cutoff in a wandering gravel-bed river. *Geomorphology,* 54, 307-232.

[79] Gartner, J.W., 2002. Estimation of suspended solids concentrations based on acoustic backscatter intensity. *Theoretical background. Turbidity and other sediment surrogates workshop.* April 30 – May 2,Reno, NV.

[80] Gessler, D., Hall, B., Spasojevic, M., Holly, F., Pourtaheri, H. & Raphelt, N., 1999. Application of 3D mobile bed, hydrodynamic model. *J. Hydr. Engrg., ASCE,* 125(7),737-749.

[81] Gonzalez, J.A., Melching, C.S. & Oberg, K.A., 1996. Analysis of open-channel velocity measurements colleted with an acoustic Doppler profiler. In: *Proceedings of the 1st International conference on new emerging concepts for rivers*, September 22-26, Chicago, Illinois, USA.

[82] Gordon, C.M., 1975. Sediment entrainment and suspension in a turbulent tidal flow. *Marine Geology*, 18, M57-M64.

[83] Goring, DJ. & Nikora, V.L., 2002. Despiking acoustic Doppler velocimeter data. *J. Hydr. Engrg., ASCE,* 128 (1), 117-126

[84] Gresho, P.M. & Sani, R.L., 2000. *Incompressible flow and the finite element method. Vol. 1. Advection-Diffusion*, Wiley & Sons, Chister, Pp. 445.

[85] Gust,G., 1990. *Method of generating precisely-defined wall shearing stresses*. U.S. Patent No. 4,973,165,1990.

[86] Hafner, T., 2008. *Uferrückbau und eigendynamische Gewässerentwicklung: Aspekte der Modellierung und Abschätzungsmöglichkeiten in der Praxis*. Berichte des Lehrstuhls und der Versuchsanstalt für Wasserbau und Wasserwirtschaft der TU München, Nr.117.

[87] Hagerty, D.J., 1991. Piping/sapping erosion. I : Basic considerations. *J. Hydr. Engrg., ASCE,* 117(8), 991-1008.

[88] Hasegawa, K., 1981. Bank erosion discharge based on a non-equilibrium theory. *Proc. JSCE, Tokyo*,316, 37-50 (in Japanese).

[89] Heritage, G. & Hetherington, D., 2007. Towards a protocol for laser scanning in fluvial geomorphology. *Earth Surface Processes and Land Forms*, 32, 66-74.

[90] Hey, R.D., 1979. Flow resistance in gravel bed rivers. *J. Hydr. Div., ASCE,* 105(4), 365-379.

[91] Holmes, R.R. & Garcia, M.H., 2002.Velocity and sediment concentration measurements over bedforms in sand-bed rivers. In: *Proceedings of the American Society of Civil Engineers Hydraulic Measurements and Experimental Methods Conference*, July 28-August 1 (CD version)

[92] Huang, CC. and Tsai, CC., 2000. New method for 3D and asymmetrical slope stability analysis. *J. of Geotechnical and Geoenvironmental Engrg.*, 126(10), 917-926.

[93] Huang, C.C., Tsai, C.C. & Chen, Y.H., 2002. Generalized method for three dimensional slope stability analysis. *J. of Geotechnical and Geoenvironmental Engrg.*,128(10), 836-848.

[94] Ikeda, S., 1981. Self-formed straight channels in sandy beds. *J. Hydr. Engrg., ASCE, 107, 389-406.*

[95] Ikeda, S., 1982. Lateral bed-load transport on side slopes. J. Hydr. Div., ASCE,108, No11.

[96] Jackson, R.G., 1976. Depositional model of point bars in the Lower Wabash River. *Journal of Sedimentary Petrology,* 46**,** 579-594.

[97] Jang, C.L. & Shimizu, Y., 2005. Numerical simulation of relatively wide, shallow channels with erodible banks. *J. Hydr. Engrg., ASCE,* 131(7),565-575.

[98] Javan, M., 1996. Brief History of Ancient Band-E-Amir Dam-Bridge. *Proceedings of the 16th Conference on Irrigation and Drainage (ICID),* Cairo, Egypt, pp. 215-227.

[99] Jia, D., Shao, X., Wang, H. & Zhou, G., 2010. Three-dimensional modelling of bank erosion and morphological changes in the Shishou bend of the middle Yangtze River. *Advances in Water Resources*, 33,348-360.

[100] Johannesson, H. & Parker, G., 1989. Velocity redistribution in meandering rivers. *J. Hydr. Engrg., ASCE,* 115(8), 1019-1039.

[101] Jones, J.A.A., 1997. Subsurface flow and subsurface erosion. In Stoddart, D.R. (Ed), *Process and form in geomorphology*, London, 74-120.

[102] Kaftori, D., Hetsroni, G. & Banerjee, S., 1995. Particle behaviuor in turbeulent boundary layer. I. Motion, deposition, and entrainment. *Phys. Fluids*, 7(5),1095-1106.

[103] Khodashenas S.R. & Paquier A., 1999. A geometrical method for computing the distribution of boundary shear tress across irregular straight open channels, *Journal of Hydrol. Res.* ,37(3),381-388

[104] Kikkawa, H., Ikeda, S. & Kitagawa, A., 1976. Flow and bed topography in curved open channels. *J. Hydr. Div., ASCE,* 102**,** 1327-1342.

[105] Kim, S-C.; Friedrichs, C.T., Maa, JP-Y. & Wright, LD., 2000. Estimating

bottom stress in tidal boundary layer from acoustic Doppler Velocimeter data. *J. Hydr. Engrg., ASCE,*126(6),399-406

[106] King, I.P.,1993. *RMA-10 A Finite Element Model for Three-Dimensional Density Stratified Flow*. Resource Modelling Associate, Sydney, NSW, Australia. (*Unpublished*).

[107] Knight, D.W., Demetriou, J.D & Hamed, M.E., 1984. Boundary shear in smooth rectangular channels. *J. Hydr. Engrg., ASCE,*110(4), 405-422.

[108] Knight, DW.,1981. Boundary shear in smooth and rough channels. *J. Hydr. Div. ASCE.*, 107(7), 839-851.

[109] Knight, D.W., Yuen, K.W.H. & Alhamid, A.A.I., 1994. *Boundary shear stress distributions in open channel flow*, in Beven, K., Chatwin P. & Millbank, J., (Eds). *Physical Mechanisms of Mixing and Transport in the Environment*. Wiley, Chapter 4, pp 51-87.

[110] Kolymbas, D., 1998. *Geotechnick – Bodenmechanik und Grundbau*. Springer-Verlag, Berlin, Pp. 427.

[111] Kolmogorov, A.N., 1933. Zur Theorie der Stetigen zufälligen Prozesse. *Math. Ann*. 108,149-160.

[112] Kolmogorov, A.N., 1931. Über die analytischen Methoden in der Wahrscheinligkeitsrechnung. *Math. Ann.* 104, 415-458.

[113] Kondolf, G.M.& Piégay, H., 2003. *Tools in fluvial geomorphology*. Chichester: Wiley.pp. 688.

[114] Kovacs, A. & Parker, G., 1994. A new vectorial bed load formulation and its application to the time evolution of straight river channels. *J. Fluid Mech.*, 267, 153-183.

[115] Kühner, W., 2003. *Sohlschubspannung und Bettbildung in Flusskrümmungen unter Beachtung alpiner Gefälleverhältnisse.* PhD. Innsbruck pp.124.

[116] Kuipers, J. & Vreugdenhil,C.B.,1973. *Calculation of two-dimensional horizontal flow*. Delft hydraulic Laboratory, Report S163, part 1.

[117] Lane, S.N., Chandler J.H. & Richards, K.S., 1994. Developments in monitoring and modelling small-scale river bed topography, *Earth Surface Processes and Land Forms,* 19, 349-368.

[118] Langendoen E.J., Simon, A. & Alonso, C.V., 2000. Modelling channel instabilities and mitigation strategies in eastern Nebraska. *Proceedings Joint Conference on Water Resources Engineering and Water Resources Planning and Management, ASCE,* 30 July-2 Aug. Minneapolis, MN, USA (published in a CD)

[119] Langendoen E.J. & Simon, A., 2008a. Modelling the evolution of incised streams. I: Model formulation and validation of flow and streambed evolution componenets. *J. Hydr. Engrg., ASCE,* 134(6),749-762.

[120] Langendoen E.J. & Simon, A.,2008b. Modelling the evolution of incised streams. II: streambank erosion. *J. Hydr. Engrg., ASCE,* 134(7),905-915.

[121] Large, A.R.G., & Heritage, G.L., 2007. Terrestrial laser scanner based instream habitat quantification using a random field approach. *Annual Conference,*

Remote Sensing and Photogrammetry Society, 11 - 14 September, Newcastle, Upon Tyre, 2007.

[122] Launder, BE. , Spalding, DB., 1972. *Lectures in mathematical models of turbulence*. Academic Press, London

[123] Lawer, D.M., 1993.The Measurement of river bank erosion and lateral channel change : A Review. *Earth Surf. Process. Landforms*,18, 777-821.

[124] Lawler, D.M., Couperthwaite, J., Bull, L. & Haris, MN., 1997a. *Bank erosion events and processes in the Upper Seven Basin*. Hydrology and Earth systems Science. 1, 523-534

[125] Lawler, D. M., Thorne C. R. & Hooke, J. M., 1997b. *Bank erosion and instability*, in Thorne, C. R., Hey, R. D. and Newson, M. D. (Eds), *Applied Fluvial Geomorphology for River Engineering and Management*, Chichester, 137-172.

[126] Li, L. & Wang, SSY., 1993. Numerical modelling of alluvial stream bank erosion. In: Wang, SSY., (Ed.), *Advances in hydro-science and engineering*, University of Mississippi, Oxford, Miss., 1, 2085-2090

[127] Lien, H.C., Hsieh, T.Y., & Yang, J.C., 1999. Bend-flow simulation using 2D depth-averaged model. *J. Hydr. Engrg., ASCE,* 125 (10),1097-1108.

[128] Lindsay, J.B. & Ashmore P.E., 2002. The Effects of Survey Frequency on Estimates of Scour and Fill in a Braided River Model, *Earth Surf. Process. Landforms,* 27, 27-43.

[129] Lippert, K., 2005. Analyse von Turbulenzmechanismen in naturnahen Fließgewässern und ihre mathematische Formulierung für hydrodynamische Modelle. *Hamburger Wasserbau-Schriften*, Heft 4, Institut für Wasserbau der TU Hamburg-Harburg, Hamburg.

[130] Lippert, K., Jung, T., Belger, G., Haase, M., Schrage, N.,2009. Kalypso: Ein Open Source Modellierungssystem für die Wasserwirtschaft. In: Bundesanstalt für Gewässerkunde (Hrsg.). *Veranstaltungen. Wasserstandsinformationsdienste der BfG für die Bundeswasserstraßen*. Koblenz..

[131] Lohnes, R. & Handy, RL., 1968. Slope angle in friable loess. *Journal of Geology*. 76, 247-258.

[132] Luppi, L., Rinaldi, M.& Darby, S.E., 2007. Modelling interactions between fluvial erosion and mass failures in cohesive riverbanks. In: Di Silvio, G., Campostrini, P., Lamberti,A. (Eds.), *Proceedings of 32nd Congress of IAHR, Harmonizing the Demands of Art and Nature in Hydraulics* .July 1-6, Venice, Italy (on CD).

[133] Luppi, L., Rinaldi,M., Teruggi, L.B., Darby,S.E. & Nardi, L., 2009. *Monitoring and numerical modelling of riverbank erosion processes: a case study along the Cecina River (central Italy) . Earth Surf. Process. Landforms*,34(4),530-546.

[134] Mahmood, K., 1971.Flow in sand bed channels. Water management technical report 11. Colorado State University. Fort Collins, CO.

[135] Malcherek,A., 2002. *Fließgewässer-Hydromechanik und Wasserbau.* Ver.3.0. Institute für Waaserwesen der Universität der Bundeswehr München.

[136] Martin-Vide, JP. & Ferrer-Boix, C., 2005. *River incision due to the gravel mining*. In Parker and Garcia, River, Coastal and Estuary Engineering, RCEM 2005. Taylor and Francis Group, London. ISBN 0 415 39270 5

[137] Mason, P.J. & Callen, N.S., 1986. On the magnitude of the subgrid scale eddy coefficient in large eddy simulations of turbulent channel flow. *J. Fluid Mech.* 162, 439 462.

[138] McAnally, W.H., 1989. STUDH: A Two-dimensional numerical model for sediment transport. In *Proceedings of the International Symposium: Sediment Transport Modelling*, August 14-18, New Orleans, LA, New York, ASCE, 659-664.

[139] McCutcheon, S.C., Martin, J.L. & Barnwell, T.O. Jr., 1993. Water Quality. In Maidment, D.R. (Ed). *Handbood of Hydrology*, McGraw-Hill, New York, NY (p. 11.3)

[140] Melcher, N.B., Costa, J.E., Haeni, F.P., Cheng, R.T., Thurman, E.M., Buursink, M., Spicer, K.A., Hayes, E., Plant, W.J., Keller, W.C. & Hayes,K., 2002. River discharge measurements by using helicopter-mounted RADAR, *Geophys. Res. Lett.*, 29(22), 2084.

[141] Milan. D.J., Heritage, G.L. & Hetherington, D., 2007. Application of a 3D Laser Scanner in the Assessment of Erosion and Deposition Volumes and Channel change in a Proglacial River, *Earth Surf. Process. Landforms,.*32, 1657-1674.

[142] Millar, R.G. & Quick, M.C., 1993. Effect of bank stability on geometry of gravel rivers. *J. Hydr. Engrg., ASCE,*119(12), 1343-1363.

[143] Millar, R.G. & Quick, M.C. 1998. Stable width and depth of gravel rivers with cohesive banks. *J. Hydr. Engrg., ASCE,* 124(10), 1005-1013.

[144] Miller, C.R., 1951. *Analysis of flow-duration rating curve method of computing sediment yield*. US Burea of Reclamation Technical Report, Denver, Colorado, 55 p.

[145] Mitasova, H., Drake, T., Harmon, R., Hofierka, J., & McNinch, J., 2002. Spatio-temporal Monitoring of Evolving Topography Using LiDAR, Real Time Kinematic GPS and Sonar Data. In *Proceedings of the Open source GIS - GRASS users conference,* Trento, Italy, 2002.

[146] Mosselman, E., 1992. *Mathematical modelling of morphological processes in rivers with erodible cohesive banks*, PhD thesis, Delft, the Netherlands.

[147] Muste, M. & Patel, V.,C., 1997. Velocity profile for particles and liquid in open-channel flow with suspended sediment. *J. Hydr. Engrg., ASCE,* 123 (9),719-725.

[148] Nagata, T., Hosoda, T. & Muramoto, Y., 2000. Numerical analysis of river channel processes with bank erosion. *J. Hydr. Engrg., ASCE,* 126(4): 243-252.

[149] Nagata, T., Hosoda, T., Muramoto, Y., Rahman, MM., 1997. Development of numerical model to forecast the channel processes with bank erosion. *Proc. 4th Japan- Chinese (Taipei) Joint Seminar on Natural Hazard Mitigation*.

[150] Nasermoaddeli, M.H.,1999. *Effect of bridge bier spacing on scour around*

bridge piers. Master Thesis. Oroumieh University,Oroumieh (in Persian language).

[151] Nasermoaddeli, M.H. & Pasche E., 2006.A multiparameter automatic convergence algorithm for flow simulation. In: Goubesville,P., Cunge,J., Guinot,V. and Liong, S. Y. (Eds), *Proceedings of 7th International Conference on Hydroinformatics 2006*, Sept. 4-8, Nice, France, Vol(4),pp. 2529-2536

[152] Nasermoaddeli, M.H. & Pasche E., 2008a. Application of terrestrial 3D laser scanner in quantification of the riverbank erosion and deposition. In: Altinakar, M.S., Kokpinar, M.A., Aydin,I., Cokgar,S. & Kirkgoz,S.(Eds), *Proceedings of International Conference on Fluvial Hydraulics, River flow 2008*, Sep. 3-5, Cesme-Ismir,Turkey, 3, 2407-2416.

[153] Nasermoaddeli, MH. & Pasche E., 2008b. Estimation of wall shear stress on a natural riverbank. In Wang,S.Y., Kawahara, M., Holtz, K.P., Tsujimoto, T. & Toda, Y., (Eds.), *Proceedings of 8th International conference on Hydro-science and Engineering*: *Advances in Hydro- Science and Engineering,* Nagoya, Japan, Sept 9-12,1425-1433 (full paper on CD).

[154] Neill, C. R., Yalin, M.S., 1969. Quantitative definition of beginning of bed movement. *J. Hydr. Div*., *ASCE*, 95, 585–588.

[155] Nezu,I. & Nakagawa,H.,1993. *Turbulence in open-channel flow*. IAHR Monograph, Balkema, Rotterdam. Pp.281.

[156] Nielsen, D.R., van Genuchten, M.T. & Biggar, J.W., 1986. Water flow and solute transport processes in the unsaturated zone. *Water Resources Research*, 22(9), 89S-108S.

[157] Nikora, V. & Goring D., 2000. Flow turbulence over fixed and weakly mobile gravel beds. *J. Hydr. Engrg., ASCE,* 126(9):679–690.

[158] Olsen, N.R.B., 2003. Three-dimensional CFD modelling of self-forming meandering channel. *J. Hydr. Engrg., ASCE,*129(5), 366-372.

[159] Osman, A.M., 1985. *Channel width response to changes in flow hydraulics and sediment load*. Ph.D., Colorado State University, Fort Collins.

[160] Osman, A.M. & Thorne, CR., 1988. River bank stability analysis. I: Theory, *J. Hydr. Engrg., ASCE,* 114(2), 134-150.

[161] Papanicolaou, N.A., Elhakim, M. & Hilldale, R., 2007. Secondary current effects on cohesive river bank erosion. *Water Resources Research,* 43, W12418.

[162] Papanicolaou, N.A. & Elhakim, M., 2007. Fluvial erosion of cohesive river banks*,* In: Di Silvio, G., Campostrini, P., Lamberti, A. (Eds.), *Proceedings of 32nd Congress of IAHR, Harmonizing the Demands of Art and Nature in Hydraulics* .July 1-6, Venice, Italy (on CD).

[163] Pasche, E., 1984, *Turbulenzmechanismen in naturnahen Fließgewässern und die Möglichkeiten ihrer mathematischen Erfassung*, Mittlg. Institut für Wasserbau und Wasserwirtschaft, RWTH Aachen, 1984.

[164] Pasche, E., Kraessig, S., Lippert, K., Nasermoaddeli, M.H., Ploeger, W. & Rath S., 2006. *Wieviel Physik braucht die Strömungsberechnung in der Ingenieurpraxis?*, Wasserbaukolloquium, Strömungssimulation im Wasserbau,

Dresdner Wasserbauliche Mitteilungen, Dresden, Germany, Heft 32, 237-260.

[165] Pasche, E., Brüning, C., Plöger, W., Teschke, U., 2005. *Möglichkeiten der Wirkungsanalyse anthropogener Veränderungen in naturnahen Fließgewässern, Hamburger Wasserbau-Schriften,* Heft 4, Institut für Wasserbau der TU-Hamburg-Harburg, Hamburg.

[166] Pavlovic, R., 1981. *Numerische Berechnung der Wärme- und Stoffausbreitung in Flüssen mit einem tiefengemittelten Modell*. Dissertation, Karlsruhe.

[167] Phillips, B.C. & Sutherland, A.J., 1989. Spatial and lag effects in bed load sediment transport. *Journal of Hydraulic Research*, 27, 115–122.

[168] Pizzuto, JE., 1984. Bank erodibility of shallow sanded streams. *Earth Surf. Process. Landforms*, John Wiley and Sons, 9, 113-124.

[169] Pizzuto, JE.,1990. Numerical simulation of gravel river widening. *Water Resources Research*. 26(9), 1971-1980.

[170] Pollen, N., Simon, A., Collison, A., 2004. *Advances in assessing the mechanical and hydrologic effects of riparian vegetation on streambank stability*. In *Riparian vegetation and fluvial geomorphology*, Bennet SJ & Simon A.,(Eds.), American Geophysical union: Washington DC.,125-140.

[171] Ploeger, W., 2007. *Sohlformen bei instationärer Strömung, Messung und Simulation.* Hamburger Wasserbau-Schriften, Heft 9, Institut für Wasserbau der TU-Hamburg-Harburg, Hamburg.

[172] Pollen, N., 2004. *The effects of riparian vegetation on stream-bank stability, mechanical and hydrological interactions. Ph.D.*, King's College, University of London, UK.

[173] Pollen, N. & Simon, A., 2005. Estimating the mechanical effects of riparian vegetation on stream bank stability using a fiber bundle model. Water Resources Research. 41: W07025.

[174] Prandtl, L., 1925. Bericht über Untersuchungen zur ausgebildeten Turbulenz. ZAMM, Bd. 5,s.136-139.

[175] Raff, D.A. & Ramirez, J.A., 2005. A physical, mechanistic and fully couples hillslope hydrology model. *Int. J. Numer. Meth. Fluids*, 49,1193-1212.

[176] Rashidi, M., Hetsroni, G. & Banerjee, S., 1990. Particle - turbulence interaction in a boundary layer. *Int. J. Multiphase Flow*, 16(6),935-949.

[177] Rhodes, D.G. & Knight, D.W., 1994. Velocity and boundary shear in a wide compound duct. *J. Hydr. Res*., IAHR, 32(5), 743 – 764.

[178] Rinaldi, M. & Casagli, N., 1999. Stability of stremabanks formed in partially saturated soils and effects of negative pore water pressures: the Sieve River (Italy). *Geomorphology,* Elsevier. 26(4), 253-277.

[179] Rinaldi, M., Casagli, N., Dapporto, S. & Gargini, A., 2004. Monitoring and modelling of pore water pressure changes and riverbank stability during flow events. *Earth Surf. Process. Landforms*, John Wiley and Sons, 29(2), 237-254.

[180] Rinaldi, M., Mengoni, B., Luppi, L. & Draby, S.E., 2008. Numerical simulation of hydrodynamics and bank erosion in a river bend. *Water Resources Research*, 44, W09428.

[181] Rodi, W., 1978. Turbulenzmodelle und ihre Anwendung auf Probleme des Wasserbaus. Habilitationsschrift, Fakultät für Bauingenieur- und Vermessungswesen, Universität Karlsruhe.

[182] Rodi, W., 1993. *Turbulence models and their application in hydraulics- A state of art Review.* 3rd Ed., IAHR Monograph. Balkema, Rotterdam, Netherland. Pp104.

[183] Rouvé, G. & Schröder, M., 1994. *Die Entwicklung eines mathematisch-numerischen Verfahrens zur Berechnung naturnaher Fließgewässer.* DFG-Abschlussbericht Ro 365/31-6, Lehrstuhl für Wasserbau und Wasserwirtschaft der RWTH Aachen.

[184] Schlichting, H., 2006. Grenzschicht-Theorie. 10. Überab. Aufl., Springer. pp799.

[185] Schmautz, M. & Aufleger, M., 2001. *Mathematische Modellierung der Strömung im Uferbereich von Fließgewässern.* Festschrift ,'75 Jahre Oskar von Miller-Institut', Berichte des Lehrstuhls und der Versuchsanstalt für Wasserbau und Wasserwirtschaft der TU München,Nr.91,Seite 214-226.

[186] Schmautz, M., 2003. *Eigendynamische Aufweitung in einer geraden Gewässerstrecke- Entwicklung und Untersuchungen an einem numerischen Model.* Berichte des Lehrstuhls und der Versuchsanstalt für Wasserbau und Wasserwirtschaft der TU München, Nr.96.

[187] Schrage, N. & Pasche, E., 2009. Efficient methods to link 1- and 2-dimensional fluvial flow models based on Finite Elements. *33rd IAHR Conference,* August 9-14,Vancouver, Canada (CD-ROM).

[188] Schröder, R., 1965. Einheitliche Berechnung gleichförmiger turbulenter Strömungen in Rohren und Gerinnen. *Der Bauingenieur*, Heft 5, 191-195.

[189] Simon, A., 1989. Shear stress determination and stream bank instability in loess- derived alluvium, West Tennessee, USA. In: DeMulder, EJ., Hageman, Pb., (Eds.), *Applied Quaternary Research*. A.A. Balkema Publishers, Rotterdam, 129-146.

[190] Simon, A., Wolfe, WJ. & Molinas, A., 1991. Mass wasting algorithms in an alluvial channel model. In *Proceedings of 5th Federal Interagency Sedimentation Conference*. 22-29 August, Las Vegas, Nevada.

[191] Simon, A. & Curini, A., 1998. Pore pressure and bank stability: the influence of matric suction. In: Abt. S. (Edt.), *Hydraulic Engineering ,98*. ASCE, Reston, 358-363.

[192] Simon, A., Shields, F.D., Ettema, R., Alonso, M.M., Garsjo, A., Curini, A. & Steffan, L., 1999. *Channel erosion on Missouri river, Montana, between Fork Peck dam and the north Dakota border*. USDA-ARS, National Sedimentation Laboratory Research Report, Oxford, MS.

[193] Simon, A., Curini, A., Darby, S.E. & Langendoen, EJ., 2000. *Bank and near-bank processes in incised channel. Geomorphology, 35(3): 193-217.*

[194] Simon, A., Collison, A.J.C., 2002. Quantifying the mechanical and hydrologic effect of riparian vegetation on streambank stability. *Earth Surf. Process.*

Landforms, 27(5), 527-546.

[195] Simon, A., Collison, A.J.C. & Layzell, A., 2003. Incorporating bank-toe erosion by hydraulic shear into ARS bank stability model: Missouri River, Eastern Montana. In: *Proc. of the World Water and Environmental Resources Congress, June 23-26, 2003, Philadelphia, PA. USA.* (published on digital media, CD).

[196] Smagorinsky, J., 1963. General circulation experiments with the primitive equations. *Monthly Weather Review*, 91(3), 99–165.

[197] Song, T, & Graf, W.H., 1994. Non-Unifrom open-channel flow over a rough bed. *Journal of Hydroscience and Hydraulic Engineering*, 12(1),1-25.

[198] Song, T, & Graf, W.H., 1996. Velocity and turbulence distribution in unsteady open-channel flows. *J. Hydr. Engrg., ASCE,* 111(8),141-154.

[199] Song, T. & Chiew, Y.M., 2001. Turbulence measurement in nonuniform open-channel flow using acoustic Doppler velocimeter (ADV*). Journal of Engineering Mechanics, ASCE*, 127(3), 219–232.

[200] Soulsby, R. L., 1983. The bottom boundary layer of shelf seas. In *Johns, B. (Ed.), Physical Oceanography of Coastal and Shelf Seas***,** Elsevier Oceanography Series, 35, Amsterdam, Ch. 5B.

[201] Spangler, M.G. & Handy, R.L., 1982. *Soil Engineering*, 4th Ed., Index Educational, New York. N.Y.

[202] Spannring, M., 1999. *Die Wirkung von Buhnen auf Strömung und Sohle eines Fließgewässers*. Berichte des Lehrstuhls und der Versuchanstalt für Wasserbau und Wasserwirtschaft der Technischen Universität München, Heft 86.

[203] Spasojevic, M & Holly, F.M., 1994. *Three-dimensional numerical simulation of mobile-bed hydrodynamics*. Contract Rep. HL-94-2, U.S. Army Engineer Waterways Experiment Station, Vicksburg, Miss.

[204] Stapleton K.R. & Huntley D.A., 1995. Seabed stress determination using the inertial dissipation method and the turbulent kinetic energy method. *Earth Surf. Process. Landforms*, 20, 807-815.

[205] Struiksama, N., 1985. Prediction of 2D bed topography in rivers. *J. Hydr. Engrg., ASCE,* 111(8), 1169-1182.

[206] Sumer, B.M. & Deigaard, R., 1981. Particle motions near the bottom in turbulent flow in an open channel. Part 2. *J. Fluid. Mech.* 109.,311-337.

[207] Taylor, G.I., 1921. Diffusion by continuous movement. *Proc. London Math. Soc.*, Ser. A20. 196-211.

[208] Taylor, G.I., 1953. Dispersion of soluble matter in solvent flowing slowly through a tube. *Proc. R. Soc. London*, Ser. A 209, 186-203.

[209] Terzaghi, K., 1936. The shear resistance of saturated soils. In *Proc. 1st Int. Conf. Soil Mech. Found. Eng*. (Cambridge, MA), Vol. 1:54-56.

[210] Terzaghi, K. & Peck, R.B., 1948. *Soil mechanics and engineering practice*. John Wiley & Sons, Inc., New York, N.Y.Pp.556.

[211] Thevenot, M. M., Prickett, T. L. & Kraus, N. C., 1992. *Tylers Beach, Virginia, dredged material plume monitoring project*. 27 September to 4 October 1991, Dredging Research Program Technical Report DRP-92-7, US Army Corps of

Engineers, Washington, D.C, 204 p.

[212] Thoma, D.P., Gupta, S.C. & Bauer, M.A., 2001. Quantifying river bank erosion with scanning laser altimetry. *International Archives of Photogrammetry and Remote Sensing*, Volume XXXIV-3/W4 Annapolis, MD., 2001,169-174.

[213] Thoma, D.P., Gupta, S.C., Bauer, M.A. & Kirchoff, C.E., 2005. Airborne laser scanning for riverbank erosion assessment, *Remote Sensing of Environment*, 95, 493–501.

[214] Thorne, C.R., 1982, *Processes and mechanisms of river bank erosion*. In: Gravel-Bed Rivers, Hey, R.D., Bathurst J.C. & Thorne, CR., (Eds.), *Gravel-Bed Rivers*. John Wiley and Sons, Chichester, England, 227-272.

[215] Thorne, C.R., 1990. Effects of vegetation on riverbank erosion and stability. In: Thornes, JB (Ed.), *Vegetation and Erosion*, Wiley, Chichester, UK, 125-144.

[216] Thorne, C.R., 1991. Bank erosion and meander migration of the Red and Mississippi rivers,USA. *Proceedings of Vienna symposium on Hydrology for Water Management of Large River Basins*, August 1991,IAHS Pub. No.201.

[217] Thorne, C.R. & Lewin, J., 1979. Bank erosion, bed material movement and planform development in a meandering river. In Rhodes, H.H. & Williams, GP. (Eds.), *Adjustments of fluvial system*. Kendall/Hunt, Dubuque, Iowa, 117-137.

[218] Thorne, C.R. & Tovey, N.K., 1981.Stability of composite river banks . *Earth Surf. Process. Landforms*, 6, 469-484.

[219] Thorne, C.R., Morphy, J.B. & Little, W.C., 1981. *Stream channel stability, Appendix D, Bank stability and bank material properties in the Bluffline streams of Northwest Mississippi.* US. Department of Agriculture Sedimentation Laboratory. Oxford. MS. 257 p.

[220] Thorne, C.R. & Abt, S.R., 1993. Analysis of river bank stability due to toe scour and lateral erosion. *Earth Surf. Process. Landforms*, John Wiley and Sons, 18, 835-843.

[221] Thorne, C.R., Hey, R.D. & Newson, M.D., 1997. *Applied fluvial geomorphology*. John Wiley and Sons, Chichester, England, Pp.376.

[222] Tracy, H.J. & Lester, C.M., 1961. *Resistance coefficients and velocity distribution in smooth rectangular channel.* U.S. Geological Survey Water Supply, paper 1592-A Geol. Survey. US Department of Interior, Washington, DC., A1-A18.

[223] Ullrich, C.R. , Hagerty, D.J. & Holmberg, R.W., 1986. Surficial failures of alluvial stream banks. *Can. Geotech. J.* , 23(3), 304-316.

[224] van Genuchten, M.Th., 1980. A closed-from equation for predicting the hydraulic conductivity of unsaturated soils. *Soil.Sci.Soc.Am.J.*, 44, 892-898.

[225] Vanoni, EA.1975. *Sedimentation Engineering*. Manuals and Reports on Eng. Practice-No. 54. ASCE Task Committee, 745 pp

[226] van Rijn, L.C., 1984a. Sediment transport. I: Bed load transport. *J. Hydr. Engrg., ASCE,* 110(10), 1431-1456.

[227] van Rijn, L.C., 1984b. Sediment transport. II: Suspended load transport. *J. Hydr. Engrg., ASCE,* 110(11), 1613-1641.

[228] van Rijn, L.C., 1984c. Sediment transport: bed forms and alluvial roughness. *J. Hydr. Engrg., ASCE,* 110(12), 1733-1754.

[229] van Rijn, LC., 1987. Mathematical modelling of morphological processes in the case of suspended sediment transport. Delft Hydr. Communication. No. 382.

[230] van Rijn, L.C., 1993. *Principles of sediment transport in rivers, estuaries and coastal seas.* Aqua publications, Netherlands.

[231] Vanoni, EA.,1975. *Sedimentation Engineering.* Manuals and reports on Eng. Practice-No. 54. ASCE Task Committee, 745 pp.

[232] Waldron, L.J., 1977. Shear resistance of root-permeated homogeneous and stratified soil. Soil Science Society of America Journal, 41, 843-849.

[233] Walling, D. E. & Webb, B. W., 1988. The reliability of rating curve estimates of suspended sediment yield: some further comments. In: Erosion and Sediment Transport Measurement (Proc. Porto Alegre Symp. Dec. 1988). IAHS Publ. no 174. 337-350.

[234] Wang, S.S.Y. and Wu, W., 2004. River Sedimentation and Morphology modelling- The state of the art and future development. *Proceedings of the 9th international symposium on River Sedimentation*, Oct. 18-21, 2007, Yichang, China.

[235] Webel, G., 1982. Turbulente Quervermischung in Gerinne Strömungen. Mitteilung,Institut für Wasserbau III, Universität Karlsruhe, Heft 21.

[236] White, W.R., Bettess, R. & Paris,E.,1982. An analytical approach to river regime. *J. Hydr. Div. ASCE,* 108(10), 1179-1193.

[237] Wieberg, P.L. and Smith, J.D., 1987. Calculations of the critical shear stress for motion of uniform and heterogeneous sediments. *Water Resources Research*, 23,1471-1480.

[238] Wilcock P.R., 1988. Methods for estimating the critical shear stress of individual fractions in mixed-size sediment. *Water Resour. Res*. 24, 1127–1135

[239] Wilke, M., 2008. *A laboratory study of the flow field in a meandering channel with an initial flat bed and movable banks, and of the subsequent evolution of bed topography and banks*. Diplom Thesis, Institut für Wasserbau der TU-Hamburg-Harburg, Hamburg.

[240] Wilson, G.V., Jardine, P.M., Luxmore, R.J., Zelazny, L.W., Lietzke, D.A. & Tod, D.E., 1991. Hydrogeomorphological processes controlling subsurface transport from an upper subcatchment of Walker Branch watershed during storm events: 1. Hydrologic transport process. *Journal of Hydrology*, 123(3-4), 297-316.

[241] Wilson, G.V., Periketi, R.K., Fox, G.A, Dabney, S.M., Shields, F.D., & Cullum, R.F., 2007. *Soil properties controlling seepage erosion contributions to streambank failure*. *Earth Surf. Process. Landforms*, 32, 447-459.

[242] Wolf, J., 1999. The estimation of shear stresses from near-bed turbulent velocities for combined wave-current flows. *Coastal Engineering,* 37, 529–543.

[243] Wolman, M.G., 1959. Factors influencing erosion of a cohesive river banks. *Earth Surf. Process. Landforms*, John Wiley and Sons, 6, 469- 484.

[244] Wolman, M.G.& Miller, J.P., 1960. Magnitude and frequency of geomorphic processes. *Journal of Geology*, 68, 54-74.

[245] Wood, A.L., Simon, A., Downs, P.W. & Thorne, C.R., 2001. Bank-toe processes in incised channels: the role of apparent cohesion in the entrainment of failed bank material. *Hydrological Processes,* 15(1), 39-61.

[246] Wren, D.G, Barkdoll, B.D., Kuhnle, R.A. & Derrow, R.W., 2000. Field techniques for suspended sediment measurements. *J. Hydr. Engrg., ASCE,* 126(2), 97-104.

[247] Wright, S. & Parker, G., 2005. Modelling downstream fining in sand-bed rivers. I: formulation. *J. Hydraulic Research*, 43(6), 613-620.

[248] Wu, T.H., McKinnell, W.P. & Swanston, D.N., 1979. Strength of tree roots and landslide in Prince of Wales Island, Alaska. *Canadian Geothechnical Journal*. 16(1),19-33.

[249] Wu, W., Rodi, W. & Wenda, T., 2000. 3D numerical modelling of flow and sediment transport in open channels. *J. Hydr. Engrg., ASCE,* 126(1), 4-15.

[250] Xu,Y., 1998. *Numerical simulation of suspended sediment transport in rivers*. Mitteilung der Institut für Wasserbau, Universität Stuttgart, Heft 98, pp.149.Dissertation.

[251] Yalin, MS., 1992. *River Mechanics.* Pergamon Press, Oxford. Pp.220.

[252] Yalin, MS. & da Silva, A.M.F., 2001. *Fluvial processes*. IAHR monograph,Netherland. 197 p.

[253] Yang, S.Q., Lim,S.-Y. & McCorquodale, J.A., *2005.* Investigation of near wall velocity in 3-D smooth channel flows. *Journal of Hydraulic Research. 43(2), 149-157.*

[254] Yang, S.Q. & Lee, J.W., 2007. Reynolds shear stress distributions in a gradually varied flow in a roughened channel. *Journal of hydraulic research*, *45(4), 462-471.*

[255] Yang, S.Q., Yu, J.X. & Wang, Y.Z., 2004. Estimation of diffusion coefficients, lateral shear stress, and velocity in open channels with complex geometry. *Water Resources Research,* 40(5), W05202, 207-217.

[256] Ye, J., McCorquodale, J.A., 1997. Depth-averaged hydrodynamic model in curvilinear collocated grid. *J. Hydr. Engrg., ASCE,* 123 (5),380–388.

[257] Zanke,U., 1977. *Berechnung von Sinkgeschwindigkeiten von Sedimenten.* Mitteilung des Franzius-Instituts für Wasserbau, Heft 46, Pp. 243, Technische Universität Hannover.

[258] Zimpfer, G.L., 1975. *Development of laboratory river channels*., PhD. thesis, Dept., of Earth Resources, Colorado State Univ., Fort Collins, Colo.

APPENDICES

A Mathematical derivations

A-1 Non-equilibrium reference concentration

A-1.1 Assuming α_0 equal to zero

Boundary condition between bed load layer and suspended load layer can be specified as following, assuming α_0=0 in Eq. (2–8) (van Rijn, 1993) :

$$\varepsilon_z \frac{\partial c}{\partial z} + w_s c = w_s (c_b - c_{b*}) \tag{A-1}$$

The above equation can be further simplified as follows:

$$c' + \underbrace{\frac{w_s}{\varepsilon_z}}_{A} c = \underbrace{\frac{w_s}{\varepsilon_z}(c_b - c_{b*})}_{B}$$

c′in the above equation is the first order derivative of c with respect to z. Assuming constant eddy diffusivity (ε_f) in respect to the depth ($\varepsilon_f = \alpha' \kappa u_* h, \varepsilon_z = \beta \phi \varepsilon_f$, α′ is a coefficient), the coefficient of c can be assumed constant (A), which results in a simple ordinary differential equation as follows:

$$c' + Ac = B$$

The above ordinary differential equation has a generic solution as follows:

$$c = e^{-\int_z^{} A d\xi} \left[\int B e^{\int_z^{} A d\xi} dz + k \right] \tag{A-2}$$

Solving the above equation yields:

$$c = e^{-Az}\left[B\int_{b}^{z} e^{Az}dz + k \right] = e^{-Az}\left[\frac{B}{A}\left(e^{Az} - e^{Ab}\right) + k \right]$$

Which is reduced to the following after simplifications:

$$c = \frac{B}{A}\left(1 - e^{A(b-z)}\right) + ke^{-Az}$$

Considering c(b) = c_b , the constant of the above equation (k) can be determined as follows:

$$c_b = \frac{B}{A}\left(1 - e^{A(b-b)}\right) + ke^{-Ab} = ke^{-Ab} \Rightarrow k = c_b e^{Ab}$$

Substituting the constant of the integration into the equation for C, it yields:

$$c = (c_b - c_{b*})\left(1 - e^{\frac{w_s}{\varepsilon}(b-z)}\right) + c_b e^{\frac{w_s}{\varepsilon}z} e^{-\frac{w_s}{\varepsilon}b} = c_b - c_{b*}\left(1 - e^{\frac{w_s}{\varepsilon}(b-z)}\right)$$

To compute the near bed non-equilibrium concentration, it is enough to set c = c_a at elevation of z = z_a, which results in the following equation, also presented in Wu et al., (2000):

$$c_b = c_2 + c_{b*}\left(1 - e^{\frac{w_s}{\varepsilon}(b-z_2)}\right) \tag{A-3}$$

A-1.2 Non-zero α_0

For determination of the non-equilibrium suspended load concentration near bed surface, assuming $\alpha_0 \neq 1$ in Eq. (2–8), similar procedure as above is repeated here, but this time including the parameter α_0.

$$\varepsilon_z \frac{\partial c}{\partial z} + w_s c = \alpha_0 w_s (c_b - c_{b*}) \tag{A-4}$$

$$c' + \underbrace{\frac{w_s}{\varepsilon_z}}_{A} c = \underbrace{\alpha_0 \frac{w_s}{\varepsilon_z}(c_b - c_{b*})}_{B}$$

$$c' + Ac = B$$

$$c = e^{-\int_z A d\xi}\left[\int B e^{\int_z A d\xi} dz + k\right]$$

$$c = e^{-Az}\left[B\int_z e^{Az} dz + k\right] = e^{-Az}\left[\frac{B}{A}\left(e^{Az}\right) + k\right]$$

$$c = \frac{B}{A} + ke^{-Az}, \qquad considering: c(b) = c_b$$

$$c_b = \frac{B}{A} + ke^{-Ab} \Rightarrow k = \left(c_b - \frac{B}{A}\right)e^{Ab}$$

$$c = \frac{B}{A} + \left(c_b - \frac{B}{A}\right)e^{A(b-z)}$$

$$@\, z = a \Rightarrow c = c_a$$

$$c_a = \frac{B}{A} + \left(c_b - \frac{B}{A}\right)e^{A(b-a)} \Rightarrow$$

$$c_b = \frac{B}{A} + \left(c_a - \frac{B}{A}\right)e^{-A(b-a)}$$

$$c_b = \frac{\alpha_0 A(c_b - c_{b*})}{A} + \left(c_a - \frac{\alpha_0 A(c_b - c_{b*})}{A}\right)e^{-A(b-a)}$$

$$c_b = \alpha_0(c_b - c_{b*}) + \left(c_a - \alpha_0(c_b - c_{b*})\right)e^{-A(b-a)} =$$

$$\alpha_0 c_b - \alpha_0 c_b e^{-A(b-a)} - \alpha_0 c_{b*} + \alpha_0 c_{b*} e^{-A(b-a)} + c_a e^{-A(b-a)}$$

$$c_b = \alpha_0 c_b\left(1 - e^{-A(b-a)}\right) + \alpha_0 c_{b*}\left(e^{-A(b-a)} - 1\right) + c_a e^{-A(b-a)}$$

$$c_b\left[1 - \alpha\left(1 - e^{-A(b-a)}\right)\right] = \alpha c_{b*}\left(e^{-A(b-a)} - 1\right) + c_a e^{-A(b-a)}$$

$$c_b = \frac{\alpha_0 c_{b*}\left(e^{-A(b-a)}-1\right)+c_a e^{-A(b-a)}}{\left[1-\alpha_0\left(1-e^{-A(b-a)}\right)\right]} \tag{A-5}$$

To examine the correctness of the above derivation, it is enough to examine if this equation reduces to the already derived simple form, when α_0 is set to 1.

$$\alpha = 1 \rightarrow c_b = \frac{c_{b*}\left(e^{-A(b-a)}-1\right)+c_a e^{-A(b-a)}}{\left[1-\left(1-e^{-A(b-a)}\right)\right]} = \frac{c_{b*}\left(e^{-A(b-a)}-1\right)+c_a e^{-A(b-a)}}{e^{-A(b-a)}}$$

$$c_b = c_{b*}\left(1-e^{A(b-a)}\right)+c_a = c_a + c_{b*}\left(1-e^{\frac{w_s}{\varepsilon_z}(b-a)}\right)$$

As it is seen, the above general equation reduces to the equation of Wu et al. (2000) for the case of α_0=1, therefore, the equation presented in Duan and French (2001) can not be correct.

A-2 Analytical function of wall shear stress for three-dimensional flow

The three-dimensional spiral flow pattern in river bend prevent correct determination of bed shear stress along the cross sectional perimeter, especially near river sidewalls, using the available common approaches. An analytical approach has been developed in the present work to enable computation of bed shear stress using detailed three-dimensional velocity measurement. In addition to computation of bed and bank shear stress distribution, it can be used to investigate the effect of outer bank cell on bank shear stress and bank erosion.

For this purpose, the momentum equation in x-direction (x: longitudinal, y: lateral and z: vertical directions) can be integrated across the stream between y_0 and y_1 (an effective near bank zone) the following can be obtained:

$$\underbrace{\int_{y_0}^{y_1}\frac{\partial}{\partial x}(\overline{u}^2+\overline{u'^2})dy}_{I}+\underbrace{\int_{y_0}^{y_1}\frac{\partial}{\partial z}(\overline{u}.\overline{w}+\overline{u'w'})dy}_{II}+\underbrace{(\overline{u}.\overline{v}+\overline{u'v'})\Big|_{y_0}^{y_1}}_{III}=\int_{y_0}^{y_1} g(\sin\theta-\frac{\partial h}{\partial x}\cos\theta)dy \tag{A-6}$$

In the above equations, u, v and w are longitudinal, lateral and vertical velocities, respectively. The bar over the mentioned parameters represents their time averaged values, while the prime shows the turbulent velocity fluctuation in the corresponding direction; h is the water depth and g is the gravity acceleration; θ is the longitudinal energy slope in the above equation.y_0 defines the bank profile as a function of elevation (z), y_1 is a function (or curve) that separates the near bank zone from the rest of the flow area across the channel. This

area should represent the effective zone contributing to the bank shear stress. This zone can be defined as a distance to the bank equal to the local water depth or defined by connecting locus of points with maximum longitudinal velocity across the river in near bank zone (Papanicolaou and Mohamed, 2007).

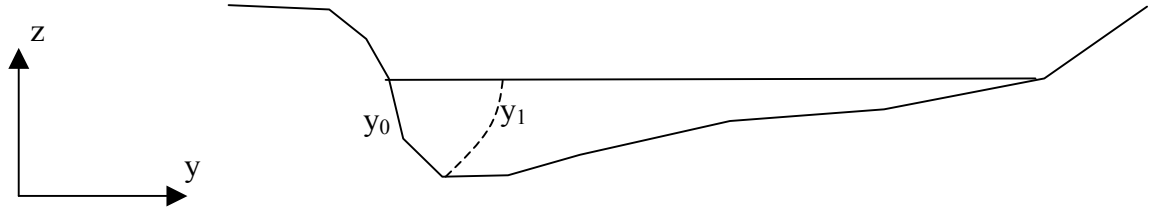

Figure A-1 Schematic presentation of the effective near bank area

Measurements are often available across a river section but not in longitudinal direction, so that the first integral (longitudinal gradient) cannot be resolved by measurements. To remove this problem, the following approach was applied.
By multiplying continuity equation by 2u and substituting the resulting equation for the first term in the first integral the following equation is obtained:

$$I = \int_{y_0}^{y_1} \frac{\partial}{\partial x}(\overline{u}^2 + \overline{u'^2})dy = \int_{y_0}^{y_1} \left(2u(\frac{\partial v}{\partial y} + \frac{\partial w}{\partial z}) - \frac{\partial \overline{u'^2}}{\partial x} \right) dy$$

Assuming that the gradient of normal Reynolds stress is negligible, the above equation reduces to the following:

$$I = \int_{y_0}^{y_1} \left(2u(\frac{\partial v}{\partial y} + \frac{\partial w}{\partial z}) \right) dy$$

Repeating the same procedure for the second integral with the boundary conditions u=w=u´w´=0 at y= y_0 and dy/dz=0, results in the following:

$$II = \int_{y_0}^{y_1} \frac{\partial}{\partial z}(\overline{u}.\overline{w} + \overline{u'w'})dy = \frac{\partial}{\partial z}\int_{y_0}^{y_1} (\overline{u}.\overline{w} + \overline{u'w'})dy - \underbrace{\frac{\partial y}{\partial z}}_{=0}(\overline{u}(y_1).\overline{w}(y_1) + \overline{u'w'(y_1)})$$

$$+ \frac{\partial y_0}{\partial z}(\underbrace{\overline{u}(y_0).\overline{w}(y_0) + \overline{u'w'(y_0)}}_{=0})$$

Applying boundary condition u = v = 0 and $u^2_{*bank}(y_0) = -\overline{u'v'}$ at y = y_0, the third term is simplified to the following:

$$III = (\overline{u}.\overline{v} + \overline{u'v'})\Big|_{y_0}^{y_1} = (\overline{u}(y_1).\overline{v}(y_1) + \overline{u'v'}(y_1)) - (\underbrace{\overline{u}(y_0).\overline{v}(y_0)}_{=0}) + \underbrace{\overline{u'v'}(y_0)}_{-u_{*bank}^2(y_0)})$$

Substituting the terms I, II and III back into the original equation and noticing that the term in the parenthesis on the right hand of the original equation is equal to the energy gradient (I_e), the following equation is obtained:

$$u_{*bank}^2(y_0) = g(y-y_0)I_e - \int_{y_0}^{y_1}\left(2u(\frac{\partial v}{\partial y} + \frac{\partial w}{\partial z})\right)dy - \frac{\partial}{\partial z}\left(\int_{y_0}^{y_1}(\overline{u}.\overline{w} + \overline{u'w'})dy\right) - \overline{u}.\overline{v}\Big|_{y_1} - \overline{u'v'}\Big|_{y_1}$$

The first term in the above equations is the pressure term. The second term reflects the momentum exchange due to non-uniformity. The third term demonstrates the secondary currents. The fourth and fifth terms are secondary currents as well as Reynolds shear stresses at distance y_1 for a given elevation (z), respectively. Given three-dimensional velocity measurements near riverbank zone, the shear stress (friction velocity) distribution over the bank surface along the outer bank can be determined using the above equation.

The most crucial term to be defined is the extent of upper limit of integration (y). It is the extent of the flow near bank, which can influence the shear stress on the bank. As a first approximation, it can be assumed to be equal to the a lateral distance to the bank, where the velocity profile across the channel reaches its maximum value, or alternatively the extent of the inner region of the flow normal to the bank. However definition of the inner region normal to the bank is not trivial.

The bed shear stress (alternatively friction velocity) distribution can be computed in the same way as for bank shear stress, but by integrating the longitudinal momentum equation over the depth as follows:

$$u_{*bed}^2 = gz(\sin\theta - \frac{\partial h}{\partial x}\cos\theta) - \left(\int_{z_0}^{z}\frac{\partial}{\partial x}(u^2 + \overline{u'^2})dz\right) - \left(\int_{z_0}^{z}\frac{\partial}{\partial y}(u.v + \overline{u'v'})dz\right) - u\cdot w\Big|_z - \overline{u'w'}\Big|_z$$

In the same manner as presented above it reduces to the following equation

$$u_{*bed}^2 = gzI_e + 2\int_{z_0}^{z}u(\frac{\partial v}{\partial y} + \frac{\partial w}{\partial z})dz - \left(\int_{z_0}^{z}\frac{\partial}{\partial y}(u.v + \overline{u'v'})dz\right) - u\cdot w\Big|_z - \overline{u'w'}\Big|_z \qquad \text{(A-7)}$$

As it is seen from the above equation, if measurements are available just under the water surface, the fourth and fifth terms on the right hand side can be neglected because just under water surface the vertical turbulent momentum exchange $\overline{u'w'} = 0$ and the vertical flow velocity (w) can be assumed zero. The rest of the terms can be then determined by detailed velocity measurements across the channel. Therefore, for z=h, the above equation reduces to:

$$u_{*bed}^2 = gzI_e + 2\int_{z_0}^{h} u\left(\frac{\partial v}{\partial y} + \frac{\partial w}{\partial z}\right)dz - \left(\int_{z_0}^{h} \frac{\partial}{\partial y}(u.v + \overline{u'v'})dz\right) \tag{A-8}$$

Using the above equation theoretical shear stress distribution across a channel in a river bend can be determined, provided that reliable velocity profile measurements in turbulent boundary layer and the whole flow is available.

B Total load transport formula

It is not intended here to present a review of available methods of computation of total equilibrium load transport but those applied in the present work.

B-1 Method of van Rijn

In this method equilibrium bed and suspended load (van Rijn, 1984a ans 1984b) are computed separately and are added to yield the total equilibrium bed load transport (van Rijn,1993).

B-1.1 Bed load formula

$$\begin{aligned} q_{b,eq} &= 0.053(s-1)^{0.5} g^{0.5} d_{50}^{1.5} T^{2.1} && T < 3 \\ q_{b,eq} &= 0.1(s-1)^{0.5} g^{0.5} d_{50}^{1.5} T^{1.5} && T \geq 3 \end{aligned} \qquad \text{(B-1)}$$

In which $q_{b,eq}$ is the equilibrium bed load transport and parameter T, D_* and s are defined as follows:

$$T = \frac{\tau - \tau_{cr}}{\tau_{cr}}$$

$$D_* = d_{50}\left[g\left(s-1\right)/\upsilon^2 \right]^{1/3}$$

$$s = \frac{\rho_s}{\rho}$$

B-1.2 Suspended load formula

$$q_{s,eq} = 0.012u \cdot h \cdot D_*^{-0.6} \left[\frac{u - u_{cr}}{\left(\left(s-1\right) g d_{50}\right)^{0.5}} \right]^{2.4} \left(\frac{d_{50}}{h} \right) \qquad \text{(B-2)}$$

In which $q_{s,eq}$ is equilibrium suspended load and u is the depth-averaged flow velocity magnitude and u_{cr} is computed as follows:

$$u_{cr} = 0.19 d_{50}^{0.1} \log\left(\frac{12h}{3d_{90}}\right) \qquad 0.0001 \le d_{50} \le 0.0005\, m$$

$$u_{cr} = 8.5 d_{50}^{0.6} \log\left(\frac{12h}{3d_{90}}\right) \qquad 0.0005 \le d_{50} \le 0.002\, ms$$

B-1.3 Total load formula

The total load formula is computed by linear addition of equilibrium bed and suspended loads as follows:

$$q_{T,eq} = q_{b,eq} + q_{s,eq}$$
$$c_{T,eq} = \frac{q_{T,eq}}{u \cdot h} \qquad \text{(B-3)}$$

In which $c_{T,eq}$ is the depth-averaged equilibrium total sediment concentration required in computation of source term in ADV-DIFF and bed evolution equations.

B-2 Method of Ackers and White

Based on the analysis of 925 sets of field and flume data, Ackers and White (1973) proposed the following formula for total equilibrium sediment transport:

$$q_t = K \cdot u \cdot d_{35} \left(\frac{u}{u_*}\right)^n \left(\frac{Y - Y_{cr}}{Y_{cr}}\right)^m \qquad \text{(B-4)}$$

$$Y = \left(\frac{u_*^n}{(g \cdot d_{35}(s-1))^{0.5}}\right)\left(\frac{u}{5.66 \log(10\, h/d_{35})}\right)^{1-n}$$

$$D_* = d_{35}\left(\frac{g(s-1)}{\upsilon^2}\right)^{1/3}$$

$$K = 10^{-3.46 + 2.79\log(D_*) - 0.98(\log(D_*))^2} \qquad 1 < D_* < 60$$
$$m = \frac{6.83}{D_*} + 1.67$$
$$n = 1 - 0.56 \log(D_*)$$
$$Y_{cr} = \frac{0.23}{D_*^{0.5}} + 0.14$$

$K = 0.25$ $D_* \geq 60$

$m = 1.78$

$n = 0$

$Y_{cr} = 0.17$

The computation of coefficients of m and K in the above equations is based on revision of the original formula by HR Waalingford (1990). In the above equations the parameters have been defined as follows:

q_t : total load transport (m^2/s)
u: depth-averaged velocity magnitude (m/s)
u_*: bed friction velocity (m/s)
Y: particle mobility parameter
Y_{cr}: critical particle mobility parameter
N, m, K: coefficients
Y: kinematic viscosity (m^2/s)
s: specific density
$d_{35'}$: representative diameter of bed material (m)

B-3 Method of Brownlie

The total sediment concentration equation suggested by Brownlie (1981) is based on over 1000 field and laboratory data.

$$c_{T,eq} = 7115 c_f (F_g - F_{g_{cr}})^{1.978} S^{0.6601} \left(\frac{h}{d_{50}} \right)^{-0.3301} \tag{B-5}$$

$$F_g = \frac{u}{\sqrt{sgd_{50}}}$$

$$F_{g_{cr}} = 4.596 \tau_c^{*0.5293} S^{-0.1405} \sigma_g^{-0.1606}$$

$$\sigma_g = \frac{1}{1.29} \log(\frac{d_{90}}{d_{50}})$$

$$\tau_c^* = 0.22 Y_* + 0.06 (10)^{-7.7 Y_*}$$

$$Y_* = \left(s \cdot R_g \right)^{-0.6}$$

$$R_g = \frac{\sqrt{g d_{50}^3}}{\upsilon}$$

In the above equations the parameters have been defined as follows:

$c_{T,eq}$: total sediment concentration (ppm)

h: flow depth (m)

S: energy slope

d_{90}, d_{50} : representative diameters of bed material (m)

C Short notes on turbulence model

The most sophisticated depth-averaged zero equation turbulence models are those considering the turbulence due to the vertical momentum exchange generated by bed surface as well as those due to horizontal momentum exchange. These turbulence models are developed by integrating the generalized Prandtl mixing length equation (Eq. 3–11) over flow depth. Following assumptions are made to enable such an integration (Schmautz, 2003):

- The horizontal gradients of velocities over water depth are assumed to be constant, allowing substituting the local flow velocities by depth-averaged flow velocities.
- The gradients of vertical velocity are ignored.

Applying the above assumptions to Eq. (3–11) yields:

$$\upsilon_t(z) = l^2 \left[\left(\frac{\partial u}{\partial z} \right)^2 + \left(\frac{\partial v}{\partial z} \right)^2 + 2\left(\frac{\partial u}{\partial x} \right)^2 + 2\left(\frac{\partial v}{\partial y} \right)^2 + \left(\frac{\partial u}{\partial y} + \frac{\partial v}{\partial x} \right)^2 \right]^{\frac{1}{2}} \tag{C-1}$$

To solve the problem of integration of the above equation over water depth, two methods are presented in the following:

a) Schmautz and Aufleger (2001) assumed that depth-averaged eddy viscosity is basically a function of velocity gradients, thereby, separate integration of mixing length and the term under root square is permissible. Moreover, the vertical gradient terms are not explicitly integrated but are approximated separately as if a uniform flow in x and y direction ($\partial/\partial x = \partial/\partial y = 0$) exists, resulting in diminishing the last three terms. The remaining terms represent the fraction of bed-generated turbulence in eddy viscosity, already introduced in Eq. (3–8). Following the above-mentioned approach the depth-averaged eddy viscosity can be determined as follows:

$$\upsilon_t = l^2 \left[\left(\frac{1}{C_{lm}^2} e^* \sigma_t \frac{u_*}{h} \right)^2 + 2\left(\frac{\partial u}{\partial x} \right)^2 + 2\left(\frac{\partial v}{\partial y} \right)^2 + \left(\frac{\partial u}{\partial y} + \frac{\partial v}{\partial x} \right)^2 \right]^{\frac{1}{2}} \tag{C-2}$$

With $l = h C_m$. The new empirical parameter (C_m) is dependent on e^*, the dimensionless diffusivity, and should be determined by trial and error or measurement. $C_m = 0.2$ for $e^* = 0.6$ and 0.27 for $e^* = 0.9$ have been suggested by Schmautz and Aufleger (2001).

b) Malcherek (2002) suggested the following formula by expanding the terms under square by Taylor series to enable integration of each term directly:

$$\upsilon_t = \frac{1}{6}\kappa h u_* + \frac{1}{40}\frac{\kappa^3 h^3}{u_*}\left[2\left(\frac{\partial u}{\partial x}\right)^2 + 2\left(\frac{\partial v}{\partial y}\right)^2 + \left(\frac{\partial u}{\partial y} + \frac{\partial v}{\partial x}\right)^2\right] \tag{C-3}$$

Schmautz (2003) showed that this equation yields almost identical results with Eqs. (Eq. C-2) in a few test trapezoidal channels and a natural one and agreed well with the result of a k-ε turbulence model (SIMK, Kölling, 1994) for the applied test cases.

D Implementation of data model in FE- and conjugate domains in FORTRAN

Table D-1 Data model developed to enable simulation of bank evolution

```
TYPE :: profile_node
 Integer             :: Fe_nodenumber
 REAL (KIND=DOUBLE) :: distance
 REAL (KIND=DOUBLE) :: elevation
 REAL (KIND=DOUBLE) :: Water_elev
 CHARACTER(LEN=9)   :: attribute !(Profile,Nose,Overhang,Front,basepoint)
END TYPE profile_node
```

```
TYPE :: profile
 INTEGE               :: CL_number
 INTEGER              :: max_nodes    ! maximum prnodes in each profile
, which is now limited to a maximum of 200.
 Type (profile_node), dimension (200) :: PRnode
 REAL (KIND=DOUBLE)   :: water_elev
 Integer              :: Rnose        ! the profile's node number of the
 nose of the right overhang
 Integer              :: Lnose
 Integer              :: Rfront       ! The profile's node number the
 undercutting front of the right bank
 Integer              :: Lfront
 logical              :: Activation   !(.TRUE. or .FALSE.)
    END TYPE profile
```

```
TYPE :: Finite_element_node
 CHARACTER (LEN =7)   :: typ              !(corner,midside)
 INTEGER              :: Node_Number      !(linkage to profile nodes
in conjugate domain)
 INTEGER              :: Profile_Number
 REAL (KIND=DOUBLE)   :: elevation, water_level
 REAL (KIND=DOUBLE)   :: sed_source
 CHARACTER (LEN =10)  :: status            !(activate, deactivate)
END TYPE finite_element_node
```

```
TYPE :: potential_nose
 INTEGER              :: node, nextnode
 REAL(kind = DOUBLE)  :: dist
END TYPE potential_nose
```

E Mesh adaptation- special cases

Depending on the constellation of nodes and amount of computed undercutting (bank retreat) special cases should be accounted for in the algorithm of mesh adaptation. The former is a consequence of spatial discretization (mesh size) and the latter due to temporal discretization (time steps). These cases are presented in the following for the case of the development of undercutting front for the first time in the riverbank profile and the case of its advancement.

E-1 Development of undercutting

Special cases may occur in the algorithm of generation of undercutting front, if water level and consequently “Nose” and “Front” of undercutting do not coincide with FE-nodes. In such cases a new node in conjugate domain is added to the profile with attributes “Nose” and /or “Front” at the corresponding positions, with their linked Fe-nodenumber data variable equal to zero.

In Figs. (E-1 a, b) this situation have been shown separately for the cases in which “Nose” and “Front” have not coincided / associated with a FE-node, respectively. Projection of those profile nodes over water surface, which are spans between “Nose” and “Front” has been depicted by vertical arrows in Fig. (E-1b). Furthermore, the mesh adaptation in case no FE-node is projected between “Nose” and “Front” has been shown in Fig. (E-1c). As it is seen from Figs. (E-1b,c), if there is no FE-node associated with profile node with attribute “Front”, then an inconsistency may occur between profiles in the two mentioned domains in the vicinity of “Front” of undercutting, which may have minimal influence on flow field computation in FE-domain, if the discretization in this zone is refined enough. Such an inconsistency is removed when the overhang fails and the node with attribute “Front” is omitted from profile domain. This will be also the case, when during the process of advancement of undercutting front, a FE-node locates over the mentioned node, thereby its vertical projection coincides with the node with attribute “Front” in profile domain, which gives rise to the situation depicted in Fig. (E-1a).

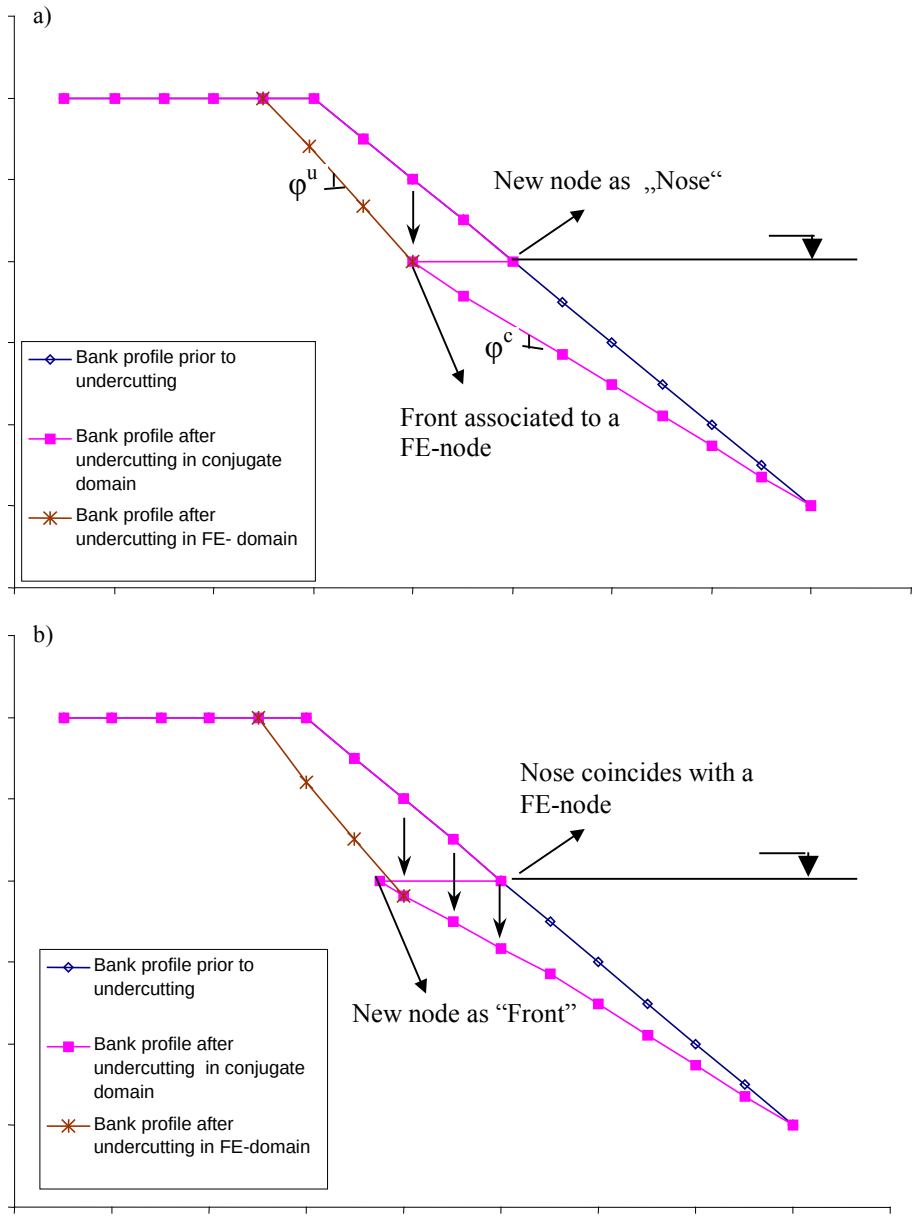

Figure E-1 Schematic illustration of mesh adaptation by generation of undercutting for the first time in a bank profile

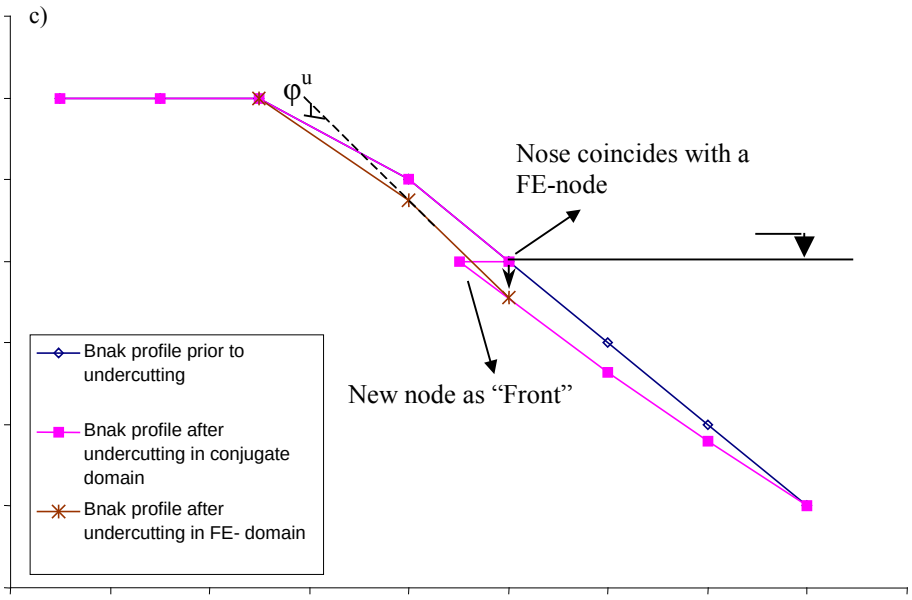

Figure E-1 Continuation from the previous page

E-2 Advancement of undercutting

In case of advancement of an existing undercutting during steady state, the old "Front" node is laterally shifted to its new position, as shown in Fig. (E-2a). Mesh adaptation becomes however, more complex in unsteady flow. In case of submergence of an already exiting overhang, the submerged zone is eliminated from overhang as shown in Fig. (4-11) in Ch. 4.2.4.While in case of drop of water stage in the river, a new undercutting may form below an existing overhang, generating a complex bank geometry. For simplification, it has been assumed that the additional overhang below an existing one fails immediately. This results in addition of a profile node at place of the actual front of the undercutting with a given attribute of "Base point". The profile of failed overhang may meet the old one below the old overhang (Fig. E-2b), at the already existing "Front" (Fig. E-2c) or comprise the existing overhang and cause to undercut the existing overhang (Fig. E-2d). The latter results in lateral advancement of the already existing "Front". In all mentioned cases the slope of the new profile over water surface is equal to unsaturated dense angle of repose (φ^u).

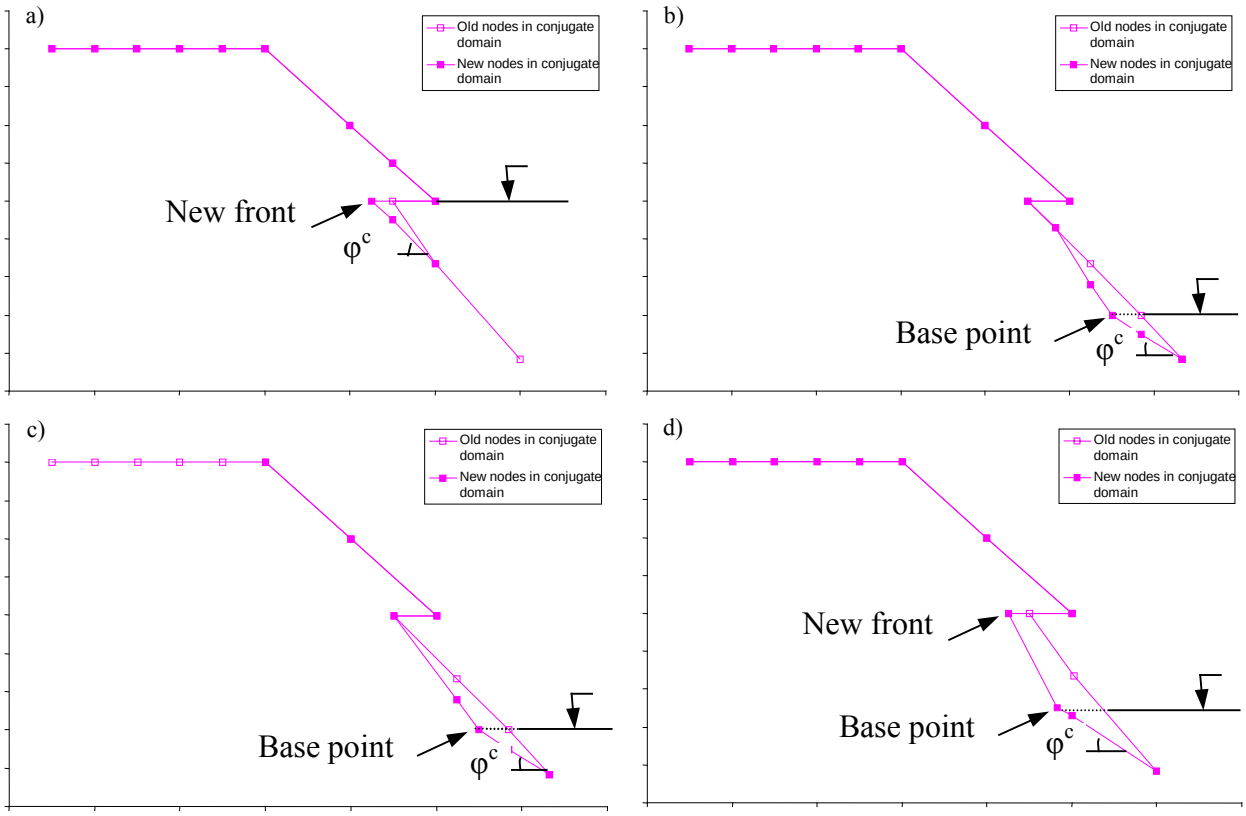

Figure E-2 Schematic illustration of mesh adaptation by advancement of undercutting during steady water stage (a), as well as by water drop in the river (b-d)

F Specifications of applied measurement instruments

F-1 Terrestrial laser scanner

Table F-1 Technical specification of laser scanner

Manufactured by		Cyra Technologies,Inc.
Measurement method		Time of flight
Laser wave length		532 (nm)
Class		2
Beam divergence/ size of the point		≈0.12 mRad / 6 mm at 50 m range
Measurement frequency		2000 Hz
Measurement range		1.5 m–100 m
Resolution		Highest: 1.2 mm at 50 m range
1 Scan pass		1.5 hours (highest resolution and max. scan range)
Measuring speed		1 Million points/ hour
Scanning resolution	Horizontal	> 1 / 3500°, 1mm/ 10 m
	Vertical	> 1 / 3500°, 1mm/ 10 m
Accuracy		6mm /50 m
Dimension (L×W×H)		31× 27 × 42
Weight		27.5 kg

F-2 Acoustic Doppler Profiler (StreamPro ADCP)

StreamPro, a state-of-the-art mini ADCP system from Teledyne RDInstrument Company was applied for measurement of flow discharge and 3D velocity profile in the present work. It has been the smallest ADCP in market at the time of application, especially developed for shallow to very shallow stream discharge measurement. The specification of the instrument has been summarized in the following table.

Table F-2 Technical specification of StreamPro ADCP: Velocity profiling

Number of cells	20
Min. cell size	2 cm
Max. cell size	10 cm
Max. measurement range	2 m
Start of the first cell	7-30 cm from transducer (depending on cell's size)
Accuracy (at cell size of a half of maximum)	±1.0 %, ±0.2 cm/s
Resolution	0.1 (cm/s)
Velocity range	±2 (m/s)
Frequency	2.0 mHz
Geometry	4 beams, ±20° beam angle
Material	Polyurethane
Weight in air	5 kg including electronics, transducer, float , and batteries (1m cable version)
Dimensions: electronics housing	15 ×20 × 10 cm
Dimensions: transducer	3.5 cm diameter × 15 cm length
Dimensions: float	44 ×70 × 11 cm

F-3 Acoustic Doppler Velocimeter (ADV)

The ADV probe Hydra® from SonTek with the unique capability of measurement of boundary distance to the sampling volume has been applied for precise three-dimensional velocity measurement in boundary layer. The probe is equipped with a pressure sensor, a tilt sensor, a compass and a temperature sensor. The General specification of the instrument has been given in the following table.

Table F-3 Technical specification of ADV

Acoustic frequency		10 MHz
Ping rate		150-250 (times per second)
Sampling method		Continuous (real time)- Single burst and multiple burst (autonomous deployment)
Sampling rate		0.1-25 Hz
Standard sampling volume		0.25 ^{cc}
Diameter of sampling volume		6 mm
Height of sampling volume	Standard	7.2 mm
	Short	1.2 mm
	Median	3.6 mm
	long	4.8 mm
Distance to the sampling volume		10 cm
Resolution		0.01 cm/s
Programmable measurement range (cm/s)	3	Max. ±30 cm/s (horizontal), Max. ±8 cm/s (vertical)
	10	Max. ±60 cm/s (horizontal), Max. ±15 cm/s (vertical)
	30	Max. ±120 cm/s (horizontal), Max. ±30 cm/s (vertical)
	100	Max. ±300 cm/s (horizontal), Max. ±75cm/s (vertical)
	250	Max. ±360 cm/s (horizontal), Max. ±90 cm/s (vertical)

Tabel F-3 Continuation from previous page

Accuracy	±1.0% of measurement range
Temperature sensor	-5 to +50
Resolution	0.01° C
Accuracy	±0.2°C
Tilt sensor	0-360° (heading), -50° to +50° (pitch and roll)
Resolution	0.1°
Accuracy	± 2° (heading), ± (pitch and roll)

F-4 Turbidity profiler (ASM-IV)

A state-of-the-art array of turbidity sensors (ASM-IV) from Argus Gesellschaft für Umweltmeßtechnik mbH has been applied for measurement of sediment transport. The specification of the instrument has been presented in the following table.

Table F-4 Technical specification of ASM-IV

Measuring method	Optical
Sensors	Backscatter infrared laser sensor (850nm)
Sensor spacing	10 mm
Number of sensors	80
Measuring interval	Min. 1 (sec.)
Sampling rate	255 samples maximum
Measuring range	50-50000 mg/l (sand), 5-5000 mg/l mud (d_{50}=20 μm)
Resolution	5%
Accuracy	±10%
Pressure sensor	0-5 bar
Resolution	0.5 %
Accuracy	± 0.3% (full range)
Temperature sensor	-10: +45
Resolution	1° C
Accuracy	±0.5°C
Weight	8 kg
Dimensions: Diameter	30 mm (sensor area), 57 mm (head)
Dimensions: length	80 cm (sensor area)

F-5 Single beam echo-sounder

A special single-beam echo-sounder has been used to measure bed elevation in extreme shallow water depth (less than 30 cm). For this purpose, the **B**lack **B**ox **E**cholot-**S**ensor (BBES-700) from the firma Dr.Fahrentholz with the following specification was applied.

Table F-5 Technical specification ASM-IV

Acoustic frequency	700 kHz
Sampling rate	Up to 40 Hz
Minimum water depth	0.10 m
Depth range	Up to 2.5 m
Weight of electronic Box	3 kg
Dimensions of electronics	225 ×125 × 200 mm

F-6 RTK-GPS system

To make the riverbed elevation data measured by single-beam echo-sounder applicable for bathymetry analysis, measuring the global coordinate of the instrument is required. This has been achieved by integrating the mentioned instrument with a **R**eal-**T**ime **K**inematic- **G**lobal **P**ositioning **S**ystem (RTK-GPS). The system uses a **D**ifferential GPS system (DGPS) comprising two GPS units, one used as a reference station or base (GPS system SR530 from firma Leica) and the other as the moving unit often called rover (GPS system 1200 from firma Leica).

The reference station is a GPS system with a known position. Its position is determined using signals received from satellites (a minimum of four satellite should be in sight of the GPS) or signals received from sending stations of net services such as SAPOS. The application of the latter method was applied since it improves the overall accuracy of the measurements. The rover unit receives signals from satellites as well as base and achieve real-time correction of positioning using signals received from base. This method improves the horizontal positioning accuracy to 1 cm and vertical accuracy to 2 cm, depending on the available number of satellites in sight of view at the time of measurements. The specifications of the GPS system 1200 is presented in the following table.

Table F-6 GPS-system 1200/SR530

GPS Technology			SmartTrack
Satellite reception			Dual Frequency
Receiver channels			12 Channels continuous tracking on L1 and L2
Satellites tracked			Up to 12 simultaneously on L1 and L2
Precision	Static	Horizontal	5 mm + 0.5 ppm /5mm +1ppm (sytem SR530)
		Vertical	10 mm + 0.5 ppm
	Kinematic	Horizontal	10 mm +1 ppm
		Vertical	20 mm +1 ppm
Position update rate			max. 20 Hz

F-7 Traverse system

The traverse system comprises a space truss and a conveying wagon. The truss was built in three units made of six ladders, each approximately 4m long. Each unit consists of two ladders connected together at a spacing of 40 cm in parallel (Fig. F-1). The three truss units were connected at feet together by inserting solid aluminium blocks into the hollow feet of the ladders in connection points and fixing them with screws. The connection zones were further reinforced by cross bracing (Fig. F-2).

The conveying wagon was built from aluminium sheet and a vertically adjustable square bar (Fig. F-2). The wagon could be moved over the truss using a conveying rope system by installing pulleys at two ends of the truss and on the wagon (Fig. F-3). The technical drawings of the wagon and the bar have been presented in Figs. (F-4) to (F-6).

The bar could be fixed remotely using a large screw (manoeuvred using two ropes) (Fig. F-2). The vertical adjustment was achieved remotely using a pulley system. The horizontal position of the bar and the probe respectively were read using a laser distance measurement system installed on one end of the truss. The vertical as well as horizontal position of the bar was measured additionally using tachymeter.

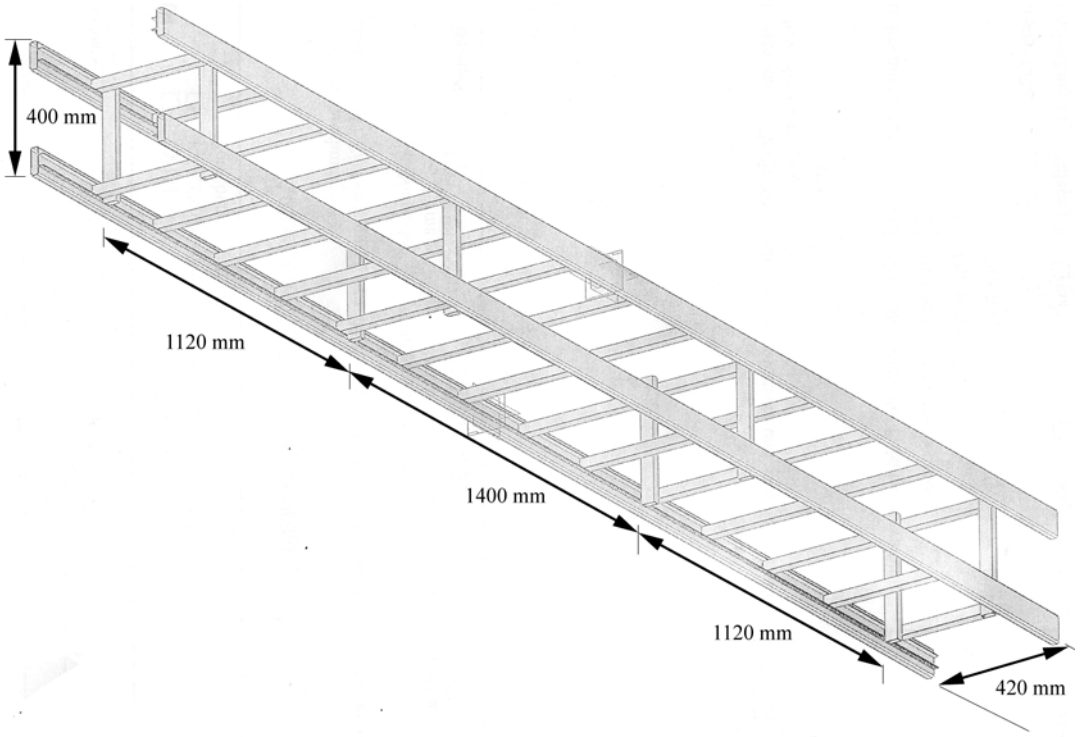

Figure F-1 One unit of the truss

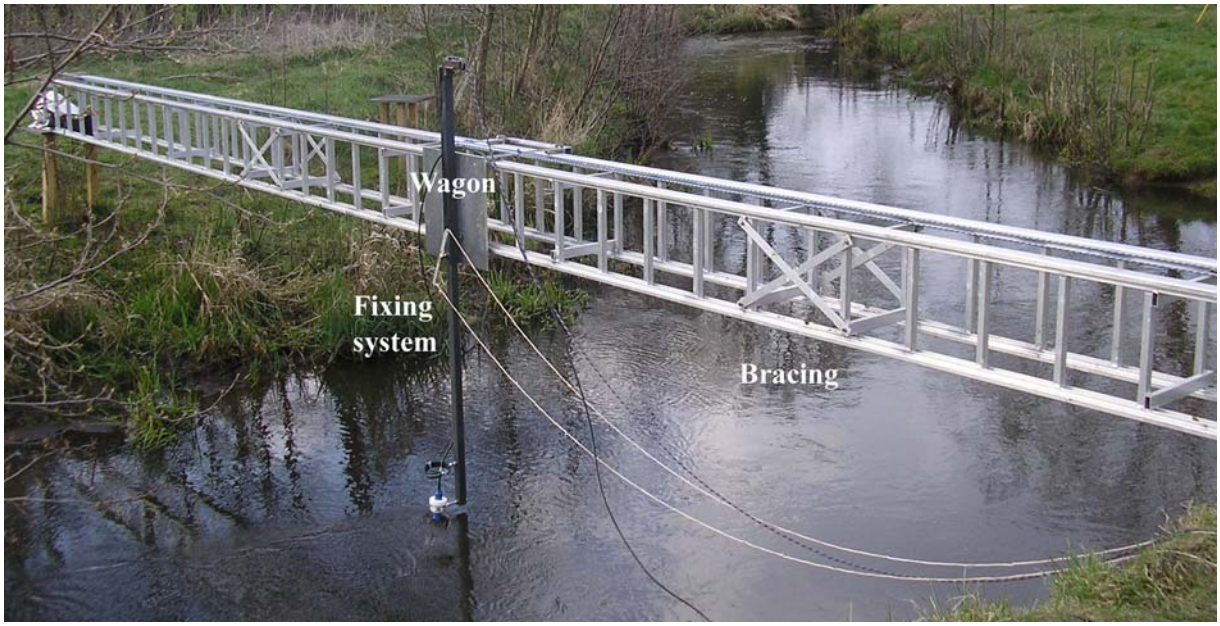

Figure F-2 Traverse system illustrating the wagon, bracing and fixing system of the bar

Figure F-3 Illustration of the remote manoeuvre and pulley system of the traverse

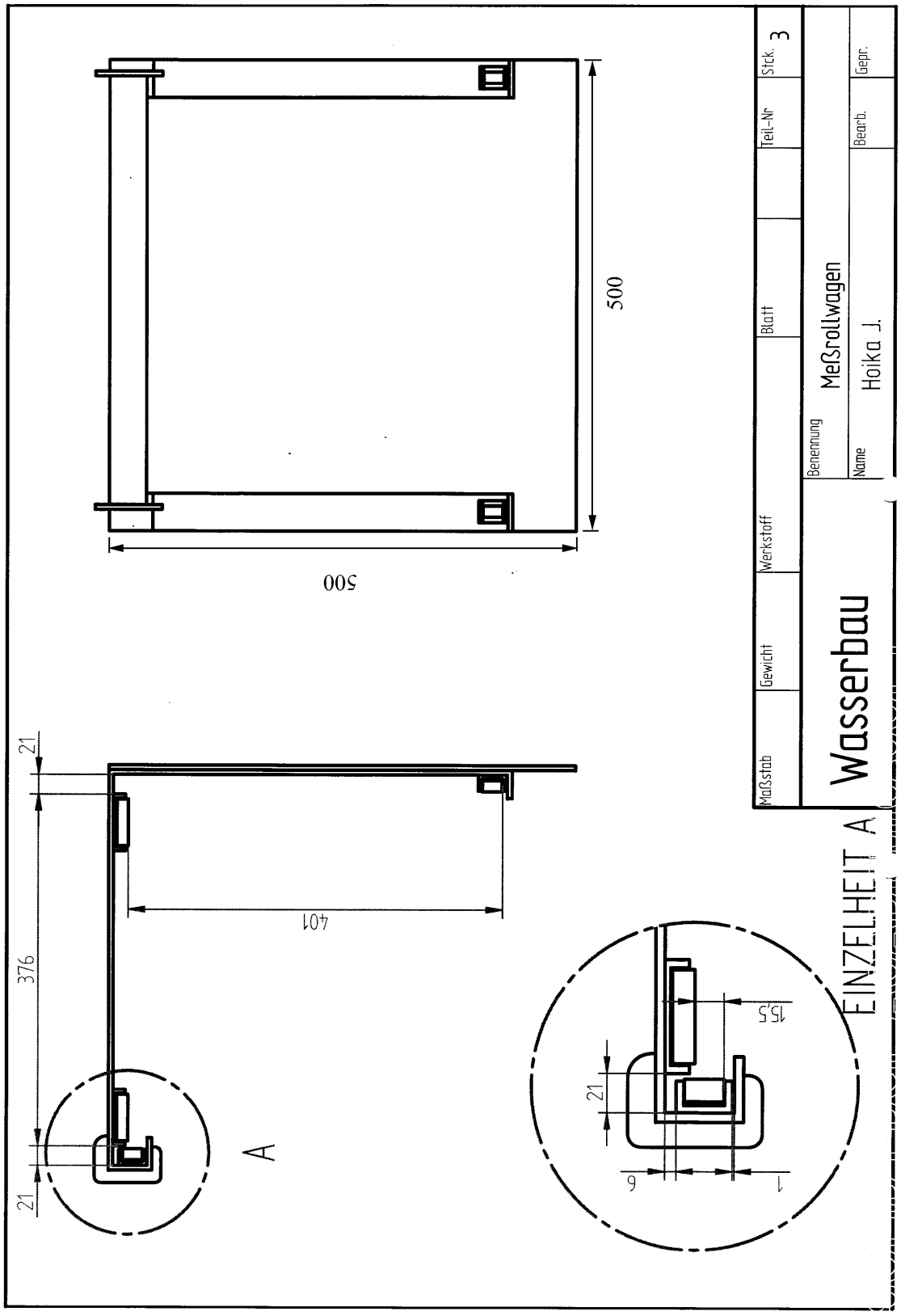

Figure F-4 Technical drawing of the traverse wagon

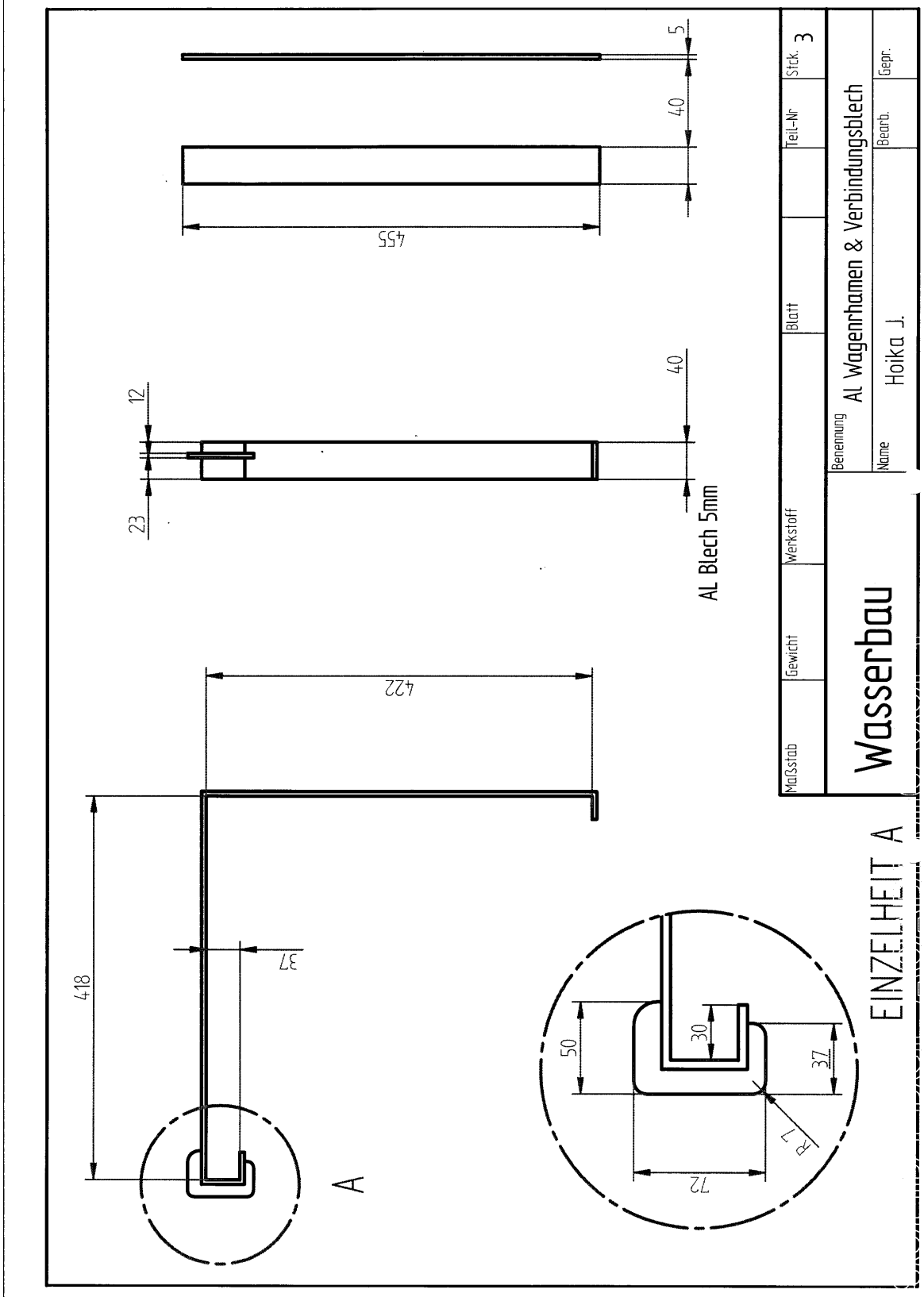

Figure F-5 Detailed technical drawing of the supporting frame of the traverse wagon

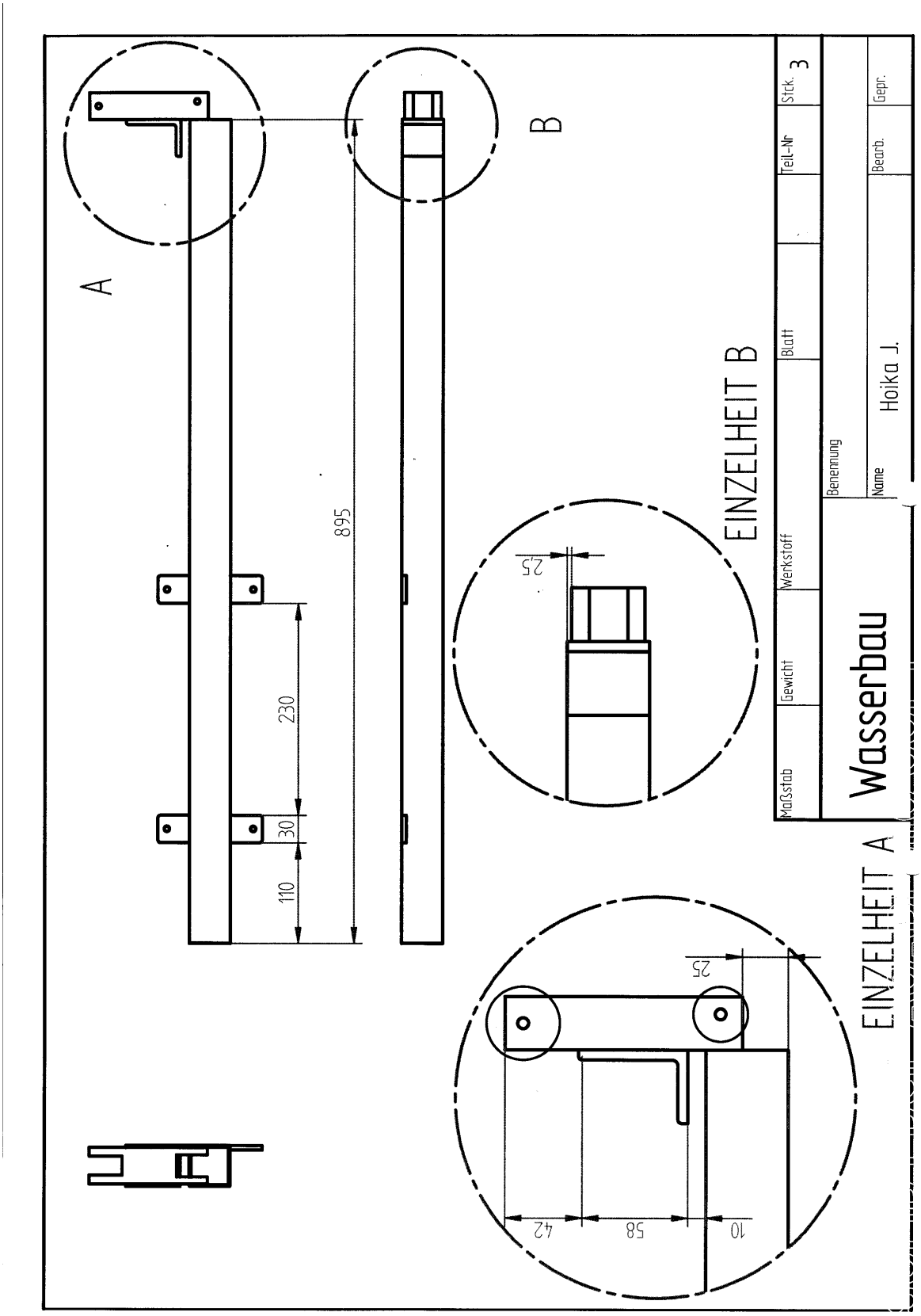

Figure F-6 Technical drawing of the adjustable bar

F-8 Remote camera

Table F-7 Specification of the remote camera

Type	Nokia PT-6
Dimensions	130 x 98 x 82 mm (including stand)
Weight	300 g
Function keys	1
Color	Pearl white
Operating temperature	–20C o to +50 C o, 4% to 100% relative operating humidity
GSM frequency bands	900/1800 MHz
Image resolution	1152x864, 640x480, 320x240, or 160x120 pixels; true color
Video clip resolution	176x144 pixels true color with audio
Media file format	Still images: JPEG; Video: H.263
Camera view angle	55 degrees, 2x digital zoom, minimum focus distance 0.5 m
Power supply	Power Supply AC-12, 100-240 VAC, Built-in back-up battery (operating time up to 12 h) Compatible with Nokia Mobile Charger LCH-12
IP Class	54
Interfaces	SMS, MMS, SMTP Internet email, and Bluetooth specification 1.1 supporting Serial Port profile

G Supplementary results of measurements

G-1 Results of sediment analysis

\\HELSINK\allgemein\labor\Protokolle\[26.05.03]\[SCHER002.XLS]Anlage (2)

Anlage .....

Projektnr.: i0506	Datei: dichte01.xls
Projektkurztitel: Scherfestigkeit Sand, Wasserbau	
Entnahmestelle:	GP / UP / RK
Entnahmetiefe:	Bodenart: Sand
Ausgeführt von: mb	Beginn: 5.9.2006 / Ende:
Geprüft von:	Datum:

Prüfprotokoll

BESTIMMUNG DER

DICHTE

DES BODENS

nach DIN 18 125 -LA (Aug. 1997)

FBL010_1

Ermittlung der Masse der feuchten Probe			
Zylinder Nr.	7	15	
Feuchte Probe + Zylinder [g]	2205,4	2015,8	
Zylinder [g]	596,8	586,6	
Feuchte Probe m [g]	1608,6	1429,2	
Ermittlung des Volumens der Probe			
Länge des Ausstechzylinders l_Z [cm]	12,0	12,0	
Länge des oberen Leerraumes l_O [cm]	0,3	0,5	
Länge des unteren Leerraumes l_U [cm]	0,0	0,9	
Länge der Probe $l = l_Z - (l_U + l_O)$ [cm]	11,7	10,6	
Innendurchmesser des Zylinders d [cm]	9,6	9,6	
Volumen der Probe $V = l * (\pi * d^2/4)$ [cm³]	846,9	767,3	
Wassergehalt			
Behälter Nr.	302	306	
Feuchte Probe + Behälter A [g]	718,79	492,57	
Trockene Probe + Behälter B [g]	668,34	459,2	
Behälter C [g]	212,63	205,89	
Wassergehalt (A-B)/(B-C)*100 [%]	11,07	13,17	
Dichte des Bodens $\rho = m/V$ [g/cm³]	1,899	1,863	
Trockendichte des Bodens ρ_d [g/cm³]	1,710	1,646	
Korndichte ρ_S [g/cm³]	2,65	2,65	
Porenanteil $n = 1 - (\rho_d / \rho_S)\ 100$ [%]	35,5	37,9	
Porenanzahl $e = (\rho_S / \rho_d) - 1$ [-]	0,55	0,61	
Anteil der wassergefüllten Poren $n_w = (\rho_d / \rho_w) * w$ [%]	18,9	21,7	
Luftporenanteil $n_a = n - n_w$ [%]	16,5	16,2	
Sättigungszahl $S_r = n_w / n$ [-]	0,53	0,57	
Proctordichte ρ_{Pr} [g/cm³]			
Verdichtungsgrad D_{Pr} [%]			

TUHH Technische Universität Hamburg-Harburg
Geotechnik und Baubetrieb
Univ.-Prof. Dr.-Ing. Jürgen Grabe
Harburger Schloßstr. 20
21079 Hamburg
Tel.: +49 (0)40 / 428 78-3782
Fax: +49 (0)40 / 428 78-4020

Figure G-1 Physical property two soil samples from riverbed and bank

TUHH
Technische Universität Hamburg-Harburg
Geotechnik und Baubetrieb
Univ.-Prof. Dr.-Ing. Jürgen Grabe
Harburger Schloßstr. 20
21079 Hamburg
Tel.: +49 (0)40 / 428 78-3782
Fax: +49 (0)40 / 428 78-4020
www.tu-harburg.de/gbt

Anlage .....
Blatt 1/2
Sep. 2006

DIREKTER SCHERVERSUCH

DIN 18 137 - DSR

Projekt Nr.: i0506
Wasserbau
Nasermoaddeli

Entnahmestelle:
Entnahmetiefe:
Bodenart: Sand
Probengüteklasse: 1

Probe Nr.		1	2	3
Anfangswassergehalt	[%]	11,1	11,1	11,1
Endwassergehalt	[%]	10,9	11,0	10,9
Einbaudichte	[g/cm³]	1,895	1,892	1,892
Konsolidierung σ	[kN/m²]	51	76	101
Konsolidierungsdauer	[h]	4	4	4
Schernormalspannung	[kN/m²]	51	76	101
Schergeschwindigkeit	mm/min	0,500	0,500	0,500
Scherfestigkeit τ	[kN/m²]	60,3	86,0	105,8

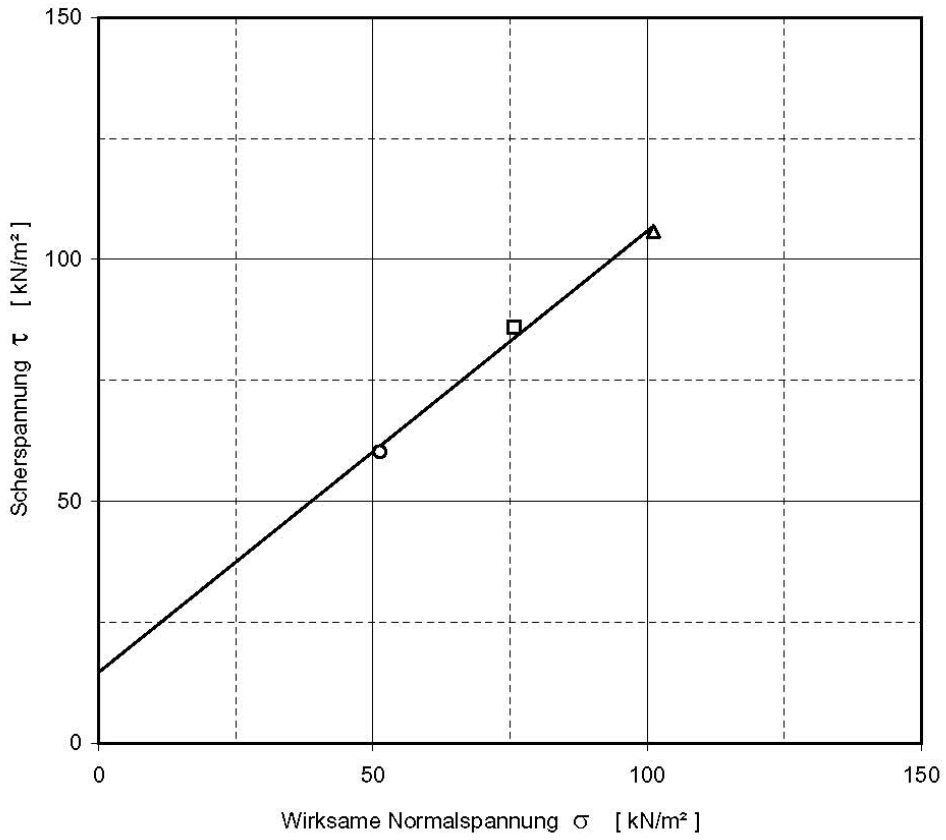

Reibungswinkel φ' = 42,3 °
Kohäsion c' = 14,6 kN/m²

Bearbeiter: .....
Geprüft von: .....

Figure G-2 Result of the direct shear test

TUHH
Technische Universität Hamburg-Harburg
Geotechnik und Baubetrieb
Univ.-Prof. Dr.-Ing. Jürgen Grabe
Harburger Schloßstr. 20
21079 Hamburg
Tel.: +49 (0)40 / 428 78-3752
Fax: +49 (0)40 / 428 78-4229
www.tu-harburg.de/gbt

Anlage .....
Blatt 2/2
Sep. 2006

DIREKTER SCHERVERSUCH

DIN 18 137 - DSR

Projekt Nr.: i0506
Wasserbau
Nasermoaddeli

Entnahmestelle:
Entnahmetiefe:
Bodenart: Sand
Probengüteklasse: 1

Probe Nr.		1	2	3
Anfangswassergehalt	[%]	11,1	11,1	11,1
Endwassergehalt	[%]	10,9	11,0	10,9
Einbaudichte	[g/cm³]	1,895	1,892	1,892
Konsolidierung σ	[kN/m²]	51	76	101
Konsolidierungsdauer	[h]	4	4	4
Schernormalspannung	[kN/m²]	51	76	101
Schergeschwindigkeit	mm/min	0,500	0,500	0,500
Scherfestigkeit τ	[kN/m²]	60,3	86,0	105,8

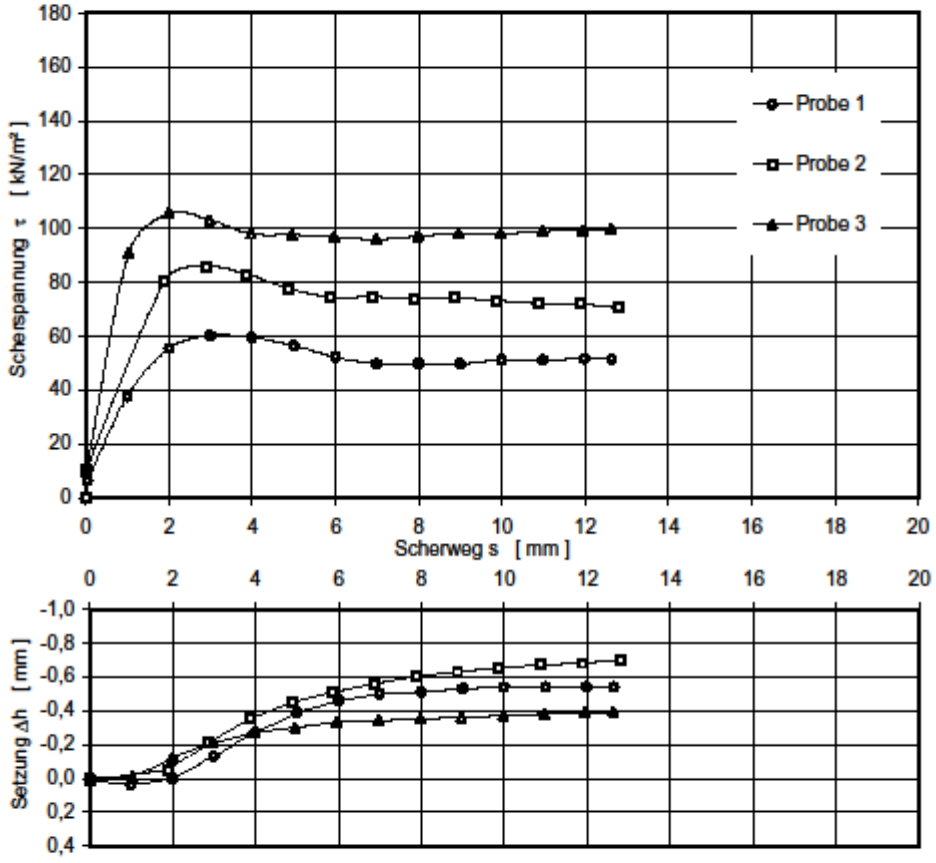

Reibungswinkel φ' = 42,3 °
Kohäsion c' = 14,6 kN/m²

Bearbeiter: .....
Geprüft von: .....

Figure G-3 Result of the direct shear test

G-2 Effect of averaging period on vertical profile of velocity

The effect of averaging period on the vertical profile of flow velocity magnitude, continuously measured by upward-looking StreamPro upstream of the bridge of Hardebek-Brokenlander Au have been presented in the following. The numbers in the title of these diagrams given in parenthesis represent the range of ensembles chosen for the analysis and date of measurement and the velocity magnitude is given in (m/s).

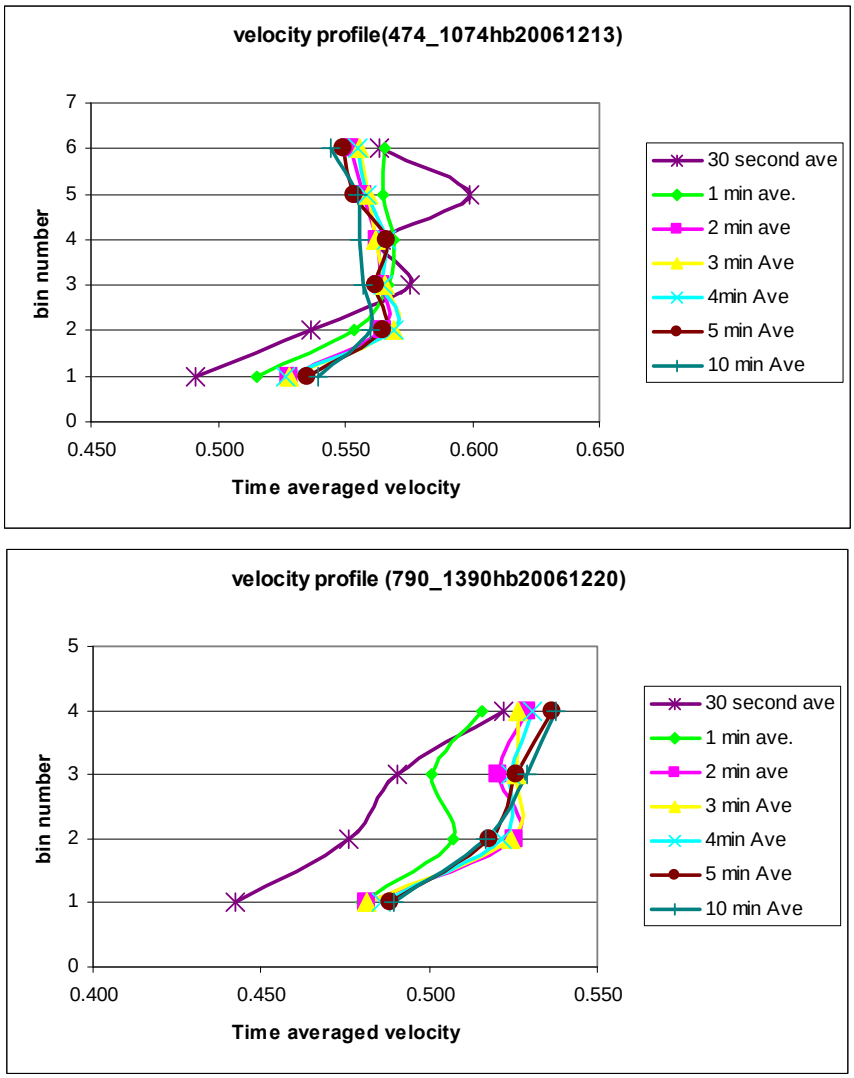

Figure G-4 Effect of averaging period on vertical distribution of velocity magnitude at Hardebek-Brokenlander Au

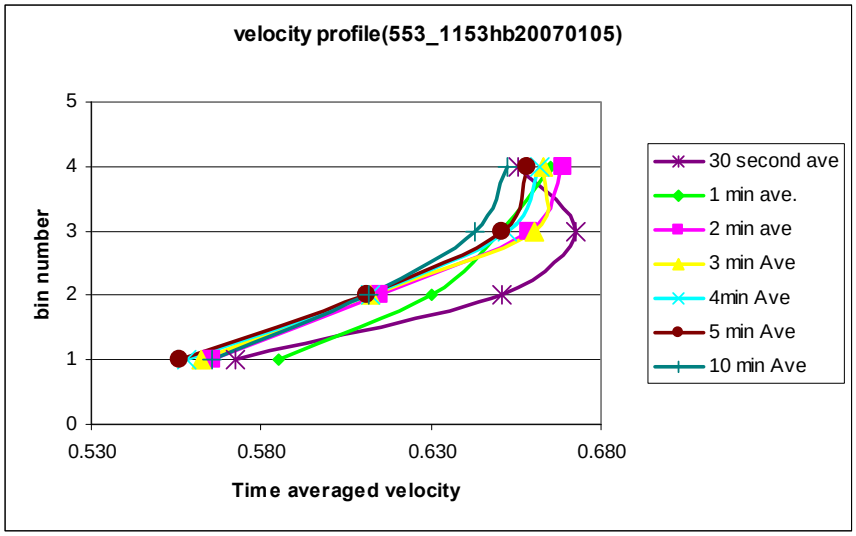

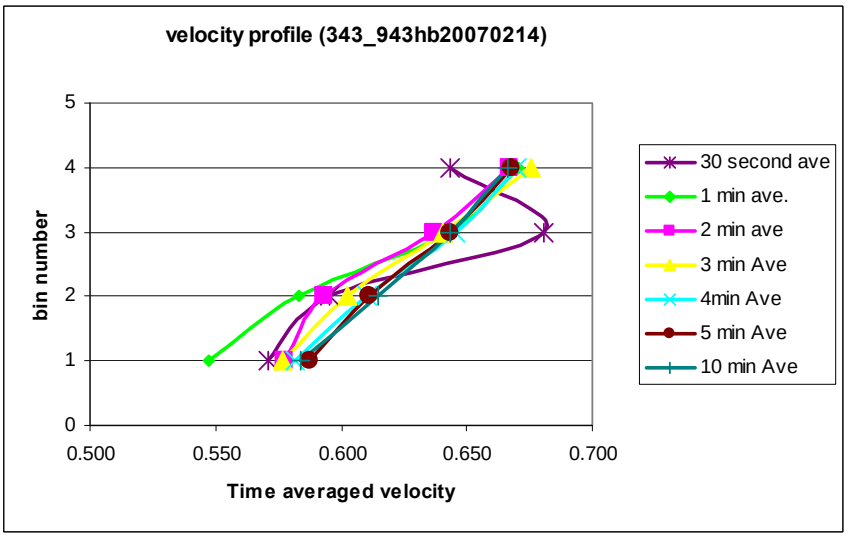

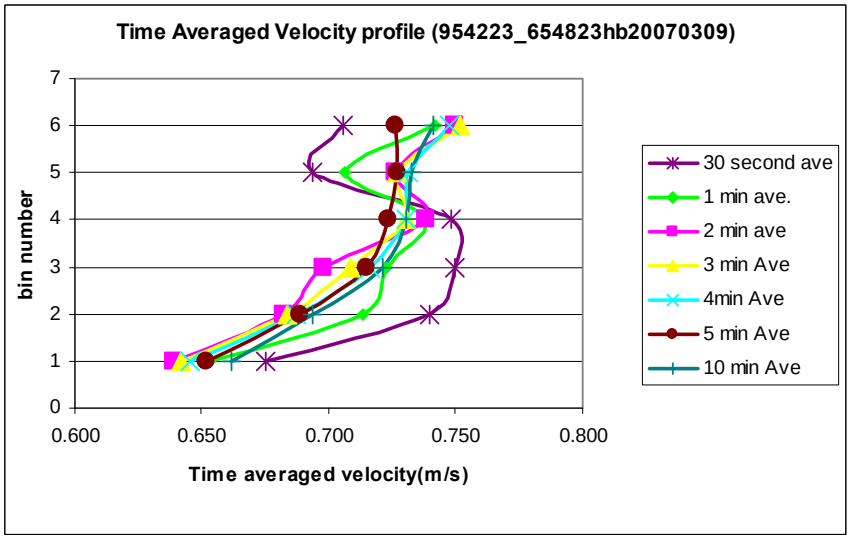

FigureG-4 : Continuation from previous page

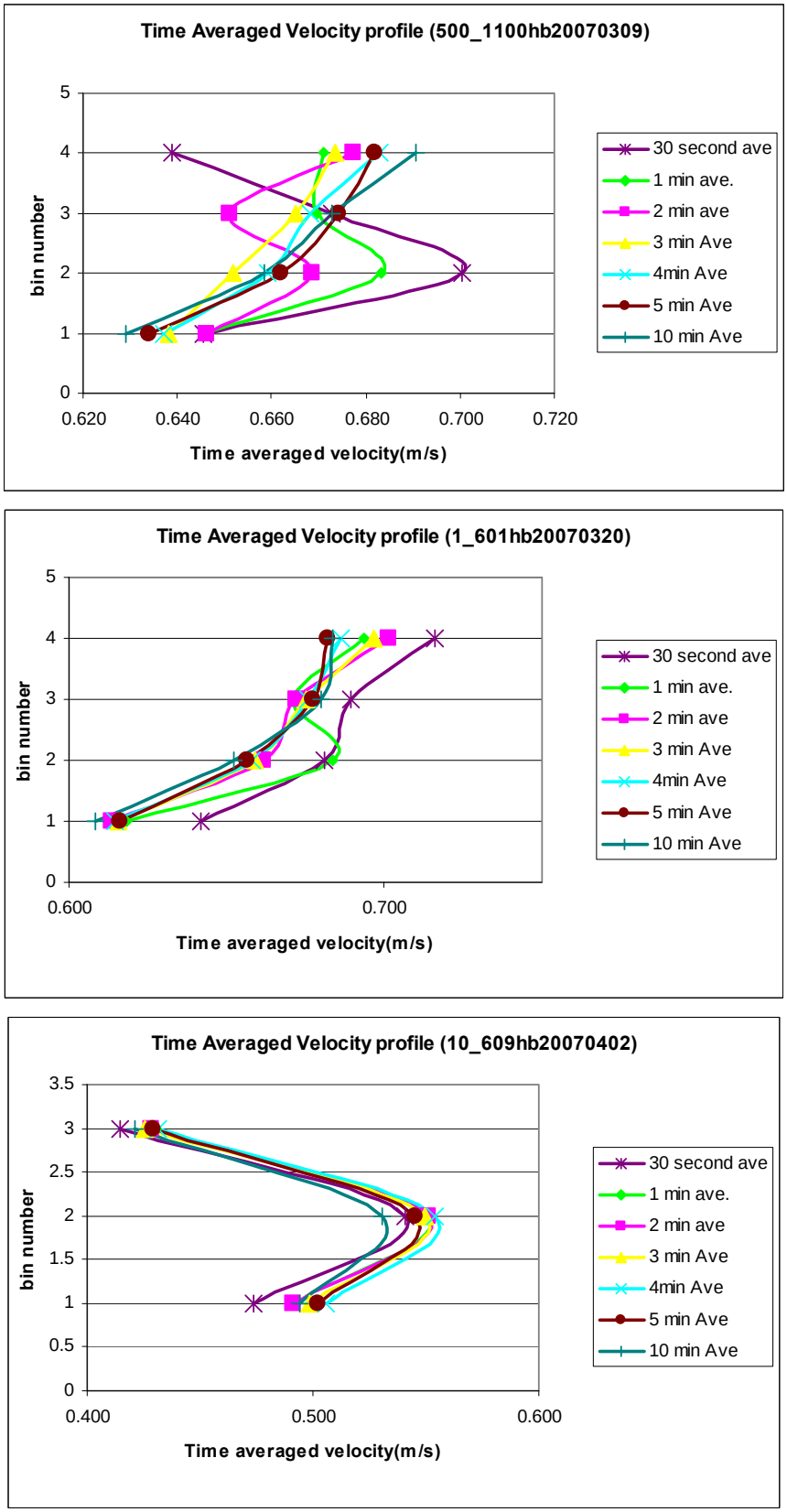

FigureG-4 : Continuation from previous page

G-3 Monitoring riverbank surface

G-3.1 Bank surface images in second measurement phase

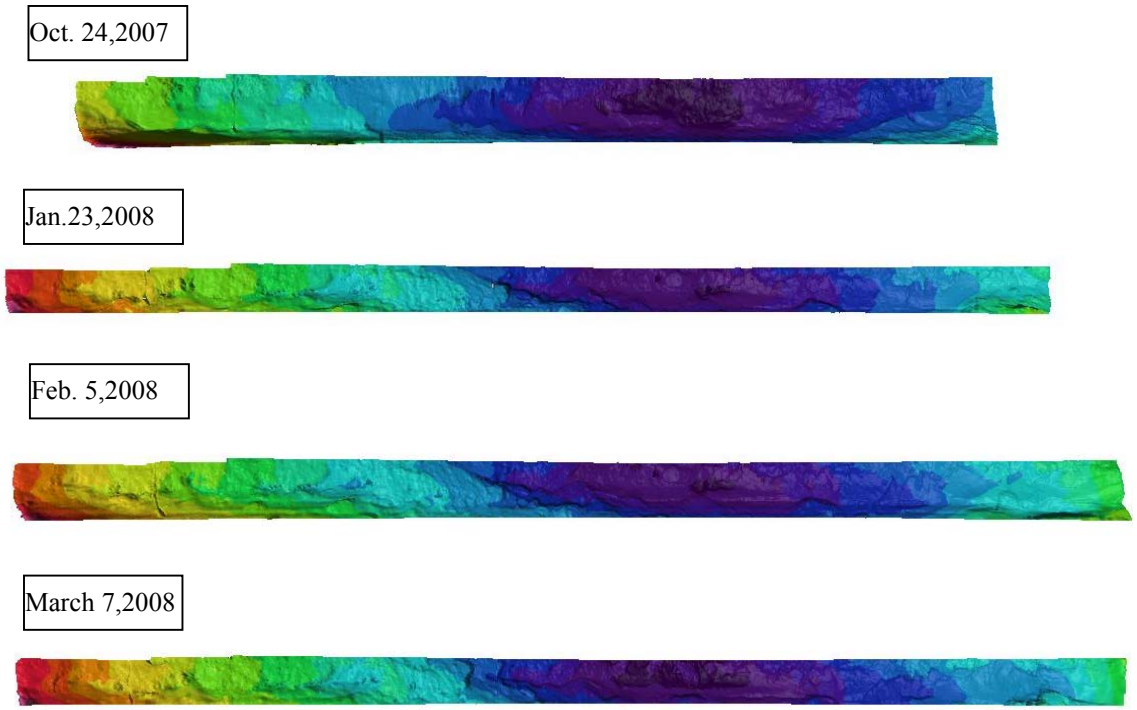

Figure G-5 Bank surface images in the second measurement period, generated using laser scanner. Depending on the distance of the point on the surface from laser scanner, the dark blue colour represents the farthest and red colour the nearest point

G-3.2 Timing of bank failure

The timing of riverbank failure in respect to the water stage has been studied using a remotely controlled camera. As it is seen from the following figures cantilever failure has occurred during water rise in the river while no failure has occurred during water drop on 25 January 2007.

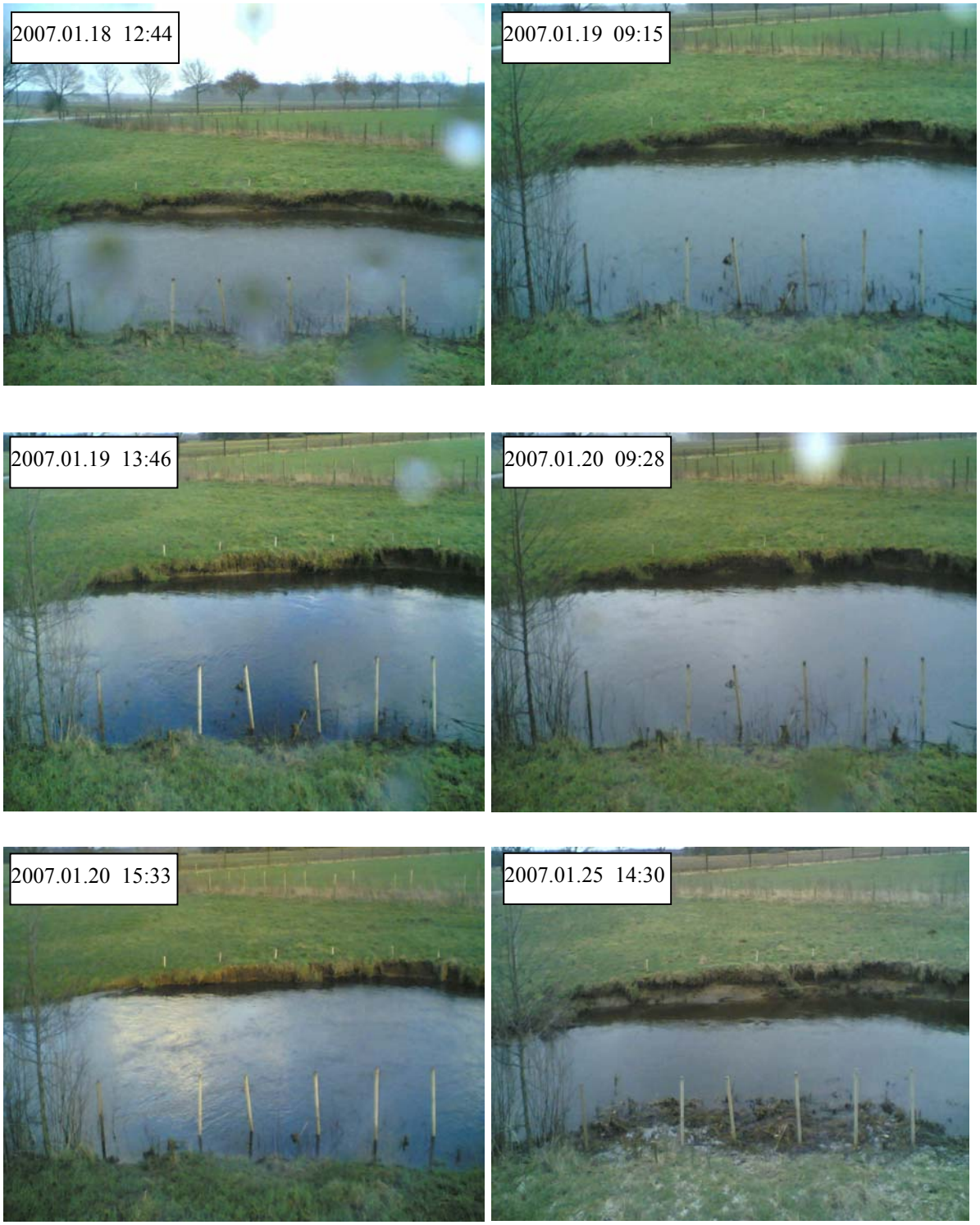

Figure G-6 Timing of bank failure at Hardebek-Brokenlander Au, captured using remotely controlled camera

H Further simulation results

H-1 Sediment transport

A qualitative investigation on the application of three different formulation of equilibrium total sediment transported (Ackers and White, van Rijn and Brownlie) has been achieved, which are presented in the following. For this purpose, a steady state sediment transport simulation with active bed (bed erosion and deposition) using Smagorinsky turbulence model and following conditions have been accomplished for the above-mentioned three formulations.

Table H-1 Simulation parameters

Time step	
Number of steady state time steps	5
Time interval (min)	5 (last time step 10)
Flow	
Discharge (m^3 /s)	1.057
Downstream water elevation (mAMSL)	12.39
Turbulence model	Smagorinsky
Sediment transport	
Initial condition (mg/l)	120
Boundary condition (mg/l)	200 mg/l
Damping coefficient of erosion/deposition	500

H-1.1 Method of van Rijn

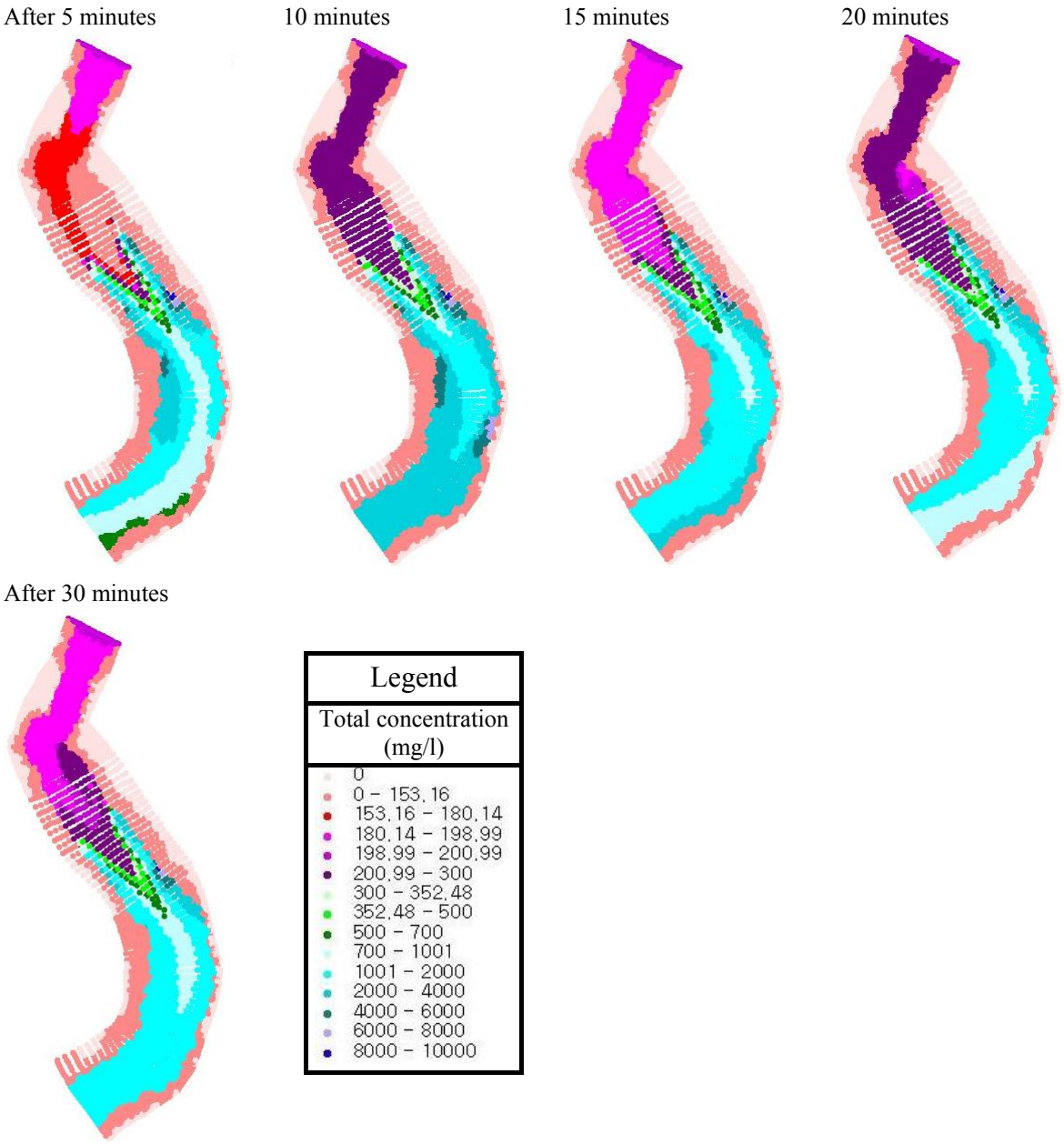

Figure H-1 Spatial distribution of total sediment concentration using van Rijn method

H-1.2 Method of Ackers and White

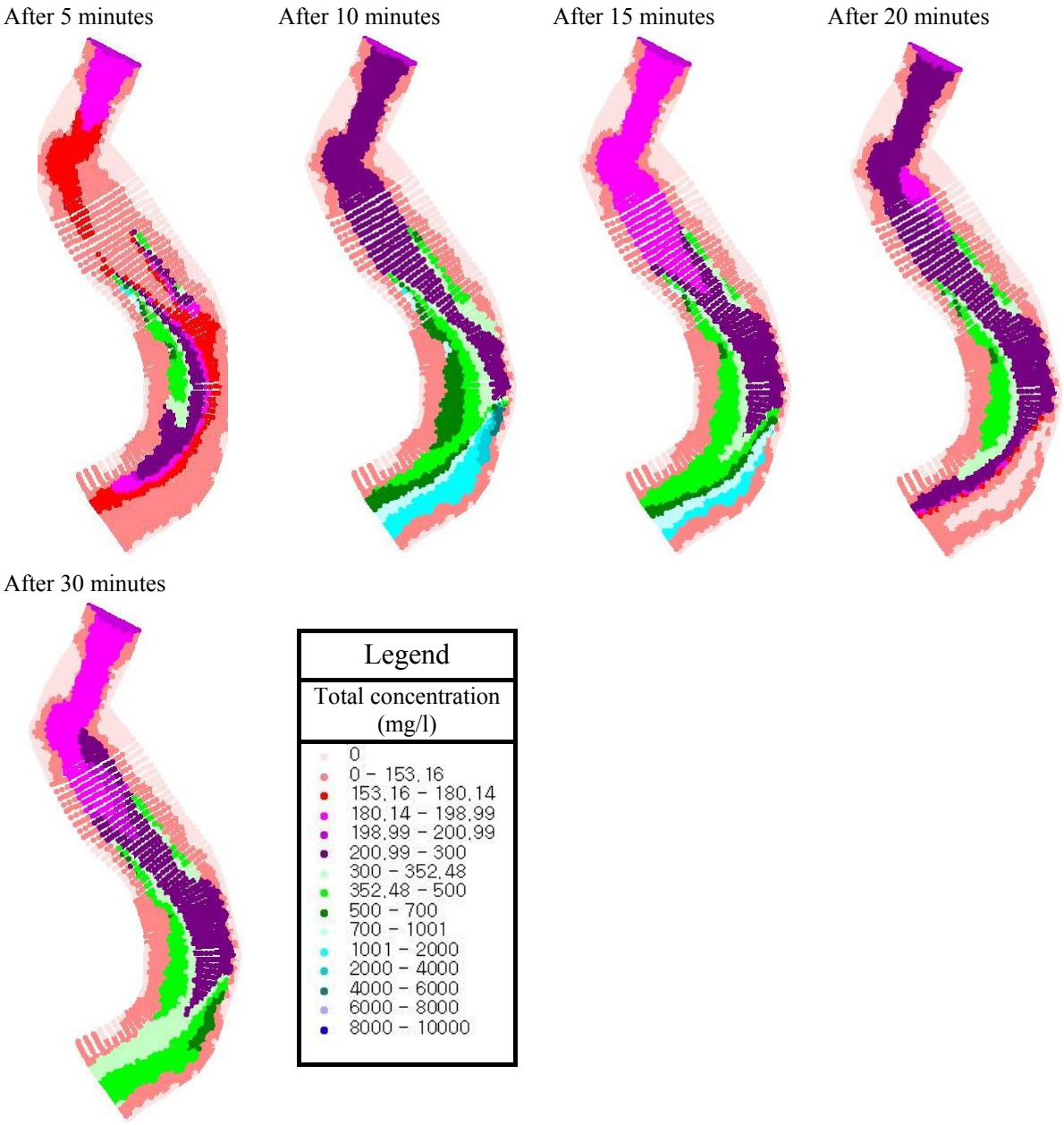

Figure H-2 Spatial distribution of total sediment concentration using Ackers-White method

H-1.3 Method of Brownlie

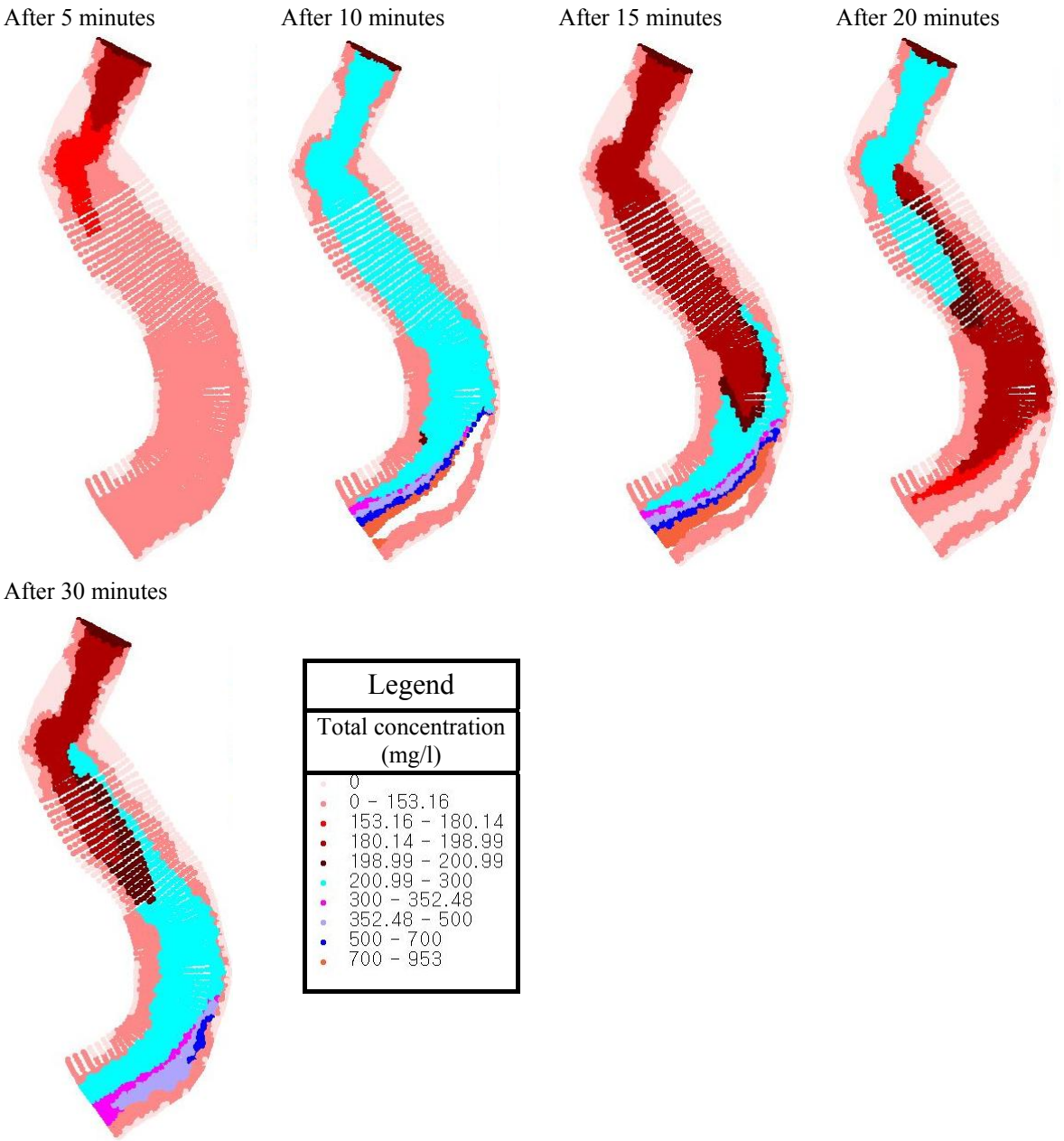

Figure H-3 Spatial distribution of total sediment concentration using Brownlie method

I Structural diagram of bank erosion algorithm

I-1 Shear Slip failure

Shear slip failure is the failure type occurring in compacted non-cohesive soils such as sandy soils. It has been found that failure surface is almost entirely confined in submerged zone. The failure slope (φ^c) has been assumed to be representable by a raised angle of repose due to the effect of compaction and cementation. The failure is assumed to occur when the slope (of a portion) of the bank exceeds the failure slope. The over-steepened area slides towards the bank-toe, which has been simulated by a cascade of sliding the over-steepened area of the elements towards the next lower element. This process causes generation of discontinuity in bank profile in form of undercutting below water stage and overhang above water stage. The slip failure algorithm and generation of such discontinuities have been demonstrated in the following figure.

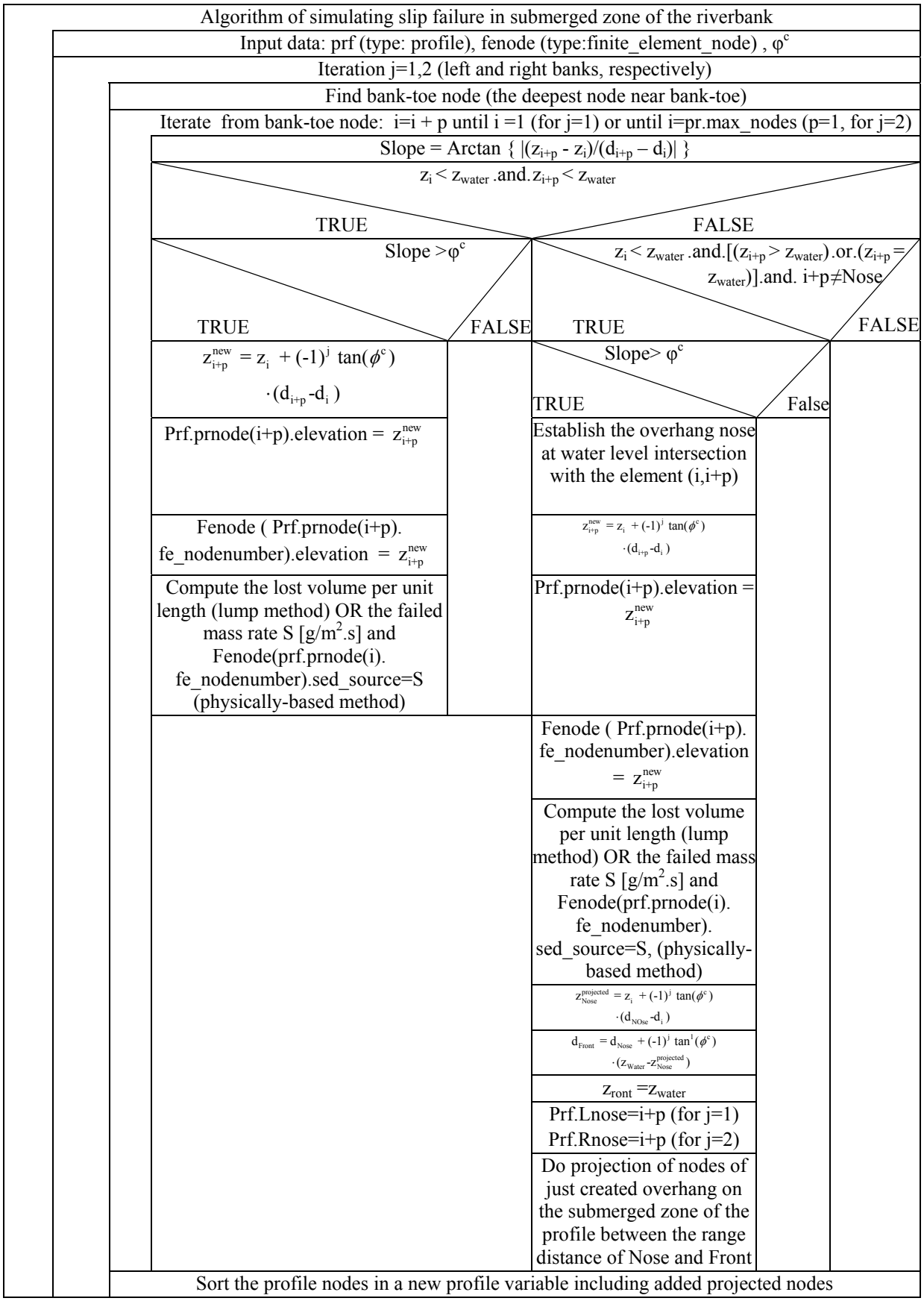

Figure I-1 Structure diagram of slip failure algorithm for profiles without an already existing overhang

I-2 Tensile cantilever failure

It is assumed that cantilever failure in form of tensile failure occurs immediately by submergence of a portion of the overhang due to the rise of water in the river. This causes to shift the undercutting front to a new position in the same elevation as the new water elevation. The lateral distance (d) of the new front of undercutting is computed using extrapolation between old and new front.

The failed area of the overhang zone is bounded to the overhang face from right (in case of left bank und vice versa for right bank), water elevation from top and lower edge of the overhang from bottom. From left side (in case of left bank) it is bounded to the new bank profile between old and new profile. This portion of the bank will be later updated using the elevation of their conjugated nodes in FE-domain. Since in this domain overhang is not existing, all submerged nodes can be subject to elevation change, including those in submerged zone of the overhang in profile domain.

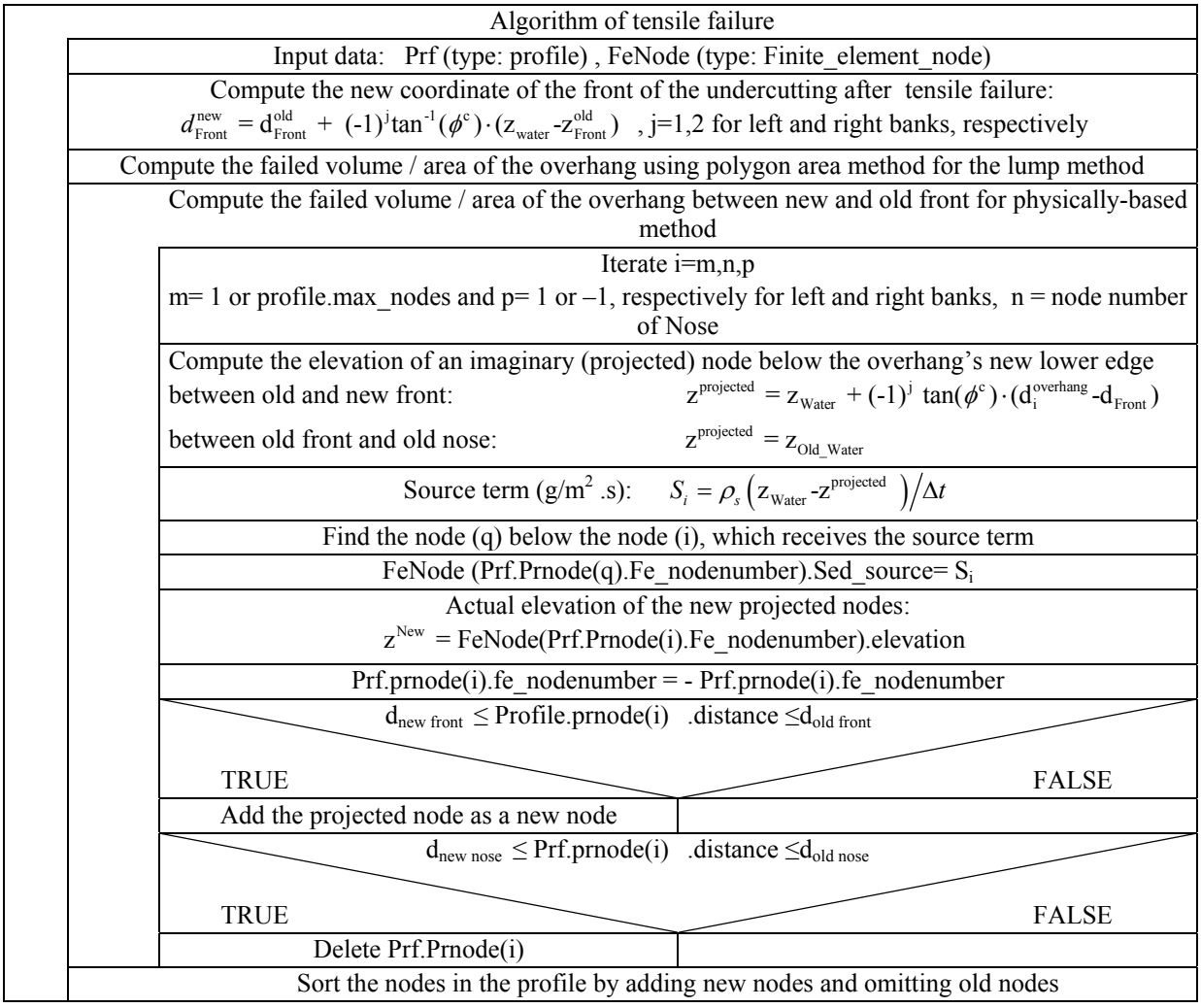

Figure I-2 Structure diagram of tensile failure algorithm

I-3 Shear cantilever failure

Cantilever failure in form of shear failure is the major form of overhang failure. It is assumed that the failure plane can be approximated with a raised angle of repose due to sediment compaction as well as matric suction. The failure occurs, when the component of active force (weight of the overhang) along the mentioned failure plane exceeds the passive forces (cohesion due matric suction as well as vegetation root).

Algorithm of shear failure	
Input data: : prf (type: profile), fenode (type:finite_element_node) , φ^u	
Iteration j=1,2 (left and right banks, respectively)	
Find the intersect of slope failure, which starts from "Front", with overhang profile	
Compute the area (A_f)of overhang being probably failed using polygon area method	
Active force per unit length:	$F_w=\rho_s.g.A_f$
Matric force per unit length:	$\psi = \rho_s \cdot g \cdot \int_{z_{front}}^{z_{int\_sect}} \left[a \cdot \left(z - z_{water}\right)^3 + b \cdot \left(z - z_{water}\right)^2 + c \cdot \left(z - z_{water}\right) \right] dz$
Cohesion force due to vegetation roots per unit length	$c_r = 1.2 T_r \frac{A_r}{A}$
$SF = \frac{c_r L_{eff.} + \psi \cdot \tan\left(\varphi^b\right) + F_w \cdot \tan\left(\varphi\right) \cdot \cos\left(\varphi^u\right)}{F_w \cdot \sin\left(\varphi^u\right)}$	
Sort the nodes into a new profile and omit Nose and Front, needs to be completed	

Figure I-3 Structure diagram of shear failure algorithm

J On the theoretical distribution of radial flow in bends

As demonstrated by Engelund (1974), Yalin (1992), etc., in a natural river, theoretical distribution of radial flow velocity can deviate substantially from that corresponding to a fully developed circular flow. There are three reasons for these deviations.

The first is that in a natural stream, in contrast to the case of circular channel, the curvature varies in downstream direction. Cross circulation thus goes through a process of growth as the meander bend is approached, and decay as the flow processes downstream of the bend. As pointed out by Chang (1988) in the process of growth and decay, the radial velocity due to cross circulation in a natural stream is always less than that corresponding to a fully developed circular flow.

The second reason for the aforementioned deviation is that the variation of channel curvature makes the flow to shift (in all its thickness) periodically left and right as it moves along the streamwise direction (Fig. J-1). This shifting is associated with a radial velocity profile, which can be either positive or negative throughout the flow depth as in Fig. (J-1c). In reality, the natural meandering flow is the result of the superimposition of cross circulatory motions on a convective base (Yalin, 1992), consequently the radial velocity profiles are the sum of a pure cross circulatory profile (as in Fig. J-1b) and a positive or negative profile of the type shown in Fig. (J-1c). This sum (Fig. J-1a) clearly yields vertical distributions of radial flow velocity diverging substantially from pure cross-circulatory flows.

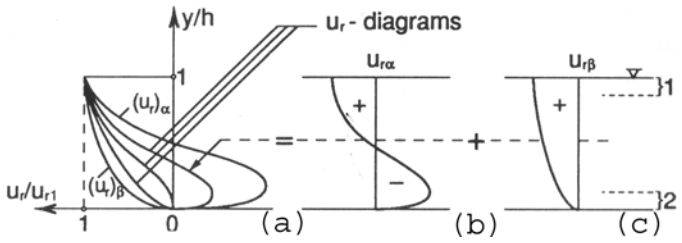

Figure J-1 Cross circulation profiles (from Yalin, 1992). A) radial velocity profile, b) pure cross circulatory profile, c) laterally oscillating flow.

Finally, the third reason is that the shape of vertical distribution of radial flow velocity depends on bed geometry, as clearly demonstrated by the measurement of Bridge (1977) and

Jackson (1976). In regions, where the flow is topographically steered away from the bars, the vertical distribution of radial velocity is entirely of the types shown in Fig. (J-1c).